T2R2 東京科学大学 リサーチリポジトリ
Science Tokyo Research Repository

# 論文 / 著書情報
# Article / Book Information

| | |
|---|---|
| 題目(和文) | 中央海嶺玄武岩を生じた母マントルの化学組成と温度の経年変化 |
| Title(English) | The secular variation of the composition and temperature of MORB-source mantle |
| 著者(和文) | 小宮剛 |
| Author(English) | Tsuyoshi Komiya |
| 出典(和文) | 学位:理学博士,<br>学位授与機関:東京工業大学,<br>報告番号:甲第3982号,<br>授与年月日:1999年3月26日,<br>学位の種別:課程博士,<br>審査員: |
| Citation(English) | Degree:Doctor of Science,<br>Conferring organization: Tokyo Institute of Technology,<br>Report number:甲第3982号,<br>Conferred date:1999/3/26,<br>Degree Type:Course doctor,<br>Examiner: |
| 学位種別(和文) | 博士論文 |
| Type(English) | Doctoral Thesis |

Powered by T2R2 (Science Tokyo Research Repository)

# The secular variation of the composition and temperature of MORB-source mantle

**by**

Tsuyoshi Komiya

**Doctor Thesis**

**Department of Applied Physics, Faculty of Science**
**Tokyo Institute of Technology**

**2-12-1, Ookayama Meguro-ku 152-8551, Tokyo JAPAN**

**e-mail: tkomiya@geo.titech.ac.jp**
**fax: +81-3-5734-3538**

**March in 1999**

# ABSTRACT

The Archean-Proterozoic boundary has been arbitrarily defined at 2500 Ma by the IUGS Subcommission on Precambrian Stratigraphy (SPS) (Plumb and James 1986). However, recent extensive dating of Precambrian terrains reveals that the evolution from "Archean-type" to "Proterozoic-type" tectonics was entirely transitional, and spanned more than 500 My. These results fueled the controversy about the driving force behind the evolution from Archean tectonics to Proterozoic tectonics (Breuer & Spohn, 1995). This paper presents the geology of five differently aged greenstone belts, together with the field occurrence and geochemistry of the greenstones. Our detailed mapping allows us to classify the greenstones in each belt and to estimate their tectonic setting based on comparison with modern accretionary complexes (Isozaki et al. 1990). In brief, our suggestion of the tectonic setting of the basalt volcanism is based on the relationships with chert layers. Namely, the greenstones are overlain by thick bedded cherts, suggesting eruption of the mid-ocean ridge basalt (MORB), while those conformably alternate with thin bedded chert or intruding thick bedded chert, suggesting formation as ocean island basalt (OIB). We have mapped the following areas: the 3.8 Ga Isua supracrustal belt (ISB), southern West Greenland; the 3.5 Ga North Pole area (NP), east Pilbara; the 3.3 Ga Cleaverville area (CLB), north Pilbara; the 2.5 Ga Beasley River area (BR), the Hamersley Group, south Pilbara; and the 1.6 Ga Glengarry Basin (KLR) in the north Yilgarn. Comparison of the composition of the least altered MORB-type samples from each area indicates the compositional and thermal secular change of upper mantle.

1: 5,000 scale mapping of the 3.8 Ga Isua supracrustal belt, the 3.5 Ga North Pole area, and the 3.3 Ga Cleaverville area shows that duplex structure composed of several horses is widespread in each. The duplexes vary in size from a few meters to several kilometers. 1: 100 scale sketches in each horse were made to remove the thrust and fold geometry, and to reconstruct the original lithostratigraphies. The reconstructed lithostratigraphies of each horse reveal a simple pattern, in ascending order from greenstone with low-K tholeiitic composition to chert/BIF. Turbidite layers cover the thick cherts in places. The cherts and the underlying low-K tholeiites nowhere contain continent- or arc-derived material. The lithostratigraphy is quite similar to Phanerozoic "oceanic plate stratigraphy," except for the poor-development and composition of the turbidites. The evidence of duplexes and "oceanic plate stratigraphy" indicates that these greenstone belts were formed as accretionary complexes. The dominantly mafic turbidite composition suggests that the accretionary complexes were formed in an intra-oceanic environment comparable to the present-day western Pacific Ocean. Two types of greenstones occur in the Isua supracrustal belt. Pillow and massive lavas are conformably overlain by thick, bedded chert layers, which are finally covered by turbidite, implying the existence of MORB. Basaltic dikes are intruded into thick chert layers, while picritic lavas are interleaved with felsic volcaniclastic sediments, implying an OIB origin (Komiya et al. 1999).

Two modes of occurrences of greenstones are present in the North Pole area; greenstones overlain by thick, bedded chert (MORB) and those conformably alternating with thin, bedded chert (OIB) (Maruyama et al. 1991). The occurrence of greenstone overlain by the thick, bedded chert in the Cleaverville area suggests an origin as MORB (Ohta et al. 1996).

Geological mapping on a 1: 5,000 scale was similarly undertaken in the Beasley River area of the Hamersley Group, and in the Kilara and Peak Hill areas of the Glengarry Basin. The former is divisible into six subunits based on lithologies: the Lower lava flow, the Lower BIF, the Middle BIF, the Komatiitic, the Rhyolite, the Upper BIF, and the Uppermost sedimentary Unit in ascending order. In the Lower lava flow Unit, no shales or terrigenous sediments are interleaved with pillow/massive lava flows, and neither lava flows nor hyaloclastite contain detrital materials, while at the top of the Lower BIF Unit, and in the Upper sedimentary Unit, there are shales, sandstones, and even conglomerates. Despite the fact that the lithostratigraphy is similar to an "oceanic plate stratigraphy," the absence of thrusts, which defines a duplex structure, does not support an origin as an accretionary complex, but as a sedimentary basin in a closing rift valley. Pillow/massive lavas in the Lower lava flow Unit were derived from mid-ocean ridge volcanism in a mature rifting system equivalent to the Red Sea in the Phanerozoic, because there are neither terrigenous materials nor vesicles in pillow/massive lavas. Despite the poor exposure, the geology of the Kilara/Peak Hill area appears to be the same as that of the Beasley River area, implying the greenstone were produced by mid-ocean ridge volcanism in a mature rift system (Pirajno et al. 1995, 1996).

861 greenstone samples, defined as the least-altered from the field and microscopic observations, were selected from ca. 6,000 samples for major, trace analyses. Moreover, rare earth elements (REE) were also analyzed on some of them. The greenstones in each area are defined as low-K tholeiitic basalt and basaltic andesite, and they are distinctly enriched in FeO* at a given MgO content, compared with modern MORB. Liquid lines of descent indicate the fractional crystallization of olivine (ol) followed by plagioclase (pl) and then clinopyroxene (cpx) for MORBs in ISB, NP, CLB, and KLR, or by cpx and then pl for those in BR, suggesting a higher degree of melting. MORBs in ISB, and NP are characterized by light REE-depleted patterns, whereas those in CLB, or BR and KLR are flat- or slightly light REE-enriched, respectively. While REE patterns of OIBs in ISB and OIB are flat- or slightly LREE-enriched.

Microprobe analyses of relict clinopyroxenes within OIB and MORB samples in NP show that the composition of both clinopyroxenes is similar to those in modern MORB. However, obvious compositional differences exist between cpx in MORBs and in OIBs in the NP. The cpx of OIBs are enriched in $Na_2O$, CaO, and $TiO_2$, but depleted in $Al_2O_3$ at a given $SiO_2$ relative to those of MORB. The relationships are similar to those between modern alkali basalt of OIB and modern MORB. Moreover, the calculated partition coefficients of $TiO_2$, $Al_2O_3$, $Na_2O$, and the MgO/FeO ratio between cpx, and whole rock range within the variations of experimental data, suggest that secondary alteration was insignificant.

FeO content and potential temperature of source mantles were estimated by comparison of the most primitive MORB in each area with recent melting experimental compilations (Hirose & Kushiro, 1993, Baker & Stolper, 1994; Kushiro, 1996). The results indicate that the mantle source of the ancient MORBs were highly enriched in FeO, and contain 10 wt % in FeO (c.f. 85-87 in $Mg^{\#}$), but that the compositional change appears not to be monotonous (Fig. 1). Moreover, the potential mantle temperature of each ancient MORB is also higher than that of modern MORB, and estimated to be ca. 1480 ˚C, but it also appears not to decrease monotonously through time (Fig. 1). Multiple saturation experiments indicate that the primitive MORBs in NP, which contains 15.2 or 11.9 wt % in MgO, are equilibrated with olivine+orthopyroxene+clinopyroxene at 15 kb and 1350 ˚C or at ca. 14 kb and ca. 1330 ˚C, respectively. These results support the potential mantle temperature estimated by the above method. The fluctuation implies the continual infilling of lower mantle material into upper mantle.

This ultra-high-pressure experiment implies new idea that some of $Fe^{2+}$ ions transformed into $Fe+Fe^{3+}$ during slab penetration into lower mantle because aluminous Mg-perovskite contains $Al^{3+}Fe^{3+}$ instead of $Mg^{2+}Si^{4+}$. The depletion of FeO content depends on $Al_2O_3$ content. Therefore, the subsidence of oceanic crust, which contains more FeO and $Al_2O_3$ relative to the underlying mantle, into lower mantle removes much amount of Fe from the slab as metallic iron. The segregated metallic iron may subside on the metallic core or float in the lower mantle. The physicochemical difference between siderophile and lithophile elements decreases at ultra-high pressure condition (Righter et al. 1997; Walter 1997). Therefore, segregation of metallic iron does not necessarily involve the depletion of siderophile elements except for some elements (e.g. P). Assuming that the production rate of metallic iron is equivalent to that of $Fe^{3+}$ in the formation of Mg-perovskite, it takes 3.1 and 5.0 billion years for the whole mantle to decrease from 10 to 8 wt % in FeO and from 29 to 21 ppm in $P_2O_5$ at the production rate of MORB in Archean.

# Contents

**THE SECULAR VARIATION OF THE COMPOSITION AND TEMPERATURE OF MORB-SOURCE MANTLE ..... 1**

**ABSTRACT ..... 2**

**CONTENTS ..... 5**

**I. PLATE TECTONICS AT 3.8 - 3.7 GA; ..... 9**

ABSTRACT ..... 10
I-1 INTRODUCTION ..... 11
I-2 GEOLOGICAL OUTLINE ..... 12
I-3 BARROVIAN-TYPE PROGRESSIVE REGIONAL METAMORPHISM ..... 14
I-4 GEOLOGY OF THE NORTHEASTERN PART OF THE ISUA SUPRACRUSTAL BELT ..... 14
I-5 GEOLOGY OF THE SOUTHERN UNIT ..... 16
I-6 RECONSTRUCTION OF LITHOSTRATIGRAPHY WITHIN A HORSE IN THE SOUTHERN UNIT ..... 16
I-7 COMPARISON OF LITHOSTRATIGRAPHY OF THE ISUA BELT WITH OCEANIC PLATE STRATIGRAPHY ..... 21
I-8 TRAVEL HISTORY OF EARLY ARCHEAN OCEANIC LITHOSPHERE IN THE ISUA BELT ..... 22
I-9 DISCUSSION ..... 24
I-10 CONCLUSIONS ..... 29
REFERENCES ..... 30
FIGURE CAPTIONS ..... 34
PHOTO CAPTIONS ..... 37

**II. GEOLOGY OF THE BEASLEY RIVER AREA AND GEOCHEMISTRY OF GREENSTONES, THE HAMERSLEY GROUP (2.5 GA), WESTERN AUSTRALIA ..... 39**

II-1 INTRODUCTION ..... 40
II-2 GEOLOGICAL OUTLINE ..... 40
II-3 GEOLOGY OF THE BEASLEY RIVER AREA, HAMERSLEY ..... 42
*II-3.1 Stratigraphic subdivisions ..... 42*
*II-3.2 Discussion on the geology of the Beasley River Area, Hamersley ..... 45*
II-4. CHEMISTRY ..... 47
*II-4.1. Sample preparation ..... 47*
*II-4.2. Analytical methods ..... 48*
*II-4.3. Major and trace element chemistry in basalts and komatiites ..... 48*
*II-4.4 Discussion on the geochemistry of the High Ti group in the pillow lava unit ..... 49*
II-5 CONCLUSIONS ..... 52
REFERENCES ..... 53

FIGURE CAPTIONS ..... 55

**III. GEOCHEMISTRY OF 3.8 GA MORB AND OIB FROM THE ISUA SUPRACRUSTAL BELT, WEST GREENLAND; IMPLICATION FOR MANTLE HETEROGENEITY OF THE MANTLE IN THE EARLY ARCHEAN ..... 57**

III-1. INTRODUCTION ..... 58
*III-1.1. Mantle heterogeneities of the modern mantle ..... 58*
*III-1.2. The early Earth differentiation recorded in the Archean rocks ..... 59*
*III-1.3. The tectonic setting of the Archean mafic/ultramafic rocks ..... 61*
III-2. GEOLOGICAL OUTLINE ..... 62
*III-2.1. Overview ..... 63*
*III-2.2. Field occurrences of pillow lava, and mafic dikes ..... 63*
III-3. CHEMISTRY ..... 64
*III-3.1. Sample preparation ..... 65*
*III-3.2. Analytical methods ..... 65*
*III-3.3. Petrography ..... 65*
III-4. RESULTS ..... 66
*III-4.1 Major and trace element chemistry in IMORBs and IOIBs ..... 66*
III-5. DISCUSSIONS ..... 67
*III-5.1. Estimate of FeO content of and pressure and temperature of partial melting of the source mantle of the IMORBs ..... 67*
*III-5.2. Origin of OIBs ..... 72*
*III-5.3. Mantle heterogeneities in the Early Archean ..... 73*
*III-5.4. Origin of mantle heterogeneity ..... 73*
III-6 CONCLUSIONS ..... 77
REFERENCES ..... 78
FIGURE CAPTIONS ..... 87

**IV. GEOCHEMISTRY OF 3.5 GA MORB AND OIB FROM THE NORTH POLE AREA, EAST PILBARA; IMPLICATION FOR MANTLE HETEROGENEITY OF THE MANTLE IN THE MIDDLE ARCHEAN ..... 89**

IV-1 INTRODUCTION ..... 90
IV-2 GEOLOGICAL OUTLINE ..... 90
*IV-2.1 Geology of the Pilbara craton ..... 90*
*IV-2.2 Geology of the North Pole area ..... 93*
IV-3 CHEMISTRY ..... 96
*IV-3.1. Sample preparation ..... 96*
*IV-3.2. Analytical methods ..... 97*
*IV-3.3. Petrography ..... 97*
IV-4 RESULTS ..... 100

*IV-4.1 Major and minor element chemistry of relict pyroxene crystals in NPMORBs and NPOIBs..... 100*
*IV-4.2 Major and trace element chemistry in NPMORBs and NPOIBs..... 100*
IV-5 DISCUSSIONS ..... 101
*IV-5.1 The estimate of the influence of secondary alteration on whole rock chemistry based on clinopyroxene composition..... 102*
*IV-5.2 The differences of composition of clinopyroxenes in NPMORBs and NPOIBs..... 102*
*IV-5.3 Estimate of FeO content of and pressure and temperature of partial melting of the source mantle of the NPMORBs..... 104*
*IV-5.4 Origin of OIBs..... 106*
*IV-5.5 Mantle heterogeneities in the Early Archean..... 107*
*IV-5.6 Origin of mantle heterogeneity..... 107*
IV-6 CONCLUSIONS ..... 109
REFERENCES ..... 110
FIGURE CAPTIONS ..... 115

**V. MELTING RELATIONS OF ARCHEAN MID-OCEAN RIDGE BASALTS: IMPLICATION FOR THERMAL EVOLUTION OF MORB SOURCE MANTLE ..... 118**

V-1 INTRODUCTION ..... 119
V-2 STARTING MATERIALS..... 120
*V-2.1 Estimate of original composition of NPMORBs..... 120*
*V-2.2 Water content in NPMORBs..... 121*
*V-2.3 Ferric to Ferrous ratio at the formation of NPMORBs..... 122*
*V-2.4 Composition of starting materials..... 122*
V-3 EXPERIMENTS ..... 123
*V-3.1 Experimental methods..... 123*
*V-3.2 Experimental results..... 123*
V-4 DISCUSSION ..... 124
*V-4.1 Interpretation of the temperature and pressure estimated by multiple saturation experiments..... 124*
*V-4.2 Estimate of potential temperature of the NPMORBs..... 125*
*V-4.3 Thermal condition of the Middle Archean mantle..... 126*
V-5 CONCLUSIONS..... 129
REFERENCES ..... 130
FIGURE CAPTIONS ..... 134

**VI. THE COMPOSITIONAL AND THERMAL EVOLUTION OF THE MORB-SOURCE MANTLE THROUGH TIME ..... 135**

VI-1 INTRODUCTION ..... 136
VI-2 EXPERIMENTS..... 137
*VI-2.1 Starting materials..... 137*
*VI-2.2 Experimental methods..... 137*

*VI-2.3 Experimental Results* ..... *138*
VI-3 GEOLOGY OF OTHER AREAS AND GEOCHEMISTRY OF GREENSTONES IN THE AREAS ..... 139
*VI-3.1 The potential temperature and Mg# of the source mantle of mid-ocean ridge basalts (MORBs) in Early Proterozoic, the Killara area, Western Australia* ..... *139*
*VI-3.2 The potential temperature of the source mantle of Al-depleted ultramafic komatiites in the Middle Archean, the Barberton Greenstone Belt, South Africa* ..... *141*
VI-4 DISCUSSIONS ..... 149
*VI-4.1 The secular change of the potential temperature of the MORB source mantle* ..... *149*
*VI-4.2 The secular change of composition of the MORB source mantle* ..... *153*
VI-5 CONCLUSIONS ..... 157
ACKNOWLEDGEMENT ..... 158
REFERENCES ..... 159
FIGURE CAPTIONS ..... 163
**ACKNOWLEDGEMENTS** ..... **171**

# I. Plate Tectonics at 3.8 - 3.7 Ga; Field Evidence from the Isua Accretionary Complex, southern West Greenland

*Tsuyoshi Komiya*,

Department of Earth and Planetary Sciences, Tokyo Institute of Technology, Tokyo 152-8551, Japan

*fax: +81-3-5734-3538* *e-mail: tkomiya@geo.titech.ac.jp*

## ABSTRACT

1:5,000 scale mapping was performed in part of the ca. 3.8 Ga Isua supracrustal belt, Isukasia area, southern West Greenland. The mapped area is divided into three units bounded by low-angle thrusts: northern, middle, and southern units. The southern unit, the best exposed, is made up of fourteen subunits (horses) with similar lithostratigraphy, bound by layer-parallel thrusts. Duplex structures are widespread in the Isua belt, and vary in size from a few meters to kilometers in scale. Duplexing proceeded from south to north, and is well-documented in the relationship between link- and roof-thrusts. The reconstructed lithostratigraphy of each horse reveals a simple pattern, which consists of greenstone with low-K tholeiitic composition, chert/BIF and turbidite in ascending order. The cherts and underlying low-K tholeiites do not contain continent- or arc-derived material. The lithostratigraphy is quite similar to Phanerozoic “oceanic plate stratigraphy”, except for the abundance of mafic material in the turbidite. The evidence of duplex structures and “oceanic plate stratigraphy” indicates that the Isua supracrustal belt is the oldest accretionary complex in the world. The dominantly mafic turbidite composition suggests that the accretionary complex was formed in an intra-oceanic environment comparable to the present-day western Pacific Ocean. The recognition of the accretionary nature of the Isua supracrustal belt supports the idea that the modern style of plate tectonics was in operation only 0.7-0.8 Gy after the formation of the Earth. The duplex polarity suggests to us that an older accretionary complex should occur to the south of the Isua accretionary complex.

## I-1 Introduction

The *ca.* 3.7 Ga Amîtsoq gneisses, with enclaves of Isua supracrustal belt at Isukasia, have long been recognized as the oldest rocks on the Earth (Moorbath et al. 1977; Nutman et al. 1993, 1996, 1997). Recently, the development of the SHRIMP method to derive protolith ages has contributed to the discovery of much older terranes. For example the Acasta gneisses in the Slave province, Northwest Territories of Canada yielded single zircon ages of 3.96 Ga (Bowring et al. 1989), 3.93 Ga granulite from Mount Sones, Enderby Land in Antarctica (Black et al. 1986), 3.85 Ga detrital zircons from metasedimentary rocks from China (Liu et al. 1992), and 4.3 Ga detrital zircons from the Narryer Complex in Yilgarn Craton, Western Australia (Froude et al. 1983). Despite these findings of much older sporadic terrains or detrital mineral grains, the 3.8 Ga Isua supracrustal rocks are still significant in so far as they retain magmatic primary features such as pillow structures (Allaart 1976; Maruyama et al. 1991, 1994) and original sedimentary structures such as rhythmic banding in BIF or graded bedding in turbidites (Nutman et al. 1984). The Isua supracrustal belt is one of the oldest terrains in the world, thus presenting a key to the understanding of tectonic processes on the early Earth.

Immediately after the establishment of the new global tectonic Paradigm the question arose as to when the modern style of plate tectonics started on the Earth (Dewey and Spall 1975). There are two opposing schools of thought. Firstly, the plate tectonic regime began at the earliest stage of the evolving earth as suggested by the geochemistry of greenstones (Condie 1972, 1982; Hart et al. 1970), geophysical considerations (Bickle 1978; Nisbet and Fowler 1983; Arndt 1983) and the geological similarities with Phanerozoic orogenic belts (Burke et al. 1976). The other school suggests that the tectonic regime until the late Proterozoic was typified by vertical movement-dominated orogenies, called the ‘millipede model’ (Wynne-Edwards 1976), or ensialic vertical tectonics (Kröner 1977, 1981; Piper 1982). The latter school listed the following features disfavoring the concept of plate tectonics in the Archean: absence of (1) ophiolites, (2) either Franciscan-type mélange or accretionary complex, and (3) blueschists, all of which characterize divergent or consuming plate boundary processes on the modern Earth. Recently, geological evidence for plate tectonics and accretion of oceanic crusts have been reported in some Archean terrains (Kusky, 1989; Hoffman 1991; Calvert et al. 1995), but some are still controversial (Bickle et al. 1994; Kusky and Winsky 1995). Here we report (1) and (2) within the Isua supracrustal belt, propose criteria for accretion of oceanic materials to continental lithosphere and discuss the features of the accretionary complex in the Isua region compared with those in the western Pacific region, especially the Japanese islands. In this paper we will use the technical terms of horse, duplex, duplexing, and roof-, floor- and link-thrust defined by McClay (1992).

## I-2 Geological Outline

The Isua supracrustal belt lies approximately 150 km northeast of Nuuk, Greenland (Fig. 1). It is part of the Akulleq terrane, which is composed of 3880-3660 Ma Amîtsoq gneiss, 2820 Ma Ikkattoq gneiss which contains some enclaves of supracrustal rocks and anorthosites (Friend et al. 1987; Nutman et al. 1989; McGregor 1993). The Akulleq terrane was intruded by the K-rich Qôrqut post-orogenic granite at about 2550 Ma, and stabilized at that time (Baadsgaard 1976; Brown et al. 1981; Moorbath et al. 1981; McGregor 1993). More recently, Friend et al. (1987) and McGregor et al. (1991) have proposed a tectonic model for the Akulleq terrane based on modern plate tectonic concepts of collision-accretion (Coney et al. 1980). The northern 3230-2980 Ma Akia, the southern 2920-2830 Ma Tasiusarsuaq, with the Akulleq terrane in-between, collided at 2820-2712 Ma. Most areas in the southwestern part of Greenland are underlain by poly-deformed amphibolite to granulite facies rocks (McGregor 1993). The northeastern part of the Akulleq terrane is an exception where a relatively less metamorphosed segment, the Isua supracrustal belt, is exposed (Fig. 1 inset). The Isua belt is, at present, exposed as a fault-bounded tectonic slice, and is in tectonic contact with the tonalitic Amîtsoq orthogneiss on both sides (McGregor 1973; Bridgwater et al. 1974).

The Isua supracrustal belt forms a 35 km-long arcuate tract and is the largest fragment of Early Archean supracrustal rock in the Akulleq terrane (Fig. 1, inset). Further to the south, Early Archean supracrustal rocks equivalent to the Isua supracrustal rocks are exposed as enclaves in the Amîtsoq gneiss. This suggests that the Isua belt was originally intruded by tonalitic rocks, which were later metamorphosed to form the Amîtsoq gneiss. The Isua supracrustal belt was affected by Barrovian-type amphibolite facies metamorphism during Archean times (Boak and Dymek 1982). In spite of metamorphism, metasomatism (Rosing et al. 1996) and polyphase ductile deformation, the original structures of the protoliths are well preserved in the northeastern part of the belt where the metamorphic grade is the lowest. The Isua belt is an exception displaying well-preserved primary structures that yield information helpful in deciphering the history of pre-3.8 Ga events on the Earth. Therefore, considerable detailed interdisciplinary work has been conducted in this district (e.g. see recent summary by Nutman 1986; Schidlowski 1988; Nutman et al. 1993, 1996, 1997; Mojzsis et al. 1996).

The authors spent two field seasons in the Isua supracrustal belt in 1990 and 1993, and completed a geologic map covering the easternmost part of the belt at a scale of 1:5,000. During our field investigations, the rock units were mapped according to their pre-metamorphic state (Maruyama et al. 1991, 1994; Komiya and Maruyama 1995). Therefore, we used the names doleritic dike, pillowed basalt, carbonate, and conglomerate, instead of homogeneous amphibolite, Garbenschiefer, calc-silicate rocks, etc. We distinguished the following five major lithologic units: (1) mafic-felsic turbidite sequence, including interlayered minor conglomerate (Photo 1,2), (2) chert and banded iron-formation (hereafter BIF) (Photo 3), (3) pillow lava, massive lava, pillow breccia, and hyaloclastite as described below (Photo 4), (4) dolerite-gabbro intrusives related to (3) (Photo 5), and (5) ultramafic

rocks (Photo 6). In addition, a large number of sills and dikes were encountered. Some are mid-Archean Ameralik amphibolite dykes displaying the characteristic large patches of plagioclase crystals (Photo 7), but the majority are of, as yet, unknown age. The noritic or high-Mg andesite dykes trending NS are the youngest rocks in the mapped area, and have been dated at 2215 Ma by SHRIMP (Nutman et al 1995).

A mylonite zone with a width of a few meters, dipping about 50° southeast, runs along both sides of the Isua belt and juxtaposes it against Amîtsoq gneiss (Photo 8) (Nutman 1984). The mylonite zone on the western boundary has a foliation characterized by the alternation of quartz-rich and feldspar-micaceous layers. Mineral lineations on the foliation dip steeply (>50°) to the ENE. Shear sense deduced from the microtextures observed in orientated thin sections indicates down-dip shear sense. Under the microscope, elongated ribbon quartz is warped into a stair-stepping morphology around the rounded feldspar porphyroclasts. Matrix quartz is dynamically recrystallized and aligned < 40° oblique to the foliation (type II S-C mylonite of Lister & Snoke 1984). The chlorite-rich parts originated from foliation-parallel veining, and show mica-fish like textures. These asymmetric textures all indicate top to the east (down slip) sense of shear (vertical simple shear, D1, of James 1976). Metamorphic conditions during mylonitization are assumed to be in the greenschist facies, because of the presence of veinlets of chlorite and the brittle deformation of feldspar. Drag folding (D2 phase of James 1976), due to dextral lateral movement, has bent the mylonitic foliation.

The eastern boundary is also defined by a mylonite zone with a 50° SE strike (Photo 9), and has dip-slip mineral lineations. Under the microscope, ribbon-quartz showing stair-step shape and S-C mylonite textures indicate top-to-the-ENE sense of shear. Biotite and white mica show ‘fish’ structures and are often recognized as tails of epidote porphyroblasts. Metamorphic conditions are assumed to have reached greenschist facies, by the same reasons as given above. The above textural features imply domal uplift of the inner gneiss, causing simple shear around the boundary between the Isua supracrustal belt and the Amîtsoq gneiss.

In spite of the recognition of pillow structures in an occurrence of amphibolite by geologists of Kyrolitselskabet Øresund A/S in the early 1970s, subsequent workers have overlooked them because they classified the rocks according to the metamorphic structure and texture, instead of protoliths (Allaart 1976). Therefore, the pillow lavas in the Isua supracrustal belt have never been well described. The pillow lava structures are sporadically preserved in areas of relatively low strain. Even under high strain, pillow structure can be recognized if the tectonic stretching is parallel to the elongated pillow tubes. The pillow lavas are relatively small, 30 to 150 cm across. Morphologies comprise: oval with cusp through pear-shaped to crescent-shaped forms, depending on secondary deformation. Relatively undeformed pillow lavas indicate the way-up (Borradaile 1982). They are composed of core (green), rim (pale green to white colored) and matrix (darker green), and some have a mantle (darker green) between the core and rim (Photo 4). They are of close-packed type with scanty matrix. They vary in size and shape depending on the flow unit. Vesicles and varioles are not visible on rims, presumably because of the secondary deformation and metamorphic

recrystallization.

## I-3 Barrovian-type progressive regional metamorphism

It had been thought that both the Isua supracrustal belt and the Amîtsoq gneiss had originally suffered amphibolite facies metamorphism and then were recrystallized under greenschist facies conditions due to retrogressive metamorphism (Boak & Dymek 1982; Nutman 1986). In this work, microscopic observations and microprobe analyses were completed on more than 750 rock samples from a NE-SW traverse from the Northern through Middle to the Southern Unit. Detailed petrographic analyses reveals that no relict minerals of high-grade amphibolitic metamorphism exist even in the least metamorphosed zone of the greenschist facies mineral assemblage. Moreover, Ca-amphiboles in the high-grade amphibolite zone possess knife-edge-bounded zoning of actinolite in the core and hornblende in the rim, suggesting the presence and preservation of the prograde metamorphic stage.

The study area is divided into four metamorphic zones based on mineral assemblages and the compositions of the metamorphic minerals (i.e. anorthite content of plagioclase) in metabasites (Fig. 3). Zone A is characterized by the greenschist mineral assemblage of chlorite (Chl), epidote (Ep), albite (Ab) and quartz (Qz). Zone B is defined by the appearance of Ca-amphiboles, either actinolite (act) and/or hornblende (Hbl), together with albite and/or oligoclase. The mineral assemblage is Chl, Ep, two amphiboles, peristeritic plagioclase (Pl) and Qz, showing the transition between greenschist and amphibolite facies. The distinctive feature of Zone C is the persistence of the peristeritic gap in plagioclase in spite of the first appearance of andesine, and the presence of two types of amphibole. The metabasites are composed of diagnostic minerals Chl, Ep, Act, Hbl, Ab, andesine and Qz. Zone D is defined by the disappearance of compositional gaps in plagioclase and Ca-amphibole. The mineral assemblage is Chl, Ep, Hbl, high-Ca plagioclase and Qz. Some rocks contain garnet and cummingtonite because of their anomalous composition (enriched in MgO, FeO and $Al_2O_3$, and MgO and FeO, respectively). The Mg value, defined by 100xMgO/(MgO+FeO), of chlorite coexisting with Hbl, Act, Ep, Pl and Qz increases progressively from 52 in Zone B to 63 in Zone C. The Fe-Mg partition coefficient between garnet and biotite also shows the progressive increase of metamorphic temperature 400 ˚C in the northern area of Zone C through 450 ˚C in the southern area of Zone C to 550 ˚C in Zone D. This suggests the metamorphic zonation represents the Barrovian-type progressive metamorphism. Isograds trend NW-SE, and cross-cut the NS-elongation of the Isua supracrustal belt, which implies post-metamorphic tectonic juxtaposition of the Isua belt into the Amîtsoq gneiss (Fig. 3). A full description of metamorphic aspects will be presented elsewhere.

## I-4 Geology of the northeastern part of the Isua supracrustal belt

The mapped area is subdivided into three units by structural breaks defined by low-

angle thrust faults, which are NS-trending/east-dipping or EW-trending/north-dipping. We term these units the Northern, Middle, and Southern Units (Fig. 1b). Each unit is composed of imbricated piles of oceanic material, such as pillowed or massive basaltic flows, hyaloclastites, BIF/chert and mafic/felsic sediments.

The Northern Unit is juxtaposed with the Middle Unit across an NS-trending fault with 20-30° dips to the east. The lower half of the Northern Unit is highly disrupted mélange (Type II, Cowan 1985), with blocks of greenstone and chert. It is comparable with examples in Phanerozoic Tethyan and circum-Pacific orogenic belts (Fig. 2a). More than 37 angular to subrounded blocks of greenstone are randomly embedded in a highly sheared muddy matrix, together with several blocks of chert with or without BIF. Moreover, magmatic structures of pillow lava, dike, gabbro and hyaloclastite have been identified in greenstone blocks, whereas bedding planes of cherts are well-preserved in chert blocks. The upper half resembles the Southern Unit in terms of structure and lithostratigraphy. It is composed of three subunits bounded by layer-parallel thrusts. Each subunit is composed of pillow lava greenstone at the bottom, overlain by layered chert/BIF. Although chert/BIF sequences are multiply deformed and cut by faults, the original lithostratigraphy can be reconstructed, as explained in the later section. Pillowed basalts covered with a hyaloclastite layer are conformably capped by thick chert/BIF sequences. BIF layers occur at the bottom of the sedimentary sequence, whereas white chert becomes more abundant through the transition of white/blue chert at the upper part. A thin graphite-bearing chert layer also occurs at the muddy chert horizon, resting on bedded chert. Basaltic dikes/sills are intruded into BIF/chert sequences in several places. The rocks in this unit suffered from relatively low-grade progressive metamorphism from greenschist facies in the eastern to epidote-amphibolite facies in the western region (Fig. 3).

The Middle Unit is cut on the south by an EW trending, gently north-dipping fault. Although Quaternary glacial drift obscured the Unit boundary, bedding planes change abruptly beyond the boundary from a NNE-strike in the Middle Unit to a NE-strike in the Southern Unit. Across the boundary, the lithostratigraphic discontinuity is obvious; chert and overlying mafic sediment predominate in the Middle Unit, whereas massive lava, pillow lava and hyaloclastite are abundant in the Southern Unit. Although the Middle Unit is mainly composed of dominantly NS-trending chert layers, near the southern margin of the Unit is found a mafic material-enriched turbidite sequence associated with felsic sandstone, mudstone, calcareous sandy shale, and even minor conglomerate crops out. Chert is mainly a white type (see the later section), and some chert layers are intercalated with impure (dolomitic) carbonate. More than 110 dykes and sills are intruded into the Middle Unit. Those are variable in thickness from tens of centimeters to tens of meters. Only two of them contain plagioclase patches, suggesting that they are Ameralik dykes. One of the Ameralik dykes intrudes the Unit-bounding fault, indicating that dyke emplacement was post-juxtaposition. The dyke itself has been metamorphosed to amphibolite facies condition. Reconstruction of the original stratigraphy is difficult because there are no key beds in the Unit, but it probably consists of several subunits, as do the other Units.

The Southern Unit occupies the major part of the mapped area. Major lithologies are basaltic lava flows, with or without pillow structures. Because various lithologies (e.g. conglomerate layers and felsic sediments) crop out throughout the Unit, we employ them as key beds in geological and structural investigations.

## I-5 Geology of the Southern Unit

The distribution pattern of the above-mentioned five major lithologies is complicated. Cherts and associated sediments form several belts, apparently converging in some cases, and diverging in the others, as indicated by layer-parallel faults (Fig. 4). Faults formed by layer-parallel shortening are common in the Isua supracrustal belt, and duplex structures are on scales of meters to a few km. Duplex structures are common in all three Units but the truncated duplex structure is most conspicuous in the Southern Unit.

At least eight major subunits (duplexes) are defined by the layer-subparallel faults, which trend NE-SW, as shown in Fig. 4. Although the faults are subparallel to the layering of the turbidite sequence, the layering is clearly cut by those faults in many places, at outcrop scale. The duplexes are, in turn, composed of several horses, and at least twelve horses can be recognized. The lithostratigraphy and chert thickness are similar among horses in each particular duplex, and these are the criteria used to define a single duplex (a duplex is indicated by a roman numeral, and the horse belonging to that duplex is indicated by a subscript Arabic numeral; e.g. $IV_2$).

We reconstructed the original lithostratigraphy within each horse by removing folds and/or thrusts, based on detailed sketches of the outcrops. The reconstructed lithostratigraphy within a horse is simple, and consists of, in ascending order, pillow basalt, chert, and turbidite (Fig. 5). Major tectonic breaks separating horses on both sides are commonly layer-parallel faults. The stratigraphic top within a horse always faces southeastward, except in a few strongly folded areas.

## I-6 Reconstruction of lithostratigraphy within a horse in the Southern Unit

The lithostratigraphy within each horse was reconstructed and compared. Centimeter-scale measurements of chert and turbidite sequences were completed on all horses. An example is shown in Fig. 5. The chert and turbidite are, in general, severely deformed compared to metabasite, and hence, particularly careful observation is necessary for the reconstruction of the original lithostratigraphy. Chert has been subdivided into the following six-types: (1) BIF-bearing, (2) white, (3) white/blue (magnetite-bearing), (4) white/green (mafic tuff-bearing), (5) muddy chert, and (6) white/gray (or brown due to weathering) chert containing thin laminated carbonate layers. The type 3 and type 4 cherts are characterized by mm to cm scale rhythmic alternations.

The mineral assemblages and abundance of minerals in the rocks reflect not only the

metamorphic grade, but also the chemical composition of the rocks. Mafic sediments (MS) can be also classified into the following five-types based on the appearance and amount of garnet. If mafic sediment is more enriched in FeO and/or MnO relative to MgO, garnet is more abundant at a given metamorphic grade. Thus, the modal amount of garnet is a marker of the relative abundance of FeO. $MS_1$ is black and massive, with few garnets. $MS_2$ is also black, but is differentiated from $MS_1$ by its rough surface and is garnet-free. $MS_3$ has quite large amounts of garnet megacrysts, and is green and massive. $MS_4$ is also black but different from $MS_1$ in terms of larger modal amounts of garnet. $MS_5$ is black to gray with a considerable amount of garnet.

In spite of complex folding, the lithostratigraphy within a horse can be reconstructed by using key beds of chert and mafic sediment lithologies. A representative example is shown in Fig. 6a, 6b. A wide variety of lithologies occur in a 80 x 30 $m^2$ area. These include rhythmically alternating white-gray chert, muddy chert, alternating felsic sandstone and mudstone, mafic sediments, carbonate, and conglomerate. The area is subdivided into four blocks (Block I to IV) by three NE-SW trending, folded thrusts ($T_1$ to $T_3$).

$T_1$, with NE-trends and SW-dips, runs along the boundary between $MS_4$ and conglomerate (Fig. 6b). $T_2$, with ENE-trends and SSE-dips, constitutes the boundary between the $MS_4$/carbonate and $MS_4$/$MS_1$ in the western area (Fig. 6c), whereas it constitutes the boundary between $MS_4$ and conglomerate in the eastern area (Fig. 6b). $T_1$ is cut by $T_2$ in the middle area. $T_3$, with ENE-trends and SSE-dips, runs along the boundary between the chert and $MS_4$, and truncates $T_2$ in the western area (Fig. 6c).

Although older folds are obscured by later deformation, and even the faults themselves are tightly folded, at least four separate generations ($F_{1a}$ to $F_{1d}$) can be observed, based on the direction and dip of the plunge of fold axes and cross-cutting relationships with thrusts. Sedimentary bedding planes ($S_0$) such as graded bedding, intercalation of conglomerate with carbonate and $MS_4$ with carbonate are well preserved in this area.

$F_{1a}$ folds have been traced throughout the eastern part of this area by using $MS_3$ and sandstone as structural markers (Fig. 6a). They are noncylindrical tight to isoclinal folds, with upright to moderately dipping, WNW-striking axial surfaces and with hinge lines plunging WNW. These folds have wavelengths of *ca.* 2 meters. $F_{1b}$ folds are noncylindrical, closed to tight, with upright to moderately dipping, NNE-striking axial surfaces and with hinge lines plunging SSW. $F_{1b}$ folds have been traced throughout the northern part by using intercalations of conglomerate with carbonate or $MS_4$ (Fig. 6a). $F_{1c}$ folds have very distinct forms. $F_{1c}$ folds are noncylindrical, closed to tight, with upright to moderately dipping, NE-striking axial surfaces and with hinge lines plunging SW (Fig. 6a). $F_{1d}$ folds are noncylindrical tight to isoclinal, with upright to moderately dipping, NE-striking axial surfaces and with hinge lines plunging SW (Fig. 6a).

The axial surface and the eastern limb of the $F_{1b}$ fold are sharply cut by $T_1$ in the middle area of Block IV (Photo 1). Moreover, the axial surface and the eastern limb of the $F_{1b}$ fold are cut by $T_1$ and its western rim is cut by $T_2$ in Block III (Fig. 6b). The axial surfaces of

$F_{1b}$ folds make a sweep to the west along thrusts, and interlimb angles decrease near the thrusts. $F_{1c}$ folds bend the axial surfaces of $F_{1a}$ and even fault surfaces of $T_1$ and $T_2$. On the other hand, $F_{1c}$ folds are truncated by $T_3$ (Fig. 6c). $F_{1d}$ fold bends $T_3$ in the western area (Fig. 6a). The foliations ($S_2$) in this area are mainly NE-SW striking and dip moderately to steeply to the southeast, and appear to be folded, with steeply SE-plunging axes ($F_2$) (Fig. 6a inset). All the rocks in this area uniformly suffered from lower amphibolite metamorphism (Fig. 3). This evidence means the juxtaposition of those blocks predates the regional amphibolite metamorphism. Superposition of the folds and thrusts described above allows us to reconstruct the original stratigraphy. The thrust and folding events are summarized in Table 1.

Block I contains a 3-5 m thick bedded chert layers capped by alternating felsic sandstone and mudstone on the top, through a few meters thick muddy chert layer. The bedded chert is intercalated with thin $MS_1$ layers in the lower part (Fig. 6c). Block II is dominated by $MS_4$ with interbedded $MS_1$, $MS_3$, $MS_5$, sandstone and carbonate. Felsic sandstone is a key bed to correlate the stratigraphy of Block I with Block Ⅱ where it is interlayered with $MS_4$ in the lower part. Toward the stratigraphic top, mafic sediments dominate, exhibiting a variety of different lithologies. $MS_3$ layers occur in the stratigraphic upper part, while $MS_1$ and $MS_5$ occur in the middle part. Thin carbonate layers are interbedded in the upper part. Among them are 10-20 cm thick Fe-rich mafic layer containing remarkably large crystals of garnet ($MS_{3,4}$) which can be used as a marker horizon. This aids helping, not only analysis of the folded structures, but also comparison of the lithostratigraphy between blocks (Fig. 6b, 6c). The overturned Block Ⅳ starts from $MS_4$ interlayered with sandstone layers through alternations of $MS_4$ and carbonate layers finally up to 4-m thick conglomerate layer (Fig. 6b, 6c). Block III is composed of alternating conglomerate and thin $MS_4$ and $MS_2$ layers with minor intercalations of carbonate layers (Fig. 6b). Although all blocks are metamorphosed to amphibolite grade, some sedimentary structures, such as cross-lamination and graded-bedding, are well preserved (Nutman et al. 1984). Using these to determine the directions of the stratigraphic top (Nutman 1986), the lithostratigraphic sequence can be reconstructed based on the above thrust/folding generations and comparison of the lithostratigraphy within each block (Fig. 7). The total thickness of the turbidite sequence is estimated to be about 70-80 m. However, due to a considerable degree of tectonic thinning, the original thickness may have been much more. The degree of deformation is measured using shapes of deformed pebbles in conglomerate layers, and the result shows that the strain ratio was 1:1.23:0.33. If such a strain ratio is applied to all lithologies, the original thickness can be estimated to be about 200 to 300 m.

Compared with reconstruction of the chert-turbidite association, it is easy to reconstruct the stratigraphy of the basaltic flow piles capped by chert, because the basalts are less deformed than the other rocks, as shown on the geologic map. A close-up view of such an example is shown in Fig. 8 and Photo 10. A northward-dipping steep wall, 80 x 300 $m^2$ in area is exposed, exhibiting a complete succession from pillow at the bottom through the hyaloclastite layers up to massive white chert bed on the top. Along the boundary between

chert and hyaloclastite, thin dolomitic carbonate pods are present. The pillow lavas are relatively small, up to 80 cm across. Morphologies range from oval with cusp, to pear-shaped, relatively undeformed pillow lavas, indicate younging towards the southwest. They are composed of cores (green), rims (pale green to white colored) and matrix (darker green), and some have mantles (darker green) between the core and rim (Photo 4). The pillow lava-hyaloclastite flow unit rests on hyaloclastite layer in the foot of wall (Fig. 8). The hyaloclastite layers on the top are divided into two sections, the upper and the lower hyaloclastite, respectively. The lower hyaloclastite layers are characterized by smooth surfaces and lack of garnet megacrysts. They consist of poorly-sorted pillow breccias set in matrix. The layers are up to 9 meters thick, and conformably cover the pillow lavas. The upper hyaloclastite layers are composed of well-sorted, fine-grained metasediments with a probable reworked origin. They are characterized by rough surfaces and garnet megacrysts. High abundance of garnet suggests that the rocks are enriched in Fe and Mn. The layers are up to 3 meters thick, and vary laterally in thickness. They conformably cover the lower hyaloclastite, and are conformably overlain by white bedded chert layers. Five subparallel dykes cut all the pillow lava flows and the overlying sedimentary units. Massive white chert beds contain thin films of either carbonate or mafic sediments, near the base.

Through detailed mapping, we obtained lithostratigraphic columnar sections for each horse (Fig. 9). Some are quite similar to each other in terms of stratigraphy and thickness of chert beds, whereas others differ. A group of horses with similar stratigraphy is regarded as belonging to a particular duplex. As a result, the following eight duplexes were recognized. All of the horses in the given duplex (e.g. III) share the same stratigraphy and thickness of chert, except for Duplex IV, in which two share both the same stratigraphy and thickness of chert, but the third shares only the stratigraphy with the others, as will be discussed later. Moreover, Duplex II has a distinct stratigraphic feature, which implies an oceanic plateau or seamount origin as will be discussed later. Duplexes I, III to VIII are described first, and II thereafter.

Duplex I is present at the structural base in the mapped area and is cut by a 50° E-dipping fault across which it is juxtaposed against the inner Amîtsoq gneiss (Fig. 4). About 50-m thick sedimentary units of white chert beds and overlying mafic turbidite sequence are exposed, but the underlying pillow lava units are mostly cut off by a 50˚ east-dipping fault (Fig. 1)

Duplex III is composed of three horses; each characterized by thick-bedded chert (30m). The basaltic layer is composed of a few pillow lava flow units, and a turbidite layer marking the top of the sequence is dominantly mafic in composition. Along a lithologic boundary between chert and mafic turbidite, a few layers of carbonate are present; each is a few tens of cm thick (Fig. 9).

Duplex IV is formed by three horses. All are characterized by thick turbidite containing felsic sandstone, mudstone and conglomerate in addition to mafic/carbonate sediments. Conglomerate layers are associated with this Duplex and are traceable over 3 to 4 km along

strike. The conglomerate layers may be related to dacite (CA volcanics) boulder-bearing, thick felsic turbidite layers, about 12 km to the southwest. Zircons from dacite pebbles yielded a well-constrained igneous age of 3807±1 Ma (Compston et al. 1986). The chert thickness in the two horses is the same (about 5 m), but that of another is quite different, at about 40 m (Fig. 9). Moreover, the lithostratigraphy of chert is also distinctive; white chert dominates in $IV_1$ and $IV_2$, while the sequence of chert is dominantly composed of blue/white chert with some layers of green/white and white chert, and even tuff and soapstone layers in $IV_3$. Nevertheless, the prominent muddy chert layers at the top of the chert sequence and the lithostratigraphy of the turbidite sequence overlying the chert are the same in all horses, suggesting the simultaneous accretion of all three at a trench, because the turbidite sequence reflects the sedimentary environment of the trench, during accretion (Kimura 1994; Kusky et al. 1997b). The different chert thicknesses amongst horses will be discussed later.

Duplex V is characterized by white chert with overlying thick blue/white chert unit (total: 40m). Near the base of the chert bed, fuchsite is present in some localities. Along the boundary between chert and underlying thick hyaloclastite layers, a thin layer of talc-bearing ultramafic rock is present. The turbidite layer is dominantly mafic in composition with minor felsic sediments (Fig. 9).

Duplexes VI, VII and VIII are not well exposed, and have been affected by thermal metamorphism by the 2.2 Ga (Nutman et al. 1995) boninitic dyke intrusions. This makes it difficult to unravel the detailed lithostratigraphy and the distribution of horses. However, a few critical exposures clearly indicate the presence of different duplexes with different lithostratigraphies. All of these are characterized by different chert thicknesses and different lithologies. Duplex VI is characterized by thin bedded blue/white chert and varied lithologies in the turbidite layers; a cm- to m-scale alternating mafic, carbonate, felsic and ultramafic sediments (Fig. 9). Duplex VII share the characteristics of thin white chert layers and the occurrence of both thick felsic and mafic sediments with distinctive carbonate layers (Fig. 9). Thick chert layers and the very thick overlying mafic sediments with ultramafic materials are present in Duplex VIII (Fig. 9).

Duplex II has a thick (up to 600 m) lithostratigraphy, which is remarkably different from the others, because chert layers appear in two stratigraphic horizons (Fig. 9). Between the lower 50-m thick and the upper 2-m thick bedded chert layers, a 190-m thick relatively undeformed mafic/felsic alternation is present. It is characterized by bimodal volcaniclastic felsic and mafic compositions. Mafic sediment contains numerous garnet megacrysts. Recent SHRIMP dating of separated zircons reveals that the felsic volcaniclastic rocks were formed at 3710±4 Ma (Nutman et al. 1997). In the lower section, the alternation is rhythmically and finely spaced. Near the base, tourmaline boulders are present (Appel 1984, 1995). In the middle section, each layer of mafic and felsic sediments becomes thick, up to 5 m. Four mafic sills are intruded into felsic sediment layers, or the boundary between felsic and mafic sediments. In the upper section, mafic sediment become dominant, interbedded with six felsic sediment layers, about 1 m thick. Thin mafic sediment layers without garnet megacrysts are

interbedded with thick mafic sediment layers with garnet megacrysts. A package of thin magnetite and green phyllite layers is intercalated into one of the thick mafic sediment layers. Near the top, a unit of very thick green phyllite with felsic sediment layers on both the sides covers the alternation of mafic sediment layers. At the top, a mafic sill is intruded. The upper 70-m thick mafic sediment layer overlying the thin chert layer is dominantly mafic in composition, and one thin felsic sediment layer is interlayered near the bottom. Mafic sediments contain no garnet megacrysts, suggesting a more Mg-rich bulk composition. Picritic lava flows are also present. The uppermost part is a thin alternation of felsic sandstone and mudstone (Fig. 9).

## I-7 Comparison of lithostratigraphy of the Isua belt with oceanic plate stratigraphy

Fig. 9 summarizes all of above-mentioned lithostratigraphies as a simplified stratigraphic column. Petrographic examination of chert indicates that no continental or arc materials occur within chert beds and underlying pillow lava flow units. Detrital materials start to appear in thin laminated chert beds precipitated after the end of major chert deposition, and become common in the turbidite layers. The sequential change of sedimentary aspects, from chert to turbidite, is common to all horses in the Isua belt. The reconstructed lithostratigraphy is quite similar to that of circum-Pacific accretionary complexes, which were formed by oceanic plate subduction during the last 450 Ma along the peripheral parts of the proto-Pacific to the present-day Pacific Ocean (Isozaki et al. 1990; Matsuda and Isozaki 1991).

The reconstructed lithostratigraphy in an accretionary prism in those Phanerozoic orogens is called “oceanic plate stratigraphy”. Representative columns are shown in Fig. 10a, which is slightly modified from the original to make the travel history of the ocean-floor on the modern Earth easy to understand. The oldest oceanic segment in the present oceans is 200 Ma off the Mariana arc, and forms a part of the Pacific plate which is being subducted under the Izu-Mariana intra-oceanic arc. Along the western margin of North and South America, spreading centers themselves are being subducted under the continents (e.g. von Huene et al. 1998). Therefore, crudely speaking, the lifetime of oceanic lithosphere from its birth at a mid-oceanic ridge to demise at the trench is 100 m.y. on average on the modern Earth. The deposition rate of bedded chert, estimated by the occurrence of radiolarian microfossils, is 1 m per 1 m.y. for Triassic to Jurassic bedded chert in Japan (Matsuda and Isozaki 1991). Thus, a 100-m thick chert bed corresponds to chert deposited over 100 m.y. A simplified oceanic plate stratigraphy is shown in Fig. 10a together with a travel history of the oceanic plate of 100 m.y. age. When the plate is formed at a mid-oceanic ridge, the oceanic crust is composed of tholeiitic basaltic flow piles. Topmost crust is partly covered by a thin bed of limestone where the ridge crest is above the carbonate compensation depth. Hydrothermal circulation of seawater at the spreading center alters the oceanic crust (ocean ridge metamorphism), and

forms massive sulfide deposits through black and white smokers locally developed on the ridge. Due to horizontal movement by ocean-floor spreading, the plate cools with time, the water depth increases, and deep-sea sediments precipitate on the ocean-floor until arrival at the trench. During the 100 m.y. of travel time from mid-oceanic ridge to a subduction zone only deep-sea sediments are precipitated on the ocean-floor. These sediments are bedded cherts formed by relatively rapid and periodical deposition of “marine snow” (radiolarians) compared to constantly supplied aeolian dust, which is transported from the continental areas. Near the trench, continent- or arc-derived turbidite starts to cover the ocean-floor. These comprise very fine-grained mudstone mixed with chert (hemipelagic sediments), outboard of the trench outer wall, which are covered by thick coarse-grained turbidites at the trench axis. The 100 Ma oceanic crust capped by 100-m thick chert and turbidite sequence is then subducted and accreted to the arc either by off-scraping at shallow levels or underplating at deeper levels.

The accretion of subducted oceanic materials in either off-scraping or underplating is through layer-parallel shortening as schematically illustrated in Fig. 10b. A competent basaltic oceanic crust overlain by semi-consolidated to unconsolidated sediments is underthrust along the décollement by oceanic plate subduction. The release of pore fluid, strain hardening and compaction, force the frictional resistance along the décollement to decrease, and cause down-stepping of the decollement. Development of décollement down-stepping at this stage results in the accretion of oceanic crust and the formation of duplex structures comprising thrust-bounded horse. The newly-accreted oceanic crust pushes up the already-accreted horses and forces them to rotate landwards. The repetition of the above process forms a duplex, which consists of several horses (Fig. 10b).

As a result of the growth of a duplex, the newly developed décollement episodically advances oceanward to push up the already-accreted duplexes and cause the formation of a younger duplex under the older duplex, as shown in Fig. 10c. Accretionary orogens develop downward and oceanward with time. Because of the contrasting physical properties of component rocks, deformation concentrates in turbidite sequences and deep-sea sediments, rather than in rigid basaltic crust at shallow levels. It is easily imagined, if seamounts, rises or plateaus were formed on a plate, those would be sandwiched on the top and bottom by deep-sea sediments before accretion at the trench. In addition, an abundance of sills and dykes would be intruded into deep-sea sediments if oceanic island magmatism developed. All of those materials formed by ocean island basalt (OIB) volcanism would be finally exposed on land, but are quite different from the normal oceanic crust and overlying sediments. Systematic rules on the mode of occurrence of accreted oceanic materials with different origins are summarized by Isozaki et al. (1990).

## I-8 Travel history of Early Archean oceanic lithosphere in the Isua belt

It has been shown that in the Southern Unit, and possibly, in the whole Isua

supracrustal belt, an accretionary complex has formed through accretion of oceanic crust to the hangingwall, by duplexing. A sequence of duplexing scenarios can be reconstructed as follows.

The structural bottom is Duplex I and the top is Duplex VIII, as judged by the southward polarity of duplexing. As illustrated in Fig. 10b, the younger horses develop downwards, therefore, the oldest duplex is VIII. Accretion proceeded from Duplex VIII, through VII, VI, V, IV, III, and II, to I with time. Within a given Duplex, the southwestern horse is the oldest horse. The similar lithostratigraphy within each horse suggests that those oceanic crust segments subducted in the same area and period. The mode of formation of the duplex structure throws light on the direction of the growth of the accretionary prism and the subduction of oceanic lithosphere. The duplex polarity is defined by the direction of convergence of faults, which divide horses, and coincides with plate convergence (Fig. 10b). The southward convergent morphology of the duplex structure is widespread over the mapped area, indicating that the Isua accretionary prism grew from south to north.

Radiometric ages are not fully available for establishing the detailed chronology within each horse. Currently available constraints on the age of the supracrustal rocks and Amîtsoq gneiss near Isua are shown on Table 2. SHRIMP data reveals that felsic sediments in Duplex II were formed at 3710 Ma, which is the only utilizable constraint for the age of deposition of oceanic materials. On the other hand, the ages of the protoliths of the Amîtsoq gneisses are 3627 to 3702 Ma in the inner area and 3695 Ma in the outer area. Judging from these data, the age of subduction of oceanic crust must be before 3702 Ma, and probably in the range 3702-3800 Ma. Tonalitic granitoids, precursors of Amîtsoq gneiss, were subsequently intruded into the Isua accretionary complex around the Isua supracrustal belt at 3627-3702 Ma. Moreover, the inner gneiss is slightly younger than the outer gneiss, and the zircon ages in the Amîtsoq gneiss are reported as 3880 Ma in the south of the Isua area (Nutman et al. 1993), suggesting that a slightly older part of the arc may be present to the south and the east of Isua.

A paleogeographic reconstruction is shown in Fig. 11 to illustrate sequential events of accretionary prisms in the Southern Unit at about 3700-3800 Ma. The arrangement of oceanic lithosphere is estimated by the order of the accretionary scenario mentioned above. Two mid-oceanic ridges are assumed to be present, because the chert thickness of Duplexes VI and IV (except IV-3) is very thin, ranging between 4 to 6 m, whereas the others are all 30-50 m. Therefore, very young oceanic plate must have subducted at the trench to form Duplexes VI and IV, suggesting the presence of a mid-oceanic ridge nearby. The chert thickness of $IV_1$ and $IV_2$ is thin, *ca.* 4 to 6 m, whereas $IV_3$ reaches 40 m thick. In spite of the difference in chert thickness, lithostratigraphy of the turbidite sequence in $IV_3$ is very similar to those of $IV_1$ or $IV_2$. This may suggest the presence of a large transform fault with lithosphere of differing ages either side. Duplex II is presumably a large oceanic plateau or seamount formed by intraoceanic off-ridge volcanism, because chert layers occur along two stratigraphic horizons and bimodal volcaniclastic sediments are intercalated with chert beds. The thick lower chert layer of Duplex II suggests that its lifetime was long, and that an old plate subducted and

accreted to the hangingwall. On the other hand, the thin upper chert layers overlying the mafic/felsic sediments suggests that within-plate volcanism occurred near the trench.

The thin (5m) chert beds in Horses $IV_2$ and $IV_3$ imply subduction of a very young oceanic plate (Fig. 12a). If a sedimentation rate typical of Phanerozoic chert is applicable, it may have been ~ 5 My. In a modern tectonic setting for such young plate subduction, the volcanic front of the calc-alkaline (CA) rock series is very close to the trench and near-trench-volcanism is present, as shown in present and past examples (e.g., Tertiary SW Japan, Takahashi 1986). When a young, hot plate subducts, the hangingwall is uplifted on a regional scale because of buoyancy. This has been well documented in young orogenic belts around the circum-Pacific region, e.g., Late Tertiary SW Japan (Takahashi 1986), and the Early Tertiary Alaska (Delong et al. 1978; Kusky et al. 1997a). In these cases, thick piles of turbidite cap the subducting oceanic crust before subduction. It is worth mentioning the lithostratigraphy of Horses $IV_2$ and $IV_3$ which are characterized by a thick quartzofeldspathic turbidite sequence which contains mafic, felsic, and silicic pebbles in several interlayered conglomerates (Photo 2). Large dacite cobbles up to 50 cm across have been described from this horizon, and their petrochemical characters show typical Archean CA series rocks mentioned above (Nutman 1986). Fig. 12 shows the arc-trench paleogeography during ridge subduction in comparison to those of normal plate subduction. Both regional uplift and fore-arc volcanism enabled the input of felsic materials into the trench.

## I-9 Discussion

The tectonics of the early Earth, especially the Early Archean, has long been controversial amongst geoscientists, particularly in the light of growing data sets, not only from field evidence, but also from computer simulation, ultrahigh-pressure experiments, and knowledge of planetary geology. Among several different interpretations, two opposing ideas have been developed: plate tectonics vs. ensialic vertical tectonics. Geologic records provide direct evidence to answer the problems. Except a few pioneering works (Hoffman 1973; Condie 1972; Burke et al. 1976), most Archean geologists did not believe in the presence of layer-parallel shortening structures in Archean orogens during the 1970s. Such structures have now been described in many Archean orogenic belts (Friend et al. 1988; Nutman et al. 1989; Maruyama et al. 1991, 1994 for southern West Greenland; Kimura et al. 1993, for the Superior province; Kusky 1989, 1990, 1991 for the Slave Province, de Wit et al. 1987ab, 1992 for the Barberton Group, South Africa; Isozaki et al. 1991; Kimura et al. 1991; Maruyama et al. 1991 for Pilbara Craton, Western Australia). To explain such nappe-stacked orogenic structures, plate tectonics has been preferentially adopted as a possible explanation (e.g. Kusky and Kidd 1992). Large-scale duplex structures have also been described in Archean orogens (e.g. Folinsbee 1968). However, such large-scale subhorizontal shortening evidence does not necessarily mean subduction of oceanic or continental plates. Such structures have been also described within continental plates, for example, in the foreland

basins such as the Cenozoic Alps-Himalayas and Caledonides in Europe and eastern USA. To demonstrate subduction of an oceanic plate, the oceanic plate stratigraphy preserved within the accretionary prism is critical, in addition to documentation of layer-parallel shortening structures in orogenic belts. Hoffman (1991) compared some Archean orogenic belts with the Phanerozoic southwestern Japan arc and speculated that Archean granite-greenstone belts may be formed as accretionary complexes. The example reported here is the first detailed documentation of structural duplexing in Archean accretionary prisms, comparable to those in Phanerozoic examples, including currently on-going consuming plate boundaries.

A continental rifting model has been used to explain the geology of the Isua supracrustal belt, but this model overlooked the ubiquitous layer-parallel thrusts. It also regards sedimentary sequences, including conglomerate, as deposited conformably in shallow marine environments, and mafic volcanics intruded into or extruded on them (e.g. Nutman 1986; Jacobsen and Dymek 1987; Dymek and Klein 1988). More recently the tectonic history of southern West Greenland was accounted for by collision-accretion (Coney et al. 1980), based on the presence of three fault-bounded blocks characterized by a geological history distinct from that of adjacent terranes (Friend et al. 1987, 1996; Nutman et al. 1989). Although such a model takes into account the growth of continental crust through collision-amalgamation after the formation of the continental crust, it does not account for the tectonic setting where basaltic lavas, and chert and turbidite with conglomerate were deposited, and the emplacement mechanism onto the continental crust. Nutman and Collerson (1991) first used the term ‘accretionary complex’ for the Isua supracrustal belt. Although they presented SHRIMP ages of the metamorphism (overgrown portion on the rim of zircons) and the formation of source rocks of detrital zircons in the quartzite in the belt, the argument as to whether the Isua supracrustal belt was formed as an accretionary complex was not presented. The present geological evidence clearly shows that pillow lava flows were extruded on the ocean-floor and chert/BIF sediments covered the piles of pillow lava flows in the open ocean, because bedded chert layers except for muddy chert, and pillow lava flow piles contain no terrigenous materials.

Geologic records preserved within turbidite sediments also give strong constraints on the type of active plate margin. If they formed along a large continental margin, they would be dominantly quartzofeldspathic. If they are formed in intra-oceanic environments, such as the western Pacific domains, they would be dominantly mafic in composition, because there are no big rivers such as the Yangtze or the Yellow River which transports huge amounts of continental materials to trenches. The sedimentary petrology of the turbidite sequences clearly indicates that the Isua accretionary complex was formed in the latter environment, because mafic sediments are dominant in the turbidite sequences. It has long been evident that isotope signatures of Isua metabasites and Amîtsoq gneiss do not support a pre-existing continental crust (Moorbath and Taylor 1981). During Archean times, especially in the Early Archean, most orogenic belts presumably formed adjacent to intra-oceanic island arcs, then grew

gradually through the collision-amalgamation process of island arcs (Condie 1982). Our present data support the idea of Condie (1982), Nutman et al. (1996) and Kusky and Vearncombe (1997).

The 3.7 to 3.8 Ga accretionary complex of the Isua supracrustal belt was formed near a CA volcano-plutonic region as demonstrated by the felsic turbidite sitting on the top of turbidite sequence, as well as dacite pebbles in a stratigraphic horizon of Duplex IV. Those petrochemical aspects are quite similar to those of Phanerozoic TTG (tonalite-trondhjemite-granodiorite) along the circum-Pacific orogenic belts, although details are different, e.g., La/Yb ratio and Eu-anomaly (Martin 1986; Nutman and Bridgwater 1986; Shimizu et al. 1988). The Amîtsoq gneiss and dacite pebbles may be one of the oldest continental materials formed by oceanic plate subduction. Orogenic belts grow with time through plate subduction by which CA volcano-plutonism creates and develops new acidic continental crust. With the growing volume of the orogen, the trench shifts oceanward with time. The Japanese islands comprise such an example. They have grown about 400-km oceanwards during the last 400 Ma by the formation of accretionary complexes and episodic intrusion of TTG every 100 Ma. Therefore, as an inevitable result, the older accretionary complex rocks are now present as enclaves within granitoids. The Cretaceous SW Japan is the Phanerozoic analogue of granite-greenstone terrain in the Precambrian. The middle Jurassic and late Permian accretionary prisms occur as enclaves within huge batholiths of TTG (Fig. 13). The Cretaceous gneiss terrain is a regionally metamorphosed granite-greenstone terrain, which is also equivalent to the Precambrian gneiss terrains (Hoffman 1991).

Table 3 is a summary of the geological evolution of the Isua area based on lithostratigraphy, deformation and metamorphism. The history after the emplacement of Amîtsoq gneiss is established from the previous work listed in the table. The Archean history of the Isua area spanned over 1 Gyr and can be subdivided into four periods. The first period records the formation of the oceanic plate at the oceanic ridge and its subsequent migration to the trench, which is well preserved in the record of formation of ‘oceanic plate stratigraphy’. The second period records the subduction and accretion of oceanic crust, which is accompanied by underplating of oceanic crust to form duplex structures. The third period records the regional metamorphism. This period is still ambiguous because it has been considered that the early mineral assemblage was overprinted by the Late Archean metamorphism (Nutman and Collerson 1991). However, mineral assemblages and microprobe analyses suggest that the regional progressive metamorphism occurred before emplacement of the Amîtsoq gneiss. Moreover, microprobe analyses show no evidence of relict minerals of the preceding higher-grade metamorphism even in the lowest grade area. And the extent of the progressive metamorphism and the trend of the foliations overprinted the duplex structure (Fig. 3, 5). The mylonite zones between the Amîtsoq gneiss and the Isua supracrustal belt did not suffer metamorphism greater than greenschist grade. This evidence suggests that the regional greenschist to amphibolite grade metamorphism postdates the formation of the duplex structures and predates the emplacement of the Amîtsoq gneiss. The timing of the

progressive metamorphism depends on the age of the intrusion across the boundary between the Isua supracrustal belt and the Amîtsoq gneiss in the southern area. Previous works presumed that the dike was correlated with the Ameralik dykes, at about 3400 Ma. The fourth period records intra-continental and continental-margin processes, including the continental growth of tonalite-trondhjemite-granodiorite plutonism (the protoliths of Amîtsoq gneiss and Ikkattoq gneiss), and collision-accretion of the Akulleq terrane with the Akia terrane and the Tasiusarsuaq terrane (Friend et al. 1987). Post-collision granitic and trondhjemitic magmatism (McGregor 1973), and 2.7 Ga regional metamorphism (Nutman and Collerson 1991) are also related to this period.

The direction of zoned growth of accretionary complexes in Isua, as inferred from unraveling the duplex structure, is northward with time. Therefore, the Isua belt is the youngest in the NE territory of Akulleq terrane in West Greenland (Fig. 1). This enables us to predict the site of the oldest accretionary prism and TTG in this area. Fig. 13 show the N-S cross section of the Isua-Amîtsoq composite terrane in comparison with the zoned growth history of southwestern Japan arc. In the southwestern Japan arc, the younger accretionary complex, the major parts of the Sanbagawa and Shimanto belts have not yet been intruded by TTG, whereas the Paleozoic to Jurassic accretionary prisms have been extensively intruded by granitoids through the zoned growth of the orogen and oceanward shifting of the trench with time. Similarly, the older accretionary complex should be penetrated by TTG, remaining as enclaves or roof pendants within TTG plutons, and those should be to the south of Isua. The Akilia association which has been defined by McGregor (1973), is the expected material for the oldest accreted oceanic materials to the north of Ivisârtoq region mapped by Chadwick and Coe (1988) and Nutman (1986). Recently Nutman et al. (1993) reported 3.88 Ga zircon age by SHRIMP separated from Amîtsoq gneiss from this region. It is the oldest age for the Amîtsoq gneisses. The subduction-accretion time of Akilia association must be earlier than 3.88 Ga, and its formation at a mid-oceanic ridge or thereafter by off-ridge volcanism must be much older.

The Isua supracrustal belt records the evidence of 3.8-3.7 Ga tectonics on the Earth, which is similar to modern plate tectonics. It also records the materials formed by the plate boundary process at that time. These give similarities and differences with materials formed by modern plate boundary processes. Differences are as follows: (1) More frequent intra-oceanic or off-ridge volcanism as demonstrated by the frequent intrusions within chert beds. This may reflect that Archean mantle is higher temperature, hence more turbulent mantle upwellings occurred in the Archean, as predicted by many workers. (2) More frequent accretion of oceanic basement than in the Phanerozoic. This may reflect thicker oceanic crust than the present. If the crust is thicker than 10 km, the mechanically weak plane easily develops within crust during subduction of oceanic plate according to recent rheological experiments (e.g. Shimamoto et al. 1993). Therefore, accretion of oceanic materials is not common during Phanerozoic subduction except during deep accretion, although sections of oceanic crust, more than 10 km thick have not yet been reported in accretionary complexes, it

must have occurred commonly in the Archean if the crust was thicker than 10 km (Hoffmann and Ranalli 1988). (3) The absence of blueschist in the Archean accretionary complex. A high geothermal gradient at the subduction zone led to Barrovian-type metamorphism instead of the high P/T type metamorphism such as that of the Sanbagawa belt (Grambling 1981; Maruyama 1997b). This is consistent with progressive metamorphism reflecting the subduction process in the Isua supracrustal belt.

In spite of those differences, many similarities are present between the Archean and the present. Although it is possible that the chert was derived from chemical precipitation at the mid-ocean ridge, the occurrence of chert beds is quite similar to Phanerozoic bedded chert, with regard to the obvious bedding planes and the lithological gradation from bottom to top. Mid-oceanic ridge volcanics are not komatiite in composition, but low-K tholeiite (Gill and Bridgwater 1979; Komiya and Maruyama 1995). Moreover, systematic compositional differences can be observed between the pillow lavas underlying the thick chert and basaltic dikes/sills intruding the chert layers (Komiya et al. 1995). Pillow lavas are enriched in $Al_2O_3$, FeO, and Y relative to basic dikes/sills at a given MgO content. The pattern of chondrite-normalized rare earth elements (REE) is light REE-depleted for pillow lavas, whereas it is flat or slightly LREE-enriched for the dikes/sills. This result is quite different from the commonly held speculation that Archean mid-oceanic ridge volcanics are komatiite (e.g., Takahashi 1990). The site of Archean komatiite formation has been speculated to be at a the spreading center (de Wit et al. 1987b), or at a hotspot seamount or huge oceanic plateaus (Storey et al. 1989; Campbell et al. 1989). For example, the Abitibi komatiites were explained to result for Archean hot-spot activity (Kimura et al. 1993), and the type locality of komatiite in the Komati Formation of the Barberton belt, as being of an oceanic plateau origin (de Wit et al. 1992). Kusky and Kidd (1992) have also suggested such an origin for the Zimbabwe komatiites. Plate tectonics had already started at least by 3.8 Ga, and presumably, back to 3.9 Ga. The common occurrence of pillow structures and conglomerate in the Isua supracrustal belt also demonstrates the presence of seawater, and the existence of a proto-ocean. Such a physical state of the early Earth is quite different from the Earth's satellite Moon, which was resurfaced heavy extraterrestrial bombardment and the related Mare volcanism (Fig. 14).

## I-10 Conclusions

(1) Our detailed mapping of the northeastern part of the Isua supracrustal belt shows that the belt consists of duplex structures. The sketches of each horse allow us to reconstruct the original lithostratigraphy. The reconstructed lithostratigraphy is quite similar to Phanerozoic 'oceanic plate stratigraphy', which consists in ascending order, of pillow/massive lava unit, bedded chert and turbidite.

(2) The discovery of the duplex structures and oceanic plate stratigraphy reveals that the Isua supracrustal belt is the oldest known Archean accretionary complex. This indicates that a kind of 'tectonics' similar to Phanerozoic plate tectonics already operated in the Early Archean.

(3) Geological evidence shows that three distinctive mafic igneous suites are present in the belt. The first is pillowed and massive lava flows with subordinate amounts of hyalocalstite layers (mainly Garbenschiefer units), which is, in turn, overlain by thick chert layers with no terrigenous materials, suggesting that the mafic rocks had been derived from oceanic ridge volcanism. The second includes the abundant doleritic dikes and sills (some homogeneous amphibolites), which nowhere intrude into the turbidite sequences but into pillowed flow units and the overlying chert layers, suggesting off-ridge volcanism origin. The third type is the abundant doleritic dikes (some homogeneous amphibolites), which also intrude into all of those units including the turbidite sequences. This may be related to post-accretionary island arc volcanism or continental rifting volcanism thereafter.

(4) The duplex polarity indicates that the Isua accretionary prism grew from the south to the north, and was followed by successive tonalitic intrusions. This idea is consistent with recent SHRIMP dating (Nutman et al. 1993), suggesting that remnants of older accretionary complexes might be preserved as enclaves and roof-pendants within Amîtsoq gneiss to the south.

(5) The oldest pillow lavas in the Isua supracrustal belt evidently shows that seawater was present in the Early Archean.

## References


Allaart, J. H., 1976, The Pre-3760 m.y. old supracrustal rocks of the Isua area, central West Greenland, and the associated occurrence of quartz-banded ironstone, *in* Windley, B. F., ed., The early history of the Earth, London, John Wiley & Sons, p. 177-189.

Appel, P. W. U., 1984, Tourmaline in the Early Archaean Isua supracrustal belt. West Greenland: Jour. Geology, v. 92, p. 599-605.

———, 1995, Tourmalinites in the 3800 Ma old Isua supracrustal belt. West Greenland: Precam. Res., v. 72, p. 227-234.

Arndt, N. T., 1983, Role of a thin, komatiite-rich oceanic crust in the Archean plate-tectonics process: Geology, v. 11, p. 372-375.

Baadsgaard, H., 1976, Further U-Pb dates on zircons from the early Precambrian rocks of the Godthaabsfjord area, West Greenland: Earth Planet. Sci. Lett., v. 33, p. 261-267.

———, Nutman, A. P., and Bridgwater, D., 1986, Geochronology and isotopic variation of the early Archaean Amîtsoq gneisses of the Isukasia area, southern West Greenland: Geochim. Cosmochim. Acta, v. 50, p. 2173-2183.

———, ———, ———, Rosing, M., McGregor, V. R., and Allaart, J. H., 1984, The zircon geochronology of the Akilia association and Isua supracrustal belt, West Greenland: Earth Planet. Sci. Lett., v. 68, p. 221-228.

Bickle, M. J., 1978, Heat loss from the Earth: A constraint on Archaean tectonics from the relation between geothermal gradients and the rate of plate production: Earth Planet. Sci. Lett., v. 40, p. 301-315.

———, Nisbet, E. G., and Martin, A., 1994, Archean greenstone belts are not oceanic crust.: Jour. Geology, v. 102, p. 121-138.

Black, L. P., Williams, I. S., and Compston, W., 1986, Four zircon ages from one rock: the history of a 3930 Ma-old granulite from Mount Sones, Enderby Land, Antarctica: Contrib. Mineral. Petrol., v. 94, p. 427-437.

Boak, J. L., and Dymek, R. F., 1982, Metamorphism of the *ca.* 3800 Ma supracrustal rocks at Isua, west Greenland: Implications from early Archean crustal evolution: Earth Planet. Sci. Lett., v. 59, p. 155-176.

Borrandaile, G. J., 1982, Tectonically deformed pillow lava as an indicator of bedding and way-up: Jour. Struct. Geol., v. 4, p. 469-479.

Bowring, S. A., Williams, I. S., and Compston, W., 1989, 3.96 Ga gneisses from the Slave province, Northwest Territories: Geology, v. 17, p. 760-764.

Bridgwater, D., McGregor, V. R., and Myers, J. S., 1974, A horizontal tectonic regime in the Archean of Greenland and its implications for early crustal thickening: Precam. Res., v. 1, p. 179-197.

Brown, M., Friend, C. R. L., McGregor, V. R., and Perkins, W. T., 1981, The late Archean Qôrqut granite complex of southern West Greenland: Jour. Geophys. Res., v. 86, p. 10617-10632.

Burke, K., Dewey, J. F., and Kidd, W. S. F., 1976, Dominance of horizontal movements, arc and microcontinental collisions during the later permobile regime, *in* Windley, B. F., ed., The early history of the Earth, London, John Wiley & Sons, p. 113-129.

Calvert, A. J., Sawyer, E. W., Davis, W. J., and Ludden, J. N., 1995, Archaean subduction inferred from seismic images of a mantle suture in the Superior Province: Nature, v. 375, p. 670-674.

Campbell, I. H., Griffiths, R. W., and Hill, R. I., 1989, Melting in an Archaean mantle plume: heads it's basalts, tails it's komatiites: Nature, v. 339, p. 697-699.

Chadwick, B., and Coe, K., 1988, 1: 100000 Ivîsartoq map sheet (64 V.2 N): Copenhagen, Geological Survey of Greenland.

Compston, W., Kinny, P. D., Williams, I. S., and Foster, J. J., 1986, The age and Pb loss behaviour of zircons from the Isua supracrustal belt as determined by ion microprobe: Earth Planet. Sci. Lett., v. 80, p. 71-81.

Condie, K. C., 1972, A plate tectonics evolutionary model of the South Pass Archaean greenstone belt, southwestern Wyoming: Proc. 24th Int. Geol. Congr., v. 1, p. 104-112.

———, 1982, Plate Tectonics and Crustal Evolution: New York, Pergamon, 310 p.

Coney, P. J., Jones, D. L., and Monger, J. W. H., 1980, Cordilleran suspect terranes: Nature, v. 288, p. 329-333.

Cowan, D. S., 1985, Structural styles in Mesozoic and Cenozoic mélanges in the western Cordillera of North America: Geol. Soc. America Bull., v. 96, p. 451 462.

DeLong, S. E., Fox, P. J., and McDowell, F. W., 1978, Subduction of the Kula ridge at the Aleutian trench: Geol. Soc. America Bull., v. 89, p. 83-95.

de Wit, M. J., Armstrong, R., Hart, R. J., and Wilson, A. H., 1987a, Felsic igneous rocks within the 3.3- to 3.5-Ga Barberton Greenstone Belt: High crustal level equivalents of the surrounding tonalite-trondhjemite terrain, emplaced during thrusting: Tectonics, v. 6, p. 529-549.

———, Hart, R. A., and Hart, R. J., 1987b, The Jamestown ophiolite complex, Barberton mountain belt: a section through 3.5 Ga oceanic crust: Jour. Afr. Earth Sci., v. 6, p. 681-730.

———, Rosing, C., Hart, R. J., Armstrong, R. A., de Ronde, C. E. J., Green, R. W. E., Tredoux, M., Peberdy, E., and Hart, R. A., 1992, Formation of an Archaean continent: Nature, v. 357, p. 553-562.

Dewey, J., and Spall, H., 1975, Pre-Mesozoic plate tectonics: How far back in Earth history can the Wilson Cycle be extended?: Geology, v. 3, p. 422-424.
Dymek, R. F., and Klein, C., 1988, Chemistry, petrology and origin of banded iron-formation lithologies from the 3800 Ma Isua supracrustal belt, West Greenland: Precam. Res., v. 39, p. 247-302.
Folinsbee, R. E., Baadsgaard, H., Cumming, G. L., and Green, D. C., 1968, A very ancient island arc, Geophys. Monogr., v. 12, Amer. Geophys. Union, Washington, p. 441-448.
Friend, C. R. L., Nutman, A. P., and McGregor, V. R., 1987, Late Archaean tectonics in the Færingehavn- Tre Brødre area, south of Buksefjorden, southern West Greenland: Jour. Geol. Soc. London, v. 144, p. 369-376.
———, ———, and ———, 1988, Late Archaean terrane accretion in the Godthåb region, southern West Greenland: Nature, v. 335, p. 535-538.
———, ———, Baadsgaard, H., Kinny, P. D., and McGregor, V. R., 1996, Timing of late Archaean terrane assembly, crustal thickening and granite emplacement in the Nuuk region, southern West Greenland: Earth Planet. Sci. Lett., v. 142, p. 353-365.
Froude, D. O., Ireland, T. R., Kinny, P. D., Williams, I. S., Compston, W., Williams, I. R., and Myers, J. S., 1983, Ion microprobe identification of 4,100-4,200 Myr-old terrestrial zircons: Nature, v. 304, p. 616-618.
Gill, R. C. O., and Bridgwater, D., 1979, Early Archaean basic magmatism in West Greenland: the geochemistry of the Ameralik dykes: Jour. Petrol., v. 20, p. 695-726.
Grambling, J. A., 1981, Pressures and temperatures in Precambrian metamorphic rocks: Earth Planet. Sci. Lett., v. 53, p. 63-68.
Hamilton, P. J., O'Nions, R. K., Bridgwater, D., and Nutman, A., 1983, Sm-Nd studies of Archaean metasediments and metavolcanics from West Greenland and their implications for the Earth's early history: Earth Planet. Sci. Lett., v. 62, p. 263-272.
Hart, S. R., Brooks, C., Krogh, T. E., Davis, G. L., and Nava, D., 1970, Ancient and modern volcanic rocks: a trace element model: Earth Planet. Sci. Lett., v. 10, p. 17-28.
Hoffman, P. F., 1973, Evolution of an early Proterozoic continental margin: the Coronation geosyncline and associated aulacogens of the northwestern Canadian shield: Philos. Trans. Royal Soc. London, v. A 273, p. 547-581.
———, 1991, On accretion of granite-greenstone terranes, in Robert, F., Sheahan, P. A., and Green, S. B., eds., Greenstone gold and crustal evolution: St. John's, Newfoundland, Geological Association of Canada, p. 32-45.
———, and Ranalli, G., 1988, Archean oceanic flake tectonics: Geophys. Res. Lett., v. 15, p. 1077-1080.
Jacobsen, S. B., and Dymek, R. F., 1988, Nd and Sr isotope systematics of clastic metasediments from Isua, West Greenland: Identification of pre-3.8 Ga differentiation crustal components: Jour. Geophys. Res., v. 93, p. 338-354.
James, P. R., 1976, Deformation of the Isua block, West Greenland: a remnant of the earliest stable continental crust: Can. Jour. Earth Sci., v. 13, p. 816-823.
Isozaki, Y., Maruyama, S., and Furuoka, F., 1990, Accreted oceanic materials in Japan: Tectonophysics, v. 181, p. 179-205.
———, ———, and Kimura, G., 1991, Middle Archean (3.3 Ga) Cleaverville accretionary complex in northwestern Pilbara block, western Australia: EOS Trans., v. 72, p. 542.
Kimura, G., 1994, The latest Cretaceous-early paleogene rapid growth of accretionary complex and exhumation of high pressure series metamorphic rocks in northwestern Pacific margin: Jour. Geophys. Res., v. 99, p. 22,147-22,164.
———, Ludden, J. N., Desrochers, J.-P., and Hori, R., 1993, A model of ocean-crust accretion for the Superior province, Canada: Lithos, v. 30, p. 337-335.
———, Maruyama, S., and Isozaki, Y., 1991, Early Archean accretionary complex in the eastern Pilbara craton, Western Australia - Detailed field occurrence in the Marble Bar area -: EOS Trans., v. 72, p. 542.
Komiya, T., and Maruyama, S., 1995, Geochemistry of the oldest MORB and OIB of the World, Isua (3.8 Ga), Greenland: EOS Trans., v. 76, p. 700.
Kröner, A., 1977, The Precambrian geotectonic evolution of Africa: Plate accretion versus plate destruction: Precam. Res., v. 4, p. 163-213.
———, 1981, Precambrian plate tectonics, *in* Kröner, A., ed., Precambrian plate tectonics, p. 57-90, Amsterdam, Elservier.
Kusky, T. M., 1989, Accretion of the Archean Slave province: Geology, v. 17, p. 63-67.
———, 1991, Structural development of an Archean orogen, western Point Lake, Northwest Territories: Tectonics, v. 4, p. 820-841.
Kusky, T. M., Bradley, D. C., and Haeussler, P., 1997a, Progressive deformation of the Chugach accretionary complex, Alaska, during a paleogene ridge-trench encounter: Jour. Struct. Geol., v. 19, p. 139-157.
———, ———, ———, and Karl, S., 1997b, Controls on accretion of flysch and mélange belts at convergent margins: Evidence from the Chugach Bay thrust and Iceworm mélange, Chugach accretionary wedge, Alaska: Tectonics, v. 16, p. 855-878.
———, and Kidd, W. S. F., 1992, Remnants of an Archean oceanic plateau, Belingwe greenstone belt,

Zimbabwe: Geology, v. 20, p. 43-46.
———, and Vearncombe, J., 1997, Structural aspects, *in* de Wit, M. J., and Ashwal, L. D., eds., Greenstone Belts, Oxford, Clarendon Press, p. 91-124.
———, and Winsky, P. A., 1995, Structural relationships along a greenstone/shallow water shelf contact, Belingwe greenstone belt, Zimbabwe: Tectonics, v. 14, p. 448-471.
Lister, G. S., and Snoke, A. W., 1984, S-C Mylonites: Jour. Struct. Geol., v. 6, p. 617-638.
Liu, D. Y., Nutman, A. P., Compston, W., Wu, J. S., and Shen, Q. H., 1992, Remnants of ≥ 3800 Ma crust in the Chinese part of the Sino-Korean craton: Geology, v. 20, p. 339-342.
Martin, H., 1986, Effect of steeper Archean geothermal gradient on geochemistry of subduction-zone magmas: Geology, v. 14, p. 753-756.
Maruyama, S., 1997a, Pacific-type orogeny revisited: Miyashiro-type orogeny proposed: The Island Arc, v. 6, p. 91-120.
———, 1997b, Initiation of return flow seawater into mantle at 750 Ma and the Proterozoic/Phanerozoic boundary: EOS Trans., v. 78, p. 826.
———, Isozaki, Y., and Kimura, G., 1991, Is the Mid-Archean barite formation from the Pilbara craton, Australia under the deep-sea environment?: EOS Trans., v. 72, p. 532.
———, Komiya, T., and Appel, P. W. U., 1994, The oldest (3.8 Ga) accretionary complex of the world, Isua, Greenland: EOS Trans., v. 75, p. 691.
———, Masuda, S., and Appel, P. W. U., 1991, The oldest accretionary complex on the Earth, Isua, Greenland: Geol. Soc. America Abs with Prog., p. A429-A430.
Matsuda, T., and Isozaki, Y., 1991, Well-documented travel history of Mesozoic pelagic chert in Japan: Tectonics, v. 10, p. 475-499.
McClay, K. R., 1992, Glossary of thrust tectonics terms, in McClay, K. R., ed., Thrust tectonics, London, Chapman & Hall, p. 419-433.
McGregor, V. R., 1973, The early Precambrian gneisses of the Godthåb district, West Greenland: Philos. Trans. Royal Soc. London, v. A273, p. 343-358.
———, 1993, Descriptive text to 1:100000 Geological map of GREENLAND Qôrqut 64 V.1 Syd.: Copenhagen, Geological Survey of Greenland, 40 p.
———, Bridgwater, D., and Nutman, A. P., 1983, The Qârusuk dykes: post-Nûk, pre-Qôrqut granitoid magmatism in the Godthåb region, southern West Greenland: Rapp. Grønlands geol. Unders., v. 112, p. 101-112.
———, Friend, C. R. L., and Nutman, A. P., 1991, The late Archean mobile belt through Godthåbsfjord, southern West Greenland: a continent-continent collision zone?: Bull. Geol. Soc. Denmark, v. 39, p. 179-197.
Michard-Vitrac, A., Lancelot, J., Allègre, C. J., and Moorbath, S., 1977, U-Pb ages single zircons from the early Precambrian rocks of West Greenland and the Minnesota River Valley: Earth Planet. Sci. Lett., v. 35, p. 449-453.
Mojzsis, S., Arrhenius, G., McKeegan, K. D., Harrison, T. M., Nutman, A. P., and Friend, C. R. L., 1996, Evidence for life on Earth before 3,800 million years ago: Nature, v. 385, p. 55-59.
Moorbath, S., Allaart, J. H., Bridgwater, D., and McGregor, V. R., 1977, Rb-Sr ages of early Archaean supracrustal rocks and Amîtsoq gneisses at Isua: Nature, v. 270, p. 43-45.
———, O'Nions, R. K., and Pankhurst, R. J., 1973, Early Archaean age for the Isua Iron Formation, West Greenland: Nature, v. 245, p. 138-139.
———, ———, and ———, 1975, The evolution of early Precambrian crustal rocks at Isua, West Greenland - Geochemical and isotopic evidence: Earth Planet. Sci. Lett., v. 27, p. 229-239.
———, and Taylor, P. N., 1981, Isotope evidence for continental growth in the Precambrian, in Kröner, A., ed., Precambrian Plate Tectonics, Amsterdam, Elservier, p. 491-525.
———, ———, and Goodwin, R., 1981, Origin of granitic magma by crustal remobilisation: Rb-Sr and Pb/Pb geochronology and isotope geochemistry of the late Archaean Qôrqut Granite Complex of southern West Greenland: Geochim. Cosmochim. Acta, v. 45, p. 1051-1060.
Nisbet, E. G., and Fowler, C. M. R., 1983, Model for Archean plate tectonics: Geology, v. 11, p. 376-379.
Nutman, A. P., 1984, Early Archaean crustal evolution of the Isukasia area, southern West Greenland *in* Kröner, A., and Greiling, R., eds., Precambrian tectonics illustrated, p. 79-93, Stuttgart, E. Schweizerbart'sche Verlagsbuchhandlung.
———, 1986, The early Archaean to Proterozoic history of the Isukasia area, southern West Greenland, v. 154: Grønlands geol. Unders. Bull., København, Denmark, 80 p.
———, Allaart, J. H., Bridgwater, D., Dimroth, E., and Rosing, M., 1984, Stratigraphic and geochemical evidence for the depositional environment of the early Archaean Isua supracrustal belt, southern West Greenland: Precam. Res., v. 25, p. 365-396.
———, Bennett, V. C., Friend, C. R. L., and Rosing, M. T., 1997, ~ 3710 and ≥ 3790 Ma volcanic sequences in the Isua (Greenland) supracrustal belt; structural and Nd isotope implications: Chem. Geol., v. 141, p. 271-287.
———, and Bridgwater, D., 1986, Early Archaean Amîtsoq tonalites and granites of the Isukasia area, southern

West Greenland: development of the oldest-known sial: Contrib. Mineral. Petrol., v. 94, p. 137-148.
———, ———, Dimroth, E., Gill, R. C. O., and Rosing, M., 1983, Early (3700 Ma) Archaean rocks of the Isua supracrustal belt and adjacent gneisses: Rapp. Grønlands geol. Unders., v. 112, p. 5-22.
———, and Collerson, K. D., 1991, Very early Archean crustal-accretion complexes preserved in the North Atlantic craton: Geology, v. 19, p. 791 794.
———, Friend, C. R. L., Baadsgaard, H., and McGregor, V. R., 1989, Evolution and assembly of Archean gneiss terranes in the Godthåbsfjord region, southern West Greenland: Structural, metamorphic, and isotope evidence: Tectonics, v. 8, p. 573-589.
———, ———, Kinny, P. D., and McGregor, V. R., 1993, Anatomy of an Early Archean gneiss complex: 3900 to 3600 Ma crustal evolution in southern West Greenland: Geology, v. 21, p. 415-418.
———, Hagiya, H., and Maruyama, S., 1995, SHRIMP U-Pb single zircon geochronology of a Proterozoic mafic dyke, Isukasia, southern West Greenland: Bull. Geol. Soc. Denmark, v. 42, p. 17-22.
———, McGregor, V. R., Friend, C. R. L., Bennett, V. C., Kinny, P. D., 1996, The Itsaq Gneiss Complex of southern West Greenland: The world's most extensive record of early crustal evolution (3,900-3,600 Ma): Precam. Res. Special Issue: The oldest rocks on Earth, v. 78, p. 1-39.
Piper, J. D. A., 1982, The Precambrian palaeomagnetic record: the case for the Proterozoic supercontinent: Earth. Planet. Sci. Lett., v. 59, p. 61-89.
Rosing, M. T., Rose, N. M., Bridgwater, D., and Thompson, H. S., 1996, Earliest part of Earth's stratigraphic record: A reappraisal of the > 3.7 Ga Isua (Greenland) supracrustal sequence: Geology, v. 24, p. 43-46.
Schidlowski, M., 1988, A 3,800-million-year isotopic record of life from carbon in sedimentary rocks: Nature, v. 333, p. 313-318.
Shimamoto, T., Seno, T. and Uyeda, S., 1993, A simple rheological model for comparative subductology: Geophys. Monogr., The Jeffreyes volume, Am. Geophys. Union, v. 76, p. 39-52.
Shimizu, H., Nakai, S., Tasaki, S., Masuda, A., Bridgwater, D., Nutman, A. P., and Baadsgaard, H., 1988, Geochemistry of Ce and Nd isotope and REE abundances in the Amîtsoq gneisses, West Greenland: Earth Planet. Sci. Lett., v. 91, p. 159-169.
Storey, M., Mahoney, J. J., Kroenke, L. W., and Saunders, A. D., 1990, Are oceanic plateau sites of komatiite formation?: Geology, v. 18, p. 376-379.
Takahashi, M., 1986, “Island arc” magmatism before and after the spreading of Japan sea: Kagaku (in Japanese), v. 56, p. 103-111.
Takahashi, E., 1990, Speculations on the Archean mantle: missing link between komatiite and depleted garnet peridotite: Jour. Geophys. Res., v. 95, p. 15941-15954.
von Huene, R., Corvalán, J., Flueh, E. R., Hinz, K., Korstgard, J., Ranero, C. R., Weinrebe, W., and the CONDOR Scientists, 1997, Tectonic control of the subducting Juan Fernández Ridge on the Andean margin near Valparaiso, Chile: Tectonics, v. 16, p. 474-488.
Wynne-Edwards, H. R., 1976, Proterozoic ensialic orogenesis: the millipede model of ductile plate tectonics: Am. Jour. Sci., v. 276, p. 927-953.

## FIGURE CAPTIONS

**Figure 1.** Geologic map of the NE part of Isua supracrustal belt. The inset map is geotectonic map of southern West Greenland, simplified after McGregor et al. (1991). Three terranes, Akia (gray), Tasiusarsuaq (gray with horizontal bars), and Akulleq are shown. Akulleq terrane is composed of Ikkattoq gneiss (dark gray with white bars), Amîtsoq gneiss (stippled), and supracrustal rocks (black). Post-collision Qôrqut granite (cross) intrude mainly Akulleq terrane. The Isua supracrustal belt is located in the northeastern corner.

**Figure 2.** (A) Geological map of the Northern Unit. The western part of the Unit is underlain by mélange equivalent to those in circum-Pacific orogenic belts in the Phanerozoic. The randomly oriented blocks of cherts and greenstones are distributed within mafic sediments. On the other hand, the eastern part is underlain by two subunits with stratigraphic sequences of pillow lava flow and the overlying bedded cherts and BIF. (B) Sketch map of the greenstone-chert sequence of the Northern Unit. See the sketch location in Fig. 2a. It is underlain by the two subunits with pillow lava flow and hyaloclastite layer capped by chert/BIF sedimentary sequence.

**Figure 3.** Progressive metamorphism in the mapped area, which is subdivided into four zones based on mineral assemblages and anorthite content (An) of plagioclase in the metabasite. The metamorphic grade ranges from greenschist facies in the northernmost area through epidote-amphibolite transition to amphibolite facies in the Southern Unit.

**Figure 4.** Distribution pattern of duplexes bounded by layer-parallel faults in the Southern Unit. Eight duplexes are defined by both lithostratigraphy within a horse and fault distribution. Duplexes consist of several horses. Simplified-cross section of piling subunits is shown. The layer-parallel boundary thrusts among horses, both inter-duplexes and intra-duplex thrusts, are left-lateral and relative direction of fault displacement is shown by small arrows. They converge to the south or west. These structures are characterized by convergence and divergence of layer-parallel faults and are duplex structures. Faults at the bottom and top are called floor- and roof-thrusts, respectively.

**Figure 5.** Representative example of lithostratigraphy within Horse $III_2$. The lithostratigraphy is composed of metabasite, chert, muddy chert and mafic sediment, in ascending order. The metabasite unit consists of a pile of pillowed basalt with massive basaltic flow and hyaloclastite. The reworked hyaloclastite with rough surfaces and numerous metamorphic garnet megaporphyroblasts occurs at the top of the unit. The chert unit is dominantly composed of a white, massive type, whereas a white/blue type occurs near the bottom. The chert unit was intruded by several basaltic sills. Some carbonate pods sporadically occur between the metabasite unit and chert unit. Mafic sediment with graded bedding covers the chert unit at the top. Muddy chert occurs as transitional

sediments between the chert unit and mafic sediments. Some carbonate layers are interleaved into muddy chert and mafic sediments. The reconstructed lithologies are compared with oceanic plate stratigraphy (See the text and Fig. 11).

**Figure 6.** (a) A sketch map to show the complex deformation patterns characteristic in the turbidite sequence. Turbidite sequence belongs to Horse $IV_2$. See the location on Fig. l. The area is subdivided into four blocks, named I, II, III and IV. The NS cross sections and reconstructed lithostratigraphy are shown in Fig. 7. Inset figure is lower hemisphere equal-area projections of poles to tectonic layering from all the blocks. Large shaded squares are eigenvectors based on a cylindrical best fit to data. Note the location of photo 1. (b) Magnified sketch map of the eastern part. (c) Magnified sketch map of the western part. (d) The outcrop in this sketch is close to the west of the sketch map (a). Although the outcrop is about 20 m far from that of sketch (a), the continuous stratigraphy can be reconstructed by means of tracing the key bed (the muddy chert layer).

**Figure 7.** A schematic NS profile of chert-turbidite unit in Fig. 6 and the reconstructed lithostratigraphy. Note the stratigraphic change from basalt and chert, through muddy chert to turbidite, including conglomerate. Note also the upward coarsening of the sedimentary body.

**Figure 8.** A sketch of Horse $III_2$ showing the stratigraphic relationship between pillow lava flow unit, hyaloclastite and reworked hyaloclastite, dolomitic carbonate pods, and massive white chert beds on the top. Location of photos 4 and 10 are shown.

**Figure 9.** Lithostratigraphies of Duplexes I to VIII in comparison with that of Mesozoic Japan (Isozaki et al. 1990). See text for details.

**Figure 10.** (a) Schematic diagrams of oceanic plate stratigraphy and the travel history of an oceanic plate, after Isozaki et al. (1991). When the plate is formed at a mid-ocean ridge, it is composed of basaltic lava flows with/without the overlying carbonate pods. The bedded chert is deposited on the oceanic crust during its migration from the ridge to the trench. Once OIB volcanism occurs on the way between the ridge and trench, its product is deposited on or intruded into the basaltic flow piles and the overlying bedded chert, and bedded chert is deposited on the complex again. Hemipelagic sediment including chert and some terrigenous pelitic sediments are deposited near the outer trench, and finally turbidite covers all units at the trench. Note the great similarity of lithostratigraphy in the Isua belt to that of Japan. (b) Mode of accretion of subducted oceanic materials, modified after McClay (1992). As a result, a duplex belt is formed from top to bottom, by successive accretion with time. Each duplex consists of several horses with similar oceanic plate stratigraphy. The duplex is cut on the top and bottom by roof- and floor-thrusts, respectively. Deformation concentrates in unconsolidated to semi-consolidated sediments; heavily deformed in the turbidite and deep-sea sediments, and less deformed in the competent oceanic crust. (c) A schematic diagram of accretion of oceanic materials at trench.

**Figure 11.** Travel history of Early Archean oceanic lithosphere in the Isua accretionary belt, West Greenland. This diagram shows paleogeographic reconstruction of accreted oceanic lithosphere, being followed by successive underthrusting of oceanic crust to form duplexes from Duplex VIII to I with time.

**Figure 12.** Comparative paleogeography of the Phanerozoic arc-trench system, ridge subduction (a) versus old plate subduction (b) after Maruyama (1997a). On the ridge subduction, regional uplift and fore-arc CA volcanism occur due to hot and buoyant plate subduction. Large amounts of sediments, including conglomerate, are supplied to the trench. The wide lateral extent of slab melting leads to more active island arc volcanism.

**Figure 13.** N-S cross-section of the SW Japanese arc (a) in comparison with NW-SE cross section of the Akulleq terrane near Isukasia, West Greenland (b). Note the 100 Ma granite-greenstone terrane in Japan. Successive oceanward growth of arc due to addition of new crust by TTG makes the older accretionary complexes “enclaves” within TTG plutons. Also note the 100 Ma gneiss terrane which has been derived from granite-greenstone terranes formed in the lower crustal levels by synchronous TTG plutonism.

**Figure 14.** A speculative cartoon showing 3.8 Ga water planet Earth and its satellite Moon. Plate tectonics had already started, however there was no solid inner core, double-layered mantle convection, no large continents. Instead a number of intra-oceanic island arcs of *ca.* 1000 oceanic microplates, abundant off-ridge volcanism related to mantle upwellings, and plume- or bombardment-triggered spreading axis, all characterized the early Earth at 3.8 Ga. One plate satellite, Moon was active only by heavy extra-terrestrial bombardments and related Mare volcanism.

## PHOTO CAPTIONS

**Photo 1.** Mafic sediment ($MS_4$) on the left and the underlying carbonate layers on the right. The boundary between the two units is a knife-edge layer-parallel fault ($T_2$), which is recognizable because carbonate layers form isoclinal folding ($F1_b$) and the folding axis is clearly cut by the fault, whereas the upper mafic sediments form rhythmic bedding without folding. The scale is 60 centimeters by carpenter's rule. The locality is Horse $IV_2$.

**Photo 2.** Conglomerate. This layer is located on the top of the lithostratigraphy of Horse $IV_2$. The gravel is polymictic, varying in size (pebble to cobble). The clasts are significantly flattened due to post-depositional deformation. This conglomerate-bearing unit is interlayered with carbonate layers in some places. The pen scale is 15 centimeters long.

**Photo 3.** Rhythmic alternation of chert and banded iron formation (upper half) and underlying mono-lithological magnetite-rich BIF. BIF crops out widely in the eastern part of the Northern Unit. The rhythmically layered BIF is highly deformed due to syn- or post-emplacement deformation.

**Photo 4.** Pillow lavas. Some basalts preserve original pillow lava structure in this figure. Each pillow consists of core (green), mantle (darker green), rim (pale green to white colored) and matrix (darker green). Each pillow is flattened by regional deformation.

**Photo 5.** A basaltic dike, cutting pillow basalt and overlying hyaloclastite layers. The hammer is on the boundary between the dike and pillowed basalt. Many drilled holes for paleomagnetism studies are visible along the sharp boundary of the intruded dike. See the location on Fig. 8.

**Photo 6.** Ultramafic rocks. The ultramafic rocks occur as discrete tectonic blocks, sedimentary debris interlayered with sandstone or talc-bearing layers intercalated by bedded chert. The photograph displays the small ultramafic tectonic massif within metabasite.

**Photo 7.** Ameralik dyke. Ameralik dykes are characterized by white patches of plagioclase megacrysts, and have been regarded as a marker for the oldest terrane in SW Greenland. The photograph shows that the dike was intruded into the bedded chert and that plagioclase xenocrysts are concentrated under the roof of the dike (sill-like) along the overlying chert (left).

**Photo 8.** The east-dipping boundary between Amîtsoq gneiss (left, white) and supracrustal belt (right, dark-colored) on the west side of the supracrustal belt. The contact is highly deformed and recrystallized to form a mylonite zone, a few meters wide.

**Photo 9.** The fault boundary between Amîtsoq gneiss (upper, white) and supracrustal belt (lower, strongly folded) on the east side of the supracrustal belt. The hammer is on the side of Amîtsoq gneiss. Supracrustal rocks are severely deformed, whereas Amîtsoq gneiss is relatively undeformed.

**Photo 10.** A photograph illustrating well-preserved pillowed basaltic flows, hyaloclastite,

reworked hyaloclastite, and the overlying bedded chert from the right to the left side. The geologist stands on the chert beds. The locality is shown on the sketch (Horse $III_2$) of Fig. 8.

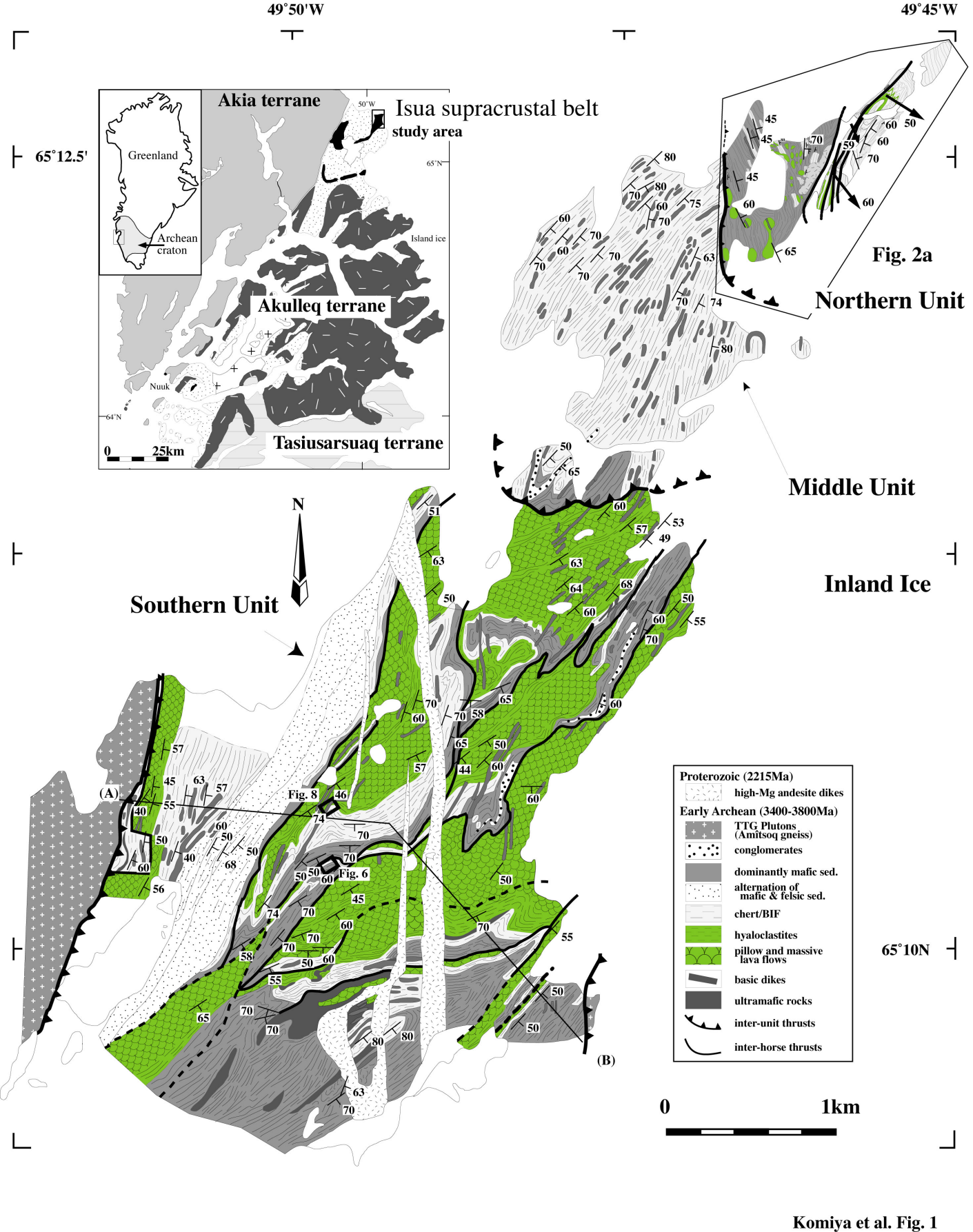


Komiya et al. Fig. 1

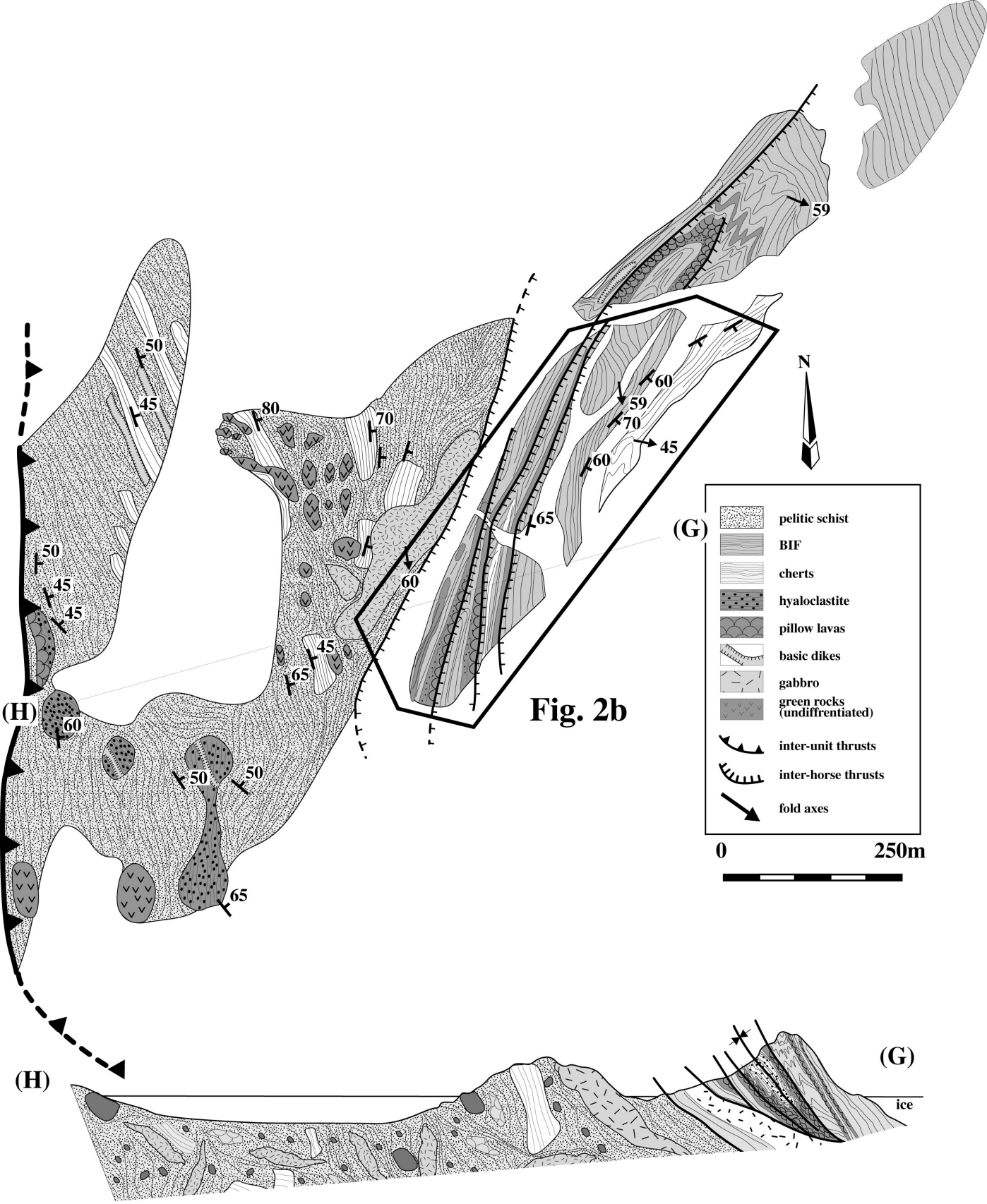


Komiya et al. Fig. 2a

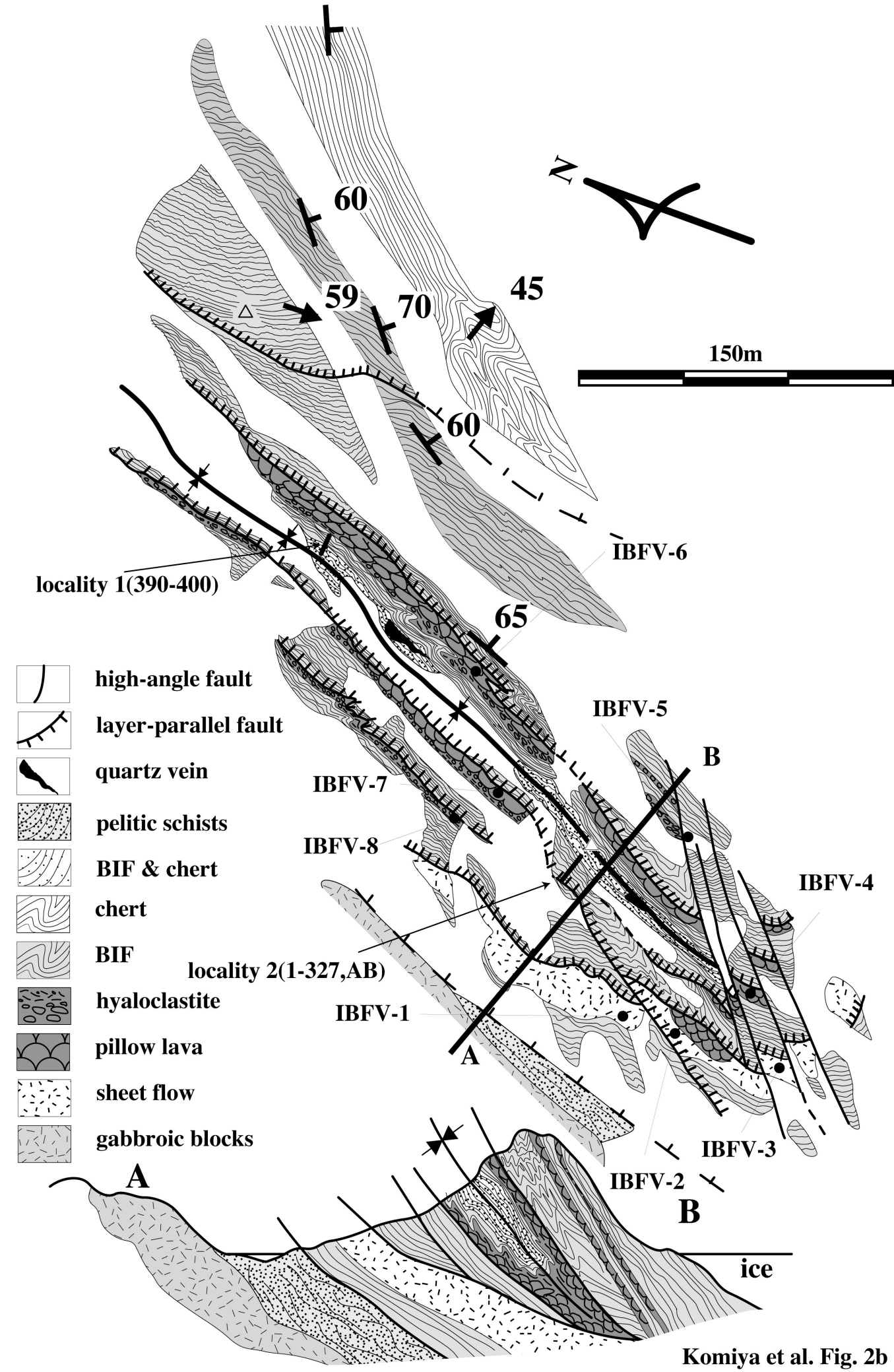


Komiya et al. Fig. 2b

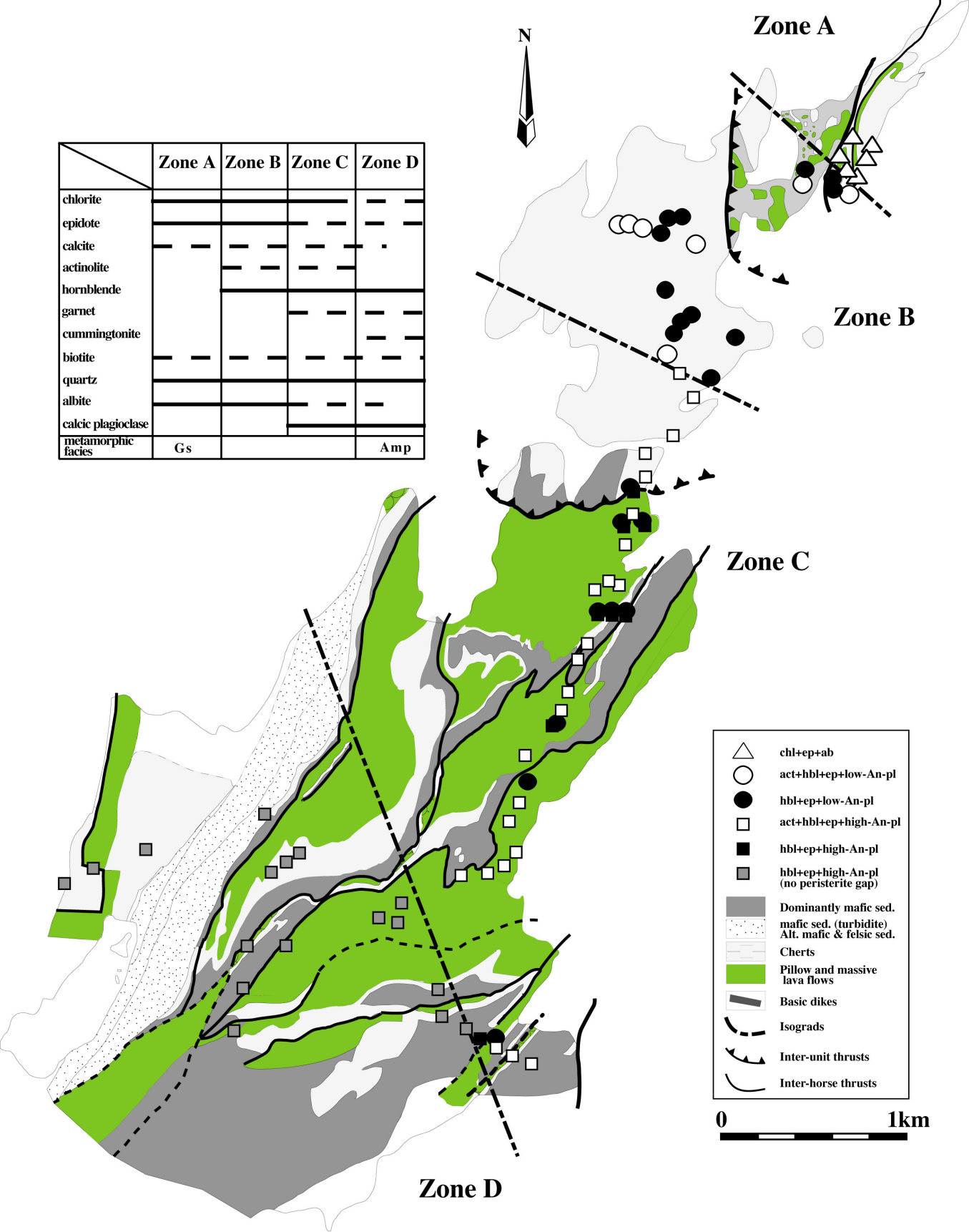


Komiya et al. Fig. 3

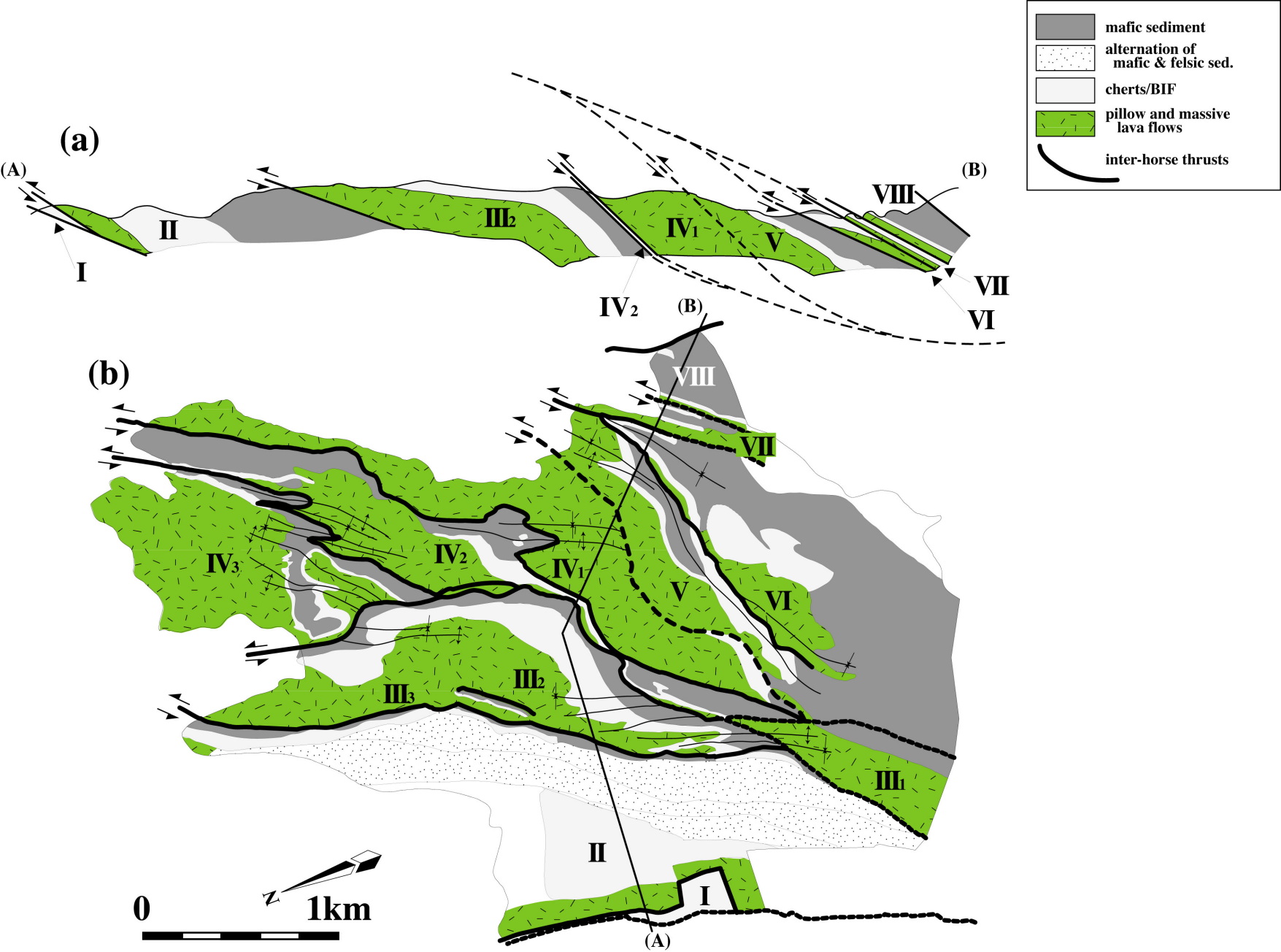


Komiya et al. Fig. 4

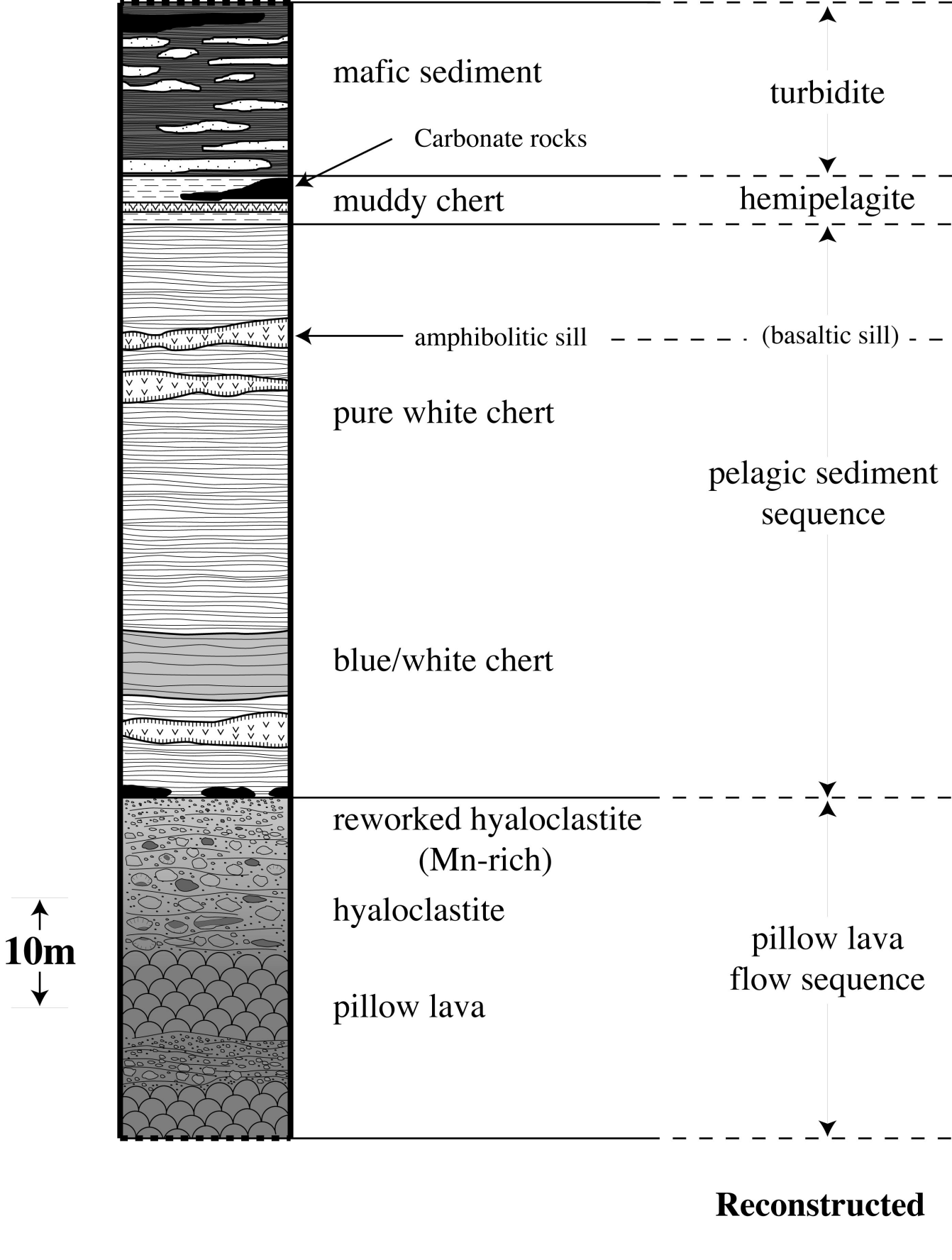


Komiya et al. Fig. 5

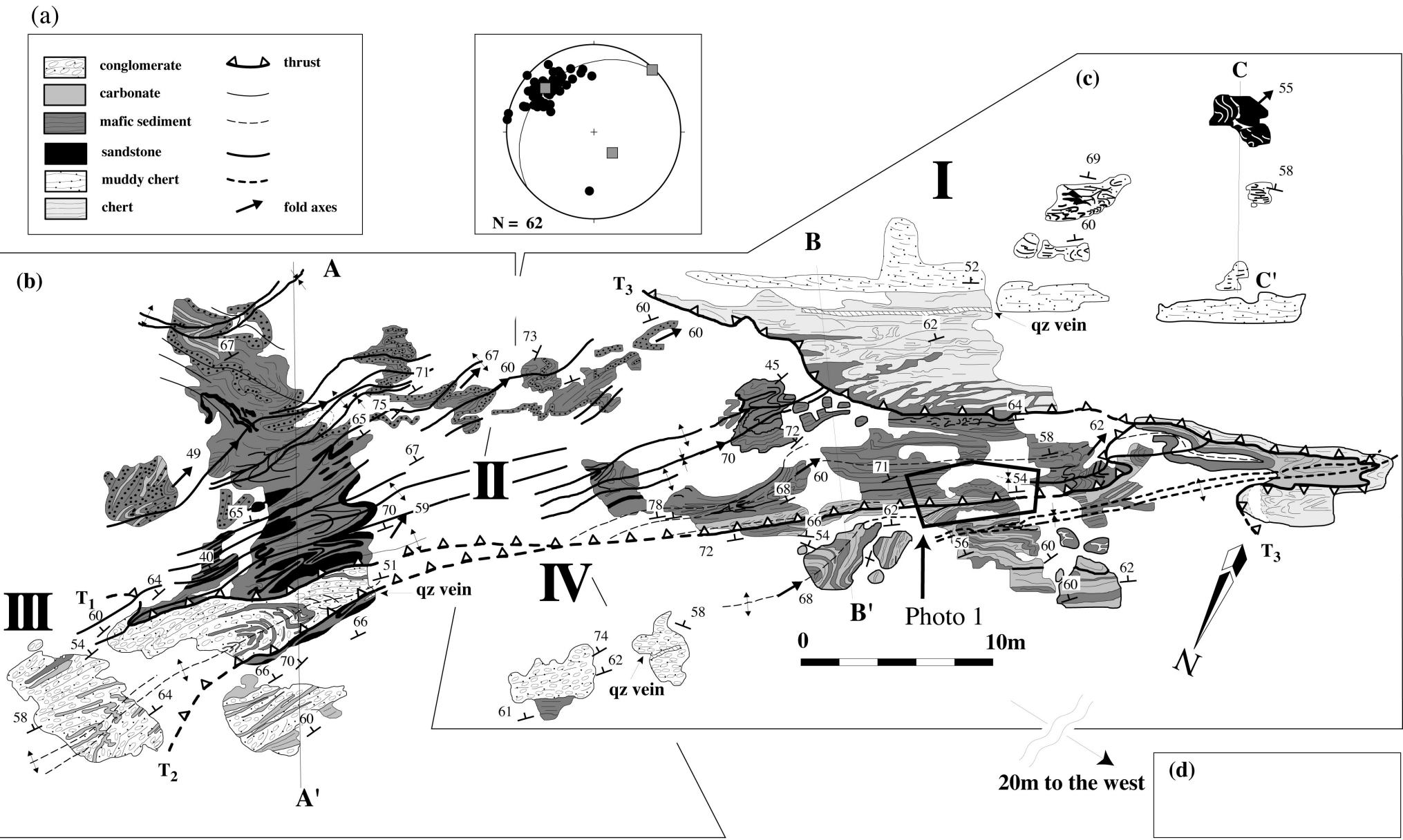


Komiya et al. Fig. 6a

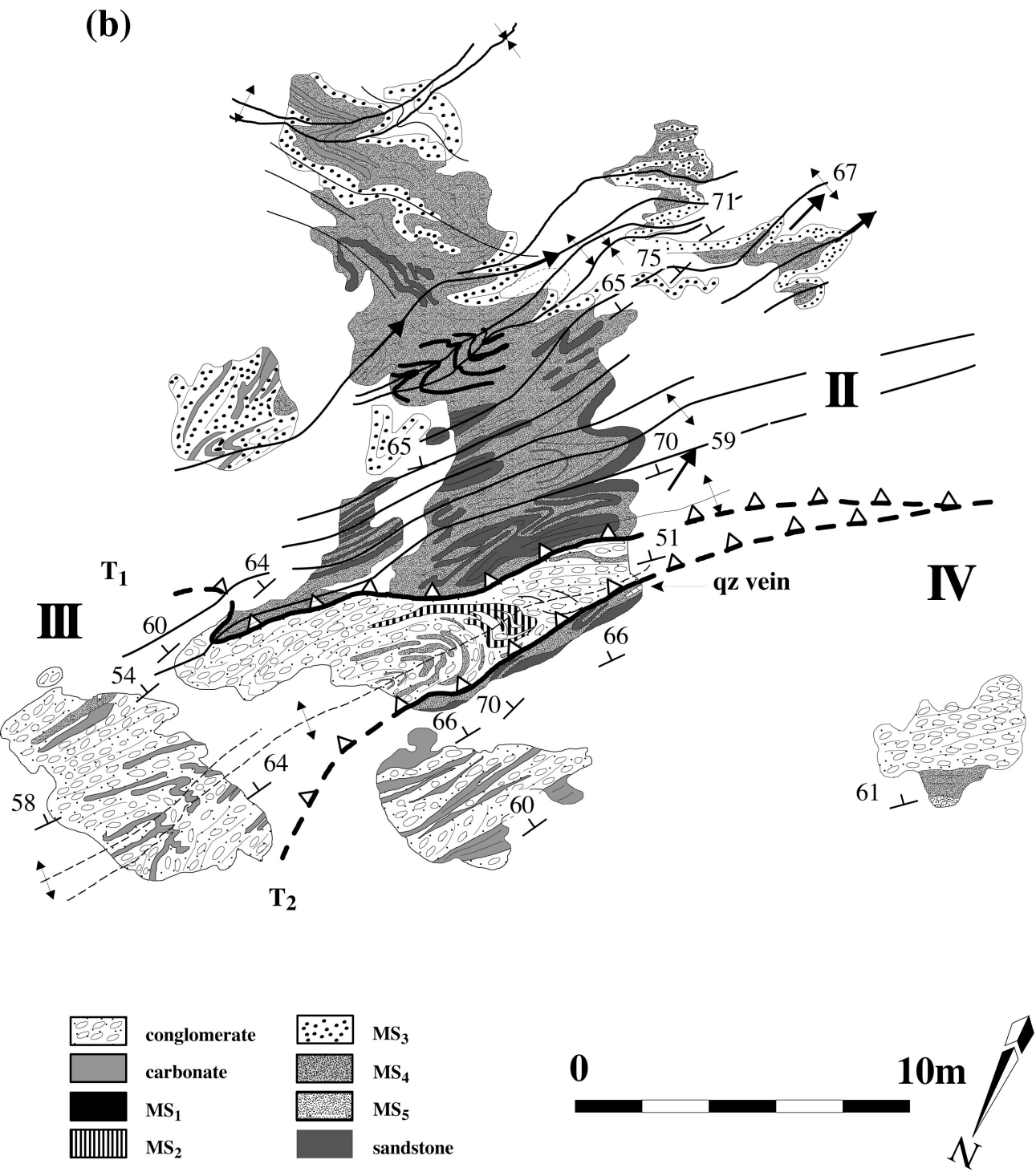


Komiya et al. Fig. 6b

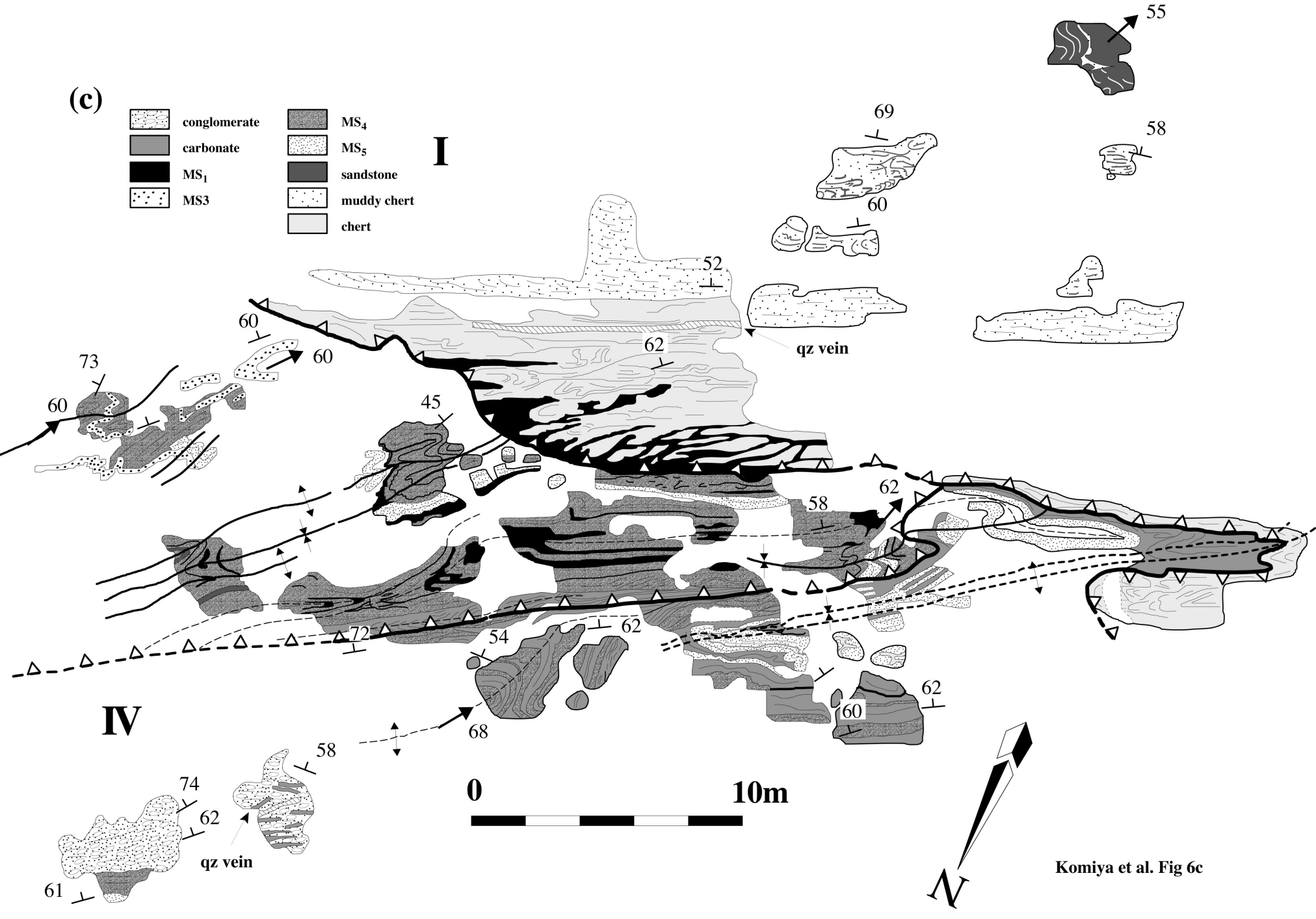


Komiya et al. Fig 6c

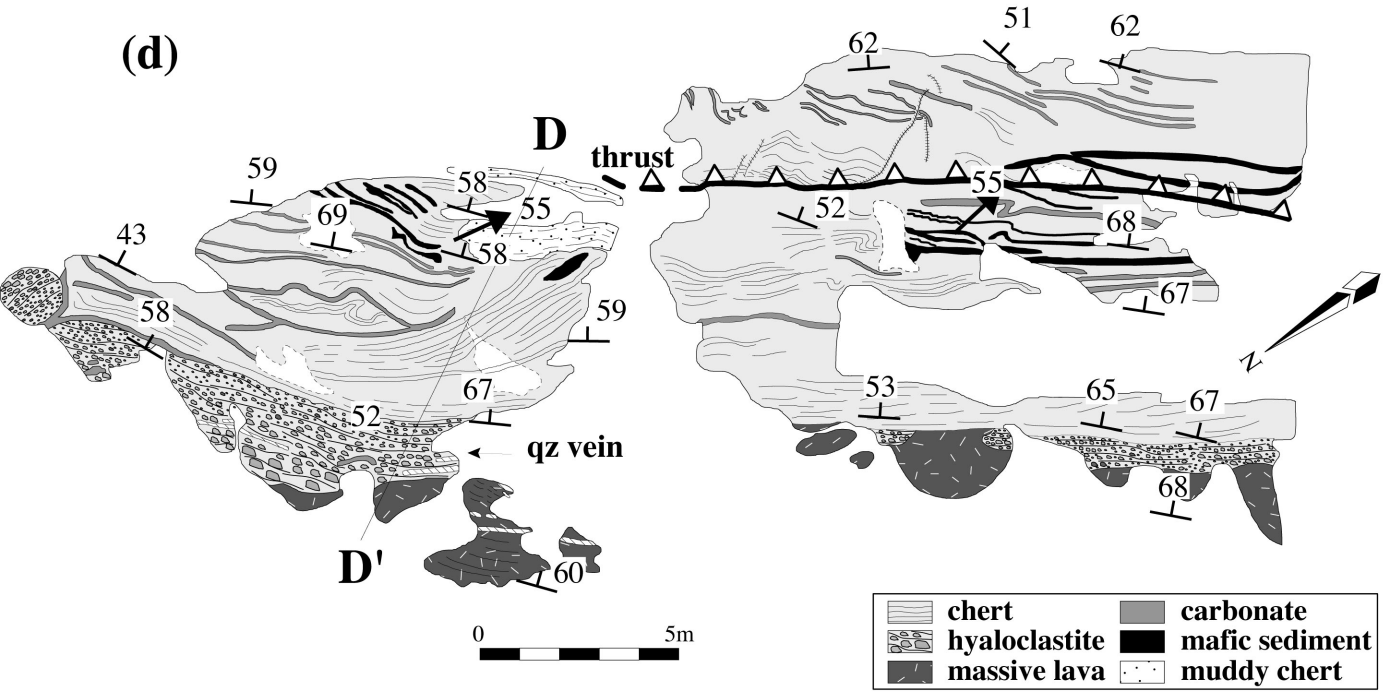


Komiya et al. Fig. 6d

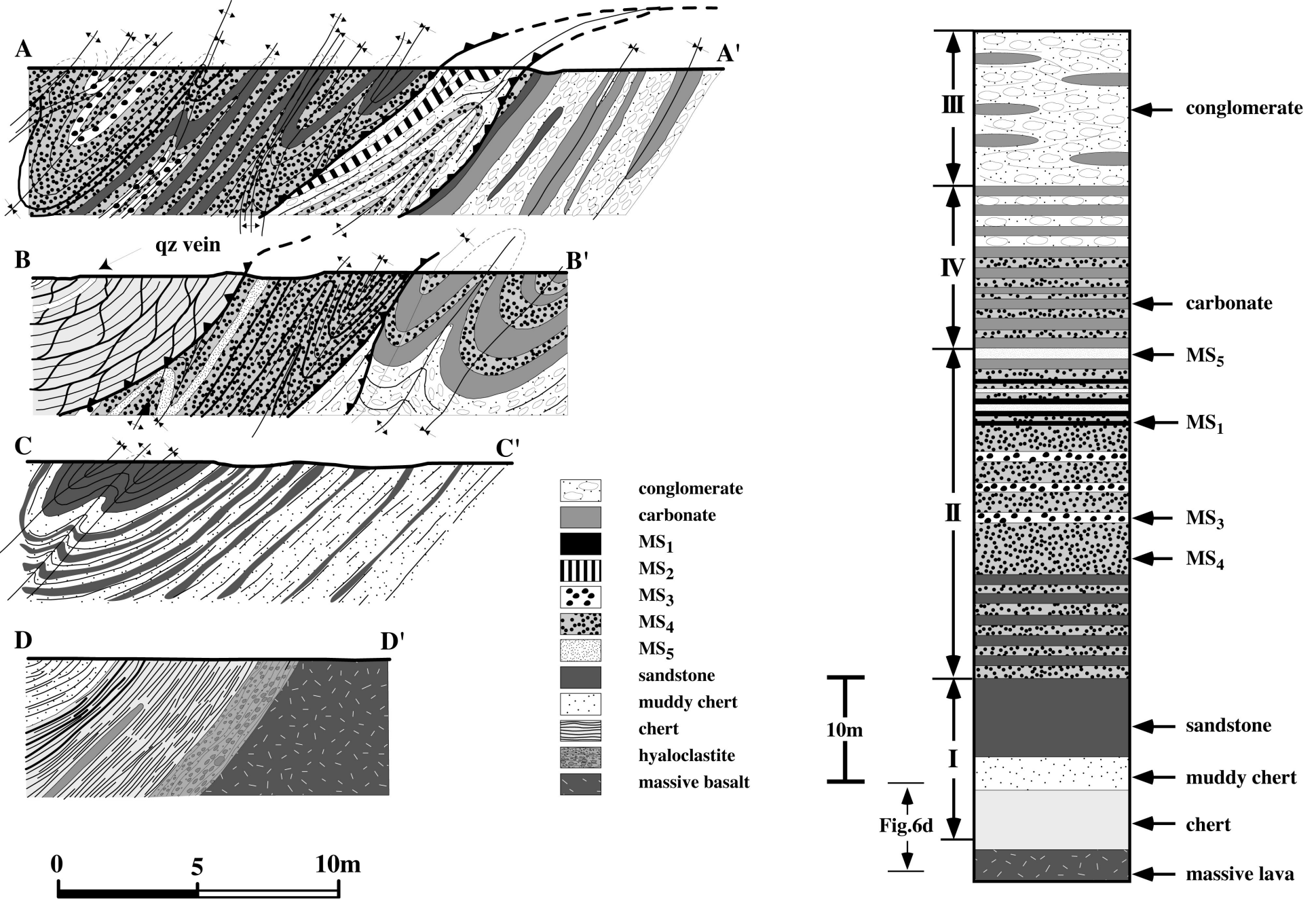


Komiya et al. Fig. 7

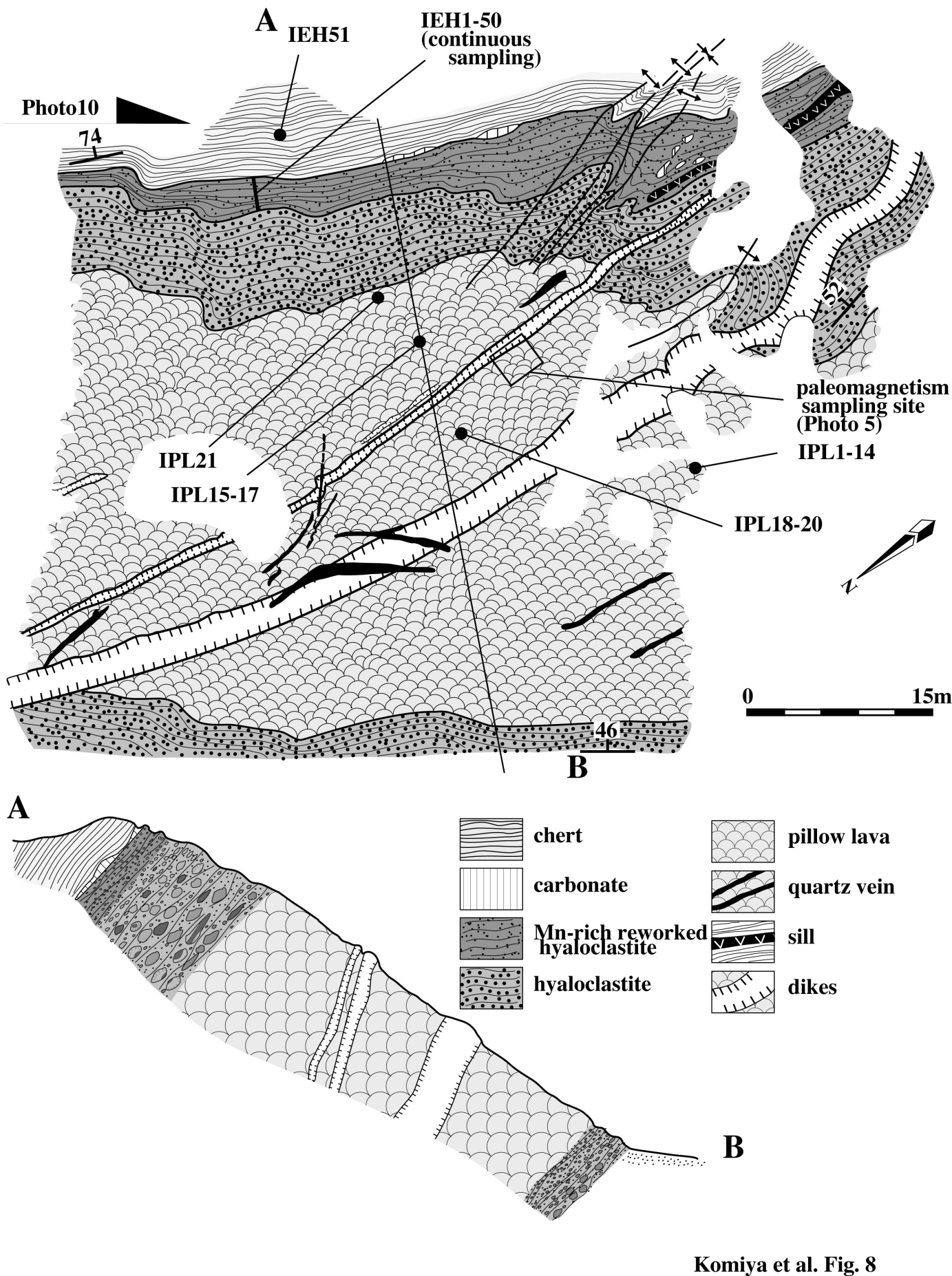


Komiya et al. Fig. 8

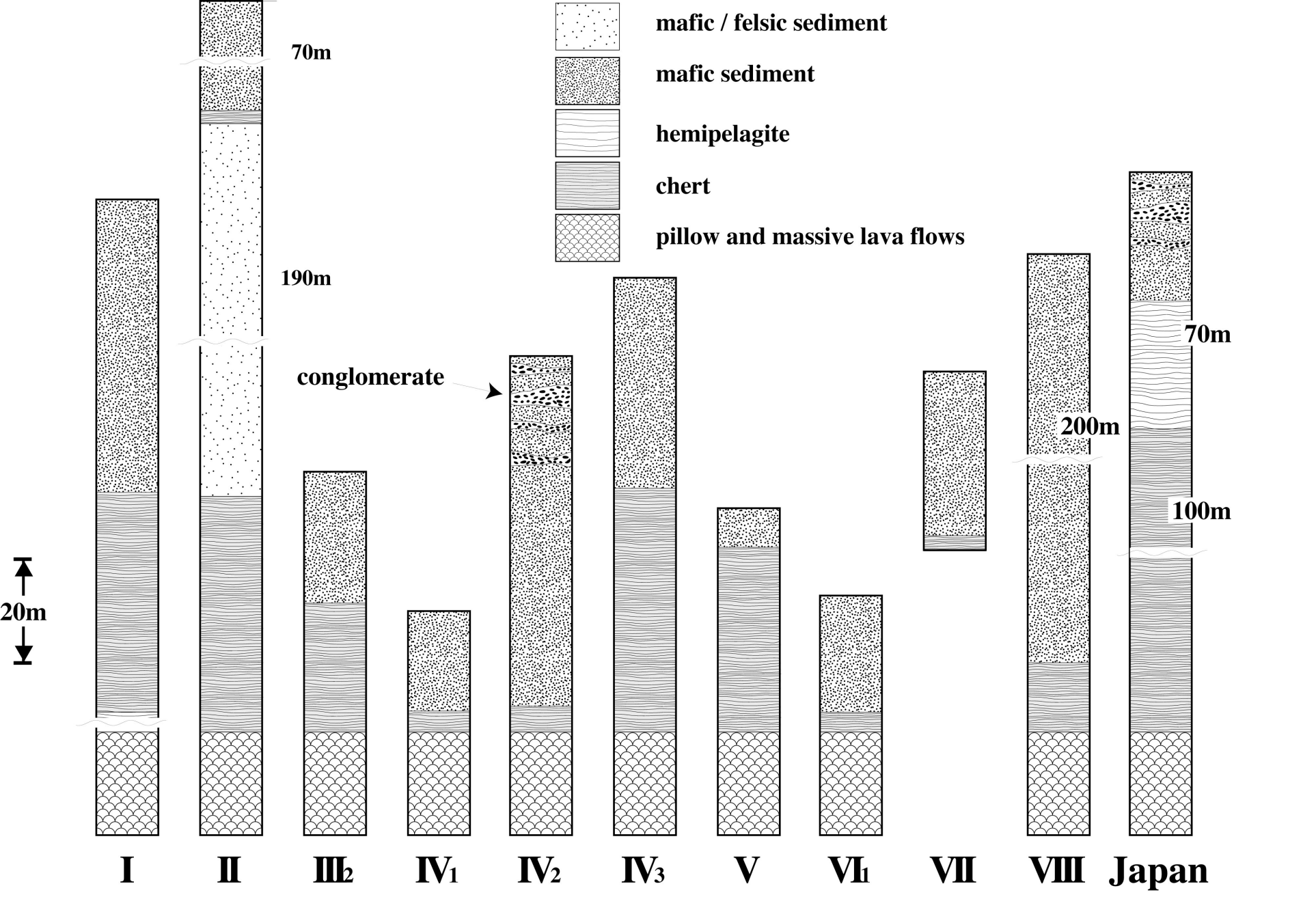


Komiya et al. Fig.9

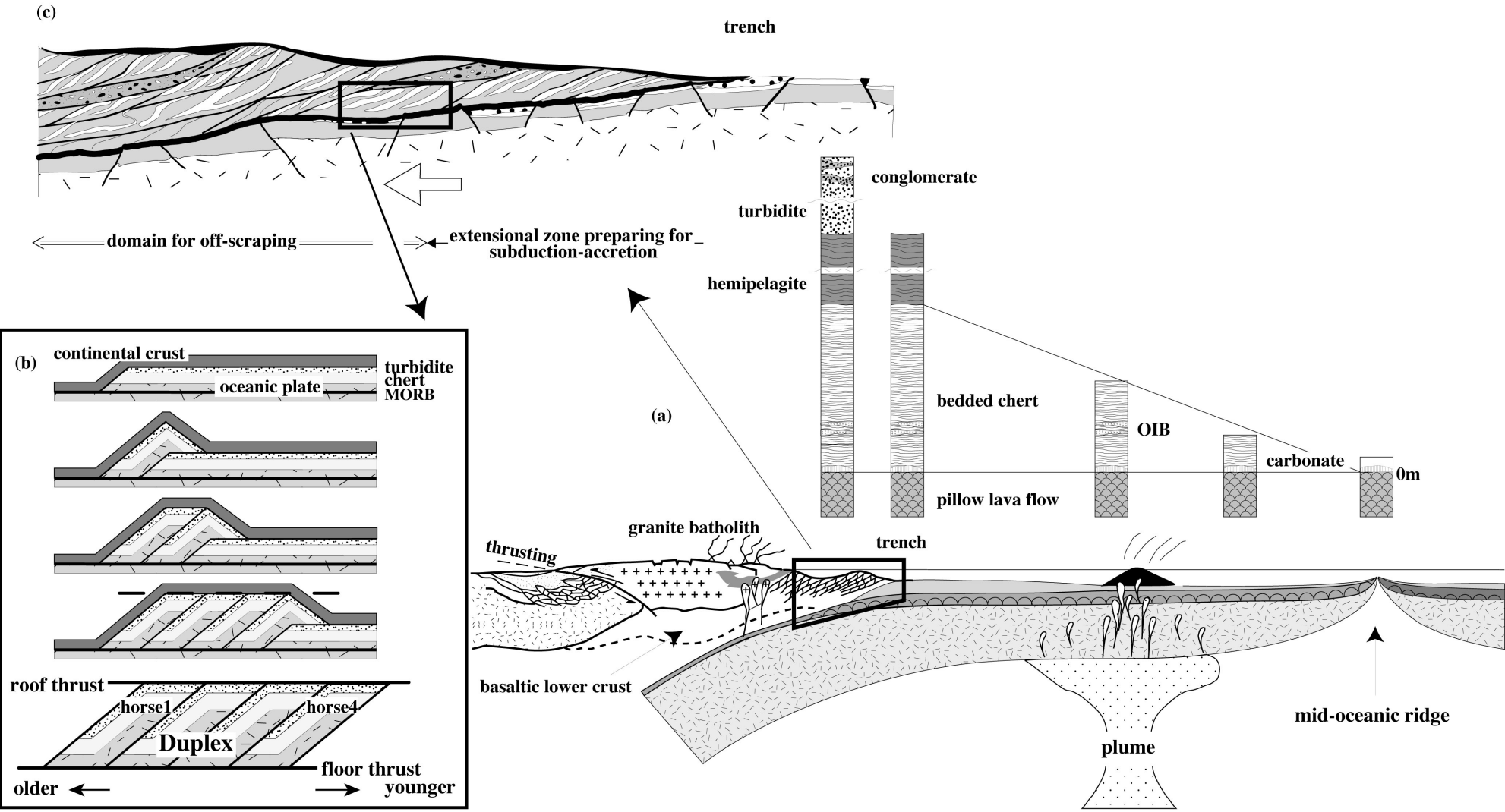


Komiya et al. Fig. 10

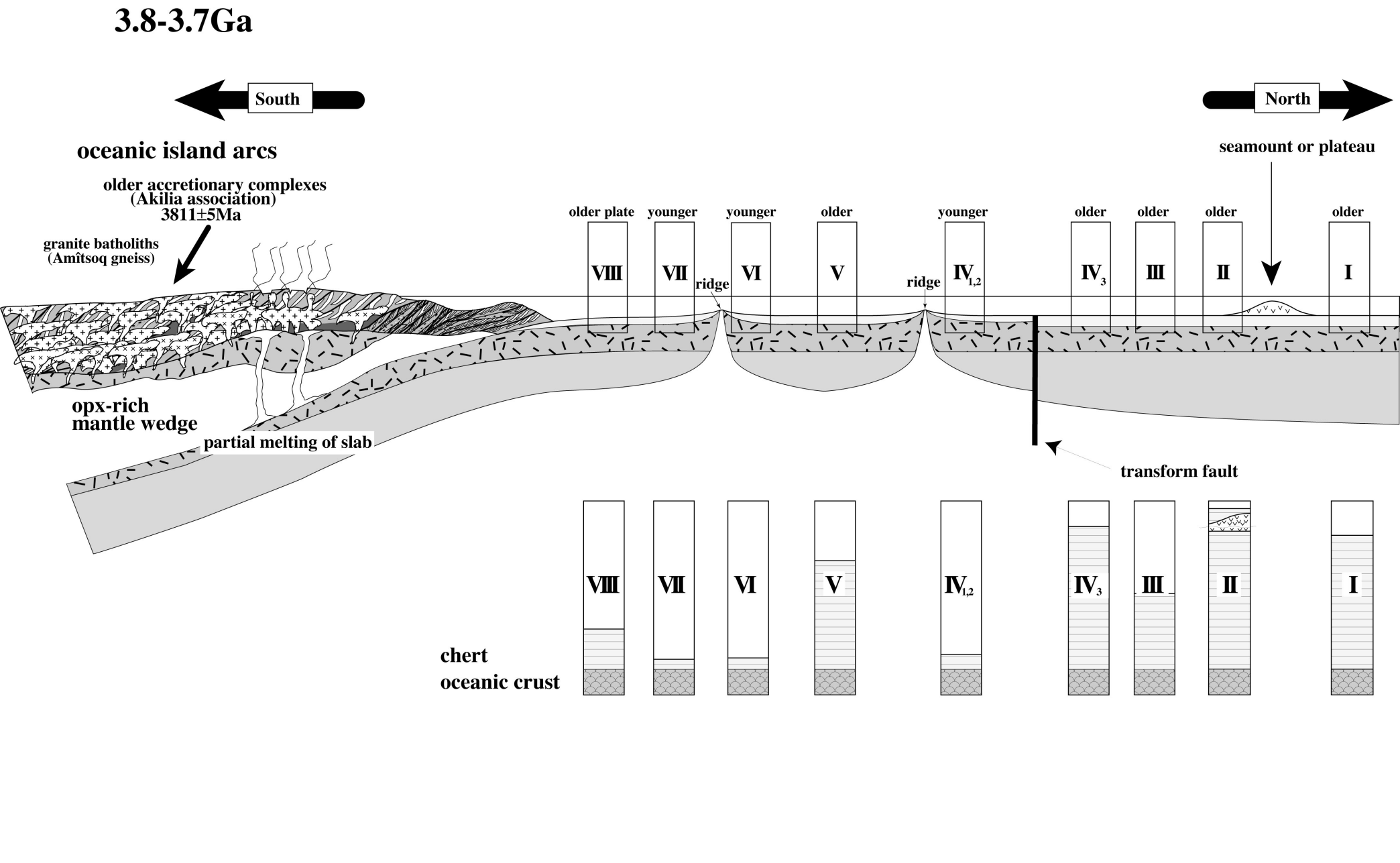


Komiya et al. Fig.11

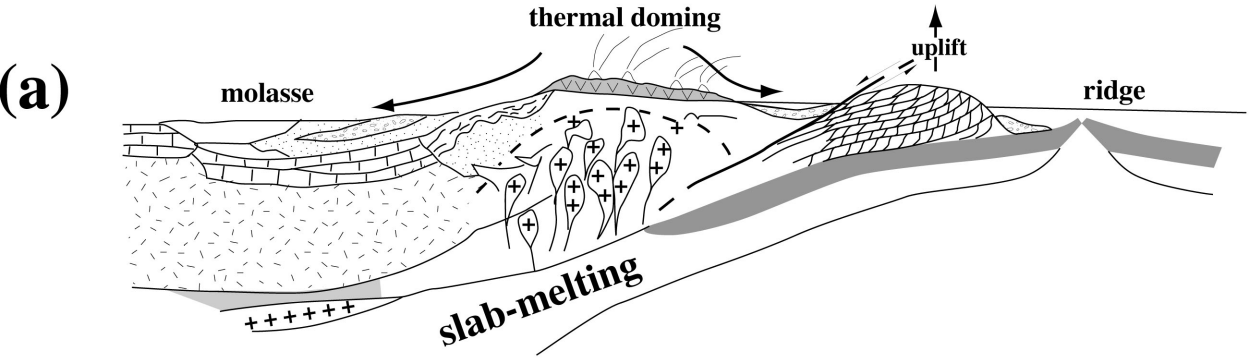


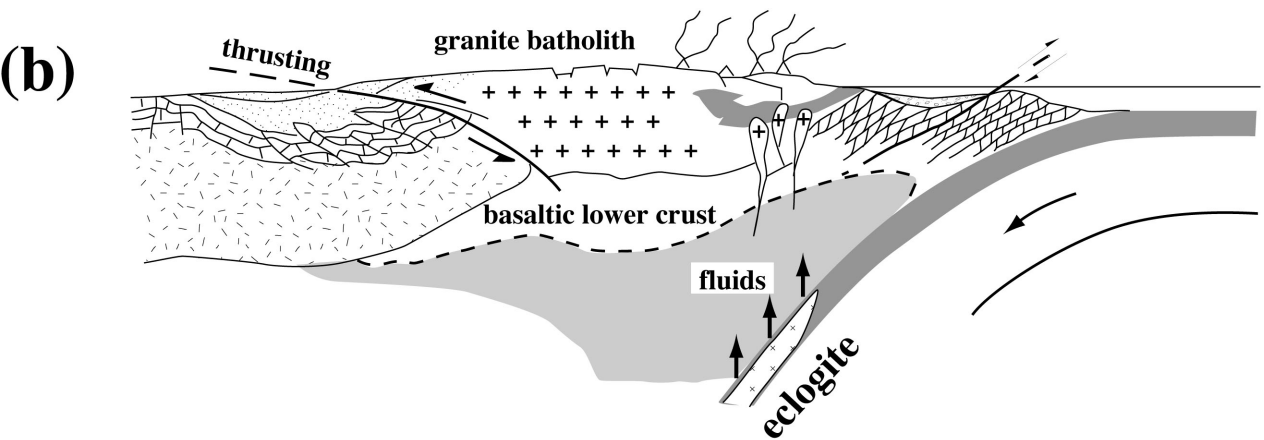


Komiya et al. Fig. 12

(a)

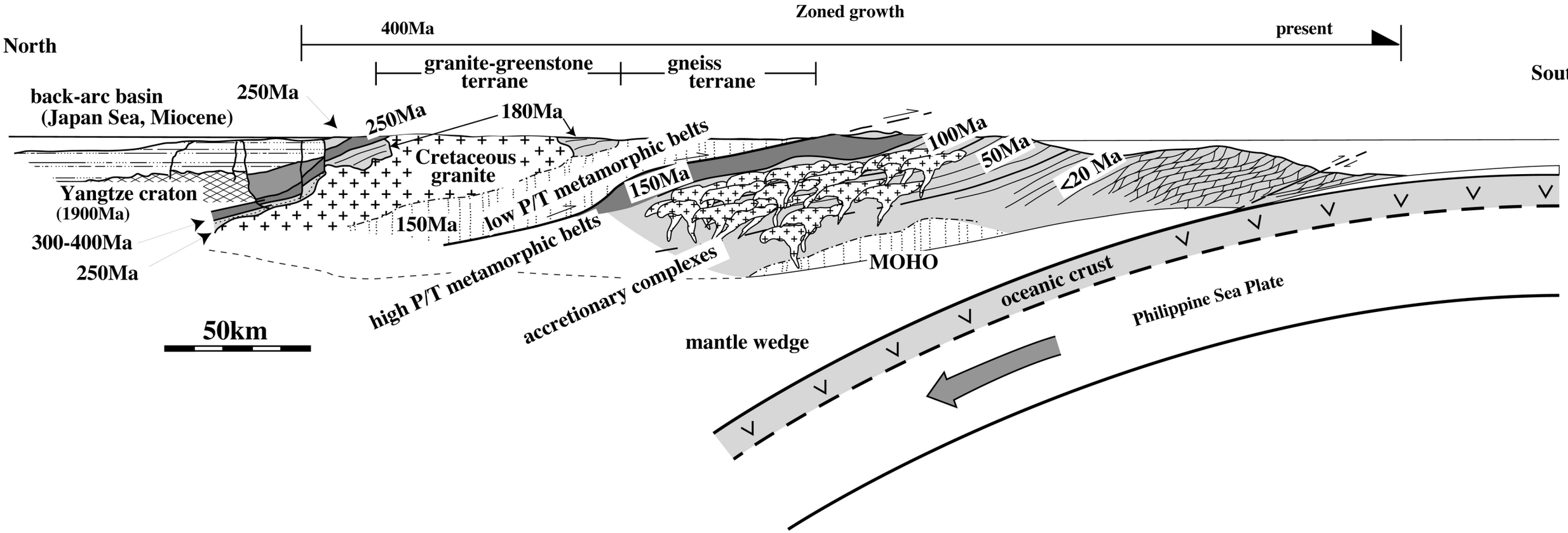


(b)

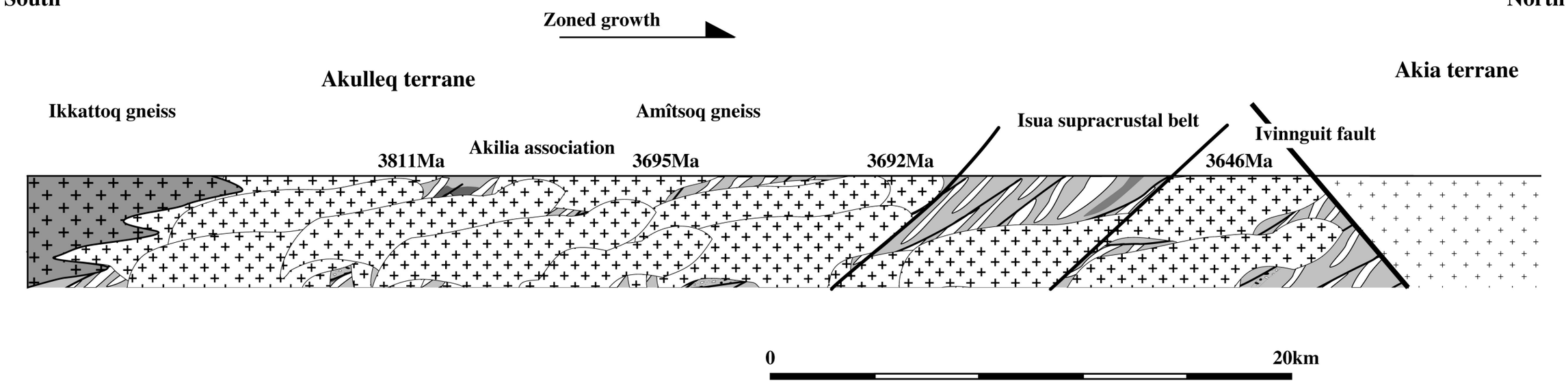


Komiya et al. Fig.13

# 3.8 Ga

## Earth

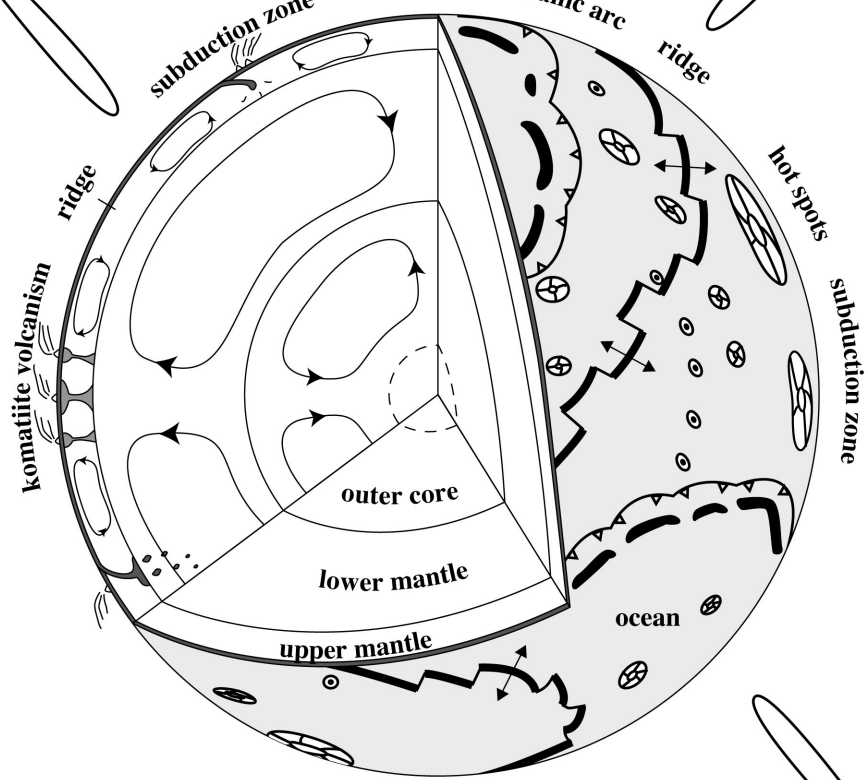


planetsimal

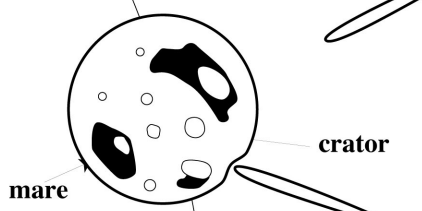


## Moon

Komiya et al. Fig. 14

'93 8

'83 7 24

'93 8 10

'93 7 25

'93 8 13

'93 7

# II. Geology of the Beasley river area and geochemistry of greenstones, the Hamersley Group (2.5 Ga), Western Australia

*Tsuyoshi Komiya*,

Department of Earth and Planetary Sciences, Tokyo Institute of Technology, Tokyo 152-8551, Japan

fax: +81-3-5734-3538 e-mail: tkomiya@geo.titech.ac.jp

## II-1 Introduction

The Archean-Proterozoic boundary has been arbitrarily defined to be at 2500 Ma by the IUGS Subcommission on Precambrian Stratigraphy (SPS) (Plumb and James 1986). However, when absolute age dating was initially unavailable, the transition from the Archean to the Proterozoic era was historically conceived in terms of a change in tectonic and sedimentation style. The Archean geological terrain is characterized by the granite-greenstone belt and gneiss terrain, and made up of greenstone belt which is composed of the thrust-bounded units of greenstone, chert and turbidite units, and the granitoid intruding them. On the other hand, the Proterozoic era had been defined by the emergence of the large flat-lying sedimentary sequences unconformably overlying on the granite-greenstone terrain. Recent extensive dating of Precambrian terrains reveals that the transition spanned more than 500 Ma; from 3.12 Ga Witwatersrand sedimentary basin, 2.95 Ga the Whim Creek belt and the Lalla Rookh basin, Western Australia, and 2.7 Ga Belingwe greenstone belt, Zimbabwe, and resulted in the controversy on the driving force of the evolution from the Archean tectonics to the Proterozoic tectonics (Breuer & Spohn, 1995). This paper presents the geology of the Beasley River area of the Hamersley Group, the Early Proterozoic sedimentary basin in Western Australia and the geochemistry of greenstones at the three stratigraphic levels. The results imply hot lower mantle material shoots up into the upper mantle at the time.

## II-2 Geological outline

In the Western Australia are made up of two large cartons; the Yilgarn Craton in the south and the Pilbara Craton in the north, respectively. The Capricorn Orogen, a major zone of deformed, low- to high-grade metamorphic rocks and granitoid intrusions lying between the Yilgarn and the Pilbara Craton, and was derived from collision of the Pilbara Craton with the Yilgarn Craton at 1.9 Ga. The Pilbara Craton is exposed over an area of 183,000 $km^2$ and is subdivided into two tectonic components: a granite-greenstone terrain (the Pilbara Supergroup), formed between 3.5 and 2.8 Ga, and a volcano-sedimentary succession in the Hamersley Basin unconformably overlying on the Supergroup (the Mount Bruce Supergroup), made up between 2.8 and 2.4 Ga. The former occurs over the northern, one thirds of the Craton, and is also exposed in several inliers further south (e.g. Wyloo, Rocklea and Milli Milli Domes, and the Sylvania Inlier) (Fig. 1). The latter is exposed in the southern two-thirds of the Craton, or forms outliers on the granite-greenstone terrain to the north (e.g. in Marble Bar area). It is made up of three stratigraphic components; Fortescue Group, Hamersley Group and Turee Creek Group in chronological order (Thorne, 1990: Hickman et al., 1990).

The Fortescue Group has maximum thickness of 6.5 km and forms about 40 percent of the outcrop area of the Hamersley Basin. The succession consists mainly of mafic volcanics,

volcaniclastic rocks, sedimentary rocks, and (platform) carbonate. Mafic and acidic intrusive igneous rocks are also in an important component locally. The Group is subdivided into six stratigraphic units; Mount Roe Basalt, Hardy Formation, Kylena Basalt, Tumbiana Formation, Maddina Basalt and Jeerinah Formation in ascending order. Detailed descriptions about those formations have been reviewed by Thorne (1990). U-Pb zircon chronological studies show that the Group were formed between ca. 2775±10 and 2684±6 Ma, felsic lava or tuff units occurring close to the base of the Group and felsic volcaniclastic units in the upper part of the Jeerinah Formation, respectively (Thorne, 1990).

The Hamersley Group conformably overlies the Fortescue Group and occupied most of the remaining 60 percent of the Hamersley Basin. It has a maximum thickness of about 2.5 km and consists mainly of banded iron formation (BIF), shale, carbonate and tuff, interlayered with mafic and felsic intrusive igneous rocks. The Hamersley Group consists of eight stratigraphic units; Marra Manba Iron Formation, Wittenoom Dolomite, Mt. Sylvia Formation, Mt. McRae Shale, Brockman Iron Formation, Weeli Wolli Formation, Woongarra Volcanics and Boolgeeda Iron Formation in ascending order. Moreover, Brockman Iron Formation is subdivided into Dales Gorge Member, Whaleback Shale Member, Joffre Member, and Yandicoogina Shale Member in order of age. The Group is characterized by abundance of banded iron-formation (BIF), but intrusive and extrusive igneous rocks (both mafic and acidic rocks) also occur pervasively, over 40 percent of the Group. The geochronology of Hamersley Group had been poorly-understood, and few U-Pb zircon ages were reported; 2,490±20 Ma from the Dales Gorge Member, and 2,470±30 Ma from Woongarra Volcanics (Compston et al. 1986). Recently SHRIMP ages, however, gave the tight constraint of the depositional and eruption ages; a tuff band in the Dales Gorge Member at 2,470±4 Ma, felsic tuffaceous sandstone in the Weeli Wolli Formation at 2,449±3 Ma, and rhyolite sheet in the Woongarra Rhyolite at 2,449±3 Ma (Barley et al. 1997).

The Turee Creek Group conformably overlies the Hamersley Group, and consists largely of argillite and sandstone, intercalated with minor carbonate and conglomerate. It occurs in scattered localities in the southern Hamersley Basin and has a maximum thickness of nearly 5 km. There are no geochronological data from this Group.

The Wyloo Group, which is an arcuate belt of Proterozoic sedimentary, unconformably covers the Hamersley Group and volcanic rocks which forms the northern margin of the Capricorn Orogen. The Wyloo Group consists of seven stratigraphic units; Beasley River Quartzite, Cheela Springs Basalt, Wooly Dolomite, Mount McGrath Formation, Duck Creek Dolomite, June Hill Volcanics, and Ashburton Formation in ascending order (Thorne and Seymour, 1991). The age of the Wyloo Group is poorly known but it is thought that the Group has a probable age of approximately 2000 Ma (Gee, 1980).

In general, rocks in the Hamersley Group have undergone very low- to low-grade metamorphism, and their metamorphic mineral assemblages indicate gradation from prehnite-pumpellyite in the south to (prehnite-) epidote-actinolite in the north (Smith et al., 1982).

Thorne and Seymour (1991) have reviewed the detailed tectonic evolution of Mount

Bruce Supergroup. The tectonic evolution is made up of seven continual events; (1) rifting of the Pilbara Craton and deposition of the Fortescue Group, (2) Hamersley Group sedimentation on a passive continental margin and the formation of oceanic crust, (3) the beginning of southward subduction and Beasley River Quartzite deposition on active (convergent) continental margin, (4) continental collision and deposition of the Mount McGrath Formation, (5) crustal loading and foreland basin subsidence leading to deposition of the Duck Creek Dolomite, (6) sedimentary infilling of the foreland basin by Ashburton Formation, and (7) deposition of the Capricorn Formation.

## II-3 Geology of the Beasley River Area, Hamersley

### II-3.1 Stratigraphic subdivisions

The Beasley River area is located in the southern edge of the Hamersley Basin and on contact of the Ashburton Basin (Fig. 1). We have carried out a geologic mapping in six summers since 1991 (Fig. 2). This area is subdivided into six subunits based on lithologies; the Lower lava flow Unit, the Lower BIF Unit, the Middle BIF Unit, the Komatiitic Unit, the Rhyolite Unit, the Upper BIF Unit, and the Uppermost sedimentary Unit, in order from the north to the south. The subdivisions by this work are compared with conventional stratigraphic subdivisions. The Lower lava flow Unit is equivalent to the Bunjinah Formation in the Fortescue Group. Both the Lower BIF Unit and the Middle BIF Unit, the Komatiitic Unit, the Rhyolite Unit, and the Upper BIF Unit are to Brockman Iron Formation, Weeli Wolli Formation Woongarra Volcanics, and the Boolgeeda Iron Formation in the Hamersley Group, respectively. And the Uppermost sedimentary Unit is equivalent to the Turee Creek Group. A meter order detailed measurement of all the stratigraphic sequence shows the systematically depositional change of the sedimentary and volcanogenic rocks, and the conformable relationships between the Units (Fig. 3 and 4). Each boundary among those Units is conformable, whereas that among layers within the Unit is also conformable. The strikes of sedimentary layers are NW-SE trending, while the dips are mostly 50˚ to 60˚ S (Fig. 3).

The Lower lava flow Unit, over 1800 meters thick, is composed mainly of piles of pillowed basalts, massive sheet flows, hyaloclastite, reworked hyaloclastite and minor dikes, and is often intercalated with thin bedded chert and felsic tuff (Fig. 2 - 4). Basaltic komatiite thick flows occur in the central stratigraphic units. Pillows form subspherical to ellipsoidal, and range from 50 to 200 cm across in size, and are well observed as tube structures in some places. Those are fringed by a dark-colored chilled margin without any traces of vesicles. Pillow lavas have no internal structures such as variolites and drain-away cavity. Most pillows form closed-packed type with minor matrix. The way-up estimated by the pillow structures is to the south. Massive lavas occur at the higher stratigraphic units. Some accompany minor amount of gabbro at the bottom. Hyaloclastite consists mainly of pillow breccias, and the

matrix without tuffaceous materials, and conformably covers on massive or pillowed basalts. Pillow breccias are mostly large, about tens cm across. The field occurrences show an autobrecciated hyaloclastite. Thin white sedimentary layers occur at the topmost part of the pillow lava flow unit. The sediments overlie on the massive basalt, and some of them are intercalated with thin chert beds. Although the extensive and severe alteration makes the composition of them obscured, the white sedimentary layers appear to be derived from felsic tuff layer. Chert layers are interlayered at the topmost of this unit. Chert layers are massive white in color and ca. 1 to 2 m thick. Some are intercalated thin felsic tuff, while contains no ferruginous beds. Both tuffaceous layer and chert are poorly traceable along the strike. Basaltic komatiites are characterized by the clinopyroxene spinifex texture, and form sheet flows. Massive ferruginous deposits unconformably cover the basaltic and komatiitic flows along the boundary between them. In this Unit, neither shales nor terrigenous sediments are interbedded, and pillow/massive lavas and hyaloclastite never contain continent- or arc-derived material.

The Lower BIF Unit, almost 600 meters thick, consists mainly of BIFs, and conformably overlies the pillow lava sequence (Fig. 2 - 4). BIF is defined as (1) silicate, (2) carbonate, or (3) oxide facies, respectively (James 1954). The fine-scales bands characterize banded iron formation. The bands forms fractal features, conventionally named 1 mm thick microband, 15 mm thick Microbands, 5 cm thick Mesobands, 50 cm thick Calamina cyclothem, 20 m thick Macrobands, and 500 m thick Broad alteration depending on the spacing on the alternation. BIFs are made up of typically of bands (mesobands) of chert; these bands in turn are separated by mesobands of fine-grained, iron-rich material. The rhythmical alternation of these two mesoband types, together form at least 80 % of the volume of most BIF, while the remaining mesobands consist of monomineralic bands made up of magnetite, carbonate (siderite), stilpnomelane, or riebeckite. BIFs can be also classified into four types based on their constitutes, as shown above; namely, chert/magnetite-, chert/siderite-, magnetite/hematite, and magnetite-dominated-type BIF. Chert mesobands normally have a significant total iron content, which is rarely less than 3 % and may reach about 30 %. This is contained in a wide variety of iron-bearing minerals, which are more coarsely crystalline than the microcrystalline quartz, and commonly concentrated into regular laminae within chert mesobands and parallel to their margins. On the other hand, mesobands of iron-rich materials consist of a fine-grained mixture of quartz, and magnetite, hematite, stilpnomelane, ankerite, and siderite, and have no regular aftbanding. Each type of BIF is distributed systematically, corresponding to the lithostratigraphy. The type of the alternation of chert with siderite occurs at the bottom of this Unit. It, 200 m thick, overlies the Lower lava flow Unit. It is laterally discontinuous, is not exposed at the eastern side. Minor altered tuffaceous layers are interbedded in the places. The type of chert/magnetite alternation pervasively occurs at any stratigraphic level, but it tends to predominate at the lower part. Thin tuffaceous and shales layers become more frequently interbedded into the chert/magnetite alternation BIF at the topmost. Each type of magnetite/hematite or monomineralic magnetite is interlayered with

chert/magnetite-type BIF at the middle stratigraphic level. On the other had, massive magnetite/hematite boulders, ca a meter across, are sporadically distributed along the river, suggesting the fluvial origin.

The Middle BIF Unit, about 180 meters, is composed mainly of chert/magnetite- and riebeckite-dominated-type BIF (Fig. 2-4). A greenstone sheet, ca. a meter thick, is intercalated between the Middle and Lower BIFs. Although the greenstone sheet is entirely altered, it appears to be basaltic in composition. Thin tuffaceous and shales layers are alternated with chert/magnetite BIF at the lower section. Even cherty conglomerate layers occur along the boundary. The chert/magnetite-type BIF layers are dominated at the lower stratigraphic sections, whereas riebeckite-dominated-type BIF layers are mono-lithologically stratified at the lower section. The riebeckite-dominated-type BIF can be divided into two groups, carbonate-free and carbonate-bearing. The origin of riebeckite is of very low-grade metamorphic and /or late diagenetic under the condition in either low pH, low $aCO_2$, or high $aNa^+$ (Miyano and Klein, 1983).

The Komatiitic Unit has a distinct feature of the repetition of basaltic flows and layers of BIFs (Fig. 2 - 4). Each basaltic flow and BIF layer are thin, but the total thickness of the pile runs up to ca. 180 meters. The deposition of BIF suggests the continual hiatus and the eruption of basalt/komatiites volcanism underwater. The thickness of this Unit and the number of the BIF layers decrease to the west, because of the thickening of the Rhyolite Unit. Basaltic flows are composed of tholeiitic massive flows and minor basaltic komatiite sheets, which are defined by the clinopyroxene spinifex texture. Tholeiitic massive flows have fine-grained zones and the inner coarse-grained doleritic zone. Vesicles are observed in the fine-grained zones. On the other hand, BIFs are classified into hematite-dominated-type and chert/magnetite-type BIF. A hematite-dominated-type BIF layer occurs at the bottom, while chert/magnetite-type BIF layers are interbedded at the middle to the upper section. BIF layers conformably rest on the basaltic flow piles. BIF layers are very thin, less than 10 m thick, and poorly traceable along strike, and appear to taper, pinch out and terminate before they can be traced for 600 m.

The Rhyolite Unit consists mainly of very thick, over 400 meters, rhyolite (Fig. 2 - 4). The common and widespread occurrence of cooling joints, amygdules, flow banding, and breccias suggests shallow-water emplacement, such as lavas (Barley et al. 1997). The Unit may be subdivided into the two sections because the thin chert/magnetite-type BIF layer is interbedded at the middle stratigraphic level. The deposition of the chert/magnetite-type BIF suggests the hiatus of rhyolite volcanism. In the lower section, fine-grained rhyolites are piled up, up to 300 m thick. The presence of the quartz paramorphs after tridymite indicates the magmatic temperatures of > 900 ˚C (Barley et al. 1997). Thin shale layers are interbedded at the three stratigraphic levels (Thorne 1990). In the upper section, two stratigraphic units of coarse-grained rhyolite occur at the bottom, whereas fine-grained rhyolite predominates at the middle and top of the section. The former contains abundant several-cm-scaled phenocrysts of quartz and/or plagioclase with minor iron oxide and pseudomorphs after pyroxene. SHRIMP

dating indicates that the rhyolite was erupted or intruded at 2,449±3 (Barley et al. 1997).

The Upper BIF Unit, 1500 m thick, is composed of chert/magnetite-type BIF, chert, and tuff (Fig. 2 - 4). The Unit has the distinct character of frequent intercalation of chert and tuff with BIF. The Unit is subdivided in two sections. The lower section is defined by the alternation of chert/magnetite-type BIF and tuffaceous layers with minor amount monolithic chert layers. The seven tuffaceous layers range from ca. 2 to 50 meters in thickness. In the upper section, chert layers become dominant. Fine-grained pale green/blue-colored laminated-chert beds cover the BIF. Moreover, they are covered by the thick alternation of chert and BIF.

The Uppermost sedimentary Unit has a distinct feature of high proportion of terrigenous materials form the lower Units (Fig. 2 - 4). The lithology changes form chemical sediments such as chert and BIF through fine-grained shales to terrigenous coarse-grained sediments such as sandstone in ascending order. The alternation of chert with shale is dominated at the bottom, thin tuff and the overlying chert layers are interbedded into the central stratigraphic level of thick chert/shale layers. The thick sedimentary packages of massive quartzite sandstone, monolithic shales, or the alternation of sandstone and shale are piled up. Massive green-colored sandstone bed is interleaved between shale and massive quartzite sandstone.

### II-3.2 Discussion on the geology of the Beasley River Area, Hamersley

The sequential change of lithostratigraphy makes a critical constraint on the environment of the deposition of volcanics and sediments. The lithostratigraphy in the accretionary complex of circum-Pacific active continental margin is characterized by “oceanic plate stratigraphy” (Matsuda & Isozaki, 1991). The oceanic plate stratigraphy is defined by piles of basaltic flow unit, pelagic sediments, hemipelagic and turbiditic sequence involving conglomerate in ascending order (Isozaki et al., 1990; Matsuda and Isozaki, 1991). The basaltic flow unit is composed of pillowed basalts, sheeted lava flows and hyaloclastite with minor amount of dolomite lenses (<20 cm) indicating its deposition above carbonate compensation depth (CCD). The pelagic sediments are made of radiolarian chert and the interlayered mudstone sediments, and contain no carbonate. Cosmic spherules are involved within the mudstone sediments. Both basaltic flow unit and pelagic sediments contain no quartzofeldspathic materials. The hemipelagite is characterized by presence of fine-grained terrigenous particles, and is more argillaceous and less siliceous than pelagic sediments. Turbiditic sequence is entirely composed of continents- or arc-derived materials. On the other hand, the lithostratigraphy of typical continental rift basin is the inverse of “oceanic plate stratigraphy”; main volcanic piles overlie the sediments (Van Houten, 1977; Hynes & Sibut, 1981; Easton, 1983). Basal deposits in rifts tend to be coarse terrigenous sediments, commonly alluvial fanglomerate. Overlying sediments become finer grained upward because of progressive subsidence within the rift. Where basal volcanism does occur in rifting, it is

characteristically subaerial and alkaline-peralkaline type (Hoffman, 1991)

The Mount Roe Basalt, lowermost stratigraphic unit of the Fortescue Group, unconformably overlies granite-greenstone basement. This formation is up to 2600 m thick, and is dominated by subaerial tholeiitic basalt with lesser amount of basaltic hyaloclastite, pillowed basalt, and continental-derived deposits. Some thin beds of fluvial sandstone are found interbedded with basalt near the base of the succession, but are not generally observed higher in the succession. Thin mudstone, sandstone, and conglomerate units of fluvial or lacustrine origin have been recorded at the base of the basalt succession. Those evidences of basal sedimentation suggest that the volcanics and sediments were deposited in the immature rift basin (Blake, 1984; Hickman & Harrison, 1986; Thorne & Blake, 1990).

On the other hand, the simplified lithostratigraphy of map area is from thick piles (>2.0 km) of pillowed basalt and hyaloclastite at the bottom, through the conformably overlying BIF, to thick terrigenous sediments at the top. Moreover, quartzofeldspathic materials that are terrigenous in origin are not contained in the Lower lava flow Unit, and the majority of the Lower and the Middle BIF Unit, whereas they become dominant in the upper Unit. The lack of terrigenous materials within pillowed basalts and BIF/chert sediments implies that those were erupted or deposited outside the limits of sedimentary influx from the continental margin. This lithostratigraphy is quite similar to "Oceanic Plate Stratigraphy" in the Phanerozoic.

Despite that the lithostratigraphy is similar to a kind of “oceanic plate stratigraphy,” lack of thrusts which defines duplex structure, do not support the origin as the accretionary complex, but as a sedimentary basin in the open rift valley. Pillow/massive lavas in the Lower lava flow Unit were derived form the volcanism in the mature rifting system equivalent to the Red Sea in the Phanerozoic, because of neither terrigenous materials nor vesicles in pillow/massive lavas. The composition of major and some trace elements of the basalts in the mature rift system are quite similar to that of MORBs in the Phanerozoic (Eissen et al., 1989; Altherr et al. 1990; Deniel et al. 1994; Stewart & Rogers, 1996). The pattern of rare earth elements of them is the same as that of transitional MORBs. Despite of relatively radiogenic Pb isotopic composition, even Nd and Sr isotopic ratios range within the variation defined by MORB source mantle. Therefore, the pillowed/massive basalts in the Lower lava flow Unit posses the chemical feature of the MORB source mantle, may be the same as for their major element composition.

The tectonic history is presumed based on the lithostratigraphy of the area (Fig. 5). Superplume presumably caused attenuation and the subsequent extension of the continental lithosphere to lead to rifting of a continent. Because lithospheric stretching cause brittle failure, block rotations and sharp differential subsidence of the upper crust, the basal sediments including the conglomerate unconformably cover the granite-greenstone terrain of the Archean Pilbara craton. Because isostatic consequence of the crustal thinning resulted in the progressive subsidence within the rift, overlying sediments become finer-grained upward. Mount Roe basalt erupted over the basal sediments or on the granite-greenstone basement.

The basaltic lavas erupted subaerially or underwater. The subaerial tholeiite formed pahoehoe flow or flood basalt flow, whereas submarine eruptions led to the formation of pillow lava and hyaloclastite. As the continental rifting advanced, spreading center became remote from the continental margins and deep under the sea so that no continental-derived sediments come to be deposited and vesicles within the lava became lesser- developed. Basaltic volcanism occurred at the significantly deep submarine environments to form pillow lavas without vesicles. Active hydrothermal activities near the spreading center resulted in the deposition of thick BIF accompanied with intermittent off-ridge volcanism. The emergence of subduction zone presumably caused the location of spreading center to migrate off the center of the plume-head (Maruyama 1994). Active plume volcanism led to not only the komatiites volcanism but also rhyolite eruption by the remelting of oceanic crust, analogous to the rhyolitic magmatism in the Iceland in the Phanerozoic (Walker, 1966; Wood, 1978; Wood et al., 1979; McDonald et al., 1990). Minor hydrothermal circulation on the hotspot resulted in the deposition of the BIF with tuffaceous and monolithic chert layers. As the oceanic plate migrated from the spreading center to the trench, terrigenous materials came to be deposited. Finally, voluminous terrigenous sediments covered all of them. Eventually they were emplaced on the continent, presumably by subduction of oceanic lithosphere under the Yilgarn..

In summary, (1) the pillowed basalts at the bottom were derived from mid-ocean ridge volcanism. (2) BIF/chert were formed as pelagic sediment by active hydrothermal circulation. (3) The plate migrated on to a hot-spot, which led to the bimodal volcanism of komatiite and rhyolite, analogous to the Phanerozoic large igneous provinces such as Iceland (Walker, 1966; Wood, 1978; Wood et al., 1979; McDonald et al., 1990). (4) Hydrothermal activity on the oceanic island caused the deposition of alternation of tuff/BIF or chert/BIF. (5) The terrigenous sediment began to be deposited accompanied with chert, which led to the deposition of alternation of chert/shales. (6) Eventually, voluminous terrigenous sediments (the Beasley River Quartzite) covered over all of them (Fig. 5, 6).

## II-4. Chemistry

### II-4.1. Sample preparation

To obtain the original magmatic composition, greenstone samples were carefully selected for the major and trace elements analyses step by step. First of all, field occurrences of greenstones and even the surrounding rocks appear to be related to the extent of the secondary alterations and the distribution of the altered zones. For example, the extensive altered zones appear at the stratigraphic top of the pillow lava flow units, or in the surroundings of large quartz veinlets such as T-chert. Such stratigraphically controlled alteration suggests a hydrothermal alteration at the formation of the magmas, accompanied

with the interaction with seawater. It is suggested that the involvement of the fluid migration from the neighboring sediments forced the composition, especially isotopic composition, disturbed during the metamorphism. Therefore, 400 greenstone samples elsewhere were preferentially collected, or thin massive lavas were also preferred. At the second stage, <1-cm-thick slabs were cut from each sample to select the rock samples without a visible internal fracture filled with quartz, chlorite and epidote minerals and the heterogeneous surfaces. Whole rock powders were prepared for 110 fresh samples, which contain neither veinlets of quartz, chlorite, and calcite, nor the heterogeneous domains even under the microscope. Slabs whose surfaces were polished were broken into small pieces, ultrasonically cleaned in de-ionized water and ethyl alcohol, dried, and powdered in a tungsten carbide shatter-box.

### II-4.2. Analytical methods

Major and some trace elements (Ni, Rb, Sr, Y, Zr, Nb, Ba, Pb, and Th) were measured by X-ray fluorescence (XRF) at Tokyo Institute of Technology and at Institute of Oceanography in Tokyo University, respectively. The analytical procedure, condition and its accuracy are described by Goto and Tatsumi (1994). Rare earth elements were determined by inductively Coupled Plasma Mass Spectrometry (ICP-MS) at Tokyo Institute of Technology. The analytical procedure, condition and its accuracy are reported elsewhere (Hirata et al. 1988).

### II-4.3. Major and trace element chemistry in basalts and komatiites

Figures 7 and 8 show the MgO versus major and trace element diagrams of basaltic and komatiitic rocks from pillow lava unit, the Lower Komatiites and the Upper Komatiites in the Beasley River area along with the modern MORBs and OIBs. The latter includes both alkaline basalts and tholeiites. Chondrite-normalized REE abundances are shown in Figure 9. Both fine-grained rock samples, which petrographically defined as aphyric or small acicular plagioclase-bearing basalts, and coarse-grained rock samples, which defined as plagioclase-phyric doleritic or clinopyroxene-plagioclase-gabbroic forms one line on the MgO diagrams. Despite of minor scattering in especially CaO and $Na_2O$ content, each type make a clear liquid line of descent except for basaltic rocks from the pillow lava unit. REE pattern of both the High Ti group and the Lower Komatiites forms slightly light REE-enriched pattern (Fig. 9).

Despite of no correlation of field occurrences, basaltic rocks pillow lava units form two distinct liquid line of descent; hereafter, named as the Low Ti group, and the High Ti group, respectively (Fig. 10). The Low Ti group has higher $SiO_2$ and $Al_2O_3$ and lower $TiO_2$, FeO*, and CaO at a given MgO content relative to the High Ti group. Especially, the compositional differences between the Low Ti group and the High Ti group increase with

decreasing MgO content. The liquid line of descent of High Ti group is similar to the modern MORBs, which is characterized abrupt increase of $SiO_2$, FeO and $TiO_2$ content and decrease of $Al_2O_3$ content due to the fractionation of plagioclase. On the other hand, the liquid line of descent of the Low Ti group does not show such features, but shows extreme increase of $SiO_2$, slightly decrease of $Al_2O_3$ and FeO, and slightly increase of $TiO_2$ at moderate MgO content. The mode of the liquid line of descent is similar to that of the modern island arc basalts. Because the detailed investigation of the Low Ti group, the Lower Komatiites and the Upper Komatiites is out of the main object of this paper, the distinct liquid line of descent of the Low Ti group is presumably caused by higher $H_2O$ content.

### II-4.4 Discussion on the geochemistry of the High Ti group in the pillow lava unit

#### II-4.4.1. $Mg^{\#}$ of source mantle of High Ti group

I here examine to estimate FeO content of source mantle, and temperature and pressure of melting. High Ti group is enriched in FeO content relative to the modern MORB at any given MgO content (Figure 11a). This difference suggests that source mantle of the High Ti group had higher FeO than that of the modern MORB.

I assumed that the Archean mantle was still a spinel- or garnet-lherzolite. This assumption leads to $Fe^{3+}/\sum Fe$ ratio of source mantle similar to that of modern upper mantle because $Fe^{3+}/\sum Fe$ ratio is controlled not only by oxygen fugacity, but also by mineral assemblage. If Archean basalts were formed within upper mantle that consisted of olivine, orthopyroxene, clinopyroxene, and spinel, $Fe^{3+}/\sum Fe$ ratio in Archean basalts would be equivalent to that of modern MORBs. Further discussion is shown elsewhere (Chapter III). Batch melting is also assumed because of its simplification.

Melting experiments of four natural peridotites KLB-1, HK66, PHN1611, and MM3 have been extensively performed using diamond aggregate method (Hirose & Kushiro 1993; Baker & Stolper 1994; Kushiro 1996). Those experiments showed $SiO_2$ content of melts is relatively independent of composition of peridotites and temperature of melting at moderate degree of melting, but quite sensitive to melting pressure, because $SiO_2$ is a major constituent element of all minerals. On the contrary, FeO* in melts strongly depends on FeO* content of peridotites, together with pressure and temperature of melting. MgO content of melts is almost proportional to degree of melting.

Some of the most primitive basalt from the High Ti group and the most primitive modern MORB are plotted along melt compositions formed by different pressures and degree of melting and from different starting materials in figure 11b. Both the High Ti group and Modern MORBs are distributed on the compositional trends defined by the melts formed at 10 or 15 kb (Fig 11a). Because the basalt of the High Ti group has relatively lower MgO content, the primary magma should have contained higher MgO. Therefore, the primary magma of the High Ti group is plotted on the partial melts at pressure of 15 – 20 kb. This

evidence suggests that average melting pressure of the High Ti group through melting column were about 15, at most up to 20 kb (Klein & Langmuir, 1987). On the other hand, the modern MORBs are formed at 10 to 15 kb, and is consistent to the high pressure experiments, 10 kb, (Fujii & Bougault 1983).

Figure 11b shows that each variation of FeO content of melt formed at 15 kb for KLB-1, HK66, and PHN1611, or 10 kb from MM3. Primitive basalt of the High Ti group is plotted toward the higher FeO content of melts from HK66 or PHN1611, whereas modern MORBs are distributed on melts from KLB-1. The composition of primary melt of the High Ti group can not be estimated because olivine is completely altered due to metamorphism. If MgO content of primary melt of the High Ti group has ca. 20 wt % in MgO, it can be formed from KLB-1 (Takahashi et al. 1993). However, because the average melting pressure should be high ca. 4.6 GPa, in the case, the High Ti group should have the garnet signatures (Salters & Hart, 1989; Bourdon et al., 1996; Salters, 1996; Hirschmann 1996; Hirschmann & Stolper, 1996). However, the High Ti group does not show garnet signature, such as heavy REE depletion. Furthermore, if the High Ti group is highly differentiated basalts from komatiites, abundance of compatible element such as Ni should be lower (Fig. 9), because Ni is more removed from the melts during crystal fractionation. The results suggest that the High Ti group was derived from more FeO*-enriched source mantle such as HK66 and PHN1611 rather than KLB-1 and MM3.

### II-4.4.2. Potential mantle temperature of source mantle of the High Ti group

The potential temperature of the Archean mantle has been estimated by previous workers since 1990 (e.g. Takahashi, 1990; Nisbet et al., 1993; Ohta et al. 1996). The former two works estimated potential temperature of Archean mantle from only MgO content in peridotitic komatiites (Takahashi 1990, Nisbet et al. 1993). However, MgO content of a primary melt strongly depends on the amount of olivine addition using olivine maximum fractionation model. Moreover, the difference of oxidation state at crystallization between the present and Archean would affect the $Mg^{\#}$ value, and the difference of oxidation state at melting between the present and Archean may be more or less present (Arculus 1985). Ohta et al. (1996) estimated the potential mantle temperature by the comparison of nine major elements in primary magma with those of experimental melts from HK66. However, $TiO_2$, $Al_2O_3$, FeO, $Na_2O$, $K_2O$, and $P_2O_5$ contents in magma are significant sensitive to those contents in source mantle. Therefore, the potential mantle temperature is estimated here by the abundance of FeO and $SiO_2$ in primitive magmas because they are relatively insensitive to the extent of crystal fractionation minor element composition of source mantle, and are strongly correlated to pressure and temperature of melting.

The potential temperature of mantle source of High Ti group was estimated based on recent experimental data in the same way mentioned in Chapter III. Figure 11b shows composition of the primitive basalt of the High Ti group along experimental melt from

PHN1611 on a $SiO_2$ versus FeO diagram. Primitive basalt of the High Ti group is plotted near the melt formed at 1425 ˚C, 15 kb or 1450, 20 kb. If the primitive basalt is the derivative from primary magma of 15 wt % in MgO, the primary magma is plotted near the melt from at 1450, 20 kb or 1400, 20 kb. Each degree of melting is 35.9, 25.0, 16.3 %, respectively according to experimental data (Kushiro 1996). Therefore, the potential mantle temperature is obtained as 1440 to 1566 ˚C of with 0.6 ˚C/km for slope of adiabat, 590 kJ/kb (140 cal/g) for heat of fusion, and 1.26 kJ $kg^{-1}{}^{\circ}K^{-1}$ (0.3 cal/g˚C) for heat capacity (Hirose & Kushiro 1998). Iwamori et al. (1995) also obtained 1320 ˚C of potential mantle temperature of modern MORBs for batch melting.

## II-5 Conclusions

(1) The geological investigation indicates that the rocks in the Beasley River area were deposited during continental rifting.

(2) The pillowed basalts at the bottom and BIF/chert were deposited within the open ocean remote from the continents because they contain no terrigenous materials. Therefore, volcanism of the pillowed basalt unit occurred at the mature stage of continental rifting, equivalent to the Red Sea in the Phanerozoic.

(3) Komatiites occur at the two stratigraphic levels. The Lower Komatiites are interbedded with tholeiitic basalts of the pillow lava units, whereas the Upper Komatiites are interlayered with thin BIF layers. Moreover, the latter is overlain by thick rhyolite flow. Komatiites were derived from off-ridge volcanism when the plate migrated on to a hot spot. The bimodal volcanism of komatiite and rhyolite is also analogous to the Phanerozoic large igneous provinces such as Iceland.

(4) The major and trace elements analyses were conducted for basalts, komatiite and rhyolite from the pillow lava unit, the Lower Komatiites, the Upper Komatiites, and the Rhyolite Unit.

(5) Basalts from the pillow lava unit are subdivided into two groups by geochemical features, especially $SiO_2$, $TiO_2$ and FeO content and the mode of liquid line of descent; the Lower Ti group and the High Ti group.

(6) High Ti group originated from FeO-enriched source mantle relative to that of the modern MORBs. The potential temperature of the source mantle is ca. 120 –220 ˚C higher than that of the modern MORBs.

## References


Altherr, R., Henjes-Kunst, F., and Baumann, A., 1990, Asthenosphere versus lithosphere as possible source for basaltic magmas erupted during formation of the Red Sea: constraints from Sr, Pb and Nd isotopes: Earth Planet. Sci. Lett., v. 96, p. 269-286.

Baker, M. B., and Stolper, E. M., 1994, Determining the composition of high-pressure mantle melts using diamond aggregates: Geochim. Cosmochim. Acta, v. 58, p. 2811-2827.

Blake, T. S., 1984, The lower Fortescue Group of the northern Pilbara Craton: stratigraphy and palaeogeography, *in* Muhling, J. R., Groves, D. I., and Blake, T. S., eds., Archaean and Proterozoic Basin of the Pilbara, Western Australia: Evolution and Mineralization potential., Geol. Dept. & Univ. Extension, Univ. Western Australia, p. 123-143.

Bourdon, B., Zindler, A., Elliott, T., and Langmuir, C. H., 1996, Constraints on mantle melting at mid-ocean ridges from global $^{238}U$-$^{230}Th$ disequilibrium data: Nature, v. 384, p. 231-235.

Breuer, D., and Spohn, T., 1995, Possible flush instability in mantle convection at the Archaean-Proterozoic transition: Nature, v. 378, p. 608-610.

Compston, W., Williams, I. S., McCulloch, M. T., Foster, J. J., Arriesns, P. A., and Trendall, A. F., 1986, Revised age for the Hamersley Group: Fifth Australian Geological Convention - Sediments Through the Ages, Abstracts Volume., Geol. Soc. Aust., Abstr., v. 3, 40 p.

Deniel, C., Vidal, P., Coulon, C., Vellutini, P.-J., and Piguet, P., 1994, Temporal evolution of mantle sources during continental rifting: The volcanism of Djibouti (Afar): J. Geophys. Res., v. 99, p. 2853-2869.

Fujii, T., and Bougault, H., 1983, Melting relations of a magnesian abyssal tholeiite and origin of MORBs: Earth Planet. Sci. Lett., v. 62, p. 283-295.

Gee, R. D., 1980, Summary of the Precambrian stratigraphy of Western Australia: West. Aust. Geol. Surv., Annual Report 1979, p. 85-90.

Goto, A., and Tatsumi, Y., 1994, Quantitative analysis of rock samples by an X-ray fluorescence spectrometer (I): The Rigaku Journal, v. 11, p. 40-59.

Hickman, A. H., 1990, Granite-Greenstone terrain, *in* Ho, S. E., Glover, J. E., Myers, J. S., and Muhling, J. R., eds., Third international Archean symposium, Excursion guidebook, p. 2-13.

Hickman, A. H., and Harrison, P. H., 1986, A review of the occurrence of, and potential for, Precambrian conglomerate-host gold mineralization within Western Australia, Geocongress ’86 Extended Abstract, Johannesburg, Geol. Soc. S. Africa, p. 301-306.

Hickman, A. H., Thorne, A. M., and Trendall, A. F., 1990, Geology of the Pilbara craton Introduction: Third international Archean symposium, Excursion guidebook, 2 p.

Hirata, T., Shimizu, H., Akagi, T., Sawatari, H., and Masuda, A., 1988, Precise determination of rare earth elements in geological standard rocks by inductively coupled plasma source mass spectrometry: Anal. Sci., v. 4, p. 637-643.

Hirose, K., and Kushiro, I., 1993, Partial melting of dry mantle peridotites at high pressures: Determination of compositions of melts segregated from peridotite using aggregates of diamond: Earth Planet. Sci. Lett., v. 114, p. 477-489.

Hirose, K., and Kushiro, I., 1998, The effect of melt segregation on polybaric mantle melting: Estimation from the inremental melting experiments: Physics of the Earth and Planetary Interiors, v. 107, p. 111-118.

Hirschmann, M., 1996, Reading garnet's signature: Nature, v. 384, p. 215-217.

Hirschmann, M. M., and Stolper, E. M., 1996, A possible role for garnet pyroxenite in the origin of the "garnet signature" in MORB: Contrib. Mineral. Petrol., v. 124, p. 185-208.

Hoffman, P. F., 1991, On accretion of granite-greenstone terranes, *in* Robert, F., Sheahan, P. A., and Green, S. B., eds., Greenstone gold and crustal evolution: St. John's, Newfoundland, Geological Association of Canada, p. 32-45.

Isozaki, Y., Maruyama, S., and Furuoka, F., 1990, Accreted oceanic materials in Japan: Tectonophysics, v. 181, p. 179-205.

Iwamori, H., McKenzie, D., and Takahashi, E., 1995, Melt generation by isentropic mantle upwelling: Earth Planet Sci. Lett., v. 134, p. 253-266.

James, H. L., 1954, Sedimentary facies of iron-formation: Econ. Geol., v. 49, p. 235-293.

Klein, E. M., and Langmuir, C. H., 1987, Global correlations of ocean ridge basalt chemistry with axial depth and crustal thickness: J. Geophys. Res., v. 92, p. 8089-8115.

Kushiro, I., 1996, Partial melting of a fertile mantle peridotite at high pressures: an experimental study using aggregates of diamond, *in* Basu, A. R., and Hart, S. R., eds., Earth processes: Reading the isotopic code, Washington D. C., AGU Monograph 95, p. 109-122.

Macdonald, R., McGarvie, D. W., Pinkerton, H., Smith, R. L., and Palacz, Z. A., 1990, Petrogenetic evolution of

the Torfajökull volcanic complex, Iceland I. Relationship between the magma types: J. Petrol., v. 31, p. 429-459.

Maruyama, S., 1994, Plume tectonics: Jour. Geol. Soc. Japan, v. 100, p. 24-49.

Matsuda, T., and Isozaki, Y., 1991, Well-documented travel history of Mesozoic pelagic chert in Japan: Tectonics, v. 10, p. 475-499.

Miyano, T., and Klein, C., 1983, Conditions of riebeckite formation in the iron-formation of the Dales Gorge Member, Hamersley Group, Western Australia: Am. Mineral., v. 68, p. 517-529.

Plumb, K. A., and James, H. L., 1986, Subdivision of Precambrian time: recommendations and suggestions by the Subcommission Precambrian Stratigraphy: Precam. Res., v. 32, p. 65-92.

Salters, V. J. M., 1996, The generation of mid-ocean ridge basalts from the Hf and Nd isotope perspective: Earth Planet. Sci. Lett., v. 141, p. 109-123.

Salters, V. J. M., and Hart, S. R., 1989, The hafnium paradox and the role of garnet in the source of mid-ocean-ridge basalts: Nature, v. 342, p. 420-422.

Smith, R. E., Perdrix, J. M., and Parks, J. R., 1982, Burial metamorphism in the Hamersley Basin, Western Australia: J. Petrol., v. 23, p. 75-102.

Stewart, K., and Rogers, N., 1996, Mantle plume and lithosphere contributions basalts from southern Ethiopia: Earth Planet. Sci. Lett., v. 139, p. 195-211.

Takahashi, E., Shimazaki, T., Tsuzaki, Y., and Yoshida, H., 1993, Melting study of a peridotite KLB-1 to 6.5 GPa, and the origin of basaltic magmas: Phil. Trans. R. Soc. London, v. A342, p. 105-120.

Thorne, A. M., 1990, Hamersley Basin Introduction: Third international Archean symposium, Excursion guidebook, 13-14 p.

Thorne, A. M., and Blake, T. S., 1990, Fortescue Group, *in* Ho, S. E., Glover, J. E., Myers, J. S., and Muhling, J. R., eds., Third international Archean symposium, Excursion guidebook, p. 14-18.

Thorne, A. M., and Seymour, D. B., 1991, Geology of the Ashburton Basin: Bull. West. Aust. Geol. Surv., p. pp141.

Trendall, A. F., 1990, The Hamersley Basin: Geology and Mineral Resources of Western Australia, Geol. Surv. West., Memoir 3, 163-189 p.

Walker, G. P. L., 1966, Acid volcanic rocks in Iceland: Bull. Volcanol., v. 29, p. 375-402.

Wood, D. A., 1978, Major and Trace element variations in the Tertiary lavas of eastern Iceland and their significances with respect to the Iceland geochemistry anomaly: J. Petrol., v. 19, p. 393-436.

Wood, D. A., Joron, J.-L., and Treuil, M., 1979a, A reappraisal of the use of trace elements to classify and discriminate between magma series erupted in different tectonic setting: Earth Planet Sci. Lett., v. 45, p. 326-336.

Wood, D. A., Joron, J.-L., Treuil, M., Norry, M. J., and Tarney, J., 1979b, Elemental and Sr-isotopic variations in basic lavas from Iceland and the surrounding ocean floor: Contrib. Mineral. Petrol., v. 70, p. 319-339.

## FIGURE CAPTIONS

**Figure 1.** Geological map of the northern Pilbara Craton (Thorne 1990) showing the distribution of the Pilbara Supergroup and the Mount Bruce Supergroup. The Pilbara Supergroup in the northern region is composed of Granite-greenstone terrane, and is exposed as inlier in the southern region. Mount Supergroup consists of, the Fortescue Group, the Hamersley Group and the Turee Creek Group in the southern region. The Fortescue Group is exposed as outlier in Marble Bar area, East Pilbara and southwest Pilbara basins. Inset map shows the location of Pilbara Craton in Western Australia. Locality of mapped area is also shown.

**Figure 2.** Geologic map of Beasley river area.

**Figure 3.** Cross section of NE-SW of the mapped area.

**Figure 4.** Lithostratigraphic column of the mapped area.

**Figure 5.** Schematic evolution of southern Pilbara area.

(A) Break up of the Pilbara Craton and deposition of the Fortescue Group,

(B) Successive break up and formation of ocean floor

(C) Hamersley Group sedimentation on a passive continental margin.

(D) Initiation of subduction and contraction of ocean floor.

(E) Beasley River Quartzite deposition on active continental margin.

(F) Continental collision and deposition of the Mount McGrath Formation

(G) Crustal loading and foreland basin subsidence leading to deposition of the Duck Creek Dolomite

(H) Deposition of Ashburton Formation in the foreland basin

(I) Deposition of the Capricorn Formation.

**Figure 6.** A cartoon of Travel history of Early Archean oceanic lithosphere in the Hamersley Group. Volcanic rocks, pillowed basalt, and komatiites and dacite, are formed at oceanic ridge and ocean island, respectively.

**Figure 7.** MgO variation diagrams of major elements for pillow lava unit, the Upper Komatiites and the Lower Komatiites. Symbols are shown in inset.

**Figure 8.** MgO variation diagrams of trace elements for pillow lava unit, the Upper Komatiites and the Lower Komatiites. Symbols are shown in inset.

**Figure 9.** Chondrite-normalized rare earth element (REE) abundances in the pillow lava unit basalt along with modern OIB and MORBs. Vales of these modern basalts are from Sun & McDonough (1989). Values of chondrite are taken from Anders & Ebihara (1982).

**Figure 10.** MgO variation diagrams of major and trace elements of basalt in the pillow lava unit. These basalts are subdivided into two groups, High Ti basalt and Low Ti basalt, by some major elements and trace element abundances. Symbols are shown in inset.

**Figure 11.** (a) MgO variation diagrams of some major elements for High Ti basalt (solid circles) along with compositional variations of modern MORBs (gray regions). Three

arrows on scattered plots indicate compositional variation of residual melts through crystal fractional fractionation of olivine, olivine+clinopyroxene and olivine+clinopyroxene+plagioclase, respectively. Abbreviations are: ol = olivine; cpx = clinopyroxene; pl = plagioclase. (b) Comparison of primitive natural basalts with partial melts formed from mantle peridotite by diamond methods. (i) $SiO_2$-MgO diagram. Symbols: a solid circle and open circles are primitive High Ti basalt and most primitive modern NMORBs, respectively. Thick arrows indicate compositional variation of partial melts produced from four mantle peridotite at different pressure, 10 kb for light gray, 15 kb for gray, 20 kb for dirk gray and 25-30 kb for black arrow respectively. This diagram indicates that both modern MORBs and High Ti basalt were formed at 10 to 15 kb. (ii) MgO-FeO diagram. Symbols: a solid circle and open circles are primitive High Ti basalt and most primitive modern NMORBs, respectively. Thick arrows indicate compositional variation of partial melts produced at 15 kb from four different mantle peridotite, HK66 for light gray, PHN1611 for gray, KLB-1 for dirk gray and MM3 for black arrow, respectively. This diagram indicates that FeO content of mantle source of modern MORBs is comparable to that of KLB-1, whereas that that of mantle source of High Ti basalt was comparable to or higher than that of HK66 and PHN1611. (iii) $SiO_2$-FeO diagram. Symbols: a solid circle and small open circles are primitive High Ti basalt and partial melts from PHN1611, respectively. Thick arrows indicate compositional variation of partial melts produced from PHN1611 at 10 to 15 kb for gray, and at 20 to 30 kb for black arrow, respectively. This diagram indicates that melting pressure and temperature of High Ti basalt was around 15 kb and 1425 ˚C. Potential mantle temperature was calculated to be 1550 ˚C using degree of melting (Kushiro 1996) and thermodynamic parameters (Hirose 1998).

**Figure 12.** Zr variation diagrams of incompatible trace elements for pillow lava unit, the Upper Komatiites and the Lower Komatiites along with modern MORB and OIB, Mare basalt and Highland basalt in Moon, Eucrite, and Orgueil. Symbols are shown in inset.

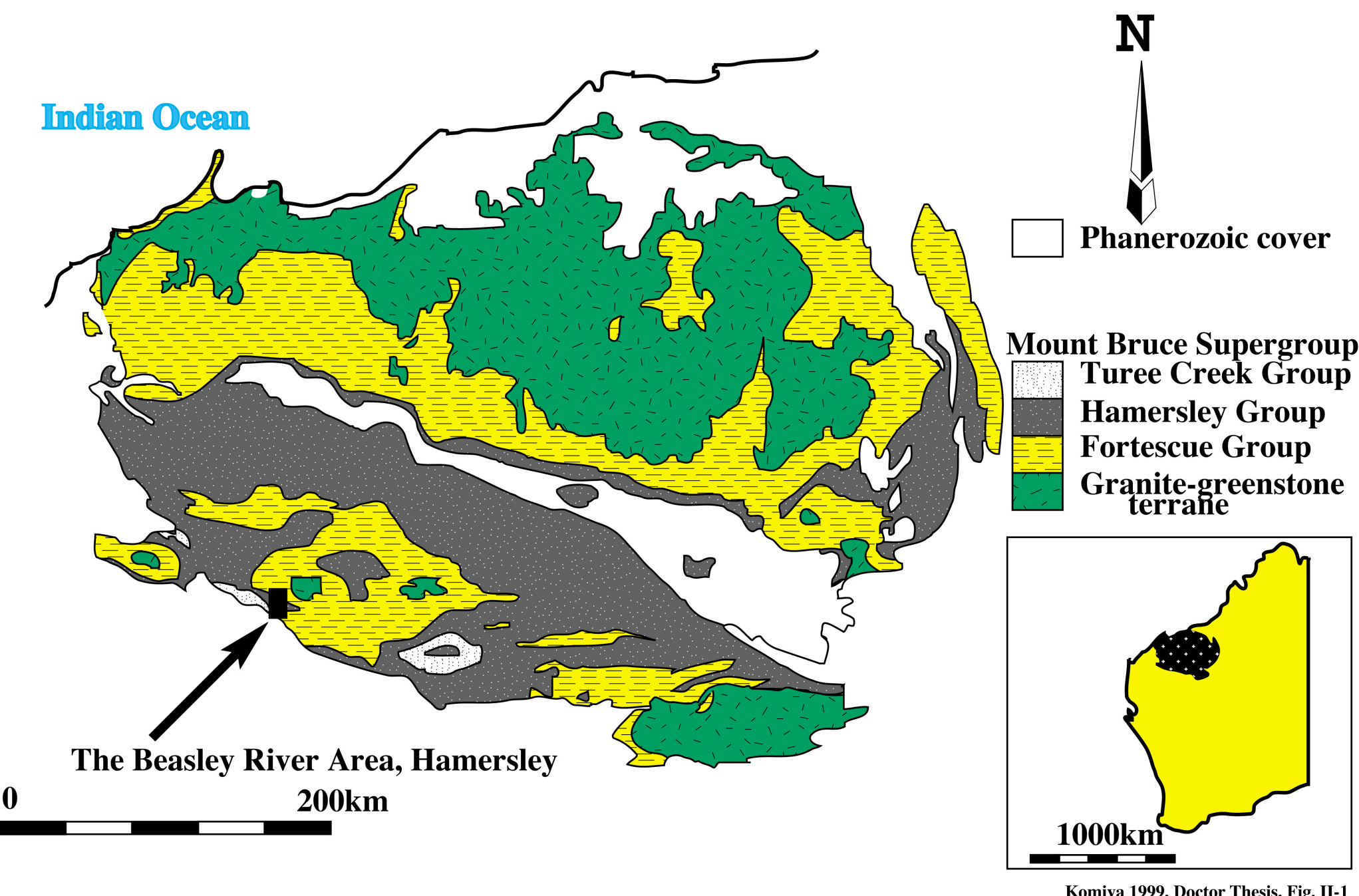


Komiya 1999, Doctor Thesis, Fig. II-1

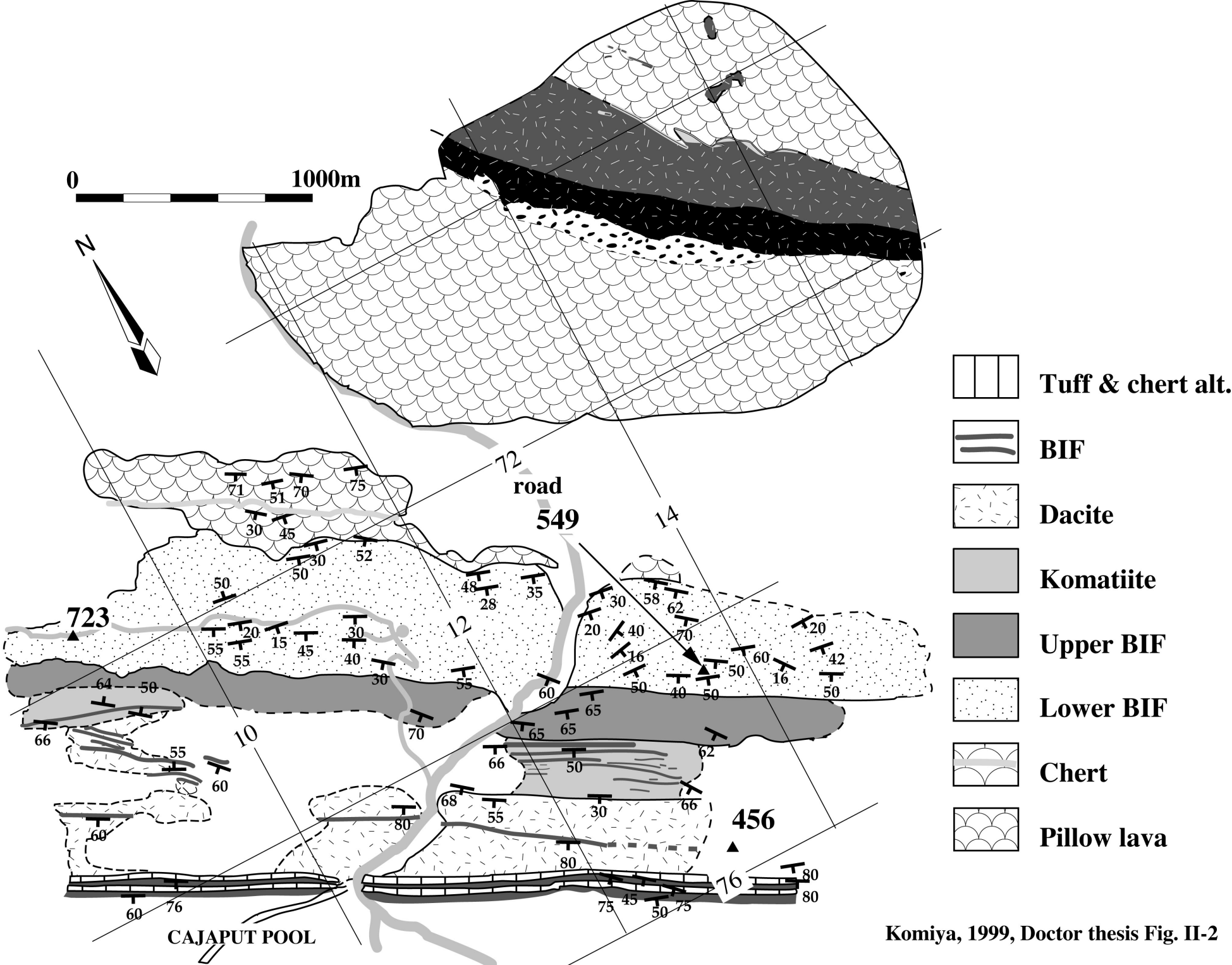


Komiya, 1999, Doctor thesis Fig. II-2

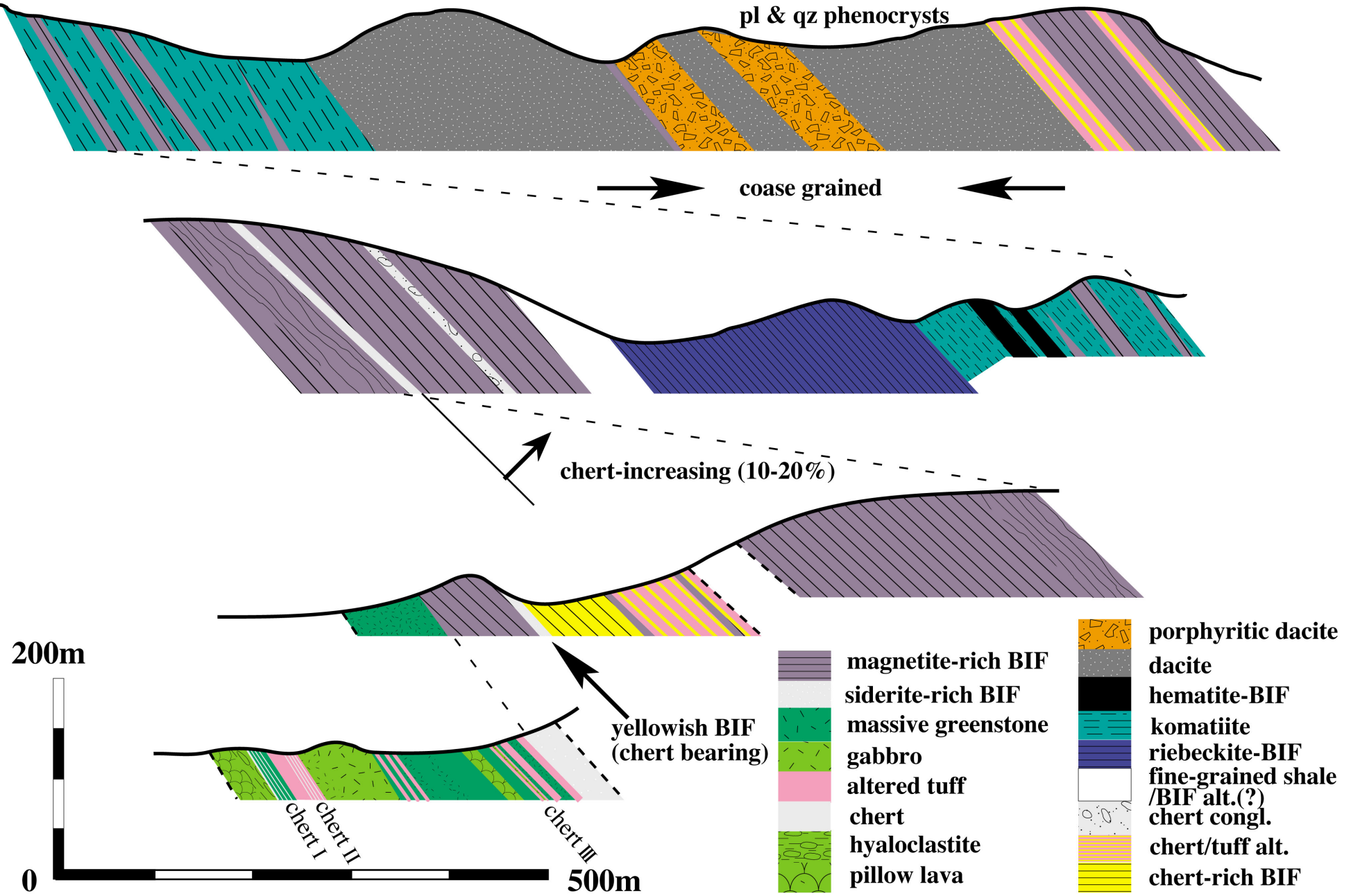


Komiya 1999, Doctor Thesis, Fig. II-3

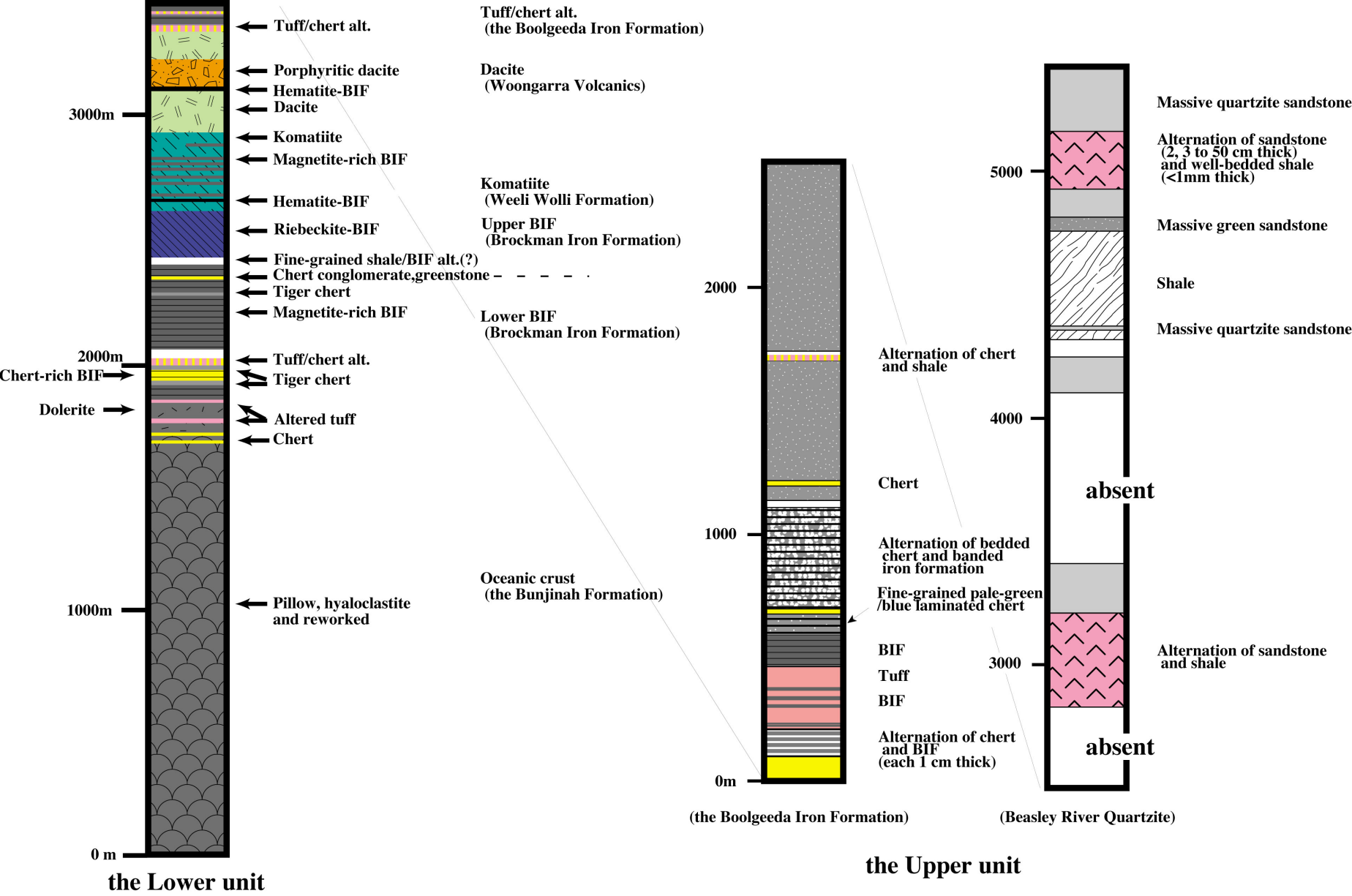


Komiya 1999 Doctor Thesis Fig. II-4

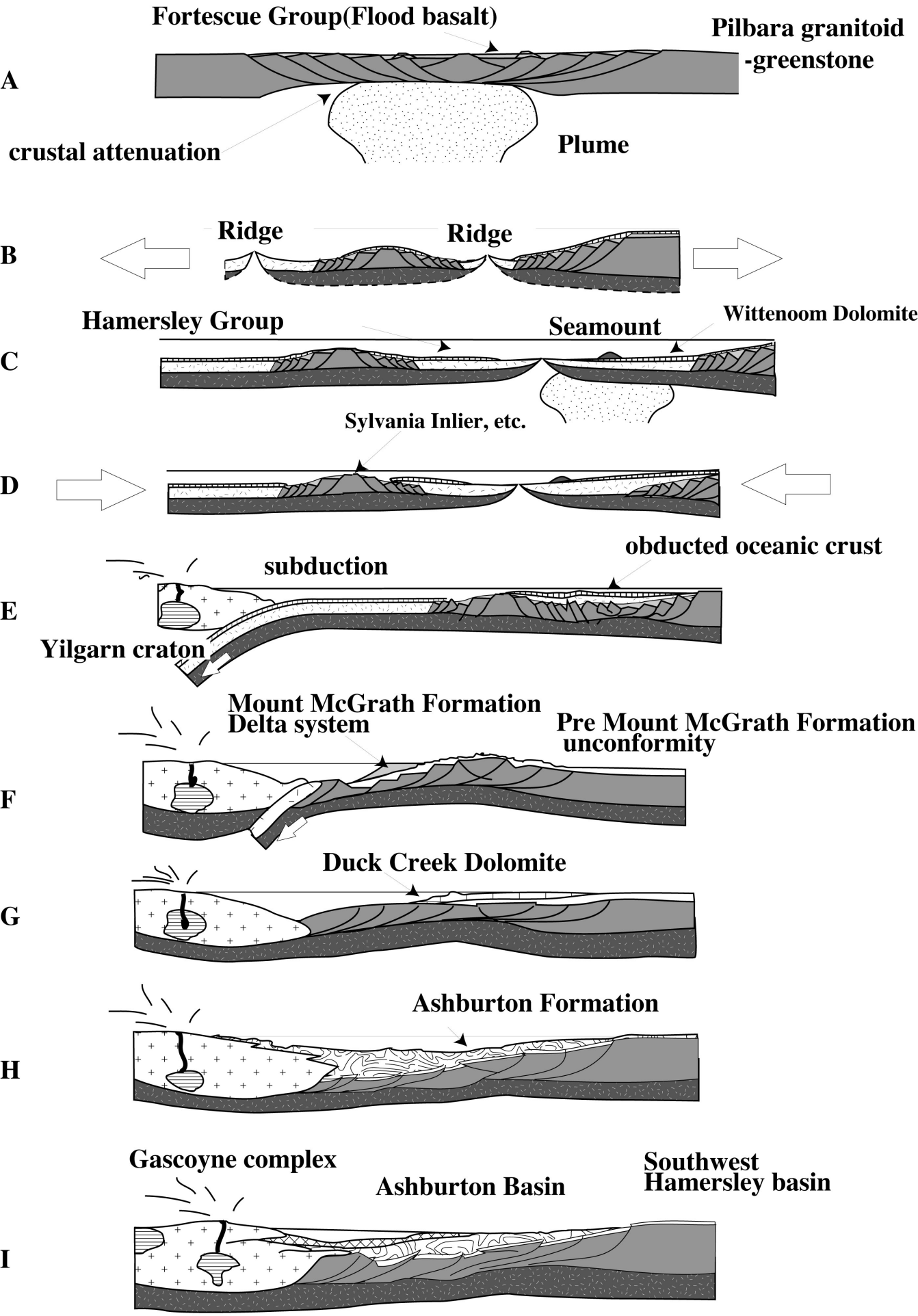


Komiya 1999 Doctor Thesis Fig.II-5

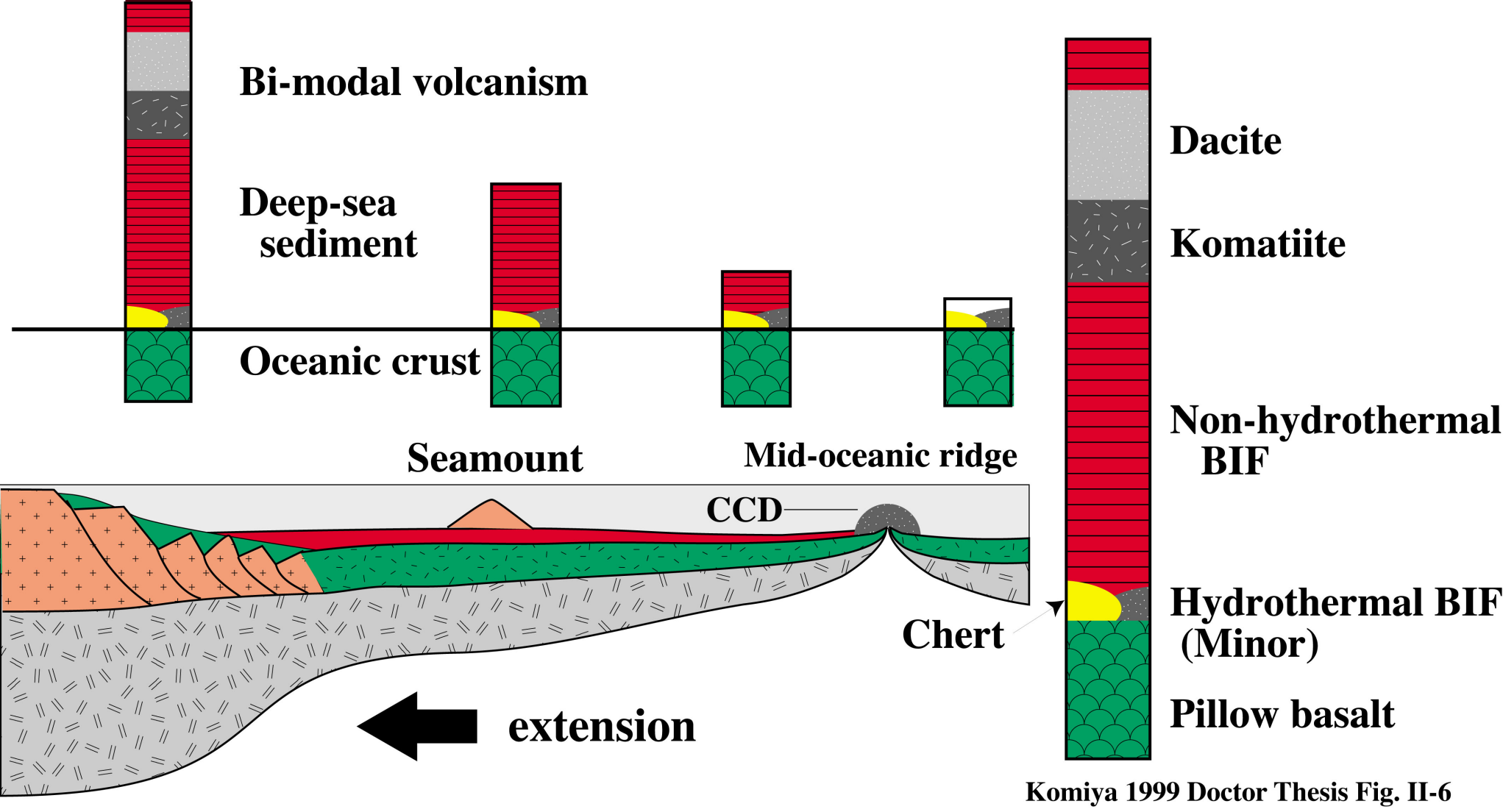


Komiya 1999 Doctor Thesis Fig. II-6

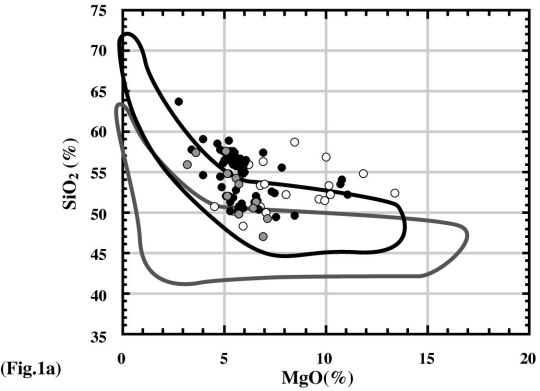


(Fig.1a)

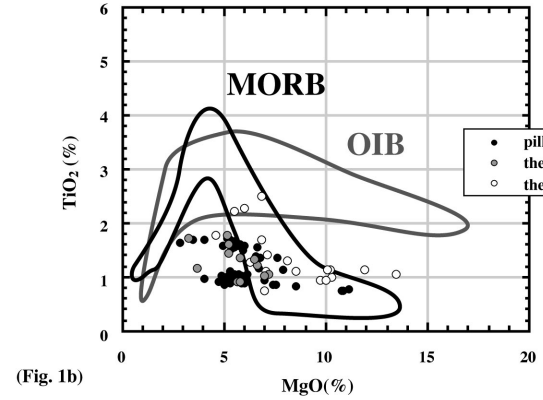


(Fig. 1b)

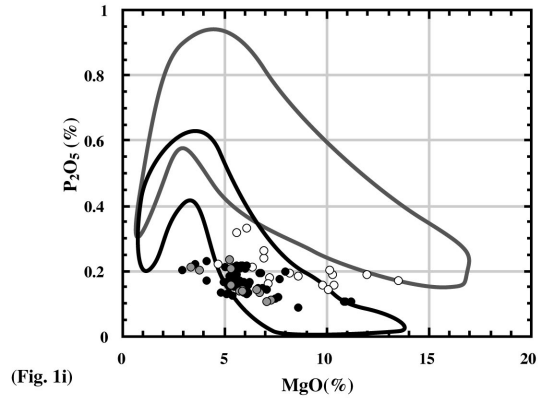


(Fig. 1i)

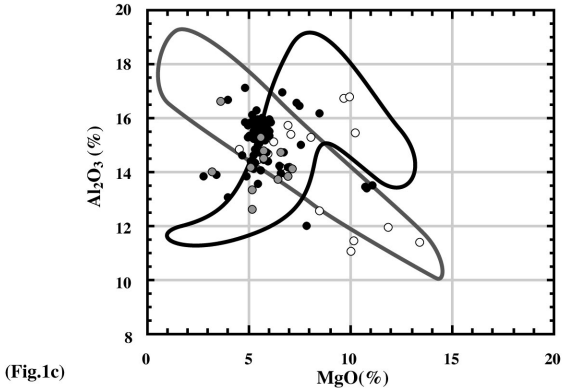


(Fig.1c)

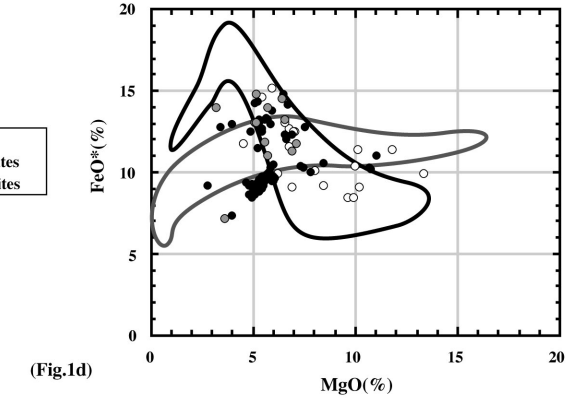


(Fig.1d)

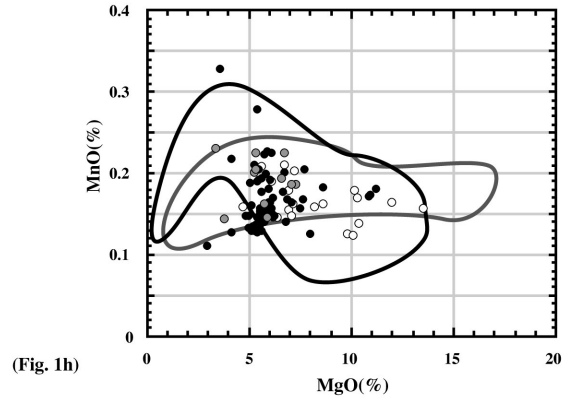


(Fig. 1h)

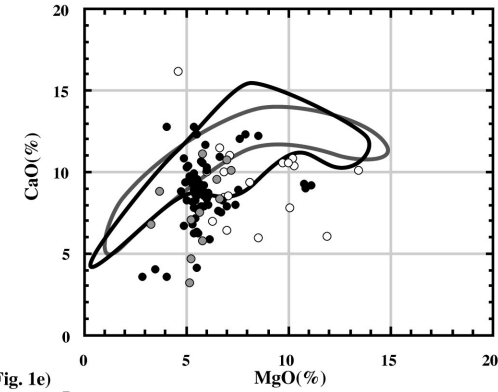


(Fig. 1e)

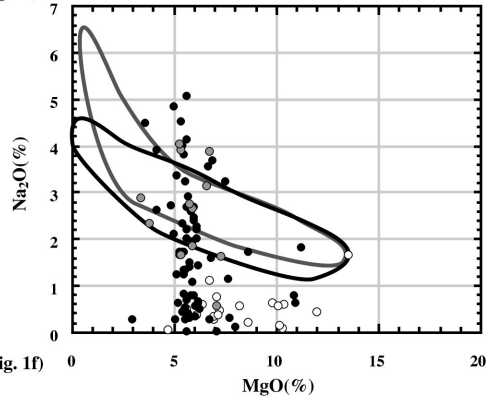


(Fig. 1f)

**Komiya 1999 Doctor Thesis Fig. II-7**

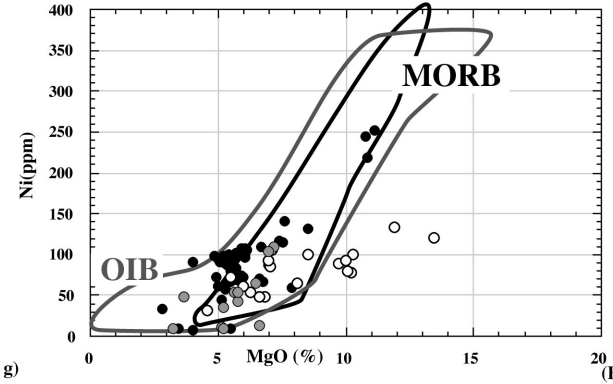


(Fig.1 g)

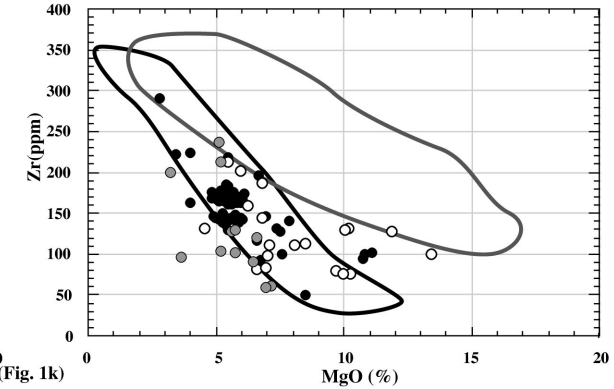


(Fig. 1k)

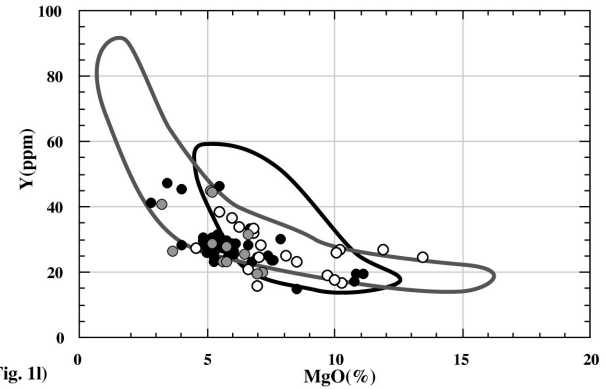


(Fig. 1l)

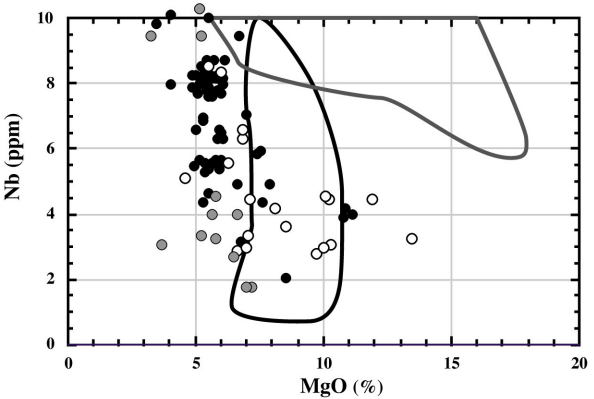


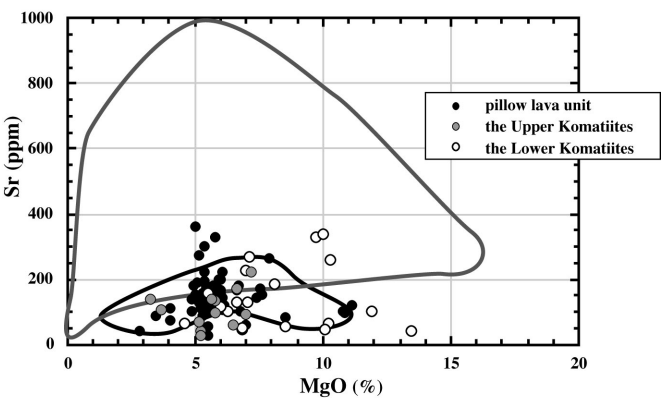


Komiya 1999 Doctor Thesis Fig. II-8

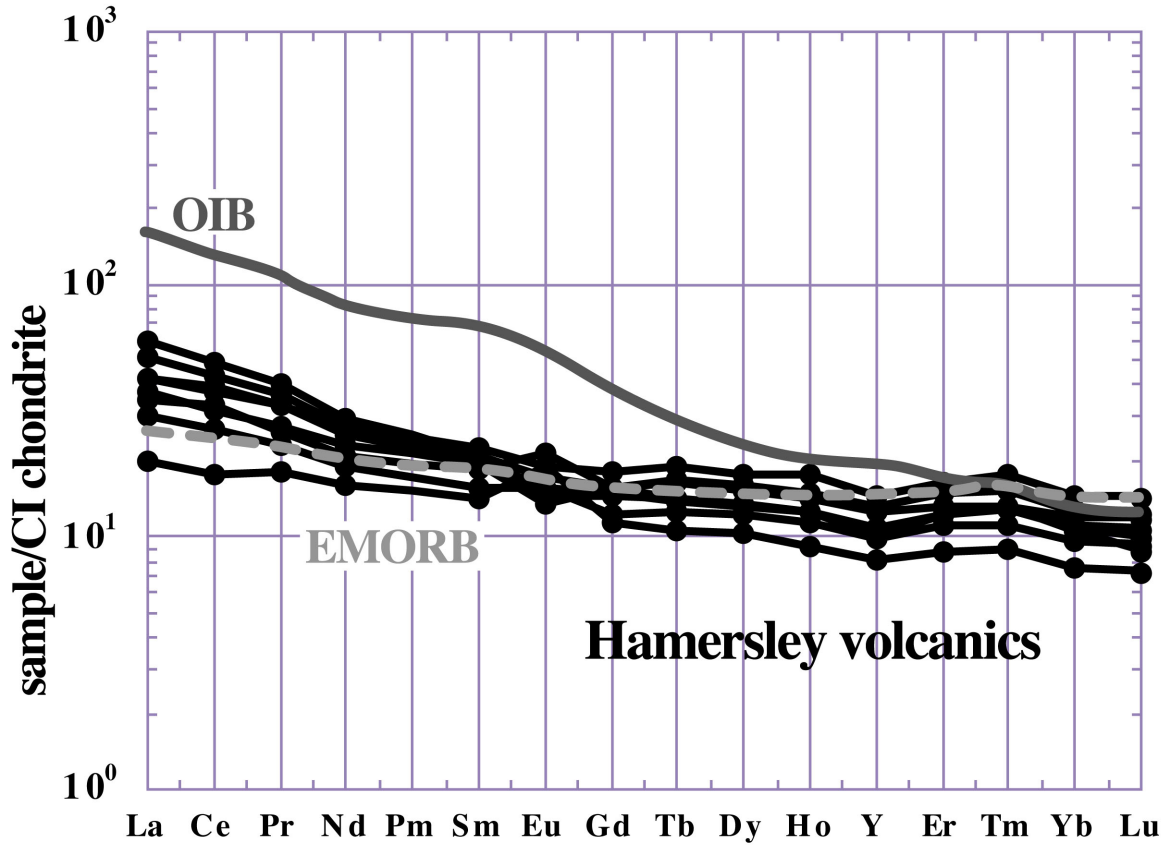


Komiya 1999 Doctor Thesis Fig. II-9

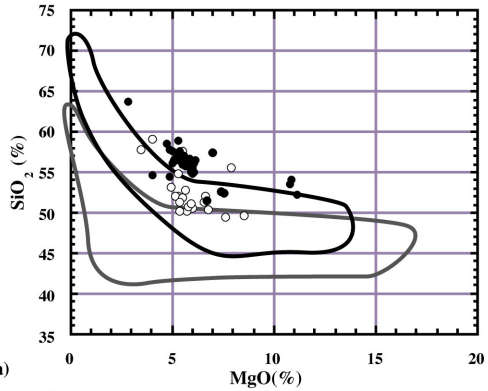


(Fig.1a)

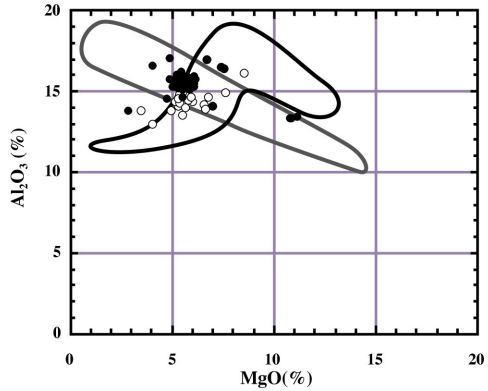


(Fig.1c)

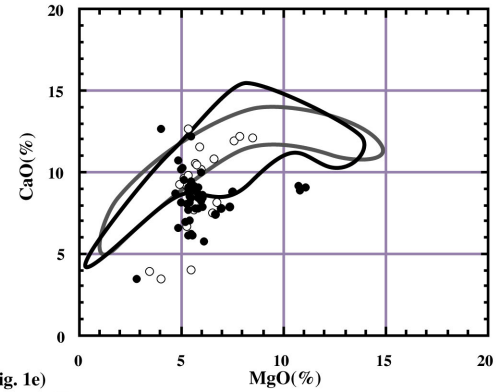


(Fig. 1e)

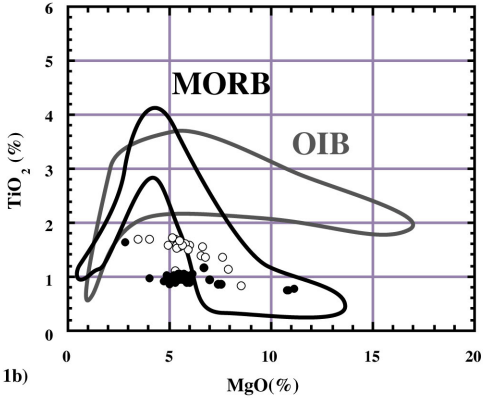


(Fig. 1b)

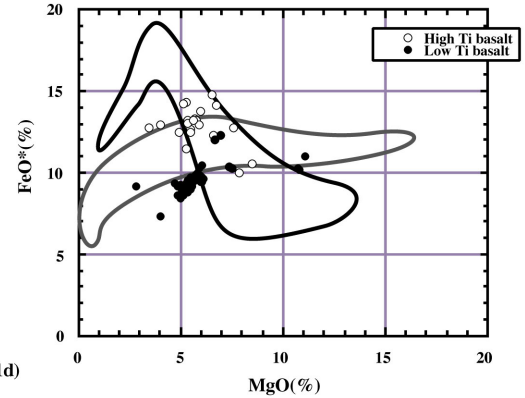


(Fig.1d)

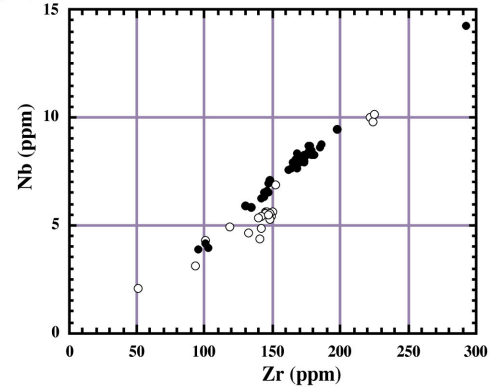


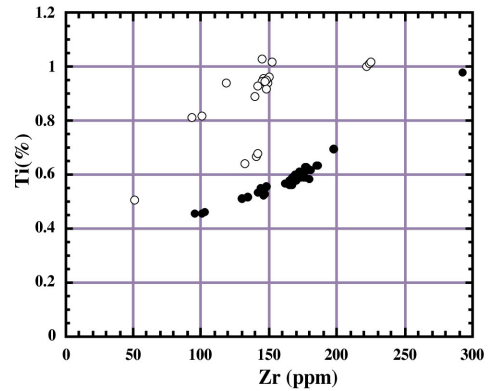


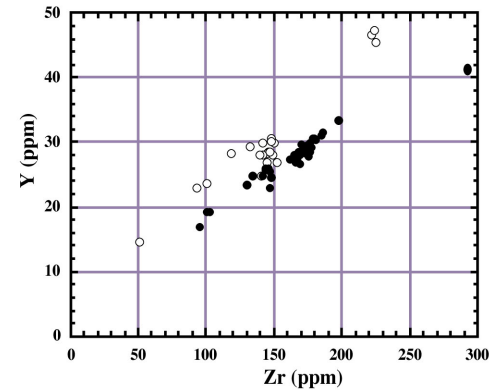


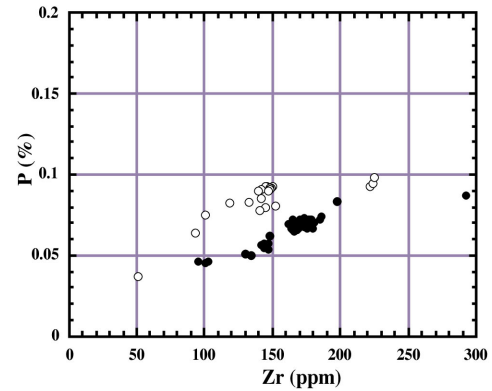

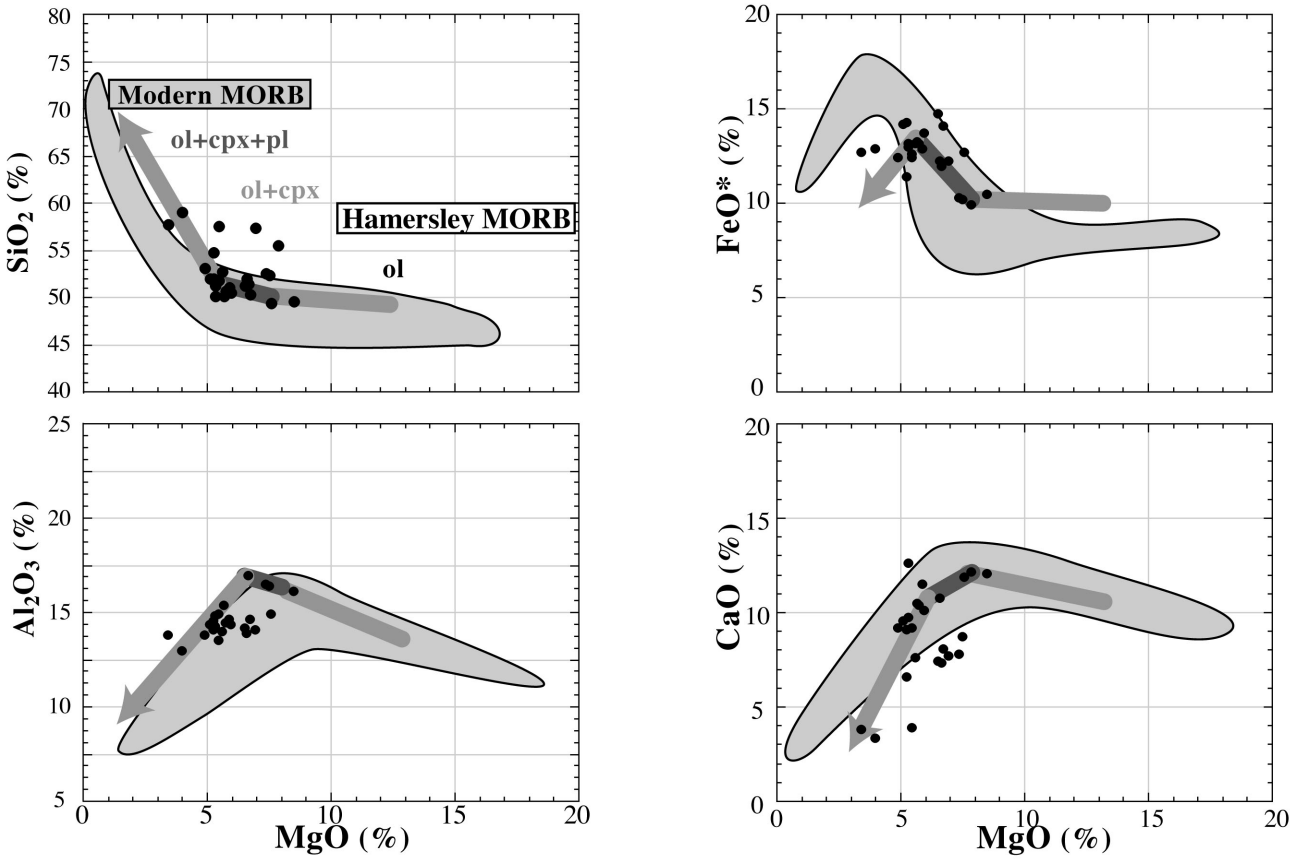


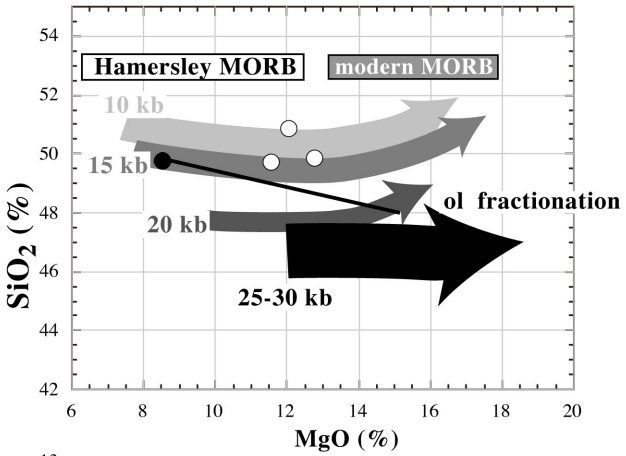


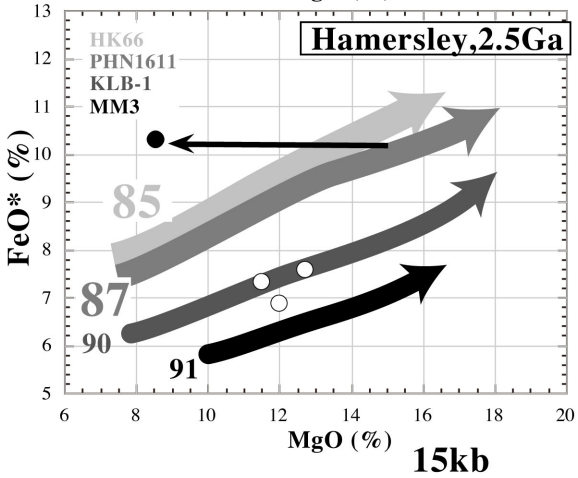


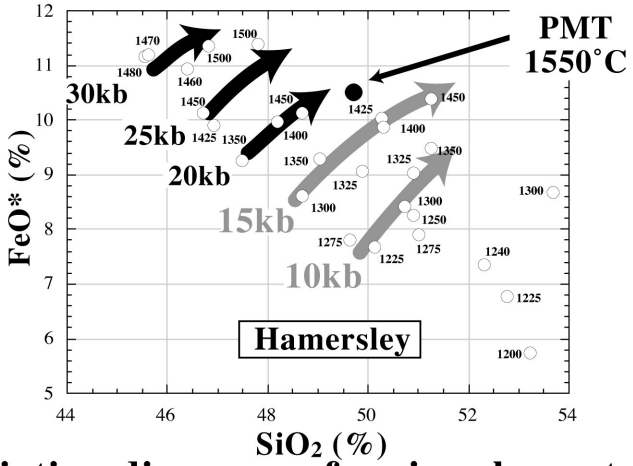


**Variation diagrams of major elements in Beasley River area (2.5Ga), compared with melt compositions by high pressure melting experiment**

## Results

**pressure-------more than10-15kb**
**FeO content in source mantle**
**-----more than10%**
**(Mg#=85-87)**
**PMT=1450-1550˚C**

Komiya 1999 Doctor Thesis Fig. II-11

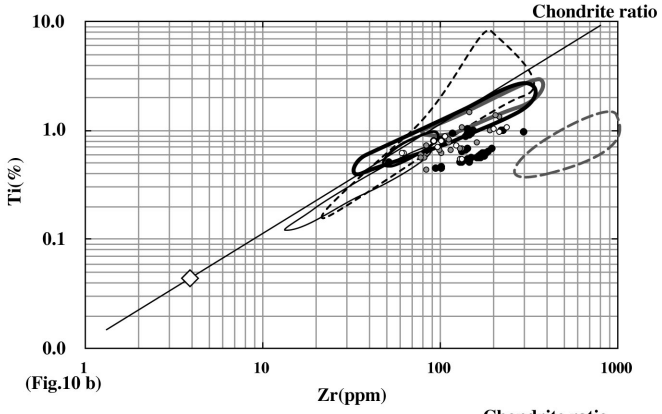


(Fig.10 b)

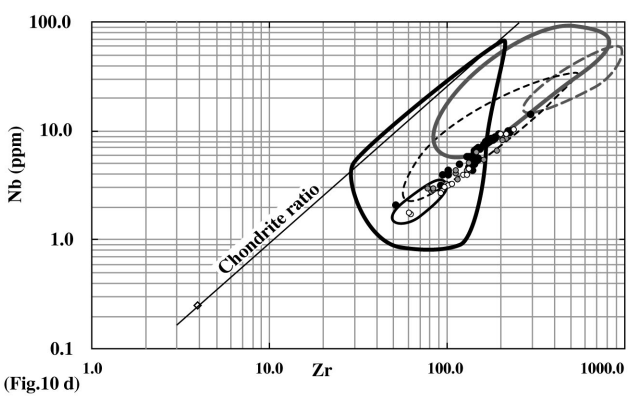


(Fig.10 d)

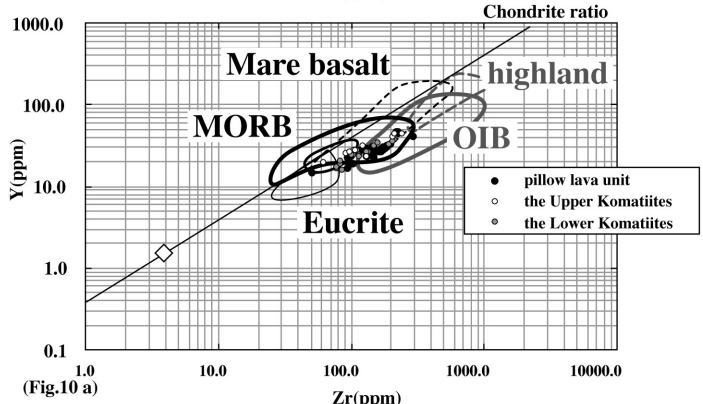


(Fig.10 a)

refractory element vs. volatile

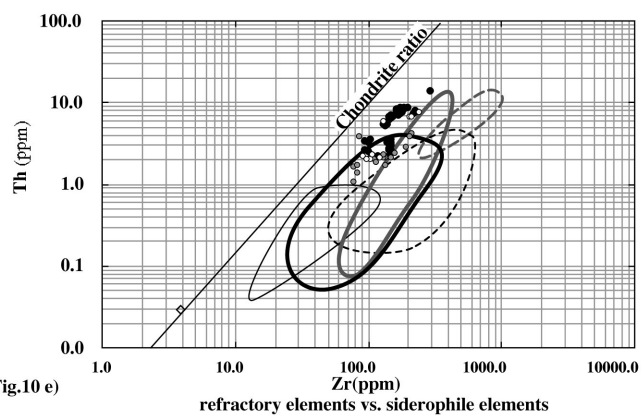


(Fig.10 e)

refractory elements vs. siderophile elements

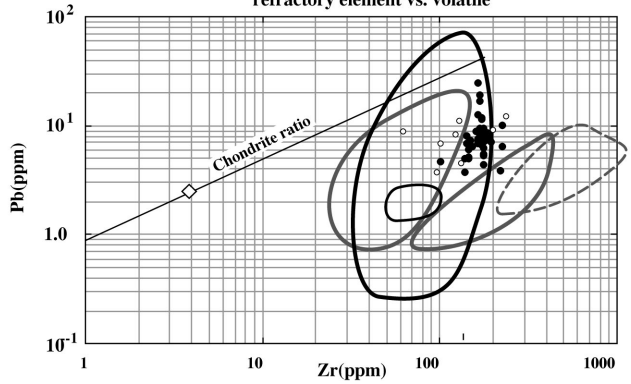


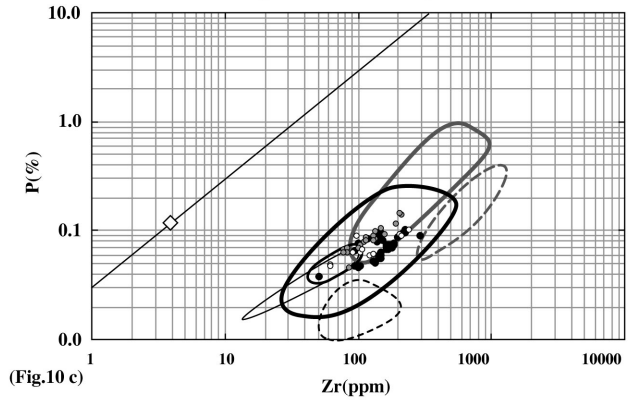


(Fig.10 c)

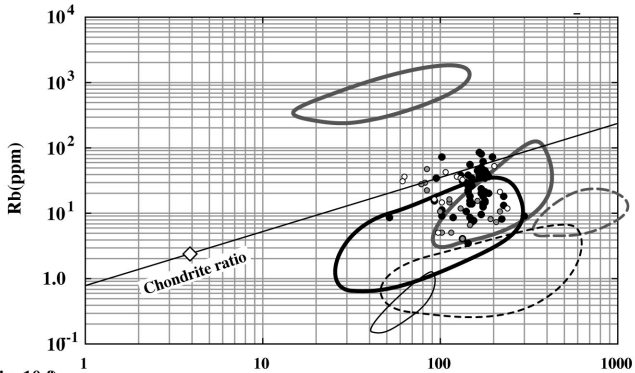


(Fig. 10 f)

refractory element vs. volatite

**Komiya 1999 Doctor Thesis Fig. II-12**

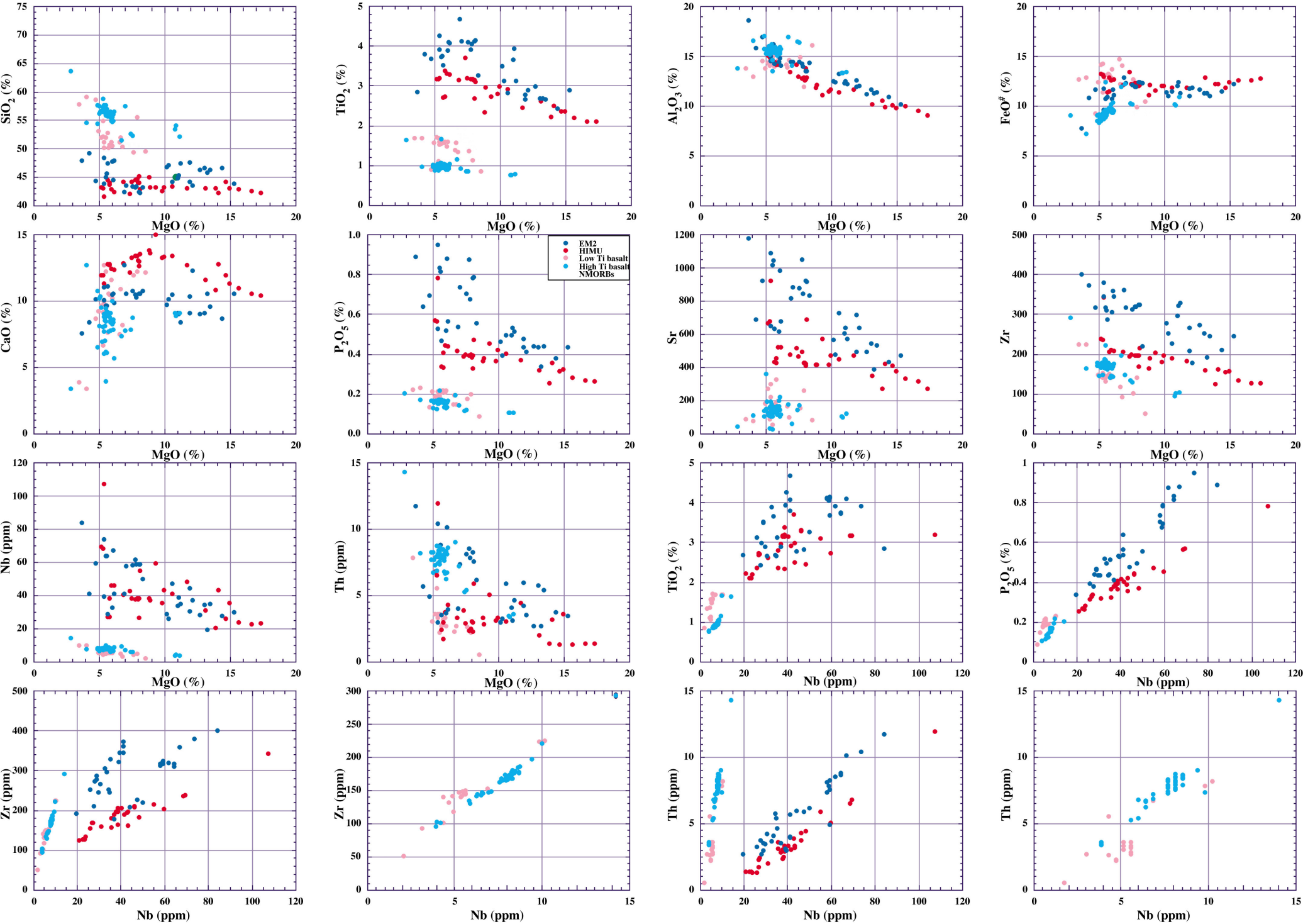


Komiya 1999 Doctor Thesis Fig. II-13

**Table 1 Chemical composition of the Low Ti basalt**

| sample | BR002 | BR003 | BR004 | BR005 | BR006 | BR007 | BR009 | BR010 | BR011 | BR012 | BR013 | BR014 | BR017 | BR021 | BR022 | BR024-2 | BR025 | BR028 | BR029 | BR030 | BR032 | BR033 | BR035 | BR128 |
|---|---|---|---|---|---|---|---|---|---|---|---|---|---|---|---|---|---|---|---|---|---|---|---|---|
| $SiO_2$ | 56.0 | 56.6 | 57.6 | 56.6 | 54.4 | 57.7 | 55.9 | 57.4 | 57.6 | 56.5 | 54.8 | 56.0 | 56.6 | 54.6 | 56.2 | 57.5 | 57.0 | 56.3 | 56.5 | 56.8 | 56.7 | 56.1 | 55.5 | 52.2 |
| $TiO_2$ | 1.04 | 1.05 | 1.03 | 1.04 | 0.96 | 1.03 | 1.00 | 0.99 | 1.00 | 1.06 | 0.89 | 1.01 | 1.02 | 0.96 | 1.00 | 0.93 | 0.95 | 0.99 | 0.95 | 0.98 | 0.94 | 0.98 | 0.95 | 0.77 |
| $Al_2O_3$ | 15.9 | 15.9 | 15.6 | 16.0 | 17.1 | 15.8 | 15.9 | 15.2 | 15.7 | 16.2 | 15.5 | 15.8 | 15.5 | 16.6 | 15.7 | 14.1 | 14.7 | 15.6 | 15.3 | 15.8 | 15.8 | 15.9 | 15.6 | 13.4 |
| FeOt | 9.76 | 8.90 | 9.24 | 9.00 | 9.09 | 8.49 | 9.44 | 9.27 | 8.37 | 9.13 | 9.36 | 9.67 | 9.86 | 7.24 | 9.58 | 12.26 | 9.25 | 9.84 | 8.81 | 8.56 | 9.08 | 9.60 | 9.81 | 10.90 |
| MnO | 0.15 | 0.13 | 0.13 | 0.14 | 0.15 | 0.13 | 0.15 | 0.14 | 0.13 | 0.14 | 0.16 | 0.15 | 0.16 | 0.13 | 0.15 | 0.16 | 0.15 | 0.16 | 0.13 | 0.13 | 0.14 | 0.15 | 0.18 | 0.18 |
| MgO | 5.7 | 5.5 | 5.4 | 5.2 | 4.9 | 4.9 | 5.5 | 5.3 | 5.0 | 5.5 | 6.0 | 5.5 | 5.8 | 4.0 | 5.9 | 7.0 | 5.5 | 5.8 | 5.1 | 5.2 | 5.4 | 6.1 | 5.8 | 11.1 |
| CaO | 7.7 | 6.2 | 6.1 | 7.0 | 10.8 | 6.5 | 9.5 | 8.0 | 8.1 | 7.0 | 10.0 | 8.5 | 7.8 | 12.7 | 8.4 | 7.8 | 9.1 | 8.8 | 10.3 | 9.5 | 9.0 | 7.9 | 8.5 | 9.1 |
| $Na_2O$ | 2.61 | 5.10 | 3.83 | 4.55 | 2.11 | 4.86 | 2.20 | 2.34 | 3.38 | 3.25 | 2.00 | 2.70 | 2.69 | 2.63 | 2.45 | - | 2.00 | 1.93 | 0.59 | 1.63 | 1.70 | 1.43 | 2.39 | 1.82 |
| $K_2O$ | 0.87 | 0.49 | 1.00 | 0.33 | 0.45 | 0.36 | 0.27 | 1.13 | 0.54 | 1.09 | 1.16 | 0.47 | 0.32 | 0.92 | 0.47 | 0.32 | 1.23 | 0.47 | 2.17 | 1.30 | 1.07 | 1.75 | 1.00 | 0.31 |
| $P_2O_5$ | 0.17 | 0.17 | 0.16 | 0.17 | 0.17 | 0.17 | 0.17 | 0.16 | 0.16 | 0.17 | 0.13 | 0.16 | 0.17 | 0.17 | 0.16 | 0.14 | 0.16 | 0.16 | 0.16 | 0.16 | 0.15 | 0.16 | 0.15 | 0.11 |
| total | 100 | 100 | 100 | 100 | 100 | 100 | 100 | 100 | 100 | 100 | 100 | 100 | 100 | 100 | 100 | 100 | 100 | 100 | 100 | 100 | 100 | 100 | 100 | 100 |
| Mg# | | | | | | | | | | | | | | | | | | | | | | | | |
| Ni | 102.2 | 94.3 | 97.0 | 97.8 | 98.1 | 97.2 | 96.3 | 96.2 | 94.3 | 99.5 | 102.6 | 97.0 | 104.4 | 90.2 | 101.6 | 87.1 | 89.3 | 99.2 | 90.9 | 96.1 | 93.6 | 99.9 | 103.1 | 251.5 |
| Rb | 33.7 | 19.1 | 39.2 | 13.9 | 19.1 | 14.8 | 12.0 | 42.0 | 20.8 | 36.1 | 37.1 | 17.8 | 12.6 | 35.7 | 19.3 | 13.2 | 45.6 | 18.9 | 80.5 | 47.6 | 38.9 | 61.0 | 38.2 | 11.0 |
| Sr | 130.6 | 103.5 | 105.7 | 109.7 | 136.1 | 101.9 | 123.2 | 158.9 | 149.8 | 170.6 | 199.0 | 153.4 | 113.4 | 111.6 | 125.6 | 61.1 | 158.4 | 153.5 | 190.9 | 127.5 | 191.7 | 219.7 | 168.6 | 120.5 |
| Y | 29.2 | 31.0 | 30.3 | 30.5 | 29.6 | 30.5 | 28.9 | 29.3 | 29.6 | 31.5 | 26.0 | 29.3 | 28.9 | 28.1 | 28.0 | 24.6 | 27.6 | 28.7 | 28.5 | 27.7 | 26.9 | 28.3 | 27.3 | 19.2 |
| Zr | 177.5 | 184.9 | 180.7 | 178.9 | 170.2 | 178.1 | 173.0 | 173.8 | 175.7 | 186.5 | 143.7 | 173.4 | 172.6 | 164.8 | 168.8 | 148.4 | 163.3 | 172.5 | 167.8 | 167.5 | 165.8 | 173.0 | 165.6 | 102.8 |
| Nb | 8.7 | 8.6 | 8.3 | 8.5 | 7.9 | 8.2 | 7.9 | 8.1 | 8.2 | 8.7 | 6.5 | 8.3 | 8.2 | 7.9 | 8.2 | 7.1 | 7.6 | 8.2 | 7.7 | 7.9 | 7.9 | 8.0 | 7.7 | 3.9 |
| Ba | 247.4 | 166.1 | 337.2 | 128.8 | 175.5 | 184.2 | 94.8 | 419.5 | 230.8 | 361.1 | 311.6 | 152.7 | 220.2 | 487.7 | 215.8 | 68.6 | 388.3 | 158.9 | 807.2 | 633.8 | 412.0 | 402.6 | 405.5 | 159.3 |
| Pb | 7.0 | 8.6 | 7.3 | 5.3 | 16.5 | 4.3 | 11.7 | 7.9 | 9.4 | 8.1 | 6.8 | 9.0 | 7.2 | 24.6 | 8.3 | 7.3 | 7.4 | 8.8 | 7.8 | 19.0 | 6.9 | 11.4 | 7.6 | 3.2 |
| Th | 8.5 | 8.7 | 7.9 | 7.9 | 8.2 | 7.7 | 8.2 | 8.8 | 8.3 | 8.4 | 6.2 | 7.6 | 8.1 | 8.2 | 7.6 | 7.2 | 7.9 | 8.4 | 7.7 | 7.3 | 7.4 | 8.2 | 7.8 | 3.6 |
| La | | | | | | | | | | | | | | | | | | | | | | | | **9.58** |
| Ce | | | | | | | | | | | | | | | | | | | | | | | | **22.2** |
| Pr | | | | | | | | | | | | | | | | | | | | | | | | **2.90** |
| Nd | | | | | | | | | | | | | | | | | | | | | | | | **11.4** |
| Sm | | | | | | | | | | | | | | | | | | | | | | | | **2.70** |
| Eu | | | | | | | | | | | | | | | | | | | | | | | | **0.77** |
| Gd | | | | | | | | | | | | | | | | | | | | | | | | **2.77** |
| Tb | | | | | | | | | | | | | | | | | | | | | | | | **0.49** |
| Dy | | | | | | | | | | | | | | | | | | | | | | | | **3.17** |
| Ho | | | | | | | | | | | | | | | | | | | | | | | | **0.67** |
| Er | | | | | | | | | | | | | | | | | | | | | | | | **1.92** |
| Tm | | | | | | | | | | | | | | | | | | | | | | | | **0.28** |
| Yb | | | | | | | | | | | | | | | | | | | | | | | | **1.73** |
| Lu | | | | | | | | | | | | | | | | | | | | | | | | **0.24** |

Total iron as FeO

**Table 1 (Continued)**

| sample | BR129 | BR132 | BR141 | 95BR001 | 95BR003 | 95BR004 | 95BR006 | 95BR007 | 95BR008 | 95BR009 | 95BR010 | 95BR012 | 95BR013 | 95BR014 | 95BR016 | 95BR023 | 95BR025 | 95BR027 | 95BR037 | 95BR041 | 95BR082 | 95BR095T |
|---|---|---|---|---|---|---|---|---|---|---|---|---|---|---|---|---|---|---|---|---|---|---|
| $SiO_2$ | 54.1 | 52.6 | 56.2 | 63.7 | 57.1 | 55.6 | 53.5 | 55.8 | 52.3 | 56.0 | 55.0 | 56.5 | 56.1 | 56.5 | 55.5 | 58.8 | 56.4 | 54.9 | 56.6 | 57.6 | 56.7 | 51.5 |
| $TiO_2$ | 0.76 | 0.87 | 0.87 | 1.63 | 0.98 | 0.94 | 0.76 | 0.94 | 0.86 | 1.00 | 0.92 | 1.05 | 0.97 | 0.96 | 0.89 | 0.88 | 0.96 | 0.92 | 0.97 | 0.98 | 0.93 | 1.16 |
| $Al_2O_3$ | 13.3 | 16.5 | 15.3 | 13.8 | 15.6 | 15.5 | 13.4 | 15.4 | 16.4 | 15.7 | 15.5 | 15.8 | 15.3 | 15.5 | 15.1 | 15.4 | 15.7 | 15.5 | 15.4 | 15.3 | 15.4 | 16.9 |
| FeOt | 10.13 | 10.24 | 9.16 | 9.10 | 9.03 | 9.71 | 10.14 | 9.40 | 10.15 | 9.61 | 10.21 | 9.54 | 9.31 | 9.44 | 9.88 | 8.90 | 9.36 | 10.40 | 9.36 | 8.74 | 9.38 | 11.91 |
| MnO | 0.17 | 0.16 | 0.16 | 0.11 | 0.14 | 0.15 | 0.17 | 0.14 | 0.17 | 0.14 | 0.16 | 0.15 | 0.14 | 0.14 | 0.16 | 0.13 | 0.16 | 0.17 | 0.15 | 0.13 | 0.15 | 0.14 |
| MgO | 10.8 | 7.4 | 5.0 | 2.8 | 5.5 | 6.0 | 10.8 | 5.6 | 7.5 | 5.6 | 6.0 | 6.1 | 6.1 | 5.4 | 5.8 | 5.3 | 5.4 | 6.1 | 5.4 | 5.4 | 5.4 | 6.7 |
| CaO | 8.9 | 7.8 | 10.2 | 3.4 | 6.1 | 8.3 | 9.1 | 9.2 | 8.8 | 8.9 | 8.6 | 5.7 | 8.4 | 8.8 | 9.1 | 8.0 | 8.5 | 8.6 | 8.1 | 7.7 | 8.7 | 7.4 |
| $Na_2O$ | 0.61 | 3.25 | 1.22 | 0.24 | 0.37 | 2.28 | 0.78 | 1.50 | 1.14 | 1.39 | 0.54 | 0.48 | 0.62 | 1.24 | 0.76 | 0.42 | 0.24 | 0.63 | 0.51 | 1.34 | 1.32 | 1.58 |
| $K_2O$ | 1.11 | 1.03 | 1.83 | 5.05 | 4.98 | 1.43 | 1.30 | 1.91 | 2.54 | 1.48 | 2.92 | 4.50 | 2.95 | 1.87 | 2.55 | 1.96 | 3.13 | 2.67 | 3.39 | 2.69 | 1.77 | 2.49 |
| $P_2O_5$ | 0.11 | 0.12 | 0.13 | 0.20 | 0.16 | 0.15 | 0.11 | 0.16 | 0.12 | 0.17 | 0.13 | 0.17 | 0.15 | 0.16 | 0.13 | 0.12 | 0.15 | 0.13 | 0.16 | 0.16 | 0.15 | 0.20 |
| total | 100 | 100 | 100 | 100 | 100 | 100 | 100 | 100 | 100 | 100 | 100 | 100 | 100 | 100 | 100 | 100 | 100 | 100 | 100 | 100 | 100 | 100 |
| Mg# | | | | | | | | | | | | | | | | | | | | | | |
| Ni | 218.8 | 116.7 | 61.1 | 33.6 | 98.9 | 98.9 | 244.9 | 94.4 | 114.9 | 95.5 | 107.0 | 105.8 | 97.0 | 91.6 | 103.4 | 89.1 | 96.7 | 107.8 | 99.2 | 87.6 | 95.6 | 108.8 |
| Rb | 72.5 | 30.9 | 54.8 | 8.7 | 13.7 | 84.1 | 32.7 | 44.2 | 36.4 | 43.1 | 17.5 | 19.7 | 22.9 | 41.0 | 25.1 | 14.9 | 9.1 | 20.9 | 20.0 | 44.4 | 42.4 | 72.5 |
| Sr | 96.7 | 145.1 | 362.6 | 41.8 | 135.2 | 164.1 | 103.1 | 160.3 | 169.7 | 157.8 | 155.1 | 118.4 | 104.9 | 151.3 | 146.9 | 32.8 | 178.9 | 144.5 | 124.9 | 154.2 | 116.4 | 179.6 |
| Y | 19.3 | 24.8 | 26.0 | 41.2 | 27.8 | 27.3 | 16.9 | 27.4 | 23.4 | 29.0 | 25.6 | 28.5 | 26.6 | 27.4 | 24.8 | 22.9 | 27.9 | 25.6 | 30.5 | 30.0 | 28.0 | 33.4 |
| Zr | 100.9 | 134.1 | 146.3 | 292.8 | 175.1 | 165.3 | 95.3 | 162.1 | 130.1 | 172.9 | 146.8 | 176.0 | 169.1 | 167.2 | 141.4 | 147.1 | 168.0 | 144.0 | 179.9 | 176.3 | 166.7 | 197.7 |
| Nb | 4.2 | 5.8 | 6.6 | 14.2 | 8.3 | 7.7 | 3.9 | 7.6 | 5.9 | 8.2 | 6.5 | 8.7 | 8.2 | 8.1 | 6.2 | 6.9 | 8.3 | 6.3 | 8.3 | 8.4 | 7.7 | 9.4 |
| Ba | 280.4 | 352.2 | 629.2 | 78.8 | 183.4 | 782.4 | 199.5 | 407.5 | 352.4 | 313.4 | 213.0 | 239.2 | 239.7 | 272.8 | 247.5 | 437.3 | 115.5 | 219.8 | 277.5 | 373.2 | 400.5 | 536.6 |
| Pb | 4.7 | 3.0 | 5.0 | 3.4 | 6.7 | 7.3 | 2.4 | 8.8 | 2.7 | 7.0 | 6.1 | 5.5 | 9.0 | 6.8 | 6.9 | 6.7 | 8.3 | 8.0 | 9.1 | 6.3 | 12.6 | 7.2 |
| Th | 3.4 | 5.3 | 6.7 | 14.3 | 8.5 | 8.3 | 3.5 | 7.9 | 5.4 | 8.0 | 6.7 | 8.6 | 8.1 | 8.1 | 6.8 | 6.9 | 8.2 | 6.7 | 8.3 | 8.1 | 7.9 | 9.0 |
| La | **12.24** | | | | | | **13.89** | | | | | | | | | | | | | | | |
| Ce | **27.3** | | | | | | **30.2** | | | | | | | | | | | | | | | |
| Pr | **3.34** | | | | | | **3.54** | | | | | | | | | | | | | | | |
| Nd | **12.8** | | | | | | **13.4** | | | | | | | | | | | | | | | |
| Sm | **2.88** | | | | | | **2.96** | | | | | | | | | | | | | | | |
| Eu | **0.87** | | | | | | **0.92** | | | | | | | | | | | | | | | |
| Gd | **2.97** | | | | | | **3.04** | | | | | | | | | | | | | | | |
| Tb | **0.50** | | | | | | **0.50** | | | | | | | | | | | | | | | |
| Dy | **3.26** | | | | | | **3.24** | | | | | | | | | | | | | | | |
| Ho | **0.69** | | | | | | **0.67** | | | | | | | | | | | | | | | |
| Er | **2.01** | | | | | | **1.94** | | | | | | | | | | | | | | | |
| Tm | **0.30** | | | | | | **0.29** | | | | | | | | | | | | | | | |
| Yb | **1.99** | | | | | | **1.82** | | | | | | | | | | | | | | | |
| Lu | **0.31** | | | | | | **0.26** | | | | | | | | | | | | | | | |

Total iron as FeO

**Table 2 Chemical composition of the High Ti basalt**

| sample | BR054 | BR133 | BR145 | BR148 | BR183 | 95BR053T | 95BR054 | 95BR055 | 95BR057 | 95BR058 | 95BR067 | 95BR092C | 95BR104 | 95BR105 | 95BR106 | 95BR107 | BR126 | BR133 | BR151 | BR184 | BR185 | BR186 | BR187 | 95BR091 |
|---|---|---|---|---|---|---|---|---|---|---|---|---|---|---|---|---|---|---|---|---|---|---|---|---|
| $SiO_2$ | 52.1 | 57.6 | 52.0 | 49.6 | 50.3 | 50.5 | 50.2 | 51.9 | 52.0 | 49.4 | 50.7 | 53.2 | 51.3 | 50.1 | 51.1 | 52.8 | 56.2 | 57.6 | 58.6 | 51.2 | 54.9 | 57.8 | 59.1 | 55.6 |
| $TiO_2$ | 1.70 | 1.67 | 1.71 | 0.84 | 1.35 | 1.59 | 1.57 | 1.55 | 1.57 | 1.37 | 1.60 | 1.57 | 1.58 | 1.53 | 1.49 | 1.58 | 1.06 | 1.67 | 0.90 | 1.38 | 1.12 | 1.69 | 1.69 | 1.13 |
| $Al_2O_3$ | 14.0 | 13.5 | 14.3 | 16.1 | 14.7 | 14.3 | 15.3 | 14.9 | 13.9 | 14.9 | 14.4 | 13.8 | 14.8 | 14.3 | 14.6 | 14.0 | 15.1 | 13.5 | 14.6 | 14.2 | 14.6 | 13.8 | 13.0 | 11.9 |
| FeOt | 14.24 | 12.38 | 14.21 | 10.47 | 14.09 | 13.76 | 13.21 | 12.57 | 12.24 | 12.69 | 13.19 | 12.38 | 13.14 | 12.94 | 12.90 | 13.20 | 9.55 | 12.38 | 9.25 | 14.74 | 11.44 | 12.74 | 12.86 | 9.88 |
| MnO | 0.28 | 0.18 | 0.21 | 0.18 | 0.17 | 0.22 | 0.20 | 0.19 | 0.20 | 0.20 | 0.23 | 0.19 | 0.20 | 0.19 | 0.19 | 0.22 | 0.14 | 0.18 | 0.15 | 0.18 | 0.19 | 0.33 | 0.22 | 0.12 |
| MgO | 5.3 | 5.5 | 5.1 | 8.5 | 6.8 | 6.0 | 5.7 | 5.5 | 6.7 | 7.6 | 5.8 | 5.0 | 5.4 | 5.4 | 5.9 | 5.7 | 5.5 | 5.5 | 4.8 | 6.6 | 5.3 | 3.5 | 4.0 | 7.9 |
| CaO | 9.1 | 3.9 | 9.7 | 12.2 | 8.2 | 10.2 | 10.6 | 9.3 | 10.9 | 11.9 | 10.5 | 9.2 | 9.9 | 12.7 | 11.6 | 7.6 | 12.2 | 3.9 | 8.7 | 7.5 | 6.7 | 3.9 | 3.4 | 12.2 |
| $Na_2O$ | 1.73 | 4.17 | 1.71 | 1.71 | 3.70 | 2.22 | 0.76 | 0.68 | 0.26 | 0.28 | 1.08 | 0.25 | 0.79 | 0.46 | 0.33 | 0.27 | - | 4.17 | 2.71 | 3.56 | 4.02 | 4.49 | 3.92 | 0.10 |
| $K_2O$ | 1.27 | 0.79 | 0.86 | 0.29 | 0.62 | 0.94 | 2.24 | 3.15 | 2.10 | 1.43 | 2.27 | 4.26 | 2.78 | 2.14 | 1.54 | 4.44 | 0.09 | 0.79 | 0.23 | 0.49 | 1.63 | 1.54 | 1.56 | 0.95 |
| $P_2O_5$ | 0.19 | 0.22 | 0.19 | 0.09 | 0.15 | 0.22 | 0.22 | 0.21 | 0.19 | 0.17 | 0.22 | 0.21 | 0.21 | 0.21 | 0.21 | 0.21 | 0.19 | 0.22 | 0.13 | 0.15 | 0.18 | 0.22 | 0.23 | 0.20 |
| total | 100 | 100 | 100 | 100 | 100 | 100 | 100 | 100 | 100 | 100 | 100 | 100 | 100 | 100 | 100 | 100 | 100 | 100 | 100 | 100 | 100 | 100 | 100 | 100 |
| Mg# | | | | | | | | | | | | | | | | | | | | | | | | |
| Ni | 59.7 | 9.0 | 44.1 | 130.5 | 66.1 | 71.4 | 83.3 | 79.2 | 70.1 | 140.0 | 69.0 | 72.1 | 66.2 | 65.2 | 73.6 | 71.3 | 66.1 | 9.0 | | | 56.6 | 8.4 | 7.0 | 58.9 |
| Rb | 7.5 | 8.1 | 20.9 | 8.3 | 15.0 | 28.5 | 21.5 | 21.2 | 8.3 | 8.8 | 33.4 | 7.0 | 25.4 | 13.3 | 10.4 | 8.6 | 4.0 | 8.1 | | | 28.2 | 17.7 | 12.8 | 3.3 |
| Sr | 146.2 | 28.0 | 271.2 | 84.7 | 101.7 | 158.2 | 182.1 | 157.0 | 164.3 | 152.6 | 329.6 | 182.2 | 220.4 | 301.7 | 196.9 | 153.6 | 55.5 | 28.0 | | | 89.2 | 89.4 | 74.0 | 263.3 |
| Y | 26.8 | 46.5 | 26.8 | 14.6 | 22.9 | 28.5 | 28.3 | 28.0 | 28.3 | 23.6 | 29.8 | 28.1 | 30.6 | 30.1 | 28.0 | 28.6 | 29.5 | 46.5 | | | 24.7 | 47.2 | 45.5 | 29.8 |
| Zr | 152.5 | 221.3 | 144.4 | 51.1 | 93.4 | 145.7 | 144.7 | 141.7 | 118.2 | 101.1 | 149.9 | 149.0 | 148.3 | 147.8 | 139.9 | 146.5 | 132.2 | 221.3 | | | 140.2 | 224.4 | 225.3 | 141.8 |
| Nb | 6.8 | 10.0 | 5.6 | 2.1 | 3.1 | 5.6 | 5.5 | 5.4 | 4.9 | 4.3 | 5.6 | 5.4 | 5.5 | 5.2 | 5.3 | 5.5 | 4.7 | 10.0 | | | 4.4 | 9.8 | 10.1 | 4.9 |
| Ba | 121.6 | 194.1 | 374.2 | 45.6 | 194.0 | 355.9 | 278.5 | 315.4 | 72.9 | 62.4 | 616.3 | 92.5 | 269.3 | 216.2 | 108.7 | 119.4 | 66.1 | 194.1 | | | 262.7 | 505.3 | 373.3 | 58.9 |
| Pb | 6.5 | 3.8 | 3.6 | 1.7 | 3.4 | 2.1 | 2.5 | 3.5 | 1.9 | 1.7 | 3.5 | 2.9 | 2.5 | 4.9 | 3.7 | 1.4 | 2.9 | 3.8 | | | 5.0 | 9.9 | 6.4 | 1.9 |
| Th | 6.7 | 7.3 | 3.6 | 0.5 | 2.7 | 2.7 | 2.8 | 3.6 | 2.3 | 2.6 | 3.2 | 3.0 | 3.3 | 3.6 | 3.3 | 2.7 | 2.2 | 7.3 | | | 5.6 | 7.8 | 8.2 | 2.2 |
| La | | | | **4.47** | | | | | | | | | | | | | | | | | | | | |
| Ce | | | | **10.4** | | | | | | | | | | | | | | | | | | | | |
| Pr | | | | **1.57** | | | | | | | | | | | | | | | | | | | | |
| Nd | | | | **7.05** | | | | | | | | | | | | | | | | | | | | |
| Sm | | | | **1.94** | | | | | | | | | | | | | | | | | | | | |
| Eu | | | | **1.00** | | | | | | | | | | | | | | | | | | | | |
| Gd | | | | **2.15** | | | | | | | | | | | | | | | | | | | | |
| Tb | | | | **0.37** | | | | | | | | | | | | | | | | | | | | |
| Dy | | | | **2.37** | | | | | | | | | | | | | | | | | | | | |
| Ho | | | | **0.48** | | | | | | | | | | | | | | | | | | | | |
| Er | | | | **1.34** | | | | | | | | | | | | | | | | | | | | |
| Tm | | | | **0.19** | | | | | | | | | | | | | | | | | | | | |
| Yb | | | | **1.21** | | | | | | | | | | | | | | | | | | | | |
| Lu | | | | **0.17** | | | | | | | | | | | | | | | | | | | | |

Total iron as FeO

**Table 3 Chemical composition of gabboric samples**

| sample | BR009 | BR010 | BR185 | BR187 | 95BR008 | 95BR055 | 95BR057 | 95BR058 | 95BR082 |
|---|---|---|---|---|---|---|---|---|---|
| $SiO_2$ | 55.9 | 57.4 | 54.9 | 59.1 | 52.3 | 51.9 | 52.0 | 49.4 | 56.7 |
| $TiO_2$ | 1.00 | 0.99 | 1.12 | 1.69 | 0.86 | 1.55 | 1.57 | 1.37 | 0.93 |
| $Al_2O_3$ | 15.9 | 15.2 | 14.6 | 13.0 | 16.4 | 14.9 | 13.9 | 14.9 | 15.4 |
| FeOt | 9.44 | 9.27 | 11.44 | 12.86 | 10.15 | 12.57 | 12.24 | 12.69 | 9.38 |
| MnO | 0.15 | 0.14 | 0.19 | 0.22 | 0.17 | 0.19 | 0.20 | 0.20 | 0.15 |
| MgO | 5.5 | 5.3 | 5.3 | 4.0 | 7.5 | 5.5 | 6.7 | 7.6 | 5.4 |
| CaO | 9.5 | 8.0 | 6.7 | 3.4 | 8.8 | 9.3 | 10.9 | 11.9 | 8.7 |
| $Na_2O$ | 2.20 | 2.34 | 4.02 | 3.92 | 1.14 | 0.68 | 0.26 | 0.28 | 1.32 |
| $K_2O$ | 0.27 | 1.13 | 1.63 | 1.56 | 2.54 | 3.15 | 2.10 | 1.43 | 1.77 |
| $P_2O_5$ | 0.17 | 0.16 | 0.18 | 0.23 | 0.12 | 0.21 | 0.19 | 0.17 | 0.15 |
| total | 100 | 100 | 100 | 100 | 100 | 100 | 100 | 100 | 100 |
| Mg# | | | | | | | | | |
| Ni | 96.3 | 96.2 | 56.6 | 7.0 | 114.9 | 79.2 | 70.1 | 140.0 | 95.6 |
| Rb | 12.0 | 42.0 | 28.2 | 12.8 | 36.4 | 21.2 | 8.3 | 8.8 | 42.4 |
| Sr | 123.2 | 158.9 | 89.2 | 74.0 | 169.7 | 157.0 | 164.3 | 152.6 | 116.4 |
| Y | 28.9 | 29.3 | 24.7 | 45.5 | 23.4 | 28.0 | 28.3 | 23.6 | 28.0 |
| Zr | 173.0 | 173.8 | 140.2 | 225.3 | 130.1 | 141.7 | 118.2 | 101.1 | 166.7 |
| Nb | 7.9 | 8.1 | 4.4 | 10.1 | 5.9 | 5.4 | 4.9 | 4.3 | 7.7 |
| Ba | 94.8 | 419.5 | 262.7 | 373.3 | 352.4 | 315.4 | 72.9 | 62.4 | 400.5 |
| Pb | 11.7 | 7.9 | 5.0 | 6.4 | 2.7 | 3.5 | 1.9 | 1.7 | 12.6 |
| Th | 8.2 | 8.8 | 5.6 | 8.2 | 5.4 | 3.6 | 2.3 | 2.6 | 7.9 |

Total iron as FeO

**Table 4 Chemical composition of aphyric samples**

| sample | BR002 | BR012 | BR013 | BR033 | BR054 | BR133 | BR141 | BR151 | BR184 | BR185 | BR186 | 95BR053T | 95BR054 | 95BR067 | 95BR091 | 95BR092C | 95BR095T | 95BR104 | 95BR105 | 95BR106 | 95BR107 |
|---|---|---|---|---|---|---|---|---|---|---|---|---|---|---|---|---|---|---|---|---|---|
| $SiO_2$ | 56.0 | 56.5 | 54.8 | 56.1 | 52.1 | 57.6 | 56.2 | 58.6 | 51.2 | 54.9 | 57.8 | 50.5 | 50.2 | 50.7 | 55.6 | 53.2 | 51.5 | 51.3 | 50.1 | 51.1 | 52.8 |
| $TiO_2$ | 1.04 | 1.06 | 0.89 | 0.98 | 1.70 | 1.67 | 0.87 | 0.90 | 1.38 | 1.12 | 1.69 | 1.59 | 1.57 | 1.60 | 1.13 | 1.57 | 1.16 | 1.58 | 1.53 | 1.49 | 1.58 |
| $Al_2O_3$ | 15.9 | 16.2 | 15.5 | 15.9 | 14.0 | 13.5 | 15.3 | 14.6 | 14.2 | 14.6 | 13.8 | 14.3 | 15.3 | 14.4 | 11.9 | 13.8 | 16.9 | 14.8 | 14.3 | 14.6 | 14.0 |
| FeOt | 9.76 | 9.13 | 9.36 | 9.60 | 14.24 | 12.38 | 9.16 | 9.25 | 14.74 | 11.44 | 12.74 | 13.76 | 13.21 | 13.19 | 9.88 | 12.38 | 11.91 | 13.14 | 12.94 | 12.90 | 13.20 |
| MnO | 0.15 | 0.14 | 0.16 | 0.15 | 0.28 | 0.18 | 0.16 | 0.15 | 0.18 | 0.19 | 0.33 | 0.22 | 0.20 | 0.23 | 0.12 | 0.19 | 0.14 | 0.20 | 0.19 | 0.19 | 0.22 |
| MgO | 5.7 | 5.5 | 6.0 | 6.1 | 5.3 | 5.5 | 5.0 | 4.8 | 6.6 | 5.3 | 3.5 | 6.0 | 5.7 | 5.8 | 7.9 | 5.0 | 6.7 | 5.4 | 5.4 | 5.9 | 5.7 |
| CaO | 7.7 | 7.0 | 10.0 | 7.9 | 9.1 | 3.9 | 10.2 | 8.7 | 7.5 | 6.7 | 3.9 | 10.2 | 10.6 | 10.5 | 12.2 | 9.2 | 7.4 | 9.9 | 12.7 | 11.6 | 7.6 |
| $Na_2O$ | 2.61 | 3.25 | 2.00 | 1.43 | 1.73 | 4.17 | 1.22 | 2.71 | 3.56 | 4.02 | 4.49 | 2.22 | 0.76 | 1.08 | 0.10 | 0.25 | 1.58 | 0.79 | 0.46 | 0.33 | 0.27 |
| $K_2O$ | 0.87 | 1.09 | 1.16 | 1.75 | 1.27 | 0.79 | 1.83 | 0.23 | 0.49 | 1.63 | 1.54 | 0.94 | 2.24 | 2.27 | 0.95 | 4.26 | 2.49 | 2.78 | 2.14 | 1.54 | 4.44 |
| $P_2O_5$ | 0.17 | 0.17 | 0.13 | 0.16 | 0.19 | 0.22 | 0.13 | 0.13 | 0.15 | 0.18 | 0.22 | 0.22 | 0.22 | 0.22 | 0.20 | 0.21 | 0.20 | 0.21 | 0.21 | 0.21 | 0.21 |
| total | 100 | 100 | 100 | 100 | 100 | 100 | 100 | 100 | 100 | 100 | 100 | 100 | 100 | 100 | 100 | 100 | 100 | 100 | 100 | 100 | 100 |
| Mg# | | | | | | | | | | | | | | | | | | | | | |
| Ni | 102.2 | 99.5 | 102.6 | 99.9 | 59.7 | 9.0 | 61.1 | | | 56.6 | 8.4 | 71.4 | 83.3 | 69.0 | 58.9 | 72.1 | 108.8 | 66.2 | 65.2 | 73.6 | 71.3 |
| Rb | 33.7 | 36.1 | 37.1 | 61.0 | 7.5 | 8.1 | 54.8 | | | 28.2 | 17.7 | 28.5 | 21.5 | 33.4 | 3.3 | 7.0 | 72.5 | 25.4 | 13.3 | 10.4 | 8.6 |
| Sr | 130.6 | 170.6 | 199.0 | 219.7 | 146.2 | 28.0 | 362.6 | | | 89.2 | 89.4 | 158.2 | 182.1 | 329.6 | 263.3 | 182.2 | 179.6 | 220.4 | 301.7 | 196.9 | 153.6 |
| Y | 29.2 | 31.5 | 26.0 | 28.3 | 26.8 | 46.5 | 26.0 | | | 24.7 | 47.2 | 28.5 | 28.3 | 29.8 | 29.8 | 28.1 | 33.4 | 30.6 | 30.1 | 28.0 | 28.6 |
| Zr | 177.5 | 186.5 | 143.7 | 173.0 | 152.5 | 221.3 | 146.3 | | | 140.2 | 224.4 | 145.7 | 144.7 | 149.9 | 141.8 | 149.0 | 197.7 | 148.3 | 147.8 | 139.9 | 146.5 |
| Nb | 8.7 | 8.7 | 6.5 | 8.0 | 6.8 | 10.0 | 6.6 | | | 4.4 | 9.8 | 5.6 | 5.5 | 5.6 | 4.9 | 5.4 | 9.4 | 5.5 | 5.2 | 5.3 | 5.5 |
| Ba | 247.4 | 361.1 | 311.6 | 402.6 | 121.6 | 194.1 | 629.2 | | | 262.7 | 505.3 | 355.9 | 278.5 | 616.3 | 58.9 | 92.5 | 536.6 | 269.3 | 216.2 | 108.7 | 119.4 |
| Pb | 7.0 | 8.1 | 6.8 | 11.4 | 6.5 | 3.8 | 5.0 | | | 5.0 | 9.9 | 2.1 | 2.5 | 3.5 | 1.9 | 2.9 | 7.2 | 2.5 | 4.9 | 3.7 | 1.4 |
| Th | 8.5 | 8.4 | 6.2 | 8.2 | 6.7 | 7.3 | 6.7 | | | 5.6 | 7.8 | 2.7 | 2.8 | 3.2 | 2.2 | 3.0 | 9.0 | 3.3 | 3.6 | 3.3 | 2.7 |

Total iron as FeO

Table 5 Chemical composition of altered samples

| sample | BR001C | BR008 | BR015 | BR018 | BR019 | BR034 | BR046 | BR047 | BR062 | LBR10 | LBR11 | BR096 | BR097 |
|---|---|---|---|---|---|---|---|---|---|---|---|---|---|
| $SiO_2$ | 54.2 | 58.7 | 55.9 | 55.8 | 55.6 | 58.0 | 46.6 | 56.9 | 49.3 | 45.8 | 75.16 | 73.6 | 73.6 |
| $TiO_2$ | 1.01 | 1.04 | 0.94 | 0.89 | 0.98 | 1.01 | 1.05 | 1.22 | 1.08 | 0.64 | 0.34 | 0.36 | 0.35 |
| $Al_2O_3$ | 15.59 | 15.65 | 15.50 | 15.34 | 15.67 | 16.71 | 15.87 | 18.05 | 16.2 | 16.0 | 11.64 | 11.78 | 11.46 |
| FeOt | 9.52 | 10.01 | 7.62 | 7.49 | 8.29 | 5.54 | 10.94 | 12.82 | 10.71 | 10.04 | 2.65 | 5.20 | 5.48 |
| MnO | 0.14 | 0.15 | 0.11 | 0.12 | 0.14 | 0.10 | 0.19 | 0.19 | 0.18 | 0.18 | 0.03 | 0.02 | 0.03 |
| MgO | 5.52 | 5.52 | 4.25 | 4.35 | 5.26 | 3.74 | 7.99 | 7.78 | 7.5 | 9.8 | 0.68 | 2.10 | 2.08 |
| CaO | 5.93 | 6.43 | 8.51 | 12.56 | 8.53 | 2.89 | 11.91 | 8.02 | 11.4 | 12.1 | 0.86 | 0.15 | 0.13 |
| $Na_2O$ | 4.29 | 3.62 | 2.24 | 1.15 | 3.27 | 0.37 | 1.35 | 3.08 | 1.79 | 1.51 | 2.64 | 0.84 | 0.57 |
| $K_2O$ | 0.68 | 0.32 | 2.23 | 0.65 | 0.38 | 8.35 | 0.35 | 0.70 | 0.12 | 0.38 | 4.55 | 5.37 | 5.36 |
| $P_2O_5$ | 0.16 | 0.17 | 0.15 | 0.15 | 0.16 | 0.17 | 0.11 | 0.12 | 0.11 | 0.06 | 0.06 | 0.07 | 0.06 |
| total | 87.5 | 91.6 | 89.8 | 91.0 | 90.0 | 91.3 | 85.5 | 96.0 | 87.7 | 86.6 | 95.97 | 100.0 | 99.7 |
| Mg# | | | | | | | | | | | | | |
| Ni | 97.2 | 83.7 | 73.8 | 75.9 | 99.9 | 89.0 | 140.8 | 119.8 | 53.7 | | | - | - |
| Rb | 27.0 | 14.5 | 75.1 | 24.4 | 15.9 | 268.0 | 11.6 | 22.4 | 29.3 | | | 107.8 | 112.5 |
| Sr | 129.4 | 108.7 | 95.1 | 96.8 | 121.5 | 56.5 | 63.3 | 236.1 | 169.7 | | | 16.2 | 13.7 |
| Y | 31.1 | 28.7 | 28.2 | 26.4 | 30.7 | 26.1 | 18.2 | 20.8 | 23.4 | | | 66.1 | 66.4 |
| Zr | 178.7 | 176.6 | 169.8 | 161.4 | 177.6 | 187.2 | 61.7 | 70.4 | 131.2 | | | 532.2 | 527.7 |
| Nb | 8.4 | 8.3 | 8.0 | 7.7 | 8.4 | 8.7 | 2.2 | 2.6 | 5.3 | | | 21.9 | 21.9 |
| Ba | 209.7 | 185.0 | 875.5 | 290.5 | 150.1 | 1890.6 | 145.2 | 83.8 | 387.6 | | | 595.2 | 486.6 |
| Pb | 6.5 | 5.8 | 7.4 | 15.7 | 8.3 | 7.3 | - | - | 8.0 | | | 5.9 | 4.5 |
| Th | 8.7 | 8.2 | 7.6 | 7.8 | 8.1 | 8.3 | - | - | 3.9 | | | 20.4 | 20.5 |

Total iron as FeO

Table 6 Chemical composition of the Lower Komatiites

| sample | 95BR019 | 95BR020 | 95BR030 | 95BR031 | 95BR032 | 95BR046 | 95BR048 | 95BR051T | 95BR064 | 95BR065 | 95BR068 | 95BR070 | 95BR075 | 95BR083 | 95BR085 | 95BR098 | 95BR100 | 95BR103 | 95BR109 |
|---|---|---|---|---|---|---|---|---|---|---|---|---|---|---|---|---|---|---|---|
| $SiO_2$ | 50.8 | 52.1 | 53.4 | 52.1 | 51.7 | 50.1 | 50.6 | 52.4 | 53.4 | 56.8 | 50.0 | 53.4 | 56.4 | 50.7 | 55.9 | 51.6 | 48.3 | 54.9 | 58.7 |
| $TiO_2$ | 2.50 | 1.00 | 1.69 | 1.31 | 0.95 | 2.22 | 1.23 | 1.04 | 1.14 | 1.13 | 1.40 | 1.11 | 0.74 | 1.78 | 1.28 | 0.94 | 2.28 | 1.13 | 1.10 |
| $Al_2O_3$ | 13.9 | 15.4 | 13.9 | 15.2 | 16.7 | 14.4 | 14.1 | 11.3 | 11.4 | 11.0 | 15.3 | 14.1 | 15.7 | 14.8 | 15.0 | 16.7 | 14.6 | 11.9 | 12.5 |
| FeOt | 12.59 | 9.01 | 11.46 | 10.03 | 8.37 | 14.51 | 12.99 | 9.80 | 11.32 | 10.33 | 12.44 | 12.40 | 8.97 | 11.69 | 9.85 | 8.36 | 15.14 | 11.29 | 9.11 |
| MnO | 0.18 | 0.14 | 0.15 | 0.16 | 0.12 | 0.21 | 0.21 | 0.16 | 0.17 | 0.18 | 0.20 | 0.16 | 0.15 | 0.16 | 0.14 | 0.12 | 0.19 | 0.16 | 0.16 |
| MgO | 6.8 | 10.3 | 6.9 | 8.1 | 9.7 | 5.5 | 6.7 | 13.4 | 10.2 | 10.1 | 7.1 | 7.0 | 7.0 | 4.6 | 6.3 | 10.0 | 6.0 | 11.9 | 8.5 |
| CaO | 9.9 | 10.3 | 8.4 | 9.3 | 10.5 | 9.5 | 11.4 | 10.0 | 10.7 | 7.7 | 10.9 | 8.4 | 6.3 | 16.1 | 6.9 | 10.5 | 9.9 | 6.0 | 5.8 |
| $Na_2O$ | 0.26 | 0.57 | 0.32 | 0.54 | 0.60 | 0.49 | 1.10 | 1.64 | 0.04 | 0.13 | 0.43 | 0.35 | 0.74 | 0.02 | 0.57 | 0.56 | 0.36 | 0.42 | 0.18 |
| $K_2O$ | 2.73 | 1.02 | 3.59 | 3.01 | 1.24 | 2.75 | 1.50 | 0.09 | 1.44 | 2.44 | 2.00 | 2.81 | 3.91 | - | 3.86 | 1.13 | 2.87 | 2.19 | 3.75 |
| $P_2O_5$ | 0.24 | 0.16 | 0.26 | 0.20 | 0.16 | 0.32 | 0.14 | 0.17 | 0.19 | 0.20 | 0.18 | 0.16 | 0.11 | 0.22 | 0.21 | 0.14 | 0.33 | 0.19 | 0.18 |
| total | 100 | 100 | 100 | 100 | 100 | 100 | 100 | 100 | 100 | 100 | 100 | 100 | 100 | 100 | 100 | 100 | 100 | 100 | 100 |
| Mg# | | | | | | | | | | | | | | | | | | | |
| Ni | 47.0 | 100.2 | 47.0 | 65.4 | 89.1 | 71.0 | 47.8 | 119.6 | 78.1 | 79.1 | 105.2 | 84.2 | 91.8 | 30.7 | 53.9 | 92.9 | 61.7 | 132.7 | 100.7 |
| Rb | 6.2 | 27.0 | 7.7 | 13.9 | 29.1 | 10.4 | 45.5 | 4.8 | 1.5 | 4.0 | 15.7 | 10.0 | 22.3 | 1.5 | 15.4 | 26.6 | 7.1 | 11.6 | 5.0 |
| Sr | 44.5 | 259.7 | 50.0 | 183.1 | 329.3 | 155.4 | 130.2 | 41.9 | 63.7 | 47.8 | 267.6 | 127.4 | 224.3 | 61.9 | 100.1 | 335.6 | 113.2 | 103.0 | 56.3 |
| Y | 31.9 | 16.7 | 33.3 | 24.9 | 19.1 | 38.3 | 20.8 | 24.3 | 26.9 | 25.9 | 28.1 | 24.3 | 15.8 | 27.3 | 34.0 | 17.7 | 36.8 | 26.7 | 23.1 |
| Zr | 146.4 | 77.3 | 189.0 | 112.8 | 81.8 | 214.7 | 83.0 | 102.3 | 134.0 | 132.0 | 112.0 | 100.5 | 84.2 | 132.7 | 160.5 | 77.5 | 203.6 | 129.2 | 115.1 |
| Nb | 6.3 | 3.0 | 6.6 | 4.1 | 2.8 | 8.5 | 2.9 | 3.2 | 4.4 | 4.5 | 4.4 | 3.3 | 3.0 | 5.1 | 5.5 | 3.0 | 8.4 | 4.4 | 3.6 |
| Ba | 39.6 | 155.1 | 83.4 | 149.5 | 76.3 | 171.2 | 120.0 | 45.7 | 33.2 | 77.6 | 166.3 | 66.7 | 272.4 | 38.2 | 208.9 | 87.7 | 131.0 | 142.7 | 62.2 |
| Pb | 2.0 | 1.0 | 0.3 | 2.0 | 1.0 | 2.9 | 1.3 | 2.1 | 1.8 | 3.4 | 1.9 | 1.1 | 2.7 | 2.9 | 2.8 | 0.1 | 3.2 | 0.2 | 1.1 |
| Th | 2.1 | 1.7 | 2.9 | 1.0 | 1.8 | 4.2 | 1.4 | 2.2 | 2.2 | 2.2 | 2.0 | 0.9 | 3.9 | 1.7 | 2.4 | 1.1 | 3.9 | 2.4 | 1.9 |
| La | | 6.94 | | | | | | 8.06 | | | | | | | | | | 10.4 | 8.98 |
| Ce | | 15.9 | | | | | | 20.2 | | | | | | | | | | 25.1 | 19.9 |
| Pr | | 2.03 | | | | | | 2.32 | | | | | | | | | | 3.03 | 2.50 |
| Nd | | 8.45 | | | | | | 9.49 | | | | | | | | | | 12.6 | 10.9 |
| Sm | | 2.15 | | | | | | 2.58 | | | | | | | | | | 3.29 | 2.83 |
| Eu | | 0.82 | | | | | | 1.16 | | | | | | | | | | 1.05 | 0.76 |
| Gd | | 2.32 | | | | | | 3.00 | | | | | | | | | | 3.64 | 3.11 |
| Tb | | 0.44 | | | | | | 0.58 | | | | | | | | | | 0.69 | 0.60 |
| Dy | | 2.86 | | | | | | 3.81 | | | | | | | | | | 4.36 | 3.76 |
| Ho | | 0.59 | | | | | | 0.80 | | | | | | | | | | 0.98 | 0.79 |
| Er | | 1.74 | | | | | | 2.34 | | | | | | | | | | 2.70 | 2.17 |
| Tm | | 0.24 | | | | | | 0.34 | | | | | | | | | | 0.40 | 0.30 |
| Yb | | 1.55 | | | | | | 2.07 | | | | | | | | | | 2.45 | 1.79 |
| Lu | | 0.22 | | | | | | 0.28 | | | | | | | | | | 0.36 | 0.22 |

Total iron as FeO

Table 7 Chemical composition of the Upper Komatiites

| sample | BR084 | BR085 | BR086 | BR089 | BR179 | BR192 | BR193 | BR195 | 95BR126 | 95BR131 | 95BR133 | 95BR134 |
|---|---|---|---|---|---|---|---|---|---|---|---|---|
| $SiO_2$ | 51.2 | 50.6 | 49.8 | 57.3 | 52.0 | 57.6 | 55.9 | 54.3 | 49.3 | 53.5 | 47.1 | 54.9 |
| $TiO_2$ | 1.22 | 1.34 | 1.35 | 1.17 | 1.46 | 1.79 | 1.72 | 0.92 | 1.05 | 0.92 | 1.04 | 1.61 |
| $Al_2O_3$ | 14.7 | 13.7 | 14.7 | 16.6 | 13.3 | 14.1 | 13.9 | 15.2 | 14.1 | 14.5 | 13.8 | 12.5 |
| FeOt | 13.14 | 14.46 | 13.86 | 7.02 | 14.69 | 12.96 | 13.87 | 11.77 | 11.64 | 10.95 | 11.18 | 12.94 |
| MnO | 0.22 | 0.19 | 0.38 | 0.14 | 0.22 | 0.20 | 0.23 | 0.16 | 0.19 | 0.14 | 0.19 | 0.20 |
| MgO | 6.6 | 6.5 | 5.8 | 3.7 | 5.3 | 5.1 | 3.3 | 5.7 | 7.2 | 5.8 | 7.0 | 5.2 |
| CaO | 8.2 | 9.4 | 11.0 | 8.7 | 6.9 | 3.0 | 6.7 | 7.4 | 10.0 | 5.6 | 10.7 | 4.5 |
| $Na_2O$ | 3.90 | 3.14 | 2.65 | 2.34 | 3.92 | 4.06 | 2.89 | 2.75 | 1.62 | 1.83 | 0.56 | 1.64 |
| $K_2O$ | 0.59 | 0.52 | 0.35 | 2.78 | 2.11 | 0.89 | 1.24 | 1.70 | 1.71 | 3.70 | 0.85 | 3.52 |
| $P_2O_5$ | 0.13 | 0.14 | 0.14 | 0.20 | 0.15 | 0.24 | 0.21 | 0.14 | 0.11 | 0.14 | 0.11 | 0.21 |
| total | 100 | 100 | 100 | 100 | 100 | 100 | 100 | 100 | 96.9 | 97.1 | 92.4 | 97.3 |
| Mg# | | | | | | | | | | | | |
| Ni | 13.1 | 64.6 | 41.4 | 47.3 | 34.1 | 9.9 | 9.5 | 53.7 | 108.6 | 52.6 | 104.5 | 9.6 |
| Rb | 35.6 | 15.6 | 14.1 | 4.9 | 41.6 | 11.6 | 50.6 | 33.0 | 35.9 | 32.0 | 29.6 | 21.1 |
| Sr | 173.0 | 60.7 | 132.9 | 106.6 | 42.1 | 68.1 | 137.8 | 136.2 | 221.6 | 96.3 | 92.7 | 26.6 |
| Y | 31.5 | 25.6 | 27.6 | 26.3 | 28.4 | 44.8 | 40.8 | 23.3 | 19.9 | 23.1 | 19.5 | 44.5 |
| Zr | 122.9 | 91.6 | 102.7 | 97.1 | 106.1 | 239.0 | 201.8 | 129.3 | 62.8 | 131.5 | 60.8 | 215.0 |
| Nb | 4.0 | 2.7 | 3.2 | 3.1 | 3.3 | 10.3 | 9.4 | 4.0 | 1.7 | 4.5 | 1.8 | 9.5 |
| Ba | 94.8 | 150.6 | 96.8 | 152.0 | 540.8 | 283.0 | 236.1 | 317.4 | 632.6 | 466.5 | 86.5 | 376.4 |
| Pb | 8.4 | 1.3 | 6.9 | 3.8 | 1.9 | 12.3 | 9.1 | 11.1 | 8.9 | 4.4 | - | 2.9 |
| Th | 2.2 | 2.2 | 2.0 | 2.1 | 2.4 | 7.9 | 6.7 | 6.1 | - | 6.1 | 0.8 | 6.7 |

Total iron as FeO

Table 8 Chemical composition of Dacites

| sample | BR109-1 | BR118 | BR121 | BR124 | BR170 | BR188-2 | BR189 | BR216 | 95BR124 | 95BR135 |
|---|---|---|---|---|---|---|---|---|---|---|
| $SiO_2$ | 88.9 | 76.6 | 75.8 | 71.5 | 84.6 | 63.7 | 72.8 | 74.2 | 75.1 | 73.8 |
| $TiO_2$ | 0.13 | 0.35 | 0.35 | 0.53 | 0.23 | 1.23 | 0.37 | 0.35 | 0.34 | 0.37 |
| $Al_2O_3$ | 5.22 | 11.70 | 12.08 | 12.16 | 8.01 | 12.78 | 12.61 | 12.01 | 11.5 | 12.2 |
| FeOt | 1.90 | 2.49 | 2.32 | 6.07 | 0.46 | 10.1 | 4.18 | 4.19 | 4.54 | 4.04 |
| MnO | 0.03 | 0.02 | 0.02 | 0.08 | 0.01 | 0.07 | 0.02 | 0.02 | 0.02 | 0.02 |
| MgO | 1.09 | 0.75 | 0.63 | 0.88 | 0.47 | 3.92 | 1.53 | 1.62 | 1.2 | 1.9 |
| CaO | 0.19 | 0.19 | 0.53 | 1.01 | 0.11 | 2.23 | 0.14 | 0.15 | 0.1 | 0.1 |
| $Na_2O$ | 0.02 | 2.08 | 1.71 | 1.58 | - | 2.78 | 0.76 | 1.34 | 5.93 | 6.26 |
| $K_2O$ | 2.25 | 5.45 | 6.25 | 5.44 | 6.12 | 1.85 | 7.09 | 5.60 | 0.66 | 0.72 |
| $P_2O_5$ | 0.05 | 0.06 | 0.06 | 0.10 | 0.05 | 0.19 | 0.07 | 0.07 | 0.07 | 0.07 |
| total | 99.8 | 99.7 | 99.7 | 99.3 | 100.1 | 98.9 | 99.5 | 99.5 | 99.5 | 99.5 |
| Mg# | | | | | | | | | | |
| Ni | - | - | - | - | - | - | 95.3 | - | - | - |
| Rb | 126.2 | 177.3 | 191.2 | 154.9 | 185.7 | 72.9 | 89.0 | 76.5 | 127.0 | 136.5 |
| Sr | 13.8 | 31.1 | 40.1 | 69.6 | 16.1 | 38.6 | 182.5 | 22.5 | 12.1 | 14.2 |
| Y | 21.4 | 60.4 | 61.0 | 54.3 | 43.1 | 79.3 | 30.2 | 89.2 | 72.4 | 99.0 |
| Zr | 202.7 | 454.6 | 461.0 | 390.3 | 320.7 | 320.4 | 199.4 | 529.4 | 514.8 | 560.4 |
| Nb | 7.6 | 17.7 | 17.7 | 16.4 | 11.5 | 16.3 | 9.2 | 22.4 | 21.4 | 22.9 |
| Ba | 384.8 | 913.9 | 1137.8 | 1352.0 | 1207.7 | 274.8 | 714.4 | 424.7 | 515.7 | 573.9 |
| Pb | 52.7 | 18.1 | 20.7 | 34.4 | 4.1 | 32.4 | 13.3 | 4.5 | 3.9 | 4.7 |
| Th | 13.8 | 28.1 | 29.4 | 23.4 | 18.5 | 12.5 | 8.6 | 20.5 | 19.1 | 20.8 |

Total iron as FeO

# III. Geochemistry of 3.8 Ga MORB and OIB from the Isua Supracrustal Belt, West Greenland; implication for mantle heterogeneity of the mantle in the Early Archean

*Tsuyoshi Komiya*,

Department of Earth and Planetary Sciences, Tokyo Institute of Technology, Tokyo 152-8551, Japan

*fax: +81-3-5734-3538* *e-mail: tkomiya@geo.titech.ac.jp*

## III-1. Introduction

The Earth is on an irreversible path toward compositional, thermal, and gravitational equilibrium through the processes of convection, melting, and differentiation. The geochemistry of continental and oceanic crust provides a basis for understanding, and a direct record of, theses processes. The geochemistry of the modern MORB and OIB shows that the (upper) mantle is very heterogeneous, and the heterogeneity may be caused by recycling of oceanic crust and/or sediments through plate tectonics. Although Large-scale chemical differentiation involved by magma ocean and core formation occurred in early Earth, any evidences of early Earth differentiation are not preserved in the modern rocks (Lee & Halliday, 1995). Moreover, although it may be also resulted from recycling of oceanic crust (Hauri 1996), it is believed that primordial mantle has still survived in the deep mantle based on high FeO content and high $^{4}He/^{3}He$ ratios in some intraoceanic basalts (Wilkinson, 1985; Stille et al., 1983; Sun, 1984; Allègre et al. 1987). Those evidences may suggest that active mantle convection homogenizes the early Earth differentiation before the Archean, and heterogeneities resulted from plate tectonics have surpassed apparent homogenization by relatively inactive mantle convection after Archean (Bowring & Housh, 1995).

Recent geological reinvestigation showed that the Isua supracrustal belt is the oldest accretionary complex (Maruyama et al. 1991, 1994; Komiya & Maruyama 1995; Komiya et al. 1999). Moreover, the field occurrences suggest that the greenstones be subdivided into three-types; which originated from mid-ocean ridge volcanism, oceanic island volcanism, and island arc or rift magmatism, respectively. Despite of many reports of geochemistry of the greenstones in the 3.8 Ga Isua supracrustal belt (Sun & Nesbitt, 1978; Gill & Bridgwater, 1979; Gill, 1979; Gill et al. 1981; Nutman 1986), those works of course did not follow this geological evidence.

This paper present the brief review of the mantle heterogeneity of the modern, and the early Earth differentiation recorded in the Archean rocks, and then the composition and temperature of the upper mantle, and the Archean mantle heterogeneity based on the geochemistry of the greenstones in the 3.8 Ga Isua supracrustal belt.

### III-1.1. Mantle heterogeneities of the modern mantle

The compilation of the isotope chemistry shows that the modern mantle is very heterogeneous (Sun, 1980; Vidal et a. 1984; Zindler & Hart, 1986; Silver et al., 1988; Weaver, 1991, Saal et al. 1998), and consists of at least five distinct components even within upper mantle (Hanan & Graham, 1996). Moreover, variations in chemical compositions of MORBs and OIBs also suggest that major element heterogeneity exist in their source mantle regions (Hauri, 1996; Langmuir & Hanson, 1980; Bryan & Dick, 1982; Kogiso et al., 1997). Although various mechanisms have been proposed for the origin, it is widely accepted that

the recycling of the oceanic crust, pelagic and terrigenous sediments into the mantle causes the heterogeneities of the mantle (Chase, 1981; Hofmann & White, 1982; Weaver, 1991; Chauvel et al., 1992; Woodhead et al., 1993; Roy-Barman & Allègre, 1995; Hirschmann & Stolper, 1996; Hauri, 1996; Kogiso et al., 1997). High pressure experiments showed that the pyrolitic mantle is transformed into perovskites and magnesiowüstite at ca. 25 GPa, whereas basaltic crust is transformed into perovskites, stishovite and aluminous phase at 27 GPa (Irifune & Ringwood, 1987, Ringwood, 1991). Those results suggest that the former basaltic crusts are accumulated and formed the megaliths along the boundary between upper and lower mantle (Ringwood, 1982; Irifune & Ringwood, 1993). If the bottom of thick piles of the former basaltic crust isostatically penetrates into the lower mantle, then the lowermost is transformed into dense mineral assemblage and delaminated to subside onto the core-mantle boundary. Recent seismic tomographies support the subducted slabs of oceanic crust on the core-mantle boundary (Fukao et al. 1992; Kendall & Silver, 1996). On the other hand, pyroxene-rich rocks are present in all types of mantle samples including xenoliths (e.g., Frey 1980; Irving 1980), ophiolites (e.g., Bouldier & Coleman 1981; Quick 1981), abyssal dredges (e.g., Dick et al. 1984; Serri et al. 1988; Bailey et al. 1992; Lee & Hart 1995; Ross & Elthon 1997) and orogenic peridotites (e.g., Suen & Frey 1987; Mukasa et al. 1991; Pearson et al. 1993). Such pyroxenites in the asthenosphere could originate from subduction of oceanic crust (e.g., Allègre & Turcotte 1986). The extremely radiogenic Pb isotope ratios of HIMU basalts suggest an enrichment both in U and Th relative to Pb in the magma source on the order of $10^9$ years ago (Tatsumoto, 1978; Hauri & Hart, 1993). That means that if mantle heterogeneities result from recycling of oceanic crust, the involved oceanic crust have independently survived in the convecting mantle for periods of time as long as several billion years.

### III-1.2. The early Earth differentiation recorded in the Archean rocks

It has been still controversial whether Archean mantle was isotopically and geochemically heterogeneous or not, because post-magmatic alterations obscured the original nature of the rocks (Gruau et al. 1996), active mantle convection may have homogenized the early heterogeneities (Abe 1993; Bowring & Housh, 1995), and tectonic setting of the basaltic volcanism are ambiguous (Condie 1985).

Archean greenstones generally suffered more or less post-magmatic modification, for example submarine weathering, hydrothermal metamorphism, regional metamorphism and metasomatism induced by granitic intrusion, so that isotopic and geochemical composition of those rocks may have been affected by such secondary effect. Therefore, it is significant of the discovery of extremely fresh komatiites in the Belingwe greenstone belt, Zimbabwe (Nisbet et al., 1987), and the measurement of isotopic compositions in relict minerals instead of bulk rocks (Hart & Brooks, 1977; Machado et al. 1986; Vervoort et al. 1994; Carignan et al., 1995ab).

Core formation, and magma ocean is expected to have caused large-scale chemical differentiation in the early Earth. However, only the geochemical evidence of magma ocean in the Earth, as yet, is the positive anomaly $\varepsilon^{142}$Nd in felsic metasedimentary rocks in the Isua supracrustal belt (Harper & Jacobsen, 1992ab, Sharma et al., 1997). Any $\varepsilon^{142}$Nd anomalies were preserved in other Archean rocks (Galer & Goldstein, 1992; Bennett & McCulloch, 1992; McCulloch & Bennett, 1992, Jacobsen & Harper, 1992). Hafnium isotopic ratio in the 3.5-Ga Aluminum depleted komatiites, Barberton Greenstone belt suggest that garnet fractionation was not caused by magma ocean, but by 3.5-Ga komatiitic magmatism. The line of those evidences suggests that the evidences of early Earth differentiation are hardly preserved, because the subsequent plate tectonics presumably resurfaced and active mantle convection presumably eliminated the mantle heterogeneities, and that if the rocks were emplaced on the continents by Early Archean, they have a narrow escape by chance from the subsequent modification. Mantle differentiation in Archean has been reported by many workers. Hart & Brooks (1977) reported the K, Rb, Cs, Sr and Ba contents and Sr- isotope ratios of seven bulk clinopyroxenes from three different areas of the Archean Abitibi belt of Canada. They showed that although the Archean mantle was similar to the mantle of today in many respects, it was most probably enriched with Cs relative to today, and that mantle evolution since 3.5 Ga can be described by a simple two-stage model, with a major development of mantle heterogeneities at about 1.7 Ga. Sun & Nesbitt (1977, 1978) reported La/Sm ratios for Archean basalts and spinifex textured peridotitic komatiites all over the world, and showed the Archean mantle had already been chemically heterogeneous based on a wide variety of the La/Sm ratios. Blichert-Toft & Albarede (1994) reported that variation of Sm/Nd ratios for Late Archean basalts and komatiites is as widely as that of modern basalts, but range of $^{143}$Nd/$^{144}$Nd ratio isn't so wide. They interpreted the chemical heterogeneities in the mantle derived from magma migration and mineralogical phase changes were stirred by so active mantle convection that they could not have been surviving for a long time. Chase and Patchett (1988) reported that both early and late Archean rocks from greenstone belt and felsic gneiss complexes exhibit positive $\varepsilon_{Nd}$ Values of +1 to +5 by 3.5 Ga. They interpreted a depleted mantle reservoir caused by extraction and temporary storage of oceanic crust materials existed very early. Sun (1984) showed that some of large variations of major, trace, rare earth, and isotope ratios from Archean mafic and ultramafic volcanics were derived from Archean mantle heterogeneities. Vervoort et al. (1994, 1996) reported that Nd and Pb isotope ratios of mafic and felsic volcanics and galenas from volcanogenic massive sulfide, and suggested that the Archean mantle was isotopically heterogeneous and these heterogeneities were developed within the first few hundred million years of Earth's history. Bennett et al. (1993) reported quite high $\varepsilon_{Nd}$ values from Early Archean mafic dikes in West Greenland, and interpreted those values as a rapid depletion of mantle within Early history of the Earth. Collerson and Regelous (1995) reported that metakomatiites and orthogneiss from the northern Labrador segment of North Atlantic Craton (NAC) yield εNd of -4 to +4. They interpreted that high values of $\varepsilon_{Nd}$ and lack of $^{142}$Nd/$^{144}$Nd anomalies from those samples

indicated that the existence of transitory depleted mantle in the early Archean (pre-4.2 Ga).

### III-1.3. The tectonic setting of the Archean mafic/ultramafic rocks

It is well-known that the geochemical characters of volcanic rocks are strongly dependent on tectonic setting such as active and passive divergent, convergent or intra-plate regime (Pearce & Cann, 1973; Wood et al., 1979; BVSP 1981; Meschede, 1986). Therefore, it is significant of the knowledge of the tectonic setting of mafic/ultramafic volcanism. The tectonic settings of Archean greenstone have been deduced mainly from the geochemical signatures, and the occurrences of greenstone.

Many workers tried to classify the greenstones based on the discrimination diagrams defined by the geochemistry of the modern basalts (Glikson 1971; Rivalenti 1976; Gill 1979; Condie, 1986, 1990, 1994; Meen, 1993). Gill (1979) and Glikson (1971) reported similarities between the Archean greenstones and modern MORBs based on major elements chemistry, and suggested that Archean mafic volcanics were derived from mid-ocean ridge. Many Archean and early Proterozoic basalts, generally speaking, have the negative anomaly in Nb, Ta, P, and Ti. In addition, the chemical compositions of many greenstones are distributed within the region defined by island arc basalts on discrimination diagrams. Therefore, Condie (1986, 1994) interpreted that Archean and early Proterozoic greenstones are the equivalent rocks to modern island arc basalts. However, despite of the some argument (Arndt, 1991; Sun & Nesbitt, 1978), Archean mantle may have been different from the modern mantle in siderophile elements, volatiles, and even major elements content (e.g. Hart et al., 1970; Sun & Nesbitt, 1977; Glikson, 1971; Gill, 1979; Gill et al., 1981; Condie, 1985,1990,1994, Ohta et al., 1996). Moreover, other differences such as the temperature of the mantle and thickness of oceanic crust, and the depth of circulation of hydrothermal fluid may have resulted in the alternative geochemical signature. For example, the modern island arc basalts are characterized by negative anomalies of Nb and Ta, which are held in refractory rutile (Brenan et al. 1994; Green 1994). But higher temperature of the Archean mantle may have caused slab melting to decompose the rutile. Even if rutile was residual during the slab melting, partition coefficient of rutile/silicate liquid pairs decreases with increasing temperature (Green 1994). Therefore, geochemical signature of negative anomaly in Nb and Ta in island arc basalt reduces during the Archean. As a result, estimates of tectonic setting based on the geochemistry appear to be insignificant.

Green (1972) suggested that Archean mafic and ultramafic suites were derived from meteoritic bombardments because his experimental results showed that the geochemistry of them required the high degree of melting. Takahashi (1990), based on his phase diagram on KLB-1, suggested that komatiites were Archean equivalent of MORBs, and that the tectosphere is the residual mantle. Tarney et al. (1976) suggested that greenstones were produced in a back-arc marginal basin setting as a analogy of the modern marginal basin " Rocas verdes" complex from S. Chile. Storey et al. (1989) suggested that Cretaceous

komatiites in Gorgona island is an obducted fragment of the oceanic Caribbean Plateau, and were formed over the Galapagos hotspot at based on the geochemistry, age, and thermal condition, and speculated that Archean komatiite were also hotspot-related oceanic plateau. Association of ultramafic komatiites and tholeiitic basalts is similar to the expected by numerical experiments, suggesting that komatiites were derived from plume volcanism (Jarvis & Campbell, 1983; Campbell et al. 1989; & Campbell & Griffiths, 1993; Griffiths & Campbell, 1990). Xenocrystic zircons were discovered from ultramafic komatiites, Kambalda, Yilgarn, suggesting that the ultramafic komatiites intruded and erupted on the older granitic basement, namely, and were derived form rift volcanism (Lesher & Arndt, 1990).

On the other hand, many studies also have estimated the tectonic setting based on the field occurrences of greenstone. A mafic intrusive-extrusive complex that grades upwards from gabbro through a zone of multiple and sheeted dykes into massive and pillowed lava flows are similar to the Phanerozoic ophiolite complex, and were derived mid-ocean ridge volcanism (Helmstaedt et al. 1986). A large ultramafic dike intruding the bottom of pile of tholeiitic pillow lava and thin ultramafic komatiites flows was presumably a remnant of sheeted dykes complex formed at mid-ocean ridge (de Wit et al. 1987b). Archean large igneous provinces may be analogous to the modern oceanic plateau because of so huge magmatism (de Wit et al. 1992). Despite of suggestion of allochthonous origin (Kusky & Kidd, 1992; Kusky & Winsky, 1995; Kusky et al., 1994), 2.7-Ga ultramafic komatiites in Belingwe greenstone belt were presumably formed by rift-volcanism because they erupted on the passive-margin sediment (Bickle et al. 1975, 1993, 1994; Blenkinsop et al., 1993, 1994; Hunter et al., 1998). Close association of dacite and basalt volcanics suggests island arcs built on oceanic crust (Sylvester et al. 1987).

Recently, the similarities of the geological features of some Archean greenstone belt to those of the Phanerozoic accretionary complex is emphasized by similar to Maruyama and co-workers; the Isua supracrustal belt (Maruyama et al., 1991b, 1994a; Komiya & Maruyama, 1995; Komiya et al., 1999); Pilbara craton (Isozaki & Maruyama, 1992; Isozaki et al., 1991; Kimura et al., 1991; Maruyama et al., 1991a; Ohta et al., 1996); Abitibi greenstone belt (Kimura et al., 1993). They emphasize “oceanic plate stratigraphy” and “duplex structure” as prime criteria of accretionary complex. They classified the greenstone into a mid-ocean ridge basalt (MORB) and a ocean island basalt (OIB), based on theory of accretionary geology (Komiya & Maruyama, 1995; Ohta et al., 1996; Komiya et al., 1998). For example, greenstones in Abitibi greenstone belt were derived from oceanic island magmatism (Kimura et al. 1993), whereas those in Cleaverville area originated from mid-ocean ridge volcanism (Ohta et al. 1996). In addition, both MORB and OIB can be observed in the Isua supracrustal belt (Komiya & Maruyama, 1995; Komiya et al. 1998)

## III-2. Geological outline

### III-2.1. Overview

The Isua supracrustal belt lies approximately 150 km northeast of Nuuk, Greenland (Fig. 1). It is part of the Akulleq terrane, which is composed of 3880-3660 Ma Amîtsoq gneiss, 2820 Ma Ikkattoq gneiss, which contains some enclaves of supracrustal rocks, and anorthosites (Friend et al. 1987, 1988; Nutman et al. 1989; McGregor 1993). The northeastern part of the Akulleq terrane is an exception where a relatively less metamorphosed segment, the Isua supracrustal belt, is exposed (Fig. 1 inset). The Isua supracrustal belt forms a 35 km-long arcuate tract and is the largest fragment of the Early Archean supracrustal rock in the Akulleq terrane (Fig. 1, inset). The belt was originally intruded by tonalitic rocks, which were later metamorphosed to form the Amîtsoq gneiss. The Isua belt is at present exposed as a fault-bounded tectonic slice, and is in tectonic contact with the tonalitic Amîtsoq orthogneiss on both sides (McGregor 1973; Bridgwater et al. 1974). The Isua supracrustal belt was affected by Barrovian-type progressive metamorphism during Archean times (Komiya et al. 1998). However, the original structures of the protoliths are well preserved in the northeastern part of the belt where the metamorphic grade is the lowest. The Isua belt is an exception displaying well-preserved primary structures that yield information helpful in deciphering the history of pre-3.8 Ga events on the Earth.

It had been regards sedimentary sequences, including conglomerate, as deposited conformably in shallow marine environments, and mafic volcanics intruded into or extruded on them, based on the continental rifting model (e.g. Nutman 1986; Jacobsen & Dymek 1987; Dymek & Klein 1988). However, recently, Komiya et al. (1998) proposed that the Isua supracrustal belt is the oldest accretionary complex, and that pillow and massive lavas and the overlying hyaloclastite layers were derived from mid-ocean ridge volcanism, and that chert/BIF sediments were deposited in the open sea.

### III-2.2. Field occurrences of pillow lava, and mafic dikes

In spite of the recognition of pillow structures in an occurrence of amphibolite by geologists of Kyrolitselskabet Øresund A/S in the early 1970s, subsequent workers have missed them because they classified the rocks based on the metamorphic structure and texture, instead of their protoliths (Allaart 1976). The pillow lava structures are sporadically preserved in areas of relatively low strain. Even under high strain, pillow structure can be recognized if the tectonic stretching is parallel to the elongated pillow tubes. Pillow lava flow unit comprises the piles of pillow lavas and hyaloclastite. At the top of pillow lava flow units, a complete succession from pillow lava flow unit on the bottom to massive white chert bed on the top through the hyaloclastite layers can be observed. Along the boundary between chert and hyaloclastite, thin dolomitic carbonate pods are present, presumably suggesting that the depth of magma eruption were shallower than carbonate-compensation-depth (CCD). The pillow lavas are relatively small, 30 to 150 cm across. Morphologies comprise: oval with cusp

through pear-shaped to crescent-shaped forms, depending on secondary deformation, relatively undeformed pillow lavas indicate the way-up (Borradaile 1982). They are composed of core (green), rim (pale green to white colored) and matrix (darker green), and some have a mantle (darker green) between the core and rim (Photo 1). The rim and the mantle may correspond, respectively, to the palagonitized sideromelane zone and tachylite zone of modern pillows (Hargraves & Ayres, 1979). They are of close-packed type with scanty matrix (Moore 1965; Jones 1969). They vary in size and shape depending on the flow unit. Vesicles and varioles are not visible on rims, presumably because of the secondary deformation and metamorphic recrystallization. The hyaloclastite layers on the top are divided into two sections, the upper and the lower hyaloclastite, respectively. The lower hyaloclastite layers are characterized by smooth surfaces and lack of garnet megacrysts. They consist of poorly-sorted pillow breccias set in matrix, and conformably cover the pillow lavas. The upper hyaloclastite layers are composed of well-sorted, fine-grained metasediments with a probable reworked origin. They are characterized by rough surfaces and a number of garnet megacrysts. High abundance of garnets suggests that the rocks are enriched in Fe and Mn. The layers are up to 3 meters thick in many places, but vary laterally in thickness. They conformably cover the lower hyaloclastite, and conformably overlain by white bedded chert layers. The pillow and massive lava units overlain by the relatively thick chert layers contains no continents- or arc-derived material, suggesting that they erupted in the open-sea environment. Geological evidences imply that they originated from mid-ocean ridge magmatism (Komiya et al. 1998). Therefore, they are here named IMORBs.

Mafic dikes are subdivided into two types by the field occurrences. Ones intrude pillow lava flow units and chert layers, but are cut by duplex-forming thrusts (Maruyama et al. 1994; Komiya et al. 1998). Some thin dikes were severely folded, and truncated by the surrounding rocks. They are dark-green colored, and range tens cm to tens m thick. They are characterized by smooth surfaces and numerous fractures normal to the outer margins. The grain size varies from coarse-grained in the center to fine-grained in the rim. However, the chilled margins of the many dikes were obscured by later metamorphism. Some were intruded across the pillow lava structures, and the bedding planes of hyaloclastites and chert, and others were emplaced as sills along the bedding planes of chert. Field occurrences suggest that these dikes emplaced between the spreading center and trench, implying that they were derived from oceanic island magmatism. Therefore, they are here named IOIBs. The second intruded across turbidite sequence, and even duplex-forming thrusts. Some dikes contain plagioclase patches, suggesting that they are Ameralik dykes. The field occurrences resemble those of the first type. They were formed as island arc volcanism or rift magmatism, because the emplacement of them postdated the accretion.

## III-3. Chemistry

### III-3.1. Sample preparation

To obtain the original magmatic composition, greenstone samples were carefully selected for the major and trace elements analyses step by step. First of all, field occurrences of greenstones and even the surrounding rocks appear to be related to the extent of the secondary alterations and the distribution of the altered zones. For example, the extensive altered zones appear at the stratigraphic top of the pillow lava flow units, or in the surroundings of large quartz veinlets (e.g. T-chert in Pilbara craton, Western Australia). Such stratigraphically controlled alteration suggests a hydrothermal alteration at the formation of the magmas, accompanied with the interaction with seawater. It is suggested that the involvement of the fluid migration from the neighboring sediments forced the composition, especially isotopic composition, disturbed during the metamorphism. Therefore, 222 greenstone samples elsewhere were preferentially collected, or thin massive lavas were also preferred. At the second stage, <1-cm-thick slabs were cut from each sample to select the rock samples without a visible internal fracture filled with quartz, chlorite and epidote minerals and the heterogeneous surfaces. Whole rock powders were prepared for 51 fresh samples, which contain neither veinlets of quartz, chlorite, and calcite, nor the heterogeneous domains even under the microscope. Slabs whose surfaces were polished were broken into small pieces, ultrasonically cleaned in de-ionized water and ethyl alcohol, dried, and powdered in a tungsten carbide shatter-box.

### III-3.2. Analytical methods

Major and some trace elements (Ni, Rb, Sr, Y, Zr, Nb, Ba, Pb, and Th) were measured by X-ray fluorescence (XRF) at Tokyo Institute of Technology and at Institute of Oceanography in Tokyo University, respectively. The analytical procedure, condition and its accuracy are described by Goto and Tatsumi (1994). Rare earth elements were determined by inductively Coupled Plasma Mass Spectrometry (ICP-MS) at Tokyo Institute of Technology. The analytical procedure, condition and its accuracy are reported elsewhere (Hirata et al. 1988).

### III-3.3. Petrography

The rock samples were collected from both pillow and massive flow unit (IMORBs), and mafic dikes (IOIBs) (Fig. 2). Although the period of the metamorphism is still controversial (e.g. Nutman & Collerson, 1991; Komiya et al., 1998), both IMORBs and IOIBs evenly suffered Barrovian-type progressive metamorphism under the greenschist to amphibolite facies condition (Komiya et al. 1998). The metamorphism causes magmatic minerals to be completely altered into metamorphic minerals; pyroxene phenocrysts are

altered to actinolite + chlorite, plagioclase to epidote + albite, and olivine to serpentine + magnetite.

The mineral assemblages in the low-grade area are defined by Chl+Ep+Ab+Qz (Zone A) in greenschist facies, and Chl+Act+Ep+Hbl+Qz+Ab (Zone B) or Chl+Act+Ep+Hbl+Qz+Ab±Pl (Zone C) in epidote-amphibolite transition. The abbreviations of mineral base on Kretz (1983). Some samples, which contain biotite and calcite, are regarded as altered samples. The original textures are preserved in most samples; for example, cumulative texture of euhedral olivine phenocrysts is observed well in some ultramafic rocks. This observation is much help in removing the samples affected by olivine accumulation from the chemical database of the IMORBs and IOIBs. In higher-grade area, the mineral assemblages are characterized by Hbl+Pl+Qz+Chl±Act±Ab±Ep. Because some samples contain biotite, calcite, and cummingtonite, they are regarded as altered samples. Even in higher-grade regions, original magmatic textures are preserved in some samples. For example, olivine cumulate rocks are defined by serpentine pseudomorphs after euhedral olivines, magnetite, and calcite pseudomorphs after clinopyroxene in matrix, and gabbroic rocks form Hbl+Chl pseudomorphs after euhedral or slightly elongated clinopyroxene phenocrysts pervasively distributed in matrix of anhedral plagioclse+chlorite+quartz, suggesting pyroxene-orthocumulate texture in Duplex VI.

## III-4. Results

### III-4.1 Major and trace element chemistry in IMORBs and IOIBs

Figures 3 and 4 show the MgO versus major and trace element diagrams of both MORBs and OIBs for the Isua supracrustal belts, along with the modern MORBs and OIBs The latter includes both alkaline basalts and tholeiites. IMORBs and IOIBs are defined as low-K tholeiite (Gill & Bridgwater, 1979; Gill, 1979; Komiya & Maruyama, 1995). Chondrite-normalized REE abundances are shown in Figure 5. Despite of minor scattering in especially CaO and $Na_2O$ content, either IMORBs or IOIBs make clear liquid lines of descent. IMORBs have clearly higher $Al_2O_3$ and lower CaO than the modern MORBs at any given MgO contents. IMORBs have lower $TiO_2$ and $Na_2O$ than the modern MORBs. They also have lower Zr, Y, and Nb at any give MgO content, and higher FeO* and MnO and lower Ni at high MgO content (> 10 wt %) relative to the modern MORBs. $SiO_2$ and $P_2O_5$, contents of IMORBs are similar to those of the modern MORBs. They have a light and middle REE-depleted pattern. The pattern of the liquid line of descent of the IMORBs is similar to that of the modern MORBs.

IOIBs have lower $Al_2O_3$ and higher FeO*, $TiO_2$, Y, Zr, and Nb at any MgO content than IMORBs at any given MgO contents. $SiO_2$, CaO, $Na_2O$, $P_2O_5$, and Ni contents of IOIBs are similar to those of IMORBs. The pattern of the liquid line of descent of the IOIBs is similar to that of the modern MORBs, rather than that of the modern OIBs. They have flat-

REE pattern.

For both IMORBs and IOIBs, samples with higher MgO contents (> 10 wt %) plot roughly along olivine fractionation curves accompanied with minor plagioclase on the MgO variation diagrams, as follows: with decreasing MgO, $TiO_2$, $Al_2O_3$, CaO $Na_2O$, $K_2O$, $P_2O_5$, and incompatible trace element, including Sr, contents and $Al_2O_3$/CaO ratios increase; $SiO_2$, FeO* and MnO contents remain almost constant; Ni concentrations decrease. These correlations suggest that the chemical variations of IMORBs and IOIBs at higher MgO contents are mainly controlled by olivine fractionation, and plagioclase plays a minor role. Clinopyroxene fractionation is still more insignificant. Plagioclase and then clinopyroxene join olivine on the liquidus at ca. 9 wt % in MgO because the slope of the liquid lines of descent increase change abruptly, $Al_2O_3$ and CaO decrease substantially with decreasing MgO (Klein & Langmuir 1987).

Petrographic observations of IMORBs and IOIBs do not support that olivine- or pyroxene- accumulation affects their liquid line of descent because the texture described above are not observed in those samples. Moreover, plagioclase- or clinopyroxene-accumulation is also not significant because with increasing MgO, $Al_2O_3$ and CaO contents decrease in those samples. Moreover, both IMORBs and IOIBs are evenly metamorphosed as described above or elsewhere (Komiya et al. 1998). Nevertheless, each makes a clear and distinctive liquid line of descent. Those evidences suggest that secondary alteration did not significantly affect the least altered samples by petrographic definition.

## III-5. Discussions

### III-5.1. Estimate of FeO content of and pressure and temperature of partial melting of the source mantle of the IMORBs

#### III-5.1.1. $Mg^{\#}$ of source mantle of the modern MORB

Field occurrences suggest that IMORBs were derived from mid-ocean ridge volcanism. I here examine to estimate FeO content of source mantle, and temperature and pressure of melting. IMORBs are enriched in FeO content relative to the modern MORB at any given MgO content (> 10 wt %). This difference suggests that source mantle of IMORBs have higher FeO than that of the modern MORB. Based on petrochemical features of the modern MORBs, drilled and dredged abyssal peridotites from mid-oceanic ridge or transform faults in the Pacific, Indian and Atlantic oceans, mantle xenoliths of volcanic rocks, and ultramafic bodies on land, the $Mg^{\#}$ value of the modern MORB source mantle can be inferred. Fo values of olivine from abyssal peridotites range 89.5 to 92 (Boyd, 1989). Xenoliths in basalts contain olivine with 90.5 to 89.2 in Fo value (Menzies, 1991). The less depleted lherzolites on the Zabargad island are composed of the typical four-phase spinel-facies assemblage of forsteritic

olivine (ca. $Fo_{90}$), enstatitic orthopyroxene, diopsidic clinopyroxene and spinel (Piccardo et al., 1988). Mg# of both pyrolite model mantle (Ringwood, 1975; Jagoutz et al. 1979: Sun, 1982; Green et al., 1979) and more recent estimates for the composition of the primitive Upper mantle (Frey et al., 1985; Bonatti et al., 1986; Zindler & Hart, 1986) also range from 88.8 to 90.1. Although recent works presume that the source mantle composition of modern MORB is equivalent to HK66 (85.3 in $Mg^{\#}$) (e.g. Kinzler 1997), the line of evidences indicates that the source mantle of the modern MORB contains ca. 90 in $Mg^{\#}$. The composition is similar to KLB-1, which contains 89.6 in $Mg^{\#}$, and equivalent to 8.10 wt % in FeO*. Recently Kushiro (1998) proposed that $Mg^{\#}$ of the source mantle of the modern MORBs should range from 89 to 85 based on the comparison of the partial melts by some experiments of recent diamond methods with most primitive basalts. However, compilation of primitive MORBs (Presnall & Hoover 1987) does not contain most primitive MORB. For example, the most primitive MORBs have 11.89 and 6.82 in MgO and FeO* respectively (Donaldson 1979), and have 12.04 and 7.84 in MgO and FeO* respectively (le Roex et al. 1981), In addition, most refractory olivine in the modern MORBs is 90.67 in Fo value (Sigurdsson 1981). Therefore, the composition of the source mantle of modern MORBs is supposed to be equivalent to that of KLB-1.

### III-5.1.2. Oxidation state of source mantle of IMORBs

Ferrous to ferric ratio in mantle is controlled by oxidation states, chemical composition, mineral assemblage, pressure, temperature, and phase chemistry; namely even by the extent of degree of melting, fractional crystallization, and presence of Fe metal and C-O-H fluid phases. The oxygen fugacity of the modern mantle is estimated various methods. At first, here, this paper presents a brief review of the oxidation of the modern mantle, and then discusses the oxidation of the Archean mantle.

#### III-5.1.2.1. Oxidation state of modern mantle

The oxygen fugacity ($fO_2$) values of the modern mantle, generally speaking, are between fayalite-magnetite-quartz (FMQ) buffer in relatively shallow depth and iron-wüstite (IW) buffer in deeper area (BVSP 1981; Arculus 1985). For example, several occurrences of Fe-Ni metallic alloys enclosed by diamond in kimberlites (Bulanova et al. 1979; Sobolev et al. 1981), which, together with hosted by the same phase (Hervig et al. 1980), indicate that the oxygen fugacity is in the vicinity of the synthetic iron-wüstite buffer during diamond growth. The discovery of ilmenite-spinel intergrowths among inclusion suites of kimberlites showed the oxygen fugacity are close to the synthetic FMQ buffer (Haggerty & Tompkins, 1983). The inclusion suites with assemblage of olivine, orthopyroxene, and ilmenite in kimberlite allowed Eggler (1983) to calculate the oxygen fugacity from FMQ buffer at relatively low pressures to slightly below the magnetite-wüstite buffer at pressures around 60 kb. The $fO_2$'s

prevailing in the spinel peridotite facies of the upper mantle are calculated from IW to more oxidized FMQ buffer, given acceptable thermodynamic data for the pure phases and crystalline solution models (O'Neill et al. 1982). The relative abundance of volatiles emitted by volcanoes was one of the major constraints that led Ringwood (1979) to infer a relatively oxidized state (FMQ buffer) for the mantle source. The evidence of presence of significant proportions of $CH_4$ in fluids trapped in diamonds suggests that the oxidation state is closed to IW buffer. The dominance of $H_2O$ and $CO_2$ in gasses associated with most active volcanism is suggestive of oxidized (FMQ) mantle source regions (Arculus 1985). The application of phase equilibrium methods to measure the oxygen fugacity at which upper mantle peridotites equilibrated (principally using the olivine-orthopyroxene-spinel assemblage, but also making use of other equilibria (O'Neill & Wall 1987; Wood & Virgo 1989; Luth et al. 1990) has led to a consensus that the upper mantle is nearly every where relatively oxidized, the majority of samples falling within –1.5 to –0.5 log-bar units of the FMQ buffer.

$Fe^{3+}/\sum Fe$ ratio in primitive spinel lherzolites and high temperature garnet lherzolites, estimated from Mössbauer determination of analyses of $Fe^{3+}/\sum Fe$ ratio in four phases remain almost constant, 2.3 ± 0.5 % (O'Neill et al 1993). Transition mantle, which consists of ß or g-spinel and majoritic garnet with/without Ca-perovskite, is expected to have $Fe^{3+}/\sum Fe$ of more than 0.05 (O'Neill et al. 1993), whereas lower mantle would have $Fe^{3+}/\sum Fe$ of 0.4 because of high solubility of $Fe^{3+}$ into perovskite.

Although pillow cores (including virtually all published whole rock analyses) typically have $Fe^{3+}/\sum Fe$ close to 0.15, equivalent to oxygen fugacities close to FMQ (Miyashiro et al. 1969; Bougault & Hekinian, 1974; Blanchard et al. 1976; Langmuir et al. 1977; Tarney et al.,1979; Byerly 1981; BVSP 1981; Sigurdsson 1981; Fornari et al. 1983; Carmichael & Ghiorso 1986; Presnall & Hoover 1987), quench glasses from the outer surfaces of MORB lavas have $Fe^{3+}/\sum Fe$ ratios of 0.07 ± 0.03 (2s), equivalent to oxygen fugacities 1-2 $\log_{10}$ units below the FMQ buffer (Christie et al. 1986). Primitive alkaline basalts should be have $Fe^{3+}/\sum Fe$ ratios of 0.12 because of the lower degree of melting (O'Neill et al. 1993).

### III-5.1.2.2. Speculation of oxidation state of Archean mantle

Oxygen fugacities of Archean mantle are very ambiguous because of no fresh samples of volcanic rocks and peridotites in the Archean terrains in the strict sense of the word. Komatiites, generally speaking, have high concentration of Cr, suggesting the significant amount of $Cr^{2+}$ as well as $Cr^{3+}$ in the source regions. More reduced basaltic melts become saturated with sulfide at lower $fS_2$'s (Naldrett 1969), so the temporal variation of the oxidation status of mantle–derived melts has relevance both to the process of sulfur transport from the mantle and to the formation of mineral deposits in the Archean (Arculus 1985). Those evidences may suggest the redox environment in the Archean mantle. However, komatiites do not have high Cr content at a given MgO content, and sulfide deposition results form interaction of ultramafic melts and terrigenous graphite-bearing sediments. The

oxidation state of the Archean mantle reduced from sulfides included in diamonds formed in a reduced Archean mantle (tectosphere) is NNO –4 to –5 (Eggler & Lorand 1994). Recently, Canil (1997) determined the correlation of oxygen fugacity with partition coefficient of V, Ti, Tb, and Sc between olivine and melt. The results suggested that 2.7 Ga ultramafic komatiites, Belingwe, crystallized under $fO_2$ condition of NNO ± 0.5, led Canil (1997) to conclude that Archean mantle was more oxidized than the present. However, the oxidation state estimated by whole rock analyses of MORBs even at present is NNO (Carmichael & Ghiorso, 1986; Carmichael 1991) because not only seawater alteration, volatile loss, and post-eruptive oxidation change ferrous to ferric, but also crystal fractionation of olivine, plagioclase and clinopyroxene increase $Fe^{3+}/\sum Fe$ ratio. The compositional variation of relict chromian spinels in ultramafic komatiites, Barberton, is similar to the modern boninites (Komiya et al. 1998a), and crystallization path of olivine, chromian spinel, clinopyroxene, plagioclase and magnetite deduced form whole rock composition of komatiites supports that the oxygen fugacity of the Archean mantle was –10 to –11 $\log_{10}$ units (Komiya et al. 1998a), equivalent to the modern MORBs (Christie et al. 1986).

I summary, the oxidation state of the Archean mantle is still controversial. However, $Fe^{3+}/\sum Fe$ ratio is controlled not only oxygen fugacity, but also mineral assemblage. If Archean basalts were formed within upper mantle, which consisted of olivine, orthopyroxene, clinopyroxene, and spinel, $Fe^{3+}/\sum Fe$ ratio in Archean basalts would be equivalent to that of modern MORBs.

### III-5.1.3. $Mg^{\#}$ of source mantle of IMORBs

The estimate of the Archean (upper) mantle composition has been still controversial because fertile mantle xenoliths have not been discovered in Archean yet. The methods of estimate of the Archean mantle composition are classified into three types; based on composition of spinifex textured peridotitic komatiites (e.g. Bickle et al., 1976; Sun & Nesbitt, 1977; Beswick 1983), then present relatively primitive (Jagoutz et al., 1979; Wänke et al., 1984), and comparison of the primitive basalts with experimental data of melting of natural peridotites (Ohta et al., 1996). This work presents FeO content of source mantle of IMORBs based on comparison of the primitive basalts with recent melting experimental data of natural peridotites. However, this estimate is mainly dependent on $SiO_2$ and FeO content because of the following three reasons. $SiO_2$ and FeO are very sensitive to pressure and temperature of melting. $SiO_2$ and FeO contents remain relatively constant during fractional crystallization. $Al_2O_3$ MnO, CaO, $Na_2O$, $K_2O$ and $P_2O_5$ content in magmas are sensitive to those abundances in mantle and those abundances in mantle are less restricted. Because this approach is not based on thermodynamical considerations (Ghiorso & Sack 1995), but entirely empirical, it can not apply to very extraordinary composition and melting condition.

Melting experiments of four natural peridotites KLB-1, HK66, PHN1611, and MM3 have been extensively performed using diamond aggregate method (Hirose & Kushiro 1993;

Baker & Stolper 1994; Kushiro 1996). Those experiments showed $SiO_2$ content of melts is relatively independent of composition of peridotites and temperature of melting at moderate degree of melting, but quite sensitive to melting pressure, because $SiO_2$ is a major constituent element of all minerals. On the contrary, FeO* in melts strongly depends on FeO* content of peridotites, together with pressure and temperature of melting. MgO content of melts is almost proportional to degree of melting. Despite of the fact that four peridotites are different each other in content major element such as $SiO_2$ and MgO, incompatible element, e.g. $Na_2O$ and $K_2O$ and mineral abundances, ratios of $SiO_2$ to MgO and FeO to MgO content vary insignificantly.

Some of most primitive IMORBs and modern MORB are plotted along melt compositions formed by different pressures and degree of melting and from different starting materials in Fig 7. Both IMORBs and Modern MORBs are distributed on the compositional trends defined by the melts formed at 10 or 15 kb (Fig 7b). This evidence suggests that average melting pressure of IMORBs through melting column were 10 to 15 kb (Klein & Langmuir, 1987), and is equivalent to that (10 kb) of modern MORB (Fujii & Bougault 1983).

Fig. 7b shows that each variation of FeO content of melt formed at 15 kb for KLB-1, HK66, and PHN1611, or 10 kb from MM3. Primitive IMORBs are plotted over melts from HK66 or PHN1611, whereas modern MORBs are distributed on melts from KLB-1. The composition of primary melt of IMORBs can not be estimated because olivine is extinct due to metamorphism. If MgO content of primary melt of IMORBs has ca. 20 wt % in MgO, IMORBs can be formed from KLB-1 (Takahashi et al. 1993). However, because the average melting pressure should be high ca. 4.6 GPa, in the case, IMORBs should have the garnet signatures (Salters & Hart, 1989; McKenzie & O'Nions 1991; Bourdon et al., 1996; Salters, 1996; Hirschmann 1996; Hirschmann & Stolper, 1996). However, IMORBs do not show garnet signature, such as heavy REE depletion, as shown later. Furthermore, if IMORBs are highly differentiated basalts from komatiites, abundance of compatible element such as Ni should be lower (Fig. 6), because Ni is more removed from the melts during crystal fractionation. The results suggest that IMORBs were derived from more FeO*-enriched source mantle such as HK66 and PHN1611 rather than KLB-1 and MM3.

The mantle of the Moon and the Mars have higher FeO content than the modern mantle of the Earth (e.g. Hartman et al., 1986 or Bertka & Holloway, 1994a,b). However, the result suggest that the source mantle of IMORBs had at most 10 % in FeO. The differences would be caused by core-formation, as discussed elsewhere.

### III-5.1.4. Potential mantle temperature of source mantle of IMORBs

The potential temperature of the Archean mantle has been estimated by previous workers since 1990 (e.g. Takahashi, 1990; Nisbet et al., 1993; Ohta et al. 1996). The former two works estimated potential temperature of Archean mantle from only MgO content in

peridotitic komatiites (Takahashi 1990, Nisbet et al. 1993). However, MgO content of a primary melt strongly depends on the amount of olivine addition using olivine maximum fractionation model because Fo content of olivine, generally speaking, is not available in many Archean komatiites and basalts (Parman et al. 1997; Komiya et al. 1998). Moreover, the difference of oxidation state of melting between the present and Archean would affect the $Mg^{\#}$ value (Arculus 1985). Ohta et al. (1996) estimated the potential mantle temperature by the comparison of nine major elements in primary magma with those of experimental melts. However, $TiO_2$, $Al_2O_3$, FeO, $Na_2O$, $K_2O$, and $P_2O_5$ contents are significant sensitive to those contents in source mantle. Therefore, I here estimate the potential mantle temperature by the abundance of FeO and $SiO_2$ in primitive magmas because they are relatively insensitive to the extent of crystal fractionation and are strongly correlated to pressure and temperature of melting.

Figure 7b shows composition of the primitive IMORBs along experimental melt from PHN1611 on a $SiO_2$ versus FeO diagram. Primitive IMORBs are plotted over the melt formed at 1325, 1400, and 1425 ˚C, 15 kb. Each degree of melting is 18.4, 26.9, 35.9 %, respectively according to experimental data (Kushiro 1996). Although a variation of compositions is possibly caused by the influence of chemical alteration, it would reflect the small perturbation of global trend (Klein & Langmuir 1989). Therefore, the potential mantle temperature is obtained 1390 to 1550 ˚C of with $Cp=1.2x10^3$ $Jkg^{-1}$, s/s=1.2x10-8 $m^3kg^{-1}°K^{-1}$, $m/m=2.4x10^{-8}$ $m^3kg^{-1}°K^{-1}$ and $S=350$ $Jkg^{-1}°K^{-1}$, which is for modern mantle (Iwamori et al., 1995). Iwamori et al. (1995) also obtained 1320 ˚C of potential mantle temperature of modern MORBs for batch melting.

**III-5.2. Origin of OIBs**

Field occurrences show that IOIBs were derived off-ridge volcanism. However, compositional variation of IOIBs is different from that of modern OIBs. Modern OIBs have lower $SiO_2$ and $Al_2O_3$ and higher FeO and $TiO_2$ than modern MORBs. Moreover, plagioclase fractionation plays significant role on liquid line of descent of modern MORBs whereas clinopyroxene fractionation is significant in modern OIBs at moderate MgO content. Those would result from high pressure of melting and crystal fractionation of OIBs. However, compositional variation of IOIBs dominated by plagioclase fractionation. Compositional variation of major and some trace elements in modern oceanic plateau is similar to that of modern MORBs (Mahoney 1987; Allan et al. 1987), reflecting olivine and the following plagioclase fractionation. IOIBs presumably originated from an oceanic plateau. Flat-REE patterns of IOIBs, and higher Nb/Y and Nb/Zr ratios are also consistent to the chemical nature of oceanic plateau (Mahoney 1987). An evidence of bimodal volcanism supports such a large igneous province (Komiya et al. 1998).

### III-5.3. Mantle heterogeneities in the Early Archean

Mafic and ultramafic volcanic rocks in Archean range from severely LREE-depleted to LREE-enriched in REE patterns (Sun & Nesbitt, 1978). LREE-enriched pattern is restricted to Al-depleted komatiite, suggesting difference of melting condition such as high-pressure garnet fractionation (Green 1975; Nesbitt et al. 1979; Ohtani, 1990). However, flat- or LREE-depleted REE patterns are pervasively observed in mafic and ultramafic volcanic rocks. Moreover, the correlation of REE patterns with major and trace elements content is described in some rocks (Sun, 1984).

REE patterns of greenstones in Isua supracrustal belt have been reported by Sun and Nesbitt (l978) and Gill et al. (1981). They are defined as Garbenschiefer samples, and the Isua supracrustal amphibolite (Sun & Nesbitt 1978) or homogeneous amphibolites (Gill et al., 1981), and are equivalent for IMORBs and IOIBs, respectively. The analyses are consistent to our results, and IOIBs form flat- or slightly LREE-enriched pattern. Although some show that severely HREE-depleted pattern or slightly Eu-negative anomaly, it is possible that they were caused by alteration (Ludden & Thompson, 1978; Sun & Nesbitt, 1978). Garbenschiefer samples have MREE-depleted patterns with strong Eu-negative anomaly, possible suffering post-magmatic alterations.

Because this work present that REE patterns of both IMORBs and IOIBs appear smooth and do not have Eu-anomaly, it is regard that later metamorphism play a minor role on abundances of rare earth elements. The distinct difference between REE pattern of IMORBs and IOIBs indicates that mantle have been already heterogeneous in the Early Archean because both magmas were formed under shallow depth condition. Moreover, source mantle of IMORBs had been depleted relative to that of IOIBs. If IOIBs originated from oceanic plateau volcanism, the source mantle should be lower mantle, analogous to modern oceanic plateau (Kogiso et al. 1997; Kimura et al. 1994). This results implies that Archean mantle have been geochemically separated into two layers similar to the modern mantle. Major and trace element concentration indicate that mantle source of IMORBs are more enriched in $Al_2O_3$, and depleted in FeO*, $TiO_2$, Y, Zr, and Nb compared with IOIBs. REE pattern of IMORBs indicates the presence of depleted source mantle in the Archean, supporting the Nd isotopic evidences (Bennett et al. 1993).

### III-5.4. Origin of mantle heterogeneity

Mantle heterogeneities of the modern mantle has been caused by long term recycling of the oceanic crust, sediments and residual peridotites through plate tectonics (Chase, 1981; Hofmann & White, 1982, Weaver, 1991, Chauvel et al., 1992, Woodhead et al., 1993; Roy-Barman & Allègre, 1995; Hirschmann & Stolper, 1996; Hauri, 1996; Kogiso et al., 1997). What caused the Archean mantle heterogeneities? We have the three causes for mantle

heterogeneity; inhomogeneous accretion of planetesimals, magma ocean and the following core formation, magmatism through plate tectonics or plume tectonics, and recycling of supracrustal rocks through plate tectonics.

A late veneer theory (Jagoutz et al. 1979; Kimura et al 1974), and heterogeneity in platinum-group elements (PGEs) in the modern fertile lherzolites (e.g. Barnes et al. 1985), non-chondritic PGEs ratios in komatiite, picrite, and basalts (Pattou et al. 1996) suggest the inhomogeneous accretion of planetesimals. However, it is still ambiguous whether major element chemistry is influenced by inhomogeneous accretion. Therefore, the discussion is deferred.

It is widely expected that magma ocean was accompanied with large-scale magmatism and stirring of mantle (e.g. Safranov, 1978; Hayashi et al. 1979 Abe 1993). Therefore, magma ocean is supposed to lead the mantle to chemical layering, but not to result in the laterally heterogeneous mantle. The liquid lines of descent of IMORBs and IOIBs indicate olivine+plagioclase fractionation rather than olivine+clinopyroxene fractionation, suggesting the moderate degree of melting. Both IMORBs and IOIBs do not have any garnet-signature, suggeting shallow-level melting. Even if fractionation of dense minerals such as garnet or magnesio-wüstite and Ca-perovskite (±Mg-perovskite) occurred during magma ocean, it did not presumably cause the differences between IMORBs and OIBs.

Large-scale magma ocean resulted in garnet (majorite)- and Mg-perovskite+magnesio-wüstite+Ca-perovskite-fractionation. Pyrope garnet involves more abundances of HREE and Y relative to LREE and Zr, whereas majorite garnet do not fractionate Y to Zr (Kato et al. 1988a; Yurimoto & Ohtani 1992). However, Neither IMORBs nor IOIBs has such a garnet-signature as HREE-depletion (Fig. 5). The fractionation of lower mantle assemblage is highly ambiguous because experimental data are insufficient yet, especially Ca-perovskite (Kato et al. 1988a) and magnesio-wüstite (Kato et al. 1988ab). The dependence of partition coefficient on the oxygen fugacity is also still ambiguous. Nevertheless, I here discuss Mg-perovskite fractionation. Mg-perovskite prefer Zr relative to Ti, Y, and Nb. Although IMORBs have higher Y/Zr ratio relative to CI chondrite (Orgueil), Ti/Zr ratio of IMORBs is similar to that of chondrites. IOIBs have Y/Zr and Ti/Zr ratios similar to the chondrites. Therefore, Mg-perovskite fractionation play insignificant role on the source mantle of IMORBs and IOIBs. Fractionation of metallic core resulted in lower ratios of Nb/Zr, P/Zr, and Pb/Zr (Ohtani et al. 1997). Both IMORBs and IOIBs are depleted in Nb, P, and Pb. In addition, Nb/Zr and P/Zr ratios range within variations of modern MORBs, suggesting core formation had already almost completed in the Early Archean. Because Pb is partitioned into metallic core relative to P (Ohtani et al. 1997), the element is supposed to be sensitive to fractionation of metals.

Pb/Zr ratio in IMORBs and IOIBs is higher than the modern MORBs, which maybe indicate the still overgrowth of metallic core after Archean. The further discussion will be presented elsewhere.

If plate tectonics also led the Archean mantle to be heterogeneous, when has plate tectonics operated? It is still controversial on the beginning of plate tectonics. During 1970s, the Archean plate tectonics supported by only some geoscientists with an enterprising spirit (Hart et al. 1970; Hoffman 1973; Condie 1972; Burke et al. 1976; Bickle 1978). However, many believed that the tectonic regime until the late Proterozoic was typified by a vertical movement-dominated orogeny, called the 'millipede model' (Wynne-Edwards 1976), or ensialic vertical tectonics (Kröner 1977, 1981; Piper 1982). During 1980s, geophysicists came to support the plate tectonics in the Archean (Burke & Kidd, 1978; Nisbet and Fowler 1983; Arndt 1983). After the second half of 1980s, geological evidences for plate tectonics and accretion of oceanic crusts have been reported in some Archean terrains (de Wit et al. 1987ab, 1992: Kusky 1989, 1991; Friend et al, 1989; Hoffman 1991; Kimura et al. 1991, 1993; Isozaki et al., 1991; Maruyama et al. 1991ab, 1994; Kusky and Winsky 1995; Calvert et al. 1995; Ohta et al. 1996; Komiya et al. 1998). Therefore, the Archean plate tectonics seemingly had the support of many geoscientists despite of insignificant minority opinion (Goodwin, 1991; 1996). However, recently some people presented the evidences against the plate tectonics in the Archean (Davies 1992; Hamilton 1993, 1998ab). I believe the Early Archean plate tectonics (Komiya et al. 1998).

The recycling of supracrustal rocks through plate tectonics played an insignificant role on the mantle heterogeneities yet, because IOIBs did not have signature of the recycling of supracrustal rocks such as Nb- and Ti- positive anomalies. Moreover, involved by the recycling of oceanic crust, IOIBs should be depleted in Pb, because Pb is removed compared with by fluids at subduction (Kogiso et al. 1997). However, neither IMORBs nor IOIBs indicate the depletion of Pb concentration. The flat-REE pattern and chondritic ratios of incompatible trace elements support that source mantle of IOIBs remained primordial (Fig. 5, 8).

As a result, magmatism at spreading center, and if plate tectonics had never operated yet, plume magmatism possibly caused the mantle to be differentiated into MORBs source and OIB source before the Early Archean. Major and trace elements composition of IMORBs and IOIBs support the hypothesis, because the extraction of the magma from mantle resulted in depletion of incompatible elements. IMORBs are depleted in incompatible elements relative to IOIBs. However, residual mantle could not possibly produce basaltic melts because of the lack of magmaphile elements. Therefore, the source mantle of IMORBs presumably involved minor amount of the residue of high-pressure materials with major amount of primordial mantle because of high content in $Al_2O_3$, Y, and HREE. Active mantle convection accompanied with plume magmatism probably caused the local differentiation of the mantle

before the Early Archean (Ogawa 1988).

If mantle heterogeneities at present are caused by recycling of oceanic crust and sediments, oceanic crust in the Early Archean is supposed to be involved in modern mantle heterogeneities because isotope evolution requires long duration, several billion years. IMORBs have higher Pb and Rb than Th and Sr, respectively compared to modern MORBs (Fig. 9), suggesting that suppression of radiogenic lead such as HIMU source mantle. Moreover, high geothermal gradient at subduction zone resulted in slab melting rather than dehydration from slab (Grambling 1981; Martin 1986; Rapp et al. 1991; Rapp & Watson 1995; Maruyama 1997). This leads to reduction of the fractionation of Pb to U or Th and Sr to Rb in subduction zone. The compositional change of subducted oceanic crust and thermal change of subduction zone through the geological time should affect secular change of mantle heterogeneities.

## III-6 Conclusions

(1) Two types of greenstones defined by their field occurrences occurred in the Isua supracrustal belt, IMORBs and IOIBs. IOIBs have lower $Al_2O_3$ and higher FeO*, $TiO_2$, Y, Zr, and Nb than IMORBs at any given MgO contents. IMORBs form LREE- and MREE-depleted REE pattern, whereas IOIBs form flat-REE pattern. The differences of field occurrence are correlated with those of the composition each other. The compositional differences indicate the mantle heterogeneities in the Early Archean, implying that the two component model is insufficient to investigate the evolution of the mantle.

(2) IMORBs have clearly higher $Al_2O_3$ and lower CaO than the modern MORBs at any given MgO contents. IMORBs have lower $TiO_2$ and $Na_2O$ than the modern MORBs. They also have lower Zr, Y, and Nb at any give MgO content, and higher FeO* and MnO and lower Ni at high MgO content (> 10 wt %) relative to the modern MORBs.

(3) Major elements chemistry of IMORBs indicates that the source mantle of IMORBs had ca. 10 wt % in FeO. The higher content of FeO and $Al_2O_3$ in the Early Archean mantle suggests that the composition of upper mantle would change through the geologic time.

(4) The estimated potential mantle temperature of source mantle of IMORBs is about 1450 ˚C, which is much lower than previous works.

(5) The mantle heterogeneities before the Early Archean caused by active plume magmatism, instead of magma ocean, the following core formation and recycling oceanic crust.

## References


Abe, Y., 1993, Thermal evolution and chemical differentiation of the terrestrial magma ocean, *in* Takahashi, E., Jeanloz, R., and Rubie, D., eds., Evolution of the Earth and Planets, Washington, IUGG and Am. Geophys. Union, p. 73-88.

Allaart, J. H., 1976, The Pre-3760 m.y. old supracrustal rocks of the Isua area, central West Greenland, and the associated occurence of quartz-banded ironstone, *in* Windley, B. F., ed., The early history of the Earth, London, John Wiley & Sons, p. 177-189.

Allan, J. F., Batiza, R., and Lonsdale, P., 1987, Petrology and chemistry of lavas from seamounts flanking the east Pacific rise axis, 21˚N: implications concerning the mantle source composition for both seamount and adjacent EPR lavas: Seamount, Islands, and Atolls: Washington, D.C., AGU Monograph, 255-282 p.

Allègre, C. J., Hamilton, B., Provost, A., and Dupre, B., 1987, Topology in isotopic multispace and origin of mantle chemical heterogeneities.: Earth Planet. Sci. Lett., v. 81, p. 319-337.

Allègre, C. J., and Turcotte, D., 1986, Implications of a two-component marble-cake mantle, Nature, 323, 123-127.

Arculus, R. J., 1985, Oxidation status of the mantle past and present: Ann. Rev. Earth Planet. Sci., v. 13, p. 75-95.

Arndt, N. T., 1983, Role of a thin, komatiite-rich oceanic crust in the Archean plate-tectonics process: Geology, v. 11, p. 372-375.

Arndt, N. T., 1991, High Ni in Archean tholeiites: Tectonophysics, v. 187, p. 411-419.

Bailey, J. C., Campsie, J., Hald, N., Dittmer, F., Fine, S., and Rasmussen, M., 1992, Petrology and geochemistry of a dredged clinopyroxenite-dolerite basal complex from the Jan Mayen volcanic province, Norweigian-Greenland sea: Mar. Geol., 105, 63-76.

Baker, M. B., and Stolper, E. M., 1994, Determining the composition of high-pressure mantle melts using diamond aggregates: Geochim. Cosmochim. Acta, v. 58, p. 2811-2827.

Bennett, V. C., and McCulloch, M. T., 1992, $^{142}$Nd-$^{143}$Nd compositions of the oldest terrestrial rocks: constraints for Early Earth differentiation: EOS Trans., v. 73, p. 621

Bennett, V. C., Nutman, A. P., and McCulloch, M. T., 1993, Nd isotopic evidence for transient, highly depleted mantle reservoirs in the early history of the Earth.: Earth Planet. Sci. Lett., v. 119, p. 299-317.

Bertka, C. M., and Holloway, J. R., 1994a, Anhydrous partial melting of an iron-rich mantle I: subsolidus phase assemblages and partial melting phase relations at 10 to 30 kbar: Contrib. Mineral. Petrol., v. 115, p. 313-322.

Bertka, C. M., and Holloway, J. R., 1994b, Anhydrous partial melting of an iron-rich mantle II: primary melt compositions at 15kbar.: Contrib. Mineral. Petrol., v. 115, p. 323-338.

Beswick, A. E., 1983, Primary fractionation and secondary alteration within an Archean ultramafic lava flow: Contrib. Mineral. Petrol., v. 82, p. 221-231.

Bickle, M. J., 1978, Heat loss from the Earth: A constraint on Archaean tectonics from the relation between geothermal gradients and the rate of plate production: Earth Planet. Sci. Lett., v. 40, p. 301-315.

Bickle, M. J., Martin, A., and Nisbet, E. G., 1975, Basaltic and peridotitic komatiites and stromatolites above a basal unconformity in the Belingwe greenstone belt, Rhodesia: Earth Planet. Sci. Lett., v. 27, p. 155-162.

Bickle, M. J., Nisbet, E. G., and Martin, A., 1994, Archean greenstone belts are not oceanic crust: J. Geol., v. 102, p. 121-138.

Bickle, M. J., Orpen, J. L., Nisbet, E. G., and Martin, A., 1993, Structure and metamorphism of the Belingwe Greenstone Belt and adjacent granite-gneiss terrain: The tectonic evolution of an Archaean craton, *in* Bickle, M. J., and Nisbet, E. G., eds., The Geology of the Belingwe Greenstone Belt, Rotterdam, Netherlands, Geol. Soc. of Zimbabwe Spec. Publ. 2, p. 39-68.

Bickle, M. J., Hawkesworth, C. J., Martin, A., Nisbet, E. G., and O'Nions, R. K., 1976, Mantle composition derived from the chemistry of ultramafic lavas: Nature, p. 577-580.

Blanchard, D. P., Rhodes, J. M., Dungan, M. A., Rodgers, K. V., Donaldson, C. H., Brannon, J. C., Jacobs, J. W., and Gibson, K., 1981, The geochemistry and petrology of basalts from Leg 37 of the Deep-Sea Drilling Project.: J. Geophys. Res., v. 81, p. 4231-4246.

Blenkinsop, T. G., Fedo, C. M., Bickle, M. J., Eriksson, K. A., Martin, A., Nisbet, E. G., and Wilson, J. F., 1993, Ensialic origin for the Ngezi Group, Belingwe greenstone belt, Zimbabwe: Geology, v. 21, p. 1135-1138.

Blenkinsop, T. G., Fedo, C. M., Bickle, M. J., Eriksson, K. A., Martin, A., Nisbet, E. G., Wilson, J. F., and Orpen, J. L., 1993, Ensialic origin for the Ngezi Group, Belingwe greenstone belt, Zimbabwe: Reply: Geology, v. 22, p. 767-768.

Blichert-Toft, J., and Albarède, F., 1994, Short-lived chemical heterogeneities in the Archean mantle with implications for mantle convection.: Science, v. 263, p. 1593-1596.

Bonatti, E., Ottonello, G., and Hamlyn, P., 1986, Peridotites from the island of Zabargad (St. John), Red Sea: Petrology and geochemistry: J. Geophys. Res., 91, 599-631.

Borrandaile, G. J., 1982, Tectonically deformed pillow lava as an indicator of bedding and way-up: Jour. Struct.

Geol., v. 4, p. 469-479.
Boudier, F., and Coleman, R. G., 1981, Cross section through the peridotite in the Samail Ophiolite, southeastern Oman mountains, J. Geophys. Res., 86, 2573-2592.
Bougault, H., and Hekinian, R., 1974, Rift valley in the Atlantic ocean near 36˚ 50'N: Petrology and geochemistry of basaltic rocks.: Earth Planet. Sci. Lett., v. 24, p. 249-261.
Bourdon, B., Zindler, A., Elliott, T., and Langmuir, C. H., 1996, Constraints on mantle melting at mid-ocean ridges from global $^{238}U$-$^{230}Th$ disequilibrium data: Nature, v. 384, p. 231-235.
Bowring, S. A., and Housh, T., 1995, The Earth's early evolution: Nature, v. 269, p. 1535-1540.
Boyd, F. R., 1989, Compositional distinction between oceanic and cratonic lithosphere: Earth Planet. Sci. Lett., 96, 15-26.
Brenan, J. M., Shaw, H. F., Phinney, D. L., and Ryerson, F. J, 1994, Rutile-aqueous fluid partitioning of Nb, Ta, Hf, Zr, U and Th: implications for high field strength element depletions in island-arc basalts: Earth, Planet., Sci, Lett., 128, 327-339.
Bridgwater, D., McGregor, V. R., and Myers, J. S., 1974, A horizontal tectonic regime in the Archean of Greenland and its implications for early crustal thickening: Precam. Res., v. 1, p. 179-197.
Brooks, C., and Hart, S. R., 1974, On the significance of komatiite: Geology, v. 2, p. 107-110.
Bryan, W. B., and Dick, H. J. B., 1982, Contrasted abyssal basalt liquidus trends: Evidence for mantle major element heterogeneity, Earth Planet. Sci. Lett., 58, 15-26.
Bulanova, G. P., Varshavskil, A. V., Leskova, N. V., and Nikishova, L. V., 1979, Central inclusions in natural diamonds; Dokl. Akad. Nauk SSSR, 244, 704-706.
Burke, K., Dewey, J. F., and Kidd, W. S. F., 1976, Dominance of horizontal movements, arc and microcontinental collisions during the later permobile regime, *in* Windley, B. F., ed., The early history of the Earth, London, John Wiley & Sons, p. 113-129.
Burke, K., and Kidd, W. S. F., 1978, Were Archean continental geothermal gradients much steeper than those of today?: Nature, v. 272, p. 240-241.
Byerly, G., 1980, The nature of differentiation trends in some volcanic rocks from the Galapagos Spreading Center: J. Geophys. Res., v. 85, p. 3797-3810.
Calvert, A. J., Sawyer, E. W., Davis, W. J., and Ludden, J. N., 1995, Archaean subduction inferred from seismic images of a mantle suture in the Superior Province: Nature, v. 375, p. 670-674.
Campbell, I. H., and Griffiths, R. W., 1993, The evolution of mantle's chemical structure: Lithos, v. 30, p. 389-399.
Campbell, I. H., Griffiths, R. W., and Hill, R. I., 1989, Melting in an Archaean mantle plume: heads it's basalts, tails it's komatiites: Nature, v. 339, p. 697-699.
Canil, D., 1997, Vanadium partitioning and the oxidation state of Archaean komatiite magmas: Nature, v. 389, p. 842-845.
Carignan, J., Machado, N., and Gariépy, C., 1995a, Initial lead isotopic composition of silicate minerals from the Mulcahy layered intrusion: Implications for the nature of the Archean mantle and the evolution of greenstone belts in the Superior Province, Canada: Geochim. Cosomchim. Acta, v. 59, p. 97-105.
Carignan, J., Machado, N., and Gariépy, C., 1995b, U-Pb isotopic geochemistry of komatiites and pyroxenes from the southern Abitibi greenstone belt, Canada: Chem. Geol., v. 126, p. 17-27.
Carmichael, I. S. E., 1991, The redox states of basic and silicic magmas: a reflection of their source regions?, Contrib. Mineral. Petrol., 106, 129-141.
Carmichael, I. S. E., and Ghiorso, M. S., 1986, Oxidation-reduction relations in basic magma: A case for homogeneous equilibria, Earth Planet. Sci. Lett., 78, 200-210.
Chase, C. G., 1981, Oceanic island Pb: two-stage histories and mantle evolution, Earth Planet. Sci. Lett., 52, 227-284
Chase, C. G., and Patchett, P. J., 1988, Stored mafic/ultramafic crust and early Archean mantle depletion: Earth Planet. Sci. Lett., v. 91, p. 66-72.
Chauvel, C., , Hofmann, A. W., and Vidal, P., 1992, HIMU-EM: The French Polynesian connection: Earth Planet. Sci. Lett., 110, 99-119.
Christie, D. M., Carmichael, I. S. E., and Langmuir, C. H., 1986, Oxidation states of mid-ocean ridge basalt glasses: Earth Planet. Sci. Lett., v. 79, p. 397-411.
Collerson, K. D., and Regelous, M., 1995, $^{143}Nd$-$^{142}Nd$ systematics of early Archean rocks from northern Labrador and implications for crust-mantle evolution of the North Atlantic craton: EOS Trans., v. 76, p. 687.
Condie, K. C., 1972, A plate tectonics evolutionary model of the South Pass Archaean greenstone belt, southwestern Wyoming: Proc. 24th Int. Geol. Congr., v. 1, p. 104-112.
Condie, K. C., 1985, Secular variation in the composition of basalts: an index to mantle evolution: J. Petrol., v. 26, p. 545-563.
Condie, K. C., 1986a, Geochemistry and tectonic setting of early Proterozoic supracrustal rocks in the southwestern United States: J. Geology, v. 94, p. 845-864.
Condie, K. C., 1990, Geochemical characteristics of Precambrian basaltic greenstones, *in* Hall, R. P., and Hughes, D. J., eds., Early Precambrian Basic Magmatism, Glasgow and London, Blackie, p. 40-55.

Condie, K. C., 1994, Greenstones through time, *in* Condie, K. C., ed., Archean Crustal Evolution, Amsterdam, Elservier, p. 85-120.
Davies, G. F., 1992, On the emergence of plate tectonics: Geology, v. 20, p. 963-966.
de Wit, M. J., Armstrong, R., Hart, R. J., and Wilson, A. H., 1987a, Felsic igneous rocks within the 3.3- to 3.5-Ga Barberton Greenstone Belt: High crustal level equivalents of the surrounding tonalite-trondhjemite terrain, emplaced during thrusting: Tectonics, v. 6, p. 529-549.
de Wit, M. J., Hart, R. A., and Hart, R. J., 1987b, The Jamestown ophiolite complex, Barberton mountain belt: a section through 3.5 Ga oceanic crust: Jour. Afr. Earth Sci., v. 6, p. 681-730.
de Wit, M. J., Rosing, C., Hart, R. J., Armstrong, R. A., de Ronde, C. E. J., Green, R. W. E., Tredoux, M., Peberdy, E., and Hart, R. A., 1992, Formation of an Archaean continent: Nature, v. 357, p. 553-562.
Dick, H. J. B., Fischer, R., and Bryan, W. B., 1984, Mineralogic variability of the uppermost mantle along mid-ocean ridges: Earth Planet. Sci. Lett., 69, 88-106.
Donaldson, C. H., 1979, An experimental investigation of the delay in nucleation of olivine in mafic magmas: Contrib. Mineral. Petrol., 69, 21-32.
Dymek, R. F., and Klein, C., 1988, Chemistry, petrology and origin of banded iron-formation lithologies from the 3800 Ma Isua supracrustal belt, West Greenland: Precam. Res., v. 39, p. 247-302.
Eggler, D. H., 1983, Upper mantle oxidation state: evidence from olivine-orthopyroxene-ilmenite assemblages: Geophys. Res. Lett., 10, 365-368.
Eggler, D. H., and Lorand, J. P., 1994, Sulfides, diamonds and mantle $fO_2$: Proc. 5th Int. Kimb. Conf., 160-169 (CPRM Brasilia, Brasilia).
Fornari, D. J., Perfit, M. R., Malahoff, A., and Embley, R., 1983, Geochemical studies of abyssal lavas recovered by DSRV Alvin from eastern Galapagos rift, Inca transform, and Ecuador rift and spatial distribution of lavas: J. Geophys. Res., v. 88, p. 10519-10529.
Frey, F. A., 1980, The origin of pyroxenites and garnet pyroxenites from Slat Lake Crater, Oahu, Hawaii: trace element evidence: Am. J. Sci., 280A, 427-449.
Frey, F. A., Sven, J., and Stockman, H., 1985, The Ronda high temperature peridotite: Geochemistry and petrogenesis: Geochim. Cosmochim. Acta, 49, 2469-2491
Friend, C. R. L., Nutman, A. P., and McGregor, V. R., 1987, Late Archaean tectonics in the Færingehavn- Tre Brødre area, south of Buksefjorden, southern West Greenland: J. geol. Soc. London, v. 144, p. 369-376.
Friend, C. R. L., Nutman, A. P., and McGregor, V. R., 1988, Late Archaean terrane accretion in the Godthåb region, southern West Greenland: Nature, v. 335, p. 535-538.
Fujii, T., and Bougault, H., 1983, Melting relations of a magnesian abyssal tholeiite and origin of MORBs: Earth Planet. Sci. Lett., v. 62, p. 283-295.
Fukao, Y., Obayashi, M., Inoue, H., and Nenbai, M., 1992, Subducting slabs stagnant in the mantle transition zone: J. Geophys. Res., 97, 4809-4822.
Ghiorso, M. S., and Sack, R. O., 1995, Chemical mass transfer in magmatic processes IV. A revised and internally consistent thermodynamic model for the interpolation and extrapolation of liquid-solid equilibria in magmatic systems at elevated temperatures and pressures: Contrib. Mineral. Petrol., v. 119, p. 197-212.
Gill, R. C. O., 1979, Comparative petrogenesis of Archaean and modern low-K tholeiites. A critical review of some geochemical aspects, *in* Ahrens, L. H., ed., Origin and Distribution of the Elements (Phys. Chem. Earth 11), Oxford, Pergamon, p. 431-447.
Gill, R. C. O., and Bridgwater, D., 1979, Early Archaean basic magmatism in West Greenland: the geochemistry of the Ameralik dykes: J. Petrol., v. 20, p. 695-726.
Gill, R. C. O., Bridgwater, D., and Allaart, J. H., 1981, The geochemistry of the earliest known basic metavolcanic rocks, at Isua, West Greenland: a preliminary investigation.,: Spec. Publs. Geol. Soc. Aust., v. 7, p. 313-325.
Glikson, A. Y., 1971, Primitive Archaean element distribution patterns: chemical evidence and geotectonic significance: Earth. Planet. Sci. Lett., v. 12, p. 309-320.
Goodwin, A. M., 1991, Precambrian geology The dynamic evolution of the continental crust, Academic Press, London, pp. 666.
Goodwin, A. M., 1996, Principles of Precambrian geology, Academic Press, London, pp. 327.
Goto, A., and Tatsumi, Y., 1994, Quantitative analysis of rock samples by an X-ray fluorescence spectrometer (I): The Rigaku Journal, v. 11, p. 40-59.
Grambling, J. A., 1981, Pressures and temperatures in Precambrian metamorphic rocks: Earth Planet. Sci. Lett., v. 53, p. 63-68.
Green, D. H., 1972, Archaean greenstone belts may include terrestrial equivalents of lunar maria ?: Earth Planet. Sci. Lett., v. 15, p. 263-270.
Green, D. H., 1975, Genesis of Archean peridotitic magmas and constraints on Archean geothermal gradients and tectonics: Geology, v. 3, p. 15-18.
Green, D. H., Hibberson, W. O., and Jaques, A. L., 1979, Petrogenesis of mid-ocean ridge basalts, *In* McElhinney, M. W. ed., The Earth: Its origin, structure and evolution, 265-299, Academic Press, London.
Green, T. H., 1994, Experimental studies of trace-element partitioning applicable to igneous petrogenesis -

Sedona 16 years later: Chem. Geol., v. 117, p. 1-36.
Griffiths, R. W., and Campbell, I. H., 1990, Stirring and structure in mantle starting plumes: Earth Planet. Sci. Lett., v. 99, p. 66-78.
Gruau, G., Chauvel, C., Arndt, N. T., and Cornichet, J., 1990, Aluminum depletion in komatiites and garnet fractionation in the early Archean mantle: Hafnium isotopic constraints: Geochim. Consmochim. Acta, v. 54, p. 3095-3101.
Gruau, G., Rosing, M., Bridgwater, D., and Gill, R. C. O., 1996, Resetting of Sm-Nd systematics during metamorphism of > 3.7-Ga rocks: implications for isotopic models of early Earth differentiation: Chem. Geol., v. 133, p. 225-240.
Hamilton, W. B., 1993, Evolution of Archean mantle and crust, In Reed Jr., J. C., et al. (eds.), Precambrian-Conterminous United States, Geol. Soc. Am., Geology of North America. v. C-2, p 597-614, 630-636.
Hamilton, W. B., 1998, Archean tectonics and magmatism: Inter. Geol. Rev., 40, 1-39.
Hamilton, W. B., 1998, Archean magmatism and deformation were not products of plate tectonics: Precam. Res., 91, 143-179.
Hanan, B. B., and Graham, D. W., 1996, Lead and Helium isotope evidence from oceanic basalts for a common deep source of mantle plumes: Science, 272, 991-995.
Haggerty, S. E., and Tompkins, L. A., 1983, Redox state of Earth's upper mantle from kimberlitic ilmenites: Nature, 303, 295-300.
Hargreaves, R., and Ayres, L. D., 1979, Morphology of Archean metabasalt flows, Utik Lake, Manitoba: Can. J. Earth Sci., v. 16, p. 1452-1466.
Harper, C. L., Jr., and Jacobsen, S. B., 1992a, Confirmation of a positive $^{142}Nd/^{144}Nd$ anomaly in 3.8 Ga Isua metasediment 715-28 relative to the Nd-b and BCR-1 standard: EOS Trans., v. 73, p. 622.
Harper, C. L., Jr., and Jacobsen, S. B., 1992b, Evidence from coupled $^{147}Sm$-$^{143}Nd$ and $^{146}Sm$-$^{142}Nd$ systematics for very early (4.5-Gyr) differentiation of the Earth's mantle: Nature, v. 360, p. 728-732.
Hart, S. R., and Brooks, C., 1977, The geochemistry and evolution of Early Precambrian Mantle: Contrib. Mineral. Petrol., v. 61, p. 109-128.
Hart, S. R., Brooks, C., Krogh, T. E., Davis, G. L., and Nava, D., 1970, Ancient and modern volcanic rocks: a trace element model: Earth Planet. Sci. Lett., v. 10, p. 17-28.
Hartmann, W. K., Phillips, R. J., and Taylor, G. J., 1986, Origin of the Moon: Houston, Lunar Planet. Inst., 781 p.
Hauri, E. H., 1996, Major-element variability in the Hawaiian mantle plume: Nature, v. 382, p. 415-419.
Hauri, E. H., and Hart, S. R., 1993, Re-Os isotope systematics of HIMU and EMII oceanic island basalts from the south Pacific Ocean, Earth Planet. Sci. Lett., 114, 353-371.
Hayashi, C., Nakazawa, K., and Mizuno, H., 1979, Earth's melting due to the blanketing effect of the primordial dense atmosphere: Earth Planet. Sci. Lett., v. 43, p. 22-28.
Helmstaedt, H., Padgham, W. A., and Brophy, J. A., 1986, Multiple dikes in Lower Kam Group, Yellowknife greenstone belt: Evidence for Archean sea-floor spreading?: Geology, v. 14, p. 562-566.
Hervig, R. L., Smith, J. V., Steele, I. M., Gurney, J. J., Meyer, H. O., and Harris, J., 1980, Diamonds: minor elements in silicate inclusions: pressure-temperature implications: J. Geophys. Res., 85, 6919-6929.
Hirata, T., Shimizu, H., Akagi, T., Sawatari, H., and Masuda, A., 1988, Precise determination of rare earth elements in geological standard rocks by inductively coupled plasma source mass spectrometry: Anal. Sci., v. 4, p. 637-643.
Hirose, K., and Kushiro, I., 1993, Partial melting of dry mantle peridotites at high pressures: Determination of compositions of melts segregated from peridotite using aggregates of diamond: Earth Planet. Sci. Lett., v. 114, p. 477-489.
Hirschmann, M., 1996, Reading garnet's signature: Nature, v. 384, p. 215-217.
Hirschmann, M. M., and Stolper, E. M., 1996, A possible role for garnet pyroxenite in the origin of the "garnet signature" in MORB: Contrib. Mineral. Petrol., v. 124, p. 185-208.
Hoffman, P. F., 1973, Evolution of an early Proterozoic continental margin: the Coronation geosyncline and associated aulacogens of the northwestern Canadian shield: Philos. Trans. R. Soc. London, v. A 273, p. 547-581.
Hofmann, A. W., and White, W. M., 1982, Mantle plumes from ancient oceanic crust: Earth Planet. Sci. Lett., 57, 421-436.
Hunter, M. A., Bickle, M. J., Nisbet, E. G., Martin, A., and Chapman, H. J., 1998, Continental extensional setting for the Archean Belingwe Greenstone Belt, Zimbabwe: Geology, v. 26, p. 883-886.
Irifune, T., and Ringwood, A. E., 1987, Phase transformations in a harzburgite composition to 26 GPa: implications for dynamical behaviour of the subducting slab: Earth Planet Sci. Lett., v. 86, p. 365-376.
Irifune, T., and Ringwood, A. E., 1993, Phase transformations in subducted oceanic crust and buoyancy relationships at depths of 600-800 km in the mantle: Earth Planet Sci. Lett., v. 117, p. 101-110.
Irving, A. J., 1980, Petrology and geochemistry of composite ultramafic xenoliths in alkalic basalts and implications for magmatic processes within the mantle: Am. J. Sci., 280A, 389-426.
Iwamori, H., McKenzie, D., and Takahashi, E., 1995, Melt generation by isentropic mantle upwelling: Earth

Planet Sci. Lett., v. 134, p. 253-266.
Isozaki, Y., and Maruyama, S., 1992, Oceanic plate stratigraphy: The prime criterion of accretionary complex: IGC Kyoto abstract, v. 2, p. 414.
Isozaki, Y., Maruyama, S., and Kimura, G., 1991, Middle Archean (3.3 Ga) Cleaverville accretionary complex in northwestern Pilbara block, western Australia: EOS Trans., v. 72, p. 542.
Isozaki, Y., Maruyama, S., and Furuoka, F., 1990, Accreted oceanic materials in Japan: Tectonophysics, v. 181, p. 179-205.
Jacobsen, S. B., and Dymek, R. F., 1988, Nd and Sr isotope systematics of clastic metasediments from Isua, West Greenland: identification of pre-3.8 Ga differentiation crustal components: J. Geophys. Res., v. 93, p. 338-354.
Jacobsen, S. B., and Harper Jr, C. L, 1992, 142Nd/144Nd in the Earth's oldest rocks and implications for the geochemistry history of the crust-mantle system: EOS Trans., v. 73, p. 622.
Jagoutz, E., Palme, H., Baddenhausen, H., Blum, K., Cendales, M., Dreibus, G., Spettel, B., Lorenz, V., and Wänke, H., 1979, The abundances of major, minor and trace elements in the earth's mantle as derived from primitive ultramafic nodules: Proc. Lunar Planet. Sci. Conf. 10th, p. 2031-2050.
Jarvis, G. T., and Campbell, I. H., 1983, Archean komatiites and geotherms: solution to an apparent contradiction: Geophys. Res. Lett., v. 10, p. 1133-1136.
Jones, J. G., 1969, Pillow lavas as depth indicators: Am. J. Sci., 267, 181-195.
Kato, T., Ringwood, A. E., and Irifune, T., 1988a, Experimental determination of element partitioning between silicate perovskites, garnet and liquids: constraints on early differentiation of the mantle: Earth Planet. Sci. Lett., v. 89, p. 123-145.
Kato, T., Ringwood, A. E., and Irifune, T., 1988b, Constraints of element partition coefficients between $MgSiO_3$ perovskite and liquid determined by direct measurements: Earth Planet. Sci. Lett., v. 90, p. 65-68.
Kendall, J. –M., and Silver, P. G., 1996, Constraints from seismic anisotropy on the mantle of the lowermost mantle, Nature, 381, 409-412.
Kimura, G., Ludden, J. N., Desrochers, J.-P., and Hori, R., 1993, A model of ocean-crust accretion for the Superior province, Canada: Lithos, v. 30, p. 337-335.
Kimura, G., Maruyama, S., and Isozaki, Y., 1991, Early Archean accretionary complex in the eastern Pilbara craton, Western Australia - Detailed field occurrence in the Marble Bar area -: EOS Trans., v. 72, p. 542.
Kimura, G., Sakakibara, M., and Okamura, M., 1994, Plumes in central Panthalassa? Deductions from accreted oceanic fragments in Japan: Tectonics, v. 13, p. 905-916.
Kinzler, R. J., 1997, Melting of mantle peridotite at pressures approaching the spinel to garnet transition: Application to mid-ocean ridge basalt petrogenesis: J. Geophys. Res., v. 102, p. 853-874.
Klein, E. M., and Langmuir, C. H., 1987, Global correlations of ocean ridge basalt chemistry with axial depth and crustal thickness: J. Geophys. Res., v. 92, p. 8089-8115.
Klein, E. M., and Langmuir, C. H., 1989, Local versus global variations in ocean ridge basalt composition: a reply: J. Geophys. Res., v. 94, p. 4241-4252.
Kogiso, T., Tatsumi, Y., Shimoda, H., and Barsczus, H. G., 1997, HIMU ocean island basalts in the southern Polynesia: new evidence for whole-mantle scale recycling of subducted oceanic crust: J. Geophys. Res., v. 102, p. 8085-8103.
Komiya, T., and Maruyama, S., 1995, Geochemistry of the oldest MORB and OIB of the World, Isua (3.8 Ga), Greenland: EOS Trans., v. 76, p. 700.
Komiya, T., Maruyama, S., Nohda, S., Masuda, T., Appel, P. W. U, Hayashi, M., and Okamoto, S., 1998, Plate tectonics at 3.8 – 3.7 Ga; Field evidence from the Isua accretionary complex, southern West Greenland; Jour. Geol. in press.
Komiya, T., Maruyama, S., Shimizu, K., and Hirose, K., 1998, Geology of Komati Fm. and mineralogy of relict igneous minerals, Barberton Greenstone Belt (3.5 Ga), South Africa, International Volcanological Congress, Cape Town
Kröner, A., 1977, The Precambrian geotectonic evolution of Africa: Plate accretion versus plate destruction: Precam. Res., v. 4, p. 163-213.
Kröner, A., 1981, Precambrian plate tectonics, *in* Kröner, A., ed., Precambrian plate tectonics, Amsterdam, Elservier, p. 57-90.
Kushiro, I., 1996, Partial melting of a fertile mantle peridotite at high pressures: an experimental study using aggregates of diamond, *in* Basu, A. R., and Hart, S. R., eds., Earth processes: Reading the isotopic code, Washington D. C., AGU Monograph 95, p. 109-122.
Kushiro, I., 1998, Compositions of partial melts formed in mantle peridotites at high pressures and their relation to those of primitive MORB: Phys. Earth Planet. Inter., 107, 103-110.
Kusky, T. M., 1989, Accretion of the Archean Slave province: Geology, v. 17, p. 63-67.
Kusky, T. M., 1991, Structural development of an Archean orogen, western Point Lake, Northwest Territories: Tectonics, v. 4, p. 820-841.
Kusky, T. M., and Kidd, W. S. F., 1992, Remnants of an Archean oceanic plateau, Belingwe greenstone belt, Zimbabwe: Geology, v. 20, p. 43-46.

Kusky, T. M., and Winsky, P. A., 1995, Structural relationships along a greenstone/shallow water shelf contact, Belingwe greenstone belt, Zimbabwe: Tectonics, v. 14, p. 448-471.
Kusky, T. M., Winsky, P. A., and Kidd, W. S. F., 1994, Ensialic origin for the Ngezi Group, Belingwe greenstone belt, Zimbabwe: Comment and reply: Geology, 22, 766-767.
Langmuir, C. H., Bender, J. F., Bence, A. E., Hanson, G. N., and Taylor, S. R., 1977, Petrogenesis of basalts from the FAMOUS area: mid-Atlantic ridge: Earth Planet. Sci. Lett., v. 36, p. 133-156.
Langmuir, C. H., and Hanson, G. N., 1980, An evaluation of major element heterogeneity in the mantle sources of basalts: Philos. Trans. R. Soc. London, A297, 383-407.
Lee, D.-C., and Halliday, A. N., 1995, Hafnium-tungsten chronometry and the timing of terrestrial core formation: Nature, v. 378, p. 771-774.
Lee, K. –L., and Hart, S. R., 1995, Os isotopic studies of abyssal peridotite: EOS Trans., Am. Geophys. Union, 76, F543.
Le Roex, A. P., Erlank, A. J., and Needham, H. D., 1981, Geochemical and mineralogical evidence for the occurrence of at least three distinct magma types in the 'Famous' region: Contrib. Mineral. Petrol., v. 77, p. 24-37.
Lesher, C. M., and Arndt, N. T., 1990, Geochemistry of komatiites at Kambalda, Western Australia: Assimilation, crystal fractionation, and lava replenishment: Int. Archean Symp. 3rd, p. pp. 149-151.
Ludden, J. N., and Thompson, G., 1978, Behaviour of rare earth elements during submarine weathering of tholeiitic basalt: Nature, v. 274, p. 147-149.
Luth, R. W., Virgo, D., Boyd, F. R., and Wood, B. J., 1990, Ferric iron in mantle-derived garnets, implications for thermobarometry and for the oxidation state of the mantle, Contrib. Mineral. Petrol., 104, 56-72.
Machado, N., Brooks, C., and Hart, S. R., 1986, Determination of initial $^{87}Sr/^{86}Sr$ and $^{143}Nd/^{144}Nd$ in primary minerals from mafic and ultramafic rocks: Experimental procedure and implications for the isotopic characteristics of the Archean mantle under the Abitibi greenstone belt, Canada: Geochim. Cosmochim. Acta, v. 50, p. 2335-2348.
Mahoney, J. J., 1987, An isotopic survey of Pacific oceanic plateaus: implications for their nature and origin: Seamounts, Islands, and Atolls: Wahington D. C., AGU Geophys. Monograph 43, 207-220 p.
Martin, H., 1986, Effect of steeper Archean geothermal gradient on geochemistry of subduction-zone magmas: Geology, v. 14, p. 753-756.
Maruyama, S., 1997, Initiation of return flow seawater into mantle at 750 Ma and the Proterozoic/Phanerozoic boundary: EOS Trans., v. 78, p. 826.
Maruyama, S., Isozaki, Y., and Kimura, G., 1991a, Is the Mid-Archean barite formation from the Pilbara craton, Australia under the deep-sea environment?: EOS Trans., v. 72, p. 532.
Maruyama, S., Komiya, T., and Appel, P. W. U., 1994a, The oldest (3.8 Ga) accretionary complex of the world, Isua, Greenland: EOS Trans., v. 75, p. 691.
Maruyama, S., Masuda, S., and Appel, P. W. U., 1991b, The oldest accretionary complex on the Earth, Isua, Greenland: Geol. Soc. Am., Abstract with programs, p. A429-A430.
McCulloch, M. T., and Bennett, V. C., 1993, Evolution of the early Earth: Constraints from $^{143}Nd$-$^{142}Nd$ isotopic systematics: Lithos, v. 30, p. 237-255.
McCulloch, M. T., and Bennett, V. C., 1994, Progressive growth of the Earth's continental crust and depleted mantle: Geochemical constraints: Geochim. Cosmochim. Acta, v. 58, p. 4717-4738.
McGregor, V. R., 1973, The early Precambrian gneisses of the Godthåb district, West Greenland: Philos. Trans. Royal Soc. London, v. A273, p. 343-358.
McGregor, V. R., 1993, Descriptive text to 1:100000 Geological map of GREENLAND Qôrqut 64 V.1 Syd.: Copenhagen, Geological Survey of Greenland, 40 p.
McKenzie, D., and Bickle, M. J., 1988, The volume and composition of melt generated by extension of lithosphere: J. Petrol., v. 29, p. 625-649.
McKenzie, D., and O'Nions, R. K., 1991, Partial melt distributions from inversion of rare earth element concentrations: Jour. Petrol., 32, 1021-1091.
Meen, W. S., 1993, Geochemical evidence for the tectonic setting of early Proterozoic metavolcanic sequences in southern Lake Superior region: J. Min. Petr. Econ. Geol., v. 88, p. 320-334.
Meschede, M., 1986, A method of discriminating between different types of mid-ocean ridge basalts and continental tholeiites with the Nb-Zr-Y diagram: Chem. Geol., v. 56, p. 207-218
Menzie, M., 1991, Oceanic peridotites, *in* Floyd, P. A., ed., Oceanic Basalts, London, Blackie, p. 363-385.
Miyashiro, A., Shido, F., and Ewing, M., 1969, Diversity and origin of abyssal tholeiite from the Mid-Atlantic Ridge near 24˚ and 30˚ north latitude: Contrib. Mineral. Petrol., v. 23, p. 38-52.
Mukasa, S. B., Shervais, J. W., Wilshire, H. G., Nielsen, J. E., 1991, Intrinsic Nd, Pb and Sr isotopic heterogeneities exhibited by the Lherz alpine peridotite massif, French Pyrenees: J. Petrol. Special Lherzolites Issue, 117-134.
Moore, J. G., 1965, Petrology of deep-sea basalt near Hawaii: Am. J. Sci., v. 263, p. 40-52.
Naldrett, A. J., 1969, A portion of the system Fe-S-O between 900 and 1080 ˚C and its application to ore magmas: J. Petrol., 10, 171-201.

Nesbitt, R. W., Sun, S. S., and Purvis, A. C., 1979, Komatiites: Geochemistry and genesis: Can. Mineral., v. 17, p. 165-186.
Nisbet, E. G., Arndt, N. T., Bickle, M. J., Cameron, W. E., Chauvel, C., Cheadle, M., Hegner, E., Kyser, T. K., Martin, A., Renner, R., and Roedder, E., 1987, Uniquely fresh 2.7 Ga komatiites from the Belingwe greenstone belt, Zimbabwe: Geology, v. 15, p. 1147-1150.
Nisbet, E. G., Cheadle, M. J., Arndt, N. T., and Bickle, M. J., 1993, Constraining the potential temperature of the Archean mantle: A review of the evidence from komatiites: Lithos, v. 30, p. 291-307.
Nisbet, E. G., and Fowler, C. M. R., 1983, Model for Archean plate tectonics: Geology, v. 11, p. 376-379.
Nutman, A. P., 1986, The early Archaean to Proterozoic history of the Isukasia area, southern West Greenland, v. 154: København, Denmark, Grønlands geol. Unders. Bull., 80 p.
Nutman, A. P., and Collerson, K. D., 1991, Very early Archean crustal-accretion complexes preserved in the North Atlantic craton: Geology, v. 19, p. 791-794.
Nutman, A. P., Friend, C. R. L., Baadsgaard, H., and McGregor, V. R., 1989a, Evolution and assembly of Archean gneiss terranes in the Godthåbsfjord region, southern West Greenland: Structural, metamorphic, and isotope evidence: Tectonics, v. 8, p. 573-589.
Ogawa, M., 1988, Numerical experiments on coupled magmatism-mantle convection system: Implications for mantle evolution and Archean continental crusts: J. Geophys. Res., v. 93, p. 15119-15134.
O'Neill, H. St. C., Oretz, N., Arculus, R. J., Wall, V. J., and Green, D. H., 1982, Oxygen fugacities from the assemblage olivine-orthopyroxene-spinel: Terra Cognita, 2, 228.
O'Neill, H. S. C., Rubie, D. C., Canil, D., Geiger, C. A., Ross II, C. R., Seifert, F., and Woodland, A. B., 1993, Ferric iron in the upper mantle and in transition zone assemblages: Implications for relative oxygen fugacities in the mantle, *in* Takahashi, E., Jeanloz, R., and Rubie, D., eds., Evolution of the Earth and Planets, Washington, IUGG and Am. Geophys. Union, p. 73-88.
O'Neill, H. St. C., and Wall, V. J.,1987, The olivine-orthopyroxene-spinel oxygen geobarometer, the nickel precipitation curve, and the oxygen fugacity of the Earth's upper mantle: J. Petrol. , 28, 1169-1191.
Ohta, H., Maruyama, S., Takahashi, E., Watanabe, Y., and Kato, Y., 1996, Field occurrence, geochemistry and petrogenesis of the Archean mid-oceanic ridge basalts (AMORBs) of the Cleaverville area, Pilbara craton, Western Australia: Lithos, v. 37, p. 199-221.
Ohtani, E., 1990, Majorite fractionation and genesis of komatiites in the deep mantle: Precam. Res., v. 48, p. 195-202.
Ohtani, E., Yurimoto, H., and Seto, S., Element partitioning between metallic liquid, silicate liquid, and lower-mantle minerals: implications for core formation of the Earth: Phys. Earth Planet. Inter., 100, 97-114.
Parman, S. W., Dann, J. C., Grove, T. L., and de Wit, M. J., 1997, Emplacement conditions of komatiite magmas from the 3.49 Ga Komati Formation, Barberton Greenstone Belt, South Africa: Earth Planet. Sci. Lett., v. 150, p. 303-323.
Pattou, L., Lorand, J. P., and Gros, M., 1996, Non-chondritic platinum-group element ratios in the Earth's mantle: Nature, v. 379, p. 712-715.
Pearce, J. A., and Cann, J. R., 1973, Tectonic setting of basic volcanic rocks determined using trace element analyses: Earth Planet. Sci. Lett., v. 19, p. 290-300.
Pearson, D. G., Davies, G. R., Nixon, P. H., 1993, Geochemical constraints on the petrogenesis of diamond facies pyroxenites from the Beni Bousera peridotite massif: J. Petrol., 34, 125-172.
Piccardo, G. B., Messiga, B., and Vannucci, R., 1988, The Zabargad peridotite-pyroxenite association: petrological constraints on its evolution: Tectonophysics, v. 150, p. 135-162.
Piper, J. D. A., 1982, The Precambrian palaeomagnetic record: the case for the Proterozoic supercontinent: Earth Planet. Sci. Lett., v. 59, p. 61-89.
Presnall, D. C., and Hoover, J. D., 1987, High pressure phase equilibrium constraints on the origin of mid-ocean ridge basalts, *in* Mysen, B. O., ed., Magmatic processes: Physicochemical Principles, p. 75-89.
Quick, J. E., 1981, Petrology and petrogenesis of the Trinity peridotite, an upper mantle diapir in the eastern Klamath mountains, northern California: J. Geophys. Res., 86, 11837-11863.
Rapp, R. B., and Watson, E. B., 1995, Dehydration melting of metabasalt at 8-32 kbar: implications for continental growth and crust-mantle recycling: Jour. Petrol., 36, 891-931.
Rapp, R. B., Watson, E. B., and Miller, C. F., 1991, Partial melting of amphibolite/eclogite and the origin of Archean trondhjemites and tonalites: Precam. Res., 51, 1-25.
Ringwood, A. E., 1975, Composition and petrology of the Earth's mantle, McGraw-Hill, New York.
Ringwood, A. E., 1979, Origin of the Earth and Moon, New York, Springer-Verlag, 295pp.
Ringwood, A. E., 1982, Phase transformations and differentiation in subducted lithosphere: Implications for mantle dynamics, basalt petrogenesis, and crustal evolution, Jour. Geology, 90, 611-643.
Ringwood, A. E., 1991, Inaugural ingerson lecture: Geochim. Cosmochim. Acta, 55, 2083-2110.
Rivalenti, G., 1976, Geochemistry of metavolcanic amphibolites from South-West Greenland, *in* Windley, B. F., ed., The Early history of the Earth, London, Wiley, p. 213-224.
Ross, K., and Elthon, D., 1997, 13. Extreme incompatible trace - element depletion of diopside in residual mantle from south of the Kane Fracture Zone, *in* Karson, J. A., Cannat, M., Miller, D. J., and Elthon, D., eds.,

Proc. ODP, Sci. Results, 153, College Stasion, TX (Ocean Drilling Program).
Roy-Barman, M., and Allègre, C. J., 1995, $^{187}Os/^{186}Os$ in oceanic island basalts: tracing oceanic crust recycling in the mantle: Earth Planet. Sci. Lett., v. 129, p. 145-161.
Saal, A. E., Hart, S. R. , Shimizu, N., Hauri, E. H., and Layne, G. D., 1998, Pb isotopic variability in melt inclusions from oceanic island basalts, Polynesia: Science, 282, 1481-1484.
Safronov, V. S., 1978, The heating of the earth during its formation: ICARUS, 33, 3-12.
Salters, V. J. M., and Hart, S. R., 1989, The hafnium paradox and the role of garnet in the source of mid-ocean-ridge basalts: Nature, v. 342, p. 420-422.
Salters, V. J. M., 1996, The generation of mid-ocean ridge basalts from the Hf and Nd isotope perspective: Earth Planet. Sci. Lett., 141, 109-123.
Serri, G., Hébert, R., and Hekinian, R., 1988, Petrology of a plagioclase-bearing olivine websterite from the Gorringe Bank (northeastern Atlantic Ocean): Can. J. Earth Sci., 25, 557-569.
Sharma, M., Papanastassiou, D. A., Wasserburg, G. J., and Dymek, R. F., 1996, The issue of the terrestrial record of $^{146}Sm$: Geochim. Cosmochim. Acta, v. 60, p. 2037-2047.
Sigurdsson, H., 1981, First-order major element variation in basalt glasses from the mid-Atlantic ridge: 29˚N to 73˚N: J. Geophys. Res., v. 86, p. 9486-9502.
Silver, P. G., Carlson, R. W., and Olson., P., 1988, Deep slabs, geochemical heterogeneity, and the large-scale structure of mantle convection: Investigation of a enduring paradox: Ann. Rev. Earth Planet. Sci., 16, 477-541.
Sobolev, N. V., Efimova, E. S., and Pospelova, L. N., 1981, Native iron in diamonds of Yakutiya and its paragenesis: Geol. Geofiz., 22, 25-28.
Stille, P., Unruh, D. M., and Tatsumoto, M., 1983, Pb, Sr, Nd and Hf isotopic evidence of multiple sources for Oahu, Hawaii basalts: Nature, p. 25-29.
Storey, M., Mahoney, J. J., Kroenke, L. W., and Saunders, A. D., 1990, Are oceanic plateau sites of komatiite formation?: Geology, v. 18, p. 376-379.
Sun, S.-S., 1980, Lead isotope study of young volcanic rocks from mid-ocean ridge, ocean islands and island arcs, Phil. Trans. Roy. Soc. London, A297, 409-445.
Sun, S.-S., 1982, Chemical composition and origin of the earth's primitive mantle: Geochim. Cosmochim. Acta, v. 46, p. 179-192.
Sun, S.-S., 1984, Geochemical characteristics of Archaean ultramafic and mafic volcanic rocks: implications for mantle composition and evolution, *in* Kröner, A., Hansen, G. N., and Goodwin, A. M., eds., Archaean Geochemistry, Berlin, Springer-Verlag, p. 25-46.
Sun, S.-S., and Nesbitt, R. W., 1977, Chemical heterogeneity of the Archean mantle, composition of the earth and mantle evolution: Earth Planet. Sci. Lett., v. 35, p. 429-448.
Sun, S.-S., and Nesbitt, R. W., 1978b, Petrogenesis of Archean ultrabasic and basic volcanics: evidence from rare earth elements: Contrib. Mineral. Petrol., v. 65, p. 301-325.
Sylvester, P. J., Atoh, K., and Schulz, K. L., 1987, Tectonic setting of late Archaean bimodal volcanism in the Michipicoten (Wawa) greenstone belt, Ontario: Can. J. Earth Sci., 24, 1120-1134.
Takahashi, E., 1990, Speculations on the Archean mantle: missing link between komatiite and depleted garnet peridotite: J. Geophys. Res., v. 95, p. 15941-15954.
Takahashi, E., Shimazaki, T., Tsuzaki, Y., and Yoshida, H., 1993, Melting study of a peridotite KLB-1 to 6.5 GPa, and the origin of basaltic magmas: Phil. Trans. R. Soc. London, v. A342, p. 105-120.
Tarney, J., Dalziel, I. W. D., and de Wit, M. J., 1976, Marginal basin " Rocas verdes " complex from S. Chile: a model for Archaean greenstone belt formation: The Early History of the Earth: London, Wiley, 131-146 p.
Tarney, J., Wood, D. A., Varet, J., Saunders, A. D., and Cann, J. R., 1979, Nature of mantle heterogeneity in the north Atlantic : evidence from Leg 49 basalts: Maurice Ewing Series 2 Deep Drilling Results in the Atlantic Ocean : Ocean Crust: Washington D.C., Am. Geophys. Union, 249-261 p.
Tatsumoto, M. 1978, Isotopic composition of lead in oceanic basalt and its implication to mantle evolution: Earth Planet. Sci. Lett., 38, 63-87.
Vervoort, J. D., and Baadsgaard, H., 1994, Depleted mantle evolution as defined by Hf isotopic data from concordant zircons: EOS Trans., v. 75, p. 690.
Vervoort, J. D., Patchett, P. J., Gehrels, G. E., and Nutman, A. P., 1996, Constraints on early Earth differentiation from hafnium and neodymium isotopes: Nature, v. 379, p. 624-627.
Vervoort, J. D., White, W. M., and Thorpe, R. I., 1994, Nd and Pb isotope ratios of the Abitibi greenstone belt: new evidence for very early differentiation of the Earth: Earth Planet. Sci. Lett., v. 128, p. 215-229.
Vidal, Ph., Chauvel, C., and Brousse, R., 1984, Large mantle heterogeneity beneath French Polynesia: Nature, 307, 536-538.
Wänke, H., Dreibus, G., and Jagoutz, E., Mantle chemistry and accretion history of the Earth., In Kröner, A., G. N. Hansen, and A. M. Goodwin (eds.), Archaean Geochemistry, Springer-Verlag, Berlin, 1-24, 1984.
Weaver, B. L., 1991, The origin of ocean island basalt end-member compositions : trace element and isotopic constraints: Earth Planet. Sci. Lett., 104, 381-397.
Wilkinson, J. F. G., 1985, Undepleted mantle composition beneath Hawaii: Earth Planet. Sci. Lett., v. 75, p. 129-

138.
Wood, D. A., Joron, J.-L., and Treuil, M., 1979a, A reappraisal of the use of trace elements to classify and discriminate between magma series erupted in different tectonic setting: Earth Planet Sci. Lett., v. 45, p. 326-336.
Wood, B. J., and Virgo, D., 1989, Upper mantle oxidation state: Ferric iron contents of lherzolite spinels by $^{57}Fe$ Mössbauer spectroscopy and resultant oxygen fugacities: Geochim. Cosmochim. Acta, 53, 1277-1291.
Woodhead, J. D., Greenwood, P., Harman R. S., and Stoffers, P., 1993, Oxygen isotope evidence for recycled crust in the source of EM-type ocean island basalts: Nature, 362, 809-813.
Wynne-Edwards, H. R., 1976, Proterozoic ensialic orogenesis: the millipede model of ductile plate tectonics: Am. J. Sci., v. 276, p. 927-953.
Yurimoto, H., and Ohtani, E., 1992, Element partitioning between majorite and liquid: a secondary ion mass spectrometric study: Geophys. Res. Lett., v. 19, p. 17-20.
Zindler, A., and Hart, S. R., 1986, Chemical geodynamics: Annu. Rev. Earth Planet. Sci., 14, 493-571.

## FIGURE CAPTIONS

**Figure 1.** Geologic map of the NE part of Isua supracrustal belt. The inset map is geotectonic map of southern West Greenland, simplified after McGregor et al. (1991). Three terranes, Akia (gray), Tasiusarsuaq (gray with horizontal bars), and Akulleq are shown. Akulleq terrane is composed of Ikkattoq gneiss (dark gray with white bars), Amîtsoq gneiss (stippled), and supracrustal rocks (black). Post-collision Qôrqut granite (cross) intrude mainly Akulleq terrane. The Isua supracrustal belt is located in the northeastern corner.

**Figure 2.** Distribution of sample locations. Symbols; solid circles are MORBs and open circles are OIBs. Determination of tectonic setting of these basalts is discussed in the text.

**Figure 3.** MgO variation diagrams of major elements for MORBs and OIBs in the Isua supracrustal belt along with modern MORB and OIB. Symbols; solid circles are MORBs and open triangles are MORBs. Compositional differences between MORBs and OIBs are present in $TiO_2$, FeO, CaO and $P_2O_5$.

**Figure 4.** MgO variation diagrams of trace elements for MORBs and OIBs in the Isua supracrustal belt along with modern MORB and OIB. Symbols; solid circles are MORBs and open triangles are MORBs. Compositional differences between MORBs and OIBs are present in Zr, Y and Nb.

**Figure 5.** Chondrite-normalized rare earth element (REE) abundances in MORBs and OIBs in the Isua supracrustal belt. IOIBs, gray lines, are characterized by flat pattern, whereas MORBs, black lines, are depleted in light-REE. Values of chondrite are taken from Anders & Ebihara (1982).

**Figure 6.** Ni-MgO plots of MORBs and OIBs in the Isua supracrustal belt along with komatiites, and modern MORB and OIB. A gray arrow indicates compositional variation of partial melts from a mantle peridotite with increasing degree of melting. A black arrow indicates compositional variation of partial melts from a mantle peridotite with increasing pressure. A broken arrow indicates compositional variation of residual melts through olivine fractionation at low pressure. Basalts are different from komatiites in Ni content at a given MgO content, especially high MgO content, because of difference of degree of melting. Symbols are shown in inset.

**Figure 7.** (a) MgO variation diagrams of some major elements for MORBs in the Isua supracrustal belt (solid circles) along with compositional variations of modern MORBs (gray regions). Three arrows on scattered plots indicate compositional variation of residual melts through crystal fractional fractionation of olivine, olivine+clinopyroxene and olivine+clinopyroxene+plagioclase, respectively. Abbreviations are: ol = olivine; cpx = clinopyroxene; pl = plagioclase. (b) Comparison of primitive natural basalts with partial melts formed from mantle peridotite by diamond methods. (i) $SiO_2$-MgO

diagram. Symbols: solid circles and open circles are primitive Isua MORBs and most primitive modern NMORBs, respectively. Thick arrows indicate compositional variation of partial melts produced from four mantle peridotite at different pressure, 10 kb for light gray, 15 kb for gray, 20 kb for dirk gray and 25-30 kb for black arrow respectively. This diagram indicates that both modern MORBs and Isua MORBs were formed at 10 to 15 kb. (ii) MgO-FeO diagram. Symbols: solid circles and open circles are primitive Isua MORBs and most primitive modern NMORBs, respectively. Thick arrows indicate compositional variation of partial melts produced at 15 kb from four different mantle peridotite, HK66 for light gray, PHN1611 for gray, KLB-1 for dirk gray and MM3 for black arrow, respectively. This diagram indicates that FeO content of mantle source of modern MORBs is comparable to that of KLB-1, whereas that that of mantle source of Isua MORBs was comparable to or higher than that of HK66 and PHN1611. (iii) $SiO_2$-FeO diagram. Symbols: solid circles and small open circles are primitive Isua MORBs and partial melts from PHN1611, respectively. Thick arrows indicate compositional variation of partial melts produced from PHN1611 at 10 to 15 kb for gray, and at 20 to 30 kb for black arrow, respectively. This diagram indicates that melting pressure and temperature of Isua MORBs was around 15 kb and 1325-1425 ˚C. Potential mantle temperature was calculated to be 1390 to 1550 ˚C using degree of melting (Kushiro 1996) and thermodynamic parameters (Hirose 1998).

**Figure 8.** Zr variation diagrams of incompatible trace elements for MORBs and OIBs in the Isua supracrustal belt along with modern MORB and OIB, Mare basalt and Highland basalt in Moon, Eucrite, and Orgueil. Symbols are shown in inset.

**Figure 9.** Compositional variation of MORBs and OIBs in the Isua supracrustal belt along with modern MORBs and OIBs in isotopic pair elements. (i) Pb-Th plots of Isua MORBs and Isua OIBs along with modern MORBs and OIBs. Symbols; solid circles and open circles indicate Isua MORBs and Isua OIBs, respectively. Isua MORBs are depleted in Pb and Th compared with Isua OIBs. Isua MORBs have high Pb/Th ratio relative to modern MORB, possibly resulting in suppression of evolution of Pb isotope in subducted oceanic crust. (ii) Sr-Rb plots of Isua MORBs and Isua OIBs along with modern MORBs and OIBs. Symbols; solid circles and open circles indicate Isua MORBs and Isua OIBs, respectively. Isua MORBs have low Sr/Rb ratio relative to modern MORB, possibly resulting in promotion of evolution of Pb isotope in subducted oceanic crust.

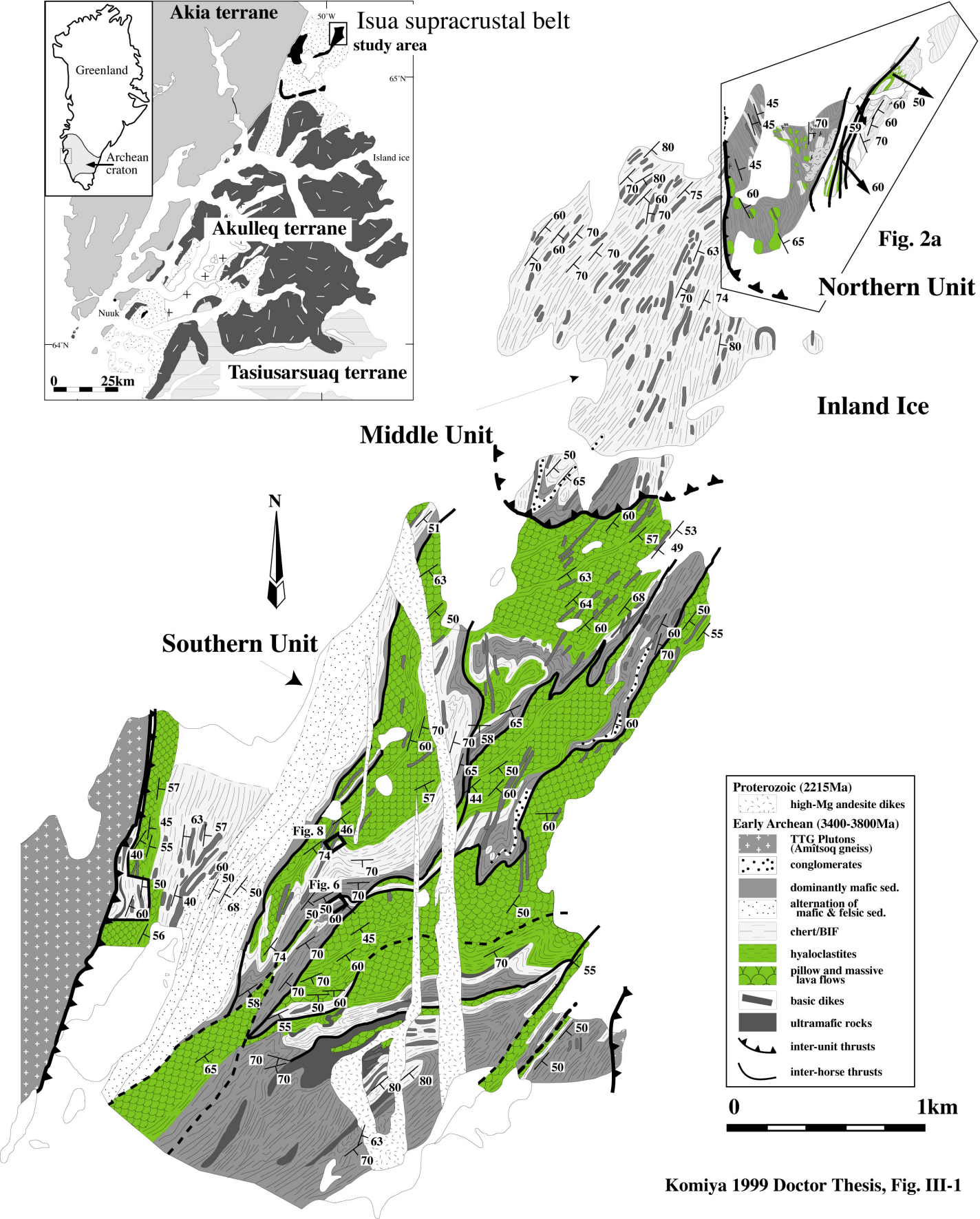


Komiya 1999 Doctor Thesis, Fig. III-1

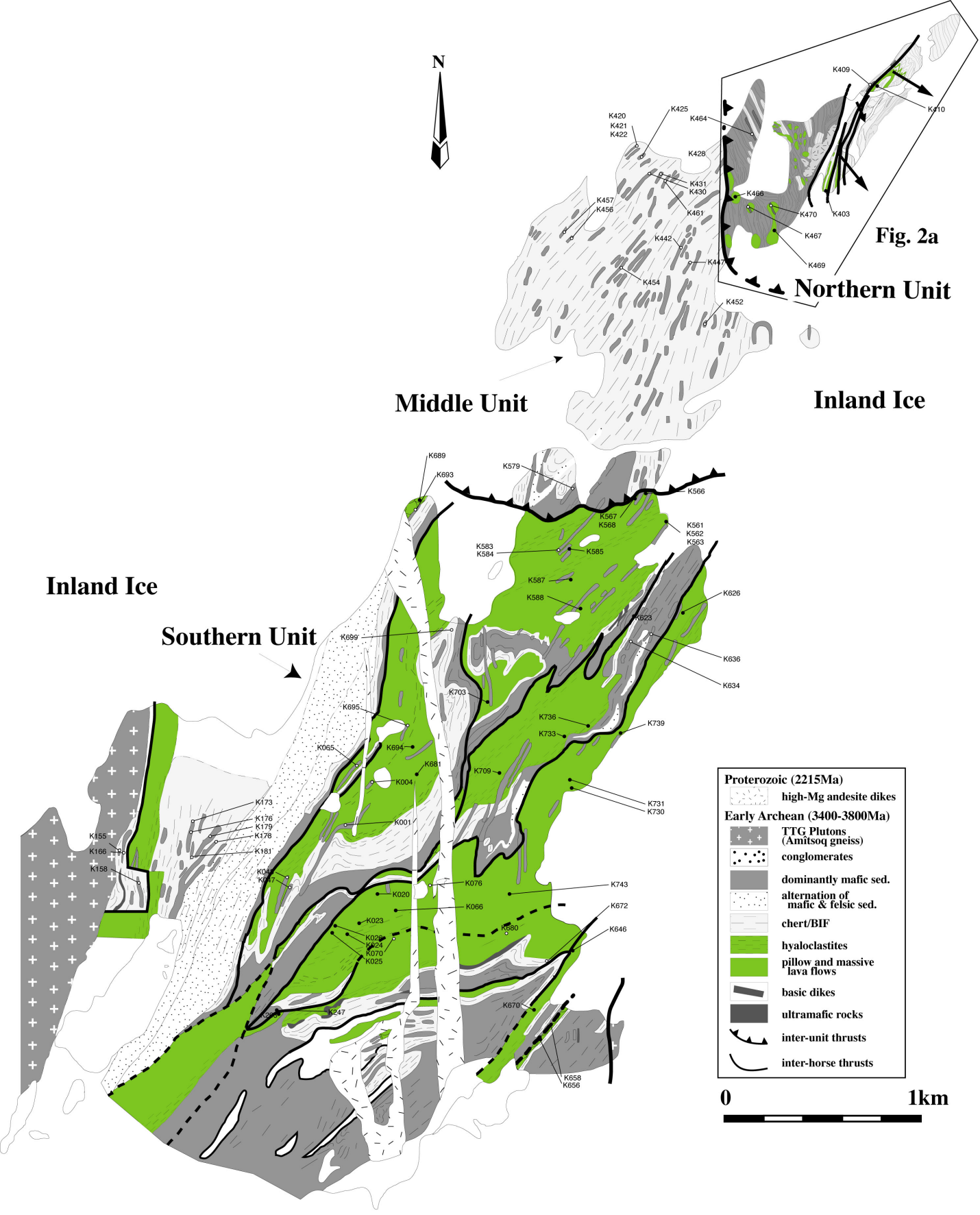


Komiya 1999 Doctor Thesis Fig. III-2

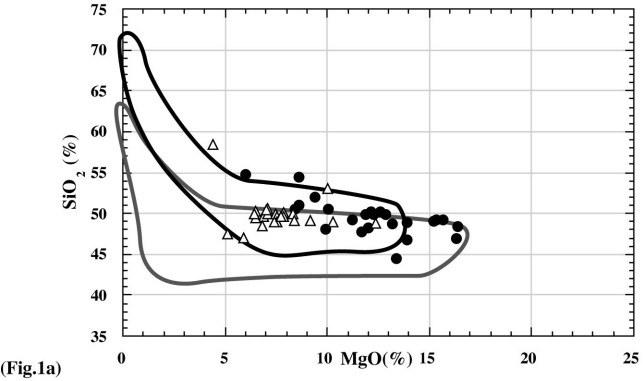


(Fig.1a)

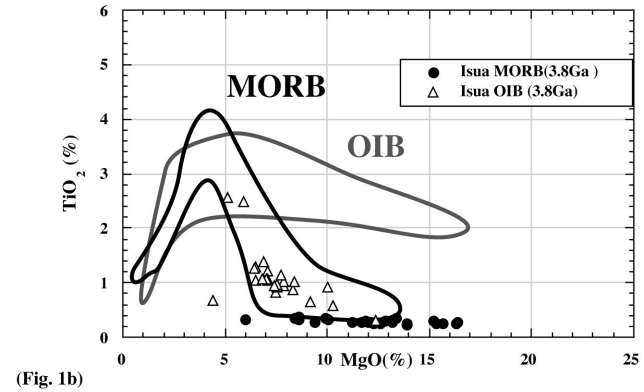


(Fig. 1b)

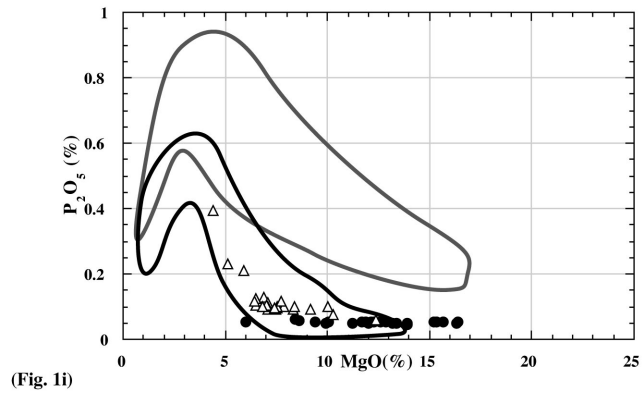


(Fig. 1i)

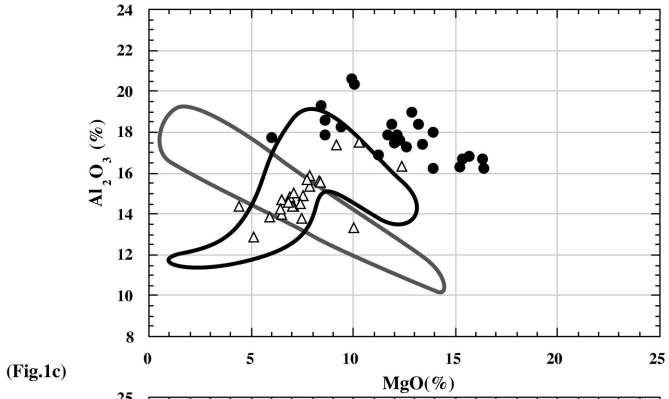


(Fig.1c)

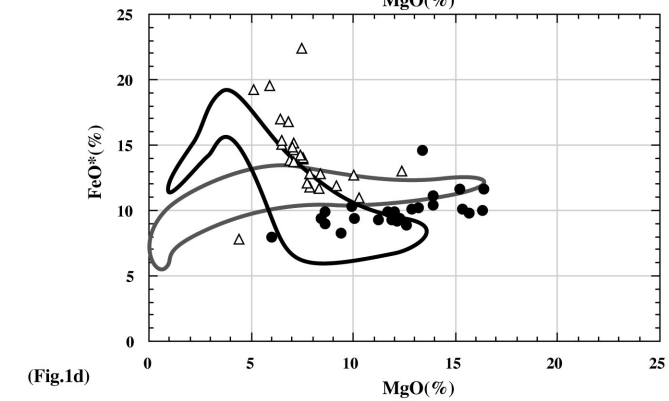


(Fig.1d)

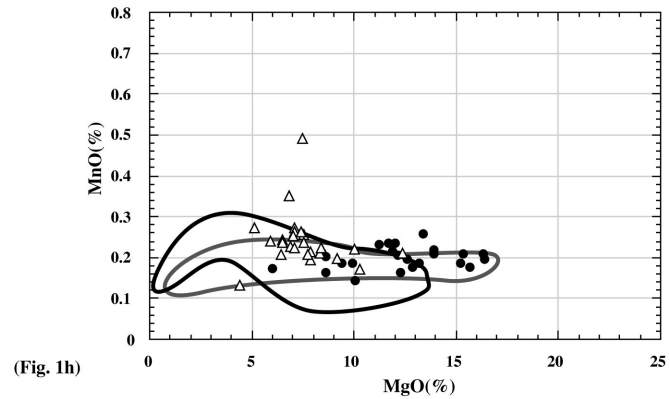


(Fig. 1h)

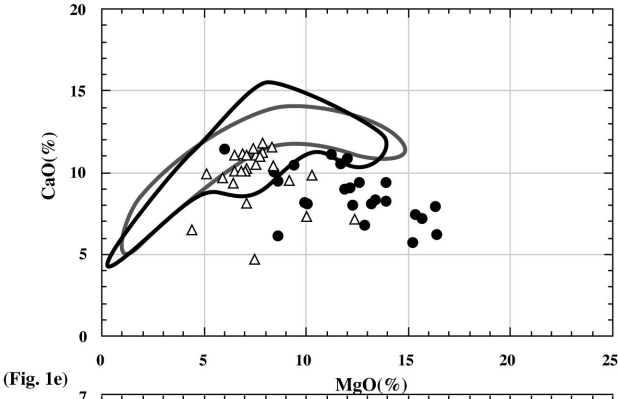


(Fig. 1e)

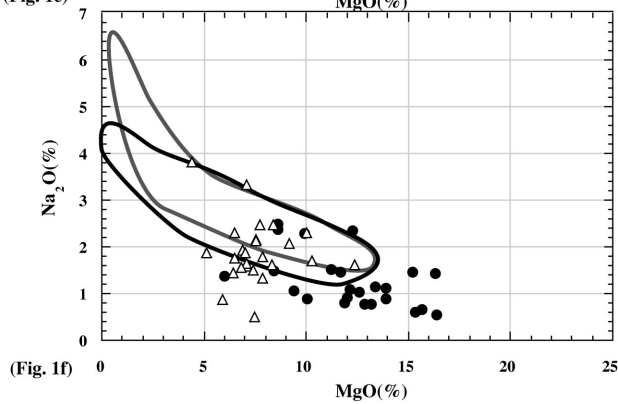


(Fig. 1f)

**Komiya 1999 Doctor Thesis Fig. III-3**

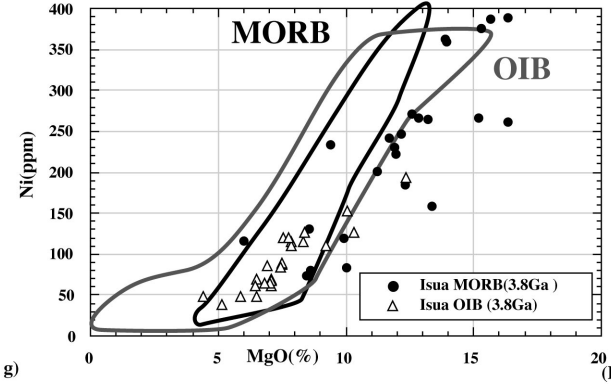


(Fig.1 g)

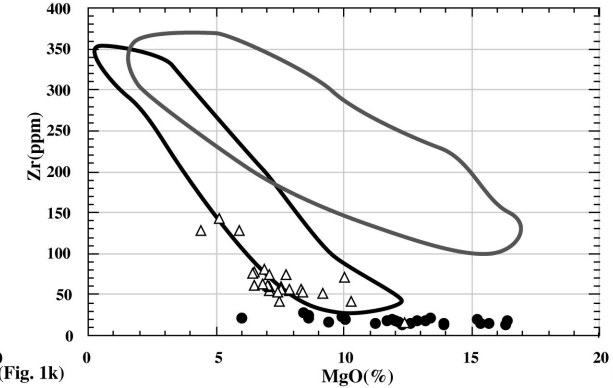


(Fig. 1k)

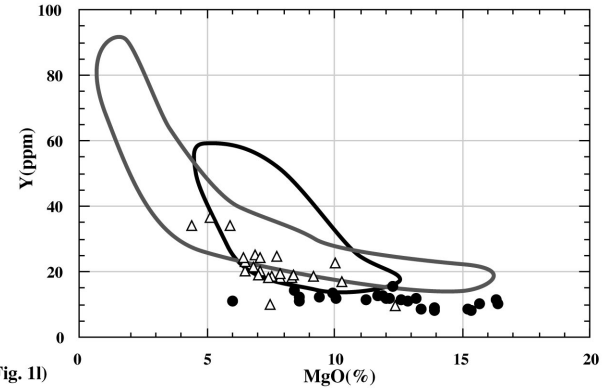


(Fig. 1l)

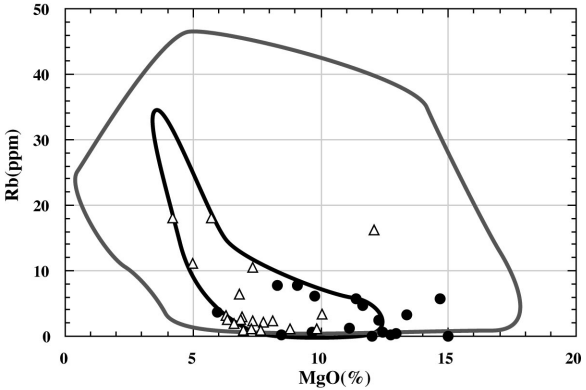


(Fig. 1j)

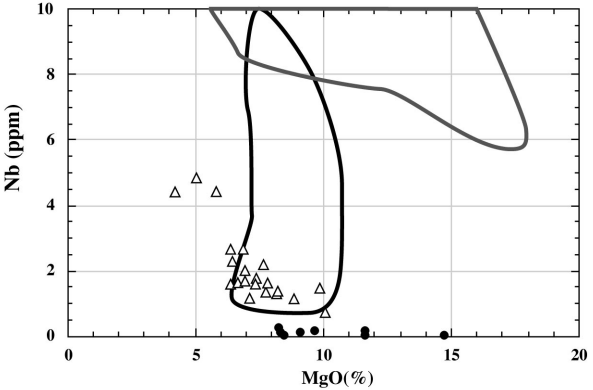


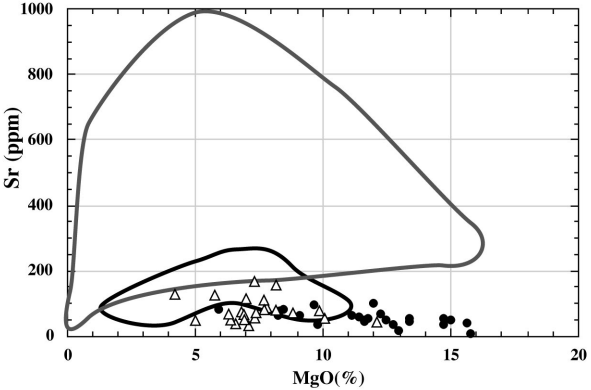


**Komiya 1999 Doctor Thesis Fig. III-4**

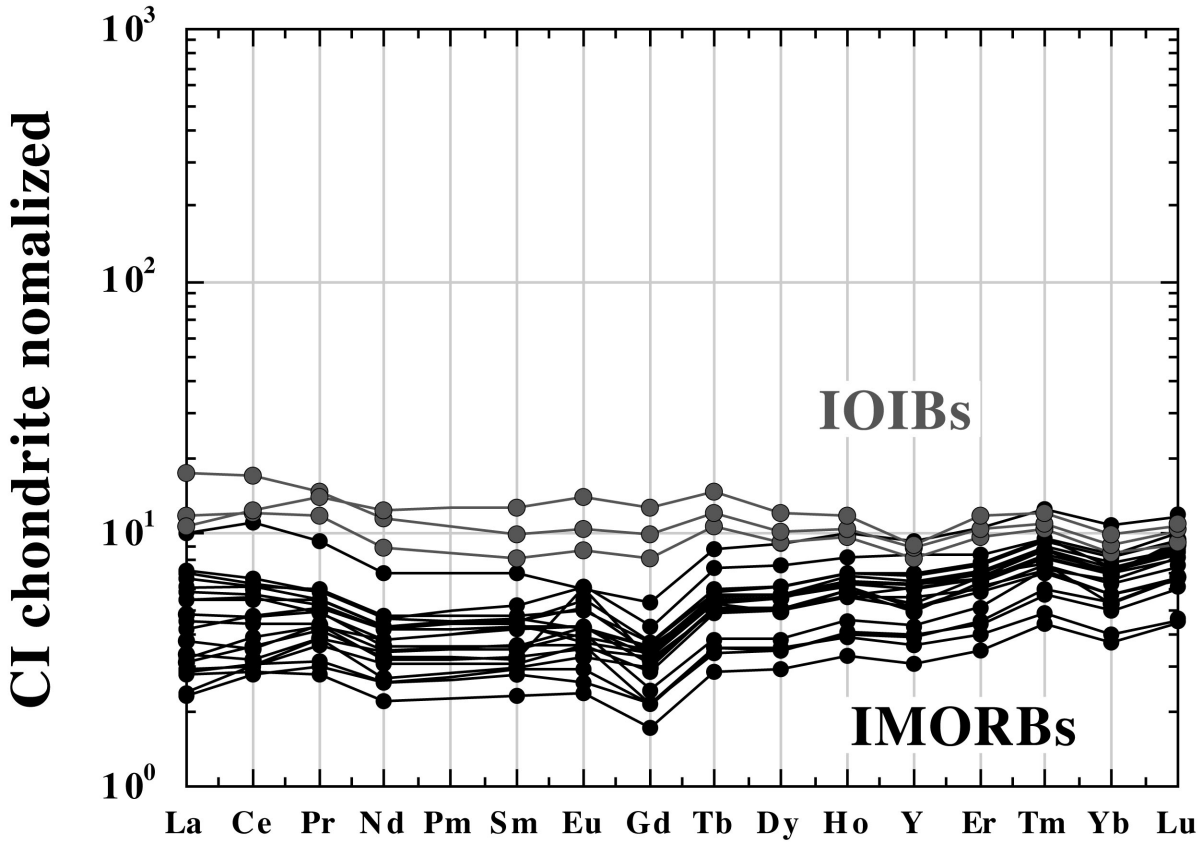


Komiya 1999 Doctor Thesis Fig. III-5

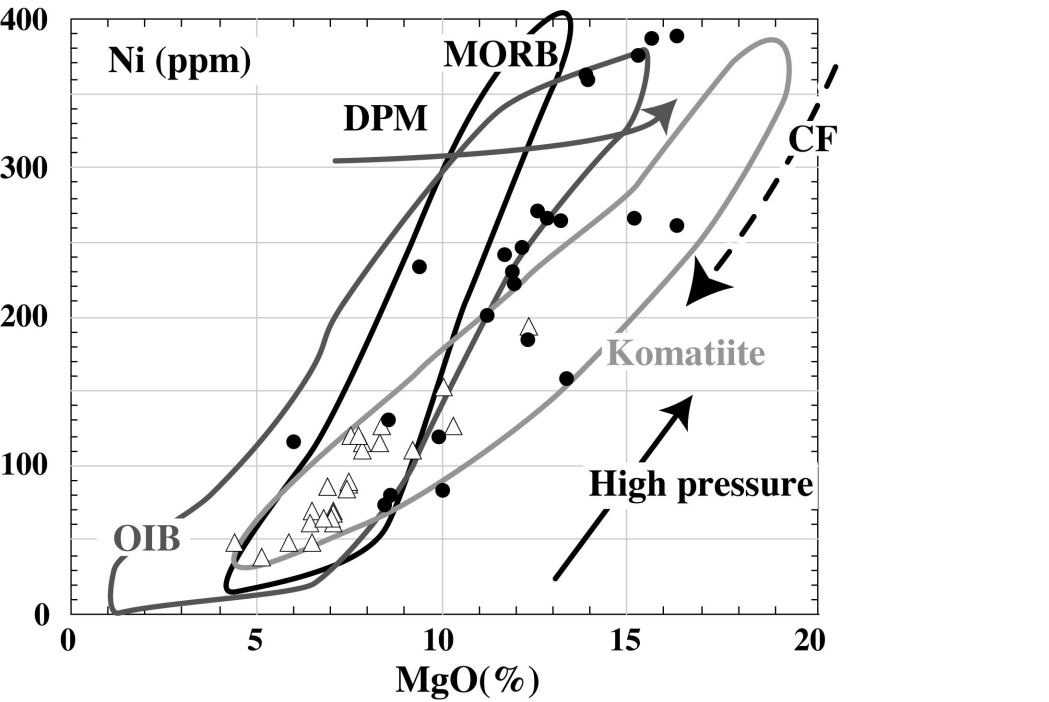


● Isua MORB(3.8Ga )
△ Isua OIB (3.8Ga)

Komiya 1999 Doctor Thesis Fig. III-6

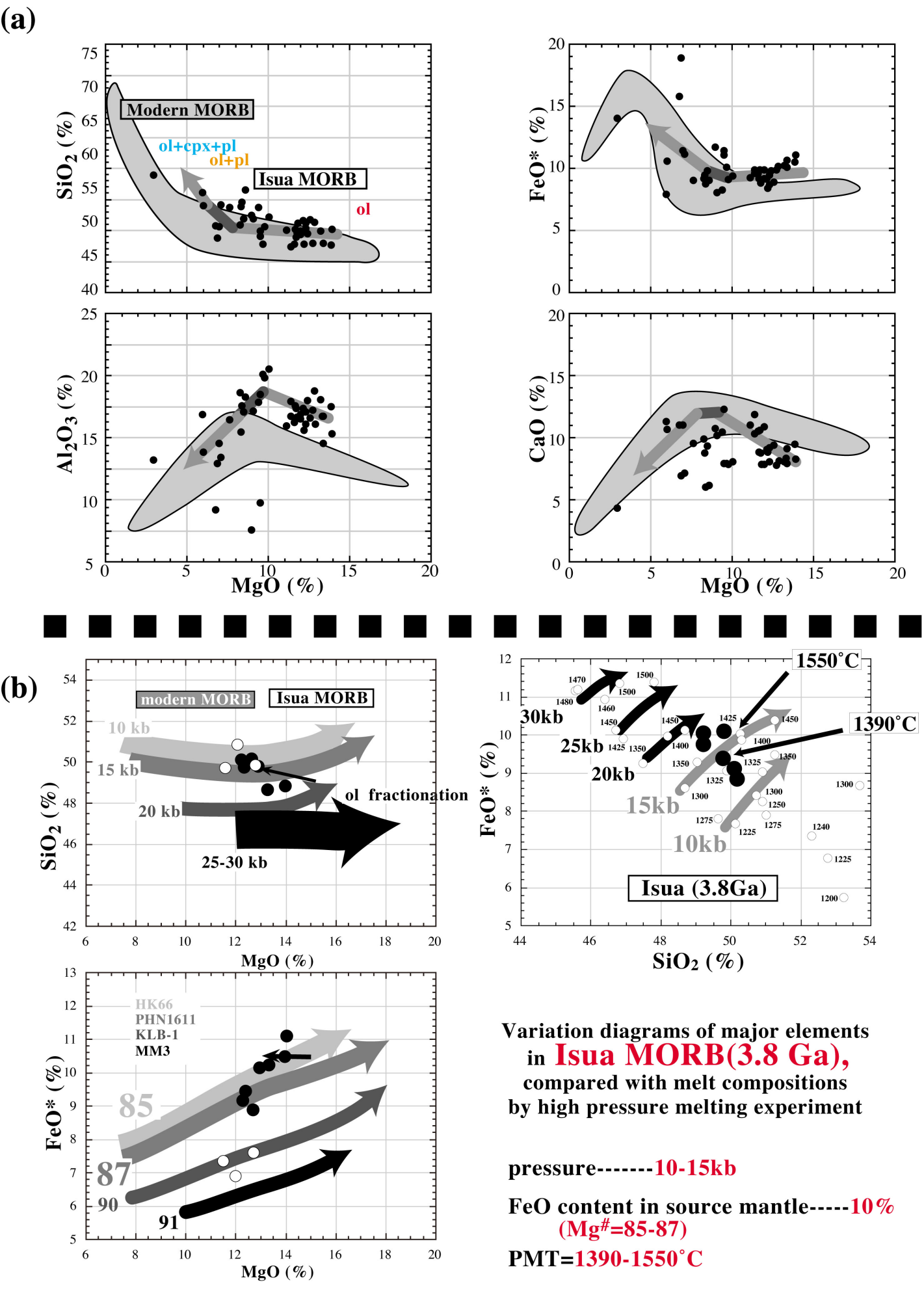


**Variation diagrams of major elements in Isua MORB(3.8 Ga), compared with melt compositions by high pressure melting experiment**

**pressure-------10-15kb**

**FeO content in source mantle-----10% ($Mg^{\#}$=85-87)**

**PMT=1390-1550˚C**

**Komiya 1999 Doctor Thesis Fig. III-7**

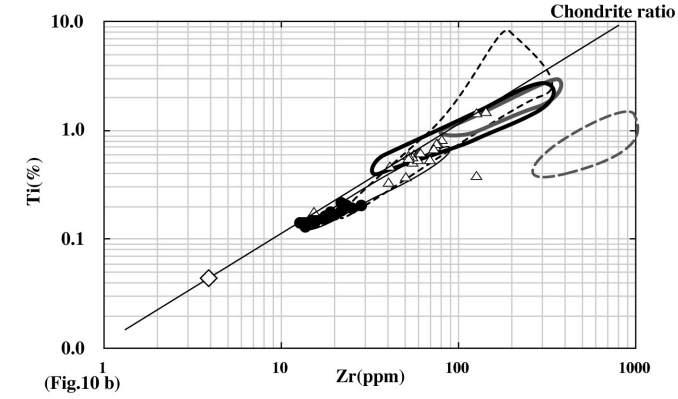


(Fig.10 b)

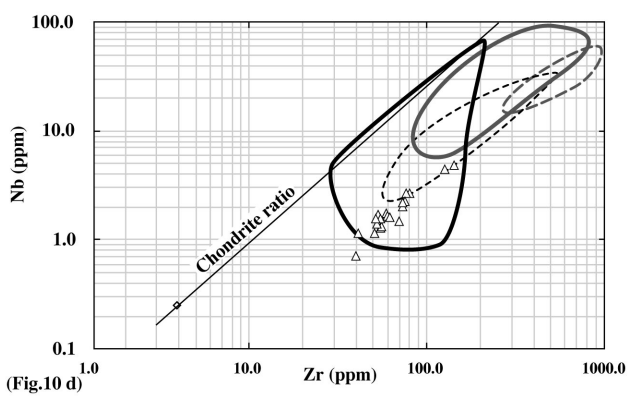


(Fig.10 d)

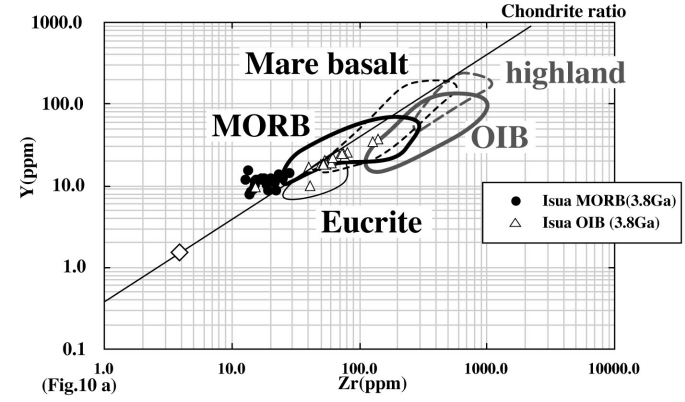


(Fig.10 a)

refractory element vs. volatile

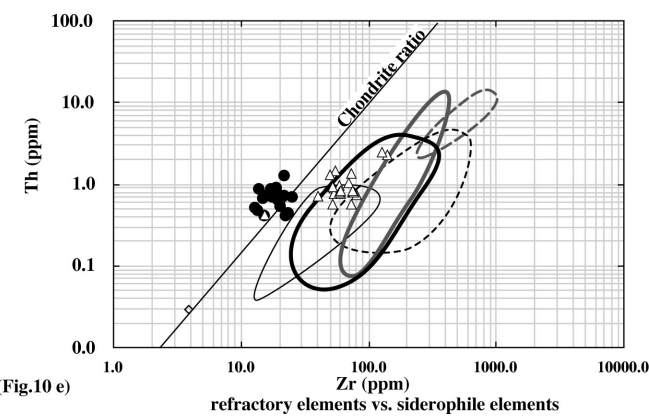


(Fig.10 e)

refractory elements vs. siderophile elements

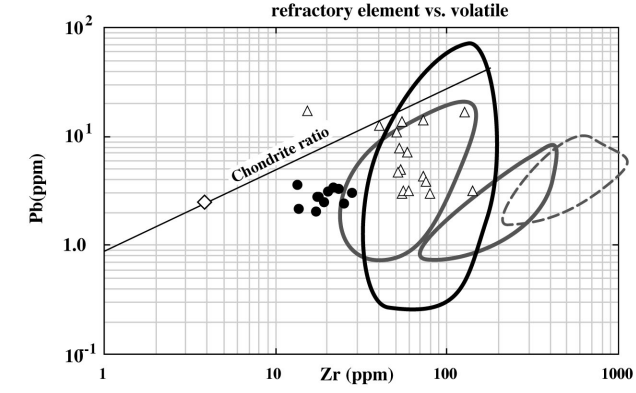


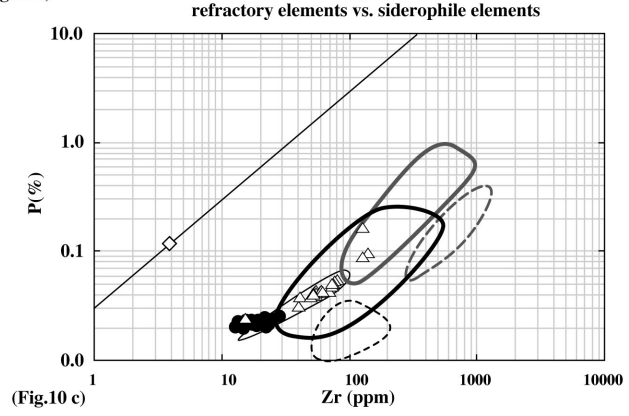


(Fig.10 c)

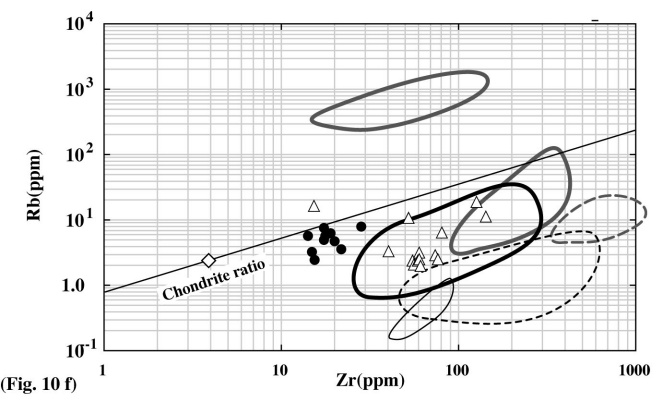


(Fig. 10 f)

refractory element vs. volatite

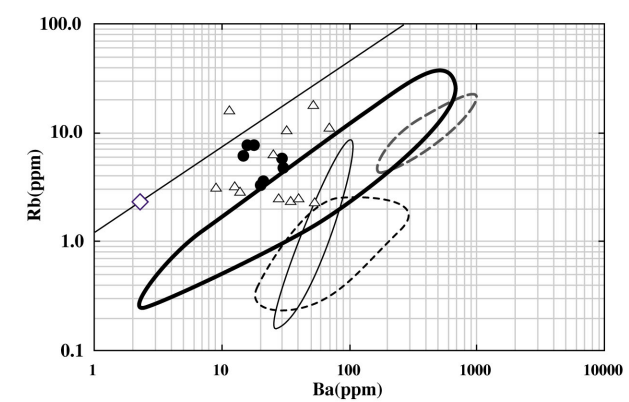


refractory element vs. volatite

**Komiya 1999 Doctor Thesis Fig. III-8**

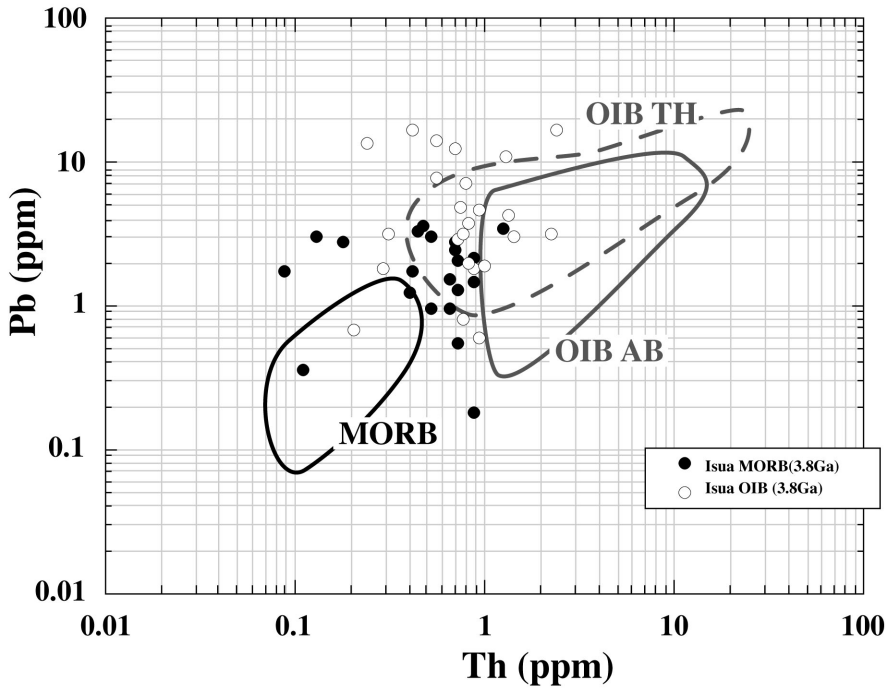


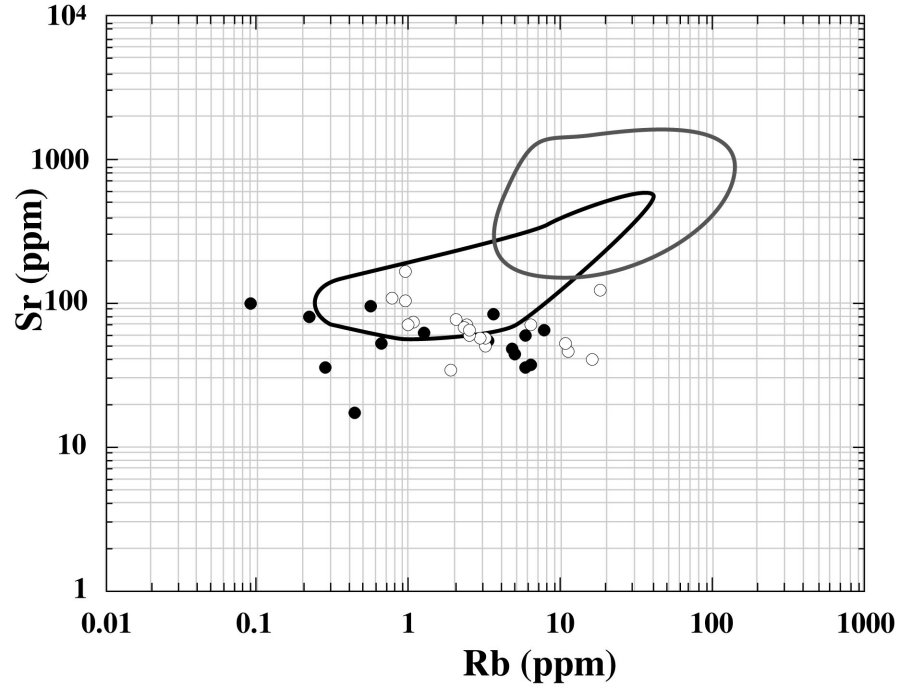


**Komiya 1999 Doctor Thesis Fig. III-9**

Table 1 Major and trace element composition of Isua MORBs

| sample | K023 | K026 | K066* | K297 | K302 | K307 | K384 | K385 | K561rim* | K562CORE | K566 | K585 | K587 | K626 | K646 | K681 | K694 | K730 | K733 | K736 | K739 | K743 | PI-MANTLE | (PILLOW) CORE | PILLOW3 | PILLOW CORE |
|---|---|---|---|---|---|---|---|---|---|---|---|---|---|---|---|---|---|---|---|---|---|---|---|---|---|---|
| $SiO_2$ | 47.25 | 49.50 | 44.63 | 46.69 | 52.75 | 46.88 | 49.20 | 48.24 | 48.73 | 50.40 | 46.95 | 48.44 | 48.72 | 48.62 | 47.43 | 45.01 | 49.01 | 48.88 | 46.77 | 46.41 | 45.01 | 47.14 | 46.82 | 50.33 | 42.99 | 54.02 |
| $TiO_2$ | 0.23 | 0.34 | 0.25 | 0.27 | 0.36 | 0.27 | 0.30 | 0.29 | 0.26 | 0.26 | 0.22 | 0.26 | 0.26 | 0.24 | 0.28 | 0.24 | 0.24 | 0.28 | 0.26 | 0.27 | 0.25 | 0.24 | 0.34 | 0.32 | 0.34 | 0.31 |
| $Al_2O_3$ | 16.05 | 18.90 | 18.32 | 15.67 | 18.03 | 17.74 | 19.81 | 18.39 | 16.92 | 17.70 | 15.58 | 17.27 | 16.74 | 17.20 | 15.76 | 16.00 | 16.85 | 18.04 | 16.98 | 17.38 | 17.34 | 16.13 | 20.05 | 17.64 | 16.83 | 17.49 |
| FeOt | 9.68 | 9.17 | 9.87 | 11.18 | 8.73 | 9.84 | 9.11 | 9.81 | 8.92 | 8.03 | 10.66 | 8.84 | 9.21 | 9.20 | 11.21 | 9.61 | 8.65 | 9.16 | 9.57 | 9.58 | 10.09 | 9.37 | 10.05 | 9.81 | 14.11 | 7.91 |
| MnO | 0.20 | 0.21 | 0.21 | 0.19 | 0.16 | 0.18 | 0.14 | 0.17 | 0.18 | 0.18 | 0.20 | 0.20 | 0.23 | 0.16 | 0.18 | 0.20 | 0.19 | 0.21 | 0.23 | 0.23 | 0.21 | 0.17 | 0.18 | 0.20 | 0.25 | 0.17 |
| MgO | 14.69 | 8.28 | 11.41 | 15.77 | 8.36 | 12.73 | 9.77 | 12.44 | 10.75 | 9.11 | 13.38 | 11.75 | 11.13 | 12.01 | 14.70 | 15.65 | 12.29 | 11.65 | 11.63 | 11.38 | 13.37 | 15.01 | 9.66 | 8.47 | 12.93 | 5.95 |
| CaO | 7.12 | 9.87 | 11.81 | 6.00 | 5.97 | 7.77 | 7.84 | 6.57 | 8.11 | 10.12 | 7.92 | 8.73 | 10.98 | 7.81 | 5.56 | 7.56 | 9.17 | 8.81 | 10.53 | 10.27 | 9.07 | 6.92 | 7.92 | 9.34 | 8.08 | 11.26 |
| $Na_2O$ | 0.57 | 1.47 | 1.06 | 0.53 | 2.42 | 0.74 | 0.87 | 0.76 | 0.82 | 1.03 | 1.06 | 1.04 | 1.49 | 2.29 | 1.41 | 1.36 | 1.02 | 0.79 | 0.88 | 1.43 | 0.87 | 0.64 | 2.24 | 2.34 | 1.12 | 1.36 |
| $K_2O$ | 0.14 | 0.26 | 0.15 | 0.03 | 0.07 | 0.10 | 0.13 | 0.06 | 0.17 | 0.20 | 0.04 | 0.02 | 0.13 | 0.07 | 0.04 | 0.06 | 0.12 | 0.15 | 0.18 | 0.18 | 0.13 | 0.04 | 0.09 | 0.13 | 0.12 | 0.17 |
| $P_2O_5$ | 0.05 | 0.06 | 0.05 | 0.05 | 0.06 | 0.05 | 0.05 | 0.05 | 0.05 | 0.05 | 0.05 | 0.05 | 0.05 | 0.05 | 0.05 | 0.05 | 0.05 | 0.05 | 0.05 | 0.05 | 0.05 | 0.05 | 0.05 | 0.06 | 0.05 | 0.05 |
| total | 95.97 | 98.06 | 97.77 | 96.37 | 96.90 | 96.31 | 97.22 | 96.78 | 94.92 | 97.07 | 96.06 | 96.62 | 98.94 | 97.63 | 96.62 | 95.74 | 97.59 | 98.03 | 97.08 | 97.17 | 96.38 | 95.73 | 97.39 | 98.63 | 96.81 | 98.69 |
| Mg# | 73.00 | 61.65 | 67.30 | 71.54 | 63.07 | 69.74 | 65.65 | 69.31 | 68.21 | 66.89 | 69.10 | 70.31 | 68.28 | 69.94 | 70.04 | 74.36 | 71.69 | 69.38 | 68.42 | 67.90 | 70.24 | 74.05 | 63.13 | 60.60 | 62.01 | 57.26 |
| Ni | 376.09 | 74.20 | 243.95 | 261.09 | 80.19 | 264.09 | 83.98 | 266.57 | 246.13 | 233.34 | 359.74 | 246.48 | 201.13 | 185.31 | 265.90 | 388.73 | 271.47 | 229.56 | 222.67 | 242.10 | 363.24 | 386.36 | 119.76 | 130.55 | 157.84 | 116.90 |
| Rb | 5.75 | 7.81 | 1.02 | - | - | 0.28 | 6.20 | 0.65 | 6.63 | 7.70 | - | - | 1.25 | 0.09 | - | - | 2.42 | 4.74 | 4.95 | 5.76 | 3.33 | 0.02 | 0.55 | 0.22 | 0.44 | 3.62 |
| Sr | 35.84 | 66.12 | 92.48 | 6.69 | 79.83 | 36.33 | 37.14 | 51.79 | 48.96 | 64.67 | 45.63 | 53.12 | 62.98 | 100.17 | 54.51 | 40.38 | 70.86 | 48.60 | 45.09 | 61.06 | 55.99 | 51.50 | 94.41 | 80.35 | 17.03 | 84.07 |
| Y | 8.34 | 14.25 | 10.69 | 10.15 | 10.98 | 11.68 | 11.99 | 10.86 | 10.16 | 12.48 | 8.01 | 11.87 | 11.40 | 15.42 | 8.79 | 11.67 | 11.67 | 12.52 | 11.84 | 12.51 | 9.15 | 10.26 | 13.61 | 12.31 | 8.78 | 10.93 |
| Zr | 14.13 | 28.05 | 16.03 | 18.64 | 21.92 | 18.66 | 19.11 | 18.87 | 16.63 | 17.26 | 13.60 | 17.14 | 15.26 | 13.40 | 19.24 | 12.65 | 15.42 | 20.15 | 17.43 | 17.83 | 14.94 | 15.21 | 23.41 | 24.92 | 22.07 | 21.69 |
| Nb | 0.04 | 0.26 | - | - | 0.12 | - | - | - | 0.00 | 0.11 | - | - | - | - | - | - | - | 0.05 | 0.16 | - | - | - | 0.17 | 0.06 | - | - |
| Ba | 6.01 | 18.04 | 4.36 | 5.83 | 25.31 | 1.67 | 14.85 | 15.27 | 15.14 | 15.92 | 10.45 | 10.51 | 15.47 | 14.41 | 9.92 | 4.83 | 6.41 | 30.31 | 2.80 | 29.74 | 20.06 | 4.87 | 23.75 | 17.28 | 5.77 | 21.01 |
| Pb | 0.36 | 3.01 | 2.11 | 0.18 | 1.30 | 0.96 | - | - | 2.45 | 2.06 | 2.16 | 1.49 | 1.25 | 3.62 | 2.48 | 0.94 | 1.75 | 3.10 | 2.83 | 2.77 | 1.57 | 0.55 | 3.32 | 2.41 | 1.72 | 3.44 |
| Th | 0.11 | 0.13 | 0.45 | 0.88 | 0.72 | 0.67 | 0.65 | 0.92 | 0.56 | 0.72 | 0.89 | 0.89 | 0.41 | 0.48 | - | 0.52 | 0.09 | 0.53 | 0.71 | 0.18 | 0.67 | 0.72 | 0.44 | 0.70 | 0.42 | 1.28 |
| La | | | 0.406 | | | | | | 0.635 | | | 0.796 | 0.750 | | | | | | 0.898 | 1.138 | | | | | 0.625 | |
| Ce | | | 1.168 | | | | | | 1.708 | | | 2.005 | 2.245 | | | | | | 2.206 | 2.912 | | | | | 2.042 | |
| Pr | | | 0.202 | | | | | | 0.271 | | | 0.355 | 0.376 | | | | | | 0.393 | 0.445 | | | | | 0.341 | |
| Nd | | | 1.060 | | | | | | 1.350 | | | 1.250 | 1.524 | | | | | | 1.478 | 1.676 | | | | | 1.762 | |
| Sm | | | 0.392 | | | | | | 0.467 | | | 0.428 | 0.458 | | | | | | 0.465 | 0.520 | | | | | 0.598 | |
| Eu | | | 0.149 | | | | | | 0.183 | | | 0.179 | 0.333 | | | | | | 0.191 | 0.227 | | | | | 0.261 | |
| Gd | | | 0.675 | | | | | | 0.754 | | | 0.271 | 0.254 | | | | | | 0.243 | 0.310 | | | | | 0.843 | |
| Tb | | | 0.154 | | | | | | 0.163 | | | 0.180 | 0.176 | | | | | | 0.189 | 0.188 | | | | | 0.170 | |
| Dy | | | 1.293 | | | | | | 1.346 | | | 1.233 | 1.235 | | | | | | 1.204 | 1.366 | | | | | 1.265 | |
| Ho | | | 0.332 | | | | | | 0.331 | | | 0.324 | 0.315 | | | | | | 0.327 | 0.353 | | | | | 0.305 | |
| Er | | | 1.126 | | | | | | 1.107 | | | 1.037 | 1.077 | | | | | | 1.106 | 1.126 | | | | | 1.021 | |
| Tm | | | 0.190 | | | | | | 0.182 | | | 0.179 | 0.178 | | | | | | 0.190 | 0.169 | | | | | 0.169 | |
| Yb | | | 1.311 | | | | | | 1.242 | | | 1.206 | 1.167 | | | | | | 1.203 | 0.901 | | | | | 1.195 | |
| Lu | | | 0.223 | | | | | | 0.206 | | | 0.220 | 0.237 | | | | | | 0.229 | 0.168 | | | | | 0.197 | |

Total iron as FeO

Table 2 Major and trace element composition of Isua MORBs, IPL series

| sample | IPL122MT | IPL018-2C2 | IPL012MN | IPL012MT | IPL012B | IPL016WR | IPL018-2C3 | IPL122R | IPL012R | IPL018-2C1 | IPL012OP | IPL021WR | IPL012C1 | IPL018-2M | IPL122C | IPL18-2C3-2 |
|---|---|---|---|---|---|---|---|---|---|---|---|---|---|---|---|---|
| $SiO_2$ | 40.0 | 47.1 | 45.3 | 43.5 | 45.8 | 43.6 | 38.2 | 42.1 | 48.7 | 38.6 | 41.1 | 41.1 | 49.1 | 44.9 | 45.7 | |
| $TiO_2$ | 0.39 | 0.31 | 0.32 | 0.29 | 0.28 | 0.32 | 0.33 | 0.32 | 0.29 | 0.32 | 0.31 | 0.31 | 0.31 | 0.30 | 0.34 | |
| $Al_2O_3$ | 21.2 | 14.5 | 15.6 | 16.3 | 11.5 | 15.8 | 15.5 | 14.4 | 12.5 | 12.9 | 13.8 | 14.6 | 17.4 | 17.6 | 17.4 | |
| FeOt | 10.2 | 9.9 | 9.8 | 11.5 | 12.0 | 9.6 | 13.0 | 11.7 | 9.1 | 13.1 | 12.1 | 10.5 | 8.2 | 11.6 | 10.6 | |
| MnO | 0.16 | 0.21 | 0.19 | 0.19 | 0.26 | 0.19 | 0.26 | 0.22 | 0.20 | 0.28 | 0.24 | 0.20 | 0.19 | 0.20 | 0.19 | |
| MgO | 10.3 | 9.3 | 8.9 | 11.2 | 10.6 | 8.9 | 12.4 | 11.1 | 7.9 | 12.3 | 11.0 | 12.1 | 7.1 | 12.1 | 10.4 | |
| CaO | 7.82 | 7.40 | 7.46 | 6.03 | 8.49 | 8.42 | 8.19 | 7.85 | 7.93 | 8.57 | 8.09 | 6.98 | 10.80 | 5.87 | 7.51 | |
| $Na_2O$ | 2.56 | 1.76 | 2.17 | 1.32 | 0.83 | 2.76 | 1.36 | 1.25 | 1.73 | 0.78 | 1.16 | 1.88 | 2.23 | 1.42 | 1.88 | |
| $K_2O$ | 0.06 | 0.08 | 0.08 | 0.05 | 0.14 | 0.11 | 0.09 | 0.09 | 0.10 | 0.10 | 0.11 | 0.46 | 0.12 | 0.04 | 0.08 | |
| $P_2O_5$ | 0.05 | 0.05 | 0.05 | 0.03 | 0.03 | 0.04 | 0.03 | 0.04 | 0.05 | 0.04 | 0.04 | 0.04 | 0.05 | 0.05 | 0.05 | |
| total | 92.7 | 90.5 | 89.9 | 90.4 | 89.8 | 89.8 | 89.2 | 89.2 | 88.5 | 87.0 | 88.1 | 88.3 | 95.6 | 94.2 | 94.2 | |
| Mg# | | | | | | | | | | | | | | | | |
| Ni | | | | | | | | | | | | | | | | |
| Rb | | | | | | | | | | | | | | | | |
| Sr | | | | | | | | | | | | | | | | |
| Y | | | | | | | | | | | | | | | | |
| Zr | | | | | | | | | | | | | | | | |
| Nb | | | | | | | | | | | | | | | | |
| Ba | | | | | | | | | | | | | | | | |
| Pb | | | | | | | | | | | | | | | | |
| Th | | | | | | | | | | | | | | | | |
| La | 2.633 | 0.742 | 1.533 | 1.540 | 0.708 | 1.017 | 1.423 | 1.715 | 1.777 | 1.168 | 0.590 | 1.414 | 1.779 | 0.592 | 0.724 | 0.826 |
| Ce | 7.531 | 1.998 | 3.972 | 4.005 | 1.993 | 3.008 | 3.772 | 4.186 | 4.334 | 3.062 | 1.983 | 3.852 | 4.333 | 1.897 | 1.959 | 2.666 |
| Pr | 0.913 | 0.345 | 0.511 | 0.514 | 0.290 | 0.458 | 0.535 | 0.578 | 0.550 | 0.426 | 0.358 | 0.476 | 0.563 | 0.291 | 0.269 | 0.421 |
| Nd | 3.593 | 1.557 | 2.108 | 2.137 | 1.252 | 2.020 | 2.220 | 2.354 | 2.248 | 1.785 | 1.699 | 1.937 | 2.318 | 1.324 | 1.135 | 1.949 |
| Sm | 1.100 | 0.469 | 0.663 | 0.666 | 0.405 | 0.653 | 0.688 | 0.713 | 0.776 | 0.567 | 0.521 | 0.651 | 0.692 | 0.454 | 0.355 | 0.662 |
| Eu | 0.352 | 0.203 | 0.222 | 0.222 | 0.138 | 0.270 | 0.216 | 0.286 | 0.338 | 0.209 | 0.226 | 0.246 | 0.318 | 0.170 | 0.136 | 0.249 |
| Gd | 1.161 | 0.450 | 0.724 | 0.735 | 0.437 | 0.676 | 0.730 | 0.773 | 0.881 | 0.616 | 0.496 | 0.709 | 0.784 | 0.456 | 0.371 | 0.651 |
| Tb | 0.328 | 0.120 | 0.198 | 0.197 | 0.118 | 0.191 | 0.203 | 0.217 | 0.254 | 0.176 | 0.131 | 0.203 | 0.215 | 0.129 | 0.104 | 0.190 |
| Dy | 2.490 | 0.897 | 1.493 | 1.500 | 0.898 | 1.449 | 1.525 | 1.659 | 1.915 | 1.355 | 0.998 | 1.532 | 1.650 | 0.955 | 0.785 | 1.393 |
| Ho | 0.590 | 0.228 | 0.364 | 0.364 | 0.223 | 0.352 | 0.368 | 0.402 | 0.449 | 0.329 | 0.252 | 0.358 | 0.403 | 0.225 | 0.190 | 0.330 |
| Er | 1.897 | 0.790 | 1.171 | 1.188 | 0.740 | 1.139 | 1.187 | 1.311 | 1.375 | 1.069 | 0.889 | 1.101 | 1.328 | 0.709 | 0.621 | 1.045 |
| Tm | 0.295 | 0.135 | 0.189 | 0.189 | 0.122 | 0.181 | 0.188 | 0.209 | 0.202 | 0.169 | 0.156 | 0.161 | 0.215 | 0.110 | 0.100 | 0.160 |
| Yb | 2.016 | 0.972 | 1.304 | 1.312 | 0.875 | 1.243 | 1.297 | 1.454 | 1.288 | 1.162 | 1.164 | 1.043 | 1.503 | 0.746 | 0.691 | 1.071 |
| Lu | 0.313 | 0.168 | 0.213 | 0.215 | 0.146 | 0.206 | 0.209 | 0.242 | 0.206 | 0.192 | 0.203 | 0.165 | 0.258 | 0.117 | 0.116 | 0.172 |

Total iron as FeO

Table 3 Major and trace element composition of altered Isua MORBs

| sample | K020 | K024 | K024MISS | K025 | K066 | K247 | K263 | K314CORE | K320 | K329 | K330 | K331 | K403 | K410 | K466 | K469 | K561rim* | K563 | K567RIM | K568CORE | K583 | K588 | K623 | K656 | K658 | K670 | K689 | K689 | K703 | K709 | K731 |
|---|---|---|---|---|---|---|---|---|---|---|---|---|---|---|---|---|---|---|---|---|---|---|---|---|---|---|---|---|---|---|---|
| $SiO_2$ | 50.3 | 47.1 | 47.4 | 52.2 | 44.6 | 52.2 | 49.3 | 56.7 | 49.9 | 52.4 | 50.9 | 49.7 | 43.9 | 42.8 | 45.8 | 36.2 | 48.7 | 46.1 | 47.6 | 49.2 | 43.2 | 47.2 | 46.8 | 48.7 | 48.6 | 48.0 | 49.4 | 49.4 | 44.2 | 46.9 | 46.7 |
| $TiO_2$ | 0.3 | 0.2 | 0.2 | 0.7 | 0.3 | 0.7 | 0.7 | 0.9 | 0.7 | 0.7 | 0.9 | 1.0 | 1.5 | 0.8 | 1.1 | 0.4 | 0.3 | 0.4 | 0.3 | 0.3 | 0.3 | 0.3 | 0.2 | 0.8 | 0.5 | 0.4 | 1.0 | 1.0 | 0.8 | 0.2 | 0.2 |
| $Al_2O_3$ | 18.7 | 16.0 | 16.0 | 14.1 | 18.3 | 15.1 | 15.6 | 14.4 | 7.2 | 14.7 | 10.0 | 10.0 | 15.6 | 14.7 | 15.2 | 18.4 | 16.9 | 22.5 | 20.5 | 20.9 | 18.2 | 17.1 | 15.6 | 11.8 | 4.8 | 18.8 | 11.3 | 11.3 | 7.8 | 13.0 | 16.5 |
| FeOt | 8.9 | 9.9 | 10.0 | 9.4 | 9.9 | 10.6 | 11.4 | 10.5 | 12.1 | 11.1 | 11.7 | 14.1 | 15.4 | 13.4 | 13.8 | 20.3 | 8.9 | 13.7 | 9.0 | 8.8 | 10.1 | 10.7 | 9.3 | 11.1 | 12.5 | 11.4 | 15.8 | 15.8 | 33.0 | 10.2 | 8.4 |
| MnO | 0.2 | 0.2 | 0.2 | 0.2 | 0.2 | 0.2 | 0.2 | 0.2 | 0.2 | 0.2 | 0.2 | 0.2 | 0.2 | 0.2 | 0.2 | 0.2 | 0.2 | 0.1 | 0.2 | 0.1 | 0.2 | 0.2 | 0.2 | 0.2 | 0.3 | 0.2 | 0.3 | 0.3 | 0.4 | 0.2 | 0.2 |
| MgO | 7.3 | 14.2 | 14.2 | 9.7 | 11.4 | 6.0 | 7.0 | 4.6 | 13.6 | 7.1 | 9.0 | 11.8 | 6.9 | 8.7 | 7.9 | 9.4 | 10.7 | 4.1 | 7.7 | 7.6 | 14.3 | 14.2 | 15.0 | 9.5 | 19.9 | 9.5 | 6.8 | 6.8 | 7.5 | 17.6 | 12.2 |
| CaO | 10.6 | 7.1 | 7.1 | 8.9 | 11.8 | 10.6 | 11.0 | 4.8 | 10.6 | 7.1 | 10.7 | 7.8 | 9.2 | 8.1 | 5.4 | 4.1 | 8.1 | 0.7 | 9.1 | 7.1 | 7.2 | 4.3 | 6.9 | 12.3 | 7.3 | 7.9 | 11.0 | 11.0 | 5.6 | 6.6 | 8.8 |
| $Na_2O$ | 1.3 | 0.5 | 0.5 | 2.5 | 1.1 | 1.9 | 2.0 | 4.7 | 0.7 | 4.5 | 2.2 | 2.8 | 0.6 | 2.2 | 2.1 | 2.2 | 0.8 | 1.9 | 2.0 | 2.1 | 1.6 | 1.0 | 1.5 | 1.8 | 0.4 | 1.4 | 2.8 | 2.8 | 0.6 | 0.6 | 2.0 |
| $K_2O$ | 0.6 | 0.1 | 0.1 | 0.3 | 0.2 | 0.5 | 0.4 | 0.1 | 0.1 | 0.1 | 0.5 | 0.1 | 0.0 | 0.1 | 0.9 | 0.1 | 0.2 | 7.3 | 0.9 | 1.3 | 0.1 | 0.2 | 0.0 | 0.3 | 0.6 | 0.1 | 0.3 | 0.3 | 0.8 | 0.0 | 0.1 |
| $P_2O_5$ | 0.1 | 0.1 | 0.0 | 0.1 | 0.0 | 0.1 | 0.1 | 0.1 | 0.1 | 0.1 | 0.1 | 0.1 | 0.1 | 0.1 | 0.1 | 0.1 | 0.0 | 0.0 | 0.1 | 0.1 | 0.0 | 0.0 | 0.0 | 0.1 | 0.1 | 0.1 | 0.1 | 0.1 | 0.1 | 0.0 | 0.1 |
| total | 98.1 | 95.3 | 95.7 | 98.1 | 97.8 | 97.8 | 97.6 | 97.0 | 95.2 | 98.0 | 96.2 | 97.6 | 93.6 | 91.0 | 92.5 | 91.4 | 94.9 | 96.8 | 97.2 | 97.4 | 95.1 | 95.1 | 95.6 | 96.4 | 95.0 | 97.7 | 98.6 | 98.6 | 100.9 | 95.4 | 95.2 |
| Mg# | 59.3 | 71.8 | 71.7 | 64.6 | 67.3 | 50.4 | 52.0 | 43.9 | 66.7 | 53.3 | 57.9 | 60.0 | 44.5 | 53.8 | 50.5 | 45.4 | 68.2 | 34.9 | 60.2 | 60.6 | 71.7 | 70.3 | 74.1 | 60.5 | 73.9 | 59.7 | 43.3 | 43.3 | 28.9 | 75.3 | 72.2 |
| Ni | 128 | 371 | 371 | 220 | 244 | 98 | 108 | 56 | 186 | 38 | 76 | 88 | 113 | 111 | 134 | 116 | 246 | 70 | 88 | 82 | 407 | 241 | 335 | 153 | 983 | 73 | 82 | 82 | 65 | 345 | 288 |
| Rb | 26.4 | 3.1 | 3.1 | 11.2 | 1.0 | 11.9 | 6.8 | 2.9 | 1.1 | 1.6 | 11.2 | 1.4 | 0.2 | 3.8 | 44.1 | 2.2 | 6.6 | 192.6 | 35.2 | 52.7 | - | 8.5 | - | 4.5 | 20.5 | 0.4 | 1.4 | 1.4 | 23.9 | 0.1 | - |
| Sr | 67 | 38 | 38 | 194 | 92 | 101 | 92 | 147 | 11 | 82 | 108 | 30 | 113 | 53 | 195 | 70 | 49 | 35 | 70 | 76 | 70 | 48 | 65 | 154 | 43 | 74 | 83 | 83 | 9 | 11 | 92 |
| Y | 12 | 9 | 9 | 13 | 11 | 17 | 20 | 12 | 16 | 15 | 14 | 19 | 30 | 16 | 20 | 5 | 10 | 6 | 10 | 11 | 11 | 11 | 9 | 16 | 10 | 13 | 18 | 18 | 15 | 13 | 12 |
| Zr | 23 | 16 | 16 | 84 | 16 | 54 | 61 | 119 | 38 | 45 | 53 | 66 | 88 | 47 | 58 | 22 | 17 | 28 | 28 | 27 | 15 | 14 | 13 | 51 | 59 | 24 | 66 | 66 | 55 | 12 | 15 |
| Nb | - | - | - | 2.2 | - | 1.4 | 1.1 | 2.5 | 0.7 | 0.7 | 1.6 | 1.6 | 2.9 | 1.3 | 1.7 | 0.7 | - | 0.5 | 0.2 | - | - | - | - | 1.4 | 1.8 | 0.2 | 1.7 | 1.7 | 1.1 | - | - |
| Ba | 18 | 5 | 5 | 136 | 4 | 26 | 16 | 6 | 10 | 17 | 51 | 13 | - | 14 | 228 | 46 | 15 | 12722 | 45 | 70 | 22 | 38 | 9 | 27 | 129 | 12 | 6 | 6 | 260 | 4 | 3 |
| Pb | 2.7 | 1.5 | 1.5 | 7.1 | 2.1 | 9.8 | 8.1 | 7.2 | 1.2 | 3.5 | 6.4 | 1.0 | 13 | 47 | 6.6 | 36.4 | 2.5 | 5.0 | 4.5 | 4.9 | 3.5 | - | 2.4 | 5.9 | 1.1 | 2.6 | 4.7 | 4.7 | 1.2 | 0.3 | 0.7 |
| Th | 0.9 | - | - | 2.1 | 0.5 | 1.6 | 1.5 | 3.5 | 0.7 | 0.7 | 0.4 | 1.0 | 0.6 | 1.1 | 0.2 | 0.9 | 0.6 | 0.9 | 0.5 | 0.8 | 0.7 | 0.2 | - | 1.4 | 0.8 | 1.0 | 0.9 | 0.9 | 0.3 | 0.2 | 0.8 |
| La | | | | | 0.406 | | | | | | | | | | | | 0.635 | | | | | | | | | | | | | | |
| Ce | | | | | 1.168 | | | | | | | | | | | | 1.708 | | | | | | | | | | | | | | |
| Pr | | | | | 0.202 | | | | | | | | | | | | 0.271 | | | | | | | | | | | | | | |
| Nd | | | | | 1.060 | | | | | | | | | | | | 1.350 | | | | | | | | | | | | | | |
| Sm | | | | | 0.392 | | | | | | | | | | | | 0.467 | | | | | | | | | | | | | | |
| Eu | | | | | 0.149 | | | | | | | | | | | | 0.183 | | | | | | | | | | | | | | |
| Gd | | | | | 0.675 | | | | | | | | | | | | 0.754 | | | | | | | | | | | | | | |
| Tb | | | | | 0.154 | | | | | | | | | | | | 0.163 | | | | | | | | | | | | | | |
| Dy | | | | | 1.293 | | | | | | | | | | | | 1.346 | | | | | | | | | | | | | | |
| Ho | | | | | 0.332 | | | | | | | | | | | | 0.331 | | | | | | | | | | | | | | |
| Er | | | | | 1.126 | | | | | | | | | | | | 1.107 | | | | | | | | | | | | | | |
| Tm | | | | | 0.190 | | | | | | | | | | | | 0.182 | | | | | | | | | | | | | | |
| Yb | | | | | 1.311 | | | | | | | | | | | | 1.242 | | | | | | | | | | | | | | |
| Lu | | | | | 0.223 | | | | | | | | | | | | 0.206 | | | | | | | | | | | | | | |

Total iron as FeO

Table 3 (Continued)

| sample | PICOREMANT | PILLOW | PILLOWACORE | PILLOWCORE2 | PILLOWCORE4 |
|---|---|---|---|---|---|
| $SiO_2$ | 52.1 | 52.0 | 47.6 | 43.9 | 56.5 |
| $TiO_2$ | 0.3 | 0.3 | 1.1 | 0.3 | 1.6 |
| $Al_2O_3$ | 16.3 | 17.1 | 14.3 | 16.2 | 14.5 |
| FeOt | 9.5 | 9.1 | 18.9 | 14.3 | 14.0 |
| MnO | 0.2 | 0.2 | 0.2 | 0.2 | 0.2 |
| MgO | 8.3 | 7.6 | 6.9 | 13.2 | 2.9 |
| CaO | 8.7 | 9.5 | 6.9 | 7.0 | 4.3 |
| $Na_2O$ | 2.0 | 2.0 | 1.4 | 0.7 | 3.5 |
| $K_2O$ | 0.1 | 0.1 | 0.3 | 0.1 | 1.3 |
| $P_2O_5$ | 0.1 | 0.1 | 0.1 | 0.0 | 0.2 |
| total | 97.6 | 98.0 | 97.6 | 96.0 | 99.0 |
| Mg# | 61.0 | 60.0 | 39.4 | 62.1 | 27.2 |
| | | | | | |
| Ni | 110 | 119 | 81 | 139 | 16 |
| Rb | 0.4 | 1.0 | 2.6 | 0.4 | 48.5 |
| Sr | 70 | 78 | 26 | 13 | 67 |
| Y | 12 | 11 | 17 | 10 | 21 |
| Zr | 24 | 22 | 61 | 23 | 243 |
| Nb | - | - | 1.9 | - | 5.3 |
| Ba | 17 | 20 | 26 | 9 | 104 |
| Pb | 2.2 | 2.1 | 1.4 | 1.5 | 3.0 |
| Th | 0.7 | 0.4 | 0.1 | 0.7 | 2.4 |
| | | | | | |
| La | | | | | |
| Ce | | | | | |
| Pr | | | | | |
| Nd | | | | | |
| Sm | | | | | |
| Eu | | | | | |
| Gd | | | | | |
| Tb | | | | | |
| Dy | | | | | |
| Ho | | | | | |
| Er | | | | | |
| Tm | | | | | |
| Yb | | | | | |
| Lu | | | | | |

Total iron as FeO

Table 4 Major and trace element composition of Isua OIBs

| samples | K001 | K004 | K048 | P065 | K076 | K155 | K166 | K179 | K181 | K285 | K345 | K409 | K421 | K425 | K428 | K430 | K457 | K458 | K461 | K464 | K470 | K508 | K579 | K636 | K672 |
|---|---|---|---|---|---|---|---|---|---|---|---|---|---|---|---|---|---|---|---|---|---|---|---|---|---|
| $SiO_2$ | 48.7 | 49.5 | 49.9 | 49.1 | 48.6 | 47.7 | 47.7 | 46.2 | 48.8 | 52.0 | 48.8 | 45.7 | 49.0 | 47.0 | 48.2 | 47.3 | 49.1 | 48.3 | 47.0 | 47.8 | 55.8 | 49.6 | 47.0 | 48.0 | 49.0 |
| $TiO_2$ | 0.8 | 0.9 | 1.0 | 1.0 | 1.4 | 0.5 | 0.3 | 2.5 | 1.0 | 0.9 | 1.2 | 2.4 | 1.0 | 0.8 | 0.9 | 0.9 | 1.0 | 1.2 | 0.6 | 1.0 | 0.6 | 1.2 | 1.0 | 0.9 | 1.1 |
| $Al_2O_3$ | 15.2 | 15.7 | 14.2 | 15.2 | 14.5 | 17.0 | 16.0 | 12.5 | 13.6 | 13.1 | 14.7 | 13.4 | 13.9 | 13.0 | 14.5 | 14.4 | 14.0 | 14.4 | 16.6 | 15.1 | 13.7 | 14.1 | 14.1 | 14.2 | 15.5 |
| FeOt | 11.4 | 11.6 | 14.4 | 12.6 | 13.5 | 10.6 | 12.7 | 18.7 | 14.6 | 12.5 | 13.4 | 18.9 | 14.7 | 21.0 | 13.6 | 13.6 | 14.5 | 15.0 | 11.3 | 12.4 | 7.5 | 16.9 | 16.3 | 14.0 | 11.9 |
| MnO | 0.2 | 0.2 | 0.3 | 0.2 | 0.2 | 0.2 | 0.2 | 0.3 | 0.2 | 0.2 | 0.2 | 0.2 | 0.3 | 0.5 | 0.2 | 0.2 | 0.2 | 0.2 | 0.2 | 0.2 | 0.1 | 0.2 | 0.3 | 0.3 | 0.2 |
| MgO | 8.2 | 7.8 | 7.0 | 7.8 | 6.8 | 10.1 | 12.1 | 5.0 | 6.3 | 9.9 | 7.0 | 5.8 | 6.9 | 7.1 | 7.4 | 7.3 | 6.9 | 6.4 | 8.8 | 8.2 | 4.2 | 6.4 | 6.6 | 7.3 | 7.7 |
| CaO | 11.3 | 11.6 | 10.1 | 11.0 | 10.9 | 9.6 | 7.0 | 9.6 | 10.8 | 7.2 | 10.8 | 9.4 | 7.9 | 4.4 | 10.2 | 10.7 | 9.8 | 9.8 | 9.1 | 10.1 | 6.2 | 9.3 | 9.8 | 11.2 | 10.8 |
| $Na_2O$ | 1.6 | 1.3 | 1.6 | 1.8 | 1.9 | 1.7 | 1.6 | 1.8 | 1.7 | 2.3 | 1.6 | 0.8 | 3.2 | 0.5 | 2.1 | 2.1 | 1.8 | 2.2 | 2.0 | 2.4 | 3.6 | 1.4 | 1.5 | 1.5 | 2.4 |
| $K_2O$ | 0.3 | 0.2 | 0.3 | 0.2 | 0.3 | 0.1 | 0.2 | 0.6 | 0.2 | 0.1 | 0.2 | 0.5 | 0.1 |  | 0.2 | 0.2 | 0.2 | 0.2 | 0.1 | 0.0 | 3.5 | 0.2 | 0.3 | 0.7 | 0.2 |
| $P_2O_5$ | 0.1 | 0.1 | 0.1 | 0.1 | 0.1 | 0.1 | 0.1 | 0.2 | 0.1 | 0.1 | 0.1 | 0.2 | 0.1 | 0.1 | 0.1 | 0.1 | 0.1 | 0.1 | 0.1 | 0.1 | 0.4 | 0.1 | 0.1 | 0.1 | 0.1 |
| total | 97.6 | 98.9 | 98.9 | 99.1 | 98.3 | 97.6 | 97.8 | 97.3 | 97.3 | 98.2 | 98.0 | 97.4 | 97.1 | 94.3 | 97.4 | 96.8 | 97.5 | 97.8 | 95.9 | 97.3 | 95.6 | 99.4 | 97.1 | 98.3 | 99.0 |
| Mg# | 56.1 | 54.4 | 46.4 | 52.4 | 47.3 | 62.8 | 62.9 | 32.4 | 43.6 | 58.6 | 48.1 | 35.2 | 45.6 | 37.6 | 49.2 | 48.9 | 45.9 | 43.1 | 58.2 | 53.9 | 50.3 | 40.4 | 42.1 | 48.3 | 53.4 |
| Ni | 115 | 115 | 61 | 109 | 85 | 127 | 192 | 37 | 47 | 153 | 68 | 47 | 68 | 87 | 119 | 88 | 64 | 68 | 109 | 125 | 47 | 60 | 64 | 84 | 120 |
| Rb | 2.4 |  | 0.8 | 2.1 | 6.4 | 3.2 | 16 | 11 | 3.1 | 1.1 | 2.9 | 18 | - | - | 2.3 | 0.9 | 2.5 | 2.5 | 1.0 | - | 18 | - | 1.9 | 10.5 | 0.9 |
| Sr | 72 | 82 | 109 | 76 | 72 | 50 | 41 | 46 | 58 | 75 | 57 | 124 | 45 | 25 | 69 | 164 | 60 | 65 | 71 | 153 | 124 | 44 | 35 | 53 | 105 |
| Y | 18 | 18 | 20 | 19 | 25 | 17 | 9.5 | 36 | 20 | 22 | 24 | 34 | 20 | 10 | 18 | 18 | 19 | 23 | 18 | 19 | 34 | 24 | 21 | 18 | 25 |
| Zr | 55 | 54 | 54 | 56 | 81 | 40 | 16 | 143 | 61 | 70 | 74 | 128 | 60 | 41 | 59 | 55 | 61 | 77 | 51 | 53 | 128 | 76 | 62 | 52 | 74 |
| Nb | 1.3 | 1.6 | 1.7 | 1.3 | 2.6 | 0.7 |  | 4.8 | 1.6 | 1.4 | 2.0 | 4.4 | 1.6 | 1.1 | 1.8 | 1.5 | 1.7 | 2.6 | 1.1 | 1.4 | 4.4 | 2.3 | 1.6 | 1.5 | 2.2 |
| Ba | 35 | 22 | 51 | 27 | 26 | 13 | 12 | 71 | 9.1 | - | 14 | 53 | 23 | 4 | 54 | 44 | 40 | 28 | 37 | 52 | 53 | 13 | 23 | 32 | 29 |
| Pb | 3.0 | 1.8 | 4.9 | 3.1 | 2.9 | 12.4 | 17.1 | 3.2 | 3.2 | 1.9 | 4.3 | 17 | 0.6 | 0.7 | 7.2 | 13 | 2.0 | 0.8 | 11 | 7.8 | 17 | 3.8 | 1.9 | 4.7 | 14 |
| Th | 1.4 | 0.9 | 0.7 | 0.3 | 0.7 | 0.7 | 0.4 | 2.3 | 0.8 | 1.0 | 1.3 | 2.4 | 0.9 | 0.2 | 0.8 | 0.2 | 0.8 | 0.8 | 1.3 | 0.6 | 2.4 | 0.8 | 0.3 | 0.9 | 0.6 |
| La |  |  |  |  |  | 2.82 |  |  |  |  |  |  |  |  |  |  |  |  | 4.17 | 2.58 |  |  |  |  |  |
| Ce |  |  |  |  |  | 7.56 |  |  |  |  |  |  |  |  |  |  |  |  | 10.7 | 7.82 |  |  |  |  |  |
| Pr |  |  |  |  |  | 1.07 |  |  |  |  |  |  |  |  |  |  |  |  | 1.36 | 1.28 |  |  |  |  |  |
| Nd |  |  |  |  |  | 4.16 |  |  |  |  |  |  |  |  |  |  |  |  | 5.35 | 5.83 |  |  |  |  |  |
| Sm |  |  |  |  |  | 1.16 |  |  |  |  |  |  |  |  |  |  |  |  | 1.43 | 1.84 |  |  |  |  |  |
| Eu |  |  |  |  |  | 0.47 |  |  |  |  |  |  |  |  |  |  |  |  | 0.57 | 0.76 |  |  |  |  |  |
| Gd |  |  |  |  |  | 0.81 |  |  |  |  |  |  |  |  |  |  |  |  | 1.01 | 1.20 |  |  |  |  |  |
| Tb |  |  |  |  |  | 0.39 |  |  |  |  |  |  |  |  |  |  |  |  | 0.43 | 0.53 |  |  |  |  |  |
| Dy |  |  |  |  |  | 2.27 |  |  |  |  |  |  |  |  |  |  |  |  | 2.53 | 2.98 |  |  |  |  |  |
| Ho |  |  |  |  |  | 0.53 |  |  |  |  |  |  |  |  |  |  |  |  | 0.57 | 0.64 |  |  |  |  |  |
| Er |  |  |  |  |  | 1.57 |  |  |  |  |  |  |  |  |  |  |  |  | 1.71 | 1.90 |  |  |  |  |  |
| Tm |  |  |  |  |  | 0.23 |  |  |  |  |  |  |  |  |  |  |  |  | 0.25 | 0.27 |  |  |  |  |  |
| Yb |  |  |  |  |  | 1.43 |  |  |  |  |  |  |  |  |  |  |  |  | 1.54 | 1.67 |  |  |  |  |  |
| Lu |  |  |  |  |  | 0.23 |  |  |  |  |  |  |  |  |  |  |  |  | 0.26 | 0.27 |  |  |  |  |  |

Table 5 Major and trace element composition of altered Isua OIBs

| samples | K047 | K070 | K158 | K173 | K176 | K178 | K189 | K265 | K378 | K420 | K422-1B | K431 | K442 | K447 | K452 | K454 | K467 | K506 | K514 | K584 | K634 | K680 | K689 | K693 | K695 | K699 |
|---|---|---|---|---|---|---|---|---|---|---|---|---|---|---|---|---|---|---|---|---|---|---|---|---|---|---|
| $SiO_2$ | 48.5 | 48.8 | 48.3 | 56.8 | 59.1 | 49.2 | 49.1 | 46.9 | 44.0 | 58.9 | 45.9 | 47.0 | 47.6 | 48.0 | 48.6 | 47.2 | 65.6 | 55.0 | 58.4 | 48.1 | 54.0 | 44.4 | 49.4 | 53.0 | 49.2 | 53.9 |
| $TiO_2$ | 1.1 | 0.9 | 0.4 | 0.8 | 0.8 | 1.0 | 1.0 | 1.9 | 0.2 | 0.4 | 0.7 | 1.0 | 1.0 | 0.6 | 0.9 | 1.2 | 0.4 | 1.0 | 0.2 | 0.6 | 0.3 | 1.1 | 1.0 | 0.4 | 1.0 | 0.6 |
| $Al_2O_3$ | 15.3 | 14.9 | 18.5 | 17.4 | 17.3 | 15.1 | 14.5 | 12.3 | 16.9 | 16.2 | 12.1 | 14.0 | 15.5 | 14.5 | 14.3 | 15.0 | 9.2 | 14.3 | 2.8 | 6.3 | 19.3 | 14.3 | 11.3 | 18.2 | 15.2 | 13.2 |
| FeOt | 12.8 | 12.2 | 10.7 | 10.6 | 8.0 | 8.9 | 13.2 | 23.2 | 10.7 | 10.3 | 29.3 | 13.8 | 12.0 | 11.8 | 13.5 | 12.5 | 19.3 | 12.5 | 8.2 | 11.9 | 6.4 | 19.0 | 15.8 | 8.0 | 12.6 | 9.5 |
| MnO | 0.2 | 0.2 | 0.2 | 0.1 | 0.1 | 0.2 | 0.2 | 0.1 | 0.3 | 0.1 | 0.4 | 0.2 | 0.2 | 0.2 | 0.2 | 0.2 | 0.5 | 0.2 | 0.3 | 0.2 | 0.1 | 0.2 | 0.3 | 0.2 | 0.2 | 0.2 |
| MgO | 7.4 | 7.7 | 9.3 | 1.6 | 3.0 | 11.2 | 7.6 | 3.5 | 12.2 | 2.1 | 7.2 | 7.7 | 7.9 | 7.9 | 7.1 | 7.1 | 1.1 | 4.7 | 4.9 | 18.6 | 6.1 | 6.7 | 6.8 | 5.6 | 7.7 | 8.1 |
| CaO | 11.2 | 11.7 | 8.1 | 5.3 | 5.0 | 8.9 | 9.7 | 4.6 | 10.6 | 3.1 | 1.4 | 5.0 | 3.3 | 10.7 | 10.8 | 11.0 | 0.9 | 7.6 | 10.4 | 10.2 | 6.8 | 10.0 | 11.0 | 11.5 | 11.1 | 8.4 |
| $Na_2O$ | 1.2 | 1.1 | 1.0 | 2.5 | 3.3 | 2.6 | 1.0 | 1.0 | 0.8 | 5.8 | 0.0 | 1.7 | 1.6 | 2.1 | 1.8 | 2.4 | 0.0 | 2.6 | 0.0 | 0.3 | 2.0 | 2.5 | 2.8 | 1.3 | 1.4 | 2.5 |
| $K_2O$ | 0.3 | 0.1 | 0.7 | 3.0 | 2.0 | 1.2 | 2.3 | 0.9 | 1.1 | 0.6 | 0.0 | 3.9 | 1.1 | 0.1 | 0.3 | 0.2 | 1.4 | 0.4 | 1.3 | 0.0 | 2.4 | 0.2 | 0.3 | 0.2 | 0.2 | 0.8 |
| $P_2O_5$ | 0.1 | 0.1 | 0.1 | 0.2 | 0.2 | 0.3 | 0.1 | 0.2 | 0.0 | 0.3 | 0.4 | 0.1 | 0.1 | 0.1 | 0.1 | 0.1 | 0.1 | 0.1 | 0.1 | 0.1 | 0.0 | 0.1 | 0.1 | 0.1 | 0.1 | 0.1 |
| total | 98.1 | 97.8 | 97.4 | 98.2 | 98.8 | 98.6 | 98.6 | 94.7 | 96.8 | 97.8 | 97.2 | 94.3 | 90.3 | 96.0 | 97.7 | 96.8 | 98.5 | 98.5 | 86.7 | 96.4 | 97.3 | 98.7 | 98.6 | 98.3 | 98.7 | 97.4 |
| Mg# | 50.8 | 52.9 | 60.7 | 20.8 | 40.2 | 69.3 | 50.5 | 21.4 | 67.1 | 26.1 | 30.5 | 49.9 | 54.0 | 54.5 | 48.4 | 50.5 | 9.2 | 40.3 | 51.8 | 73.4 | 62.6 | 38.4 | 43.3 | 55.3 | 52.3 | 60.3 |
| Ni | 109 | 97 | 82 | 36 | 38 | 65 | 82 | 26 | 363 | 1 | 25 | 94 | 114 | 92 | 71 | 110 | 17 | 52 | 343 | 793 | 231 | 97 | 82 | 59 | 104 | 96 |
| Rb | 1.7 | 0.1 | 56 | 331 | 116 | 6.2 | 96 | 47 | 37 | 49 | - | 200 | 49 | 0.5 | 3.1 | 1.4 | 84 | 11.0 | 51.0 | 0.7 | 104 | 0.6 | 1.4 | 3.8 | 3.3 | 36 |
| Sr | 174 | 68 | 48 | 177 | 328 | 84 | 126 | 44 | 43 | 84 | 3 | 133 | 79 | 131 | 139 | 96 | - | 192 | 10 | 6 | 114 | 177 | 83 | 96 | 78 | 274 |
| Y | 20 | 20 | 15 | 19 | 21 | 23 | 19 | 31 | 8 | 22 | 18 | 11 | 16 | 14 | 18 | 23 | 19 | 19 | 5 | 13 | 5 | 23 | 18 | 14 | 18 | 14 |
| Zr | 69 | 56 | 21 | 204 | 196 | 73 | 57 | 118 | 15 | 194 | 90 | 54 | 52 | 34 | 54 | 73 | 99 | 119 | 25 | 79 | 20 | 68 | 66 | 24 | 56 | 88 |
| Nb | 1.6 | 1.3 | - | 5.8 | 5.3 | 2.2 | 1.9 | 3.7 | - | 4.7 | 2.3 | 1.6 | 1.3 | 0.7 | 1.5 | 2.3 | 3.0 | 3.4 | 0.5 | 1.8 | 0.0 | 1.9 | 1.7 | 0.2 | 1.6 | 2.6 |
| Ba | 35 | 13 | 23 | 182 | 249 | 36 | 101 | 199 | 35 | 258 | - | 2233 | 76866 | 2123 | 355 | 290 | 693 | 101 | 9 | 0 | 368 | 67 | 6 | 25 | 21 | 250 |
| Pb | 8.9 | 2.0 | 13 | 21 | 13 | 8.5 | 8.8 | 3.5 | 1.0 | 5.7 | 1.1 | 4.1 | 2.8 | 5.4 | 2.2 | 11 | 2.6 | 26 | 3.4 | - | 20 | 5.0 | 4.7 | 2.0 | 3.1 | 9.2 |
| Th | 1.1 | 1.0 | 0.2 | 6.1 | 5.0 | 1.1 | 0.1 | 1.7 | 0.4 | 10.2 | 7.1 | 0.8 | 1.7 | 0.5 | 0.6 | 1.1 | 3.2 | 2.8 | 0.6 | 2.1 | 1.1 | 0.2 | 0.9 | 0.7 | 0.9 | 2.7 |
| La | | | | | | | | | | | | | | | | | | | | | | | | | | |
| Ce | | | | | | | | | | | | | | | | | | | | | | | | | | |
| Pr | | | | | | | | | | | | | | | | | | | | | | | | | | |
| Nd | | | | | | | | | | | | | | | | | | | | | | | | | | |
| Sm | | | | | | | | | | | | | | | | | | | | | | | | | | |
| Eu | | | | | | | | | | | | | | | | | | | | | | | | | | |
| Gd | | | | | | | | | | | | | | | | | | | | | | | | | | |
| Tb | | | | | | | | | | | | | | | | | | | | | | | | | | |
| Dy | | | | | | | | | | | | | | | | | | | | | | | | | | |
| Ho | | | | | | | | | | | | | | | | | | | | | | | | | | |
| Er | | | | | | | | | | | | | | | | | | | | | | | | | | |
| Tm | | | | | | | | | | | | | | | | | | | | | | | | | | |
| Yb | | | | | | | | | | | | | | | | | | | | | | | | | | |
| Lu | | | | | | | | | | | | | | | | | | | | | | | | | | |

**Total iron as FeO**

Table 6 Major and trace element composition of ultramafic rocks

| samples | K163 | K164 | K294 | K296 | K325 | K327 | K390 | K673 | K674 | K749-1 | K749-2 | K751 |
|---|---|---|---|---|---|---|---|---|---|---|---|---|
| $SiO_2$ | 43.6 | 45.1 | 32.4 | 35.7 | 44.2 | 43.2 | 38.9 | 54.5 | 48.9 | 55.4 | 47.2 | 59.9 |
| $TiO_2$ | 0.4 | 0.4 | 0.0 | 0.0 | 0.3 | 0.2 | 0.2 | 0.6 | 0.8 | 0.2 | 0.9 | 0.5 |
| $Al_2O_3$ | 4.2 | 4.6 | 2.2 | 2.7 | 14.3 | 11.4 | 1.0 | 14.1 | 12.2 | 6.4 | 13.7 | 16.5 |
| FeOt | 11.5 | 11.5 | 9.0 | 8.6 | 9.3 | 10.1 | 20.3 | 9.5 | 12.7 | 13.4 | 15.6 | 6.6 |
| MnO | 0.2 | 0.2 | 0.2 | 0.1 | 0.2 | 0.2 | 0.2 | 0.1 | 0.2 | 0.4 | 0.3 | 0.1 |
| MgO | 29.9 | 30.7 | 34.7 | 36.5 | 11.9 | 22.3 | 35.1 | 10.0 | 9.6 | 9.4 | 6.7 | 2.5 |
| CaO | 3.4 | 3.1 | 0.2 | 0.1 | 5.3 | 6.6 | 0.6 | 5.1 | 10.4 | 9.7 | 10.3 | 4.4 |
| $Na_2O$ | 0.1 | 0.1 | - | 0.0 | 3.6 | 0.3 | 0.0 | 3.6 | 0.8 | 2.6 | 1.4 | 1.5 |
| $K_2O$ | 0.0 | 0.0 | - | - | 1.9 | 0.0 | - | 0.5 | 2.2 | 0.1 | 0.4 | 4.3 |
| $P_2O_5$ | 0.1 | 0.1 | 0.0 | 0.0 | 0.1 | 0.1 | 0.0 | 0.1 | 0.1 | 0.1 | 0.1 | 0.2 |
| total | 93.3 | 95.8 | 78.7 | 83.9 | 90.9 | 94.5 | 96.4 | 98.2 | 97.8 | 97.7 | 96.6 | 96.5 |
| Mg# | 82.3 | 82.7 | 87.3 | 88.3 | 69.5 | 79.7 | 75.4 | 65.2 | 57.4 | 55.5 | 43.4 | 40.3 |
| Ni | 1539 | 1590 | 1686 | 1959 | 199 | 720 | 2821 | 123 | 216 | 70 | 68 | 57 |
| Rb | 43 | 37 | - | - | 116 | 4 | - | 239 | 103 | 37 | 27 | 97 |
| Sr | 7.2 | 7.8 | 2.5 | 2.2 | 8.6 | 7.8 | 2.1 | 13.0 | 17.6 | 3.9 | 19.1 | 13.1 |
| Y | 44 | 46 | 3.6 | 4.3 | 15 | 16 | 12 | 83 | 62 | 73 | 55 | 196 |
| Zr | 0.7 | 0.7 | - | - | - | 0.1 | - | 2.2 | 1.6 | 1.4 | 1.7 | 5.1 |
| Nb | - | - | - | - | 407 | 2.0 | - | 221 | 163 | 27 | 20 | 194 |
| Ba | 2.3 | 2.5 | - | - | 9.1 | 0.2 | 1.1 | 8.4 | 67 | 4.5 | 0.4 | 14 |
| Pb | - | - | - | - | 88 | - | - | 19 | 50 | - | 3.3 | 130 |
| Th | 0.4 | 0.7 | 0.3 | 0.3 | 0.7 | 0.3 | 0.2 | 2.6 | 1.7 | 2.3 | 0.2 | 6.5 |

**Total iron as FeO**

Table 7 Major and trace element composition of sedimentary rocks

| samples | K229A | K229B | K233 | K386 | K387 | KOMI |
|---|---|---|---|---|---|---|
| $SiO_2$ | 46.0 | 44.2 | 49.8 | 46.7 | 47.0 | 54.0 |
| $TiO_2$ | 0.3 | 0.4 | 0.4 | 0.2 | 0.4 | 1.0 |
| $Al_2O_3$ | 18.2 | 20.9 | 21.0 | 16.0 | 19.6 | 13.8 |
| FeOt | 9.1 | 13.9 | 11.2 | 9.5 | 10.9 | 12.3 |
| MnO | 0.2 | 0.1 | 0.2 | 0.2 | 0.2 | 0.2 |
| MgO | 11.0 | 4.4 | 3.8 | 15.9 | 9.6 | 4.5 |
| CaO | 11.1 | 1.4 | 2.8 | 5.8 | 7.8 | 6.4 |
| $Na_2O$ | 0.9 | 2.2 | 1.4 | 0.5 | 1.9 | 4.1 |
| $K_2O$ | 0.3 | 7.2 | 6.1 | 0.0 | 0.0 | 0.9 |
| $P_2O_5$ | 0.0 | 0.0 | 0.0 | 0.0 | 0.1 | 0.1 |
| total | 97.1 | 94.7 | 96.6 | 94.8 | 97.4 | 97.3 |
| Mg# | | | | | | |
| Ni | 232 | 65 | 78 | 369 | 71 | 52 |
| Rb | 12 | 196 | 178 | - | - | 32 |
| Sr | 58 | 39 | 63 | 19 | 50 | 168 |
| Y | 10 | 7 | 10 | 10 | 12 | 20 |
| Zr | 18 | 25 | 32 | 15 | 26 | 125 |
| Nb | - | 0.7 | 0.8 | - | 0.2 | 3.4 |
| Ba | 20 | 10721 | 9424 | 2 | 10 | 729 |
| Pb | 2.2 | 5.5 | 6.4 | 0.1 | - | 5.6 |
| Th | 0.0 | 1.0 | 0.9 | 0.7 | 0.7 | 2.9 |

Total iron as FeO

# IV. Geochemistry of 3.5 Ga MORB and OIB from the North Pole area, east Pilbara; implication for mantle heterogeneity of the mantle in the Middle Archean

*Tsuyoshi Komiya*,

Department of Earth and Planetary Sciences, Tokyo Institute of Technology, Tokyo 152-8551, Japan

*fax: +81-3-5734-3538* *e-mail: tkomiya@geo.titech.ac.jp*

# IV-1 Introduction

Archean orogenic belts are subdivided in to two groups; high grade gneiss terrain and granite-greenstone belt. The former includes the Akulleq terrane with the Isua supracrustal belt, southern West Greenland and Acasta gneiss, Slave Province, Canada. The latter includes North Pole area and Cleaverville area, Pilbara Craton, Barberton Greenstone Belt in South Africa, Belingwe Greenstone Belt in Zimbabwe and Abitibi Greenstone Belt. in Canada. Although the latter is, generally speaking, characterized by low grade metamorphism, some rocks are metamorphosed to amphibolite facies. North Pole area is a unique greenstone belt because the area is one of the oldest greenstone belts but is least metamorphosed. Therefore, not only primary magmatic structure but also primary magmatic minerals are well preserved, which allows us to study the detailed investigation of magmatic process in the Archean. Moreover, the insignificant metamorphism and very wide-spread outcrops lead to many detailed interdisciplinary works (e.g. Schopf 1994)

North Pole area is an Archean accretionary complex, which is characterized by duplex structure and oceanic plate stratigraphy. The geological evidences allow us to determine the tectonic setting of greenstones in North Pole area. The field occurrences of greenstones and the surrounding rocks indicate that two types of greenstone occur in this area; one originated from mid-ocean magmatism and another was derived from oceanic island magmatism. This work presents the brief geological review for the North Pole area as an accretionary complex, and geochemistry of two types of greenstones. This study indicates that mantle had been already heterogeneous, that the Middle Archean mantle was enriched in FeO content, and the potential temperature of the Middle Archean mantle was about 100 ˚C higher than that of the modern mantle.

# IV-2 Geological outline

### IV-2.1 Geology of the Pilbara craton

The Pilbara craton occurs in the northern part of Western Australia (Fig. 1). It is exposed over an area of 183,000 $km^2$ and has two different tectonic components. One is a granite-greenstone belt, and forms between 3.6 to 2.8 Ga. The other is volcano-sedimentary succession, Mount Bruce Supergroup, which unconformably overlies granite-greenstone belt. The granite-greenstone is exposed over the northern third of the craton, 60,000 $km^2$ between Karratha and Nullagine. The volcano-sedimentary succession of the Hamersley Basin is preserved over the southern two-thirds of the craton. Pilbara craton is bordered tectonically on the south by the 1.9 Ga Capricorn Orogen and Paterson Orogen and on the east by the Paterson Orogen, whereas on the both the north and west are hidden beneath Phanerozoic cover deposits of the Canning and Carnarvon Basins.

### IV-2.1.1 Pilbara Supergroup

All the Archean greenstones of the Pilbara were grouped by Hickman (1983) as the Pilbara Supergroup. It is subdivided into three groups: Warrawoona, Gorge Creek, and Whim Creek Groups in ascending order of stratigraphy (Hickman, 1983). Basement of the Pilbara Supergroup had been unknown. However, the new unit, the Coonterunah succession which unconformably underlies middle part of Warrawoona Group was discovered nearby the Strelley Pool Chert (Buick et al., 1995). This succession, at least 5.5 km thick, is dominated by a bimodal suite of volcanic rocks with compositional units ~1 km thick. The mafic units consist of sparsely amygdaloidal tholeiitic pillowed and massive basalt with minor magnesian basalt, komatiitic basalt (>11% MgO), and coarse-grained volcaniclastic rocks. The felsic units contain massive, highly amygdaloidal dacite with subordinate dacite porphyry and hyaloclastic rhyolite. This unconformity cuts the Coonterunah succession and granitoids of the Carlindi batholith, which intruded into the Coonterunah succession. The age of the succession is 3515.12 ± 2.7 Ma, determined by zircon U-Pb geochronology (Buick et al., 1995). These zircons were obtained from rhyolites in middle part of the Coonterunah succession.

#### Warrawoona Group

The Warrawoona Group is the lowermost part of Pilbara Supergroup. It is composed of mainly mafic rocks, minor felsic volcanics, bedded chert, and volcano-derived epiclastic sediments. The total thickness of Warrawoona Group is about 15 km. These rocks were metamorphosed under greenschist facies condition. Lipple (1975) had divided the Warrawoona Group into the following two subgroups: Talga Talga Subgroup and Salgash Subgroups. The Duffer Formation separated these subgroups. The Talga Talga Subgroup is composed of the North Star Basalt, the McPhee Formation, and the Mount Ada Basalt in upward sequence (Hickman, 1983). The Salgash Subgroup comprises Towers Formation, Apex Basalt, Panorama Formation, and Euro Basalt in ascending order. The Wyman Formation had been considered that belonged to an uppermost part of the Warrawoona Group (Hickman, 1983) However, Hickman (1990) interpreted that the Wyman Formation did not belong to the Salgash Subgroup because it locally unconformably overlay the Salgash Subgroup. Furthermore, Barley (1993) divided the Warrawoona Megasequence (previously the Warrawoona Group) into three subgsequences: Talga Talga, Duffer, and Salgash subsequences. Duffer subsequence consists of the Duffer Formation and the Panorama Formation. A study of the cherts and volcanic sediments shows that they were deposited in shallow, subaquerious environments (e.g. Barley et al., 1979; Dunlop and Buick, 1981; Lowe, 1983; Buick and Dunlop, 1990; Nijman et al., 1998).

#### Gorge Creek Group

The Gorge Creek Group, which unconformably rest on the Warrawoona Group, is composed of psammitic and pelitic rocks, ferruginous metasediments, tholeiitic pillowed

basalt, banded iron formation, ferruginous chert, shale, and acidic tuff. This group is divided into the following six formations: the Corboy Formation, Charteris Basalt, Cleaverville Formation, Honeyeater Basalt, Lalla Rookh Sandstone, and Mosquito Creek Formation. This Group has a total thickness up to 15 km. Chemical sedimentary rocks and fine-grained clastic rocks are largely restricted to the lower part of the succession. Isotopic evidence from unit immediately underlying and overlying the Gorge Creek Group indicates an age range of 3.3 – 3.0 Ga. The Upper part of this group, the Lalla Rookh Sandstone and Mosquite Creek Formation, is characterized by rift-related trough deposition or fault-bounded basin (Eriksson, 1981; Krapez, 1984). These upper sedimentary sequences, the Lalla Rookh Sandstone and Mosquite Creek Formation, are called the DeGrey Group and there unconformably overlie on the Honeyeater Basalt.

**Whim Creek Group**

The 3.0 Ga Whim Creek Group is composed of the Warambie Basalt, Mons Cupri Volcanics, and Rushall Slate. It unconformably overlies the Warrawoona Group and the Mosquito Creek Formation. It is overlain unconformably by the Mount Roe Basalt (about 2775 Ma) in the lowermost part of the Fortescue Group. Barley and others (1984) interpreted the Whim Creek Group contains a partly subaerial sequence of calc-alkaline volcanics and associated epiclastic sediments which show shallow-water and deep-water facies. The depositional environment of the Whim Creek Groups is terrestrial to marine environments within a rapidly subsiding ensialic graben or pull-apart basin (Barley, 1987).

**IV-2.1.2 Mount Bruce Super Group**

Mount Bruce Super Group occurs over the northern third of the Craton, and is also exposed in several inliers further south (e.g. Wyloo, Rocklea and Milli Milli Domes, and the Sylvania Inlier) (Fig. 1). The latter is exposed in the southern two-thirds of the craton, form outliers on the granite-greenstone terrain to the north (e.g. in Marble Bar area), and has three stratigraphic components; Fortescue Group, Hamersley Group and Turee Creek Group in chronological order (Thorne, 1990: Hickman et al., 1990).

**Fortescue Group**

The Fortescue Group has maximum thickness of 6.5 km and forms about 40 percent of the outcrop area of the Hamersley Basin. The succession consists mainly of mafic volcanics, volcaniclastic rocks, sedimentary rocks, and (platform) carbonate. Mafic and acidic intrusive igneous rocks are also in an important component locally. The Group is subdivided into six stratigraphic units; Mount Roe Basalt, Hardy Formation, Kylena Basalt, Tumbiana Formation, Maddina Basalt and Jeerinah Formation in ascending order. Detailed descriptions about those formations have been reviewed by Thorne (1990). U-Pb zircon chronological studies show that the Group were formed between ca. 2775±10 and 2684±6 Ma, felsic lava or tuff units

occurring close to the base of the Group and felsic volcaniclastic units in the upper part of the Jeerinah Formation, respectively (Thorne, 1990).

**Hamersley Group**

The Hamersley Group conformably overlies the Fortescue Group and occupied most of the remaining 60 percent of the Hamersley Basin. It has a maximum thickness of about 2.5 km and consists mainly of banded iron formation (BIF), shale, carbonate and tuff, interlayered with mafic and felsic intrusive igneous rocks. The Hamersley Group consists of eight stratigraphic units; Marra Manba Iron Formation, Wittenoom Dolomite, Mt. Sylvia Formation, Mt. McRae Shale, Brockman Iron Formation, Weeli Wolli Formation, Woongarra Volcanics and Boolgeeda Iron Formation in ascending order. Moreover, Brockman Iron Formation is subdivided into Dales Gorge Member, Whaleback Shale Member, Joffre Member, and Yandicoogina Shale Member in order of age. The Group is characterized by abundance of banded iron-formation (BIF), but intrusive and extrusive igneous rocks (both mafic and acidic rocks) also occur pervasively, over 40 percent of the Group. The geochronology of Hamersley Group had been poor-understood, and few U-Pb zircon ages were reported; 2490±20 Ma from the Dales Gorge Member, and 2470±30 Ma from Woongarra Volcanics (Compston et al. 1986). Recently SHRIMP ages, however, gave the tight constraint of the depositional and eruption ages; a tuff band in the Dales Gorge Member at 2,470±4 Ma, felsic tuffaceous sandstone in the Weeli Wolli Formation at 2449±3 Ma, and rhyolite sheet in the Woongarra Rhyolite at 2449±3 Ma (Barley et al. 1997).

**Turee Creek Group**

The Turee Creek Group conformably overlies the Hamersley Group, and consists largely of argillite and sandstone, intercalated with minor carbonate and conglomerate. It occurs in scattered localities in the southern Hamersley Basin and has a maximum thickness of nearly 5-km. There are no geochronological data from this Group.

**Wyloo Group**

The Wyloo Group, which is an arcuate belt of Proterozoic sedimentary, unconformably covers the Hamersley Group and volcanic rocks which forms the northern margin of the Capricorn Orogen. The Wyloo Group consists of seven stratigraphic units; Beasley River Quartzite, Cheela Springs Basalt, Wooly Dolomite, Mount McGrath Formation, Duck Creek Dolomite, June Hill Volcanics, and Ashburton Formation in ascending order (Thorne and Seymour, 1991). The age of the Wyloo Group is poorly known but it is thought that the Group has a probable age of approximately 2000 Ma (Gee, 1980).

**IV-2.2 Geology of the North Pole area**

### IV-2.2.1 Previous Works

The North Pole area of the East Pilbara greenstone belt is about 160 km south of Port Headland and 50 km west of Marble Bar. The area is formed a typical granite-greenstone belt, which belongs to the Warrawoona group (Hickman 1983). Bedded chert and greenstone are dominated, with minor amount of T-chert and veinlets or layers of barite. T-chert (tectonically controlled chert) is distinguished from normal sedimentary chert by lack of internal banding and its discordant relations to adjacent strata (Dunbar and Rodgers, 1961). Hickman (1973) first reported existence of T-chert in the North Pole area in Pilbara Craton. T-chert was originally considered that the chert was formed as fumarole or feeder to bedded sedimentary chert units. However, this interpretation was rejected two observation: (1) the intrusive chert is injected along fault plane which displace the sedimentary chert units; and (2) the T-chert penetrates the layered succession above the level of the highest sedimentary chert. These rocks are exposed over an area of 20 x 10 $km^2$. The thick bedded cherts, is called “chert-barite unit” because it contains large amount of barite, is the lowermost concordant sedimentary unit in the North Pole area (Hickman, 1973). The stratigraphic definition of these thick cherts in the Warrawoona Group is still controversial. Hickman (1973) had suggested that these cherts lay near the base of the Talga Talga Subgroup in the Warrawoona Group. Thereafter, Hickman (1981,1983) revised that these thick sedimentary chert and greenstones belonged to Towers Formation. Whereas, Lowe (1983) and co-workers interpreted that the Strelley Pool Chert (Towers Formation), to the north of North Pole area, was the stratigraphic equivalent of the thickest cherts in other area but North Pole was not. The thick cherts in North Pole area was arranged structurally about 10 km below the Strelley Pool Chert. Many previous workers have interpreted that origin of these thick cherts were shallow-water environment. Evidences of the shallow-water environment are roughly divided into four groups: (1) sedimentary structures of bedded cherts (e.g. laminae, ripple mark, etc.), (2) presence of evaporites (barite and carbonates), (3) size and amount of vesicles in metamorphosed, pillowed basalt, and (4) sulfur isotope data of barite (e.g. Dunlop et al., 1978; Barley et al., 1979; Walter et al., 1980; Dunlop and Buick, 1981; Nijman et al., 1998). Maruyama et al. (1991), however, suggested that these chert and barite unit have been formed in deep-sea environments, which correspond to Mid-Ocean Ridge, and that the North Pole area has been formed as a thrust-imbricated accretionary complex. The accretionary complex is composed of thrust-imbricated piles primarily pillowed basalts (500 m +) with minor sheeted dikes and the overlying bedded cherts (30 m +) with or without volcaniclastic or terrigenous sediments.

### IV-2.2.2 Geochronology

Zircon U-Pb dating yielded an age of 3459 ± 18 Ma for the North Pole Adamellite (Thorpe et al., 1992a). The age of a felsic rocks, belong to the Duffer Formation, on southern part of the area (Panorama Ridge) is 3458 ± 1.9 Ma (Thorpe et al., 1992a, b) and 3464 ± 2 Ma

(Buick et al., 1995). Pidgeon (1978) dated a felsic volcanics unit in the Duffer Formation at 3452 ± 16 Ma by the U-Pb zircon method. This age is consistent with a Rb-Sr isochron age of 3506 ± 62 for the Duffer Formation at Warrery Gap on the western side of the Corunna Downs Batholith (Cooper et al., 1982). The North Star Basalt, at the base of Warrawoona Group, yielded a 3560 ± 32 Ma Sm-Nd isochron age (Hamilton et al., 1981). Furthermore, Gruau et al. (1987) has reported Sm-Nd isochron age at 3712 ± 98 for komatiites, high-Mg basalt and tholeiites from the North Star Basalt and the Mount Ada Basalt, which are stratigraphically equivalent to the Unit I, the Unit II, and part of the Unit III as shown below. Gruau et al. (1987), however, suggested that this might be an artifact of mixing material from isotopically heterogeneous sources. A more recent U-Pb zircon method at 3449 ± 3 Ma and 3470 ± 3 Ma have been reported by Thorpe et al. (1992a) for felsic schist of Mount Ada Basalt from Pyramid Well. McNaughton et al. (1993), however, has reported that the ages from 3.24 Ga to 3.31 Ga for doleritic sill from the McPhee Formation of middle part of the Talga Talga Subgroup. These ages are younger than ages of the overlying Duffer Formation. Galena from vein barite in Unit I (chert-barite unit) gives a model age of 3490 Ma [data of Richards et al. (1981) re-calculated by Thorpe et al. (1992b)].

### IV-2.2.3 New geological interpretation of the North Pole area

This area is divided into the thrust-bounded five units: the Unit I to V in ascending order (Fig. 2). These consist of the greenstones and conformably overlying bedded cherts. These units are concentrically distributed around intruded adamellite. The Unit I, the Unit II, and the Unit III exposed all over the area except for western part. On the other hand, the Unit IV and Unit V exposed only southern part and northern part marginally. The Unit I and Unit II correspond to the lower part of Talga Talga Subgroup in Warrawoona Group (Lipple, 1975). They are considered as equivalent to the North Star Basalt (Hickman, 1983) The Unit III corresponds to the middle part of the Talga Talga Subgroup which is upper part of the North Star basalt and lower part of Mount Ada Basalt. The Unit IV corresponds to the upper part of the Mount Ada Basalt, the Duffer Formation (Hickman, 1983), and the Panorama Formation (DiMarco and Lowe, 1989a, b). Therefore, bedded cherts at the top of the unit correspond to the part of the Towers Formation. The Unit V corresponds to lowermost part of the Apex basalt (Hickman, 1983) or the Euro Basalt (DiMarco and Lowe, 1989a, b).

The Unit I is the lowermost unit in this area. This unit consists of the basaltic and doleritic greenstones, up to 2000 m, and the bedded cherts, up to 70m. Massive or pillowed basaltic flows, several to tens of meters thick, are dominated, with the minor amount of hyaloclastitic breccia in the upper part, whereas massive basaltic, doleritic or gabbroic rocks become predominate in the lower area. In this unit, pillowed basalts have low vesicularity and pillow size is smaller than those in the other units. Although rarely, these flows in the uppermost area are intercalated thin bedded cherts. Alteration trends to become severe from the lower to the upper. These greenstones are conformably covered with the bedded cherts,

which ranges in thickness from several meters to tens of meters. These bedded cherts are discontinuously distributed due to the high angle normal faults. These cherts are intercalated with numerous bedded barites. The bedded barites are ubiquitous distributed in this unit. Furthermore, veinlets of barite with or without T-chert intrude into the strongly altered greenstones. 75% T-cherts of all occur in this unit and are gathered upper part of this unit. The largest of all the T-chert dikes is 2 km long, and tens of meters wide. The T-cherts intruded into greenstones and lower part of bedded chert but neither intruded into the uppermost bedded chert nor through the bedded chert layers.

The Unit II structurally and stratigraphically overlies the Unit I. This unit is also composed of bedded, up to 40 m thick and greenstones. This unit, however, has T-cherts less than the Unit I. T-cherts intruded into only upper part of the unit. The bedded cherts contain no bedded barite. The greenstones in the Unit II are similar to those in the Unit I in field occurrences. However, total thickness of the unit (~1000 m) is less than the Unit I.

The Unit III, 1500m thick, is distinct from two units in lithology. This unit is composed predominantly of massive and pillowed lava of basalt and pyroxene spinifex-bearing komatiite, which intercalated, discontinuous, thin bedded cherts, 0.2 to 10 m thick. The pillows of greenstones trend to be larger than those in any other units. These pillowed greenstones have significant amount of vesicles in the outer margin.

The Unit IV consists of predominantly greenstones, felsic lava, and minor, thin, intercalated, bedded cherts. The lower part of this unit consists of komatiitic, high-Mg basaltic greenstones, similar to the upper part of the Unit III. The felsic lava, up to 400m thick, is restricted in top of this unit. The lava are intercalated thin bedded cherts and pillowed and massive greenstones.

The Unit V overlies the bedded cherts of the uppermost of Unit IV along thrust. This unit is similar to Unit III. Nevertheless, the total thickness is thin, only 600m, relative to the Unit III.

## IV-3 Chemistry

### IV-3.1. Sample preparation

To obtain the original magmatic composition, greenstone samples were carefully selected for the major and trace elements analyses step by step. First of all, field occurrences of greenstones and even the surrounding rocks appear to be related to the extent of the secondary alterations and the distribution of the altered zones. For example, the extensive altered zones appear at the stratigraphic top of the pillow lava flow units, or in the surroundings of large quartz veinlets such as T-chert. Such stratigraphically controlled alteration suggests a hydrothermal alteration at the formation of the magmas, accompanied with the interaction with seawater. It is suggested that the involvement of the fluid migration

from the neighboring sediments forced the composition, especially isotopic composition, disturbed during the metamorphism. Therefore, 2,500 greenstone samples elsewhere were preferentially collected, or thin massive lavas were also preferred. At the second stage, <1-cm-thick slabs were cut from each sample to select the rock samples without a visible internal fracture filled with quartz, chlorite and epidote minerals and the heterogeneous surfaces. Whole rock powders were prepared for 112 fresh samples, which contain neither veinlets of quartz, chlorite, and calcite, nor the heterogeneous domains even under the microscope. Slabs whose surfaces were polished were broken into small pieces, ultrasonically cleaned in de-ionized water and ethyl alcohol, dried, and powdered in a tungsten carbide shatter-box.

### IV-3.2. Analytical methods

Major and some trace elements (Ni, Rb, Sr, Y, Zr, Nb, Ba, Pb, and Th) were measured by X-ray fluorescence (XRF) at Tokyo Institute of Technology and at Institute of Oceanography in Tokyo University, respectively. The analytical procedure, condition and its accuracy are described by Goto and Tatsumi (1994). Rare earth elements were determined by inductively Coupled Plasma Mass Spectrometry (ICP-MS) at Tokyo Institute of Technology. The analytical procedure, condition and its accuracy are reported elsewhere (Hirata et al. 1988). Chemical compositions of minerals were determined by the electron probe microanalyzer (JEOL-JXA-8800) housed at Tokyo Institute of Technology. All analyses were performed with accelerating voltage 15 kV, 12 nA beam current and counting time 10-40 s. Oxide ZAF correction methods was employed.

### IV-3.3. Petrography

The rock samples were collected from Unit I and II (NPMORBs), and Unit III (NPOIBs) all over the map area (Fig. 2). Rocks in North Pole area were metamorphosed under from prehnite-pumpellyite through greenschist to lower amphibolite facies condition. The mode of the progressive metamorphic zonation is very distinct because of the repetition of metamorphic grade at Unit-boundary thrust, suggesting the hydrothermal metamorphism (Terabayashi & Masuda, 1996, per. comm.). On the other hand, the subsequent contact aureole is also observed within a narrow band of the surrounding of North Pole adamellite.

The mineral assemblages are defined by Pum+Cal±Prh or Ep+Pum±Prh±Cal in prehnite-pumpellyite facies Ep+Pum±Cal or Ep-Pum+Act±Cal in transition of prehnite-pumpellyite to greenschist facies, Ep+Act±Cal and Act±Cal in greenschist facies, and Hbl±Cal in lower amphibolite facies. Chlorite and albite/plagioclase pervasively occur with minor amounts of quartz, phengite, magnetite and sphene. The pervasive presence and significant amount of calcite characterize the metamorphism in North Pole area, suggesting high $fCO_2$ in metamorphic fluids. The mineral assemblage of Act+Rt+Cal in some altered

rocks in Unit I also support high $fCO_2$ in metamorphic fluids (Kitajima 1998, per. comm.). Metamorphic zonation will be discussed elsewhere (Terabayashi et al. 1998; Kitajima et al. 1998). The distinct feature of metamorphism is abundance of calcite. However, calcite-free rock samples collected for chemical analyses.

Relict minerals of clinopyroxene, and chromian spinels are well preserved in many coarse-grained rocks. However, many clinopyroxenes are overgrown by metamorphic fine-grained actinolite needles. Although olivine relict minerals are well preserved in olivine cumulate zone of a thick komatiite flow in Unit III, most olivine phenocrysts are completely altered to chlorite elsewhere.

Magmatic textures are well preserved all over the area because neither metamorphism nor deformation is significant on fabrics of greenstones. Rock samples are classified into two groups based on the magmatic texture, fine-grained and coarse-grained types, respectively. Fine-grained type includes aphyric, fine-grained plagioclase-bearing, fine-grained clinopyroxene-bearing basalts and clinopyroxene-spinifex basaltic komatiites, whereas coarse-grained type is characterized by coarse-grained plagioclase-phyric and coarse-grained clinopyroxene-phyric basalts, plagioclase-clinopyroxene-dolerite or gabbro, and quartz-plagioclase-gabbro. Minor amounts of olivine-cumulate rocks and olivine-clinopyroxene rocks samples occur in Unit III.

The aphyric basalts contain no phenocrysts, and are characterized by fine-grained chlorite, actinolite, and fibrous or acicular –plagioclase with fine-grained epidote. Those rocks occur in outer margin of pillow lavas and massive flows. However, alterations along concentric fissures within pillow lavas obliterate the primary features in some rocks.

The fine-grained plagioclase-bearing basalts have plagioclase laths or needles in the matrix of chlorite and actinolite with minor amount of small epidote grains. Plagioclase laths are up to 100 μm long, whereas needles are up to 150 μm in length. The plagioclase grains are evenly distributed, up to 20 % in volume. Although the plagioclase-bearing basalts are observed in all Units, they are distributed mainly in Unit I and II. Some forms intersertal texture with minor amount of small anhedral clinopyroxene grains.

The fine-grained clinopyroxene-bearing basalts are characterized by small equigranular clinopyroxenes, in the matrix of chlorite and actinolite with minor amount of small epidote grains. Clinopyroxene grains are subrounded to spherical, are up to 50 μm across. The clinopyroxene grains are pervasively distributed, up to 20 % in volume. Although the clinopyroxene-bearing basalts are observed in Unit II and III, they are distributed mainly in Unit III.

The clinopyroxene-spinifex basaltic komatiites have clinopyroxene-needles, tens mm in length with in the matrix of chlorite, actinolite and anhedral plagioclase with minor amount of chromian spinels. The clinopyroxene-bearing basaltic komatiites occur in three localities. A minor thin basaltic komatiite flow, 5 m thick and 50 m long, occurs accompanied with pillowed basalt and gabbroic rocks in Unit II. Although it has spinifex sequence of chilled margin, randomly-oriented small clinopyroxene spinifex and randomly-oriented large

clinopyroxene spinifex in descending order, neither olivine-cumulate nor gabbroic zone is involved. Thick major basaltic komatiite flow, ca. 100 m thick and over 15 km long, overlies the thick-bedded chert of Unit II. Thin-bedded chert, 5 m thick, covers the basaltic flow. It is characterized by the distinctive magmatic layering. Basal chilled margin (tens cm thick), cumulate zone (ca. 80 m thick), clinopyroxene-spinifex zone (ca. 10 m thick), and columnar-jointed zone (2 m thick), and upper chilled margin (tens cm thick) in ascending order. Cumulate zone range from olivine-dominated in the bottom, through olivine-clinopyroxene-phyric to clinopyroxene-plagioclase phyric in the upper area. Olivines are euhedral to slightly elongate, accompanied with minor amount of euhedral chromian spinels and inter-granular anhedral or oikocrystic clinopyroxenes. Clinopyroxene grains in olivine-clinopyroxene-phyric pyroxenite or clinopyroxene-plagioclase-phyric gabbro is large and subhedral to euhedral. Clinopyroxene spinifex is oriented-grown normal to flow plane at lower half of the spinifex zone. The spinifex clinopyroxenes are over one meter long. On the other hand, randomly-oriented clinopyroxene spinifex predominates in upper half of spinifex zone. The size of spinifex grains ranges from less than one mm in upper part to over 5 cm in lower part, with scattering of grain size at the same stratigraphic level. A minor thin basaltic komatiite flow, 10 m thick and 50 m long, occurs accompanied with pillowed basalt and pillow breccias in Unit III. It is dominated by the randomly-oriented clinopyroxene spinifex with thin topmost chilled margin, 10 cm thick.

The coarse-grained plagioclase-phyric basalts contain relatively large plagioclase laths and euhedral columns in the matrix of chlorite and actinolite with minor epidote. The size of plagioclase grains range from 150 μm to 3 mm in length. The volume of plagioclase varies from 20 % to 75 %. Although the plagioclase-phyric basalts are observed in all Units, they are distributed mainly in Unit I and II.

The coarse-grained clinopyroxene-phyric basalts contain relatively large equigranular clinopyroxenes, in the matrix of chlorite and actinolite with minor amount of small epidote grains. Clinopyroxene grains are subrounded to spherical, and range from 50 μm to 200 μm across. The clinopyroxene grains are pervasively distributed, 20 to 60 % in volume. The clinopyroxene-phyric basalts are observed in Unit II and III. Although they are distributed mainly in Unit III, they occur as thick pile of 10-m thick clinopyroxene-phyric basaltic flows near a large gabbroic body in southern Unit II.

The plagioclase-clinopyroxene dolerite or gabbro forms ophitic to subophitic texture. Plagioclase laths vary from 200 μm to 3 mm in size, wrapped within large oikocrystic clinopyroxenes with minor amount of magnetite and matrix chlorite. Minor large brown hornblendes are also interspersed in the matrix. The brown hornblendes are euhedral and overgrown by bluish-green actinolite. Large euhedral magnetite grains are also pervasive.

The quartz-plagioclase-gabbro contains euhedral plagioclase, euhedral angular quartz in the matrix of chlorite, actinolite and magnetite. Because quartz grains are angular and euhedral, they are presumed to be primary. However, no late stage crystallization phases such as pigeonite and orthopyroxene are preserved, possibly due to metamorphism and/or

alteration.

## IV-4 Results

### IV-4.1 Major and minor element chemistry of relict pyroxene crystals in NPMORBs and NPOIBs

Clinopyroxenes in NPMORBs include large equigranular clinopyroxenes in clinopyroxene-phyric basalts, and large oikocrystic clinopyroxenes in plagioclase-clinopyroxene gabbro. Clinopyroxenes in NPOIBs include large equigranular clinopyroxenes in clinopyroxene-phyric basalts and large clinopyroxene oikocrysts enclosing euhedral olivines in olivine-clinopyroxene cumulate in a thick komatiites flow.

Pyroxenes in NPMORBs and NPOIBs are defined as augite or ferroaugite, and are distributed within the variation of clinopyroxenes in modern MORBs (Fig. 3). Many pyroxenes have compositionally normal zoning within the outer rim. The estimated minimum temperature of clinopyroxene saturation is ca. 1250 ˚C or 1200 ˚C for NPMORBs or NPOIBs, respectively. Clinopyroxenes in NPOIBs are similar to those of tholeiitic OIBs.

Figure 4 shows the compositional differences between relict clinopyroxenes in NPMORBs and NPOIBs in major and minor elements. Clinopyroxenes in NPMORBs are subdivided into two types based on their composition; high-Ti group and low-Ti group. All large oikocrystic clinopyroxenes in plagioclase-clinopyroxene gabbro belong to low-Ti group, whereas large equigranular clinopyroxenes in clinopyroxene-phyric basalts belong to both types. However, no samples contain both groups of clinopyroxenes. Clinopyroxenes in NPOIBs belong to moderate-Ti group.

The clinopyroxenes of OIBs are enriched in $Na_2O$, CaO, and $TiO_2$, but depleted in $Al_2O_3$ at the given $SiO_2$, relative to those of low-Ti group of MORBs. On the other hand, the clinopyroxenes of OIBs are enriched in $Na_2O$ and CaO, depleted in $TiO_2$, and equivalent in Al at the given $SiO_2$ relative to those of high-Ti group of MORBs. Clinopyroxenes in NPOIBs are enriched in jadeite and Ca-tschermak molecule relative to those in NPMORBs. Clinopyroxenes of Low-Ti group in NPMORBs have higher Al and lower Ti contents at a given Si content, and lower jadeite component, relative to those of modern MORBs. Clinopyroxenes of high-Ti group also have higher Al and Ti contents at a given Si content, and lower jadeite component, relative to those of modern MORBs (Fig. 5).

### IV-4.2 Major and trace element chemistry in NPMORBs and NPOIBs

Figures 6 and 7 show the MgO versus major and trace element diagrams of both MORBs and OIBs for North Pole area, along with the modern MORBs and OIBs. The latter includes both alkaline basalts and tholeiites. NPMORBs and NPOIBs are defined as low-K tholeiite affinities. Both NPMORBs and NPOIBs include fine-grained basaltic and doleritic

rocks. Chondrite-normalized REE abundances are shown in Figure 8. Despite of minor scattering in especially CaO and $Na_2O$ content, both fine-grained NPMORBs (NPMORBs-I) and NPOIBs (NPOIBs-I) make clear liquid lines of descent.

NPMORBs-I has lower $Al_2O_3$ than the modern MORBs at high MgO contents (> 10 wt %). NPMORBs-I has lower $TiO_2$ and $P_2O_5$ than the modern MORBs at low MgO contents (< 7 wt %). It also has lower Zr and Y at any give MgO content (especially low MgO), and higher FeO* and MnO at high MgO content (> 10 wt %) relative to the modern MORBs. $SiO_2$, CaO, Ni, Sr, and $Na_2O$ contents of NPMORBs-I are similar to those of the modern MORBs. They have a slightly light and middle REE-depleted pattern. The pattern of the liquid line of descent of the NPMORBs-I is similar to that of the modern MORBs.

NPOIBs-I appears to be more dispersed than MORB-I. However, the former has lower CaO and slightly higher $Al_2O_3$ at moderate MgO content. Moreover, the former is enriched $SiO_2$, $Na_2O$, $P_2O_5$, Zr, Y, and Nb, whereas depleted in Ni. Concentrations of $Al_2O_3$, FeO, MnO, and CaO in NPOIBs-I are equivalent to those of NPMORBs-I at high MgO content. The pattern of the liquid line of descent of the NPOIBs is similar to that of the modern MORBs, rather than that of the modern OIBs. They have slightly LREE-enriched pattern.

Coarse-grained samples are relatively scattered relative to fine-grained samples (Fig. 6, and 7). Although many samples are distributed around the liquid line of descent defined by fine-grained samples, some are plotted off. Clinopyroxene-phyric dolerite/gabbro has relatively lower $Al_2O_3$, less than 10 wt %, and higher CaO at high MgO content, whereas plagioclase-phyric dolerite/gabbro has relatively higher $Al_2O_3$, $Na_2O$ and Sr, and lower $TiO_2$, FeO*, $P_2O_5$ and Y content at low MgO content. Plagioclase-clinopyroxene-dolerite/gabbro is bimodal on MgO contents, more than 10 wt % or less than 5 wt %. High MgO dolerite/gabbro appears to be plotted on the liquid line of descent.

For both NPMORBs-I and NPOIBs-I, samples with higher MgO contents (> 8 wt %) plot roughly along olivine fractionation curves accompanied with minor plagioclase on the MgO variation diagrams, as follows: with decreasing MgO, $TiO_2$, $Al_2O_3$, CaO $Na_2O$, $K_2O$, $P_2O_5$, and incompatible trace element, including Sr, contents and $Al_2O_3$/CaO ratios increase; $SiO_2$, FeO* and MnO contents remain almost constant; Ni concentrations decrease. These correlations suggest that the chemical variations of NPMORBs-I and NPOIBs-I at higher MgO contents are mainly controlled by olivine fractionation, and plagioclase plays a minor role. Clinopyroxene fractionation is still more insignificant. Plagioclase and then clinopyroxene join olivine on the liquidus at ca. 8 wt % in MgO because the slope of the liquid lines of descent increase change abruptly, $Al_2O_3$ and CaO decrease substantially with decreasing MgO (Klein & Langmuir 1987).

## IV-5 Discussions

## IV-5.1 The estimate of the influence of secondary alteration on whole rock chemistry based on clinopyroxene composition

Petrographic observation and major element chemistry indicate that clinopyroxenes are saturated just after plagioclase in NPMORBs. Plagioclase-join lead to abruptly changing the slop of liquid line of descent. During olivine fractionation, on a plot of MgO versus $Al_2O_3$, $Al_2O_3$ increases with decreasing MgO; when plagioclase joins olivine on the liquidus, however, the slop of the liquid line eof descent changes abruptly and $Al_2O_3$ decreases substantially with decreasing MgO. On the other hand, on a plot of MgO versus $TiO_2$, $TiO_2$ increases slightly with decreasing MgO; in plagioclase crystallizing, however, the slop of the liquid line of descent changes abruptly and $TiO_2$ increases substantially with decreasing MgO. Thus, precise MgO content where plagioclase joins olivine on the liquidus can be estimated from the mode of the liquid line of descent. Moreover, substantial increase of $TiO_2$ content on $Mg^{\#}$ versus $TiO_2$ diagram allows us to estimate the precise partition coefficient, defined by $Kd^{FeO-MgO}=(Fe^{2+}/Mg^{2+})^{cpx}/(Fe^{2+}/Mg^{2+})^{liq}$.

Figure 9a shows $Mg^{\#}$ value versus $Al_2O_3$ content in NPMORBs-I, indicating that plagioclase joins olivine at 60 in Mg#, equivalent to 8.5 wt % in MgO. Figure 9b shows Mg# value versus $TiO_2$ content in NPMORBs-I and the calculated melt equilibrated with clinopyroxene phenocrysts. The melt composition is calculated using the partition coefficient, $Kd^{FeO-MgO} = 0.26$ for $Mg^{\#}$ (Sisson & Grove 1993, Tormey et al. 1987) and $D_{Ti} = 0.20$ for Ti content (Green 1994), respectively. Despite of slight dispersion due to less accuracy of microprobe analyses, the calculated compositions are plotted on the liquid line of descent defined by NPMORBs-I. If $TiO_2$ content remained during metamorphism because $TiO_2$ empirically is regarded as immobile element, Figure 9b indicates that secondary alteration play insignificant role on $Mg^{\#}$ value.

Figures 9c and 9d show the composition of the clinopyroxenes phenocrysts and host clinopyroxene-bearing samples. Because the host samples defined as clinopyroxene-phyric basalts with large equigranular pyroxenes or plagioclase-clinopyroxene-gabbro, whole rock composition do not directly reflect the magmatic composition. Therefore, partition coefficient of Ti is relatively high. Despite of compositional variation of clinopyroxenes within one sample, calculated partition coefficient of Mg and Fe between clinopyroxene and whole rocks are distributed within the range calculated from the modern MORB and the included clinopyroxenes.

## IV-5.2 The differences of composition of clinopyroxenes in NPMORBs and NPOIBs

Both the compositions of clinopyroxenes in NPMORBs and NPOIBs are similar to those in MORBs and tholeiitic OIBs (Fig. 5). However, some differences are also between clinopyroxenes in NPMORBs and NPOIBs, and those in MORBs. Clinopyroxenes in NPMORBs have lower wollastonite component, compared with those in modern MORBs.

The estimated minimum temperature of clinopyroxene saturation is ca. 1250 ˚C for NPMORBs (Lindsley 1983), indicating early saturation of clinopyroxene for NPMORBs. Relatively lower concentration of Ti and Na in clinopyroxenes of NPMORBs is consistent to the bulk composition of NPMORBs.

Some compositional differences are also between the clinopyroxenes in NPMORBs and those in NPOIBs. The clinopyroxenes of NPOIBs are enriched in $Na_2O$, CaO, and $TiO_2$, but depleted in $Al_2O_3$ at the given $SiO_2$, relative to those of NPMORBs. The estimated minimum temperature of clinopyroxene saturation is ca. 1250 ˚C for NPMORBs and 1200 ˚C for NPOIBs (Lindsley 1983). In varying the degree, these differences are similar to the differences between the clinopyroxenes in modern MORBs and modern OIBs (or alkali OIBs) (Maruyama 1976; Nisbet & Pearce 1977). Ca content in clinopyroxenes depends on temperature (Lindsley 1983), pressure, $SiO_2$ activity (Davidson & Lindsley 1994), water content (Gaetani et al. 1993; Parman et al. 1997). But pressure dependence is relatively insignificant at less than 5 kb. The difference in $SiO_2$ activities of NPMORBs and NPOIBs also makes a minor contribution to the difference of Ca content in clinopyroxenes because $SiO_2$ content is similar each other. Water content is supposed to plays a significant role on higher wollastonite component in clinopyroxenes. Higher water content in melt breaks Si-O chains in the silicates to increase $SiO_2$ activity (Kushiro 1975). Moreover, high water content changes appearance temperature of the silicate phases to varying degrees. Especially, the liquidus volume of plagioclase shrinks to delay plagioclase-saturation, relative to other phases such as olivine and clinopyroxene. The late fractionation of plagioclase leads to higher $Al_2O_3$ in clinopyroxene and magmas at moderate MgO content. The relative location of the refraction of liquid line of descent of NPMORBs and NPOIBs on MgO versus $Al_2O_3$ and CaO diagrams due to plagioclase-join is consistent to the later fractionation of plagioclase in NPOIBs. Figure 10 shows the ternary diagrams of cpx-pl-ol and cpx-pl-qz (Tormey et al. 1987; Grove et al. 1992; Gaetani et al. 1993; Sisson & Grove 1993). Both figures indicate that NPMORBs crystallized under the low-pressure anhydrous condition, whereas NPOIBs under the relative high-pressure hydrous condition. The compositional difference between NPMORBs and NPOIBs causes high $Al_2O_3$ content of clinopyroxenes in some flows of NPMORBs than that in NPOIBs (Fig. 11)

Although higher $Na_2O$ content or jadeite component of clinopyroxenes in OIBs is caused by compositional differences of magmas, OIBs presumably crystallized at higher level because of insignificant difference of $Na_2O$ content in NPOIBs from that in NPMORBs. Figure 4 shows the mode of coupling substitution of minor elements. The plots of $Na+{}^{IV}Al$ against ${}^{VI}Al+2Ti+Cr$ elucidate the oxidation state of these elements. If all the Fe in pyroxenes were $Fe^{2+}$, and Ti and Cr were in the 4+ and 3+ states, respectively the data would be plot on the 45 ˚ line on such diagrams. Chemical data for pyroxenes from NPOIBs plot on or towards the $Na+{}^{IV}Al$ axis, indicating moderate $Fe^{3+}$ in these pyroxenes. In contrast, pyroxenes from NPMORBs plot on the other side of the 45 ˚ line, towards ${}^{VI}Al+2Ti+Cr$ which indicates the presence of $Ti^{3+}$ and/or $Cr^{2+}$, and reflects the lower oxygen fugacity. However, ${}^{VI}Al+2Ti+Cr$ in

pyroxenes from NPMORBs appear to be extreme low. Such extreme high concentration in $^{VI}$Al+2Ti+Cr reported in some meteorites, such as Stannern and Nuevo Laredo (BVSP 1981). Some pyroxenes in NPMORBs have extremely high abundance of $TiO_2$, up to 4.72 wt %. Moreover, some pyroxenes of them include “exsolution grain” of a Ti phase. Further investigation is required for determining the origin of high Ti content in some pyroxenes.

### IV-5.3 Estimate of FeO content of and pressure and temperature of partial melting of the source mantle of the NPMORBs

#### IV-5.3.1 $Mg^{\#}$ of source mantle of NPMORBs

Field occurrences suggest that NPMORBs were derived from mid-ocean ridge volcanism. I here examine to estimate FeO content of source mantle, and temperature and pressure of melting. NPMORBs are enriched in FeO content relative to the modern MORB at any given MgO content (> 10 wt %). This difference suggests that source mantle of NPMORBs had higher FeO than that of the modern MORB.

I assumed that the Archean mantle was still a spinel- or garnet-lherzolite. This assumption leads to $Fe^{3+}/\sum Fe$ ratio of source mantle similar to that of modern upper mantle because $Fe^{3+}/\sum Fe$ ratio is controlled not only oxygen fugacity, but also mineral assemblage. If Archean basalts were formed within upper mantle, which consisted of olivine, orthopyroxene, clinopyroxene, and spinel, $Fe^{3+}/\sum Fe$ ratio in Archean basalts would be equivalent to that of modern MORBs. Further discussion is shown elsewhere. Batch melting is also assumed because of its simplification.

Melting experiments of four natural peridotites KLB-1, HK66, PHN1611, and MM3 have been extensively performed using diamond aggregate method (Hirose & Kushiro 1993; Baker & Stolper 1994; Kushiro 1996). Those experiments showed $SiO_2$ content of melts is relatively independent of composition of peridotites and temperature of melting at moderate degree of melting, but quite sensitive to melting pressure, because $SiO_2$ is a major constituent element of all minerals. On the contrary, FeO* in melts strongly depends on FeO* content of peridotites, together with pressure and temperature of melting. MgO content of melts is almost proportional to degree of melting.

Some of most primitive NPMORBs and modern MORB are plotted along melt compositions formed by different pressures and degree of melting and from different starting materials in Fig 12b. Both NPMORBs and Modern MORBs are distributed on the compositional trends defined by the melts formed at 10 or 15 kb (Fig 12b). This evidence suggests that average melting pressure of NPMORBs through melting column were 10 to 15 kb (Klein & Langmuir, 1987), and is equivalent to that (10 kb) of modern MORB (Fujii & Bougault 1983).

Fig. 12b shows that each variation of FeO content of melt formed at 15 kb for KLB-1, HK66, and PHN1611, or 10 kb from MM3. Primitive NPMORBs are plotted over melts from

HK66 or PHN1611, whereas modern MORBs are distributed on melts from KLB-1. The composition of primary melt of NPMORBs can not be estimated because olivine is extinct due to metamorphism. If MgO content of primary melt of NPMORBs has ca. 20 wt % in MgO, NPMORBs can be formed from KLB-1 (Takahashi et al. 1993). However, because the average melting pressure should be high ca. 4.6 GPa, in the case, NPMORBs should have the garnet signatures (Salters & Hart, 1989; McKenzie & O'Nions 1991; Bourdon et al., 1996; Salters, 1996; Hirschmann 1996; Hirschmann & Stolper, 1996). However, NPMORBs do not show garnet signature, such as heavy REE depletion (Fig. 8). Furthermore, if NPMORBs are highly differentiated basalts from komatiites, abundance of compatible element such as Ni should be lower (Fig. 7), because Ni is more removed from the melts during crystal fractionation. The results suggest that NPMORBs were derived from more FeO*-enriched source mantle such as HK66 and PHN1611 rather than KLB-1 and MM3.

The mantle of the Moon and the Mars have higher FeO content than the modern mantle of the Earth (e.g. Hartman et al., 1986 or Bertka & Holloway, 1994a,b). However, the result suggest that the source mantle of NPMORBs had at most 10 % in FeO. The differences would be caused by core-formation, as discussed elsewhere.

### IV-5.3.2 Potential mantle temperature of source mantle of NPMORBs

The potential temperature of the Archean mantle has been estimated by previous workers (e.g. Takahashi, 1990; Nisbet et al., 1993; Ohta et al. 1996) since the establishment of concepts of potential mantle temperature (McKenzie & Bickle 1988). The former two works estimated potential temperature of Archean mantle from only MgO content in peridotitic komatiites (Takahashi 1990, Nisbet et al. 1993). However, MgO content of a primary melt strongly depends on the amount of olivine addition using olivine maximum fractionation model because Fo content of olivine, generally speaking, is not available in many Archean komatiites and basalts (Parman et al. 1997; Komiya et al. 1998). Moreover, the difference of oxidation state of melting between the present and Archean would affect the $Mg^{\#}$ value (Arculus 1985). Ohta et al. (1996) estimated the potential mantle temperature by the comparison of nine major elements in primary magma with those of experimental melts. However, $TiO_2$, $Al_2O_3$, FeO, $Na_2O$, $K_2O$, and $P_2O_5$ contents are significant sensitive to those contents in source mantle. Therefore, I here estimate the potential mantle temperature by the abundance of FeO and $SiO_2$ in primitive magmas because they are relatively insensitive to the extent of crystal fractionation and are strongly correlated to pressure and temperature of melting.

Figure 12b shows composition of the primitive NPMORBs along experimental melt from PHN1611 on a $SiO_2$ versus FeO diagram. Primitive NPMORBs are plotted over the melt formed at 1325, 1400, and 1425 ˚C, 15 kb. Each degree of melting is 18.4, 26.9, 35.9 %, respectively according to experimental data (Kushiro 1996). Although a variation of compositions is possibly caused by the influence of chemical alteration, it would reflect the

small perturbation of global trend (Klein & Langmuir 1989). Therefore, the potential mantle temperature is obtained 1390 to 1550 ˚C of with Cp=1.2x10$^{3}$ Jkg$^{-1}$, s/s=1.2x10-8 m$^{3}$kg$^{-1}$°K$^{-1}$, m/m=2.4x10$^{-8}$ m$^{3}$kg$^{-1}$°K$^{-1}$ and S=350 Jkg$^{-1}$°K$^{-1}$, which is for modern mantle (Iwamori et al., 1995). Iwamori et al. (1995) also obtained 1320 ˚C of potential mantle temperature of modern MORBs for batch melting.

**IV-5.4 Origin of OIBs**

Field occurrences show that NPOIBs were derived off-ridge volcanism. Moreover, thick basaltic komatiite flow occurs at the bottom of the Unit III. A large gabbroic body also is emplaced in Unit II, where a feeder dike runs towards the top-covering chert from. However, except with komatiitic rocks, compositional variation of NPOIBs is different from that of modern OIBs. Modern OIBs have lower $SiO_2$ and $Al_2O_3$ and higher FeO and $TiO_2$ than modern MORBs. Moreover, plagioclase fractionation plays significant role on liquid line of descent of modern MORBs whereas clinopyroxene fractionation is significant in modern OIBs at moderate MgO content. Although clinopyroxene fractionation is slightly of significance in NPOIBs relative to NPMORBs, it is no much for that in modern OIBs. Significant clinopyroxene fractionation would result from high pressure of melting and crystal fractionation of OIBs, presumably involved with hydrous source mantle. However, compositional variation of NPOIBs dominated by plagioclase fractionation. Compositional variation of major and some trace elements in modern oceanic plateau is similar to that of modern MORBs (Mahoney 1987; Allan et al. 1987), reflecting olivine and the following plagioclase fractionation. NPOIBs presumably originated from an oceanic plateau. Flat-REE patterns of NPOIBs, and higher Nb/Y and Nb/Zr ratios are also consistent to the chemical nature of oceanic plateau (Mahoney 1987). An evidence of bimodal volcanism of basalt/basaltic komatiite with huge rhyolite bodies in the eastern area Unit II supports such a large igneous province. Composition of clinopyroxene phenocrysts and whole rocks of NPOIBs suggests the significant amount of water at least at the crystal fractionation. Moreover, significant amount of vesicles and amygdules filled with quartz and calcite within the outer margin of pillowed basalts in Unit III support the involvement of significant water content in NPOIBs. These observation is consistent to recent evidences for hydrous komatiites (Arndt et al. 1977, 1986, 1998; Stone et al. 1995ab, 1997; Lewis & Williams 1973; Saverikko 1985, 1990; Dan & de Wit 1985; Echeverría & Aitkan 1986; Hill et al. 1995; Hanski & Smolkin 1995; Grove et al. 1994, 1995, 1997; Parman et al. 1997). However, the tectonic setting is presumed to be subduction zone because of its high water content (Brooks & Hart 1974; Allègre 1982; Parman et al. 1997). Our evidences suggest that NPOIBs with basaltic komatiites were derived at oceanic island or plateau through the plume magmatism and its source mantle would be hydrous. The result implies that the source mantle involved recycling oceanic crusts. Water content of source mantle can not be obtained, but appears to be low because of lack of vesicles at outermost margin of pillow lavas and komatiite flows

(McDonough & Danyushevsky 1995; Shimizu et al. 1997; Komiya et al. 1998b).

### IV-5.5 Mantle heterogeneities in the Early Archean

Mafic and ultramafic volcanic rocks in Archean range from severely LREE-depleted to LREE-enriched in REE patterns (Sun and Nesbitt, 1978). LREE-enriched pattern is restricted to Al-depleted komatiite, suggesting difference of melting condition such as high-pressure garnet fractionation (Green 1975; Nesbitt et al. 1979; Ohtani, 1990). However, flat- or LREE-depleted REE patterns are pervasively observed in mafic and ultramafic volcanic rocks. Moreover, the correlation of REE patterns with major and trace elements content is described in some rocks (Sun, 1984).

Because this work present that REE patterns of both NPMORBs and NPOIBs appear smooth and do not have Eu-anomaly, it is regard that later metamorphism play a minor role on abundances of rare earth elements. The distinct difference between REE pattern of NPMORBs and NPOIBs indicates that mantle have been already heterogeneous in the Middle Archean because both magmas were formed under shallow depth condition. Moreover, source mantle of NPMORBs had been depleted relative to that of NPOIBs. If NPOIBs originated from oceanic plateau volcanism, the source mantle should be or involve lower mantle, analogous to modern oceanic plateau (Kogiso et al. 1997; Kimura et al. 1994). This results implies that Archean mantle have been geochemically separated into two layers similar to the modern mantle. Major and trace element concentration indicate that mantle source of NPMORBs are more enriched in $Al_2O_3$, and depleted in FeO*, $TiO_2$, Y, Zr, and Nb compared with NPOIBs. REE pattern of IMORBs indicates the presence of depleted source mantle in the Archean, supporting the Nd isotopic evidences (Silver et al. 1988; Bennett et al. 1993).

### IV-5.6 Origin of mantle heterogeneity

Mantle heterogeneities of the modern mantle has been caused by long term recycling of the oceanic crust, sediments and residual peridotites through plate tectonics (Chase, 1981; Hofmann & White, 1982, Weaver, 1991, Chauvel et al., 1992, Woodhead et al., 1993; Roy-Barman & Allègre, 1995; Hirschmann & Stolper, 1996; Hauri, 1996; Kogiso et al., 1997). Active magmatism through plume tectonics and/or plate tectonics led the mantle to be heterogeneous in the Early Archean (Komiya & Maruyama 1995; Chapter III in this paper). What caused mantle heterogeneities by the Middle Archean? The three causes for mantle heterogeneity are supposed; inhomogeneous accretion of planetesimals, magma ocean and the following core formation, magmatism through plate tectonics or plume tectonics, and recycling of supracrustal rocks through plate tectonics.

It is expected that the inhomogeneous accretion of planetesimals and magma ocean

and the following core formation led to the large-scale mantle heterogeneity at the formation of the Earth. However, except for rare evidences (Barnes et al. 1985; Pattou et al. 1996; Harper & Jacobsen 1992), no vestiges are preserved in even the Early Archean rocks (Gruau et al. 1988; Kato et al. 1998a). Therefore, it is supposed that mantle convection completely erased mantle heterogeneities by the Early Archean (Abe 1993).

Archean plate tectonics has become widely accepted (e.g. de Wit et al. 1987ab, 1992; Kusky 1989, 1990, 1991, Ohta et al 1996; Komiya et al 1998), despite of several objection (Goodwin 1991, 1996; Davies 1992; Hamilton 1993, 1998ab).

The recycling of supracrustal rocks through plate tectonics played an insignificant role on the mantle heterogeneities in the Early Archean (Chapter III). However, the composition of clinopyroxenes and liquid line of descent of NPOIBs indicate that the source mantle of NPOIBs was more or less hydrous. Although the source of the incorporated water can not be determined as yet, it was presumably subducted oceanic crust. NPOIBs are enriched in incompatible trace elements compared with NPMORBs, but their ratios are similar each other. NPOIBs did not have signature of the recycling of supracrustal rocks such as Nb- and Ti-positive anomalies. Moreover, involved by the recycling of oceanic crust, NPOIBs should be depleted in Pb, because Pb is removed compared with by fluids at subduction (Kogiso et al. 1997). However, neither NPMORBs nor NPOIBs indicates the depletion of Pb concentration each other, despite of relative depletion in Pb compared with IMORBs and IOIBs. The mantle in transition zone, which is composed of ß-spinels and majorite, can contain significant amount of water (Kawamoto et al. 1996). The source mantle of NPOIBs may involve minor amount of such mantle. The slightly enriched REE pattern and depletion of Y content support that source mantle of IOIBs contained transition zone mantle materials (Fig. 7, 8, and 13).

As a result, magmatism at spreading center, and if plate tectonics had never operated yet, plume magmatism possibly mainly caused the mantle to be differentiated into MORBs source and OIB source. In addition, involvement of mantle materials in transition zone also, more or less, played a role in mantle heterogeneities. Major and trace elements composition of NPMORBs and NPOIBs support the hypothesis, because the extraction of the magma from mantle resulted in depletion of incompatible elements. NPMORBs are depleted in incompatible elements relative to NPOIBs. However, residual mantle could not possibly produce basaltic melts because of the lack of magmaphile elements. Therefore, the source mantle of IMORBs presumably involved minor amount of the residue of high-pressure plume magmas with major amount of primordial mantle because of lower content in $Al_2O_3$, Y, and HREE. Active mantle convection accompanied with plume magmatism probably caused the local differentiation of the mantle before the Early Archean (Ogawa 1988).

## IV-6 Conclusions

(1) Two types greenstones defined by their field occurrences occurred in North Pole area, NPMORBs and NPOIBs. NPOIBs have lower $Al_2O_3$ and higher FeO*, $TiO_2$, Y, Zr, and Nb than NPMORBs at any given MgO contents. NPMORBs form LREE- and MREE-depleted REE pattern, whereas NPOIBs form slightly LREE-enriched pattern. The differences of field occurrence are correlated with those of the composition each other. The compositional differences indicate the mantle heterogeneities in the Middle Archean, implying that the two component model is insufficient to investigate the evolution of the mantle.

(2) Correlations among compositions of clinopyroxenes and whole rocks indicate that secondary alteration played an insignificant role on the concentration of al least Ti, MgO and FeO. The compositions of clinopyroxenes and whole rocks of NPOIBs indicate the involvement of water during crystal fractionation, suggesting that the source mantle was wer.

(3) NPMORBs have lower $TiO_2$ and $Na_2O$ than the modern MORBs. They also have lower Zr, Y, and Nb at any give MgO content, and higher FeO* and MnO and lower Ni at high MgO content (> 10 wt %) relative to the modern MORBs.

(4) Major elements chemistry of NPMORBs indicates that the source mantle of NPMORBs had ca. 10 wt % in FeO. The higher content of FeO* in the Middle Archean mantle suggests that the composition of upper mantle would change through the geologic time.

(5) The estimated potential mantle temperature of source mantle of NPMORBs is about 1450 ˚C, which is much lower than previous works.

## References


Allan, J. F., Batiza, R., and Lonsdale, P., 1987, Petrology and chemistry of lavas from seamounts flanking the east Pacific rise axis, 21˚N: implications concerning the mantle source composition for both seamount and adjacent EPR lavas: Seamount, Islands, and Atolls: Washington, D.C., AGU Monograph, 255-282 p.

Allègre, C. J., 1982, Genesis of Archaean komatiites in a wet ultramafic subducted plate, in Arndt, N. T., and Nisbet, E. H., eds., Komatiites, London, George Allen and Unwin, 495-500.

Arculus, R. J., 1985, Oxidation status of the mantle past and present: Ann. Rev. Earth Planet. Sci., v. 13, p. 75-95.

Arndt, N. T., 1986, Spinifex and swirling olivines in a komatiites lava lake, Munro Township, Canada: Precam. Res., 34, 139-155.

Arndt, N. T., Naldrett, A. J., and Pyke, D. R., 1977, Komatiitic and iron-rich tholeiitic lavas of Munro Township, Northeast Ontario: J. Petrol., v. 18, p. 319-369.

Arndt, N. T., Ginibre, C., Chauvel, C., Albarède, F., Cheadle, M., Herzberg, C., Jenner, G., and Lahaye, Y., 1998, Were komatiites wet?: Geology, 26, 739-742.

Baker, M. B., and Stolper, E. M., 1994, Determining the composition of high-pressure mantle melts using diamond aggregates: Geochim. Cosmochim. Acta, v. 58, p. 2811-2827.

Barley, M. E., 1987, The Archean Whim Creek belt, an ensialic fault-bounded basin in the Pilbara block, australia: Precam. Res., v. 37, p. 199-215.

Barley, M. E., 1993, Volcanic, sedimentary and tectostratigraphic environments of the ca. 3.46 Ga Warrawoona Megasequence: a review: Precambrian Research, v. 60, p. 47-67.

Barley, M. E., Dunlop, J. S. R., Glover, J. E., and Groves, D. I., 1979, Sedimentary evidence for an Archaean shallow-water volcanic-sedimentary facies, eastern Pilbara Block, Western Australia: Earth and Planetary Science Letters, v. 43, p. 74-84.

Barley, M. E., Sylvester, G. C., Groves, D. I., Borley, G. D., and Rogers, N., 1984, Archaean calc-alkaline volcanism in the Pilbara Block, Western Australia: Precam. Res., v. 24, p. 285-319.

Bennett, V. C., Nutman, A. P., and McCulloch, M. T., 1993, Nd isotopic evidence for transient, highly depleted mantle reservoirs in the early history of the Earth.: Earth Planet. Sci. Lett., v. 119, p. 299-317.

Bertka, C. M., and Holloway, J. R., 1994a, Anhydrous partial melting of an iron-rich mantle I: subsolidus phase assemblages and partial melting phase relations at 10 to 30 kbar: Contrib. Mineral. Petrol., v. 115, p. 313-322.

Bertka, C. M., and Holloway, J. R., 1994b, Anhydrous partial melting of an iron-rich mantle II: primary melt compositions at 15kbar.: Contrib. Mineral. Petrol., v. 115, p. 323-338.

Basaltic Volcanism Study Project (BVSP): Basaltic Volcanism on the Terrestrial Planet.: New York, Pergamon Press, 1286 p., 1981

Bourdon, B., Zindler, A., Elliott, T., and Langmuir, C. H., 1996, Constraints on mantle melting at mid-ocean ridges from global $^{238}U$-$^{230}Th$ disequilibrium data: Nature, v. 384, p. 231-235.

Brooks, C., and Hart, S. R., 1974, On the significance of komatiite: Geology, v. 2, p. 107-110.

Buick, R., and Dunlop, J. S. R., 1990, Evaporitic sedements of Early Archaean age from the Warrawoona Group, North Pole, Western Australia: Sedimentology, v. 37, p. 247-277.

Buick, R., Thornett, J. R., McNaughton, N. J., Smith, J. B., Barley, M. E., and Savage, M., 1995, Record of emergent continental crust ca. 3.5 billion years ago in the Pilbara craton of Australia: Nature, v. 375, p. 574-577.

Cooper, J. A., James, P. R., and Rutland, R. W. R., 1982, Isotopic dating and structural relationships of granitoids and greenstones in the east Pilbara, Western Australia: Precam. Res., v. 18, p. 199-236.

Chase, C. G., 1981, Oceanic island Pb: two-stage histories and mantle evolution, Earth Planet. Sci. Lett., 52, 227-284

Chauvel, C., , Hofmann, A. W., and Vidal, P., 1992, HIMU-EM: The French Polynesian connection: Earth Planet. Sci. Lett., 110, 99-119.

Cooper, J. A., James, P. R., and Rutland, R. W. R., 1982, Isotopic dating and structural relationships of granitoids and greenstones in the east Pilbara, Western Australia: Precam. Res., v. 18, p. 199-236.

Dann, J. C., and de Wit, M. J., 1995, Remapping the komatiite type section, Barberton greenstone belt: vesicle, intrusions, and deformation: Montreal, International Conference on Tectonics and Metallogeny of Early/Mid Precambrian Orogenic Belts, Precambrian '95, 55.

Davies, G. F., 1992, On the emergence of plate tectonics: Geology, v. 20, p. 963-966.

Davidson, P. M., and Lindsley, D. H., 1994, Effect of Ca content and $SiO_2$ activity on augite + olivine equilibria: Am. Mineral., v. 79, p. 1123-1124.

DiMarco, M. J., and Lowe, D. R., 1989a, Petrography and provenance of silicified early Archaean volcaniclastic sandstones, eastern Pilbara Block, Western Australia: Sedimentology, v. 36, p. 821-836.

DiMarco, M. J., and Lowe, D. R., 1989b, Stratigraphy and sedimentology of an early Archean felsic volcanic sequence, eastern Pilbara Block, Western Australia. with special reference to the Duffer Formation and

implications for crustal evolution: Precambrian Research, v. 44, p. 147-169.
Dunbar, C. E., and Rodgers, J., 1961, Principles of stratigraphy: New York, John Wiley and Sons, 248 p.
Dunlop, J. S. R., and Buick, R., 1981, Archaean epiclastic sediments derived from mafic volcanics, North Pole, Pilbara Block, Western Australia: Special Publications Geological Society of Australia, v. 7, p. 225-233.
Dunlop, J. S. R., Muir, M. D., Milne, V. A., and Groves, D. I., 1978, A new microfossil assemblage from the archaean of Western Australia: Nature, v. 274, p. 676-678.
Echeverría, L. M., and Aitken, B. G., 1986, Pyroclastic rocks: another manifestation of ultramafic volcanism on Gorgona Island, Columbia: Contrib. Mineral. Petrol., v. 92, p. 428-436.
Eriksson, K. A., 1981, Archaean platform-to-trough sedimentation, East Pilbara Block, Australia, *in* Glover, J. E., and Goves, D. I., eds., Archaean Geology, Spec. Publ. 7, Geol. Soc. Aust., Perth, p. 235-244.
Fujii, T., and Bougault, H., 1983, Melting relations of a magnesian abyssal tholeiite and origin of MORBs: Earth Planet. Sci. Lett., v. 62, p. 283-295.
Gaetani, G. A., Grove, T. L., and Bryan, W. B., 1993, The influence of water on the petrogenesis of subduction-related igneous rocks: Nature, v. 365, p. 332-334.
Goto, A., and Tatsumi, Y., 1994, Quantitative analysis of rock samples by an X-ray fluorescence spectrometer (I): The Rigaku Journal, v. 11, p. 40-59.
Green, D. H., 1975, Genesis of Archean peridotitic magmas and constraints on Archean geothermal gradients and tectonics: Geology, v. 3, p. 15-18.
Green, T. H., 1994, Experimental studies of trace-element partitioning applicable to igneous petrogenesis - Sedona 16 years later: Chem. Geol., v. 117, p. 1-36.
Grove, T. L., de Wit, M. J., and Dann, J., 1995, Wet komatiites and Archean mantle conditions: Montreal, International Conference on Tectonics and Metallogeny of Early/Mid Precambrian Orogenic Belts, Precambrian ’95, 29.
Grove, T. L., de Wit, M. J., and Dann, J. C., 1997, 4.4.2. Komatiites from the Komati type section, Barberton, South Africa, *in* de Wit, M. J., and Ashwal, L. D., eds., Greenstone belts, Oxford, Oxford university press, p. 438-453.
Grove, T. L., Gaetani, G. A., and de Wit, M. J., 1994, Spinifex textures in 3.49 Ga Barberton Mountain Belt komatiites: evidence for crystallization of water-bearing, cool magmas in the Archean: EOS Trans. Am. Geophys. Union 75 supple., p. 654.
Grove, T. L., Kinzler, R., and Bryan, W. B., 1992, Fractionation of mid-ocean basalt (MORB), Mantle Flow and Melt Generation at Mid-Ocean Ridges, Washington D. C., AGU Monograph 71, p. 281-310.
Gruau, G., Chauvel, C., Arndt, N. T., and Cornichet, J., 1990, Aluminum depletion in komatiites and garnet fractionation in the early Archean mantle: Hafnium isotopic constraints: Geochim. Consmochim. Acta, v. 54, p. 3095-3101.
Gruau, G., Jahn, B. M., Glikson, A. Y., Davy, R., Hickman, A. H., and Chauvel, C., 1987, Age of the Archean Talga-Talga Subgroup, Pilbara Block, Western Australia, and early evolution fo the mantle: new Sm-Nd isotopic evidence: Earth and Planetary Science Letters, v. 85, p. 105-116.
Hamilton, P. J., Evensen, N. M., O'Nions, R. K., Glikson, A. Y., and Hickman, A. H., 1981, Sm-Nd dating of the North Star Basalt, Warrawoona Group, Pilbara Block, Western Australia: Geol. Soc. Aust. Spec. Publ., v. 7, p. 187-192.
Hanski, E. J., and Smolkin, V. F., 1995, Iron- and LREE-enriched mantle source for early Proterozoic intraplate magmatism as exemplified by the Pechengas ferropicrites, Kola Peninsula, Russia: Lithos, 34, 107-125.
Hartmann, W. K., Phillips, R. J., and Taylor, G. J., 1986, Origin of the Moon: Houston, Lunar Planet. Inst., 781 p.
Hickman, A. H., 1973, The North Pole barite deposits, Pilbara Goldfield: Ann. Rep. Geol. Surv. West. Aust. for 1972, p. 57-60.
Hickman, A. H., 1981, Crustal evolusion of the Pilbara Block, Western Austarlia, *in* Glover, J. E., and Groves, D. I., eds., Archaean Geology, Perth, Geological Scociety of Australia Incorporation, p. 57-69.
Hickman, A. H., 1983, Geology of the Pilbara Block and its environs: West. Aust. Geol. Surv. Bull., v. 127, 268 p.
Hickman, A. H., 1990, Granite-Greenstone terrain, *in* Ho, S. E., Glover, J. E., Myers, J. S., and Muhling, J. R., eds., Third international Archean symposium, Excursion guidebook, p. 2-13.
Hickman, A. H., Thorne, A. M., and Trendall, A. F., 1990, Geology of the Pilbara craton Introduction: Third international Archean symposium, Excursion guidebook, 2 p.
Hill, R. E. T., Barnes, S. J., Gole, M. J., and Dowling, S. E., 1995, The volcanology of komatiites as deduced from field relationships in the Norseman-Wiluna greenstone belt, Western Australia: Lithos, 34, 159-188.
Hirata, T., Shimizu, H., Akagi, T., Sawatari, H., and Masuda, A., 1988, Precise determination of rare earth elements in geological standard rocks by inductively coupled plasma source mass spectrometry: Anal. Sci., v. 4, p. 637-643.
Hirose, K., and Kushiro, I., 1993, Partial melting of dry mantle peridotites at high pressures: Determination of compositions of melts segregated from peridotite using aggregates of diamond: Earth Planet. Sci. Lett., v. 114, p. 477-489.

Hirschmann, M., 1996, Reading garnet's signature: Nature, v. 384, p. 215-217.
Hirschmann, M. M., and Stolper, E. M., 1996, A possible role for garnet pyroxenite in the origin of the "garnet signature" in MORB: Contrib. Mineral. Petrol., v. 124, p. 185-208.
Hofmann, A. W., and White, W. M., 1982, Mantle plumes from ancient oceanic crust: Earth Planet. Sci. Lett., 57, 421-436.
Iwamori, H., McKenzie, D., and Takahashi, E., 1995, Melt generation by isentropic mantle upwelling: Earth Planet Sci. Lett., v. 134, p. 253-266.
Kato, T., Ringwood, A. E., and Irifune, T., 1988a, Constraints of element partition coefficients between $MgSiO_3$ perovskite and liquid determined by direct measurements: Earth Planet. Sci. Lett., v. 90, p. 65-68.
Kato, T., Ringwood, A. E., and Irifune, T., 1988b, Experimental determination of element partitioning between silicate perovskites, garnet and liquids: constraints on early differentiation of the mantle: Earth Planet. Sci. Lett., v. 89, p. 123-145.
Kawamoto, T., Hervig, R., and Holloway, J. R., 1996, Experimental evidence for a hydrous transition zone in the early Earth's mantle: Earth Planet. Sci. Lett., v. 142, p. 587-592.
Kimura, G., Sakakibara, M., and Okamura, M., 1994, Plumes in central Panthalassa? Deductions from accreted oceanic fragments in Japan: Tectonics, v. 13, p. 905-916.
Klein, E. M., and Langmuir, C. H., 1987, Global correlations of ocean ridge basalt chemistry with axial depth and crustal thickness: J. Geophys. Res., v. 92, p. 8089-8115.
Klein, E. M., and Langmuir, C. H., 1989, Local versus global variations in ocean ridge basalt composition: a reply: J. Geophys. Res., v. 94, p. 4241-4252.
Kogiso, T., Tatsumi, Y., Shimoda, H., and Barsczus, H. G., 1997, HIMU ocean island basalts in the southern Polynesia: new evidence for whole-mantle scale recycling of subducted oceanic crust: J. Geophys. Res., v. 102, p. 8085-8103.
Kogiso, T., Tatsumi, Y., and Nakano S., 1997, Trace element transport during dehydration process in the subducted oceanic crust: 1. Experiments and implications for the origin of oceanic island basalts: Earth Planet. Sci. Lett., 148, 193-205.
Komiya, T., and Maruyama, S., 1995, Geochemistry of the oldest MORB and OIB of the World, Isua (3.8 Ga), Greenland: EOS Trans., v. 76, p. 700.
Komiya, T., Maruyama, S., Nohda, S., Masuda, T., Appel, P. W. U., Hayashi, M., and Okamoto, S., 1998a, Plate tectonics at 3.8 – 3.7 Ga; Field evidence from the Isua accretionary complex, southern West Greenland; Jour. Geol. in press.
Komiya, T., Maruyama, S., Shimizu, K., and Hirose, K., 1998b, Geology of Komati Fm. and mineralogy of relict igneous minerals, Barberton Greenstone Belt (3.5 Ga), South Africa, International Volcanological Congress, Cape Town
Krapez, B., 1984, Sedimentation in a small, fault-bounded basin-the Lalla Rookh Sandstone, East Pilbara Block, *in* Muhling, J. R., Groves, D. I., and Blake, T. S., eds., Geol. Dept. & Univ. Extension, Univ. West. Aust., Publ. 9, Archaean & Proterozoic basins of the Pilbara, Western Australia, p. 89-110.
Kushiro, I. 1975, On the nature of silicate melt and its significance in magma genesis: regularities in the shift of the liquidus boundaries involving olivine, pyroxene, and silica minerals: Am. J. Sci., 275, 411-431.
Kushiro, I., 1996, Partial melting of a fertile mantle peridotite at high pressures: an experimental study using aggregates of diamond, *in* Basu, A. R., and Hart, S. R., eds., Earth processes: Reading the isotopic code, Washington D. C., AGU Monograph 95, p. 109-122.
Lewis, J. D., and Williams, J. R., 1973, The petrology of an ultramafic lava near Murphy Well. Eastern Goldfields, Western Australia: Geological Survey of Western Australia, Ann. Rep., 1972, 60-68.
Lindsley, D. H., 1983, Pyroxene thermometry: Am. Mineral., v. 68, p. 477-493.
Lipple, S. L., 1975, Definitions of new and revised stratigraphic units of the eastern Pilbara region: Ann. Rep. Geol. Soc. West. Aust. for 1974, p. 58-63.
Lowe, D. R., 1983, Restricted shallow-water sedimentation of Early Achean stromatolitic and evaporitic strata of the Strelley Pool Chert, Pilbara Block, Western Australia: Precambrian Research, v. 19, p. 239-283.
Mahoney, J. J., 1987, An isotopic survey of Pacific oceanic plateaus: implications for their nature and origin: Seamounts, Islands, and Atolls: Wahington D. C., AGU Geophys. Monograph 43, 207-220 p.
Maruyama, S., 1976, Chemical natures of the Sawadani greenstone complex in Chichibu belt, eastern Shikoku: J. Geol. Soc. Jpn., v. 82, p. 183-197.
McDonough, W. F., and Danyushevsky, L. V., 1995, Water and sulfer contents of melt inclusions from Archean komatiites: EOS Trans., v. 76, p. S266.
McKenzie, D., and Bickle, M. J., 1988, The volume and composition of melt generated by extension of lithosphere: J. Petrol., v. 29, p. 625-649.
McKenzie, D., and O'Nions, R. K., 1991, Partial melt distributions from inversion of rare earth element concentrations: Jour. Petrol., 32, 1021-1091.
McNughton, N. J., Compston, W., and Barley, M. E., 1993, Constraints on the age of the Warrawoona Group, eastern Pilbara Block, Western Australia: Precambrian Research, v. 60, p. 69-98.
Nesbitt, R. W., Sun, S. S., and Purvis, A. C., 1979, Komatiites: Geochemistry and genesis: Can. Mineral., v. 17,

p. 165-186.
Nijima, W., Bruijne, K. C. H. d., and Valkering, M. E., 1998, Growth fault control of Early Archaean cherts,barite mounds and chert-barite veins, North Pole Dome, Eastern Pilbara, Western Australia: Precambrian Research, v. 88, p. 25-52.
Nisbet, E. G., Cheadle, M. J., Arndt, N. T., and Bickle, M. J., 1993, Constraining the potential temperature of the Archean mantle: A review of the evidence from komatiites: Lithos, v. 30, p. 291-307.
Nisbet, E. G., and Pearce, J. A., 1977, Clinopyroxene composition in mafic lavas from different tectonic settings: Contrib. Mineral. Petrol., v. 63, p. 149-160.
Ohta, H., Maruyama, S., Takahashi, E., Watanabe, Y., and Kato, Y., 1996, Field occurrence, geochemistry and petrogenesis of the Archean mid-oceanic ridge basalts (AMORBs) of the Cleaverville area, Pilbara craton, Western Australia: Lithos, v. 37, p. 199-221.
Ohtani, E., 1990, Majorite fractionation and genesis of komatiites in the deep mantle: Precam. Res., v. 48, p. 195-202.
Parman, S. W., Dann, J. C., Grove, T. L., and de Wit, M. J., 1997, Emplacement conditions of komatiite magmas from the 3.49 Ga Komati Formation, Barberton Greenstone Belt, South Africa: Earth Planet. Sci. Lett., v. 150, p. 303-323.
Pattou, L., Lorand, J. P., and Gros, M., 1996, Non-chondritic platinum-group element ratios in the Earth's mantle: Nature, v. 379, p. 712-715.
Pidgeon, R. T., 1978, 3450 m.y.-old volcanics in the aarchaean layered greenstone succession of the Pilbara Block, Western Australia: Earth Planet. Sci. Lett., v. 37, p. 421-428.
Richards, J. R., Flecher, I. R., and Blockley, J. G., 1981, Pilbara galenas: Precise isotopic assay of the oldest Australian leads; model ages and growth curve implications: Mineral. Deposita, v. 16, p. 7-30.
Roy-Barman, M., and Allègre, C. J., 1995, $^{187}Os/^{186}Os$ in oceanic island basalts: tracing oceanic crust recycling in the mantle: Earth Planet. Sci. Lett., v. 129, p. 145-161.
Salters, V. J. M., and Hart, S. R., 1989, The hafnium paradox and the role of garnet in the source of mid-ocean-ridge basalts: Nature, v. 342, p. 420-422.
Salters, V. J. M., 1996, The generation of mid-ocean ridge basalts from the Hf and Nd isotope perspective: Earth Planet. Sci. Lett., 141, 109-123.
Saverikko, M., 1985, The pyroclastic komatiite complex at Sattasvaara in northern Finland: Bull. Geo. Soc. Finland, 57, 55-87.
Saverikko, M., 1990, Komatiitic explosive volcanism and its tectonic setting in Finland, the Fennoscandian (Baltic) Shield: Bull. Geo. Soc. Finland, 62, 3-38.
Schopf, J. W., 1994, The oldest known records of life: Early Archean stromatolites, microfossils, and organic matter, *In* Bengtson, S. ed., Early life on Eath. Nobel Symposium No. 84., New York, Columbia Univ.Press, 193-206.
Shimizu, K., Komiya T., Maruyama, S., and Hirose, K., 1997, Water content of melt inclusion in Cr-spinel of 2.7 Ga komatiite from Belingwe Greenstone Belt, Zimbabwe: EOS Trans. Am. Geophys. Union, 78, 750.
Silver, P. G., Carlson, R. W., and Olson., P., 1988, Deep slabs, geochemical heterogeneity, and the large-scale structure of mantle convection: Investigation of a enduring paradox: Ann. Rev. Earth Planet. Sci., 16, 477-541.Sisson, T. W., and Grove, T. L., 1993a, Experimental investigation of the role of $H_2O$ in calc-alkaline differentiation and subduction zone magmatism: Contrib. Mineral. Petrol., v. 113, p. 143-166.
Stone, W. E., Crocket, J. H., and Dickin, A. P., 1995, Origin of Archean ferropicrites: Geochemical constraints from the Boston Creek flow, Abitibi greenstone belt, Ontario, Canada: Chemical Geology, v121, p. 51-71..
Stone, W. E., Crocket, J. H., and Fleet, M. E., 1995, Differentiation processes in an unusual iron-rich alumina-poor Archean ultramafic/mafic igneous body, Ontario: Contrib. Mineral. Petrol., v. 119, p. 287-300.
Stone, W. E., Deloule, E., Larson, M. S., and Lesher, C. M., 1997, Evidence for hydrous high-MgO melts in the Precambrian: Geology, v. 25, p. 143-146.
Sun, S.-S., 1984, Geochemical characteristics of Archaean ultramafic and mafic volcanic rocks: implications for mantle composition and evolution, *in* Kröner, A., Hansen, G. N., and Goodwin, A. M., eds., Archaean Geochemistry, Berlin, Springer-Verlag, p. 25-46.
Sun, S.-S., and Nesbitt, R. W., 1978b, Petrogenesis of Archean ultrabasic and basic volcanics: evidence from rare earth elements: Contrib. Mineral. Petrol., v. 65, p. 301-325.
Takahashi, E., 1990, Speculations on the Archean mantle: missing link between komatiite and depleted garnet peridotite: J. Geophys. Res., v. 95, p. 15941-15954.
Takahashi, E., Shimazaki, T., Tsuzaki, Y., and Yoshida, H., 1993, Melting study of a peridotite KLB-1 to 6.5 GPa, and the origin of basaltic magmas: Phil. Trans. R. Soc. London, v. A342, p. 105-120.
Thorpe, R. I., Hickman, A. H., Davis, D. W., Mortensen, J. K., and Trendall, A. F., 1992a, Constraints to models for lead evolution from precise zircon U-Pb geochronology for the Marble Bar region, Pilbara Craton, Western Australia, *in* Glover, J. E., and Ho, S. E., eds., The Archaean: Terrains, Processes and Metallogeny, Geology Department (Key Centre) and University Extension, The University of Western Australia Publication 9, p. 395-406.
Thorpe, R. I., Hickman, A. H., Davis, D. W., Mortensen, J. K., and Trendall, A. F., 1992b, U-Pb zircon

geochronology of Archean felsic units in the Marble Bar region, Pilbara Craton: Precam. Res., v. 56, p. 169-189.
Tormey, D. R., Grove, T. L., and Bryan, W. B., 1987, Experimental petrology of normal MORB near the Kane Fracture Zone: 22-25˚ N, mid-Atlantic ridge: Contrib. Mineral. Petrol., v. 96, p. 121-139.
Walter, M. R., Buick, R., and Dunlop, J. S. R., 1980, Stromatolites 3,400-3,500 Myr old from the North Pole area, Western Australia: Nature, v. 284, p. 443-445.
Weaver, B. L., 1991, The origin of ocean island basalt end-member compositions : trace element and isotopic constraints: Earth Planet. Sci. Lett., 104, 381-397.
Woodhead, J. D., Greenwood, P., Harman R. S., and Stoffers, P., 1993, Oxygen isotope evidence for recycled crust in the source of EM-type ocean island basalts: Nature, 362, 809-813.

## FIGURE CAPTIONS

**Figure 1.** Geological map of the northern Pilbara Craton (Hickman 1990) showing the distribution of the Pilbara Supergroup and the Mount Bruce Supergroup. The Pilbara Supergroup in the northern region is composed of Granite-greenstone terrane, and is exposed as inliers in the southern region. Mount Supergroup consists of the Fortescue Group, the Hamersley Group and the Turee Creek Group in the southern region. The Fortescue Group is exposed as outliers in Marble Bar area, East Pilbara and southwest Pilbara basins. Inset map shows the location of Pilbara Craton in Western Australia. Locality of mapped area, North Pole area is also shown.

**Figure 2.** Geological map of North Pole area (Kabashima 1998 per. commun.).

**Figure 3.** Compositions of relict igneous pyroxenes in MORBs and OIBs in North Pole area projected in terms of Wo-En-Fs. End members of pyroxene are calculated by Lindsley's (1983) method. Symbols; solid and open circles indicate pyroxenes from MORBs and those from OIBs in North Pole area. Compositional fields with solid black line, broken black line and gray line are from modern MORB, alkaline OIB and tholeiitic OIB, respectively.

**Figure 4.** Binary plots of major and minor elements of relict igneous pyroxenes in MORBs and OIBs in North Pole area. Symbols; solid and open circles indicate pyroxenes from MORBs and those from OIBs in North Pole area.

**Figure 5.** Binary plots of major and minor elements of relict igneous pyroxenes in modern MORB, tholeiitic OIB and alkaline OIB along with in North Pole MORBs. Symbols are shown in inset.

**Figure 6.** MgO variation diagrams of major elements for MORBs and OIBs in the North Pole area along with modern MORB and OIB. Symbols are shown as solid circles; coarse-grained MORBs, solid circles with an inner white open circle; fine-grained MORBs, open circles; OIBs, and open circles with inner small solid circle; fine-grained OIBs. Coarse-grained samples, in general, are distributed more widely in composition relative to fine-grained samples, influenced by accumulation of crystallized phases.

**Figure 7.** MgO variation diagrams of trace elements for MORBs and OIBs in the North Pole area along with modern MORB and OIB. Symbols are the same as in Figure 6.

**Figure 8.** Chondrite-normalized rare earth element (REE) abundances in MORBs and OIBs in North Pole area. IOIBs, gray lines, are slightly enriched in light-REE, whereas MORBs, black lines, are slightly depleted in light-REE. Values of chondrite are taken from Anders & Ebihara (1982).

**Figure 9.** (a) $Al_2O_3$-$Mg^{\#}$ plots of fine-grained North Pole MORBs. A bending is present at about 60 in $Mg^{\#}$. The bending is caused by initiation of crystallization of plagioclase. (b) $TiO_2$-$Mg^{\#}$ plots of fine-grained North Pole MORBs and the calculated compositions from relict igneous clinopyroxenes using an appropriate partition coefficient. Symbols

are shown in inset. Compositional variation of the calculated compositions corresponds to that of fine-grained MORBs. (c) $TiO_2$-$Mg^{\#}$ plots of fine-grained North Pole MORBs and relict igneous clinopyroxenes along with modern MORB and euhedral clinopyroxenes in modern MORBs. Symbols are shown in inset. Numbers indicates the calculated partition coefficient of Ti between clinopyroxene and whole rock with the clinopyroxene. (d) Fe/Mg ratio of clinopyroxene versus Fe/Mg ratio of whole rock sample with the clinopyroxene diagram. Solid circles are North Pole MORBs. Number attached with black line is an apparent distribution function of Fe and Mg between melt and clinopyroxene.

**Figure 10.** (a) Normative composition of North Pole MORBs and OIBs projected from silica on to cpx-pl-ol pseudo-ternary phase diagram (Gaetani et al. 1993). Also shown are pseudo-invariant points of ol-pl-cpx determined by melting experiments performed at 2 kb, under $H_2O$-saturated condition and at 1 atm, under dry condition (Gaetani et al. 1993). Solid circles and open circles are North Pole MORBs and OIBs, respectively. (b) Normative composition of North Pole MORBs and OIBs projected from ol on to cpx-pl-qz pseudo-ternary phase diagram (Gaetani et al. 1993). Also shown are calculated olivine+clinopyroxene LLD and olivine+clinopyroxene+plagioclase saturation boundaries at 2 kb, H2O-saturated conditions and at 1 atm, dry condition (Gaetani et al. 1993). Solid circles and open circles are North Pole MORBs and OIBs, respectively.

**Figure 11.** $Al_2O_3/TiO_2$-MgO plots of North Pole MORBs and OIBs. Solid circles and open circles are North Pole MORBs and OIBs, respectively. $Al_2O_3$ to $TiO_2$ ratio of North Pole MORBs is higher than that of OIBs.

**Figure 12.** (a) MgO variation diagrams of some major elements for coarse-grained (solid circles) and fine-grained MORBs (solid-circles with inner white circle) in the North Pole (solid circles) along with compositional variations of modern MORBs (gray regions). Three arrows on scattered plots indicate compositional variation of residual melts through crystal fractional fractionation of olivine, olivine+clinopyroxene and olivine+clinopyroxene+plagioclase, respectively. Abbreviations are: ol = olivine; cpx = clinopyroxene; pl = plagioclase. (b) Comparison of primitive natural basalts with partial melts formed from mantle peridotite by diamond methods. (i) $SiO_2$-MgO diagram. Symbols: solid black circles, solid gray circles and open circles are primitive North Pole MORBs, starting materials of high-pressure experiments (see also Chapter V) and most primitive modern NMORBs, respectively. Thick arrows indicate compositional variation of partial melts produced from four mantle peridotite at different pressure, 10 kb for light gray, 15 kb for gray, 20 kb for dirk gray and 25-30 kb for black arrow respectively. This diagram indicates that both modern MORBs and North Pole MORBs were formed at 10 to 15 kb. (ii) MgO-FeO diagram. Symbols: solid black circles, solid gray circles and open circles are primitive North Pole MORBs, starting materials of high-pressure experiments (see also Chapter V) and most primitive modern NMORBs, respectively. Thick arrows indicate compositional variation of partial melts produced at

15 kb from four different mantle peridotite, HK66 for light gray, PHN1611 for gray, KLB-1 for dirk gray and MM3 for black arrow, respectively. This diagram indicates that FeO content of mantle source of modern MORBs is comparable to that of KLB-1, whereas that that of mantle source of North Pole MORBs was comparable to or higher than that of HK66 and PHN1611. (iii) $SiO_2$-FeO diagram. Symbols: a solid circle and small open circles are primitive North Pole MORBs and partial melts from PHN1611, respectively. Thick arrows indicate compositional variation of partial melts produced from PHN1611 at 10 to 15 kb for gray, and at 20 to 30 kb for black arrow, respectively. This diagram indicates that melting pressure and temperature of North Pole MORBs was around 15 kb and 1325-1425 ˚C. Potential mantle temperature was calculated to be 1390 to 1550 ˚C using degree of melting (Kushiro 1996) and thermodynamic parameters (Hirose 1998).

**Figure 13.** Zr variation diagrams of incompatible trace elements for MORBs and OIBs in the North Pole along with modern MORB and OIB, Mare basalt and Highland basalt in Moon, Eucrite, and Orgueil. Symbols are the same as in Figure 6.

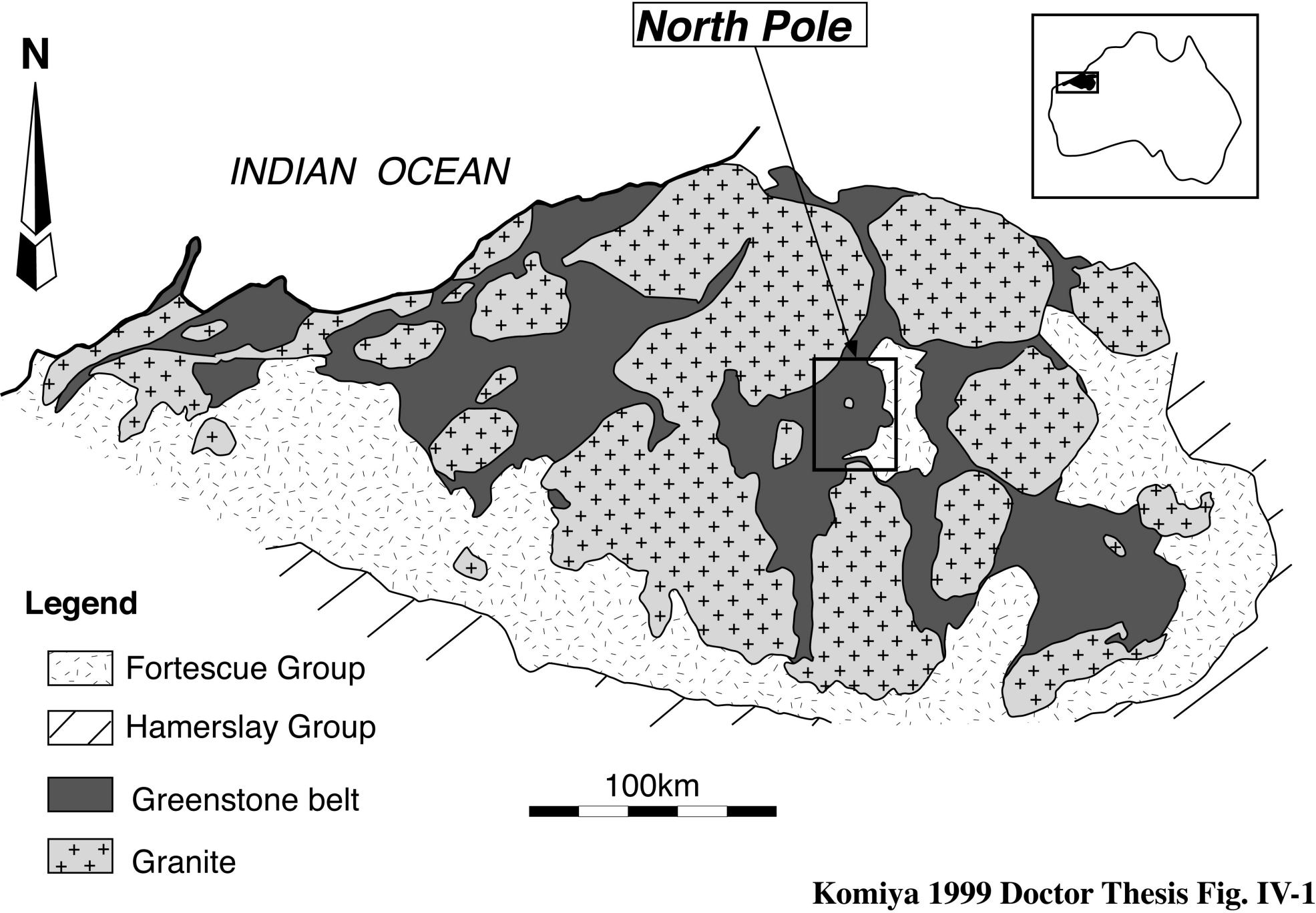


Komiya 1999 Doctor Thesis Fig. IV-1

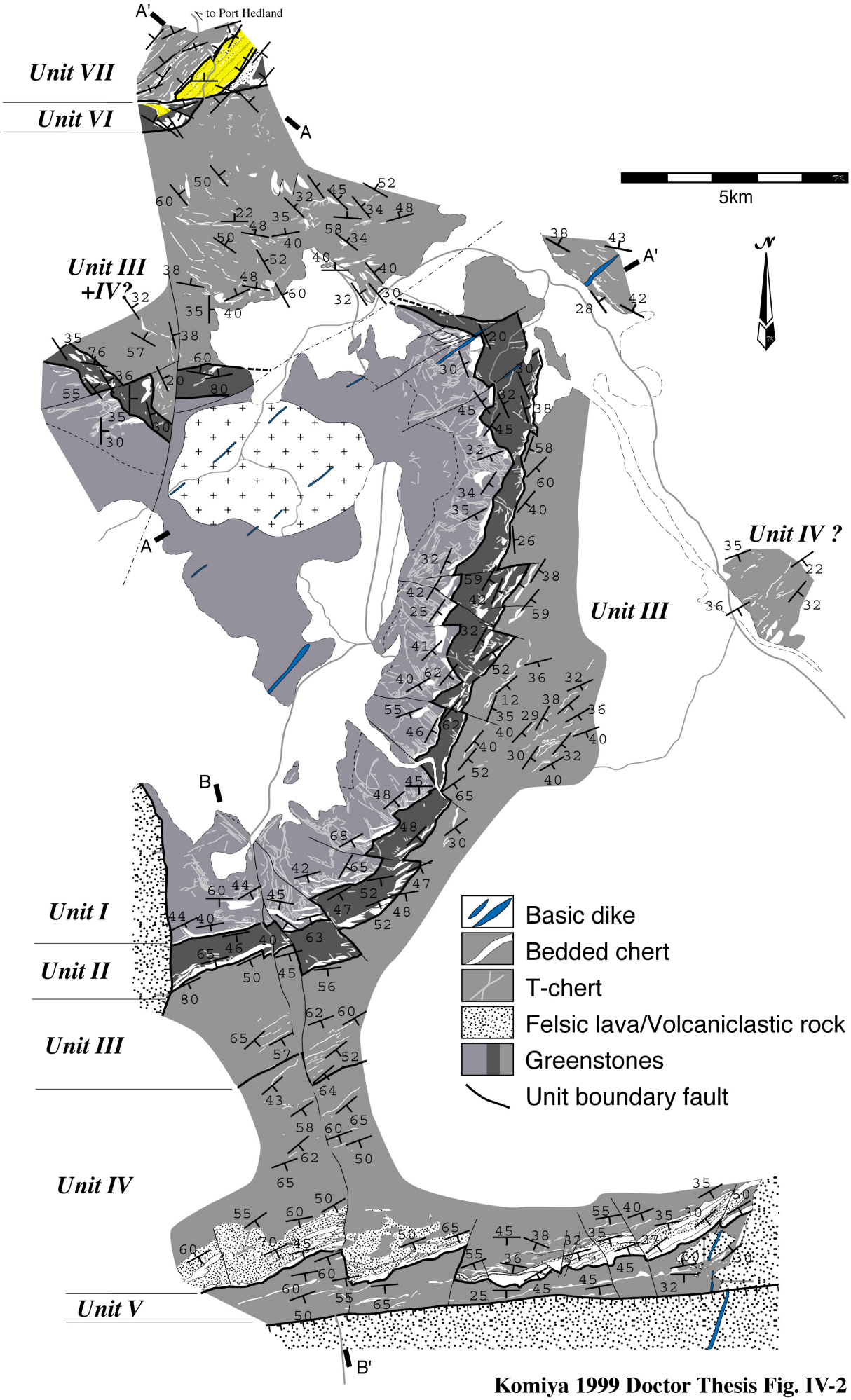


**Komiya 1999 Doctor Thesis Fig. IV-2**

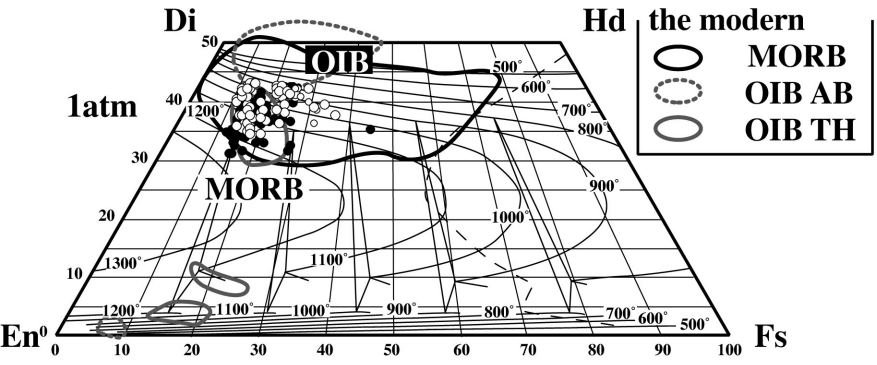


Komiya 1999 Doctor Thesis Fig. IV-3

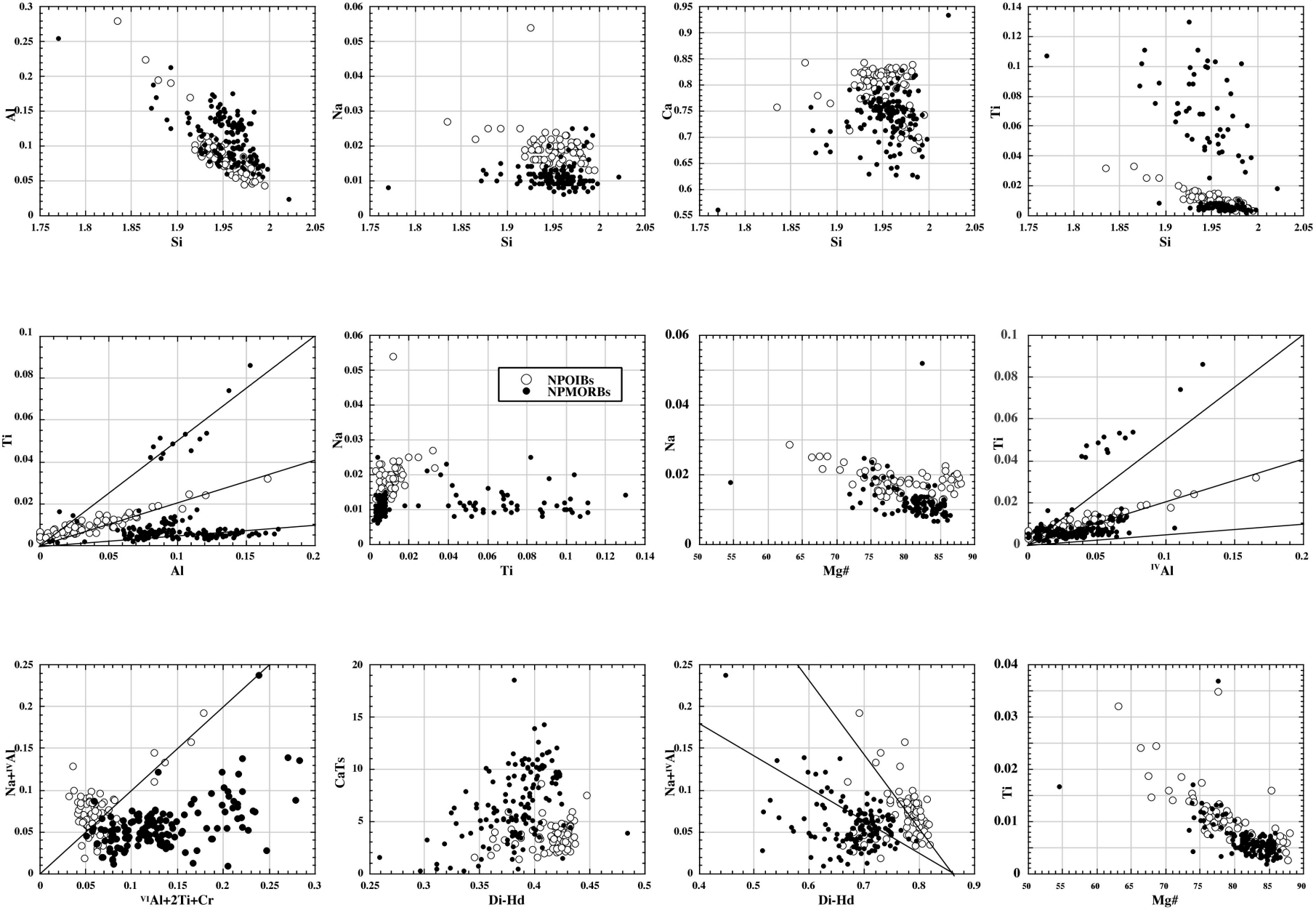


**Komiya 1999 Doctor Thesis Fig. IV-4**

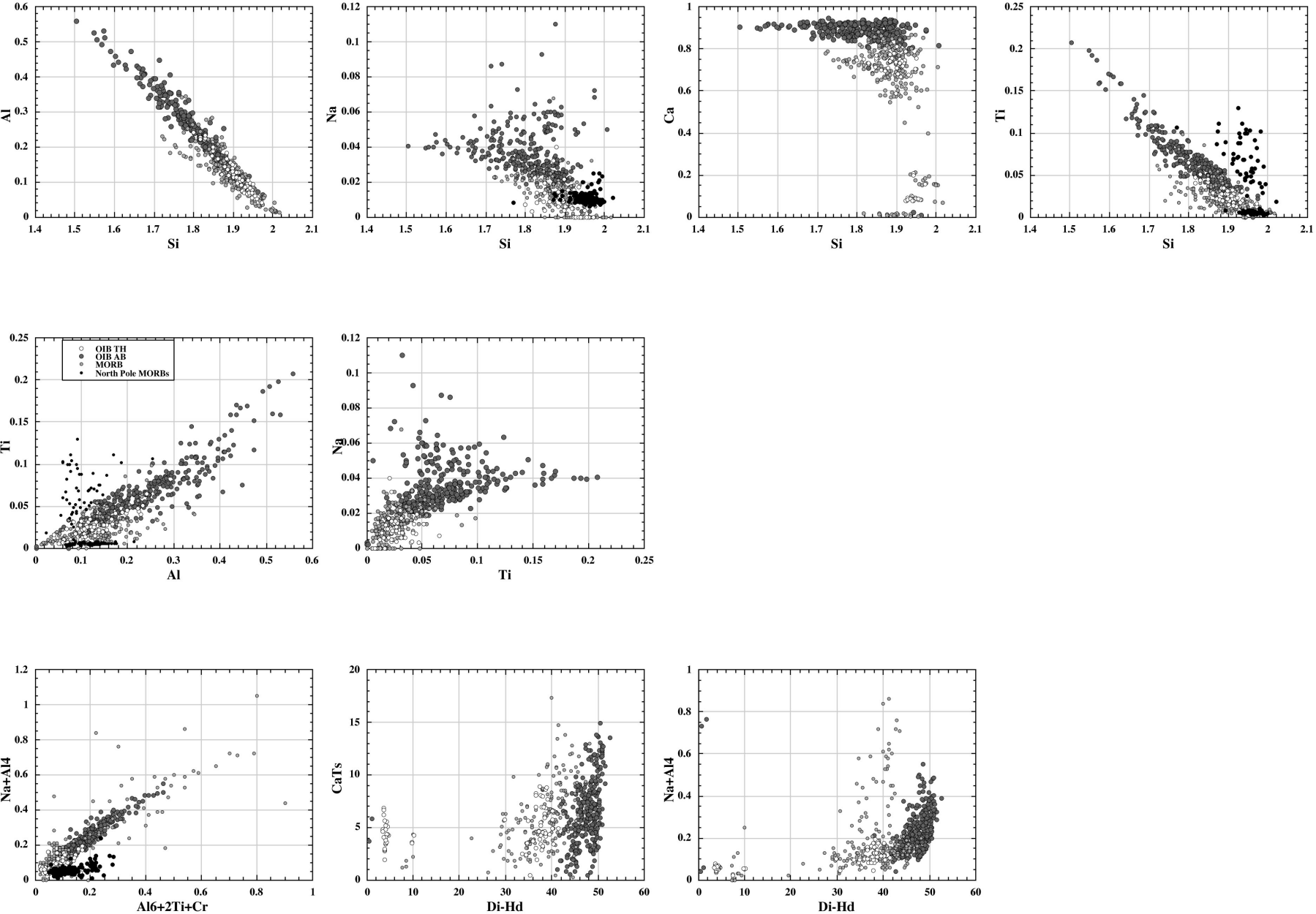


**Komiya 1999 Doctor Thesis Fig. IV-5**

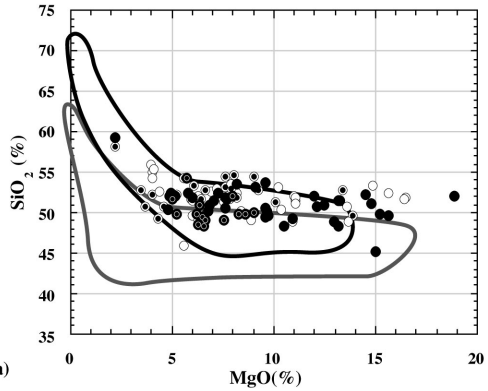


(Fig.1a)

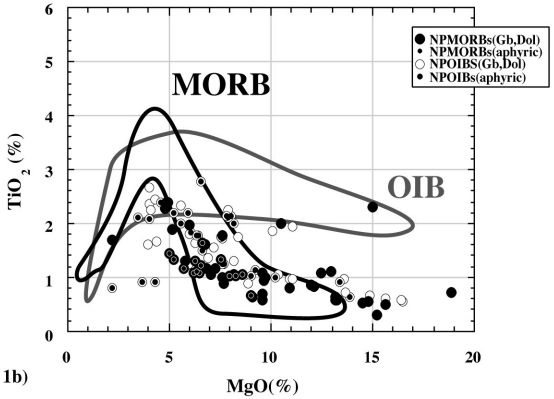


(Fig. 1b)

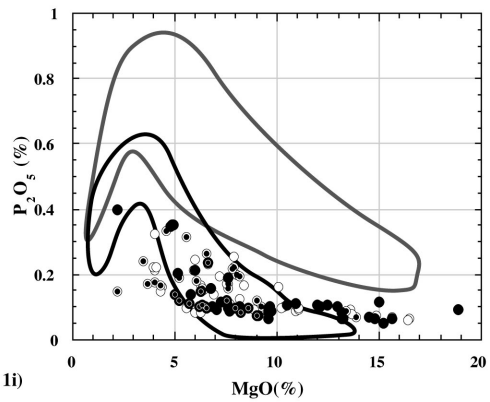


(Fig. 1i)

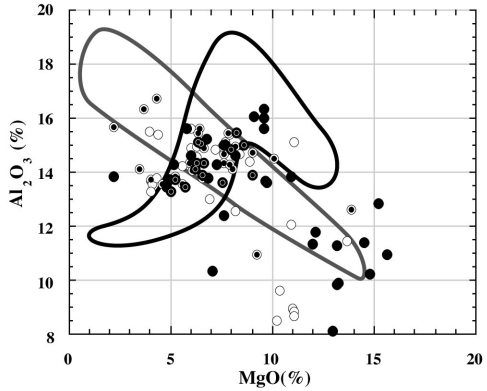


(Fig.1c)

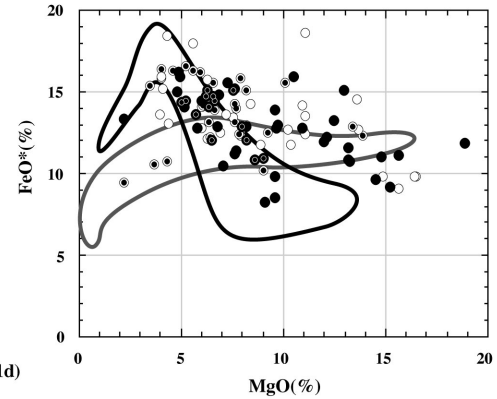


(Fig.1d)

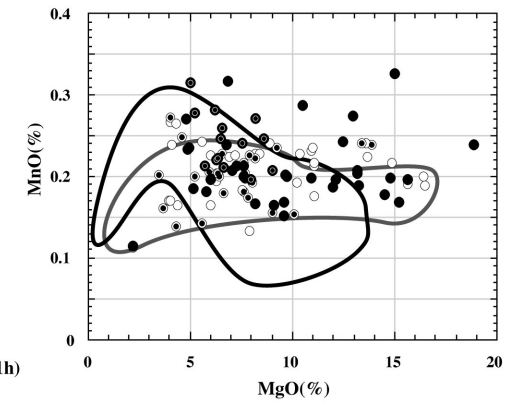


(Fig. 1h)

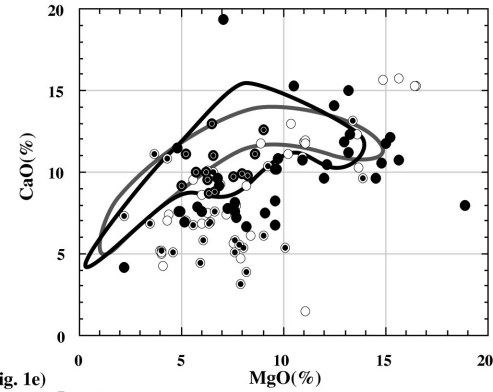


(Fig. 1e)

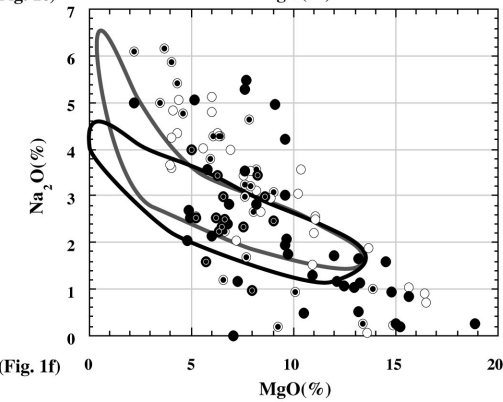


(Fig. 1f)

**Komiya 1999 Doctor Thesis Fig. IV-6**

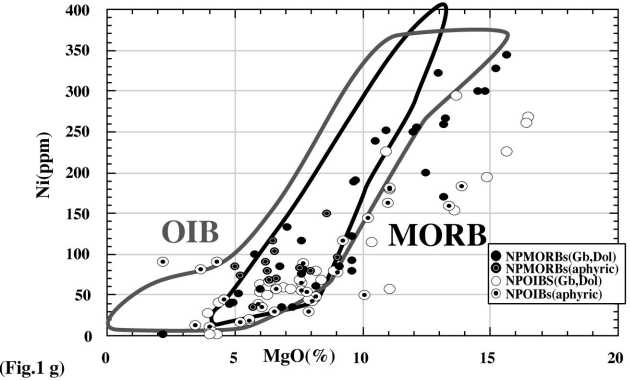


(Fig.1 g)

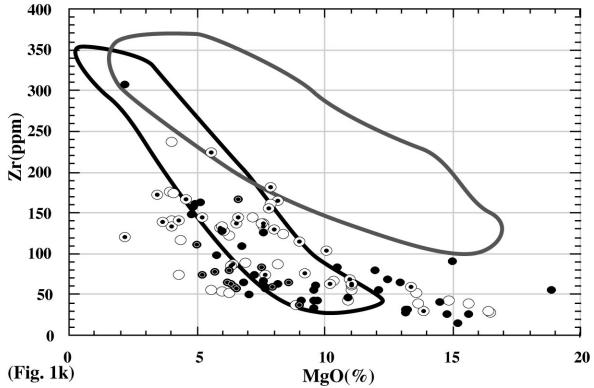


(Fig. 1k)

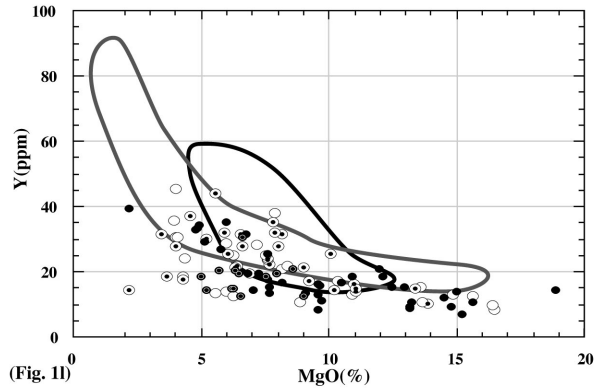


(Fig. 1l)

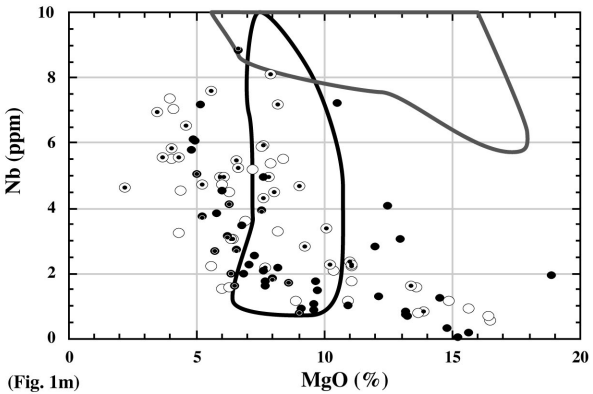


(Fig. 1m)

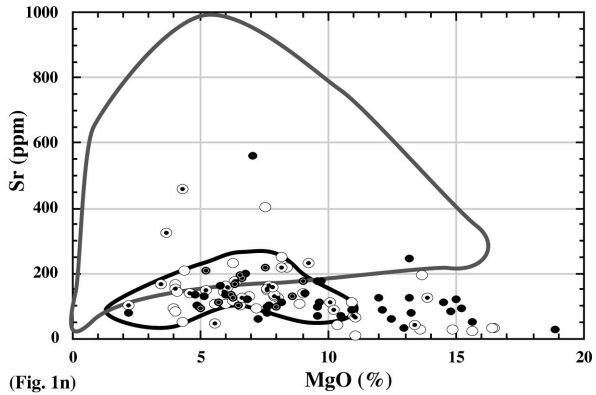


(Fig. 1n)

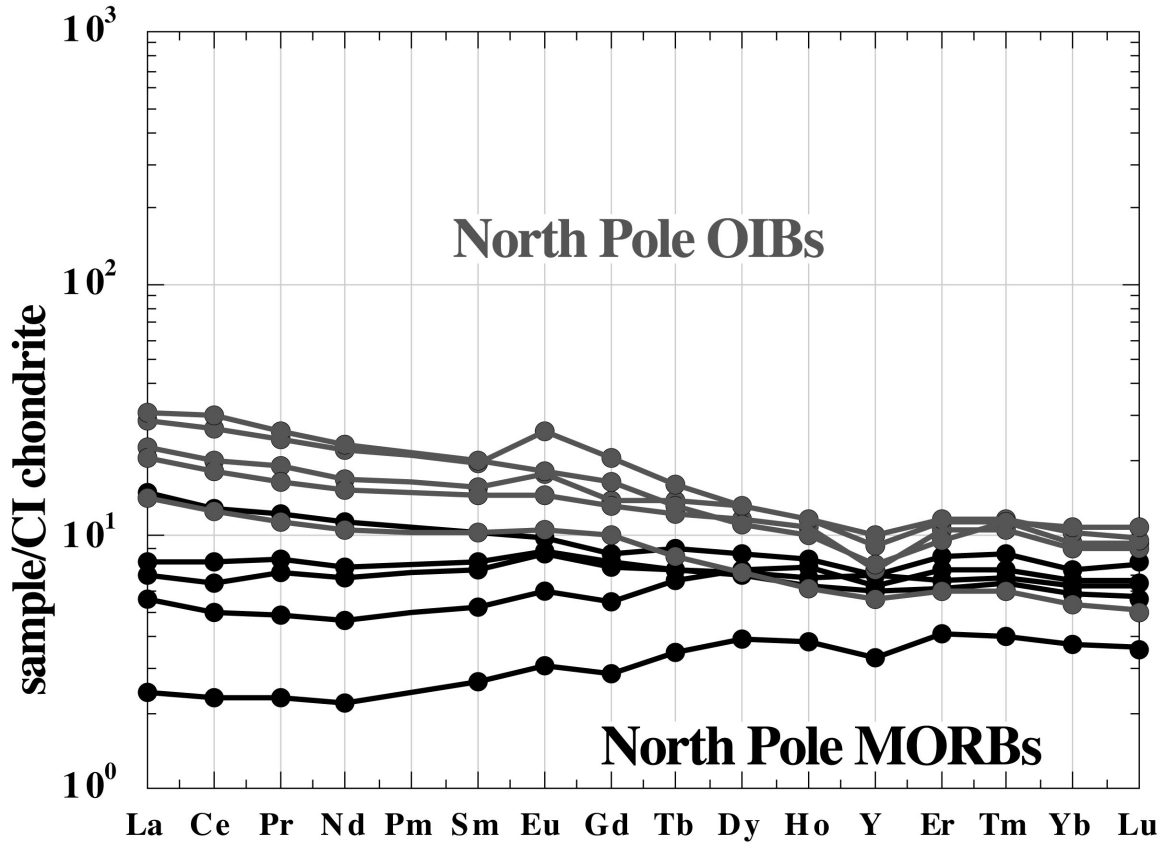


Komiya 1999, Doctor Thesis Fig. IV-8

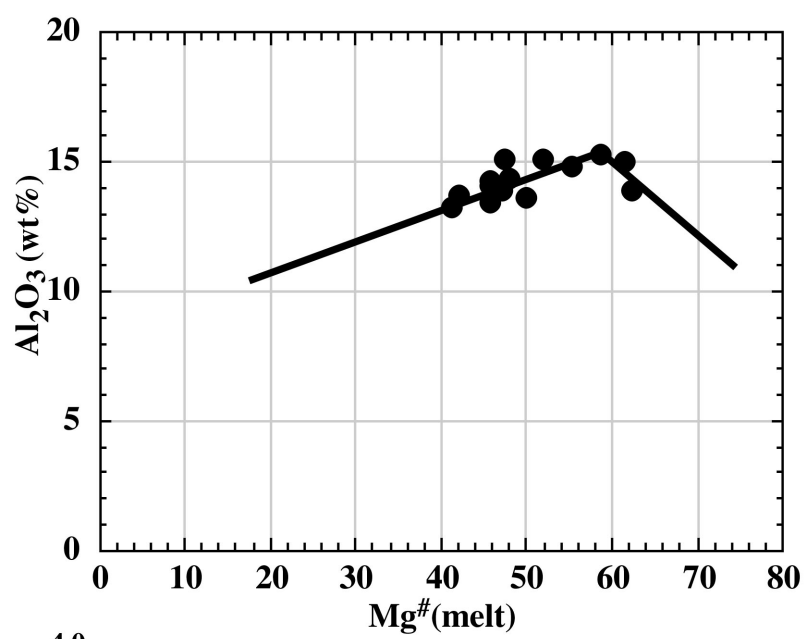


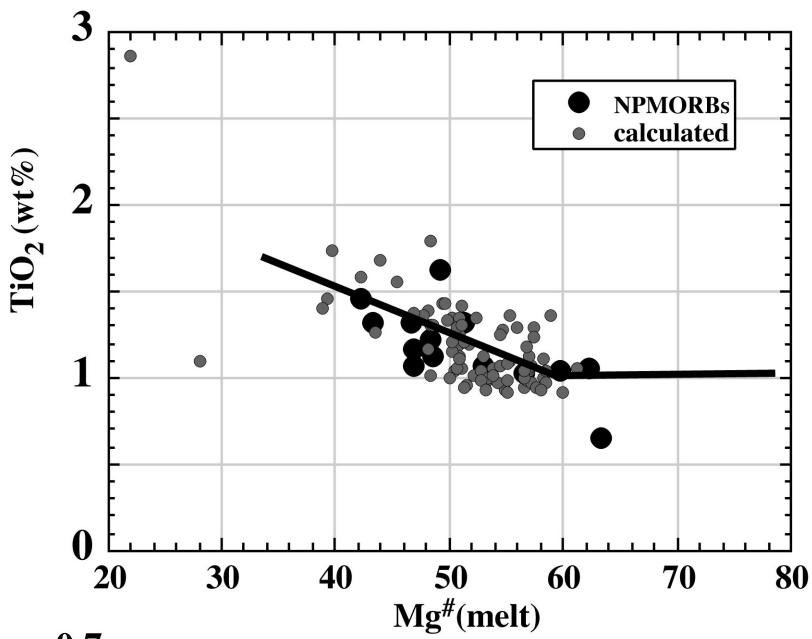


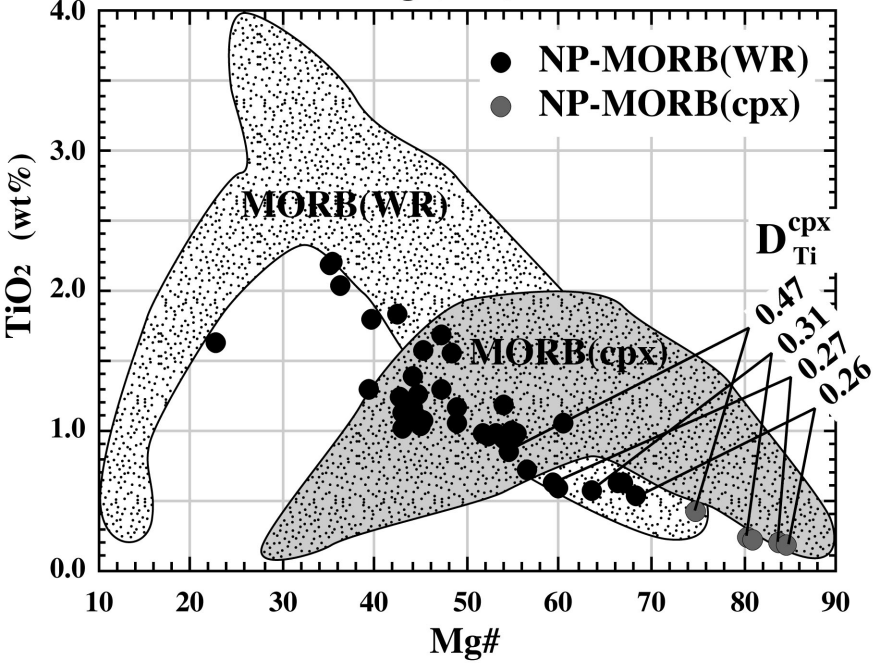


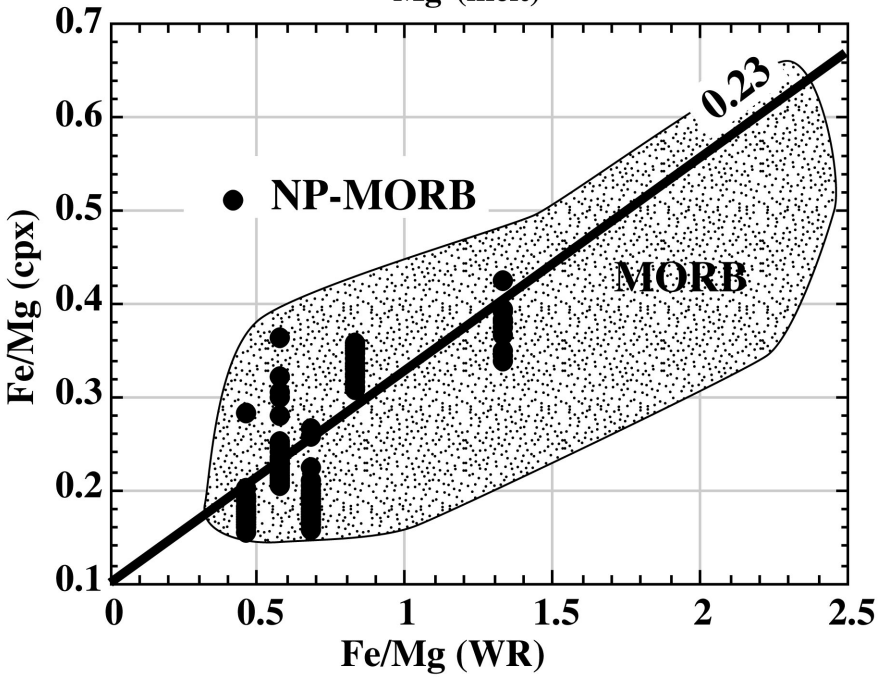


Komiya 1999, Doctor Thesis Fig. IV-9

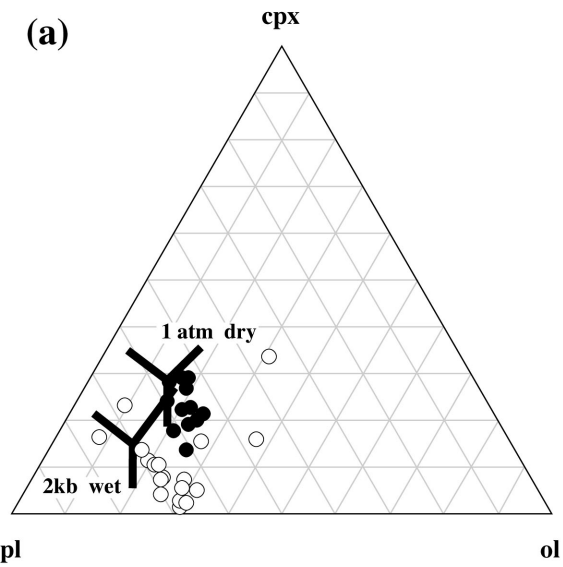


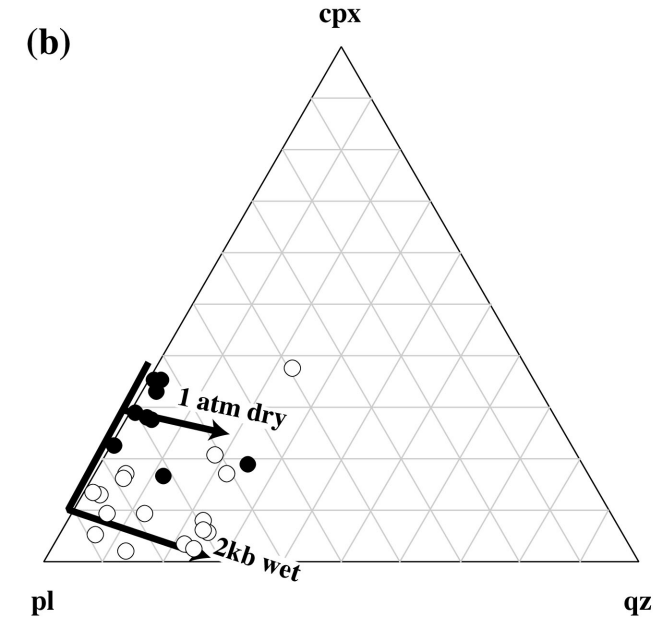


Komiya 1999, Doctor Thesis Fig. IV-10

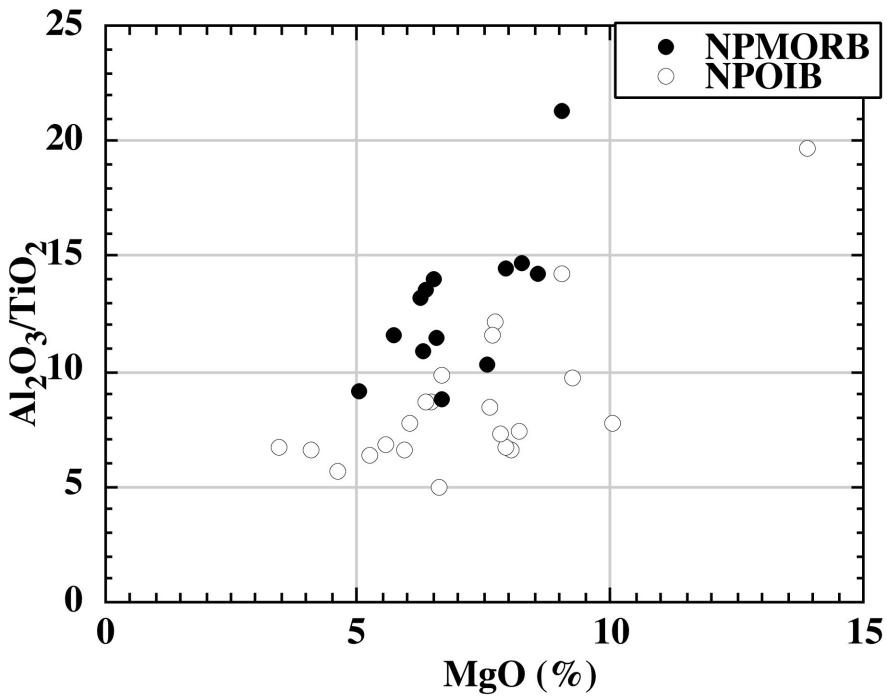


Komiya 1999, Doctor Thesis Fig. IV-11

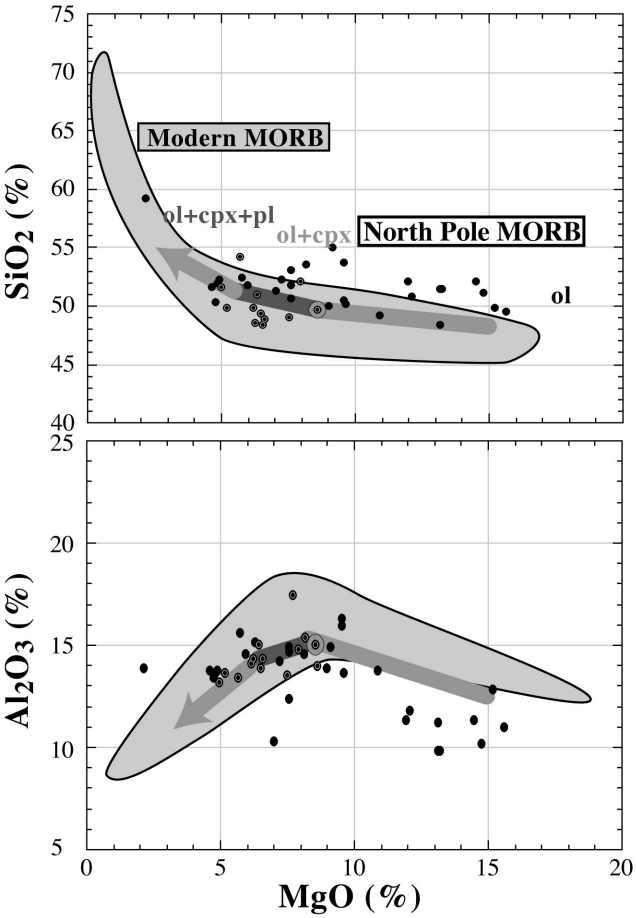


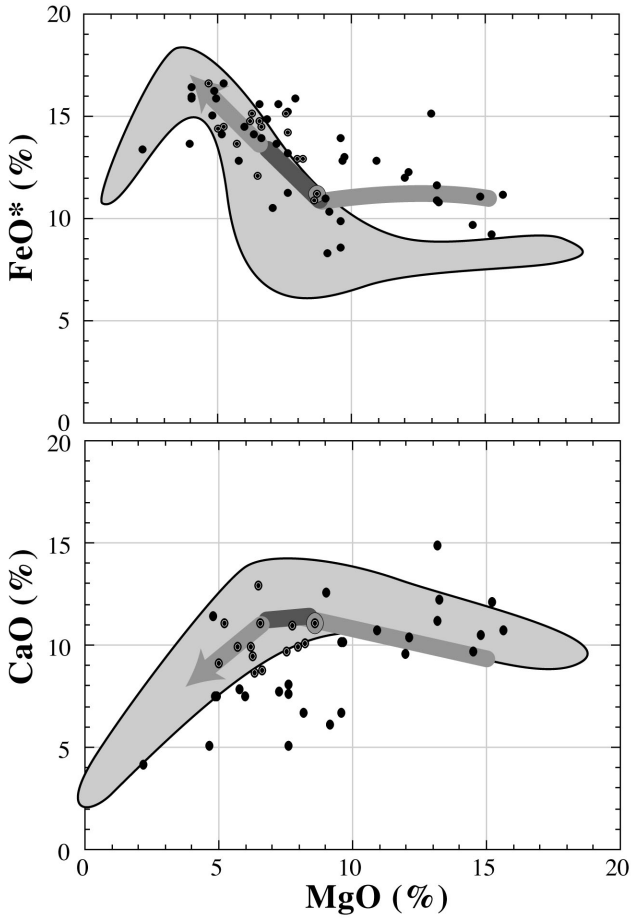


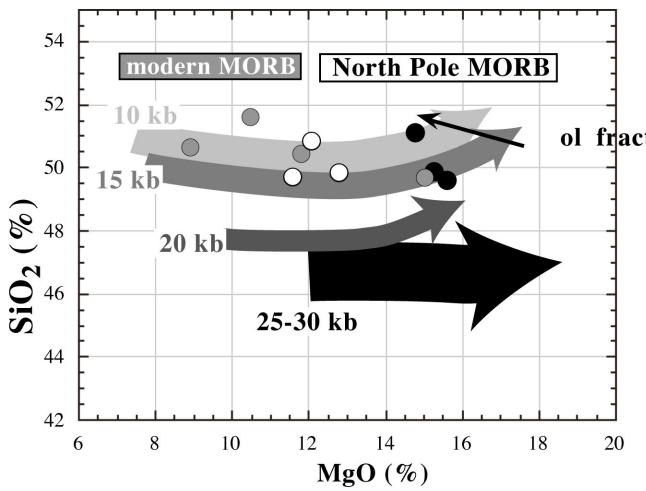


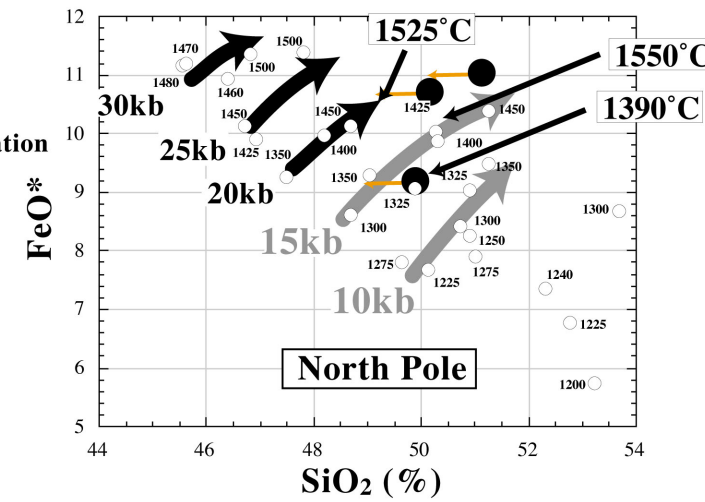


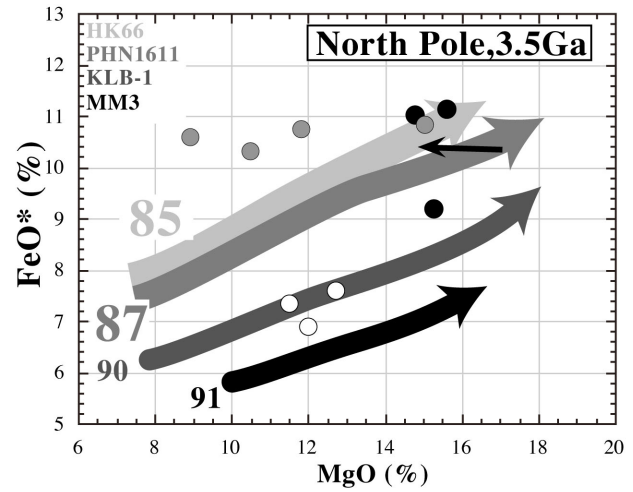


**Variation diagrams of major elements in North Pole MORB(3.5Ga), compared with melt compositions by high pressure melting experiment**

## Results

**pressure-------10-15kb**

**FeO content in source mantle-----**
**Mg#=85-87(FeO 10%)**

**PMT= ca. 1480˚C**

**Komiya 1999, Doctor Thesis Fig. IV-12**

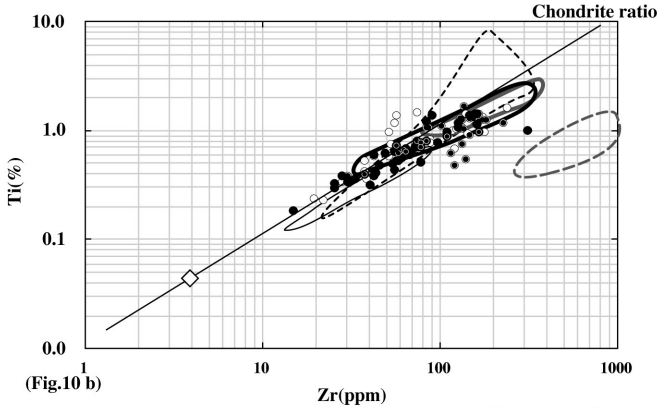


(Fig.10 b)

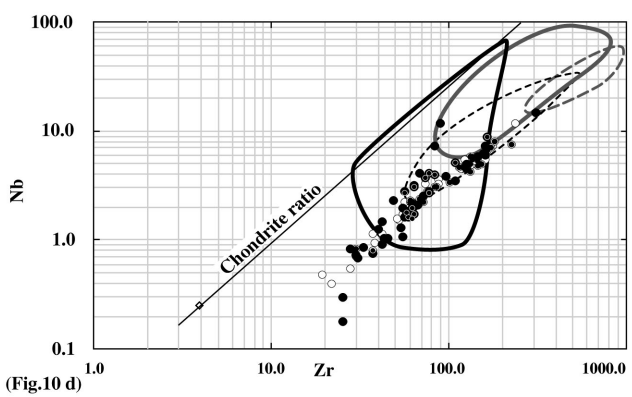


(Fig.10 d)

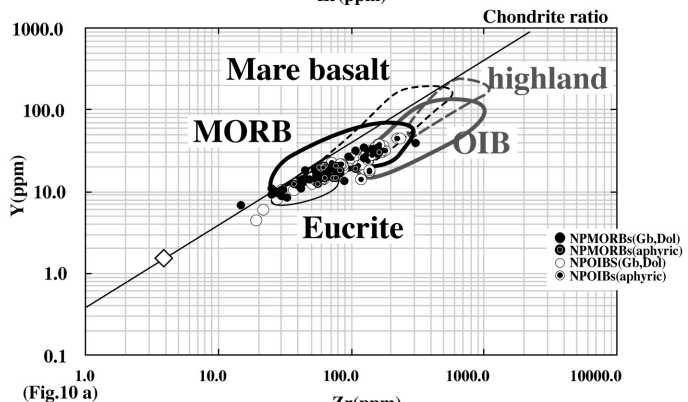


(Fig.10 a)

refractory element vs. volatile

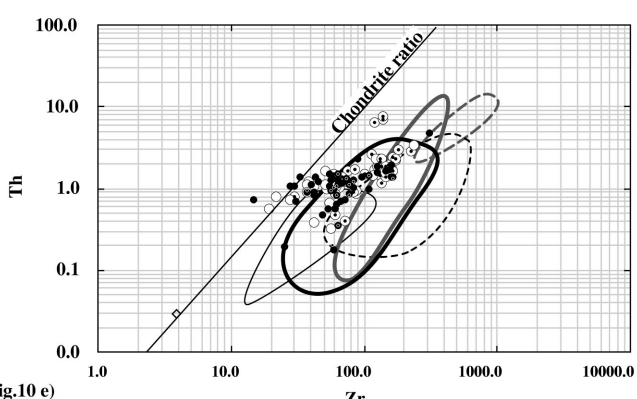


(Fig.10 e)

refractory elements vs. siderophile elements

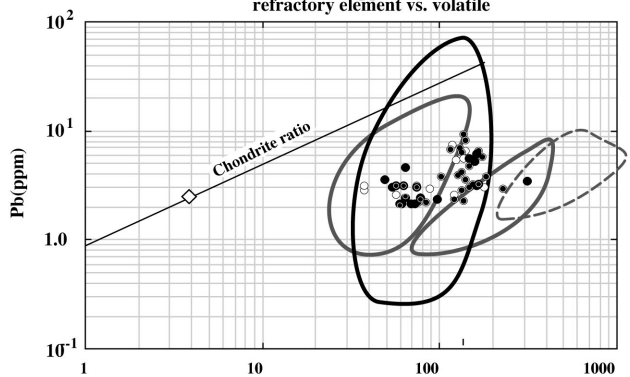


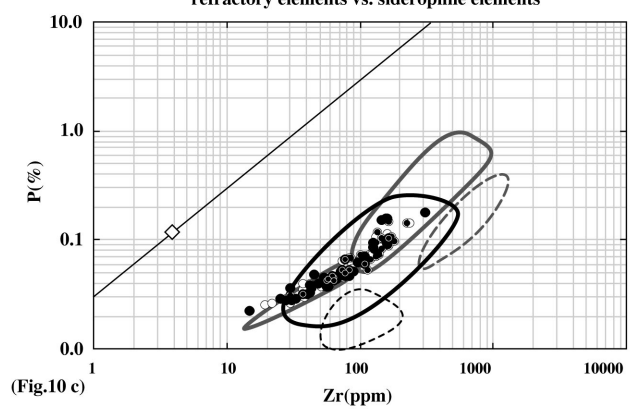


(Fig.10 c)

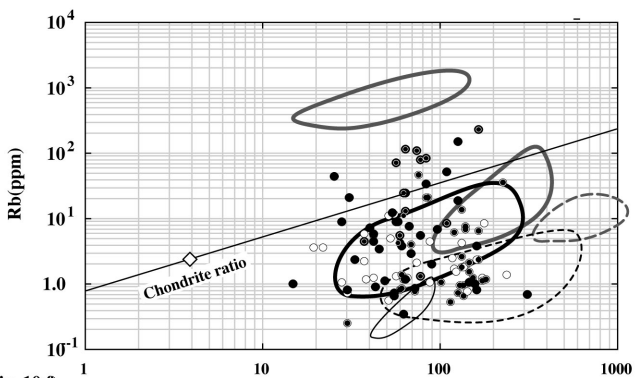


(Fig. 10 f)

refractory element vs. volatite

**Komiya 1999 Doctor Thesis Fig. IV-13**

Table 1 Chemical composition of aphyric MORBs

| sample | 95NP010 | E204 | E205 | E206 | E208 | E209 | E214 | F237 | B106 | E148 | E152 | 95NP106 | 97NP101 | 95NP507 |
|---|---|---|---|---|---|---|---|---|---|---|---|---|---|---|
| SiO2 | 49.4 | 49.0 | 49.1 | 48.3 | 49.8 | 49.9 | 48.5 | 51.0 | 52.1 | 54.2 | 50.0 | 49.8 | 51.6 | 50.0 |
| TiO2 | 1.07 | 1.63 | 1.33 | 1.22 | 1.07 | 1.32 | 1.31 | 1.12 | 1.03 | 1.17 | 0.65 | 1.06 | 1.45 | 1.04 |
| Al2O3 | 15.1 | 14.4 | 13.6 | 13.9 | 14.1 | 13.7 | 14.3 | 15.1 | 14.8 | 13.4 | 13.9 | 15.0 | 13.3 | 15.3 |
| FeOt | 12.0 | 14.4 | 15.1 | 14.7 | 14.8 | 14.4 | 15.1 | 14.1 | 12.8 | 13.6 | 11.0 | 10.8 | 14.4 | 11.7 |
| MnO | 0.25 | 0.21 | 0.24 | 0.26 | 0.28 | 0.28 | 0.22 | 0.22 | 0.20 | 0.21 | 0.21 | 0.25 | 0.31 | 0.27 |
| MgO | 6.50 | 6.66 | 7.54 | 6.56 | 6.23 | 5.24 | 6.30 | 6.33 | 7.94 | 5.74 | 9.01 | 8.57 | 5.03 | 8.24 |
| CaO | 13.0 | 8.84 | 9.74 | 11.1 | 9.98 | 11.1 | 9.53 | 8.68 | 9.95 | 9.96 | 12.6 | 11.1 | 9.15 | 9.56 |
| Na2O | 2.34 | 2.48 | 2.35 | 2.98 | 2.52 | 2.51 | 3.43 | 2.23 | 0.96 | 1.59 | 2.45 | 2.98 | 4.00 | 3.41 |
| K2O | 0.20 | 2.20 | 0.94 | 0.85 | 1.14 | 1.43 | 1.16 | 1.16 | 0.08 | 0.01 | 0.12 | 0.38 | 0.66 | 0.38 |
| P2O5 | 0.10 | 0.24 | 0.12 | 0.10 | 0.10 | 0.12 | 0.15 | 0.10 | 0.10 | 0.11 | 0.07 | 0.09 | 0.14 | 0.09 |
| total | 100 | 100 | 100 | 100 | 100 | 100 | 100 | 100 | 100 | 100 | 100 | 100 | 100 | 100 |
| Mg# | 49.0 | 45.1 | 47.1 | 44.2 | 42.9 | 39.3 | 42.7 | 44.5 | 52.4 | 42.9 | 59.4 | 58.5 | 38.4 | 55.7 |
| | | | | | | | | | | | | | | |
| Ni | 117 | 69 | 84 | 104 | 90 | 74 | 79 | 68 | 79 | 35 | 96 | 150 | 85 | 144 |
| Rb | 5.4 | 227.1 | 83.2 | 72.0 | 111.3 | 110.0 | 80.2 | 24.2 | 4.2 | 1.3 | 4.4 | 13 | 8.3 | 11 |
| Sr | 102 | 185 | 219 | 195 | 132 | 208 | 123 | 165 | 95 | 110 | 177 | 128 | 94 | 149 |
| Y | 19 | 31 | 18 | 13 | 15 | 15 | 15 | 20 | 19 | 21 | 12 | 21 | 19 | 20 |
| Zr | 60 | 167 | 83 | 57 | 64 | 74 | 79 | 63 | 59 | 78 | 38 | 64 | 110 | 62 |
| Nb | 1.6 | 8.9 | 3.9 | 2.7 | 3.1 | 3.7 | 4.1 | 2.0 | 1.8 | 2.7 | 0.8 | 1.7 | 5.1 | 1.6 |
| Ba | 176 | 344 | 161 | 317 | 160 | 134 | 171 | 1093 | 115 | 163 | 241 | 86 | 123 | 146 |
| Pb | 2.1 | 3.3 | 1.7 | 3.2 | 2.5 | 3.1 | 2.4 | 3.2 | 0.9 | 0.6 | 0.6 | 0.5 | 1.2 | 1.4 |
| Th | 1.0 | 1.3 | 1.2 | 0.9 | 1.5 | 1.3 | 1.1 | 0.8 | 0.2 | 0.8 | 0.9 | 0.3 | 1.4 | 1.0 |

Total iron as FeO

Table 2 Chemical composition of coarse-grained MORBs

| sample | 95NP005 | 95NP012 | A120 | C179 | C183 | C209 | D144B | E197 | E200 | F167 | C011 | C017 | C018 | C182 | C232 | F219 | G136 | B091 | B101 | B164 | C094 | D122 | E067 | E072 | E104 | E174 | E174-2 | E177 |
|---|---|---|---|---|---|---|---|---|---|---|---|---|---|---|---|---|---|---|---|---|---|---|---|---|---|---|---|---|
| SiO2 | 51.5 | 50.2 | 50.2 | 51.4 | 51.5 | 48.4 | 50.6 | 51.9 | 49.0 | 49.4 | 49.6 | 51.1 | 50.8 | 45.2 | 51.0 | 49.6 | 52.0 | 59.2 | 51.8 | 52.5 | 53.5 | 52.0 | 50.5 | 51.0 | 52.4 | 52.4 | 52.0 | 50.3 |
| TiO2 | 0.64 | 1.61 | 0.93 | 1.05 | 0.59 | 2.01 | 1.78 | 1.97 | 1.10 | 1.08 | 0.50 | 0.55 | 0.83 | 2.31 | 1.08 | 0.99 | 0.72 | 1.69 | 1.00 | 1.31 | 1.06 | 1.89 | 0.59 | 1.16 | 1.18 | 2.40 | 2.38 | 2.28 |
| Al2O3 | 9.80 | 15.2 | 13.7 | 10.3 | 9.86 | 6.39 | 12.4 | 14.6 | 8.12 | 15.6 | 11.0 | 10.2 | 11.8 | 4.9 | 6.6 | 13.6 | 8.0 | 13.9 | 15.0 | 15.6 | 14.6 | 14.3 | 16.0 | 13.8 | 14.3 | 13.7 | 13.7 | 13.4 |
| FeOt | 11.5 | 12.9 | 12.8 | 10.4 | 10.8 | 15.9 | 15.2 | 14.5 | 15.1 | 13.9 | 11.1 | 11.0 | 12.3 | 20.1 | 13.2 | 13.0 | 11.9 | 13.3 | 11.2 | 12.8 | 12.9 | 14.1 | 9.8 | 14.8 | 15.6 | 15.9 | 16.2 | 15.0 |
| MnO | 0.21 | 0.24 | 0.20 | 0.21 | 0.19 | 0.29 | 0.21 | 0.20 | 0.27 | 0.17 | 0.20 | 0.20 | 0.20 | 0.33 | 0.24 | 0.20 | 0.24 | 0.11 | 0.20 | 0.18 | 0.17 | 0.18 | 0.17 | 0.32 | 0.21 | 0.23 | 0.23 | 0.27 |
| MgO | 13.2 | 6.77 | 9.69 | 7.08 | 13.3 | 10.5 | 7.65 | 6.01 | 13.0 | 9.62 | 15.6 | 14.8 | 12.1 | 15.0 | 12.5 | 9.75 | 18.8 | 2.20 | 7.62 | 5.79 | 8.17 | 5.18 | 9.60 | 6.83 | 7.28 | 4.92 | 4.91 | 4.80 |
| CaO | 11.2 | 9.63 | 10.2 | 19.4 | 12.3 | 15.3 | 8.12 | 7.55 | 11.9 | 8.27 | 10.7 | 10.5 | 10.5 | 11.7 | 14.1 | 10.8 | 8.00 | 4.17 | 7.58 | 7.83 | 6.66 | 6.93 | 10.2 | 9.17 | 7.80 | 7.57 | 7.56 | 11.4 |
| Na2O | 1.65 | 2.39 | 2.09 | 0.00 | 1.14 | 0.48 | 3.54 | 2.14 | 1.03 | 1.93 | 0.83 | 0.93 | 1.16 | 0.24 | 1.07 | 1.73 | 0.25 | 5.01 | 5.28 | 3.55 | 2.82 | 5.06 | 3.00 | 2.83 | 1.15 | 2.53 | 2.69 | 2.04 |
| K2O | 0.14 | 0.93 | 0.15 | 0.00 | 0.30 | 0.67 | 0.26 | 0.94 | 0.42 | 0.00 | 0.40 | 0.61 | 0.29 | 0.12 | 0.15 | 0.15 | 0.02 | 0.00 | 0.23 | 0.26 | - | 0.15 | 0.03 | 0.00 | - | - | - | - |
| P2O5 | 0.06 | 0.16 | 0.10 | 0.09 | 0.06 | 0.10 | 0.19 | 0.21 | 0.10 | 0.10 | 0.06 | 0.06 | 0.10 | 0.11 | 0.10 | 0.09 | 0.09 | 0.40 | 0.10 | 0.14 | 0.10 | 0.20 | 0.07 | 0.10 | 0.12 | 0.35 | 0.35 | 0.35 |
| total | 100 | 100 | 100 | 100 | 100 | 100 | 100 | 100 | 100 | 100 | 100 | 100 | 100 | 100 | 100 | 100 | 100 | 100 | 100 | 100 | 100 | 100 | 100 | 100 | 100 | 100 | 100 | 100 |
| Mg# | 67.0 | 48.3 | 57.5 | 54.7 | 68.7 | 54.0 | 47.3 | 42.5 | 60.4 | 55.3 | 71.4 | 70.5 | 63.7 | 57.1 | 62.8 | 57.3 | 73.8 | 22.8 | 54.8 | 44.6 | 53.0 | 39.5 | 63.5 | 45.1 | 45.4 | 35.6 | 35.0 | 36.2 |
| Ni | 259 | 86 | 188 | 133 | 266 | 239 | 116 | 57 | 323 | 121 | 345 | 301 | 256 | 622 | 200 | 191 | 407 | 2 | 77 | 100 | 62 | 51 | 92 | 35 | 35 | 40 | 40 | 38 |
| Rb | 8.7 | 51.0 | 3.8 | 1.1 | 21.2 | 33.5 | 18.1 | 151.0 | 23.7 | 0.6 | 42.5 | 44.3 | 11.9 | 2.0 | 2.9 | 4.4 | 0.7 | 0.7 | 7.5 | 6.6 | 0.3 | 3.8 | 2.3 | 1.2 | 0.9 | 0.8 | 1.0 | 1.0 |
| Sr | 124 | 200 | 112 | 560 | 76 | 68 | 80 | 135 | 30 | 67 | 49 | 82 | 88 | 121 | 58 | 176 | 25 | 76 | 97 | 161 | 108 | 127 | 174 | 121 | 60 | 98 | 99 | 133 |
| Y | 9.4 | 32 | 16 | 14 | 11 | 17 | 25 | 35 | 15 | 16 | 11 | 9.4 | 19 | 14 | 15 | 11 | 14 | 40 | 17 | 27 | 17 | 29 | 8 | 19 | 20 | 34 | 33 | 33 |
| Zr | 28 | 109 | 61 | 49 | 31 | 84 | 126 | 128 | 65 | 55 | 26 | 26 | 55 | 90 | 68 | 42 | 55 | 307 | 67 | 98 | 63 | 163 | 33 | 64 | 73 | 160 | 157 | 147 |
| Nb | 0.8 | 3.5 | 1.8 | 2.3 | 0.7 | 7.2 | 5.0 | 4.5 | 3.1 | 1.1 | 0.2 | 0.3 | 1.3 | 11.7 | 4.1 | 1.5 | 2.0 | 14.7 | 2.1 | 3.9 | 2.2 | 7.2 | 0.8 | 2.0 | 2.6 | 6.1 | 6.1 | 5.8 |
| Ba | 162 | 4269 | 179 | 445 | 834 | 271 | 101 | 307 | 202 | 16 | 114 | 171 | 73 | 1398 | 83 | 412 | 62 | 26 | 658 | 252 | 30 | 114 | 41 | 41 | 27 | 52 | 63 | 838 |
| Pb | 0.0 | 1.8 | 2.2 | 3.6 | 1.1 | 0.7 | 0.6 | 1.1 | 1.3 | - | - | 1.9 | 3.1 | 1.7 | 2.1 | 1.9 | 1.7 | 3.5 | 0.8 | 2.4 | 1.5 | 3.2 | 1.4 | 4.7 | 2.2 | 6.2 | 5.3 | 5.7 |
| Th | 1.0 | 1.0 | 0.5 | 0.5 | 0.7 | 1.0 | 1.6 | 1.8 | 1.1 | 1.0 | 0.2 | -0.3 | 0.5 | 2.3 | 1.1 | 0.8 | 1.4 | 4.6 | 0.7 | 1.4 | 0.6 | 1.9 | 1.4 | 1.3 | 0.7 | 1.4 | 1.6 | 1.6 |
| La | | | | | | | | | | | 1.39 | 1.64 | | | | | | | | | | | | | | | | |
| Ce | | | | | | | | | | | 3.25 | 3.95 | | | | | | | | | | | | | | | | |
| Pr | | | | | | | | | | | 0.47 | 0.65 | | | | | | | | | | | | | | | | |
| Nd | | | | | | | | | | | 2.24 | 3.10 | | | | | | | | | | | | | | | | |
| Sm | | | | | | | | | | | 0.78 | 1.05 | | | | | | | | | | | | | | | | |
| Eu | | | | | | | | | | | 0.35 | 0.46 | | | | | | | | | | | | | | | | |
| Gd | | | | | | | | | | | 1.13 | 1.46 | | | | | | | | | | | | | | | | |
| Tb | | | | | | | | | | | 0.25 | 0.26 | | | | | | | | | | | | | | | | |
| Dy | | | | | | | | | | | 1.85 | 1.71 | | | | | | | | | | | | | | | | |
| Ho | | | | | | | | | | | 0.43 | 0.37 | | | | | | | | | | | | | | | | |
| Er | | | | | | | | | | | 1.23 | 1.06 | | | | | | | | | | | | | | | | |
| Tm | | | | | | | | | | | 0.18 | 0.16 | | | | | | | | | | | | | | | | |
| Yb | | | | | | | | | | | 1.15 | 1.05 | | | | | | | | | | | | | | | | |
| Lu | | | | | | | | | | | 0.17 | 0.16 | | | | | | | | | | | | | | | | |

Total iron as FeO

Table 2 (Continued)

| sample | E182 | E313 | E313-2 | G211 | E166 | E171 | E278 | G055 | G214 |
|---|---|---|---|---|---|---|---|---|---|
| SiO2 | 53.7 | 51.7 | 51.7 | 53.1 | 48.4 | 52.2 | 49.9 | 52.1 | 49.2 |
| TiO2 | 0.69 | 0.89 | 0.89 | 0.64 | 0.57 | 0.53 | 0.31 | 0.87 | 0.81 |
| Al2O3 | 16.3 | 15.0 | 15.0 | 16.0 | 11.3 | 11.4 | 12.8 | 11.3 | 13.8 |
| FeOt | 8.48 | 11.4 | 11.4 | 8.27 | 10.8 | 9.65 | 9.20 | 11.9 | 12.8 |
| MnO | 0.15 | 0.20 | 0.20 | 0.17 | 0.20 | 0.18 | 0.17 | 0.19 | 0.20 |
| MgO | 9.60 | 7.71 | 7.71 | 9.11 | 13.2 | 14.5 | 15.2 | 12.0 | 10.9 |
| CaO | 6.72 | 7.24 | 7.24 | 7.51 | 15.0 | 9.66 | 12.2 | 9.61 | 10.7 |
| Na2O | 4.21 | 5.47 | 5.47 | 4.96 | 0.52 | 1.60 | 0.18 | 1.72 | 1.28 |
| K2O | 0.00 | 0.23 | 0.23 | 0.14 | 0.00 | 0.26 | 0.00 | 0.19 | 0.09 |
| P2O5 | 0.08 | 0.08 | 0.08 | 0.07 | 0.08 | 0.07 | 0.05 | 0.11 | 0.11 |
| total | 100 | 100 | 100 | 100 | 100 | 100 | 100 | 100 | 100 |
| Mg# | 66.8 | 54.6 | 54.6 | 66.3 | 68.4 | 72.8 | 74.7 | 64.1 | 60.4 |
| | | | | | | | | | |
| Ni | 80 | 82 | 81 | 85 | 170 | 300 | 328 | 250 | 252 |
| Rb | 0.9 | 8.9 | 8.7 | 5.6 | 0.8 | 7.3 | 1.0 | 5.5 | 3.4 |
| Sr | 95 | 101 | 100 | 140 | 247 | 112 | 91 | 126 | 86 |
| Y | 13 | 15 | 14 | 13 | 8.9 | 12 | 6.7 | 21 | 18 |
| Zr | 43 | 59 | 57 | 42 | 31 | 40 | 15 | 79 | 46 |
| Nb | 1.0 | 1.7 | 1.6 | 0.9 | 0.7 | 1.2 | 0.0 | 2.8 | 1.0 |
| Ba | 32 | 898 | 899 | 177 | 27 | 85 | 62 | 441 | 118 |
| Pb | 1.3 | 0.2 | 0.5 | 0.9 | 1.1 | 1.2 | 0.4 | 0.9 | 0.8 |
| Th | 1.4 | 1.3 | 1.3 | 0.9 | 1.0 | 1.1 | 0.7 | 1.2 | 1.2 |
| | | | | | | | | | |
| La | | | | | 1.70 | 3.56 | 0.56 | | |
| Ce | | | | | 4.84 | 8.07 | 1.39 | | |
| Pr | | | | | 0.74 | 1.12 | 0.21 | | |
| Nd | | | | | 3.46 | 5.31 | 0.98 | | |
| Sm | | | | | 1.13 | 1.49 | 0.37 | | |
| Eu | | | | | 0.46 | 0.54 | 0.17 | | |
| Gd | | | | | 1.25 | 1.67 | 0.55 | | |
| Tb | | | | | 0.25 | 0.32 | 0.13 | | |
| Dy | | | | | 1.66 | 2.10 | 0.93 | | |
| Ho | | | | | 0.35 | 0.45 | 0.21 | | |
| Er | | | | | 1.02 | 1.35 | 0.64 | | |
| Tm | | | | | 0.15 | 0.19 | 0.09 | | |
| Yb | | | | | 1.01 | 1.24 | 0.61 | | |
| Lu | | | | | 0.16 | 0.20 | 0.09 | | |

Total iron as FeO

Table 3 Chemical composition of altered MORBs

| sample | 95NP014 | 95NP047 | 95NP050 | C100 | C178 | C206 | C233 | E190 | E207 | F137 | F148 | F149 | F175 | F238 | F240 | B075 | B092 | B107 | C079 | C092 | E060 | E123 | E151 | E321 | G223 |
|---|---|---|---|---|---|---|---|---|---|---|---|---|---|---|---|---|---|---|---|---|---|---|---|---|---|
| SiO2 | 50.5 | 43.2 | 48.4 | 51.5 | 48.3 | 48.4 | 46.8 | 48.3 | 48.6 | 49.4 | 50.2 | 60.3 | 44.9 | 48.5 | 48.7 | 62.0 | 50.0 | 48.7 | 47.5 | 66.0 | 52.0 | 47.6 | 49.0 | 66.0 | 51.1 |
| TiO2 | 1.02 | 1.19 | 1.01 | 1.05 | 1.12 | 1.55 | 0.94 | 1.10 | 1.24 | 0.52 | 0.63 | 1.87 | 0.98 | 1.19 | 1.33 | 1.92 | 1.78 | 0.94 | 0.72 | 0.58 | 1.39 | 1.16 | 0.72 | 0.57 | 0.69 |
| Al2O3 | 13.4 | 8.61 | 14.7 | 15.0 | 15.7 | 15.0 | 6.1 | 15.4 | 13.6 | 6.61 | 7.38 | 11.8 | 14.9 | 12.0 | 10.2 | 14.5 | 13.6 | 13.9 | 13.6 | 10.3 | 10.3 | 13.9 | 13.7 | 10.3 | 14.7 |
| FeOt | 13.0 | 16.1 | 11.3 | 15.3 | 11.9 | 11.2 | 13.3 | 12.0 | 13.4 | 11.1 | 11.3 | 16.7 | 10.2 | 13.6 | 13.8 | 12.5 | 13.5 | 11.9 | 11.6 | 10.2 | 12.3 | 12.8 | 11.1 | 9.9 | 8.56 |
| MnO | 0.25 | 0.29 | 0.20 | 0.06 | 0.22 | 0.19 | 0.24 | 0.28 | 0.26 | 0.21 | 0.21 | 0.17 | 0.19 | 0.20 | 0.25 | 0.03 | 0.13 | 0.21 | 0.21 | 0.05 | 0.19 | 0.19 | 0.22 | 0.05 | 0.18 |
| MgO | 6.28 | 15.8 | 8.21 | 11.3 | 5.22 | 7.16 | 12.4 | 5.36 | 6.31 | 20.6 | 17.3 | 3.89 | 6.17 | 8.95 | 8.94 | 3.24 | 6.42 | 7.78 | 7.38 | 8.53 | 5.43 | 6.88 | 8.09 | 8.39 | 10.5 |
| CaO | 10.2 | 8.74 | 9.57 | 0.20 | 11.4 | 9.79 | 12.9 | 10.1 | 8.69 | 6.54 | 7.75 | 0.45 | 9.78 | 4.94 | 10.1 | 0.31 | 4.15 | 8.39 | 8.24 | 0.16 | 14.0 | 9.38 | 9.47 | 0.17 | 4.43 |
| Na2O | 3.40 | 0.09 | 1.85 | - | 3.10 | 2.36 | 1.04 | 1.14 | 3.10 | 0.21 | 0.94 | - | 2.56 | 3.52 | 1.87 | - | 4.08 | 0.63 | 2.64 | -0.25 | - | 1.19 | 3.98 | - | 4.34 |
| K2O | 0.14 | 0.07 | 1.45 | - | 0.25 | 0.96 | 0.11 | 2.86 | 1.22 | 0.02 | 0.02 | 0.36 | 0.08 | 0.11 | 1.06 | 1.76 | 0.00 | 0.08 | - | -0.01 | - | - | 0.02 | - | 0.11 |
| P2O5 | 0.09 | 0.11 | 0.09 | 0.07 | 0.11 | 0.15 | 0.09 | 0.12 | 0.11 | 0.07 | 0.08 | 0.27 | 0.09 | 0.10 | 0.12 | 0.19 | 0.19 | 0.09 | 0.07 | 0.04 | 0.11 | 0.10 | 0.07 | 0.06 | 0.08 |
| total | 99.8 | 96.0 | 98.0 | 95.9 | 98.6 | 98.1 | 95.4 | 97.9 | 97.9 | 96.5 | 97.0 | 97.4 | 91.0 | 94.6 | 97.9 | 97.7 | 95.4 | 93.9 | 93.3 | 96.7 | 96.9 | 94.6 | 97.7 | 96.3 | 95.7 |
| Ni | 129 | 807 | 119 | 207 | 99 | 89 | 283 | 91 | 86 | 498 | 402 | 17 | 124 | 115 | 134 | 57 | 48 | 93 | 63 | 322 | 138 | 82 | 82 | 179 | 101 |
| Rb | 1.6 | 5.7 | 86 | 0.5 | 4.3 | 111 | 1.7 | 126 | 113 | 0.8 | 1.1 | 11 | 4.5 | 4.5 | 82 | 50 | 1.1 | 4.2 | 1.2 | 0.3 | 0.8 | 0.9 | 1.4 | 0.7 | 5.2 |
| Sr | 112.1 | 35.1 | 153 | 9.3 | 142 | 172 | 48 | 126 | 211 | 18 | 22 | 11 | 62 | 100 | 79 | 22 | 152 | 114 | 124 | 11 | 412 | 151 | 89 | 9 | 217 |
| Y | 20.1 | 13.5 | 21 | 20 | 23 | 25 | 12 | 16 | 14 | 12 | 15 | 47 | 14 | 15 | 20 | 28 | 28 | 16 | 13 | 14 | 15 | 21 | 13 | 8 | 14 |
| Zr | 59.5 | 63.9 | 60 | 54 | 66 | 95 | 58 | 137 | 70 | 42 | 54 | 237 | 56 | 64 | 93 | 168 | 157 | 56 | 44 | 33 | 71 | 71 | 41 | 25 | 46 |
| Nb | 1.5 | 8.1 | 1.0 | 1.5 | 1.7 | 3.6 | 3.7 | 6.0 | 3.6 | 1.4 | 1.8 | 8.8 | 1.8 | 2.5 | 4.4 | 8.0 | 7.1 | 1.6 | 0.9 | 0.9 | 2.5 | 2.0 | 1.0 | 0.5 | 1.1 |
| Ba | 297.8 | 26.6 | 1062 | 50 | 232 | 169 | 118 | 3735 | 256 | 47 | 22 | 33 | 17 | 274 | 167 | 137 | 540 | 59 | 390 | 85 | 88 | 602 | 131 | 342 | 6728 |
| Pb | 2.0 | 0.2 | 4.1 | 0.7 | 1.3 | 2.2 | 1.0 | 2.8 | 2.5 | 1.1 | 1.1 | 0.9 | 1.4 | 1.9 | 1.0 | 5.4 | 3.6 | 1.4 | 0.6 | 0.4 | 4.6 | 1.4 | 0.9 | 5.0 | 2.9 |
| Th | 0.7 | 1.2 | 0.8 | 0.8 | 1.1 | 1.1 | 0.4 | 2.2 | 0.6 | 0.8 | 1.5 | 1.3 | 0.6 | 0.6 | 1.7 | 2.7 | 2.5 | 1.2 | 1.0 | 0.3 | 1.0 | 1.0 | 0.7 | 0.2 | 0.7 |

Total iron as FeO

Table 4 Chemical composition of aphyric OIBs

| sample | B159 | B171 | E332 | F188 | G066 | 95NP154 | 95NP174 | 95NP033 | 95NP034 | 95NP063 | 95PN001 | B082 | B085 | E027 | E028 | E046 | E047 | E228 | E231 | E255 | G093 | G119 | G119-2 | G177 |
|---|---|---|---|---|---|---|---|---|---|---|---|---|---|---|---|---|---|---|---|---|---|---|---|---|
| $SiO_2$ | 49.6 | 51.9 | 51.7 | 58.1 | 52.7 | 49.6 | 52.1 | 54.6 | 51.3 | 54.3 | 53.4 | 54.4 | 53.1 | 52.2 | 54.4 | 51.8 | 53.0 | 51.6 | 52.7 | 52.8 | 50.7 | 51.7 | 51.1 | 49.3 |
| $TiO_2$ | 0.64 | 1.25 | 2.19 | 0.80 | 1.13 | 2.79 | 2.07 | 2.15 | 1.87 | 2.00 | 1.83 | 1.03 | 1.73 | 2.19 | 1.24 | 2.01 | 2.12 | 2.14 | 2.10 | 1.51 | 2.39 | 1.79 | 1.78 | 0.92 |
| $Al_2O_3$ | 12.6 | 15.1 | 14.3 | 15.7 | 10.9 | 13.8 | 13.7 | 14.1 | 14.5 | 13.6 | 14.1 | 14.7 | 14.7 | 13.8 | 14.3 | 15.0 | 14.3 | 15.5 | 14.1 | 14.9 | 13.5 | 15.6 | 15.4 | 16.7 |
| FeOt | 12.3 | 14.0 | 16.2 | 9.5 | 12.5 | 15.6 | 16.4 | 12.8 | 15.6 | 16.3 | 14.2 | 10.2 | 14.2 | 16.6 | 13.2 | 15.1 | 15.8 | 12.4 | 15.4 | 13.9 | 16.3 | 12.2 | 13.1 | 10.7 |
| MnO | 0.24 | 0.20 | 0.20 | 0.11 | 0.24 | 0.23 | 0.27 | 0.19 | 0.15 | 0.14 | 0.20 | 0.16 | 0.22 | 0.20 | 0.18 | 0.22 | 0.23 | 0.17 | 0.20 | 0.18 | 0.25 | 0.20 | 0.20 | 0.14 |
| MgO | 13.9 | 7.7 | 5.90 | 2.20 | 9.26 | 6.59 | 4.07 | 8.02 | 10.1 | 5.58 | 6.05 | 9.03 | 7.61 | 5.22 | 7.64 | 8.19 | 7.91 | 7.83 | 3.44 | 6.64 | 4.59 | 6.45 | 6.36 | 4.33 |
| CaO | 9.6 | 8.0 | 4.46 | 7.27 | 10.4 | 10.0 | 5.21 | 5.33 | 5.39 | 6.74 | 5.87 | 6.10 | 5.06 | 6.99 | 5.8 | 3.9 | 3.2 | 5.6 | 6.8 | 7.6 | 5.0 | 6.9 | 6.8 | 10.9 |
| $Na_2O$ | 1.01 | 1.70 | 3.78 | 6.10 | 0.18 | 1.19 | 5.88 | 2.66 | 0.94 | - | 4.29 | 3.09 | 3.24 | 2.55 | 2.97 | 3.57 | 3.21 | 4.63 | 4.98 | 2.24 | 4.76 | 4.27 | 4.28 | 5.42 |
| $K_2O$ | -0.02 | 0.00 | 0.99 | 0.12 | 2.48 | - | 0.05 | - | - | 1.26 | - | - | - | 0.01 | 0.05 | 0.05 | 0.00 | 0.00 | 0.00 | 0.02 | 0.37 | 0.72 | 0.73 | 0.19 |
| $P_2O_5$ | 0.07 | 0.11 | 0.21 | 0.15 | 0.10 | 0.26 | 0.18 | 0.20 | 0.16 | 0.32 | 0.18 | 0.12 | 0.17 | 0.19 | 0.16 | 0.20 | 0.22 | 0.22 | 0.24 | 0.23 | 0.33 | 0.15 | 0.16 | 0.17 |
| total | 100 | 100 | 100 | 100 | 100 | 100 | 100 | 100 | 100 | 100 | 100 | 100 | 100 | 100 | 100 | 100 | 100 | 100 | 100 | 100 | 100 | 100 | 100 | 100 |
| Mg# | 66.8 | 49.6 | 39.3 | 29.3 | 56.8 | 42.9 | 30.7 | 52.8 | 53.5 | 37.9 | 43.2 | 61.2 | 48.8 | 35.9 | 50.8 | 49.1 | 47.1 | 52.9 | 28.5 | 45.9 | 33.4 | 48.5 | 46.3 | 41.8 |
| Ni | 184 | 89 | 39 | 90 | 117 | 29 | 11 | 42 | 51 | 18 | 35 | 78 | 64 | 16 | 55 | 48 | 29 | 53 | 13 | 57 | 44 | 67 | 66 | 91 |
| Rb | 0.2 | 0.7 | 13.3 | 6.0 | 45.2 | 0.9 | 1.7 | 0.9 | 1.1 | 35 | 0.7 | 0.5 | 0.7 | 1.5 | 2.5 | 2.4 | 1.2 | 1.2 | 1.1 | 2.0 | 6.4 | 20.6 | 20.4 | 7.5 |
| Sr | 125 | 160 | 141 | 103 | 233 | 100 | 152 | 123 | 112 | 45 | 155 | 137 | 146 | 146 | 150 | 218 | 128 | 158 | 165 | 124 | 136 | 175 | 174 | 458 |
| Y | 10 | 22 | 32 | 14 | 17 | 31 | 28 | 28 | 26 | 44 | 25 | 21 | 24 | 30 | 24 | 31 | 32 | 35 | 32 | 28 | 37 | 22 | 21 | 18 |
| Zr | 30 | 73 | 132 | 121 | 76 | 137 | 133 | 129 | 103 | 225 | 128 | 114 | 137 | 145 | 133 | 164 | 181 | 155 | 173 | 145 | 166 | 86 | 85 | 140 |
| Nb | 0.8 | 2.2 | 5.0 | 4.6 | 2.8 | 5.5 | 5.8 | 4.5 | 3.4 | 7.6 | 4.9 | 4.7 | 5.9 | 4.7 | 4.3 | 7.2 | 8.1 | 5.0 | 6.9 | 5.3 | 6.5 | 3.1 | 3.1 | 5.6 |
| Ba | 102 | 53 | 129 | 104 | 174 | 15 | 47 | 493 | 665 | 182 | 11 | 716 | 113 | 1039 | 219 | 315 | 389 | 181 | 27 | 392 | 148 | 150 | 152 | 213 |
| Pb | 1.8 | 0.39 | 4.3 | 2.3 | 2.2 | 2.3 | 2.9 | 7.1 | 3.9 | 2.9 | 4.0 | 6.7 | 9.5 | 4.8 | 6.5 | 6.6 | 3.8 | 3.2 | 5.7 | 3.1 | 1.5 | 0.8 | 2.2 | 8.4 |
| Th | 0.77 | 0.39 | 1.4 | 6.4 | 1.6 | 1.1 | 2.2 | 1.8 | 1.5 | 2.8 | 1.8 | 2.6 | 1.8 | 1.3 | 2.0 | 2.4 | 2.9 | 1.9 | 2.2 | 1.8 | 1.6 | 1.7 | 0.9 | 6.8 |
| La | | | | | 6.76 | | | | 7.49 | | | | | | | | | | | | | | | |
| Ce | | | | | 16.6 | | | | 19.1 | | | | | | | | | | | | | | | |
| Pr | | | | | 2.20 | | | | 2.40 | | | | | | | | | | | | | | | |
| Nd | | | | | 10.3 | | | | 10.9 | | | | | | | | | | | | | | | |
| Sm | | | | | 2.80 | | | | 2.87 | | | | | | | | | | | | | | | |
| Eu | | | | | 1.41 | | | | 1.00 | | | | | | | | | | | | | | | |
| Gd | | | | | 4.05 | | | | 3.29 | | | | | | | | | | | | | | | |
| Tb | | | | | 0.57 | | | | 0.47 | | | | | | | | | | | | | | | |
| Dy | | | | | 3.23 | | | | 2.77 | | | | | | | | | | | | | | | |
| Ho | | | | | 0.63 | | | | 0.56 | | | | | | | | | | | | | | | |
| Er | | | | | 1.88 | | | | 1.58 | | | | | | | | | | | | | | | |
| Tm | | | | | 0.26 | | | | 0.26 | | | | | | | | | | | | | | | |
| Yb | | | | | 1.72 | | | | 1.85 | | | | | | | | | | | | | | | |
| Lu | | | | | 0.24 | | | | 0.27 | | | | | | | | | | | | | | | |

Total iron as FeO

Table 5 Chemical composition of coarse-grained OIBs

| sample | B099 | B100 | D109 | E109 | E126 | E126-2 | 95NP164 | 95NP166 | 95NP173 | 95NP059 | 95NP069 | 95NP110 | 95PN009 | A099 | C115 | C116 | C117 | C119 | C128 | C136 | D016 | D065 | D129 | D132 | E034 | E035 | E050 | E227 | E256 | G196 | G260 | G272 | G273 | G279 | G279-2 |
|---|---|---|---|---|---|---|---|---|---|---|---|---|---|---|---|---|---|---|---|---|---|---|---|---|---|---|---|---|---|---|---|---|---|---|
| $SiO_2$ | 53.3 | 49.7 | 52.5 | 50.7 | 42.4 | 42.1 | 55.0 | 55.9 | 50.3 | 52.0 | 52.7 | 48.9 | 51.6 | 48.9 | 51.9 | 51.7 | 49.0 | 51.4 | 52.5 | 55.4 | 46.0 | 52.4 | 49.2 | 49.0 | 50.2 | 51.3 | 54.3 | 53.5 | 52.9 | 50.7 | 52.7 | 53.2 | 51.9 | 51.9 | 51.1 |
| $TiO_2$ | 0.66 | 1.26 | 0.61 | 0.96 | 0.39 | 0.39 | 2.36 | 1.61 | 1.05 | 1.14 | 1.66 | 0.71 | 1.79 | 0.98 | 0.56 | 0.58 | 1.65 | 1.94 | 1.37 | 2.24 | 2.34 | 1.30 | 2.44 | 0.88 | 1.75 | 1.74 | 2.68 | 2.26 | 1.56 | 0.92 | 0.91 | 0.98 | 1.05 | 0.98 | 0.98 |
| $Al_2O_3$ | 5.2 | 14.9 | 5.19 | 7.51 | 3.20 | 3.19 | 13.7 | 15.5 | 9.61 | 14.6 | 15.4 | 11.4 | 15.6 | 12.0 | 5.05 | 5.00 | 14.9 | 15.1 | 13.0 | 13.5 | 14.2 | 12.6 | 13.8 | 14.4 | 14.7 | 14.9 | 13.3 | 15.4 | 14.8 | 16.4 | 6.42 | 8.51 | 8.91 | 8.82 | 8.64 |
| FeOt | 9.8 | 14.1 | 9.07 | 14.6 | 16.0 | 16.6 | 15.8 | 13.6 | 11.8 | 12.2 | 13.1 | 12.7 | 12.8 | 14.2 | 9.78 | 9.85 | 15.8 | 18.6 | 12.5 | 15.2 | 18.0 | 12.9 | 18.4 | 11.8 | 14.2 | 13.4 | 15.9 | 12.3 | 13.6 | 10.6 | 12.9 | 12.7 | 12.6 | 12.4 | 13.5 |
| MnO | 0.22 | 0.17 | 0.19 | 0.24 | 0.27 | 0.27 | 0.27 | 0.17 | 0.23 | 0.20 | 0.16 | 0.22 | 0.23 | 0.23 | 0.19 | 0.20 | 0.19 | 0.18 | 0.22 | 0.24 | 0.24 | 0.23 | 0.27 | 0.24 | 0.23 | 0.18 | 0.17 | 0.13 | 0.23 | 0.16 | 0.24 | 0.19 | 0.24 | 0.21 | 0.22 |
| MgO | 14.9 | 6.0 | 15.6 | 13.6 | 33.5 | 33.2 | 4.00 | 3.96 | 10.3 | 6.26 | 4.39 | 13.7 | 6.01 | 10.9 | 16.5 | 16.4 | 6.27 | 11.0 | 6.93 | 4.11 | 5.56 | 8.21 | 4.29 | 8.85 | 8.42 | 7.57 | 4.01 | 7.93 | 7.21 | 3.71 | 13.4 | 10.2 | 11.0 | 11.1 | 11.1 |
| CaO | 15.7 | 8.6 | 15.7 | 12.3 | 4.28 | 4.26 | 5.02 | 5.16 | 13.0 | 10.1 | 7.40 | 10.3 | 6.83 | 11.0 | 15.3 | 15.3 | 7.49 | 1.43 | 9.29 | 4.22 | 9.49 | 9.13 | 7.04 | 11.8 | 6.11 | 5.68 | 5.1 | 4.7 | 7.4 | 11.2 | 13.2 | 11.1 | 11.8 | 12.0 | 11.8 |
| $Na_2O$ | 0.22 | 5.14 | 1.02 | 0.05 | - | - | 3.60 | 3.67 | 3.56 | 3.42 | 5.07 | 1.87 | 4.79 | 1.52 | 0.70 | 0.91 | 4.35 | - | 3.97 | 4.82 | 4.04 | 3.12 | 4.35 | 2.94 | 2.65 | 3.45 | 4.25 | 3.54 | 2.05 | 6.15 | 0.26 | 3.04 | 2.21 | 2.55 | 2.49 |
| $K_2O$ | 0.00 | 0.12 | 0.02 | - | 0.02 | 0.03 | 0.03 | 0.23 | 0.01 | 0.04 | 0.05 | 0.14 | 0.15 | 0.17 | 0.01 | 0.02 | 0.28 | 0.43 | 0.12 | 0.02 | 0.05 | 0.02 | 0.05 | 0.05 | 0.01 | 0.03 | 0.01 | 0.04 | - | 0.18 | - | 0.01 | 0.14 | 0.01 | 0.01 |
| $P_2O_5$ | 0.07 | 0.08 | 0.07 | 0.09 | 0.06 | 0.06 | 0.21 | 0.22 | 0.10 | 0.16 | 0.16 | 0.08 | 0.24 | 0.09 | 0.06 | 0.06 | 0.08 | 0.09 | 0.14 | 0.22 | 0.10 | 0.12 | 0.15 | 0.09 | 0.16 | 0.17 | 0.33 | 0.26 | 0.20 | 0.17 | 0.09 | 0.10 | 0.10 | 0.10 | 0.10 |
| total | 100 | 100 | 100 | 100 | 100 | 100 | 100 | 100 | 100 | 100 | 100 | 100 | 100 | 100 | 100 | 100 | 100 | 100 | 100 | 100 | 100 | 100 | 100 | 100 | 100 | 100 | 100 | 100 | 100 | 100 | 100 | 100 | 100 | 100 | 100 |
| Mg# | 73.0 | 43.1 | 75.5 | 62.4 | 78.9 | 78.1 | 31.0 | 34.1 | 61.0 | 47.8 | 37.5 | 65.8 | 45.6 | 57.9 | 75.0 | 74.8 | 41.5 | 51.4 | 49.7 | 32.5 | 35.5 | 53.1 | 29.3 | 57.2 | 51.3 | 50.1 | 30.9 | 53.5 | 48.5 | 38.5 | 64.9 | 58.9 | 60.9 | 61.4 | 59.3 |
| Ni | 194 | 62 | 226 | 153 | 1089 | 1093 | 5.1 | 28 | 115 | 59 | 41 | 295 | 53 | 227 | 269 | 261 | 50 | 56 | 59 | 4.5 | 20 | 79 | 1.2 | 80 | 68 | 69 | 0.5 | 44 | 57 | 82 | 160 | 145 | 163 | 180 | 182 |
| Rb | 1.2 | 4.9 | 1.1 | 0.6 | 3.6 | 3.5 | 1.8 | 8.4 | 1.2 | 1.7 | 2.4 | 5.6 | 4.2 | 5.5 | 1.0 | 0.7 | 10.7 | 11.2 | 4.3 | 1.2 | 1.3 | 1.0 | 2.0 | 2.1 | 1.5 | 1.7 | 1.4 | 2.4 | 0.7 | 6.9 | 0.8 | 1.1 | 4.0 | 1.4 | 0.9 |
| Sr | 27 | 105 | 23 | 26 | 21 | 21 | 168 | 90 | 43 | 231 | 206 | 192 | 162 | 110 | 30 | 30 | 117 | 10 | 127 | 142 | 108 | 248 | 51 | 107 | 216 | 404 | 81 | 134 | 93 | 323 | 40 | 87 | 69 | 62 | 62 |
| Y | 13 | 14 | 12 | 15 | 4.5 | 6.1 | 30 | 36 | 17 | 25 | 24 | 11 | 29 | 13 | 8.1 | 9.4 | 13 | 14 | 19 | 31 | 13 | 21 | 18 | 11 | 22 | 25 | 45 | 38 | 28 | 18 | 15 | 14 | 16 | 14 | 15 |
| Zr | 42 | 53 | 38 | 52 | 20 | 22 | 140 | 176 | 66 | 122 | 116 | 38 | 134 | 43 | 28 | 30 | 52 | 56 | 88 | 174 | 56 | 87 | 74 | 37 | 125 | 137 | 238 | 162 | 144 | 138 | 59 | 63 | 68 | 61 | 62 |
| Nb | 1.1 | 1.5 | 0.9 | 1.5 | 0.5 | 0.4 | 5.5 | 7.4 | 2.1 | 4.5 | 4.5 | 0.8 | 4.7 | 1.2 | 0.5 | 0.7 | 1.6 | 1.7 | 3.6 | 7.0 | 2.2 | 3.3 | 3.2 | 1.1 | 5.5 | 5.9 | 11.9 | 5.4 | 5.2 | 5.5 | 1.6 | 2.3 | 2.4 | 2.2 | 2.3 |
| Ba | 36 | 83 | 74 | 7.1 | 6.6 | 8.3 | 34 | 162 | 19 | 91 | 114 | 777 | 84 | 69 | 47 | 130 | 492 | 141 | 65 | 66 | 92 | 676 | 59 | 36 | 858 | 4794 | 26 | 39 | 410 | 384 | 542 | 13 | 43 | 8.5 | 26 |
| Pb | 1.8 | 1.2 | 0.4 | 0.7 | 0.5 | 0.3 | 6.6 | 3.1 | 1.2 | 2.6 | 7.5 | 2.9 | 1.6 | - | - | 0.58 | 0.8 | 1.8 | 1.5 | 1.9 | 2.6 | 2.9 | 3.2 | 3.1 | 5.4 | 5.6 | 1.2 | 1.2 | 1.9 | 3.6 | 1.6 | 0.1 | 1.1 | 1.2 | 1.2 |
| Th | 1.1 | 0.95 | 1.2 | 1.6 | 0.5 | 0.8 | 2.0 | 2.6 | 1.0 | 1.7 | 1.4 | 1.1 | 1.9 | 0.37 | 0.72 | 0.00 | 1.1 | 0.66 | 0.83 | 2.1 | 0.32 | 0.90 | 1.2 | 0.9 | 2.2 | 2.2 | 3.4 | 1.8 | 1.5 | 7.3 | 1.5 | 1.1 | 1.3 | 0.9 | 0.5 |
| La | | | | 5.43 | | | | | | | | | | | 3.24 | | | | | | | | | | | | | | | | 4.89 | | | | |
| Ce | | | | 12.71 | | | | | | | | | | | 7.56 | | | | | | | | | | | | | | | | 11.32 | | | | |
| Pr | | | | 1.73 | | | | | | | | | | | 1.00 | | | | | | | | | | | | | | | | 1.52 | | | | |
| Nd | | | | 7.95 | | | | | | | | | | | 4.71 | | | | | | | | | | | | | | | | 7.17 | | | | |
| Sm | | | | 2.29 | | | | | | | | | | | 1.42 | | | | | | | | | | | | | | | | 2.10 | | | | |
| Eu | | | | 0.99 | | | | | | | | | | | 0.56 | | | | | | | | | | | | | | | | 0.81 | | | | |
| Gd | | | | 2.76 | | | | | | | | | | | 1.93 | | | | | | | | | | | | | | | | 2.62 | | | | |
| Tb | | | | 0.51 | | | | | | | | | | | 0.29 | | | | | | | | | | | | | | | | 0.45 | | | | |
| Dy | | | | 3.25 | | | | | | | | | | | 1.68 | | | | | | | | | | | | | | | | 2.91 | | | | |
| Ho | | | | 0.64 | | | | | | | | | | | 0.33 | | | | | | | | | | | | | | | | 0.61 | | | | |
| Er | | | | 1.84 | | | | | | | | | | | 0.95 | | | | | | | | | | | | | | | | 1.72 | | | | |
| Tm | | | | 0.26 | | | | | | | | | | | 0.13 | | | | | | | | | | | | | | | | 0.24 | | | | |
| Yb | | | | 1.61 | | | | | | | | | | | 0.87 | | | | | | | | | | | | | | | | 1.51 | | | | |
| Lu | | | | 0.24 | | | | | | | | | | | 0.12 | | | | | | | | | | | | | | | | 0.23 | | | | |

Total iron as FeO

Table 6 Chemical composition of altered OIBs

| sample | D108 | B109 | E313 | F187 | 95NP052 | 95NP056 | 95NP083 | 95NP065 | 95NP090 | 95NP101 | 95NP104 | 95NP107 | B092 | C160 | C172 | E006 | G120 | G161 | G093 |
|---|---|---|---|---|---|---|---|---|---|---|---|---|---|---|---|---|---|---|---|
| $SiO_2$ | 44.7 | 49.4 | 49.1 | 54.6 | 55.1 | 55.9 | 51.3 | 55.8 | 44.7 | 47.8 | 47.6 | 48.4 | 50.0 | 49.1 | 52.4 | 50.1 | 49.3 | 50.8 | 49.0 |
| $TiO_2$ | 1.68 | 0.59 | 0.84 | 0.83 | 0.81 | 0.79 | 2.06 | 1.49 | 1.55 | 1.52 | 2.72 | 1.72 | 1.78 | 1.68 | 1.47 | 1.58 | 1.76 | 1.75 | 2.31 |
| $Al_2O_3$ | 14.0 | 5.07 | 14.3 | 15.5 | 14.5 | 15.0 | 13.2 | 13.9 | 13.6 | 13.3 | 12.2 | 13.0 | 13.6 | 13.4 | 12.5 | 13.7 | 13.6 | 13.8 | 13.1 |
| FeOt | 16.0 | 8.84 | 10.9 | 9.49 | 9.35 | 9.37 | 13.8 | 12.3 | 14.5 | 13.1 | 14.4 | 14.2 | 13.5 | 13.3 | 15.5 | 12.3 | 14.7 | 12.7 | 15.7 |
| MnO | 0.22 | 0.35 | 0.19 | 0.12 | 0.12 | 0.15 | 0.17 | 0.12 | 0.18 | 0.18 | 0.18 | 0.22 | 0.13 | 0.17 | 0.17 | 0.23 | 0.25 | 0.21 | 0.24 |
| MgO | 6.63 | 14.4 | 7.33 | 2.80 | 2.59 | 4.14 | 2.43 | 2.32 | 8.61 | 6.72 | 3.81 | 4.16 | 6.42 | 5.24 | 6.53 | 5.67 | 3.31 | 4.64 | 4.44 |
| CaO | 7.68 | 15.4 | 6.88 | 5.63 | 6.56 | 6.38 | 6.50 | 4.06 | 6.33 | 6.72 | 8.44 | 7.69 | 4.15 | 6.23 | 4.03 | 6.08 | 6.17 | 5.30 | 4.88 |
| $Na_2O$ | 4.06 | 0.40 | 5.19 | 5.34 | 2.38 | 2.60 | 3.08 | 5.01 | 0.72 | 2.28 | 1.36 | 0.21 | 4.08 | 4.05 | - | 3.41 | 4.16 | 4.79 | 4.60 |
| $K_2O$ | 0.41 | - | 0.22 | 0.39 | 1.54 | 1.32 | 0.05 | 0.11 | - | - | - | 0.70 | - | - | 0.34 | 0.08 | 0.30 | 0.06 | 0.35 |
| $P_2O_5$ | 0.08 | 0.07 | 0.08 | 0.15 | 0.15 | 0.14 | 0.24 | 0.20 | 0.14 | 0.14 | 0.31 | 0.23 | 0.19 | 0.17 | 0.19 | 0.15 | 0.13 | 0.17 | 0.32 |
| total | 95.5 | 94.5 | 95.0 | 94.9 | 93.1 | 95.8 | 92.9 | 95.3 | 90.3 | 91.8 | 91.0 | 90.5 | 93.9 | 93.2 | 93.1 | 93.3 | 93.6 | 94.2 | 95.0 |
| Mg# | | | | | | | | | | | | | | | | | | | |
| Ni | 52 | 201 | 81 | 99 | 84 | 93 | 19 | 20 | 60 | 58 | - | 29 | 48 | 37 | 36 | 57 | 0.4 | 44 | 44 |
| Rb | 7.3 | 0.8 | 8.7 | 15 | 65 | 36 | 2.5 | 4.8 | 1.3 | 0.5 | 1.2 | 21 | 1.1 | 0.3 | 9.3 | 3.6 | 5.6 | 3.2 | 6.4 |
| Sr | 31 | 39 | 100 | 219 | 206 | 684 | 139 | 67 | 38 | 61 | 57 | 41 | 152 | 209 | 24 | 134 | 113 | 256 | 136 |
| Y | 13 | 10 | 14 | 19 | 17 | 17 | 33 | 41 | 22 | 22 | 42 | 37 | 28 | 25 | 36 | 27 | 23 | 27 | 37 |
| Zr | 53 | 31 | 57 | 137 | 137 | 136 | 200 | 197 | 92 | 94 | 191 | 195 | 157 | 135 | 167 | 110 | 105 | 134 | 166 |
| Nb | 1.5 | 0.9 | 1.6 | 5.1 | 5.3 | 5.4 | 9.7 | 8.5 | 2.8 | 2.9 | 7.9 | 6.7 | 7.1 | 5.2 | 6.0 | 3.5 | 3.8 | 5.2 | 6.5 |
| Ba | 344 | 44 | 899 | 491 | 450 | 957 | 215 | 135 | 75 | 281 | 12 | 194 | 540 | 53 | 73 | 218 | 182 | 67 | 148 |
| Pb | 1.0 | 1.9 | 0.5 | 9.1 | 9.6 | 7.0 | 5.1 | 5.4 | 1.1 | 3.9 | 0.8 | 1.3 | 3.6 | 2.7 | 0.9 | 7.9 | 3.6 | 3.4 | 1.5 |
| Th | 0.6 | 1.2 | 1.3 | 6.5 | 8.2 | 6.4 | 3.3 | 2.6 | 1.2 | 0.5 | 1.9 | 2.6 | 2.5 | 1.7 | 1.8 | 1.7 | 1.2 | 1.8 | 1.6 |

Total iron as FeO

# V. Melting relations of Archean mid-ocean ridge basalts: implication for thermal evolution of MORB source mantle

*Tsuyoshi Komiya*,

Department of Earth and Planetary Sciences, Tokyo Institute of Technology, Tokyo 152-8551, Japan

*fax: +81-3-5734-3538* *e-mail: tkomiya@geo.titech.ac.jp*

## V-1 Introduction

The compositional and isotopic evolution of the Earth has been relatively well discussed (e.g. Allègre et al. 1980; Galer & Goldstein 1991; McCulloch & Bennett 1994). Nevertheless, thermal evolution of the Earth has not been investigated so much well (e.g. Richter 1985; Davies 1992; Ogawa 1997). Especially, direct observations of the temperature of ancient mantle appear to be insufficient to construct the models compared to the investigation of compositional and isotopic evolution. Therefore, the lack of data of ancient thermal condition appears to make computational calculation of the thermal evolution of the Earth ambiguous.

It was widely accepted before 1970s that the Earth has evolved in a very nearly steady thermal state, because it was thought that the rate of heat loss from the Earth would be similar to the rate of heat production in chondritic earth (Urey 1956; Birch 1958; Tozer 1965, 1972). However, in 1980s, estimates of the heat loss incorporating revised calculation of the heat loss from oceanic regions indicated that the heat loss form the Earth are about 30 % higher than would be expected for steady state heat flow from a chondritic Earth (Davies 1980; Sclater et al. 1980, Pollack 1980). On the other hand, many geological evidences for the steady state thermal evolution of the Earth were reported in the last half 1970s; for example, (1) similarity of the geothermal gradient of Archean-aged continental lithospheres to the Phanerozoic continental geothermal gradient (Burke & Kidd 1978), (2) similarity of the metamorphic facies series between Archean and more recent rocks (Windley 1976; Watson 1978), (3) the similarity of the height of mountain between the Archean and the modern (England & Bickle 1984), and (4) The presence of the Archean-aged diamond in kimberlite (Richardson et al. 1984). Nevertheless, Some geological evidences against the steady state of thermal evolution are also reported; for example, (1) the eruptions of extreme high temperature magmas of ultramafic komatiitic magma (Green et al. 1975; Bickle et al. 1977; Arndt & Nisbet 1982; Bickle 1982), and (2) estimate of bulk composition of the Earth (Jagoutz et al. 1979). Bickle (1978) proposed the plate tectonics in the Archean because of explaining the apparent contradiction. Jordan (1975ab, 1978, 1981, 1988) strongly advocated that the continental lithosphere was chemically distinct from the normal mantle, and that the thickness was not controlled by the temperature of the mantle. Richter (1985) calculated the thermal evolution of the mantle assuming of double-layered mantle convection and chemical distinct tectosphere, and solved the paradox.

In 1990s, despite of the some previous works (Richter 1985; 1988), the significance of the combination of magmatism and mantle convection come to be recognized (Ogawa 1988, 1994). In addition, Ogawa (1997) showed that the Archean-Proterozoic boundary was a turning point from the large-scale melting and chemical layering of the mantle to thermal convection of solid-state mantle. Moreover, the presence of instability in mantle convection at the Archean-Proterozoic transition was suggested by computer simulations (Breuer & Spohn

1995). The calculation implies the episodic evolution of the mantle instead of gradual change of the mantle. Since the last half of 1980s, the evidences of the Archean plate tectonics have been reported in many Archean terrains (e. g. de Wit et al. 1987ab; Kusky 1991; Ohta et al. 1996; Komiya et al. 1998). However, operation of the plate tectonics conflicts with the high temperature of the Archean mantle, because heat loss through the plate tectonics is relatively low (Davies 1992). Therefore, estimate of the Archean mantle temperature becomes significant for not only the thermal history of the mantle but also Archean tectonics.

This work estimated the potential mantle temperature of source mantle of the 3.5 Ga MORB based on the multiple saturation experiments of the most primitive Archean MORB from the 3.5 Ga North Pole area.

## V-2 Starting materials

### V-2.1 Estimate of original composition of NPMORBs

Two types of basalt are recognized in North Pole area; NPMORBs and NPOIBs, respectively. The formers occur in Unit I and II, which are covered with thick-bedded chert, suggesting that it was derived from mid-ocean ridge volcanism based on accretionary geology. On the other hand, the latters occur in Unit III, which are repeatedly interbedded by thin chert layers, suggesting that they originated from oceanic island magmatism. A komatiite flow at the bottom and minor amount of basaltic komatiites flows all over the area of the Unit III also support the estimated tectonic setting (Campbell et al. 1989; Campbell & Griffiths 1993)

To obtain the original magmatic composition, greenstone samples were carefully selected for the major and trace elements analyses step by step. First of all, field occurrence of greenstones appears to be related to the extent of the secondary alterations and the distribution of the altered zones. For example, the extensive altered zones appear at the stratigraphic top of the pillow lava flow units, or in the surroundings of large quartz veinlets such as T-chert. Such stratigraphically controlled alteration suggests a hydrothermal alteration right after eruption, accompanied with the interaction with seawater. It is suggested that the involvement of the fluid from the neighboring sediments also disturbs the composition, especially isotopic composition. Therefore, about 2,500 greenstone samples elsewhere were preferentially collected from least altered area, remote from the T-chert and sedimentary layers. Massive lavas are preferred to pillow lavas because many pillow suffered low-temperature hydrothermal alteration along concentric fissures. At the second stage, <1-cm-thick slabs were cut from each sample to select the rock samples without a visible internal fracture filled with quartz, chlorite and epidote minerals and the heterogeneous surfaces. Whole rock powders were prepared for 112 fresh samples, which contain neither veinlets of quartz, chlorite, and calcite, nor the heterogeneous domains even under the microscope. Slabs whose surfaces were polished were broken into small pieces, ultrasonically cleaned in de-ionized

water and ethyl alcohol, dried, and powdered in a tungsten carbide shatter-box.

Petrographic observation and major element chemistry indicate that clinopyroxenes are saturated just after plagioclase in NPMORBs. Plagioclase-join leads to abruptly changing the slope of liquid line of descent. During olivine fractionation, on a plot of MgO versus $Al_2O_3$, $Al_2O_3$ increases with decreasing MgO; when plagioclase joins olivine on the liquidus, however, the slopes of the liquid line of descent changes abruptly and $Al_2O_3$ decreases substantially with decreasing MgO. On the other hand, on a plot of MgO versus $TiO_2$, $TiO_2$ increases slightly with decreasing MgO; in plagioclase crystallizing, however, the slope of the liquid line of descent changes abruptly and $TiO_2$ increases substantially with decreasing MgO. Thus, precise MgO content where plagioclase joins olivine on the liquidus can be estimated from the mode of the liquid line of descent. Moreover, substantial increase of $TiO_2$ content on $Mg^{\#}$ versus $TiO_2$ diagram allows us to estimate the precise partition coefficient, defined by $Kd^{FeO-MgO}=(Fe^{2+}/Mg^{2+})^{cpx}/(Fe^{2+}/Mg^{2+})^{liq}$. Figure 9a in Chapter IV shows $Mg^{\#}$ value versus $Al_2O_3$ content in NPMORBs-I, indicating that plagioclase joins olivine at 60 in Mg#, equivalent to 8.5 wt % in MgO. Figure 9b in Chapter III shows $Mg^{\#}$ value versus $TiO_2$ content in NPMORBs-I and the calculated melt equilibrated with clinopyroxene phenocrysts. The melt composition is calculated using the partition coefficient, $Kd^{FeO-MgO} = 0.26$ for $Mg^{\#}$ (Sisson & Grove 1993, Tormey et al. 1987) and $D_{Ti} = 0.20$ for Ti content (Green 1994), respectively. Despite of slight dispersion due to less accuracy of microprobe analyses, the calculated compositions are plotted on the liquid line of descent defined by NPMORBs-I. If $TiO_2$ content remained during metamorphism because $TiO_2$ empirically is regarded as immobile element, the evidence indicates that secondary alteration plays insignificant role on $Mg^{\#}$ value.

NPMORBs-I has lower $Al_2O_3$ than the modern MORBs at high MgO contents (> 10 wt %). NPMORBs-I has lower $TiO_2$ and $P_2O_5$ than the modern MORBs at low MgO contents (< 7 wt %). It also has lower Zr and Y at any given MgO content (especially low MgO), and higher FeO* and MnO at high MgO content (> 10 wt %) relative to the modern MORBs. $SiO_2$, CaO, Ni, Sr, and $Na_2O$ contents of NPMORBs-I are similar to those of the modern MORBs. They have a slightly light and middle REE-depleted pattern. The pattern of the liquid line of descent of the NPMORBs-I is similar to that of the modern MORBs.

### V-2.2 Water content in NPMORBs

Higher water content in melt breaks Si-O chains in the silicates to increase $SiO_2$ activity (Kushiro 1975). Moreover, high water content changes appearance temperature of the silicate phases to the varying degrees. Especially, the liquidus volume of plagioclase shrinks to delay plagioclase-saturation, relative to other phases such as olivine and clinopyroxene. The late fractionation of plagioclase leads to higher $Al_2O_3$ in magmas at moderate MgO content. The refraction of liquid line of descent of NPMORBs is located at 8.2 wt % in MgO on MgO versus $Al_2O_3$, and is equivalent to the modern MORBs (Klein & Langmuir 1987). Both the ternary diagrams of cpx-pl-ol and cpx-pl-qz (Tormey et al. 1987; Grove et al. 1992;

Gaetani et al. 1993; Sisson & Grove 1993) indicate that NPMORBs crystallized under the low-pressure anhydrous condition (see the Figure 10 in Chapter IV). Water content affects the composition of clinopyroxenes. Higher water content leads to higher $Al_2O_3$ and CaO content in clinopyroxenes (Gaetani et al. 1993; Parman et al. 1997). Clinopyroxenes in NPMORBs have as higher $Al_2O_3$ and CaO contents as those in NPOIBs (see the Figure 4 in Chapter IV). Therefore, NPMORBs had insignificant water, equivalent to modern MORBs, ca. 0.12 wt % (Sobolev & Chaussidon 1996).

### V-2.3 Ferric to Ferrous ratio at the formation of NPMORBs

Ferric to ferrous ratio in mantle is controlled not only by oxidation states (Hill & Roeder 1973; Kress & Carmichael 1989, 1991), but also chemical composition (Hill & Roeder 1973; Mo et al. 1982; Kress & Carmichael 1989, 1991), mineral assemblage (O'Neill et al. 1993), pressure (BVSP 1981; Mo et al. 1982; Kress & Carmichael 1989, 1991), temperature (e.g. Miyashiro 1973; Kress & Carmichael 1989, 1991), and phase chemistry (O'Neill et al. 1993; Wood & Rubie 1996; McCammon 1997; McCammon et al. 1997). For example, $Fe^{3+}/\sum Fe$ in NMORBs has been long believed to be about 0.1 to 0.15, based on the whole rocks chemistry (e.g. Miyashiro et al. 1969). If $Fe^{3+}/\sum Fe$ ration remains constant during magma ascent, MORB should be formed around the FMQ buffer condition, equivalent to $\log fO_2$=-7. Therefore, assuming that the degree of melting is 12 % and distribution of $Fe^{3+}$ among the solid phases of peridotite, $D^{sol/liq}_{Fe2O3}$=0.2, source mantle should have 0.389 wt % in $Fe_2O_3$. However, $Fe^{3+}/\sum Fe$ ratio of fresh glasses mid-ocean ridge basalt is only 0.07±0.03, equivalent to FMQ-2 (Christie et al. 1986), because fractional crystallization, volatile loss, sea-water alteration cause $Fe^{3+}/\sum Fe$ ratio to increase. Therefore, mantle source has 0.145 wt % in $Fe_2O_3$; namely, $Fe^{3+}/\sum Fe$ ratio is 0.018. The calculation is consistent to the Mössbauer analyses of natural primitive lherzolites, $Fe^{3+}/\sum Fe$=0.023±0.005 under FMQ condition (O'Neill et al. 1993). Supposing melting under IW buffer condition, the source mantle has $Fe^{3+}/\sum Fe$=0.005, and 0.044 wt % in $Fe_2O_3$. Very low $Fe_2O_3$ content should be of insignificance on melting relation. In addition, as far as source mantle consists of mineral assemblage of peridotite, $Fe_2O_3$ content must be suppressed because those minerals such as olivine, orthopyroxene, and clinopyroxene contain insignificant amount of $Fe_2O_3$ (O'Neill et al. 1993).

Therefore, graphite capsules are preferred to maintain the low $Fe^{3+}/\sum Fe$ ratio during the experiment.

### V-2.4 Composition of starting materials

The sample used in this study, 97NP106, is the most primitive one of NPMORBs-I. The rock sample was collected from Unit I in the southern region of North Pole area.

Starting materials are prepared as mixtures of a powdered natural rock sample

97NP106 with synthetic olivine mixture from analytical reagent grade chemicals. Both rock powder and analytical reagent grade chemicals are carefully ground under alcohol and heated at 1000 ˚C for three hours before measurement. Four starting mixes were prepared for the experiments with different amounts of synthetic olivine mixtures.

In Table 1, the results of XRF analysis of 97NP106 and of microprobe analysis of the glass fused of four stating mixes just above the liquidus are shown. Four starting mixes have 8.70, 10.3, 11.8, and in MgO, respectively.

## V-3 Experiments

### V-3.1 Experimental methods

The high-pressure melting experiments were carried out in graphite capsules in a solid-media apparatus using the hot piston-out method described by Boyd and England (1967). Pyrex glass sleeves with graphite heater were used in the 3/4-inch diameter furnace assemblies. Temperature was measured and controlled by $Pt/Pt_{90}Rh_{10}$ thermocouples. Temperature is precise within 2- 3 ˚C and has not been corrected for pressure effects. The experiments were made in the pressure range between 10 and 20 kbar, and in the temperature range between 980 and 1340 ˚C. Run durations ranged from 15 to 20 minutes because long run duration using graphite capsules causes the precipitation of metal blobs such as iron and nickel. Identification and chemical analyses of phase were made with a scanning electron microprobe (JEOL JSM5310) with Link EDS systems and the electron probe microanalyzer (JEOL-JXA-8800) housed at Tokyo Institute of Technology. Analytical conditions were 15 kV accelerating voltage, 1 nA specimen current and 60 – 80s counting time for a scanning electron microprobe, whereas were accelerating voltage 15 kV, 12 nA beam current and counting time 10-40 s for microprobe. Oxide ZAF correction method was employed for microprobe measurements.

### V-3.2 Experimental results

The results of melting experiments are summarized in Table 2 and Fig. 2-5. The results are consistent to similar experiments for modern island arc basalts and modern MORBs (Tatsumi 1982, 1983ab; Fujii & Bougault 1983).

For 97NP106, which has 8.60 wt % in MgO, at any pressure, clinopyroxene is the liquidus phase and followed by orthopyroxene. Olivine does not join the liquidus volume at any pressure. The temperatures are above liquidus for most runs. The phase relationships suggest that if multiple saturation point were to exist, the point should be located at less than 10 kbar (Fig. 2).

For the start 1, which has 10.1 wt % in MgO, at any pressure, clinopyroxene is the liquidus phase and followed by orthopyroxene and plagioclase. Olivine does not join the

liquidus volume at any pressure. The phase relationships suggest that if multiple saturation point were to exist, the point should be located at less than 10 kbar (Fig. 3).

For the start 2, which has 11.9 wt % in MgO, olivine is the liquidus phase at less than 12.5 kbar, and followed by clinopyroxene. At above this pressure, clinopyroxene is the liquidus phase and followed by orthopyroxene and then plagioclase. Orthopyroxene also appears very near the liquidus at 15 kbar. These phase relations suggest that the start 2 magma coexists with a lherzolitic mineral assemblage at about 13.5 kbar and 1340 ˚C (point A in Fig. 4).

For the start 3, which has 15.1 wt % in MgO, olivine is the liquidus phase at less than 15 kbar, and followed by orthopyroxene and clinopyroxene. Orthopyroxene is the liquidus phase at high pressure. These phase relations indicate that the start 3 magma coexists with a lherzolitic mineral assemblage at about 15 kbar and 1350 ˚C (point B in Fig. 5).

Plagioclase sometimes failed to crystallize in short-duration runs as pointed out by Bender et al. (1978). It is because the rates of nucleation and growth of plagioclase in basaltic melts are very small, compared to other ferromagnesian minerals (Donaldson 1979; Fujii & Bougault 1983). In run #12, amorphous plagioclase is present around quench crystal plagioclase.

## V-4 Discussion

### V-4.1 Interpretation of the temperature and pressure estimated by multiple saturation experiments.

Before the first half of 1980s, more or less, a single composition was introduced as the primary magmas of MORBs. Therefore, multiple saturation experiment (Kushiro & Thompson 1972; Kushiro 1973; Fujii & Bougault 1983) and melting experiments of natural peridotite (Jaques & Green 1980; Stolper 1980; Elthon & Scarfe 1984; Presnall & Hoover 1984; Fujii & Scarfe 1985; Falloon & Green 1987, 1988) was conducted for the estimate of the depth and temperature. In the latter case, the estimated temperature and pressure depends on the composition of natural peridotite In the former case, estimated temperature and the pressure would depend on the composition of selected starting material. It is because the extent of olivine fractionation is poorly restricted. Despite of presence of two opposing schools for MORBs genesis, high pressure picritic (O'Hara 1968; Green et al. 1979; Stolper 1980; Elthon & Scarfe 1984) or shallow level tholeiitic primary magma (Kushiro & Thompson 1972; Kushiro 1973; Presnall et al. 1979; Fujii & Bougault 1983), the temperature and pressure for MORB genesis were estimated. However, in the late half of 1980s, the outline of melting mechanism for the modern MORBs was established (Klein & Langmuir 1987; Bickle 1986; McKenzie & Bickle 1988). The most impressive change would be the accumulation of small melt batches from wide pressure range for MORB magma. Many evidences for fractional melting are reported in 1990s (e.g. Johnson et al. 1990; Sinton et al.

1993; Sobolev & Shimizu 1993; Iwamori 1993). Recently, the presence of small amount of melts that involved garnet fractionation in MORBs is controversial (Shen & Forsyth 1995; Hirschmann 1996; Stolper & Hirschmann 1996; Kinzler 1997). Therefore, the interpretation of the temperature and pressure estimated by multiple saturation experiments is ambiguous and controversial. Hirose and Kawamura (1994) demonstrated that both the melting processes, incremental melting and batch melting, can generate melts with similar major element compositions from the identical source if mantle melts isobarically, although higher temperature is required for incremental melting. Moreover, both the melting processes could generate melts with similar major element compositions even if accumulation of polybaric incremental melts govern the melting mechanism (Hirose & Kushiro 1998). It contrasts with case of isobaric melting, however, that the higher potential temperature is required for batch melting to generate melt with a similar major element composition. The difference of potential temperature for batch and fractional meting is estimated about 40 ˚C. Therefore, the potential mantle temperature is estimated in this study, assuming batch melting.

**V-4.2 Estimate of potential temperature of the NPMORBs**

The estimate of potential temperature of the Archean mantle has been reported since 1990 (e.g. Takahashi 1990; Nisbet et al., 1993; Ohta et al. 1996). Ones estimated potential temperature of Archean mantle from only MgO content in peridotitic komatiites (Takahashi 1990; Nisbet et al., 1993). MgO content of primary magma were estimated using olivine maximum fractionation model. The estimate, however, very severely depends on the amount of added olivine and the dependence of partition coefficient on composition, temperature and pressure even if the composition of most magnesian olivine phenocrysts is known. On the other hand, Ohta et al. (1996) compared the estimated primary magma with experimental melts from natural peridotite. However, the composition of primary magma depends on not only temperature and pressure at melting but also the composition of peridotites. In addition, $Al_2O_3$ and CaO content of magma are dependent on the extent of fractional crystallization. The estimated temperature and pressure is inconsistent to the trace elements chemistry, e.g. REE pattern (Ohta et al. 1996).

The temperature and pressure estimated by multiple saturation experiments are, of course, independent of the composition of source mantle. While, because they are dependent on the composition of selected stating materials, the most primitive and its derivatives of 97NP106 are prepared. Experimental results indicate that NPMORBs magma was formed at 13 to 15 kbar, and 1340 to 1350 ˚C. Assuming 0.6 ˚C/km for slope of adiabat, 590 kJ/kb (140 cal/g) for heat of fusion, and 1.26 kJ $kg^{-1}{}^{\circ}K^{-1}$ (0.3 cal/g˚C) for heat capacity, potential mantle temperature is calculated. Because the calculation of potential mantle temperature requires the degree of melting, degree of melting is estimated based on melting experiments of PHN1611 (Kushiro 1996; Hirose & Kushiro 1998). The degree of melting that NPMORBs magma is formed at 15 kbar and 1350 ˚C is estimated as 20.3 %. It is shown by calculation that the

mantle which produces 20.3 partial melt at 15 kbar and 1350 ˚C has 1420 ˚ C of potential mantle temperature. If the primary melts of the modern NMORBs have about 50.5, 12, and 7.2 wt % in $SiO_2$, MgO and FeO respectively, the potential mantle temperature is estimated as about 1300 ˚C (see the Figure 12b in Chapter IV). Thickness of oceanic crust indicates that the potential temperature of the modern upper mantle is 1320 ˚C, assuming the batch melting (Iwamori et al. 1995). Because in fact, MORBs are produced through the fractional melting, potential mantle temperature estimated by the composition of the MORBs possibly tends to be lower than that by the thickness of oceanic crust (Hirose & Kushiro 1998).

On the other hand, the potential mantle temperature was estimated by comparison of the primitive NPMORBs and experimental melts from PHN1611. The detailed procedures for estimate of the composition and potential temperature of source mantle are shown elsewhere (Chapter III and IV). Primitive NPMORBs are plotted over the melt formed at 1325, 1400, and 1425 ˚C, at 15 kbar. Each degree of melting is 18.4, 26.9, 35.9 %, respectively according to experimental data (Kushiro 1996). Therefore, the potential mantle temperature is obtained as 1384 to 1566 ˚C. Such the high potential mantle temperature resulted in thick oceanic crust, about 20-km thick (Klein & Langmuir 1987; McKenzie & Bickle 1988; Iwamori et al. 1995)

Although the potential mantle temperature estimated by multiple saturation experiments is within that by comparison of the primitive MORBs with experimental melts, the latter tends to be higher than the former. It is probably because the composition of source mantle is different from the PHN1611, especially in $Al_2O_3$ and CaO. The starting materials are plotted on Walker's ol-pl-qz ternary projections (Walker et al. 1979). It is recognized that despite of the different compositions of peridotites, isobaric compositional trends of the melts form as single lines in the projections (Fig 1, see also the Hirose & Kushiro 1993) whereas, isothermal compositional trends severely depend on the composition of peridotite, especially at low temperature (Fig. 1). Figure 1 also shows the melt of start 2 can be formed at 15 kbar 1350 ˚C, which is consistent of the multiple saturation experiments. However, the expected melting pressure and temperature are inconsistent to the results of multiple saturation for the melts of 97NP106, start 1 and start 3. The results imply that the 97NP106, the start 1 and the start 3 are not primary magmas.

If the potential mantle temperature was 1420 ˚C, ascending mantle would pass the solidus temperature of PHN1611 mantle at more than 30 kb. The calculations suggest NPMORBs should have the garnet signature (Hirschmann & Stolper 1996). However, NPMORBs have LREE-depleted REE pattern as shown above, and apparent garnet signature is not recognizable in REE pattern of NPMORBs. However, Y/Zr ratio of NPMORBs is lower than the chondritic ratio, implying garnet signature.

### V-4.3 Thermal condition of the Middle Archean mantle

The melting temperature of komatiites is relatively well constrained (e.g. Takahashi 1990; Nisbet et al. 1993). However, it is widely accepted that komatiite was not produced

from normal upper mantle, but from plume source mantle at higher pressure or highly wet mantle (e.g. Takahashi & Scarfe 1985; Inoue & Sawamoto 1992). Therefore, the potential mantle temperature estimated from the komatiite magma does not possibly represent that of normal upper mantle in the Archean. On the other hand, the potential temperature of source mantle of MORBs was reported from only 3.3 Ga Cleaverville MORBs, about 1400 ˚C (Ohta et al. 1996). Moreover, it seems that their results have some contradictions, for example lack of garnet signature and unreasonable thermal parameters.

Our estimate of the potential temperature of 3.5 Ga MORBs source mantle, 1420 ˚C is much lower than previous works, 1900 ˚C (Nisbet et al. 1993). One of the reasons is because the former represents the potential temperature of normal upper mantle, whereas the latter represents the plume source mantle. Higher temperature of mantle results in double-layered mantle convection because of high Rayleigh numbers. Therefore, it is thought that the Archean mantle whose potential temperature was high enough to produce komatiites, over 1900 ˚C convected in double-layered. However, if the potential mantle temperature is 1420 ˚C, even single-layered convection can release the heat from the mantle (Richter 1985). Phase change from γ-spinel+garnet+Ca-perovskite to Mg-perovskite+magnesiowüstite+Ca-perovskite at 650 km induces the layered convection if the Clapeyron slope of the reaction is low, -4 to –8 MPa/K (Christensen & Yuen 1985). Although effect of phase change on the mode of mantle convection in the Archean will be discussed elsewhere (Chapter VI), the Archean mantle was certainly inclined to convect in double-layered in than the modern. Nevertheless, low heat loss from the mantle through only plate tectonics leads to increase of mantle temperature when mantle is about 50 ˚C hotter than at present. The calculation appears to be inconsistent to the geological evidences of plate tectonics (Davies 1992). However, the episodic mantle overturn or active plume volcanism would account for the apparent inconsistency (Breuer & Spohn 1995).

Assuming that the thickness of lithosphere is rheologically controlled by the temperature at the bottom of the lithosphere, the Archean lithosphere would be less than 30 km thick when the potential mantle temperature, was 1420 ˚C (Richter 1985). The calculation suggests the presence of the partial molten layer beneath the lithosphere, 60 km thick. It has been long regarded as inconsistency with the geological observation because of the lack of evidences of large-scale magmatism on the continents (Bickle 1978). However, if any continent was underlain by the thick tectosphere in the Archean, high potential mantle temperature did not necessarily lead to large-scale volcanism on the continents. On the other hand, thin oceanic plate led to high geothermal gradient, suggesting the presence of partial molten layer beneath oceanic plate. Although this idea is not new (Nisbet & Walker 1982), it allows us to explain the occurrences of Al-undepleted komatiites in the Archean.

Al-undepleted komatiites occur widely in the Archean terrains. These magmas are characterized by high degree of melting and no garnet signature. Any normal adiabatic decompressional melting can not produce such magmas because higher degree of melting requires the beginning of melting at higher pressure. However, the presence of partial molten

layer in steady state does not require the high pressure melting, which is consistent to the geochemistry of Al-undepleted komatiites and the occurrences of relatively thick and long flows (Arndt et al. 1977). The duration of presence of the partial molten layer depends on the heat loss from the mantle. High activity of magmatism leads to high heat loss and decreasing potential mantle temperature, which appears to be consistent to the limited occurrences of komatiites in the Archean.

## V-5 Conclusions

(1) Multiple saturation experiments were conducted in the pressure range between 10 and 20 kbar, and in the temperature range between 980 and 1340 ˚C using the four derivatives from most primitive 3.5 Ga MORBs, collected from the North Pole area, Pilbara Craton.

(2) The start 2, 11.9 wt % in MgO, and start 3, 15.1 wt % in MgO, have the multiple saturation point of olivine+orthopyroxene+clinopyroxene+liquid, which is located at 1340 ˚C, 13.5 kbar and 1350 ˚C, 15 kbar, respectively.

(3) The potential mantle temperature, 3.5 Ga is estimated as 1420 ˚C, assuming that the composition of source mantle is the same composition as PHN1611.

(4) The estimated potential mantle temperature is only 120 ˚C higher than that of modern mantle.

(6) High potential mantle temperature leads to the partial molten layer beneath oceanic lithosphere. Al-undepleted komatiites, which are characterized by high degree of melting and no garnet signature, presumably were derived from plume magmatism from the region.

## References

Basaltic Volcanism Study Project (BVSP): Basaltic Volcanism on the Terrestrial Planet: New York, Pergamon Press, 1286 p., 1981.

Allègre, C. J., Brévart, O., B., D., and Minster, J.-F., 1980, Isotopic and chemical effects produced in a continuously differentiating convecting Earth mantle: Phil. Trans. R. Soc. London, v. A297, p. 447-477.

Arndt, N. T., 1977, Thick, Layered peridotite - gabbro lava flows in Munro Township, Ontario: Can. J. Earth Sci., v. 14, p. 2620-2637.

Arndt, N. T., and Nisbet, E. G., 1982, Komatiites, London, George Allen & Unwin, p. 526.

Bender, J. F., Hodges, F. N., and Bence, A. E., 1978, Petrogenesis of basalts from the project FAMOUS area: experimental study from 0 to 15 kbars: Earth Planet. Sci. Lett., v. 41, p. 277-302.

Bickle, M. J., 1978, Heat loss from the Earth: A constraint on Archaean tectonics from the relation between geothermal gradients and the rate of plate production: Earth Planet. Sci. Lett., v. 40, p. 301-315.

Bickle, M. J., 1982, The magnesium content of komatiitic liquids, *in* Arndt, N. T., and Nisbet, E. G., eds., Komatiites, London, George Allen & Unwin, p. 479-494.

Bickle, M. J., 1986, Implications of melting for stabilisation of the lithosphere and heat loss in the Archaean: Earth Planet. Sci. Lett., v. 80, p. 314-324.

Bickle, M. J., Ford, C. E., and Nisbet, E. G., 1977, The petrogenesis of peridotitic komatiites: evidence from high-pressure melting experiments: Earth Planet. Sci. Lett., v. 37, p. 97-106.

Birch, F., 1958, Differentiation of the Mantle: Geol. Soc. Am. Bull., v. 69, p. 483-485.

Breuer, D., and Spohn, T., 1995, Possible flush instability in mantle convection at the Archaean-Proterozoic transition: Nature, v. 378, p. 608-610.

Burke, K., and Kidd, W. S. F., 1978, Were Archean continental geothermal gradients much steeper than those of today?: Nature, v. 272, p. 240-241.

Campbell, I. H., and Griffiths, R. W., 1993, The evolution of mantle's chemical structure: Lithos, v. 30, p. 389-399.

Campbell, I. H., Griffiths, R. W., and Hill, R. I., 1989, Melting in an Archaean mantle plume: heads it's basalts, tails it's komatiites: Nature, v. 339, p. 697-699.

Christensen, U. R., and Yuen, D. A., 1985, Layered convection induced by phase transitions: J. Geophys. Res., v. 90, p. 10291-10300.

Christie, D. M., Carmichael, I. S. E., and Langmuir, C. H., 1986, Oxidation states of mid-ocean ridge basalt glasses: Earth Planet. Sci. Lett., v. 79, p. 397-411.

Davies, G. F., 1980, Thermal histories of convective earth models and constraints on radiogenic heat production in the earth: J. Geophys. Res., v. 85, p. 2517-2530.

Davies, G. F., 1992, On the emergence of plate tectonics: Geology, v. 20, p. 963-966.

de Wit, M. J., Armstrong, R., Hart, R. J., and Wilson, A. H., 1987a, Felsic igneous rocks within the 3.3- to 3.5-Ga Barberton Greenstone Belt: High crustal level equivalents of the surrounding tonalite-trondhjemite terrain, emplaced during thrusting: Tectonics, v. 6, p. 529-549.

de Wit, M. J., Hart, R. A., and Hart, R. J., 1987b, The Jamestown ophiolite complex, Barberton mountain belt: a section through 3.5 Ga oceanic crust: Jour. Afr. Earth Sci., v. 6, p. 681-730.

Donaldson, C. H., 1979, An experimental investigation of the delay in nucleation of olivine in mafic magmas: Contrib. Mineral. Petrol., v. 69, p. 21-32.

Elthon, D., and Scarfe, C. M., 1984, High-pressure phase equilibria of a high-magnesia basalt and the genesis of primary oceanic basalts: Am. Mineral., v. 69, p. 1-15.

England, P., and Bickle, M., 1984, Continental thermal and tectonic regimes during the Archean: Jour. Geol., v. 92, p. 353-367.

Falloon, T. J., and Green, D. H., 1987, Anhydrous partial melting of MORB, pyrolite and other peridotite compositions at 10 kb: Implications for the origin of primitive MORB glasses: Mineral. Petrol., v. 37, p. 181-219.

Falloon, T. J., and Green, D. H., 1988, Anhydrous partial melting of peridotite from 8-35 kb and the petrogenesis of MORB: J. Petrol., p. 379-414.

Fujii, T., and Bougault, H., 1983, Melting relations of a magnesian abyssal tholeiite and origin of MORBs: Earth Planet. Sci. Lett., v. 62, p. 283-295.

Fujii, T., and Scarfe, C. M., 1985, Composition of liquids coexisting with spinel lherzolite at 10 kbar and genesis of MORBs: Contrib. Mineral. Petrol., v. 90, p. 18-28.

Gaetani, G. A., Grove, T. L., and Bryan, W. B., 1993, The influence of water on the petrogenesis of subduction-related igneous rocks: Nature, v. 365, p. 332-334.

Galer, S. J. G., and Goldstein, S. L., 1991, Early mantle differentiation and its thermal consequences: Geochim. Cosmochim. Acta, v. 55, p. 227-239.

Green, D. H., Hibberson, W. O., and Jaques, A. L., 1979, Petrogenesis of mid-ocean ridge basalts, *in*

McElhinney, M. W., ed., The Earth: its origin, structure and evolution, London., Academic Press.
Green, D. H., Nicholls, I. A., Viljoen, M., and Viljoen, R., 1975, Experimental demonstration of the existence of peridotitic liquids in earliest Archean magmatism: Geology, v. 3, p. 11-14.
Green, T. H., 1994, Experimental studies of trace-element partitioning applicable to igneous petrogenesis - Sedona 16 years later: Chem. Geol., v. 117, p. 1-36.
Grove, T. L., Kinzler, R., and Bryan, W. B., 1992, Fractionation of mid-ocean basalt (MORB), Mantle Flow and Melt Generation at Mid-Ocean Ridges, Washington D. C., AGU Monograph 71, p. 281-310.
Hill, R., and Roeder, P., 1974, The crystallization of spinel from basaltic liquid as a function of oxygen fugacity: Am. Mineral., v. 82, p. 709-729.
Hirose, K., and Kawamura, K., 1994, A new experimental approach for incremental batch melting of peridotite at 1.5 GPa: Geophys. Res. Lett., v. 21, p. 2239-2242.
Hirose, K., and Kushiro, I., 1993, Partial melting of dry mantle peridotites at high pressures: Determination of compositions of melts segregated from peridotite using aggregates of diamond: Earth Planet. Sci. Lett., v. 114, p. 477-489.
Hirose, K., and Kushiro, I., 1998, The effect of melt segregation on polybaric mantle melting: Estimation from the incremental melting experiments: Physics of the Earth and Planetary Interiors, v. 107, p. 111-118.
Hirschmann, M., 1996, Reading garnet's signature: Nature, v. 384, p. 215-217.
Hirschmann, M. M., and Stolper, E. M., 1996, A possible role for garnet pyroxenite in the origin of the "garnet signature" in MORB: Contrib. Mineral. Petrol., v. 124, p. 185-208.
Inoue, T., and Sawamoto, H., 1992, High pressure melting of pyrolite under hydrous condition and its geophysical implication: High-pressure Research: Application to Earth and Planetary Sciences: Tokyo and AGU, Washington D. C ., Terra, 323-331 p.
Iwamori, H., 1993, A model for disequilibrium mantle melting incorporating melt transport by porous and channel flows: Nature, v. 366, p. 734-737.
Iwamori, H., McKenzie, D., and Takahashi, E., 1995, Melt generation by isentropic mantle upwelling: Earth Planet Sci. Lett., v. 134, p. 253-266.
Jagoutz, E., Palme, H., Baddenhausen, H., Blum, K., Cendales, M., Dreibus, G., Spettel, B., Lorenz, V., and Wänke, H., 1979, The abundances of major, minor and trace elements in the earth's mantle as derived from primitive ultramafic nodules: Proc. Lunar Planet. Sci. Conf. 10th, p. 2031-2050.
Jaques, A. L., and Green, D. H., 1980, Anhydrous melting of peridotite at 0-15 kb pressure and the genesis of tholeiitic basalts: Contrib. Mineral. Petrol., v. 73, p. 287-310.
Johnson, K. T. M., Dick, H. J. B., and Shimizu, N., 1990, Melting in the oceanic mantle: an ion microprobe study of diopsides in abyssal peridotites: J. Geophys. Res., v. 95, p. 2661-2678.
Jordan, T. H., 1975a, The continental tectosphere: Rev. Geophys. Space Phys., v. 13, p. 1-12.
Jordan, T. H., 1975b, Lateral heterogeneity and mantle dynamics: Nature, v. 257, p. 745-750.
Jordan, T. H., 1978, Composition and development of the continental tectosphere: Nature, v. 274, p. 544-548.
Jordan, T. H., 1981, Continents as a chemical boundary layer: Phil. R. Soc. London, v. A301, p. 359-373.
Jordan, T. H., 1988, Structure and formation of the continental tectosphere: Jour. Petrol., p. 11-37.
Kinzler, R. J., 1997, Melting of mantle peridotite at pressures approaching the spinel to garnet transition: Application to mid-ocean ridge basalt petrogenesis: J. Geophys. Res., v. 102, p. 853-874.
Klein, E. M., and Langmuir, C. H., 1987, Global correlations of ocean ridge basalt chemistry with axial depth and crustal thickness: J. Geophys. Res., v. 92, p. 8089-8115.
Komiya, T., Maruyama, S., Nohda, S., Masuda, T., Appel, P. W. U., Hayashi, M., and Okamoto, S., 1998, Plate tectonics at 3.8 ≲ 3.7 Ga; Field evidence from the Isua accretionary complex, southern West Greenland: Jour. Geol.
Kress, V. C., and Carmichael, I. S. E., 1989, The lime-iron-silicate melt system: Redox and volume systematics: Geochim. Cosmochim. Acta, v. 53, p. 2883-2892.
Kress, V. C., and Carmichael, I. S. E., 1991, The compressibility of silicate liquids containing $Fe_2O_3$ and the effect of composition, temperature, oxygen fugacity and pressure on their redox states: Contrib. Mineral. Petrol., v. 108, p. 82-92.
Kushiro, I., 1973, Origin of some magmas in oceanic and circum-oceanic regions: Tectonophys., v. 17, p. 211-222.
Kushiro, I., 1975, On the nature of silicate melt and its significance in magma genesis: regularities in the shift of the liquidus boundaries involving olivine, pyroxene, and silica minerals: Am. J. Sci., v. 275, p. 411-431.
Kushiro, I., 1996, Partial melting of a fertile mantle peridotite at high pressures: an experimental study using aggregates of diamond, *in* Basu, A. R., and Hart, S. R., eds., Earth processes: Reading the isotopic code, Washington D. C., AGU Monograph 95, p. 109-122.
Kushiro, I., and Thompson, R. N., 1972, Origin of some abyssal tholeiites from the Mid-Atlantic Ridge: Carnegie Inst. Washington, Yearb., v. 71, p. 403-406.
Kusky, T. M., 1991, Structural development of an Archean orogen, western Point Lake, Northwest Territories: Tectonics, v. 4, p. 820-841.
McCammon, C., 1997, Perovskite as a possible sink for ferric iron in the lower mantle: Nature, v. 387, p. 694-

696.
McCammon, C., Hutchison, M., and Harris, J., 1997, Ferric iron content of mineral inclusions in diamonds from São Liz: A view into the lower mantle: Science, v. 278, p. 434-436.
McCulloch, M. T., and Bennett, V. C., 1994, Progressive growth of the Earth's continental crust and depleted mantle: Geochemical constraints: Geochim. Cosmochim. Acta, v. 58, p. 4717-4738.
McKenzie, D., and Bickle, M. J., 1988, The volume and composition of melt generated by extension of lithosphere: J. Petrol., v. 29, p. 625-649.
Miyashiro, A., 1973, Metamorphism and Metamorphic Belts: London, George Allen & Unwin, 492 p.
Miyashiro, A., Shido, F., and Ewing, M., 1969, Diversity and origin of abyssal tholeiite from the Mid-Atlantic Ridge near 24˚ and 30˚ north latitude: Contrib. Mineral. Petrol., v. 23, p. 38-52.
Mo, X., Carmichael, I. S. E., Rivers, M., and Stebbins, J., 1982, The partial molar volume of $Fe_2O_3$ in multicomponent silicate liquids and the pressure dependence of oxygen fugacity in magmas: Mineral. Mag., v. 45, p. 237-245.
Nisbet, E. G., Cheadle, M. J., Arndt, N. T., and Bickle, M. J., 1993, Constraining the potential temperature of the Archean mantle: A review of the evidence from komatiites: Lithos, v. 30, p. 291-307.
Nisbet, E. G., and Walker, D., 1982, Komatiites and the structure of the Archaean mantle: Earth Planet. Sci. Lett., v. 60, p. 105-113.
O'Hara, M. J., 1968, Are ocean floor basalts primary magma?: Nature, v. 220, p. 683-686.
O'Neill, H. S. C., Rubie, D. C., Canil, D., Geiger, C. A., Ross II, C. R., Seifert, F., and Woodland, A. B., 1993, Ferric iron in the upper mantle and in transition zone assemblages: Implications for relative oxygen fugacities in the mantle, *in* Takahashi, E., Jeanloz, R., and Rubie, D., eds., Evolution of the Earth and Planets, Washington, IUGG and Am. Geophys. Union, p. 73-88.
Ogawa, M., 1988, Numerical experiments on coupled magmatism-mantle convection system: Implications for mantle evolution and Archean continental crusts: J. Geophys. Res., v. 93, p. 15119-15134.
Ogawa, M., 1994, Effects of chemical fractionation of heat-producing elements on mantle evolution inferred from a numerical model of coupled magmatism-mantle convection system: Phys. Earth Planet. Inter., v. 83, p. 101-127.
Ogawa, M., 1997, A bifurcation in the coupled magmatism-mantle convection system and its implications for the evolution of the Earth's upper mantle: Phys. Earth Planet. Inter., v. 102, p. 259-276.
Ohta, H., Maruyama, S., Takahashi, E., Watanabe, Y., and Kato, Y., 1996, Field occurrence, geochemistry and petrogenesis of the Archean mid-oceanic ridge basalts (AMORBs) of the Cleaverville area, Pilbara craton, Western Australia: Lithos, v. 37, p. 199-221.
Parman, S. W., Dann, J. C., Grove, T. L., and de Wit, M. J., 1997, Emplacement conditions of komatiite magmas from the 3.49 Ga Komati Formation, Barberton Greenstone Belt, South Africa: Earth Planet. Sci. Lett., v. 150, p. 303-323.
Pollack, H. N., 1980, The heat flow from the earth: A review, *in* Davies, P. A., and Runcorn, S. K., eds., Mechanisms of continental drift and plate tectonics, New York, Academic, p. 183-192.
Presnall, D. C., Dixon, J. R., O'Donnel, T. H., and Dixon, S. A., 1979, Generation of mid-ocean ridge tholeiite: J. Petrol., v. 20, p. 3-35.
Presnall, D. C., and Hoover, J. D., 1984, Composition and depth of origin of primary mid-ocean ridge basalts: Contrib. Mineral. Petrol., v. 84, p. 170-178.
Richardson, S. H., Gurney, J. J., Erlank, A. J., and Harris, J. W., 1984, Origin of diamonds in old enriched mantle: Nature, v. 310, p. 198-202.
Richter, F. M., 1985, Models for the Archean thermal regime: Earth Planet. Sci. Lett., v. 73, p. 350-360.
Richter, F. M., 1988, A major change in the thermal state of the Earth at the Archean-Proterozoic boundary: Consequences for the nature and preservation of continental lithosphere: Jour. Petrol., p. 39-52.
Sclater, J. G., Jaupart, C., and Galson, D., 1980, The heat flow through oceanic and continental crust and the heat loss from the earth: Rev. Geophys. Space Phys., v. 18, p. 269-311.
Shen, Y., and Forsyth, D. W., 1995, Geochemical constraints on initial and final depths of melting beneath mid-ocean ridges: J. Geophys. Res., v. 100, p. 2211-2237.
Sinton, C. W., Christie, D. M., Coombs, V. L., Nielsen, R. L., and Fisk, M. R., 1993, Near-primary melt inclusions in anorthite phenocrysts from the Galapagos Platform: Earth Planet. Sci. Lett., v. 119, p. 527-537.
Sisson, T. W., and Grove, T. L., 1993, Experimental investigation of the role of $H_2O$ in calc-alkaline differentiation and subduction zone magmatism: Contrib. Mineral. Petrol., v. 113, p. 143-166.
Sobolev, A. V., and Chaussidon, M., 1996, $H_2O$ concentrations in primary melts from supra-subduction zones and mid-ocean ridges: Implications for $H_2O$ storage and recycling in the mantle: Earth Planet. Sci. Lett., v. 137, p. 45-55.
Stolper, E. M., 1980, A phase diagram for mid-ocean ridge basalts: Preliminary results and implications for petrogenesis: Contrib. Mineral. Petrol., v. 74, p. 13-27.
Takahashi, E., 1990, Speculations on the Archean mantle: missing link between komatiite and depleted garnet peridotite: J. Geophys. Res., v. 95, p. 15941-15954.
Takahashi, E., and Scarfe, C. M., 1985, Melting of peridotite to 14 GPa and the genesis of komatiites: Nature, v.

315, p. 566-568.
Tatsumi, Y., 1982, Origin of high-magnesian andesites in the Setouchi volcanic belt, southwest Japan, II. Melting phase relations at high pressures: Earth Planet. Sci. Lett., v. 60, p. 305-317.
Tatsumi, Y., 1983a, Generation of arc basalt magmas and thermal structure of the mantle wedge in subduction zones: J. Geophys. Res., v. 88, p. 5815-5825.
Tatsumi, Y., 1983b, High magnesian andesites in the Setouchi volcanic belt, southwest Japan and their possible relation to the evolutionary history of the Shikoku inter-arc basin, Geodynamics of the Western Pacific-Indonesian region Geodynamic series, volume 11, Washington D. C., Am. Geophys. Union, p. 331-341.
Tormey, D. R., Grove, T. L., and Bryan, W. B., 1987, Experimental petrology of normal MORB near the Kane Fracture Zone: 22-25˚ N, mid-Atlantic ridge: Contrib. Mineral. Petrol., v. 96, p. 121-139.
Tozer, D. C., 1965, Heat transfer and convection currents: Phil. R. Soc. London, v. A258, p. 252-271.
Tozer, D. C., 1972, The present thermal state of the terrestrial planets: Phys. Earth Planet. Inter., v. 6, p. 182-197.
Urey, H. C., 1956, The cosmic abundance of potassium, uranium, and thorium and the heat balances of the earth, moon, and Mars: Proc. Natl. Acad. Sci. U. S., v. 42, p. 889-891.
Walker, D., Shibata, T., and Delong, S. E., 1979, Abyssal tholeiites from the Oceanographer Fracture Zone II Phase equilibria and mixing: Contrib. Mineral. Petrol., v. 70, p. 111-125.
Watson, J. V., 1978, Precambrian thermal regimes: Phil. R. Soc. London, v. A288, p. 431-440.
Windley, B. F., 1976, New tectonic models for the evolution of Archean continents and oceans, *in* Windley, B. F., ed., The early history of the Earth, London, John Wiley & Sons, p. 105-111.
Wood, B. J., and Rubie, D. C., 1996, The effect of alumina on phase transformations at the 660-kilometer discontinuity from Fe-Mg partitioning experiments: Science, v. 273, p. 1522-1524.

## FIGURE CAPTIONS

**Figure 1.** Normative composition of starting materials projected from cpx on to pl-ol-qz pseudo-ternary phase diagram (Walker et al. 1979). Also shown are normative compositions of the isobaric (thick broken line) and isothermal (solid line) compositional trends defined by the partial melts from (a) PHN1611 (Kushiro 1996), (b) KLB-1 (Hirose & Kushiro 1993) and (c) HK66 (Hirose & Kushiro 1993) with isoplethes of degree of melting (fine broken line). Numbers attached with thick broken line, solid line and fine broken line are melting pressure, melting temperature and degree of melting, respectively.

**Figure 2.** Melting phase relations of the Start 0, which is most primitive aphyric MORB in North Pole area. No multiple saturation point defined by olivine+clinopyroxene+orthopyroxene+liquid is present, suggesting that this magma was not derived directly from partial melting of a mantle peridotite, but was affected by some crystal fractionations. Abbreviations are: ol = olivine; cpx = clinopyroxene; opx = orthopyroxene; liq = liquid.

**Figure 3.** Melting phase relations of the Start 1, which is a mixture of most primitive aphyric MORB in North Pole area with amounts of the equilibrated olivine. No multiple saturation point defined by olivine+clinopyroxene+orthopyroxene+liquid is present, suggesting that this magma was not derived directly from partial melting of a mantle peridotite, but was affected by some crystal fractionations. Abbreviations are the same as in Figure 2.

**Figure 4.** Melting phase relations of the Start 2, which is a mixture of most primitive aphyric MORB in North Pole area with amounts of the equilibrated olivine. A multiple saturation point defined by olivine+clinopyroxene+orthopyroxene+liquid is present around 14 kb, 1325 ˚C, suggesting that this magma was coexisting with a mantle peridotite. Abbreviations are the same as in Figure 2.

**Figure 5.** Melting phase relations of the Start 3, which is a mixture of most primitive aphyric MORB in North Pole area with amounts of the equilibrated olivine. A multiple saturation point defined by olivine+clinopyroxene+orthopyroxene+liquid is present around 15 kb, 1350 ˚C, suggesting that this magma was coexisting with a mantle peridotite. Abbreviations are the same as in Figure 2.

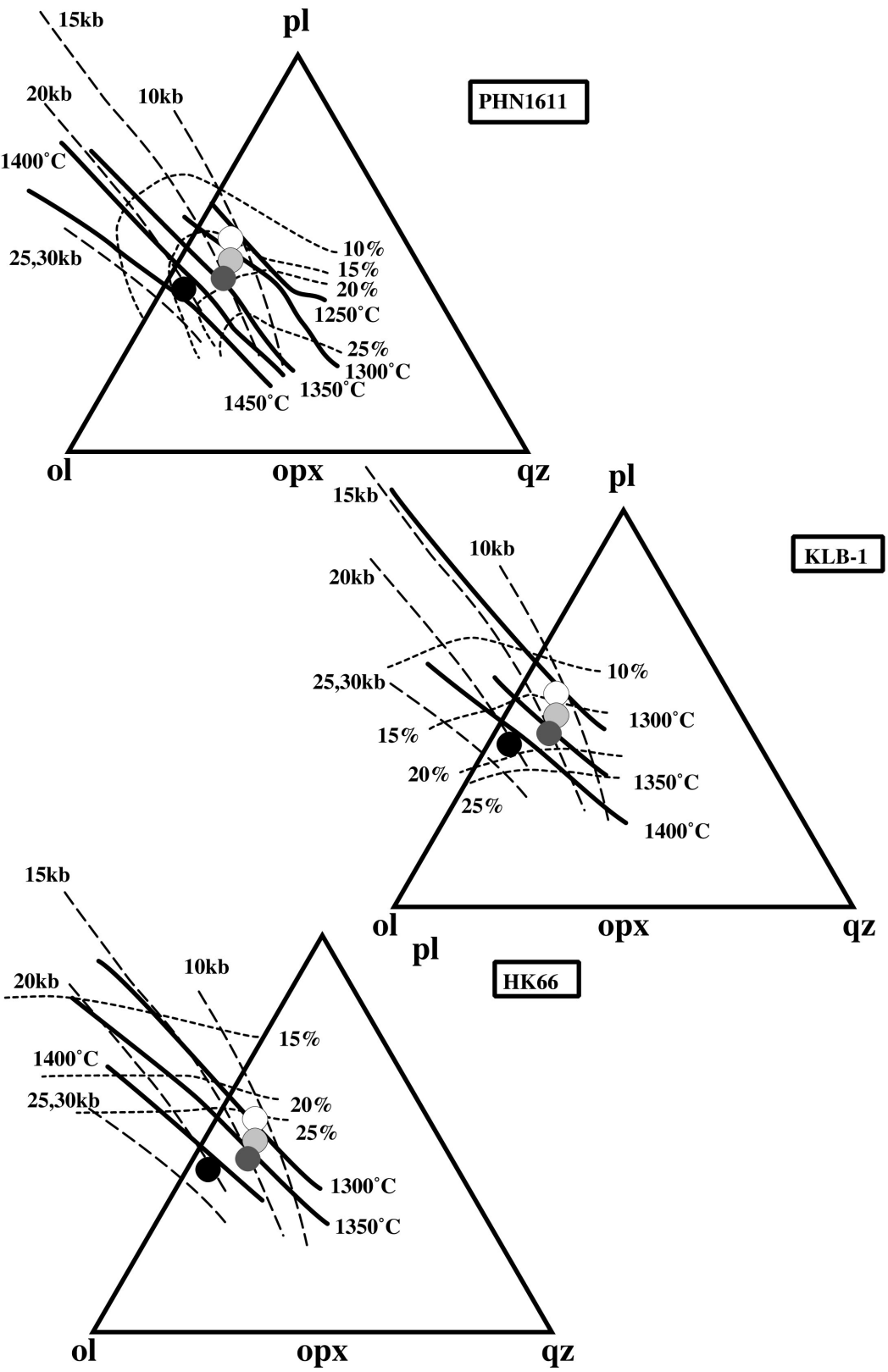


Komiya 1999 Doctor Thesis Fig. V-1

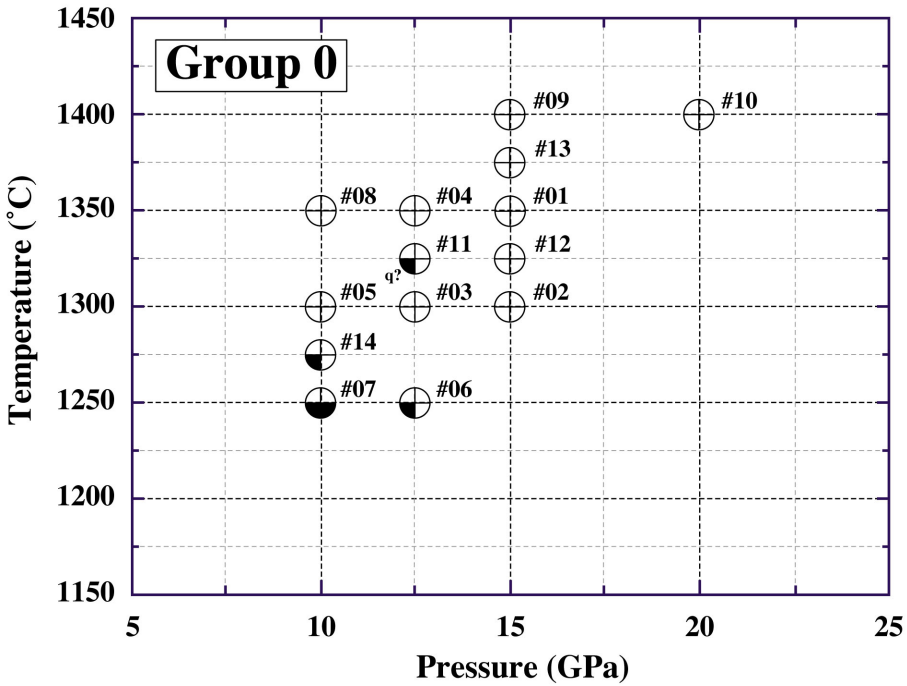


Komiya 1999, Doctor Thesis Fig. V-2

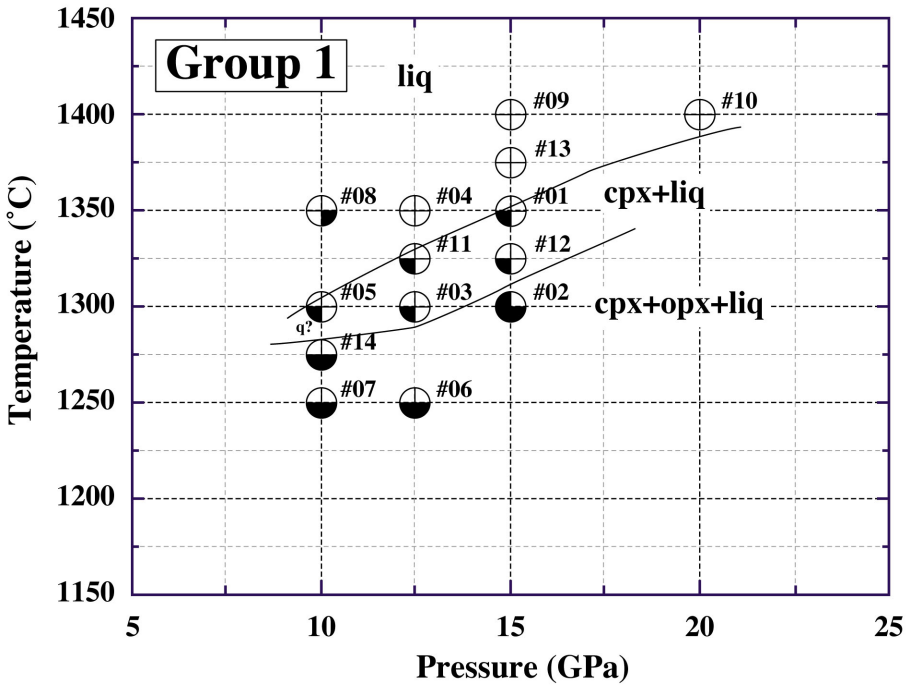


Komiya 1999, Doctor Thesis Fig. V-3

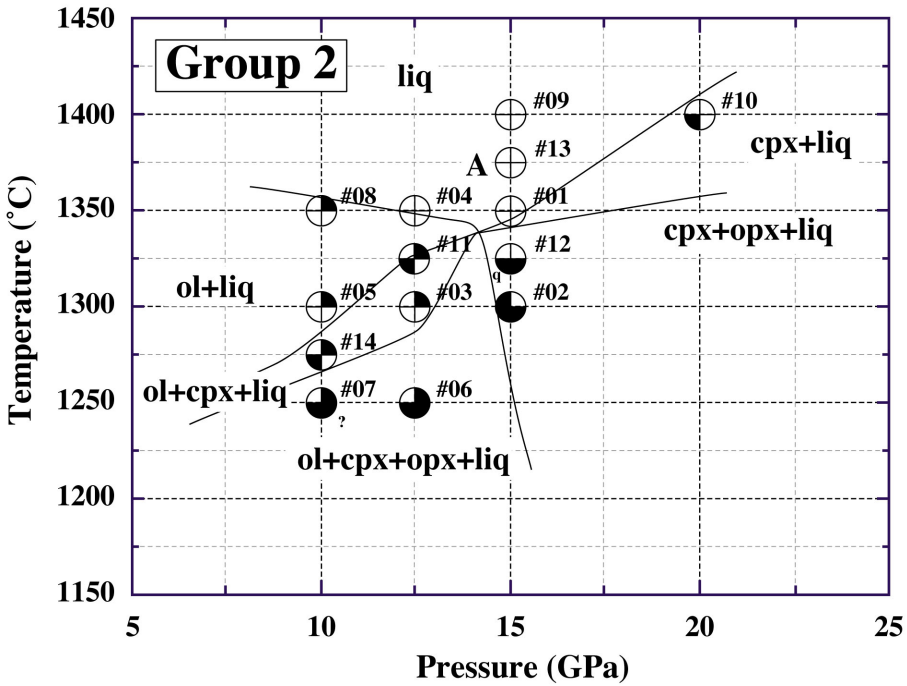


Komiya 1999, Doctor Thesis Fig. V-4

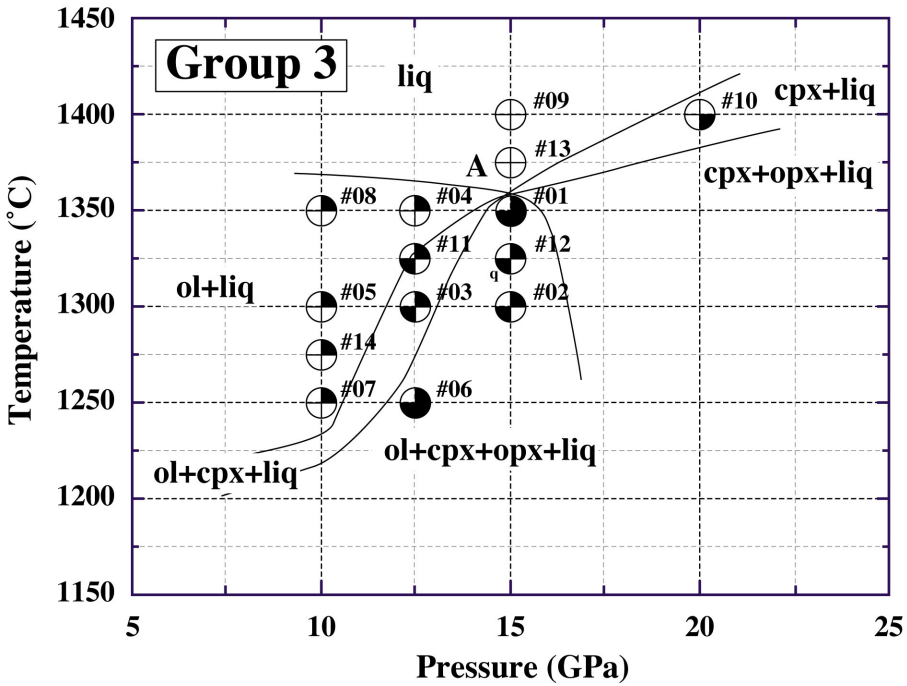


Komiya 1999, Doctor Thesis Fig. V-5

Table 1 Chemical data for starting materials (major elements in wt %)

| sample | 97NP106 | start1 | start2 | start3 | 97NP106* | start1* | start2* | start3* |
|---|---|---|---|---|---|---|---|---|
| $SiO_2$ | 49.8 | 49.3 | 48.9 | 48.2 | 50.8(0.68) | 51.2(0.59) | 50.5(0.66) | 49.3(0.55) |
| $TiO_2$ | 1.10 | 1.05 | 1.00 | 0.91 | 1.11(0.13) | 0.92(0.11) | 0.91(0.10) | 0.88(0.15) |
| $Al_2O_3$ | 15.0 | 14.4 | 13.6 | 12.4 | 14.9(0.39) | 13.9(0.23) | 13.4(0.33) | 12.3(0.19) |
| FeO | 10.8 | 10.9 | 11.0 | 11.1 | 10.6(0.70) | 10.3(0.27) | 10.6(0.49) | 10.6(0.62) |
| MnO | 0.20 | 0.20 | 0.20 | 0.20 | 0.17(0.21) | 0.18(0.11) | 0.21(0.17) | 0.00(0.00) |
| MgO | 8.60 | 10.1 | 11.9 | 15.2 | 8.70(0.23) | 10.3(0.31) | 11.8(0.39) | 15.1(0.45) |
| CaO | 11.1 | 10.6 | 10.1 | 9.19 | 10.5(0.62) | 9.89(0.72) | 9.69(0.37) | 8.85(0.29) |
| $Na_2O$ | 3.00 | 2.87 | 2.73 | 2.48 | 2.87(0.24) | 2.86(0.24) | 2.51(0.21) | 2.55(0.12) |
| $K_2O$ | 0.40 | 0.38 | 0.36 | 0.33 | 0.37(0.04) | 0.40(0.03) | 0.38(0.06) | 0.29(0.09) |
| $P_2O_5$ | 0.10 | 0.10 | 0.09 | 0.08 | | | | |
| total | 100.1 | 100.0 | 100.0 | 100.0 | 100.0 | 100.0 | 100.0 | 100.0 |
| | | | | | | | | |
| Mg# | 58.7 | 62.2 | 65.8 | 70.9 | 59.4 | 64.0 | 66.6 | 71.7 |

Total iron as FeO

Table 2a Experimental run data on 97NP106

| Run No. | P (kbar) | T (℃) | Time | phase present |
|---|---|---|---|---|
| #7 | 10 | 1250 | 15 | gl+cpx+opx |
| #14 | 10 | 1275 | 15 | gl+cpx |
| #5 | 10 | 1300 | 10 | gl |
| #8 | 10 | 1350 | 15 | gl |
| #6 | 12.5 | 1250 | 15 | gl+cpx |
| #3 | 12.5 | 1300 | 10 | gl |
| #11 | 12.5 | 1325 | 15 | gl+cpx |
| #4 | 12.5 | 1350 | 10 | gl |
| #2 | 15 | 1300 | 10 | gl |
| #12 | 15 | 1325 | 15 | gl |
| #1 | 15 | 1350 | 10 | gl |
| #13 | 15 | 1375 | 15 | gl |
| #9 | 15 | 1400 | 15 | gl |
| #10 | 20 | 1400 | | gl |

Table 2b Experimental run data on start1

| Run No. | P (kbar) | T (℃) | Time | phase present |
|---|---|---|---|---|
| #7 | 10 | 1250 | 15 | gl+cpx+opx |
| #14 | 10 | 1275 | 15 | gl+ol+cpx |
| #5 | 10 | 1300 | 10 | gl+cpx |
| #8 | 10 | 1350 | 15 | gl+opx |
| #6 | 12.5 | 1250 | 15 | gl+cpx+opx |
| #3 | 12.5 | 1300 | 10 | gl+cpx |
| #11 | 12.5 | 1325 | 15 | gl+cpx |
| #4 | 12.5 | 1350 | 10 | gl |
| #2 | 15 | 1300 | 10 | gl+opx+cpx+pgl |
| #12 | 15 | 1325 | 15 | gl+cpx |
| #1 | 15 | 1350 | 10 | gl+cpx |
| #13 | 15 | 1375 | 15 | gl |
| #9 | 15 | 1400 | 15 | gl |
| #10 | 20 | 1400 | | gl |

Table 2c Experimental run data on start2

| Run No. | P (kbar) | T (℃) | Time | phase present |
|---|---|---|---|---|
| #7 | 10 | 1250 | 15 | gl+ol+cpx+opx(?) |
| #14 | 10 | 1275 | 15 | gl+ol+cpx |
| #5 | 10 | 1300 | 10 | gl+ol |
| #8 | 10 | 1350 | 15 | gls+ol |
| #6 | 12.5 | 1250 | 15 | gl+ol+opx+cpx |
| #3 | 12.5 | 1300 | 10 | gl+ol+opx(?) |
| #11 | 12.5 | 1325 | 15 | gl+ol+cpx |
| #4 | 12.5 | 1350 | 10 | gl |
| #2 | 15 | 1300 | 10 | gl+opx+cpx+pl |
| #12 | 15 | 1325 | 15 | gl+opx+q-cpx |
| #1 | 15 | 1350 | 10 | gl |
| #13 | 15 | 1375 | 15 | gl |
| #9 | 15 | 1400 | 15 | gl |
| #10 | 20 | 1400 | | gl+cpx |

Table 2d Experimental run data on start3

| Run No. | P (kbar) | T (℃) | Time | phase present |
|---|---|---|---|---|
| #7 | 10 | 1250 | 15 | gl+ol |
| #14 | 10 | 1275 | 15 | gl+ol |
| #5 | 10 | 1300 | 10 | gl+ol |
| #8 | 10 | 1350 | 15 | gl+ol |
| #6 | 12.5 | 1250 | 15 | gl+ol+cpx+opx |
| #3 | 12.5 | 1300 | 10 | gl+ol+cpx |
| #11 | 12.5 | 1325 | 15 | gl+ol+cpx |
| #4 | 12.5 | 1350 | 10 | gl+ol |
| #2 | 15 | 1300 | 10 | gl+ol+cpx |
| #12 | 15 | 1325 | 15 | gl+opx+q-cpx |
| #1 | 15 | 1350 | 10 | gl+ol+opx+cpx |
| #13 | 15 | 1375 | 15 | gl |
| #9 | 15 | 1400 | 15 | gl |
| #10 | 20 | 1400 | | gl+opx+q-cpx |

gl=glass, ol=olivine, pl=plagioclase, opx=orthopyroxene, cpx=clinopyroxene, q-cpx=quench crystal of clinopyroxene

# VI. The compositional and thermal evolution of the MORB-source mantle through time

*Tsuyoshi Komiya*,

Department of Earth and Planetary Sciences, Tokyo Institute of Technology, Tokyo 152-8551, Japan

*fax: +81-3-5734-3538* *e-mail: tkomiya@geo.titech.ac.jp*

## VI-1 Introduction

Many evidences for slab penetration into lower mantle are reported by seismic observations and possibly high-pressure experiments in the Phanerozoic. The evidences of seismic observations are from the residual sphere analysis of body-wave travel times (Jordan 1977; Creager & Jordan 1984, 1986a), a suite of unusually broad and complex shear waves from two deep-focus events approximately along the strike of the slab (Silver & Chan 1986; Beck & Lay 1986), three–dimensional tomography (Dziewonski 1984; Woodhouse & Dziewonski 1987; Fukao et al. 1992), and three-dimensional P-wave velocity variation near the core-mantle boundary (Creager & Jordan 1986b; Morelli & Dziewonski 1987; Gudmundsson et al. 1986). On the other hand, high-pressure experiments indicate that slab tends to be stagnated along the upper-lower mantle boundary, because of the negative slope of Clapeyron curve of post-spinel transformation (Ito & Yamada 1982; Ito & Takahashi 1989), or of the higher pressure transformation of the subducted oceanic crust relative to the surrounding mantle (Irifune & Ringwood 1987, 1993; Ringwood 1991). However, inertia of slab descending motion prevents the slab from stagnation on the boundary (Ito & Sato 1992). Because slab becomes warm enough to comprise dense mineral assemblage in its stagnation on the boundary, still relatively cold plate can penetrate into the lower mantle. Because thick pile of oceanic crust isostatically penetrates into the lower mantle across the boundary, its basement comes to comprise the dense mineral assemblage to subside into the lower mantle (Irifune & Ringwood 1987, 1993; Hirose et al. 1998).

It has been long suggested that high temperature of the mantle leaded to double-layered convection because of high Rayleigh number in the Archean. However, some differences between the Archean and Phanerozoic are expected to result in the slab penetration in to the lower mantle in the Archean. For example, oceanic crust in the Archean had lower $Mg^{\#}$ value and lower $Al_2O_3$ content because of higher degree of melting. The compositional differences lead to transformation into the perovskite-bearing mineral assemblage in the oceanic crust at lower pressure (Irifune et al. 1996). Moreover, the higher potential temperature of the mantle leads to the thinning of the oceanic lithosphere. Therefore, oceanic lithosphere was presumably dominated by the oceanic crust and harzburgite relative to the modern oceanic lithosphere (Arndt 1983). On the other hand, the higher potential mantle temperature led the surrounding mantle to transform into the dense lower mantle at the lower pressure.

This paper presents the preliminary results of high-pressure experiments of the Archean oceanic crust. The secular change of the composition and temperature of the upper mantle will be discussed based on the estimated potential temperature and composition of the mantle in Chapter III, IV, and V.

## VI-2 Experiments

Two kinds of ultra-high pressure experiments were conducted for two purposes with multianvil apparatus. One of the purposes is the investigation for transformation of the Archean oceanic crust at upper-lower mantle boundary. Another ultra-high pressure experiment is conducted under the controlled oxygen fugacity, for the measurement of solubility of FeO iron into Mg-perovskite. Although the latter is still on going, the present will also present some preliminary results.

### VI-2.1 Starting materials

Three different starting materials were used in this study. Two materials are natural greenstone samples from 3.5 Ga North Pole area. Another sample is a primitive modern NMORB, MAR02 (Hirose et al. 1998). One of the Archean MORBs is a primitive NPMORB, B106, which has 8.91 wt % in MgO. Another of the Archean MORBs is a coarse-grained NPMORB, C017, which has 14.3 wt % in MgO. Although the latter contains many clinopyroxene and plagioclase phenocrysts and forms the gabbroic texture, it is plotted on the higher MgO extension of liquid line of descent on the MgO versus major element diagrams. The chemical compositions are shown in table 1 and Figure 1.

To obtain glass starting materials, the one atmosphere melting were performed at $pO_2 = 10^{-8}$ bar with the Pt-loop method (), where $pO_2$ was controlled by changing the mixing ratio of $CO_2$ and $H_2$ gases. In order to minimize iron loss, very thin Pt wire (0.05 mm) was used as a loop. The compositions of starting materials were confirmed with electron microprobe (Table 1).

Four starting mixes, $(Mg_{0.9}Fe_{0.1})SiO_3$+8%$AlO_{1.5}$, $(Mg_{0.9}Fe_{0.1})SiO_3$+6%$AlO_{1.5}$, $(Mg_{0.9}Fe_{0.1})SiO_3$+4%$AlO_{1.5}$, and $(Mg_{0.7}Fe_{0.3})SiO_3$+8%$AlO_{1.5}$ were prepared for another experiments from analytical reagent grade chemicals (Table 3). The samples were synthesized in the piston-cylinder apparatus, with oxide mixtures as starting material. The mixtures were prepared by weighing the heat-treated oxides, MgO, $Al_2O_3$, $Fe_2O_3$ and $SiO_2$, in the above composition, followed by grinding under alcohol in an agate mortar. The oxide mixtures were then placed in a $CO_2$-CO gas-mixing furnace at temperature 1473 K for 24 hours. To reduce the $Fe^{3+}$ to $Fe^{2+}$, the oxygen fugacity ($fO_2$) was controlled at about $10^{-10.50}$. This oxygen fugacity between the iron-wüstite ($10^{-11.91}$) and wüstite-magnetite ($10^{-9.10}$) buffers at 1473 K. The treated mixtures were reground and was set in graphite capsules within outer sealed platinum capsules. The capsules were then run in the piston-cylinder apparatus for 5 minutes 1500 K and 1.0 GPa and then quenched.

### VI-2.2 Experimental methods

High-pressure and high-temperature experiments were conducted in a uniaxial multianvil (MA6-8 type) apparatus, driven by a 1500-ton hydraulic press with a ram diameter of 20 inches, at the Geophysical Laboratory. The runs were made in a pressure of 25.5, 26, and 27 GPa, and at 1500 ˚C. Run duration was 12, 8, and 6 hours, respectively. In all the present experiments, MgO pressure medium of 8 mm edge length octahedron was used, where a few percent of $Cr_2O_3$ was added in order to reduce heat loss by radiation. Toshiba (F grade) tungsten carbide cubes with 3-mm truncated edge length were used for all the experiments. Lanthanum chromite furnace was used for heat insulation. A ribbon of Re foil was used for capsules. Details of experimental configurations and pressure calibration for the 8/3 assembly were described elsewhere (Bertka & Fei 1997; Hirose & Fei 1998). Boron nitride capsules with Re outer capsule instead of graphite inner capsule were used for the experiment under the controlled oxygen fugacity. Temperature was measured with W5%Re-W26%Re (type C) thermocouple, which was put axially in contact with the sample capsule. All experiments were run under dry condition. Multiple samples with different compositions were loaded in a Re capsule, separated by thin Re disks, in single experiments to compare to each other (Fei et al. 1991; Hirose & Fei 1998).

Phase relations and major element chemical compositions were determined with an electron microprobe (JEOL-JXA8800) housed in the Tokyo Institute of Technology. All analyses were performed with accelerating voltage 15 kV, 12 nA beam current and counting time of 10-40 s. Phase relation were examined also with the micro-focused X-ray diffractometer and micro-Raman spectroscopy at Tokyo Institute of Technology.

**VI-2.3 Experimental Results**

Experimental conditions and mineral assemblage of run products are summarized in table 2. At 25.5 GPa, the mineral assemblages of majorite+stishovite+Ca-perovskite+Al-phase were observed in all specimens. Mineral assemblage of MAR02 is the same as the previous work (Hirose et al. 1998). Minor amounts of an aluminous phase (Al-phase) are also recognized (Hirose et al. 1998). At 26 GPa, the Al-bearing Mg-perovskite joins subsolidus phase assemblage of majorite, stishovite and Ca-perovskite in C017 and B106. Therefore, the mineral assemblages are defined by Mg-perovskite, majorite, stishovite, Ca-perovskite, and Al-phase. MAR02 is also composed of Mg-perovskite, majorite, stishovite, and Ca-perovskite (Hirose et al. 1998) The phase assemblage at 27 GPa is Al-bearing Mg-perovskite, stishovite, Ca-perovskite, Al-phase, and trace majorite. The mineral assemblage of MAR02 is the same as that in previous work (Hirose et al. 1998) (Fig. 2a). Th results suggests that FeO and $Al_2O_3$ content in subducted oceanic crust play an insignificant role on the P and T condition of phase change. This is probably because FeO and $Al_2O_3$ content in MORBs exceed their solubilities in Mg-perovskite, and another phase, such as magnesiowüstite and an aluminous phase are precipitated.

Another experiment was conducted under the controlled oxygen fugacity, at 27 GPa,

2000 ˚C. A natural peridotite, KLB-1 and a synthetic mix, En70+8%Al are used as starting material. Although the deformation of boron nitride capsule did not allow us to recover a sample En70+8%Al, KLB-1 sample was collected much enough to determine and analyze the phases. The run charge contained Mg-perovskite, magnesiowüstite, majoritic garnet, and minor Ca-perovskite. The partition coefficient of iron and magnesium between Mg-perovskite and magnesiowüstite are shown figure 2b with the compilation of previous works (Ito et al. 1984; Ito & Takahashi 1989; Fei et al. 1991; Irifune 1994; McFarlane et al. 1994; Wood & Rubie 1996; McCammon et al. 1997). It is widely accepted that the limited amount of ferrous ion can dissolve into Mg-perovskite (e.g. Fei et al. 1996), because the high iron content modifies the crystal structure (Kudoh et al. 1990). However, iron content in Mg-perovskite increase with $Al_2O_3$ content (Wood & Rubie 1996; McCammon 1997; McCammon et al. 1997). The observation is considered as the coupled substitutions of $Al^{3+}$ and $Fe^{3+}$ for $Mg^{2+}$ and $Si^{\cdot}$ respectively. Our experimental results also support the interpretation (Fig. 2b). Wood and Rubie (1996) showed the substitution is independent of oxygen fugacity based on diamond cell experiments using various capsules with different oxygen fugacity. However, this experiments indicate $Kd^{FeO^*\text{-}MgO}=(Fe^*/Mg^{2+})^{mw}/(Fe^*/Mg^{2+})^{pv}$ is similar to $Kd^{FeO\text{-}MgO}=(Fe^{2+}/Mg^{2+})^{mw}/(Fe^{2+}/Mg^{2+})^{pv}$ of natural mw and perovskite inclusions within diamonds (McCammon et al. 1997). The evidences imply $Fe_2O_3$ content in Mg-perovskite more or less depends on oxygen fugacity. The coupled substitution of $Al^{3+}Fe^{3+}$ for $Mg^{2+}Si^{4+}$ is accompanied with deoxidization of $Fe^{2+}$ into Fe (Wood & Rubie 1996; Miyajima per. commun. 1998). Many metallic iron blobs with high Re content were also observed in this experiments. Although involvement of partial molten Re capsule can not necessarily ruled out, this evidence may indicate the deoxidization of $Fe^{2+}$ into Fe.

## VI-3 Geology of other areas and geochemistry of greenstones in the areas

### VI-3.1 The potential temperature and Mg# of the source mantle of mid-ocean ridge basalts (MORBs) in Early Proterozoic, the Killara area, Western Australia

The Glengarry Basin was formed at the Middle Proterozoic, 1.6 to 1.9 Ga, by the oblique subduction of oceanic plate (Pirajno et al. 1995, 1996). Despite of poor outcrops, the lithostratigraphy indicates that the deposition was formed at the mature stage of rifting (Pirajno et al. 1995, 1996). Therefore, the tholeiitic basalts in this area are equivalent to the pillowed basalt in the Hamersley in the Early Proterozoic or tholeiitic basalts from the Red Sea in the Phanerozoic.

Figures 3a show the MgO versus major element diagrams of basaltic rocks from the Killara area along with the modern MORBs and OIBs (Table 8 and 9). The latter includes both alkaline basalts and tholeiites. Chondrite-normalized REE abundances are shown in Figure 4. The REE patters forms slightly light REE-enriched. Only fine-grained rock samples, which petrographically defined as aphyric or small acicular plagioclase-bearing basalts are

analyzed and plotted on the Figure 3a. Despite of minor scattering in especially CaO content, it forms a clear liquid line of descent.

Field occurrences indicate that the Killara basalts were derived by the volcanism at the mature stage of continental rifting as shown elsewhere. The liquid line of descent forms abrupt increase of $SiO_2$ and FeO, and decrease of $Al_2O_3$ and CaO at moderate MgO content, similar to that of the modern MORBs. The Killara MORBs have higher $SiO_2$ content relative to the modern MORBs. Moreover, it is suggested that the Killara MORBs have higher $SiO_2$ and FeO, and lower $Al_2O_3$ ad CaO at the high MgO content, compared with the modern MORBs. The Killara MORBs are enriched in FeO content relative to the modern MORB (Figure 3a). This difference suggests that source mantle of the Killara MORBs had higher FeO than that of the modern MORB. However, the difference of FeO content appears relatively small.

Assuming that the mantle was still a spinel- or garnet-lherzolite, $Fe^{3+}/\sum Fe$ ratio of source mantle is possibly similar to that of modern upper mantle because $Fe^{3+}/\sum Fe$ ratio is controlled not only by oxygen fugacity, but also by mineral assemblage. Batch melting is also assumed because of its simplification. Melting experiments of four natural peridotites KLB-1, HK66, PHN1611, and MM3 have been extensively performed using diamond aggregate method (Hirose & Kushiro 1993; Baker & Stolper 1994; Kushiro 1996). Those experiments showed $SiO_2$ content of melts is relatively independent of composition of peridotites and temperature of melting at moderate degree of melting, but quite sensitive to melting pressure, because $SiO_2$ is a major constituent element of all minerals. On the contrary, FeO* in melts strongly depends on FeO* content of peridotites, together with pressure and temperature of melting. MgO content of melts is almost proportional to degree of melting.

The most primitive Killara MORBs and modern MORB are plotted along melt compositions formed by different pressures and degree of melting and from different starting materials in figure 3b. The Killara MORBs are plotted toward the higher $SiO_2$ content of the melts formed at 10 kb, whereas Modern MORBs are distributed on the compositional trends defined by the melts formed at 10 or 15 kb (Fig 3b). Because the Killara MORBs have relatively lower MgO content, the primary magma should have contained higher MgO. Therefore, the primary magma of the Killara MORBs is plotted on the partial melts at pressure of 10 to 15 kb. This evidence suggests that average melting pressure of the Killara MORBs through melting column were about 10, kb (Klein & Langmuir, 1987). On the other hand, the modern MORBs are formed at 10 to 15 kb, and is consistent to the high pressure experiments, 10 kb, (Fujii & Bougault 1983).

Figure 3b shows that each variation of FeO content of melt formed at 15 kb for KLB-1, HK66, and PHN1611, or 10 kb from MM3. Primitive magma of Killara MORBs is plotted toward the higher FeO content of melts from HK66 or PHN1611, whereas modern MORBs are distributed on melts from KLB-1. The composition of primary melt of the Killara MORBs can not be estimated because olivine is completely altered due to metamorphism. If MgO content of primary melt of the Killara MORBs has ca. 20 wt % in MgO, it can be formed

from KLB-1 (Takahashi et al. 1993). However, because the average melting pressure should be high ca. 4.6 GPa, in the case, the Killara MORBs should have the garnet signatures (Salters & Hart, 1989; Bourdon et al., 1996; Salters, 1996; Hirschmann 1996; Hirschmann & Stolper, 1996). However, the Killara MORBs does not show garnet signature, such as heavy REE depletion (Fig. 4). The results suggest that the Killara MORBs was derived from more FeO*-enriched source mantle such as HK66 and PHN1611 rather than KLB-1 and MM3.

The potential temperature of the Archean mantle has been estimated by previous workers since 1990 (e.g. Takahashi, 1990; Nisbet et al., 1993; Ohta et al. 1996). The potential mantle temperature was estimated by the abundance of FeO and $SiO_2$ in primitive magmas because they are relatively insensitive to the extent of crystal fractionation and are strongly correlated to pressure and temperature of melting. Figure 3b shows composition of the primitive basalt of the Killara MORBs, along experimental melt from PHN1611 on a $SiO_2$ versus FeO diagram. Primitive basalt of the Killara MORBs is plotted near the melt formed at 1350 ˚C, 10 kb. If the primitive basalt is the derivative from primary magma of 15 wt % in MgO, the primary magma is plotted near the melt from at 1425, 15 kb or 1400, 15 kb. Each degree of melting is 29.2, 35.9, 26.9 %, respectively according to experimental data (Kushiro 1996). Therefore, the potential mantle temperature is obtained as 1470 to 1570 ˚C of with 0.6 ˚C/km for slope of adiabat, 590 kJ/kb (140 cal/g) for heat of fusion, and 1.26 kJ $kg^{-1}°K^{-1}$ (0.3 cal/g˚C) for heat capacity (Hirose & Kushiro 1998). Iwamori et al. (1995) also obtained 1320 ˚C of potential mantle temperature of modern MORBs for batch melting.

### VI-3.2 The potential temperature of the source mantle of Al-depleted ultramafic komatiites in the Middle Archean, the Barberton Greenstone Belt, South Africa

The Barberton Greenstone Belt is *ca.* 3.5 Ga greenstone belt, located at the northeastern edge of the Kaapvaal craton, and is characterized by Al-depleted peridotitic komatiites. The Barberton Greenstone Belt, the Swaziland Supergroup, is subdivided into the volcanosedimentary Onverwacht Group and the overlying sedimentary Fig Tree and Moodies Groups (Viljoen & Viljoen, 1969). The Onverwacht Group comprises the lower ultramafic unit (the Tjakastad Subgroup) and the overlying mafic to felsic unit (Geluk Subgroup), and they are bounded by the Middle marker chert layers at the boundary. The Tjakastad Subgroup is underlain by the Sandspruit, Theespruit, and Komati Formations in ascending order, and is composed mainly of peridotitic and basaltic komatiites, basalt, chert and banded iron formation, together with minor clastic sediments and felsic intrusions. The Geluk Subgroup consists of the Hooggenoeg, Kromberg, and Swartkoppie Formations in ascending order, and contains basaltic komatiite, basalt, dacite, chert and banded iron formation, together with minor ultramafic komatiite, clastic sediment, and felsic intrusives.

Figure 5a shows the geological map of the Komati Formation in Barberton Greenstone Belt in South Africa. The Komati Formation is subdivided into two units by the lithology. The lower area is characterized by the alternation of piles of peridotitic komatiite flows with

basaltic flows. The ultramafic komatiites are thin, 20 cm to 15 m thick, and form piles of many flows. The pillow structures are pervasively recognized in the basaltic flow. Pillowed and massive basaltic flows have white spherical structure, several cm across. The white spherules are called ocelli, caused by liquid immiscibility (Ferguson & Currie 1972), crustal contamination (de Wit et al. 1987) or secondary alteration. Basaltic komatiite flow conformably overly the basaltic flow in the upper area of Komati Fm. Basaltic komatiites are characterized by clinopyroxene spinifex texture. Some basaltic komatiites form pillow lava structure, but another form massive lava. Small clinopyroxene-spinifex crystals are recognizable in the core of the pillow lava. Peridotitic komatiites are classified into two types based on the volcanic occurrence; peridotitic komatiites flows with/without olivine spinifex texture and intrusives of sills and dikes. The latters have the adcumulate texture with euhedral olivine, augite and bronzite oikocrysts, and titaniferous hornblende. There is obvious relationship between stratigraphy and vesicularity of peridotitic komatiite lava flow. Thick peridotitic komatiite flows at the bottom of the Komati Formation has no vesicles, while many thin peridotitic komatiite flows at the intermediate stratigraphic level have many vesicles at both upper and lower chilled margins. In addition, hyaloclastite with highly vesicularity occurs at this stratigraphic level (Dann, 1998). At the upper stratigraphic level, peridotitic komatiites without spinifex texture become dominated rather than spinifex texture-bearing peridotitic komatiites, and have no vesicles. This area of the Komati formation is bounded by two types of thrusts; one type is composed of four thrusts with NE-trending and NW-dipping, and another type consists of three thrusts with EW-trending and N-dipping. The direction of the deformation of the former thrusts is top to the north, while that of the latter thrusts is also top to the north (Fig. 5a). The latter include the Komati Fault. In addition, outcrop-scale duplex structures exist around the boundary between the Komati and Hooggenoeg Formations. Therefore, the geological structure indicates that Komati Formation forms thrust-bounded imbricate structure.

Figure 5b is geological map of the Hooggenoeg Formation, overlying the Komati Formation. The Hooggenoeg Formation mainly comprises basaltic lavas and intrusives, basaltic komatiite, ultramafic komatiite lava and intrusives, dacite, qz-porphyry intrusives and chert and volcanic sandstone. In the lower zone, pillow and massive basaltic lavas are dominated, while basaltic and peridotitic komatiite, dacite and bedded chert are predominant in the upper area. The dips and strikes of bedded chert layers range mainly from 30 to 85 south-dipping, and from 75 to 85 west-direction, respectively. Many layer-parallel shear zones are present especially in the upper zone. Especially, the sear zones exist on the bedded chert layers. In addition, there are outcrop-scale duplex structures in some places all over the Hooggenoeg Formation. The direction of the movement is top to the east. The geological structure of the Hooggenoeg Formation is also thrust-bound imbricate structure. Recently, petrology, geochemistry and geology of the Phanerozoic accretionary complex showed that obvious and simple relationship between field occurrence of greenstones and their tectonic setting (summarized by Ogawa and Taniguchi, 1989; Isozaki et al., 1990). Massive and

pillowed basaltic greenstones overlain by thick-bedded chert have MORB-affinity geochemistry and tholeiitic characteristics of relict igneous augites (Sugisaki et al., 1979; Taira et al., 1988; Kimura & Mukai, 1991; Okamoto et al., 2000; Hashimoto & Kimura, 1999). In addition, Japanese island arc experienced ridge-subductions at least three times (Isozaki, 1996). At the final ridge-subduction in the Tertiary, MORB magmatism occurred around the subduction zone. The oceanic crust formed at the ridge subduction also accreted to Japanese island arc to make the Tertiary accretionary complex, the Shimanto Belt. Greenstones with MORB-affinity geochemistry alternate with mudstone in some places in Shimanto Belt (e.g. Maeda & Kagami, 1996), and the field occurrence is quite similar to the alternation between pillowed basalt and mudstone in the Taitao peninsula in southwestern Chile, where an on-going ridge-subduction occurs (Nelson et al., 1993; Komiya unpubl. data). On the other hand, greenstones with OIB- and oceanic plateau-affinity of whole rock and relict igneous pyroxenes composition repeatedly alternate with thin bedded chert (meters to centimeters thick), or are capped by limestone (e.g. Kimura et al., 1994; Nishimura et al., 1979; Kimura, 1994; Kimura et al., 1992; Matsuda & Ogawa, 1993; Maruyama & Yamasaki, 1978). Especially, it is worth mentioning that both greenstones with MORB- and OIB-affinity geochemistry occur in small areas, and that the field occurrence of the greenstones follows the above-mentioned rule (Shimizu, 1979; Suzuki, 1988; Ueda et al., 2000). Comparison of geological and sedimentary structures between the Phanerozoic accretionary complexes and the Barberton Greenstone Belt showed that the Barberton Greenstone Belt was accretionary complex, which consists of oceanic island magmatic basalt and komatiite and pelagic sediments. On the other hand, the structural movement of some shear zones and duplex structures show that the accretionary complex had grown from west to east, and from north to south.

Figure 6 shows geological map of the Schapenburg greenstone remnant. The Schapenburg greenstone remnant in the Barberton Greenstone Belt is composed of ultramafic komatiite, basaltic komatiite, gabbro, basalt, BIF/chert, and psammitic/pelitic gneiss, and was intruded by granitoids and eventually by younger dikes. Previous work suggested conformable cyclically repetition of ultramafic and basaltic komatiites (Anhaeusser, 1983). However, the remnant comprises at least fourteen layer parallel thrust-bounded subunits (horses). Figure 7 is a sketch map of outcrops at the boundary between two thrust-bounded horses. The deformation is concentrated along the boundary to form shear zone. The movement of the deformation is top to the east. Duplex structures with outcrop scale are obvious in some places. The subunits have the similar lithostratigraphy one another, which consist of ultramafic komatiites, basaltic komatiite, and chert/BIF in ascending order. Shear zones are remarkable only at the top and bottom of the lithostratigraphy. Despite that the lithostratigraphy is quite thin, it is similar to “oceanic plate stratigraphy” in the Phanerozoic accretionary complex (Isozaki et al., 1990). The lines of evidence of duplex structure and “oceanic plate stratigraphy” imply that the Schapenburg greenstone remnant was mid-Archean accretionary complex, comparable to the oldest accretionary complex in the Isua

supracrustal belt (Komiya et al., 1999). Chert layers are relatively thin and discontinuous. In addition, some layers are conformably interlayered with basaltic greenstone. The field occurrence of mafic/ultramafic volcanics and bedded chert layers suggests that the Schapenburg remnant originated from oceanic island and plateau, according to accretionary geology (Isozaki et al., 1990).

Figure 8 shows sketch maps of the peridotitic komatiite at the intermediate stratigraphic level, which are composed of the seven thin komatiite flows. Despite of the difference in thickness, each flow is composed of basal chilled margin, equant olivine cumulate, oriented olivine spinifex zone, random-olivine spinifex zone and invisible random spinifex zone and topmost chilled margin in ascending order in this outcrop. The stratigraphy is equivalent to the previous works (Arndt et al. 1977; Arndt 1994; Grove et al. 1997). Chilled margins occur only at the topmost and bottom, and no chilled margin runs between oriented olivine-spinifex zone and equant olivine cumulate zone. The observations are inconsistent to the interpretations by Grove and co-workers which suggested spinifex zone intruded into the massive ultramafic rocks (Grove et al 1997). Small but visible vesicles occur at both the top and the basal chills in some flows (Fig. 8, 9). Nevertheless, no vesicles are present on the top surface of the chilled margin, suggesting that the magma was under-saturated in $H_2O$ at the eruption. These flows appear to be thinner than others. Size of vesicles increases inward (Fig. 9). Figure 10 is the sketch of relatively thick ultramafic komatiite flow at the stratigraphic bottom. The inner stratigraphy is similar to the thin flow, but is characterized by the presence of foliated zone (B1). The flow consists of basal chilled margin, equant olivine cumulate, oriented olivine spinifex zone, foliated zone, random-olivine spinifex zone and invisible random spinifex zone and topmost chilled margin in ascending order in this outcrop. The flow contains no vesicles not only at the chilled margin but also in the spinifex zone.

Figure 11 shows the progressive metamorphism in this area. Metamorphic zones are defined by mineral assemblage and the composition of amphibole and plagioclase in Tholeiitic basalt in Komati Fm. Metabasite in the upper zone is characterized by actinolite and albite, suggesting greenschist facies condition. The mineral assemblages of metabasites in the middle zone are characterized by hornblende+albite, hornbelnde+albite+calcic plagioclase, actinolite+hornblende+calcic plagioclase, suggesting the transition zone from the greenschist to amphibolite facies. Metabasites in the lower zone contain hornblende and calcic plagioclase, indicating amphibolite facies. The irregular variation of the compositions of amphiboles and plagioclase is caused by the variation of bulk compositions, but also presumably by the repetition of metamorphic grade along thrust.

Olivines are found all over the Komati Fm., especially in olivine cumulate zone of peridotitic komatiite flows and poikilitic komatiitic sills and dikes (Fig. 12a). However, the olivines have distinct compositions between in low-grade and in high-grade metamorphosed zones. Figure 13 shows the compositions of olivines in olivine cumulate zone in the ultramafic komatiite flows from the lower metamorphic grade zone and higher metamorphic grade zone. Olivines in the severely metamorphic zone have relatively higher Fo value, up to

93.5, but are highly dispersed in Ni and Mn contents at given Fo value. In addition, the olivines are characterized by high ratio of secondary magnetite to serpentine and inconsistency between the direction of c-axis of relict olivine and that of its pseudomorph. The lines of evidence indicate that olivines in high-grade metamorphic zone originated from the metamorphism. The olivines in low-grade metamorphic zone have relatively lower Fo value, and have characteristics of low ratio of secondary magnetite to serpentine and consistency between the direction of c-axis of relict olivine and that of its pseudomorph. Olivines coexisting with Type II (mentioned later) clinopyroxenes are relatively magnesian, and range from 90.5 to 92.8 in Fo value, whereas olivines enclosed by Type III clinopyroxene and orthopyroxene oikocrysts are less magnesian and have the Fo values from 87.2 to 88.5. The less metamorphosed olivines define a clear single compositional trend of Ni or Mn, which corresponds the calculated olivine-fractionation trend on Fo diagram. Most refractory olivine of the less metamorphosed olivines has 92.8 in Fo value, suggesting that the primary magma of ultramafic komatiite is at least 26.5 wt % in MgO (Komiya et al., 1998).

Clinopyroxenes are also found all over the Komati and the Hooggenoeg Formations (Fig. 12ab). but some of them suffered post-magmatic modification on the composition. Figure 14 shows the composition of clinopyroxene in a single sample of ultramafic komatiite. The pyroxenes vary so much in composition, but forms distinct two compositional trends. One trend is defined by increasing wollastonite content with increasing $Mg^{\#}$, whereas another trend is defined by decreasing wollastonite content with increasing $Mg^{\#}$. The former is caused by secondary alteration including subsolidus interaction with fluids, analogous to the hydrothermal clinopyroxenes of the Skaergaard intrusion (Manning & Bird 1986). The latter originates from the magmatic differentiation.

Primary relict igneous clinopyroxenes are subdivided into three types by the occurrence and composition (Fig. 15). Type I clinopyroxene is calcic clinopyroxenes with spinifex texture. Type II clinopyroxene crystallized from interstitial melt among olivine grains in cumulate zone, and formed euhedral column to oikocrysts, depending on the crystallinity. Type III clinopyroxene forms poikilitic texture, accompanied by inclusions of euhedral olivines, oikocrystic bronzite and intercumulus igneous hornblende, and is found in komatiitic sills and dikes.

Type I is enriched in wollastonite component and has the large compositional variation (Fig. 16). It is still controversial whether the high wollastonite content was caused by high $H_2O$ content (Gaetani et al., 1993; Parman et al., 1997) or high cooling rate (Kinzler & Grove, 1985). Clinopyroxenes of Type II display quite distinctive compositional zonation from pigeonite in the core through augite in the mantle to highly aluminous augite along the rim (Fig. 17 and 18). The ratio of volume of pigeonite in the core to augite in the mantle/rim increases from the stratigraphic bottom to the top in the Komati Fm (Fig. 19). Especially, no pigeonitic cores exist within clinopyroxene grains at the stratigraphic bottom of the Komati Fm. Figure 17 shows the compositions of augite and pigeonite from type II ultramafic komatiites. Figure 18 shows the textual relationships between augite, pigeonite and aluminous

augite, suggesting that olivine is followed by pigeonite, augite and aluminous augite. Although any pigeonite is enclosed by augite, pyroxene geotherm indicates that pigeonite crystallized at the almost same temperature (Figure 17). The line of evidences suggests that the ultramafic komatiites had only small amount of water, less than 0.4 wt % (Figure 15b). Pyroxene geotherm (Lindsley, 1983) indicates that the clinopyroxenes crystallized from 1300 ˚C. Parman and others (1997) showed that crystallization of augite preceded that of pigeonite in peridotitic komatiites with high water content (more than 0.4 wt %). The texture indicates presence of water in the host magma at the crystallization, and degassing of $H_2O$ with decreasing depth of seawater due to piling up of komatiite and basaltic flows. Olivines in cumulate zones of peridotitic komatiites with type II-clinopyroxenes, form a clear single liquid line of descent, and range from 90.5 to 92.8 in Fo value (Fig. 13a). Clinopyroxenes of Type III are more magnesian, up to 89.5 in $Mg^{\#}$ value than the coexisting olivines, 87.2 in Fo value (Fig. 20). The coexisting orthopyroxenes are relatively magnesian, up to 90.6 in $Mg^{\#}$ (Fig. 20). The compositional relationship indicates that olivine, clinopyroxene, and orthopyroxene crystallized in almost equilibrium, consistent to the poikilitic texture. Pyroxene geotherm indicates that clinopyroxene and orthopyroxene crystallized from 1200 ˚C. Highly titaniferous hornblende occurs as intercumulus phase among olivine, orthopyroxene and clinopyroxene grains, suggesting $H_2O$-saturation in highly evolved magma. Relict igneous olivine phenocrysts define a single liquid line of descent in cumulate zone with type II and III-clinopyroxenes, but olivines from type III, 87.2 to 88.5 in Fo value, are less magnesian than those from type II, 90.5 to 92.8 in Fo value. The compositional evidence is consistent that both types of ultramafic komatiites were differentiated from the same primary magma.

Figures 23 and 24 show compositional variations within chromian spinels enclosed by olivine and clinopyroxene, respectively. Chromian spinels within olivine phenocrysts or serpentine pseudomorphs after olivine have high $Cr_2O_3$, FeO and MnO and low MgO content. Extreme high abundance of MnO in those chromian spinels is unique of all the chromian spinels in any terrestrial rocks. Chromian spinels within clinopyroxene phenocrysts form distinctive compositional zoning. They have high MgO, and low $Cr_2O_3$, FeO and MnO in the core. However, they have higher MnO and FeO in the outer margin or along the fissures. Figure 25 shows compositional variations of isolated chromian spinels and chromian spinels enclosed by various phases such as olivine, clinopyroxene, orthopyroxene, and hornblende along with chromian spinels in the modern MORBs and boninites on the calculated $Fe^{3+}$ versus Al diagram. Cores of chromian spinels enclosed by clinopyroxenes are plotted on the estimated compositional trends of fractional crystallization. On the other hand, the calculated $Fe^{3+}$ content in other chromian spinels increases with decreasing Al content, suggesting that the compositions suffered from recrystallization during solidification of magma (Ridley 1977; Wilkinson & Hensel 1988) or secondary alteration at the metamorphism. Figures 26a and 26b show compositional variations of fresh chromian spinels within clinopyroxene phenocrysts along with chromian spinels in the modern MORBs and boninites on $Mg^{\#}$ versus $Cr^{\#}$, and Ti versus $Fe^{3+}/(Fe^{3+}+Cr+Al)$ ratio diagrams. Chromian spinels from ultramafic komatiites form a

compositional variation similar to those of boninites. Chromian spinels in ultramafic komatiites have higher $Fe^{3+}$ compared with those of modern MORBs, suggesting that $Fe^{3+}/\sum Fe$ ratio of ultramafic komatiites was higher than that of modern MORBs. The high $Fe^{3+}/\sum Fe$ ratio was presumably caused by the melting of transition mantle, which can contain higher $Fe^{3+}$ content than peridotitic mantle. The pattern of REE elements and $Al_2O_3$ content of Al-depleted komatiites support the speculation.

Type III ultramafic komatiite contains highly titaniferous hornblende, kaersutite (Fig. 27). The shape of them is irregular and is dependent of the outlines of the surrounding minerals. The hornblende crystals are colorless to brown in color, and have clear cleavages. The color corresponds to the Ti content of the hornblende, and varies from colorless to brown with increasing Ti content. Colorless areas appear to be near the high Ca-augite or salite. The observation suggest that colorless hornblende suffered from secondary chemical modification possibly due to the interaction of metamorphic or hydrothermal fluid.

Here, potential mantle temperature of ultramafic komatiites will be estimated from combination of the sequence of fractional crystallization and recent experimental result (Parman et al. 1997). Igneous texture of fresh ultramafic komatiites indicates the sequence of fractional crystallization pass from olivine through pigeonite to augite as shown above. In additions, augite was crystallized just after pigeonite (Fig. 17a). Therefore, ultramafic komatiite magma would contain ca. 0.5 wt % in $H_2O$ when pigeonite joined olivine on the liquidus (Figure 17b), suggesting that the primary magma would contain about 0.4 % in $H_2O$. The result is different from the previous works, which showed ultramafic komatiites had over 4.2 wt % (Parman et al. 1997). Moreover, the result is consistent to FTIR and ion-probe analyses of melt inclusions of Al-undepleted ultramafic komatiite (McDonough & Danyushevsky 1995; Shimizu et al. 1997). Parman et al. (1997) regarded that primary magma has 23.2 wt % in MgO, whereas Fo value of olivines phenocrysts indicate the primary magma should have 26.5 wt % in MgO. Because increasing 3 % MgO content results in increase of liquidus temperature by 60 ˚C at 1 atm (Nisbet et al. 1993), the liquidus temperature of ultramafic komatiites is estimated as about 1500 ˚C based on the experimental results of ultramafic komatiites (Parman et al. 1997). The degree of melting was estimated as about 36 % by the abundance of incompatible elements such as $TiO_2$, assuming that the source mantle would be pyrolitic in $TiO_2$ content. The potential mantle temperature was estimated as about 1700 ˚C based on the melting experiments at relatively lower pressure (Hirose 1997), because of lack of melting experiments of slightly hydrous peridotite at high pressure (Figure 28). Although the thickness of oceanic plate cannot be estimated, the oceanic plate was supposed 60-km thick, average thickness in the Archean (Chapter V). The difference of mineral assemblage may affect the estimate of potential mantle temperature because spinel can contain much water relative to olivine, orthopyroxene, and clinopyroxene. The estimated potential mantle temperature means maximum because the difference leads to increasing the solidus temperature at the higher pressure.

## VI-4 Discussions

### VI-4.1 The secular change of the potential temperature of the MORB source mantle

Many previous works estimated the mantle temperature of the Archean from the composition of the komatiites (Green et al. 1975; Takahashi 1990; Nisbet et al. 1993). Therefore, it is considered that the Archean mantle was much hotter than the modern mantle. However, it is poorly understood where komatiites were formed (e.g. Green et al. 1975; Takahashi & Scarfe 1985; Inoue & Sawamoto 1992). In addition, it becomes widely supposed that komatiites were derived from plume-related magmatism (e.g. Campbell et al. 1989; Campbell & Griffiths 1993).

Recently Maruyama and co-workers proposed the determination methods of geological setting of greenstone based on the accretionary geology, analogous to the Phanerozoic accretionary complex (Maruyama et al. 1991ab; Isozaki et al. 1991; Kimura et al 1993; Ohta et al. 1996; Komiya et al. 1998). The results indicate that the Archean MORBs were FeO enriched tholeiites instead of komatiites (Ohta et al. 1996; Komiya et al. 1998). Therefore, the potential mantle temperature estimated from the komatiite magma does not represent that of normal upper mantle in the Archean, but represent that of plume source mantle. The potential temperature of source mantle of MORBs was reported from only 3.3 Ga Cleaverville MORBs, about 1400 ˚C (Ohta et al. 1996).

This doctor thesis presents the potential mantle temperature of MORBs source mantle with different age (in Chapter II to VI). The potential temperature of 3.5 Ga plume source mantle is also presented in this chapter. Figure 29 shows the secular variation of the potential temperatures of source mantles of MORBs and plume-related magma. The estimated potential mantle temperature with each age except for that of 3.5 Ga North Pole area involves the uncertainty of about 100 ˚C, caused by uncertainty of the composition of primary magma, insufficiency of experimental data, and influence of secondary alteration on especially $SiO_2$ content. Magmatic process (Klein & Langmuir 1989) and small temporal change of potential mantle temperature (Reynolds et al. 1992) may also play significant role on the large uncertainty.

Secular change of potential temperature of upper mantle was obtained in Figure 29, assuming that MORBs with different age represent a typical MORB from the normal ridge segment with the age. The potential temperature of present-day mantle is estimated by three methods: thickness of oceanic crust (McKenzie & Bickle 1988; Iwamori et al. 1995), rare earth element inversion (McKenzie & O'Nions 1991; White et al. 1992), major element inversion (e.g. McKenzie & Bickle 1988; Kinzler 1997; Hirose & Kushiro 1998). Thickness of oceanic crust vary from ca. 2.1 ±0.6 km in very slow spreading ridges through 4.0 ±1.3 km in fracture zones and 7.1±0.8 km in normal ridges to 10.7 ±1.6 plume affected oceanic ridge (White et al. 1992). Oceanic ridges directly above a rising mantle plume, such as Iceland and possible Ontong-Java plateau have very thick oceanic crust, 18.5 ± 0.5 km (White et al. 1997).

However, subaerial or subglacial magmatism occurs instead of submarine eruption on Iceland because of very thick oceanic crust. Pillow lava is formed even by subglacial eruption, but not by subaerial eruption. Subaerial eruption leads to toe structure with rare exception (Jones 1968). There are some differences between submarine pillow lava and subglacial pillow lava (Wells et al. 1979). For example, subglacial pillows tend to be more widely separated from one another, with the intervening spaces filled by palagonitized hyaloclastite. Pillow lavas with subcircular or elliptical outlines and hollow layered pillows are common in subglacial exposures (Wells et al. 1979). Small amount of hyaloclastite and common occurrence of closed-pack-type pillow lava in Archean greenstone belt are incompatible to subglacial or subaerial eruption. Moreover, the overlying bedded chert without tidal structure or perturbed sedimentary structure is considered as pelagic or deep-sea sediment. Therefore, even if the paleoenvironment of investigated areas were affected by mantle plume, they did not lie directly above a rising mantle plume. Despite of minor influence of small amount of exposed continental crust and short life span of oceanic lithosphere, if amount of water in Archean was comparable to that at present, axial depth of oceanic ridge should be also comparable. Then variation of thickness of oceanic crust is limited to *ca.* 3000 m. Inversion of thickness of oceanic crust showed potential mantle temperature varied from 1343 ˚C for 8-km thick oceanic crust to 1385 ˚C for 11-km thick oceanic crust (Iwamori et al. 1995). REE inversion showed potential mantle temperature varied from 1330 ˚C for 8-km thick oceanic crust to 1365 ˚C for 11-km thick oceanic crust (White et al. 1992). Major element inversion also indicated that potential mantle temperature varied from ca. 1416 ˚C for 8-km thick oceanic crust to ca. 1449 ˚C for 11-km thick oceanic crust (Kinzler 1997). Namely, possible spatial variation of potential mantle temperature plays insignificant role on the estimated secular variation. Recently, depth of water at oceanic ridge in middle Archean was estimated to be comparable to present-day depth of water, based on fluid circulation and ocean floor metamorphism in North Pole area (Kitajima & Maruyama 1997 per. Commun.).

Despite of large error, figure 29 indicates some significant and new observation. Firstly, the Archean mantle was only about 100 to 200 ˚C higher than the modern mantle. The estimated temperature is much lower than that by previous works, 1900 ˚C (Takahashi 1990; Nisbet et al. 1993). Higher temperature of mantle makes mantle convection double-layered because of high Rayleigh numbers. Therefore, it is thought that the Archean mantle was necessarily convected in double-layered. However, if the potential mantle temperature ranged from *ca.* 1400 to 1550 ˚C in the Archean, even single-layered convection can release the heat from the mantle (Richter 1985). Phase change from γ-spinel+garnet+Ca-perovskite to Mg-perovskite+magnesiowüstite+Ca-perovskite at 650 km induces the layered convection if the Clapeyron slope of the reaction is low, -4 to –8 MPa/K (Christensen & Yuen 1985). However, the modern mantle convects in whole mantle because of the involvement of subsidence of slab into the lower mantle and ascent of superplume from the lower mantle.

Figure 33 shows the phase relations of KLB-1 in 0 to 30 GPa, and 1200 to 2600 ˚C (Herzberg & Zhang 1996). P-T paths of the mantle with three different potential mantle

temperatures are also drawn on figure 33. Each P-T path corresponds to the Archean normal upper mantle, 1450 ˚C in PMT, the modern normal upper mantle, 1330 ˚C, and the Archean plume-source mantle, 1700 ˚C. P-T condition of phase change from majorite-bearing to perovskite-bearing oceanic crust are also shown based on experimental data of this work and Hirose et al. (1998) in Figure 33.

Although the depth of upper-lower mantle boundary (ULB) decreases with potential temperature of the mantle, difference of potential mantle temperature by 150 ˚C plays insignificant role on the depth of ULB, by only *ca.* 7 km (Fig. 33). Moreover, large temperature difference, even by 400 ˚C leads to small difference of depth of phase, by at most *ca.* 4 km (Fig. 33). Although the temperature of slab rather than surrounding mantle is critical on whether slab penetrates into lower mantle, it depends strongly on thermal structure of slab. Therefore, temperature of slab at ULB is still poorly known. The temperature of slab depends primarily on the velocity of the slab penetration, which is the function of dip angle of the subduction (Ito & Sato 1992). The dip angle of subduction is proportional to the age of slab. Lifetime of oceanic plate is supposed to have been shorter in Archean than in Phanerozoic because plate moved faster (Dewey & Windley 1981; Nisbet & Fowler 1983) and/or the size of plate was smaller (Hargraves 1986) in order to release much heat from the mantle. This prevents the slab from penetrating not only into the lower mantle but also into the mantle transition zone.

The plate motion depends not only on ridge push and mantle drug force but also on slab pull. In the Phanerozoic, the latter is more significant. Hotter potential mantle temperature leads to thicker oceanic crust, ca. 17 km at 1450 ˚C (Fig. 30), whereas thickness of oceanic plate decrease with increasing potential mantle temperature (Table 6). Maximum thickness of Archean and preset-day oceanic lithosphere calculated by simple thermal conductivity indicates that thickness of Archean oceanic plate was less than *ca.* 71 km, whereas that of present-day oceanic lithosphere is more than 190 km. Moreover, it is thought that another small-scale mantle convection keeps the thickness of plate constant beneath relative older lithosphere (e.g. Richter & Parsons 1975). Therefore, at present, even 200 Ma oceanic lithosphere are at most *ca.* 100 km thick. In Archean, its short lifetime, 20 m.y., led to thin oceanic lithosphere (Fig. 30). Therefore, slab pull increases and slab resistance decrease (Arndt 1983; Richter 1985). Recently Davies (1992) emphasized that Archean oceanic plate with thick oceanic crust and harzburgite could not subduct at trench because its density was lighter than the underlying asthenosphere. However, his logic is unsound, because initiation of subduction occurs from difference of density between the two lithospheres, instead of the underlying mantle. Therefore, initiation of subduction is independent of potential mantle temperature.

Higher potential mantle temperature may result directly in higher geothermal gradient in subduction zone. Figure 32 shows phase relation of hydrous MORB with geothermal gradient of Archean subduction zone estimated from Isua supracrustal belt. Higher geothermal gradient prevents the subducted oceanic crust from changing into eclogite or high-

pressure granulite. Therefore, some considered that plate tectonics had not operated yet in Archean (e.g. Hamilton 1998). However, slab melting leaves eclogite (ρ=3.55) or high-pressure granulite (ρ=3.47) as residue, which are dense than ambient mantle (ρ=3.34) (Fig. 32). Therefore, Archean oceanic lithosphere with thick basaltic crust could easily subduct into upper-lower mantle boundary.

Subducted oceanic plate tends to be stagnated on upper-lower mantle boundary because both oceanic crustal portion and the underlying mantle portion have Mg-perovskite-bearing phase assemblage at relatively higher pressure (Fig. 33). It may be possible that a subducted oceanic lithosphere penetrates into the lower mantle due to inertia of descending slab. However, even if isostatic, Archean oceanic lithosphere could subside into the lower mantle because of its thick basaltic crust (Fig.34). Phase change from majoritic garnet to Mg-perovskite in basalt system takes place by 40 km deeper than that in peridotite system (Fig. 33 and 34). Therefore, subducted oceanic lithosphere is stagnated to produce megaliths mainly of basaltic materials along upper-lower mantle boundary. Isostasy indicates that once megaliths grow up to 80 km thick, the basement delaminated to sink into lower mantle (Fig. 34). High production rate of oceanic crust at ridge in Archean indicates that it takes only 100 M.y. for 80-km thick subducted oceanic crust to be stored over upper-lower mantle boundary. Moreover, high potential mantle temperature led to the harzburgite-dominated lithosphere, which may have allowed the slab to penetrate into the lower mantle (Irifune & Ringwood 1987). Therefore, slab penetrated into the lower mantle in the Archean as well as in the Phanerozoic. Namely, episodic whole mantle convection predominated even in the Archean. Despite of presence of highly depleted mantle (Silver et al. 1988; Bennett et al. 1993, McCulloch & Bennett 1994), no magmas from complementary enriched mantle have been reported in the Archean, suggesting that subducted oceanic crusts ware not homogenized but were stagnated somewhere (Chase & Patchett 1988; Blichert-Toft & Albarède 1993, 1994). Subducted oceanic crusts were presumably stagnated in the lower mantle as well as in the bottom of upper mantle.

Secondly, the temperature of upper mantle has not been decreasing gradually but episodically. The potential mantle temperature remained constant from 3.8 to 2.5 Ga, about 150 ˚C higher than the modern. Moreover, potential mantle temperature appears to have been relatively lower at 3.3 Ga, whereas it appears to be higher at 2.5 Ga. The effect of global variation of potential mantle temperature, analogous to the modern upper mantle (Klein & Langmuir 1987, 1989; Klein et al. 1991; Kinzler 1997) can not be ruled out on higher potential mantle temperature at 2.5 Ga. However, active magmatism including ultramafic komatiites was reported around the Archean-Proterozoic boundary (Arndt et al. 1977; Nisbet et al. 1977; Hall 1980). Therefore, the higher potential mantle temperature may represent the average at 2.5 Ga. Recently Ogawa (1997) proposed that mantle temperature may have remained constant based on the computer simulation in the Archean. Although our geological investigation indicated that plate tectonics had already operated in the Archean, his calculation is consistent to this result.

Constancy of potential mantle temperature through the Archean may be because the hotter lower mantle materials were injected episodically or continuously into the upper mantle. Mantle over turn is also expected by computer simulations (Breuer & Spohn 1995). Relatively higher potential temperature of the early Archean mantle may represent the rejuvenation by involvement of lower mantle materials. Further investigation will be required for the quantification of mantle overturn and the accompanied rejuvenation of upper mantle.

**VI-4.2 The secular change of composition of the MORB source mantle**

It is widely supposed that the Earth was made of chondritic meteorites (Ringwood 1966). Therefore, the average composition of the whole mantle is supposed to equivalent to that of chondrite except for the depletion of volatile and siderophile elements, due to heat generation during the accretion and the segregation of iron metal in the following core formation, respectively. The imaginary mantle, which has such primitive composition, is called primordial mantle or primitive mantle. However, chondritic mantle model also involves some inconsistencies. For example, depletion of Si relative to Mg in the (upper) mantle is well known. The cause is still controversial; for example, fractionation into the lower mantle (Liu 1982; Anderson 1982, 1983; Taylor & McLennan 1985), volatility-controlled process in the solar nebula prior to accretion of the Earth (Ringwood 1979; 1989), and fractionation of metallic Si into the iron core (Ringwood 1979). The first idea is inconsistent to the ultra-high pressure experiments (Kato et al. 1988; Kesson & Fitz Gerald 1991). The second idea is supported by Preliminary data (Ringwood 1989), but there appears to be no gainsaying the ignorance of composition of another planet.

On the other hand, the mantle compositions estimated by the meteorites have higher FeO content than the modern ultramafic mantle nodules (e.g. Jagoutz et al. 1979). This difference may be caused by secular change of the composition of the mantle (e.g. Glikson 1971, 1979; Sun & Nesbitt 1977) or fractionation into the lower mantle (e.g. Anderson 1982). Archean basalts have higher FeO content than modern MORB (Glikson 1971; Gill 1979). Therefore, it was thought that Archean mantle was more enriched in FeO relative to modern mantle. In later 1970s, composition of Archean mantle was estimated from liquid line of descent of Al-undepleted komatiite (Bickle et al. 1977; Sun & Nesbitt 1977; Sun 1982; Beswick 1983). It is thought that Al-undepleted komatiite was produced by high degree of melting at moderate pressure, 3 to 7 GPa. Therefore, only olivine was left in residue. Liquid line of descent of Al-undepleted komatiite indicates that Archean mantle had slightly higher FeO content than modern upper mantle but less than the estimate from Archean basalt (table 7). The discrepancy is because the liquid line of descent is derived not from fractional melting but from crystallization of magma, and because MgO content of primitive mantle was assumed to be 42 to 45 %. Chemical variation of magma through fractional crystallization is quite different from that through mixing of residual magma and crystallized olivine on FeO vs. MgO diagram. Liquid line of descent of Al-undepleted ultramafic komatiite indicates a trend

of mixing of residual magma with olivine (e.g. Arndt 1994). However, if komatiite magma left only olivine behind, composition of mantle source except for Ni can be estimated from liquid line of descent liquid line of descent, involved by fractional melting (Fig. 36). Because distribution function of Ni between olivine and melt is dependent on pressure (Taura et al. 1998), the estimated concentration is slightly higher (Fig. 36). This work also estimated FeO content of source mantle of Al-undepleted komatiite from data of Al-undepleted komatiite in Belingwe greenstone belt and Abitibi greenstone belt (Fig. 36). The result indicates that Archean mantle had about 9.1 to 10.1 wt % in FeO (Fig. 36). Moreover, FeO content of mantle source was estimated to be 9.6 wt % from most primitive magma of Al-undepleted komatiite using distribution function of FeO and MgO between olivine and melt (table 7). These evidences indicate that Archean mantle was still more enriched in FeO, compared to modern mantle.

Major elements analyses of the MORBs with different age indicate that the Archean mantle had a higher FeO content than the modern upper mantle (Fig. 29, and see the text in Chapter II, III, and IV). Moreover, FeO content of the MORB source mantle did not change gradually through time, but changed abruptly after the Proterozoic. The mode of secular change of the FeO content appears similar to that of the potential mantle temperature (Fig. 29).

Depletion in FeO may have been caused by the storage of FeO-enriched oceanic crust in the upper or lower mantle (Chase & Patchett 1988). The idea is consistent to geochemistry of the modern oceanic island basalt (e.g. Hauri 1996; Kogiso et al. 1997). However, this idea can not explain why modern MORBs can be produced from the residual mantle, again. Namely, if the source mantle of MORBs involved the recycled oceanic crust, the depletion in only FeO cannot be explained.

This ultra-high-pressure experiment implies new idea that some of $Fe^{2+}$ ions transformed into $Fe+Fe^{3+}$ during slab penetration into the lower mantle because aluminous Mg-perovskite contains $Al^{3+}Fe^{3+}$ instead of $Mg^{2+}Si^{4+}$ as shown above (Fig. 2b). The depletion of FeO content depends on $Al_2O_3$ content. Therefore, the subsidence of oceanic crust, which contain more FeO and $Al_2O_3$ relative to the underlying mantle, into lower mantle removes much FeO content from the slab as metallic iron. The segregated metallic iron may subside on the metallic core or float in the lower mantle. However, Sun (1982, 1984) emphasized that metallic core had never grown after Archean based on ratio of siderophile to lithophile element such as $P_2O_5/TiO_2$. However, these works compared komatiite and picrite with different age to modern NMORBs (Fig. 31; Fig. 2 of Sun 1984). Comparison of Archean MORBs with modern MORB indicated obvious secular variation of $P_2O_5/TiO_2$ ratio (Fig. 31). Therefore, extraction of metallic iron is consistent to secular change of siderophile element. Moreover, Pb, a chalcophile element may be also enriched in the 3.8 Ga MORBs, relative to the modern MORBs. However, there are not obvious secular variations of Ni and platinum group elements (PGEs) abundances. Ni and PGEs behave as compatible element at mantle melting. Although some PGEs like Re are thought to be highly incompatible elements,

modern MORBs have much less Re content than upper mantle (e.g. Keays 1982), suggesting that PGEs, even Re, behave as compatible elements. The physicochemical difference between siderophile and lithophile elements, in general, decreases at ultra-high pressure condition (Hillgren et al. 1994; Righter et al. 1997; Walter 1997). Namely, partition coefficients of P, Ni, PGEs between metallic liquid and silicate liquid decrease to *ca.* 3.1, 40 and 100 at 27 GPa, 1400 ˚C, ΔIW=+2 (Righter et al. 1997; Walter 1997; table 4). Therefore, segregation of metallic iron plays significant role on abundance of incompatible siderophile element such as P, but insignificant role on abundance of compatible element (table 4). Here, I will estimate the amount of metallic iron precipitated from the subducted oceanic crust in slab penetration into the lower mantle. Some parameters are summarized on table 4. The calculation indicates that assuming that the production rate of metallic iron is equivalent to that of $Fe^{3+}$, it takes 26 b.y. to reduce FeO content in whole mantle from 10.2 wt % to 8.1 wt % at the production rate of MORBs in the Phanerozoic (table 5). On the other hand, the production rate of MORBs in the Archean allows FeO content of whole mantle to decrease from 10.2 to 8.1 wt % in only 3.1 b.y. (table 5). Moreover, phosphorus content falls from 29 to 21 ppm in only 5 b.y. (table 5). The estimated NiO content of modern upper mantle varies from 0.24 to 0.31 wt % (Jagoutz et al. 1979). If a obvious secular change of NiO content is recognized, Archean mantle should have been higher than 0.31 wt % in Ni content. The calculation indicates that it is at least 15 b.y. before NiO content to fall from 0.3 to 0.25 ppm (table 5), suggesting no secular change of Ni content. PGEs also indicate no secular change, similar to Ni (table 5). On the other hand, if MORBs is produced at production rate of Archean, the Earth experienced the geochemical whole mantle convection three times (table 5). Therefore, MORB mantle source involved the recycled oceanic crust that passed by the lower mantle (Fig. 35) and it is significantly depleted in FeO, whereas are insignificantly depleted in other elements. The feature is consistent to geochemistry of modern MORBs, whose model age is calculated as about 1.7 to 4.5 Ga by Pb isotope (Silver et al. 1988).

## VI-5 Conclusions

(1) Ultra-high pressure experiments indicate that compositional difference between the Archean and modern MORBs plays insignificance role on the depth of slab penetration.
(2) Ultra-pressure experiments suggests that metallic iron is segregated form slab at phase change from majorite to perovskite. The amount of segregated iron metal depends on $Al_2O_3$ content.
(3) Potential mantle temperature of upper mantle in the Archean was 150 to 200 ˚C higher than in the Phanerozoic. The result suggests that episodic whole mantle convection dominated even in the Archean.
(4) The potential temperature of upper mantle does decrease not gradually, but episodically. Especially, the potential mantle temperature decreased significantly after the Proterozoic.
(5) The Archean upper mantle had higher FeO content than the modern upper mantle. The secular change was not also gradual but probably continual.
(6) The depletion of FeO content in the upper mantle may be caused by the segregation of metallic iron during slab penetration into the lower mantle.

## Acknowledgement

I wish to thank them for assisting in the acquisition of analytical data and high pressure experiments: Drs. Kei Hirose and Yingwei Fei (multi-anvil apparatus), Prof. Eiichi Takahashi (XRD), and Mr. Katayama (Laser Raman).

Working in Killara area, special thanks to Kouki Kitajima for supporting field works and arranging data.

Investigating in South Africa, although author can not fully discuss the geology and geochemistry of Barberton area for want of space in the manuscript, he wishes to thank Dr. Marthinus Cloete for the time he took to show author aspects of the mountain land that I would otherwise not have seen or been able to discuss. Author also wishes to acknowledge them for assisting in field survey and fruitful discussions: Drs. Kei Hirose, Kenji Shimizu, Toshiaki Tsunogae, Hikaru Iwamori, Hiroaki Ozawa, Kenji Nishikawa, and more recently Kazuaki Okamoto, Hiroshi Ohta, and Noriyuki Takahashi.

Investigating mantle evolution and dynamics, author wishes to thank Drs. Kei Hirose and Shigenori Maruyama for valuable discussions and revising his early draft.

## References


Anderson, D. L., 1982, Chemical composition and evolution of the mantle, *in* Akimoto, S., and Manghnani, M. H., eds., High-pressure research in geophysics, Tokyo, Center for Academic Publications, p. 301-318.

Anderson, D. L., 1983, Chemical composition of the mantle: J. Geophys. Res., v. 88, p. B41-B52, 1341-1352.

Arndt, N. T., 1983, Role of a thin, komatiite-rich oceanic crust in the Archean plate-tectonics process: Geology, v. 11, p. 372-375.

Arndt, N. T., 1994, Archean komatiites, *in* Condie, K. C., ed., Archean Crustal Evolution, Amsterdam, Elsevier, p. 11-44.

Arndt, N. T., Naldrett, A. J., and Pyke, D. R., 1977, Komatiitic and iron-rich tholeiitic lavas of Munro Township, Northeast Ontario: J. Petrol., v. 18, p. 319-369.

Baker, M. B., and Stolper, E. M., 1994, Determining the composition of high-pressure mantle melts using diamond aggregates: Geochim. Cosmochim. Acta, v. 58, p. 2811-2827.

Barnes, S.-J., 1998, Chromite in komatiites, 1. magmatic controls on crystallization and composition: Jour. Petrol., v. 39, p. 1689-1720.

Beck, S. L., and Lay, T., 1986, Test of the lower mantle slab penetration hypothesis using broadband S waves: Geophys. Res. Lett., v. 13, p. 1007-1010.

Bennett, V. C., Nutman, A. P., and McCulloch, M. T., 1993, Nd isotopic evidence for transient, highly depleted mantle reservoirs in the early history of the Earth.: Earth Planet. Sci. Lett., v. 119, p. 299-317.

Bertka, C. M., and Fei, Y., 1997, Mineralogy of the Martian interior up to core-mantle boundary pressures: J. Geophys. Res., v. 102, p. 5251-5264.

Blichert-Toft, J., and Albarède, F., 1993, Short-lived chemical heterogeneities in the Archean mantle with implications for mantle convection.: EOS Trans., v. 74, p. 656.

Blichert-Toft, J., and Albarède, F., 1994, Short-lived chemical heterogeneities in the Archean mantle with implications for mantle convection.: Science, v. 263, p. 1593-1596.

Bourdon, B., Zindler, A., Elliott, T., and Langmuir, C. H., 1996, Constraints on mantle melting at mid-ocean ridges from global $^{238}U$-$^{238}Th$ disequilibrium data: Nature, v. 384, p. 231-235.

Breuer, D., and Spohn, T., 1995, Possible flush instability in mantle convection at the Archaean-Proterozoic transition: Nature, v. 378, p. 608-610.

Campbell, I. H., and Griffiths, R. W., 1993, The evolution of mantle's chemical structure: Lithos, v. 30, p. 389-399.

Campbell, I. H., Griffiths, R. W., and Hill, R. I., 1989, Melting in an Archaean mantle plume: heads it's basalts, tails it's komatiites: Nature, v. 339, p. 697-699.

Chase, C. G., and Patchett, P. J., 1988, Stored mafic/ultramafic crust and early Archean mantle depletion: Earth Planet. Sci. Lett., v. 91, p. 66-72.

Christensen, U. R., and Yuen, D. A., 1985, Layered convection induced by phase transitions: J. Geophys. Res., v. 90, p. 10291-10300.

Creager, K. C., and Jordan, T. H., 1984, Slab penetration into the lower mantle: J. Geophys. Res., v. 89, p. 3031-3049.

Creager, K. C., and Jordan, T. H., 1986a, Slab penetration into the lower mantle beneath the Mariana and other island arcs of the northwest Pacific: J. Geophys. Res., v. 91, p. 3573-3589.

Creager, K. C., and Jordan, T. H., 1986b, A spherical structure of the core-mantle boundary from *PKP* travel times: Geophys. Res. Lett., v. 13, p. 1497-1500.

de Wit, M. J., Hart, R. A., and Hart, R. J., 1987, The Jamestown ophiolite complex, Barberton mountain belt: a section through 3.5 Ga oceanic crust: Jour. Afr. Earth Sci., v. 6, p. 681-730.

Dewey, J. F., and Windley, B. F., 1981, Growth and differentiation of continental crust:: Phil. R. Soc. London, v. A301, p. 189-206.

Dziewonski, A. M., 1984, Mapping the lower mantle: determination of lateral heterogeneity in P velocity up to degree and order 6: J. Geophys. Res., v. 89, p. 5929-5952.

Fei, Y., Mao, H.-K., and Mysen, B. O., 1991, Experimental determination of element partitioning and calculation of phase relations in the MgO-FeO-$SiO_2$ system at high pressure and high temperature: J. Geophys. Res., v. 96, p. 2157-2169.

Fei, Y., Wang, Y., and Finger, L. W., 1996, Maximum solubility of FeO in $(Mg,Fe)SiO_3$-perovskite as a function of temperature at 26 GPa: Implication for FeO content in the lower mantle: J. Geophys. Res., v. 101, p. 11525-11530.

Ferguson, J., and Currie, K. L., 1972, Silicate immiscibility in the ancient basalts of the Barberton Mountain Land, Transvaal: Nature Phys. Sci., v. 235, p. 86-89.

Fujii, T., and Bougault, H., 1983, Melting relations of a magnesian abyssal tholeiite and origin of MORBs: Earth Planet. Sci. Lett., v. 62, p. 283-295.

Fukao, Y., Obayashi, M., Inoue, H., and Nenbai, M., 1992, ubducting slabs stagnant in the mantle transition

zone: J. Geophys. Res., v. 97, p. 4809-4822.
Gaetani, G. A., Grove, T. L., and Bryan, W. B., 1993, The influence of water on the petrogenesis of subduction-related igneous rocks: Nature, v. 365, p. 332-334.
Glikson, A. Y., 1971, Primitive Archaean element distribution patterns: chemical evidence and geotectonic significance: Earth. Planet. Sci. Lett., v. 12, p. 309-320.
Glikson, A. Y., 1979, Siderophile and lithophile trace element evolution of the Archaean mantle: J. Aust. Geol. Geophys., v. 4, p. 253-279.
Green, D. H., Nicholls, I. A., Viljoen, M., and Viljoen, R., 1975, Experimental demonstration of the existence of peridotitic liquids in earliest Archean magmatism: Geology, v. 3, p. 11-14.
Grove, T. L., de Wit, M. J., and Dann, J. C., 1997, 4.4.2. Komatiites from the Komati type section, Barberton, South Africa, *in* de Wit, M. J., and Ashwal, L. D., eds., Greenstone belts, Oxford, Oxford university press, p. 438-453.
Gudmundsson, O., Clayton, R. W., and Anderson, D. L., 1986, CMB topography inferred from ISC *PcP* travel times: EOS Trans., Am. Geophys. Union, v. 67, p. 1100.
Hall, R. P., 1980, The tholeiitic and komatiitic affinities of the Malene metavolcanic amphibolites from Ivisârtoq, southern West Greenland: Rapp. Grønlands Geol. Unders., v. 97, p. 20pp.
Hargraves, R. B., 1986, Faster spreading or greater ridge length in the Archean?: Geology, v. 14, p. 750-752.
Hauri, E. H., 1996, Major-element variability in the Hawaiian mantle plume: Nature, v. 382, p. 415-419.
Herzberg, C., and Zhang, J., 1996, Melting experiments on anhydrous peridotite KLB-1: Compositions of magmas in the upper mantle and transition zone: J. Geophys. Res., v. 101, p. 8271-8295.
Hirose, K., 1997, Melting experiments on lherzolite KLB-1 under hydrous conditions and generation of high-magnesian andesitic melts: Geology, v. 25, p. 42-44.
Hirose, K., and Fei, Y., 1998, Majorite-perovskite transformation on the join $MgSiO_3$-$Mg_3Al_2Si_3O_{12}$ and its role in the dynamics at the 660-km discontinuity: Physics of the Earth and Planetary Interiors, v. submitted.
Hirose, K., Fei, Y., Ma, Y., and Mao, H., 1998, The fate of subducted basaltic crust in the Earth's lower mantle: Nature, v. in press.
Hirose, K., and Kushiro, I., 1993, Partial melting of dry mantle peridotites at high pressures: Determination of compositions of melts segregated from peridotite using aggregates of diamond: Earth Planet. Sci. Lett., v. 114, p. 477-489.
Hirose, K., and Kushiro, I., 1998, The effect of melt segregation on polybaric mantle melting: Estimation from the inremental melting experiments: Physics of the Earth and Planetary Interiors, v. 107, p. 111-118.
Hirschmann, M., 1996, Reading garnet's signature: Nature, v. 384, p. 215-217.
Hirschmann, M. M., and Stolper, E. M., 1996, A possible role for garnet pyroxenite in the origin of the "garnet signature" in MORB: Contrib. Mineral. Petrol., v. 124, p. 185-208.
Inoue, T., and Sawamoto, H., 1992, High pressure melting of pyrolite under hydrous condition and its geophysical implication: High-pressure Research: Application to Earth and Planetrary Sciences: Tokyo and AGU, Washington D. C ., Terra, 323-331 p.
Irifune, T., 1994, Absence of an aluminous phase in the upper part of the Earth's lower mantle: Nature, v. 370, p. 131-133.
Irifune, T., Koizumi, T., and Ando, J., 1996, An experimental study of the garnet-perovskite transformation in the systme $MgSiO_3$-$Mg_3Al_2Si_3O_{12}$: Phys. Earth Planet. Int., v. 96, p. 147-157.
Irifune, T., and Ringwood, A. E., 1987, Phase transformations in a hartzburgite composition to 26 GPa: implications for dynamical behaviour of the subducting slab: Earth Planet Sci. Lett., v. 86, p. 365-376.
Irifune, T., and Ringwood, A. E., 1993, Phase transformations in subducted oceanic crust and buoyancy relationships at depths of 600-800 km in the manlte: Earth Planet Sci. Lett., v. 117, p. 101-110.
Isozaki, Y., Maruyama, S., and Kimura, G., 1991, Middle Archean (3.3 Ga) Cleaverville accretionary complex in northwestern Pilbara block, western Australia: EOS Trans., v. 72, p. 542.
Ito, E., and Sato, H., 1992, Effect of phase transformations on the dynamics of the descending slab, *in* Syono, Y., and Manghnani, M. H., eds., High-pressure Research: Application to Earth and Planetary Sciences, Washington, D. C., AGU, p. 257-262.
Ito, E., and Takahashi, E., 1989, Postspinel transformation in the system $Mg_2SiO_4$-$Fe_2SiO_4$ and some geophysical implications: J. Geophys. Res., v. 94, p. 10637-10646.
Ito, E., Takahashi, E., and Matsui, Y., 1984, The mineralogy and chemistry of the lower mantle: an implication of the ultrahigh-pressure phase relations in the system MgO-FeO-$SiO_2$: Earth Planet. Sci. Lett., v. 67, p. 238-248.
Ito, E., and Yamada, H., 1982, Stability relations of silicate spinels, ilmenites, and perovskites, *in* Akimoto, S., and Manghnani, M. H., eds., High-pressure research in geophysics, Tokyo, Center for Academic Publications, p. 405-419.
Iwamori, H., McKenzie, D., and Takahashi, E., 1995, Melt generation by isentropic mantle upwelling: Earth Planet Sci. Lett., v. 134, p. 253-266.
Jagoutz, E., Palme, H., Baddenhausen, H., Blum, K., Cendales, M., Dreibus, G., Spettel, B., Lorenz, V., and Wänke, H., 1979, The abundances of major, minor and trace elements in the earth's mantle as derived from

primitive ultramafic nodules: Proc. Lunar Planet. Sci. Conf. 10th, p. 2031-2050.
Jordan, T. H., 1977, Lithospheric slab penetration into the lower mantle beneath the Sea of Okhotsk: J. Geophys., v. 43, p. 473-496.
Kato, T., Ringwood, A. E., and Irifune, T., 1988, Constraints of element partition coefficients between $MgSiO_3$ perovskite and liquid determined by direct measurements: Earth Planet. Sci. Lett., v. 90, p. 65-68.
Kesson, S. E., and Fitz Gerald, J. D., 1991, Partitioning of MgO, FeO, NiO, MnO and $Cr_2O_3$ between magnesian silicate perovskite and magnesiowüstite: implications for the origin of inclusions in diamond and the composition of the lower mantle: Earth Planet. Sci. Lett., v. 111, p. 229-240.
Kimura, G., Ludden, J. N., Desrochers, J.-P., and Hori, R., 1993, A model of ocean-crust accretion for the Superior province, Canada: Lithos, v. 30, p. 337-335.
Kinzler, R. J., 1997, Melting of mantle peridotite at pressures approaching the spinel to garnet transition: Application to mid-ocean ridge basalt petrogenesis: J. Geophys. Res., v. 102, p. 853-874.
Kinzler, R. J., and Grove, T. L., 1985, Crystallization and differentiation of Archean komatiite lavas from northeast Ontario: phase equilibrium and kinetic studies: Am. Mineral., v. 70, p. 40-51.
Klein, E. M., and Langmuir, C. H., 1987, Global correlations of ocean ridge basalt chemistry with axial depth and crustal thickness: J. Geophys. Res., v. 92, p. 8089-8115.
Klein, E. M., and Langmuir, C. H., 1989, Local versus global variations in ocean ridge basalt composition: a reply: J. Geophys. Res., v. 94, p. 4241-4252.
Klein, E. M., Langmuir, C. H., and Staudigel, H., 1991, Geochemistry of basalts from the Southeast Indian Ridge, 115˚-138˚: J. Geophys. Res., v. 96, p. 2089-2107.
Kogiso, T., Tatsumi, Y., Shimoda, H., and Barsczus, H. G., 1997, HIMU ocean island basalts in the southern Polynesia: new evidence for whole-mantle scale recycling of subducted oceanic crust: J. Geophys. Res., v. 102, p. 8085-8103.
Komiya, T., Maruyama, S., Nohda, S., Masuda, T., Appel, P. W. U., Hayashi, M., and Okamoto, S., 1998a, Plate tectonics at 3.8 – 3.7 Ga; Field evidence from the Isua accretionary complex, southern West Greenland: Jour. Geol.
Komiya, T., Maruyama, S., Shimizu, K., and Hirose, K., 1998b, Geology of Komati Fm. and mineralogy of relict igneous minerals, Barberton Greenstone Belt (3.5 Ga), South Africa: International Volcanological Congress, Cape Town.
Kudoh, Y., Prewitt, C. T., Finger, L. W., Darovskikh, A., and Ito, E., 1990, Effect of iron on the crystal structure of $(Mg,Fe)SiO_3$ perovskite: Geophys. Res. Lett., v. 17, p. 1481-1484.
Kushiro, I., 1996, Partial melting of a fertile mantle peridotite at high pressures: an experimental study using aggregates of diamond, *in* Basu, A. R., and Hart, S. R., eds., Earth processes: Reading the isotopic code, Washington D. C., AGU Monograph 95, p. 109-122.
Kushiro, I., 1998, Compositions of partial melts formed in mantle peridotites at high pressures and their relation to those of primitive MORB: Physics of the Earth and Planetary Interiors, v. 107, p. 103-110.
Lindsley, D. H., 1983, Pyroxene thermometry: Am. Mineral., v. 68, p. 477-493.
Liu, L. G., 1982, Chemical inhomogeneity of the mantle: geochemical considerations: Geophys. Res. Lett., v. 9, p. 124-126.
Manning, C. E., and Bird, D. K., 1986, Hydrothermanl clinopyroxenes of the Skaergaard intrusion: Contrib. Mineral. Petrol., v. 92, p. 437-447.
Maruyama, S., Isozaki, Y., and Kimura, G., 1991a, Is the Mid-Archean barite formation from the Pilbara craton, Australia under the deep-sea environment?: EOS Trans., v. 72, p. 532.
Maruyama, S., Masuda, S., and Appel, P. W. U., 1991b, The oldest accretionary complex on the Earth, Isua, Greenland: Geol. Soc. Am., Abstract with programs, p. A429-A430.
McCammon, C., 1997, Perovskite as a possible sink for ferric iron in the lower mantle: Nature, v. 387, p. 694-696.
McCammon, C., Hutchison, M., and Harris, J., 1997, Ferric iron content of mineral inclusions in diamonds from São Liz: A view into the lower mantle: Science, v. 278, p. 434-436.
McCulloch, M. T., and Bennett, V. C., 1994, Progressive growth of the Earth's continental crust and depleted mantle: Geochemical constraints: Geochim. Cosmochim. Acta, v. 58, p. 4717-4738.
McDonough, W. F., and Danyushevsky, L. V., 1995, Water and sulfer contents of melt inclusions from Archean komatiites: EOS Trans., v. 76, p. S266.
McFarlane, E. A., Drake, M. J., and Rubie, D. C., 1994, Element partitioning between Mg-perovskite, magnesiowüstite, and silicate melt at conditions of the Earth's mantle: Geochim. Cosmochim. Acta, v. 58, p. 5161-5172.
Moore, G., Righter, K., and Carmichael, I. S. E., 1995, The effect of dissolved water on the oxidation state of iron in natural silicate liquids: Contrib. Mineral. Petrol., v. 120, p. 170-179.
Morelli, A., and Dziewonski, A. M., 1987, Topography of the core-mantle boundary and lateral homogeneity of the liquid core: Nature, v. 325, p. 678-683.
Nisbet, E. G., Bickle, M. J., and Martin, A., 1977, The mafic and ultramafic lavas of the Belingwe greenstone belt, Rhodesia: J. Petrol., v. 18, p. 521-566.

Nisbet, E. G., Cheadle, M. J., Arndt, N. T., and Bickle, M. J., 1993, Constraining the potential temperature of the Archean mantle: A review of the evidence from komatiites: Lithos, v. 30, p. 291-307.
Nisbet, E. G., and Fowler, C. M. R., 1983, Model for Archean plate tectonics: Geology, v. 11, p. 376-379.
Ogawa, M., 1997, A bifurcation in the coupled magmatism-mantle convection system and its implications for the evolution of the Earth's upper mantle: Phys. Earth Planet. Inter., v. 102, p. 259-276.
Ohta, H., Maruyama, S., Takahashi, E., Watanabe, Y., and Kato, Y., 1996, Field occurrence, geochemistry and petrogenesis of the Archean mid-oceanic ridge basalts (AMORBs) of the Cleaverville area, Pilbara craton, Western Australia: Lithos, v. 37, p. 199-221.
Parman, S. W., Dann, J. C., Grove, T. L., and de Wit, M. J., 1997, Emplacement conditions of komatiite magmas from the 3.49 Ga Komati Formation, Barberton Greenstone Belt, South Africa: Earth Planet. Sci. Lett., v. 150, p. 303-323.
Pirajno, F., Adamides, N. G., Occhipinti, S., Swager, C. P., and Bagas, L., 1996, Geology and tectonic evolution of the Early Proterozoic Glengarry Basin, Western Australia: Western Australia Geological Survey, Annual Review 1994-95, p. 71-80.
Pirajno, F., Occhipinti, S., Le Blanc Smith, G., and Adamides, N., 1995, Pillow lavas in the Peak Hill and Glengarry terranes: Western Australia Geological Survey, Annual Review 1993-94, p. 63-66.
Reynolds, J. R., Langmuir, C. H., Bender, J. F., Kastens, K. A., and Ryan, W. B. F., 1992, Spatial and temporal variability in the geochemistry of basalts from the East Pacific Rise: Nature, v. 359, p. 493-499.
Richter, F. M., 1985, Models for the Archean thermal regime: Earth Planet. Sci. Lett., v. 73, p. 350-360.
Righter, K., Drake, M. J., and Yaxlley, G., 1997, Prediction of siderophile element metal-silicate partition coefficients to 20 GPa and 2800 ˚C: the effects of pressure, temperature, oxygen fugacity, and silicate and metallic melt compositions: Physics of the Earth and Planetary Interiors, v. 100, p. 115-134.
Ridley, W. I., 1977, The crystallisation trends of spinels in Tertiary basalts from Rhum and Muck and their petrogenetic significance: Contrib. Mineral. Petrol., v. 64, p. 243-255.
Ringwood, A. E., 1966, The chemical composition and origin of the earth, *in* Hurley, P. M., ed., Advances in Earth Sciences, MIT Press, p. 287-356.
Ringwood, A. E., 1979, Origin of the Earth and Moon: New York, Springer-Verlag, 295 p.
Ringwood, A. E., 1989, Significance of the terrestrial Mg/Si ratio: Earth Planet. Sci. Lett., v. 95, p. 1-7.
Ringwood, A. E., 1991, Inaugural ingerson lecture: Geochim. Cosmochim. Acta, v. 55, p. 2083-2110.
Salters, V. J. M., 1996, The generation of mid-ocean ridge basalts from the Hf and Nd isotope perspective: Earth Planet. Sci. Lett., v. 141, p. 109-123.
Salters, V. J. M., and Hart, S. R., 1989, The hafnium paradox and the role of garnet in the source of mid-ocean-ridge basalts: Nature, v. 342, p. 420-422.
Scowen, P. A. H., Roeder, P. L., and Helz, R. T., 1991, Reequilibration of chromite within Kilauea Iki lava lake, Hawaii: Contrib. Mineral. Petrol., v. 107, p. 8-20.
Shimizu, K., T., K., Maruyama, S., and Hirose, K., 1997, Water content of melt inclusion in Cr-spinel of 2.7 Ga komatiite from Belingwe Greenstone Belt, Zimbabwe: EOS Trans, Am. Geophys. Union, v. 78, p. 750.
Silver, P. G., Carlson, R. W., and Olson., P., 1988, Deep slabs, geochemical heterogeneity, and the large-scale structure of mantle convection: Investigation of a enduring paradox: Ann. Rev. Earth Planet. Sci., v. 16, p. 477-541.
Silver, P. G., and Chan, W. W., 1986, Observations of body wave multipathing from broadband seismograms: evidence for lower mantle slab penetration beneath the Sea of Okhotsk: J. Geophys. Res., v. 91, p. 13787-13802.
Sun, S.-S., and Nesbitt, R. W., 1977, Chemical heterogeneity of the Archean mantle, composition of the earth and mantle evolution: Earth Planet. Sci. Lett., v. 35, p. 429-448.
Takahashi, E., 1986, Origin of basaltic magmas. - implications from peridotite melting experiments and olivine fractionation model -: Bull. Volcanol. Soc. Jap., v. 30, p. 17-40.
Takahashi, E., 1990, Speculations on the Archean mantle: missing link between komatiite and depleted garnet peridotite: J. Geophys. Res., v. 95, p. 15941-15954.
Takahashi, E., and Scarfe, C. M., 1985, Melting of peridotite to 14 GPa and the genesis of komatiites: Nature, v. 315, p. 566-568.
Takahashi, E., Shimazaki, T., Tsuzaki, Y., and Yoshida, H., 1993, Melting study of a peridotite KLB-1 to 6.5 GPa, and the origin of basaltic magmas: Phil. Trans. R. Soc. London, v. A342, p. 105-120.
Taylor, S. R., and McLennan, S. M., 1985, The continental crust: Its composition and evolution: Oxford, Balckwell, 312 p.
Walter, M. J., 1997, One step to Earth: Nature, v. 387, p. 453.
Wilkinson, J. F. G., and Hensel, H. D., 1988, The petrology of some picrites from Mauna Loa and Kilauea volcanoes, Hawaii: Contrib. Mineral. Petrol., v. 98, p. 326-345.
Wood, B. J., and Rubie, D. C., 1996, The effect of alumina on phase transfomations at the 660-kilometer discontinuity from Fe-Mg partitioning experiments: Science, v. 273, p. 1522-1524.
Woodhouse, J. H., and Dziewonski, A. M., 1987, Models of the upper and lower mantle from waveforms of mantle waves and body waves: EOS. Trans., Am. Geophys. Union, v. 68, p. 356-357.

## FIGURE CAPTIONS

**Figure 1.** Composition of starting materials for ultra-high pressure experiments. MgO variation diagrams of major elements for MORBs in the North Pole area along with modern MORB. Starting materials are natural greenstone samples of North Pole MORBs. Large gray circles, solid circles, and open circles indicate starting materials, coarse-grained MORBs, and fine-grained MORBs, respectively.

**Figure 2.** (a) Phase relations of two North Pole MORBs under anhydrous condition along with those of a primitive modern MORB (Hirose et al. 1998). Abbreviations are: mj = majorite; cpx = clinopyroxene; st = stishovite; Ca-pv = Calcium-perovskite; Mg-pv = Magnesium perovskite. (b) (i) Distribution function of total Fe and Mg between magnesiowüstite and Mg-perovskite versus $Al_2O_3$ content in Mg-perovskite. Symbols are shown in inset. A gray solid symbol is distribution function of ferrous and magnesium between a natural magnesiowüstite and the coexisting orthopyroxene transformed from Mg-perovskite within a diamond. Numbers are temperature controlled in experiments. (ii) Fe/Mg ratio in magnesiowüstite versus Fe/Mg ratio in Mg-perovskite. Symbols are shown in inset. Symbols for element are materials of capsules.

**Figure 3.** (a) MgO variation diagrams of some major elements for Killara MORBs (solid circles) along with compositional variations of modern MORBs (gray regions). Three arrows on scattered plots indicate compositional variation of residual melts through crystal fractional fractionation of olivine, olivine+plagioclase and olivine+plagioclase+clinopyroxene, respectively. Abbreviations are: ol = olivine; cpx = clinopyroxene; pl = plagioclase. (b) Comparison of primitive natural basalts with partial melts formed from mantle peridotite by diamond methods. (i) $SiO_2$-MgO diagram. Symbols: solid circles and open circles are primitive Killara MORBs and most primitive modern NMORBs, respectively. Thick arrows indicate compositional variation of partial melts produced from four mantle peridotite at different pressure, 10 kb for light gray, 15 kb for gray, 20 kb for dirk gray and 25-30 kb for black arrow respectively. This diagram indicates that both modern MORBs and Killara MORBs were formed at 10 to 15 kb. (ii) MgO-FeO diagram. Symbols: solid circles and open circles are primitive Killara MORBs and most primitive modern NMORBs, respectively. Thick arrows indicate compositional variation of partial melts produced at 15 kb from four different mantle peridotite, HK66 for light gray, PHN1611 for gray, KLB-1 for dirk gray and MM3 for black arrow, respectively. This diagram indicates that FeO content of mantle source of modern MORBs is comparable to that of KLB-1, whereas that that of mantle source of High Ti basalt was comparable to or higher than that of HK66 and PHN1611. (iii) $SiO_2$-FeO diagram. Symbols: solid circles and small open circles are primitive Killara MORBs and partial melts from PHN1611, respectively. Thick arrows indicate compositional variation of partial melts produced from PHN1611 at 10 to 15 kb for gray,

and at 20 to 30 kb for black arrow, respectively. This diagram indicates that melting pressure and temperature of High Ti basalt was around 10 kb and 1350 ˚C. Potential mantle temperature was calculated to be 1450 to 1500 ˚C using degree of melting (Kushiro 1996) and thermodynamic parameters (Hirose 1998).

**Figure 4.** Chondrite-normalized rare earth element (REE) abundances in Killara MORBs (fine black lines with circles) along with modern OIB (gray line), EMORB (broken light gray line) and NMORB (black solid line). Vales of these modern basalts are from Sun & McDonough (1989). Values of chondrite are taken from Anders & Ebihara (1982).

**Figure 5.** (a) Geologic map of the Komati Formation. The inset map is geotectonic map of Barberton Greenstone Belt, simplified after Anhaeusser et al. (1983). (b) Geological map of the Hooggenoeg Formation.

**Figure 6.** Geological map of the Schapenburg remnant. The remnant comprises ultramafic komatiite, basaltic komatiite, gabbro, basalt, BIF/chert, and psammitic/pelitic gneiss, and was intruded by granitoids and eventually by younger dikes. Previous work suggested conformable cyclically repetition of ultramafic and basaltic komatiites (Anhaeusser, 1983). However, the remnant comprises at least fourteen layer parallel thrust-bounded subunits (horses).

**Figure 7.** Sketch map of the boundary between horses. The horses are bounded by a layer-parallel thrust, whose direction of movement is top to the east.

**Figure 8.** Sketch map of type locality of a pile thin olivine spinifex flows at the stratigraphic intermediate level in Spinifex Stream. Small vesicles are present in topmost and bottom chilled margin of olivine spinifex Flows VI, V and I.

**Figure 9.** A photo of chilled margin of Flow VI and topmost chilled margin of Flow V. Small are present at the bottom of chilled margin of Flow VI and the topmost chilled margin and the underlying fine-grained randomly-oriented olivine-spinifex zone of Flow V. Size of vesicles increases from top to spinifex zone.

**Figure 10.** Sketch map of two thick olivine spinifex flows at the stratigraphic bottom of the Komati Formation. The komatiite flows have no vesicles. Open circles are sample localities.

**Figure 11.** (a) Compositional variations of metamorphic Ca-amphiboles in tholeiitic flows interlayered olivine-spinifex komatiite flows. The compositions are shown in a quadrilateral, which is a part of Hallimond's triangular diagram. Open circles are compositions of actinolite and hornblende, which are separated by a compositional break. Solid circles are composition of amphiboles, which have no compositional break. Compositional variations of Ca-amphiboles along the Tr-$Prg_{60}Ts_{40}$ line with increasing metamorphic grade. (b) Compositional variations of Ca-amphiboles from northern to southern area of Komati Formation, projected onto the Tr-$Prg_{60}Ts_{40}$ line. Numbers at left side are identifications of sample. Numbers at right side are $Mg^{\#}$ of Ca-amphiboles. (c) Variations of An content of plagioclase in tholeiitic flows from northern to southern area of Komati Formation.

**Figure 12.** (a) Distribution of relict igneous minerals in the Komati Formation. Augitic pyroxenes are widely preserved all over the Komati Formation. Olivine is also present both at the upper and lower area of the Komati Formation, but the olivine at the lower area is metamorphic based on the crystal property and Ni and Mn contents. Pigeonitic pyroxene exists only at the stratigraphic upper level, indicating the presence of water in the host magma at the crystallization, and degassing of $H_2O$ with decreasing depth of seawater due to piling up of komatiite and basaltic flows. (b) Distribution of relict igneous minerals in the Hooggenoeg Formation.

**Figure 13.** (a) NiO and MnO versus Fo value of relict igneous olivines from ultramafic komatiites in low metamorphic grade area. Gray and black lines indicate the calculated liquid line of descent of olivine fractionation in NiO and MgO content, respectively. Maximum Fo value is 92.8, indicating that a primary ultramafic komatiite is 26.5 wt % in MgO. The difference of symbols indicates difference of samples containing olivines. (b) NiO and MnO versus Fo value of relict igneous olivines from ultramafic komatiites in moderate- to high metamorphic grade area. Gray and black lines indicate the calculated liquid line of descent of olivine fractionation in NiO and MgO content, respectively. Squares and circles are NiO and MnO content, respectively. Many olivines have higher Fo content up to 93.5.

**Figure 14.** Compositions of relict igneous pyroxenes in ultramafic komatiites projected in terms of Wo-En-Fs. End members of pyroxene were calculated by Lindsley's method (Lindsley 1983). Solid circles indicate compositions of pyroxenes. Pyroxenes vary significantly from diopside through augite and pigeonite to enstatite in composition. (b) Compositions of relict igneous pyroxenes in an ultramafic komatiite, BC210, are shown in a quadrilateral, which is a part of Wo-En-Fs ternary diagram (Lindsley 1983). Despite of pyroxenes within a single sample, the pyroxenes vary significantly from diopside and salite to augite in composition. Two compositional variations are present: One indicates that $Mg^{\#}$ in clinopyroxenes increases with increasing Wo content. The other indicates that $Mg^{\#}$ in clinopyroxenes decreases with increasing Wo content.

**Figure 15.** Back-scattered electron image of ultramafic komatiites, and composition of igneous pyroxenes. Pyroxenes in ultramafic komatiites are classified into three types based on the texture; spinifex-textured clinopyroxenes (type I), euhedral to subhedral clinopyroxenes (type II) from inter-cumulus melt at the cumulate layer of ultramafic komatiite, clinopyroxene oikocrysts (type III), together with euhedral olivine, orthopyroxene oikocrysts and minor intercumulus titaniferous brown hornblende in ultramafic komatiite dikes and sills. Type I clinopyroxene has calcic augite and salite composition. Type II clinopyroxene formed euhedral column to sub-oikocrysts, depending on the crystallinity. The composition of the clinopyroxenes discontinuously changes from pigeonite in the core through augite in the mantle to highly aluminous augite along the rim in the stratigraphic intermediate to upper level of the Komati Formation. On the other hand, the clinopyroxene in the stratigraphic lower level has

augitic composition. Type III clinopyroxene is augitic in the composition, and is often accompanied with bronzitic pyroxene oikocrysts, and titaniferous hornblende.

**Figure 16.** Compositions of relict igneous pyroxene in a thin olivine-spinifex ultramafic komatiite flow projected in terms Wo-En-Fs. End members of pyroxenes were calculated by Lindsley's method (Lindsley 1983). Solid circles indicate compositions of pyroxenes from BC430. Gray region indicates compositional variation of pyroxenes from olivine-spinifex komatiite flows (Parman et al. 1997).

**Figure 17.** (a) Compositions of relict igneous pyroxene in a ultramafic komatiite flow, which has phase assemblage of olivine+pigeonite+Calcic clinopyroxene+Aluminous augite, BC198, projected in terms Wo-En-Fs. End members of pyroxenes were calculated by Lindsley's method (Lindsley 1983). Solid circles, gray solid circles and open circles are pigeonite, Calcic clinopyroxene, and aluminous augite, respectively. Open fields with solid line and with broken indicate compositional variation of clinopyroxenes produced at 2 kb under hydrous condition and at 1 atm under anhydrous condition, respectively. Gray region indicates compositional variation of pyroxenes from olivine-spinifex komatiite flows (Parman et al. 1997). (b) Phase appearance temperature in proportion to water content, modified after Fig. 5 of Parman et al. (1997). Sequence of phase appearance changes from ol+csp+pig+aug under less hydrous condition to ol+csp+aug+pig (opx) under higher hydrous condition.

**Figure 18.** Compositional distribution within clinopyroxene from BC198, whose phase assemblage is ol+pig+calcic clinopyroxene+aluminous clinopyroxene. (a) Zoning patters in clinopyroxene with euhedral outline of ca. 300 μm from pigeonitic core through augitic mantle to thin aluminous augite margin along a white line. Light gray, broken black and gray lines are $SiO_2$, MgO and CaO content, respectively. Black and dirk gray lines are twice of FeO content, and 10 times of $Al_2O_3$ content. (b-e) Distribution of $SiO_2$, $Al_2O_3$, FeO, MgO and CaO content within clinopyroxene. (f) Variation in $Mg^{\#}$ within clinopyroxene. (g) SEM image of clinopyroxene. (h) Back-scattered electron image of clinopyroxene.

**Figure 19.** Back-scattered electron image of type II clinopyroxenes in the cumulate zone of ultramafic komatiite flows depending on the stratigraphic level of the Komati Formation. Volume of pigeonitic core decreases from the stratigraphic top to intermediate of the Formation. No pigeonitic core is present at the bottom. The relationship between stratigraphy and volume of pigeonitic core suggests paleo-bathymetric change of seawater at the eruption of magma on the oceanic plateau due to piling of basalt and komatiite flows.

**Figure 20.** Compositions of relict igneous pyroxene on compositional variation of increase of Mg# with increasing Wo content in a ultramafic komatiite dike, which has phase assemblage of olivine+Calcic clinopyroxene+orthopyroxene+hornblende, BC210, projected in terms Wo-En-Fs. End members of pyroxenes were calculated by Lindsley's method (Lindsley 1983). Solid circles indicate compositions of all the pyroxenes of

from BC210. Open circles indicate compositions of orthopyroxene and the coexisting clinopyroxene. Open fields with solid line and with broken indicate compositional variation of clinopyroxenes produced at 2 kb under hydrous condition and at 1 atm under anhydrous condition, respectively. Gray region indicates compositional variation of pyroxenes from olivine-spinifex komatiite flows (Parman et al. 1997).

**Figure 21.** Summary of composition of type II pyroxenes all over the Komati Formation.

**Figure 23.** Compositional distribution within a chromian spinel enclosed by an olivine from BC210, whose phase assemblage is ol+clinopyroxene+orthopyroxene+hornblende. (a) Zoning patters in chromian spinel of ca. 120 μm along a black line. Dirk gray, gray and light gray lines are $Cr_2O_3$, FeO, and MgO content, respectively. Black solid and broken lines are four times of $Al_2O_3$ content, and 10 times of MnO content. (b) Zoning pattern of $Cr^{\#}$ (gray broke line) and $Mg^{\#}$ (light broken line). Distribution of $Al_2O_3$ (c), $Cr_2O_3$ (d), FeO (f), MgO (g) and MnO (i) content within chromian spinel. Variation in $Mg^{\#}$ (e) and $Cr^{\#}$ (h) within chromian spinel. (i) Back-scattered electron image of chromian spinel.

**Figure 24.** Compositional distribution within two chromian spinels enclosed by a clinopyroxene from BC210, whose phase assemblage is ol+clinopyroxene+orthopyroxene+hornblende. (a) Zoning patters in chromian spinels of ca. 50 μm along a black line. Dirk gray, gray and light gray lines are $Cr_2O_3$, FeO, and MgO content, respectively. Black solid and broken lines are four times of $Al_2O_3$ content, and 10 times of MnO content. (b) Zoning pattern of $Cr^{\#}$ (gray broke line) and $Mg^{\#}$ (light broken line). Distribution of $Al_2O_3$ (c), $Cr_2O_3$ (d), FeO (f), MgO (g) and MnO (i) content within chromian spinel. Variation in $Mg^{\#}$ (e) and $Cr^{\#}$ (h) within chromian spinel. (i) Back-scattered electron image of chromian spinel.

**Figure 25.** Plot of $Fe^{3+}$ versus Al in chromian spinels from ultramafic komatiites (calculated to 4 oxygen anions). The ferric iron content was determined by assuming stoichiometry, and an ideal $XY_2O_4$ formula, where X = ($Fe^{2+}$, Ni, Mn, Mg) and Y = ($Cr^{3+}$, $Fe^{3+}$, Al). Ti was assumed to be present as an ulvöspinel component. Also shown are compositional fields of chromian spinel from boninite and modern MORB. Two arrows indicate compositional variation through crystal fractionation of olivine and minor chromian spinels and through recrystallization of post-entrapment during cooling of magma and/or metamorphism. Symbols are chromian spinels in matrix, gray solid circles with black outline, chromian spinels within orthopyroxene, gray solid circles, chromian spinels within olivine, dirk gray solid circles, chromian spinels within clinopyroxene, black solid circles, and chromian spinels within hornblende, open circles. Circle and square represent core and rim of chromian spinel, respectively.

**Figure 26.** (a) Plot of $Cr^{\#}$, defined by Cr/(Cr+Al) ratio, versus $Mg^{\#}$, defined by Mg/(Mg+$Fe^{2+}$) ratio, in core of chromian spinels within clinopyroxene from ultramafic komatiites. (a) Plot of $Fe^{3+}/(Fe^{3+}+Cr^{3+}+Al^{3+})$ ratio, versus Ti in core of chromian spinels within clinopyroxene from ultramafic komatiites (calculated to 4 oxygen anions). The ferric iron content was determined by assuming stoichiometry, and an ideal $XY_2O_4$ formula,

where X = ($Fe^{2+}$, Ni, Mn, Mg) and Y = ($Cr^{3+}$, $Fe^{3+}$, Al). Ti was assumed to be present as an ulvöspinel component. Also shown are compositional fields of chromian spinel from boninite and modern MORB. An arrow indicates compositional variation through crystal fractionation of olivine and minor chromian spinels. Open circles are composition of core of chromian spinels within clinopyroxene.

**Figure 27.** Compositional variations and textures of igneous and metamorphic Ca-amphiboles in ultramafic komatiite, BC210. (a) The compositions are shown in a quadrilateral, which is a part of Hallimond's triangular diagram. (b) $TiO_2$ content of the amphiboles, projected onto the Tr-$Prg_{60}Ts_{40}$ line. (c) Plots of $TiO_2$ content versus $Mg^{\#}$ of the amphiboles. (d) Plots of $Fe^{3+}$ to total Fe ratio versus Ti of the amphiboles (calculated to 23 oxygen anions). (e) Variation of $Mg^{\#}$ of the amphiboles, projected onto the Tr-$Prg_{60}Ts_{40}$ line. (f) Textures of igneous amphiboles, back-scattered electron image. Color of the amphiboles becomes light near a secondary clinopyroxene (cpx) and rim of the amphiboles, suggesting post-magmatic recrystallization of igneous amphibole. Origins of amphiboles, igneous or metamorphic are determined by texture (See also the text). Open circles are compositions of metamorphic amphiboles. Gray solid circles are compositions of igneous amphiboles near hydrothermal and metamorphic amphiboles. Black solid circles are compositions of igneous amphiboles.

**Figure 28.** Melting phase relations of peridotite KLB-1 under anhydrous and slightly hydrous, 0.5 wt % in $H_2O$, condition. Wet solidus is extended to high pressure based on a melting phase relation at low pressure under slightly hydrous condition, 0.5 wt % in $H_2O$ (Hirose 1997). P-T paths for anhydrous (black thick line) and hydrous (gray line) mantle melting with no chemical isolation of melt are calculated from the model by Iwamori et al. (1995). The liquidus curve is assumed to be the same as those for dry melting.

**Figure 29.** Estimated secular changes of potential mantle temperature of Upper mantle (black line) and plume source (light gray line), and FeO content of Upper mantle (gray line) since Archean. The left vertical axis represents potential temperature of mantle, whereas the right vertical axis represents FeO content of upper mantle. It means that Archean mantle was not necessarily similar to PHN1611 or HK66 in major elements, but was comparable to them in FeO content or $Mg^{\#}$.

**Figure 30.** Comparison of inner structure and thickness of oceanic lithospheres between Archean and present. Thin oceanic lithosphere with thick oceanic crust in Archean makes an excellent contrast with thick oceanic lithosphere with thin oceanic crust (See also the text). Inset diagram is P-T-X paths for mantle melting with no chemical isolation of melt (Iwamori et al. 1995). Average thickness of oceanic crust from Archean upper mantle, PMT = 1450 ˚C reached about 17 km.

**Figure 31.** (a) $TiO_2$ versus $P_2O_5$ plot to estimate the $TiO_2/P_2O_5$ ration for the mantle with different age. Measured $(P_2O_5)_m$ value for each sample was corrected by a chondrite-normalized $Eu^*$/Nd ratio of that sample to account for deviation of its REE pattern and

$TiO_2/P_2O_5$ ratio from the primitive mantle with chondritic REE abundances. Symbols for Ancient MORBs are the same as Figure 25 (b). Data sources for komatiites and picrite with different ages and modern MORB are from Sun (1984). (b) $TiO_2$ versus $P_2O_5$ content plot of Ancient MORBs and the modern MORB. Symbols are shown in inset. Gray and open circle fields are compositional variations of Ancient MORBs and the modern MORB.

**Figure 32.** Phase relations of a hydrous MORB, modified after Okamoto (1998). The residues through partial melting are shown above wet solidus of a MORB under $H_2O$-saturated condition (Rapp et al. 1995). Also shown is an Archean geothermal gradient at subduction zone (Komiya et al. 1998).

**Figure 33.** Phase relations of anhydrous peridotite KLB-1 (fine black lines), modified after Figure 1 of Herzberg & Zhang (1996) and anhydrous Archean MORB (thick gray lines). Symbols are defined as follows: L, liquid; Ol, olivine; Opx, orthopyroxene; Cpx, clinopyroxene; Grt, garnet; Mw, magnesiowüstite; MgPv, magnesium perovskite; CaPv, calcium perovskite; ß, modified spinel $(Mg, Fe)_2SiO_4$, γ, spinel $(Mg, Fe)_2SiO_4$. Also shown are P-T paths of uprising mantle with 1330, 1450, and 1700 ˚C in PMT and of descending slab.

**Figure 34.** Comparison of densities of a subducted oceanic lithosphere and ambient mantle along the upper-lower mantle boundary in Archean. The subducted oceanic lithosphere is heavier than the ambient mantle above the boundary, whereas is lighter just below the boundary. However, the subducted oceanic lithosphere becomes heavier than the surrounding mantle again below about 750-km depth. Calculation of simple isostasy indicates that oceanic lithosphere could be stagnated up to 80 km thick along the boundary. Inset diagram indicates change of the densities of subducted MORB and the ambient pyrolitic mantle in a proportion to the pressure (Hirose et al. 1998).

**Figure 35.** Cartoon of material circulation in whole mantle in Archean. Formation of continental crust at subduction zones, segregation of iron blobs in slab penetration into lower mantle and recycling of FeO-poor subducted oceanic lithosphere and primitive mantle from lower mantle have changed the chemical composition of the Earth's mantle through geologic time.

**Figure 36.** Chemical variations of Al-undepleted peridotitic komatiites from Belingwe Greenstone Belt and Abitibi Greenstone Belt (Bickle et al. 1975; Arndt 1977; Arndt et al. 1977; Arth et al. 1977; Nisbet et al. 1977; Nisbet et al. 1987; Arndt 1986; McDonough & Ireland 1993). Symbols are shown in inset. (a) Plot of $TiO_2$ versus MgO content in Al-undepleted komatiite from the Abitibi Greenstone Belt (Arndt 1986), showing that they plot on an olivine control line. Average MgO content of bulk olivines accumulated as cumulate is calculated to be 51.7 wt %. Assuming that source mantle had 37 to 39 wt % in MgO, it had 2.4 to 2.2 wt % in $TiO_2$. (b) Plot of FeO* versus MgO content, showing that they plot on an olivine control line. Average FeO* content of bulk olivines accumulated as cumulate is calculated to be 7.1 wt %. Assuming that source

mantle had 37 to 39 wt % in MgO, it had 9.5 to 9.2 wt % in FeO*. (c) Plot of $TiO_2$ versus MgO content in Al-undepleted komatiite from Belingwe Greenstone Belt and Abitibi Greenstone Belt. Assuming that source mantle had 37 to 39 wt % in MgO, it had 2.5 to 0.9 wt % in $TiO_2$. (d) Plot of FeO* versus MgO content, showing that they plot on an olivine control line from A to B. Black line indicates compositional variation of residual melts, caused by extra-addition of crystallized olivine to magma from A to B, and by crystal fractional fractionations of olivine+chromian spinel from B to C, of olivine+clinopyroxene from C to D, of clinopyroxene from D to E, and clinopyroxene+sulfide from D to F. Gray line indicates the compositional variation of the olivine crystallized from primitive magma, 26.5 wt % in MgO to the differentiated magma, 20 wt % in MgO. Assuming that source mantle had 37 to 39 wt % in MgO, it had 10.1 to 9.1 wt % in FeO*. (e) Plot of NiO versus MgO content, showing that they plot on olivine control line at low pressure. Gray line indicates the compositional variation of the olivine crystallized from primitive magma, 26.5 wt % in MgO to the differentiated magma, 20 wt % in MgO. Assuming that source mantle had 37 to 39 wt % in MgO, it had 0.24 to 0.31 wt % in NiO. However, because melting pressure is much higher, up to 7 GPa, than that of crystal fractionation. Assuming that distribution function of Ni and Mg between olivine and melt at high pressure is 1.2 (Taura et al. 1998), mantle source had 0.26 wt % in NiO at 37.2 wt % in MgO.

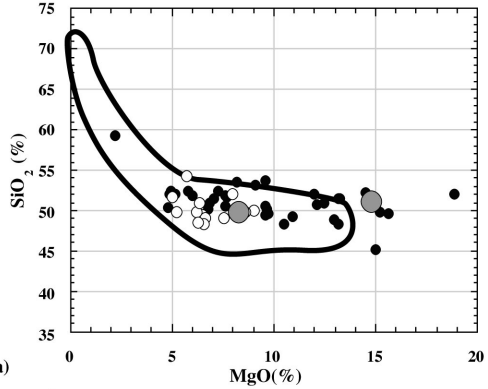


(Fig.1a)

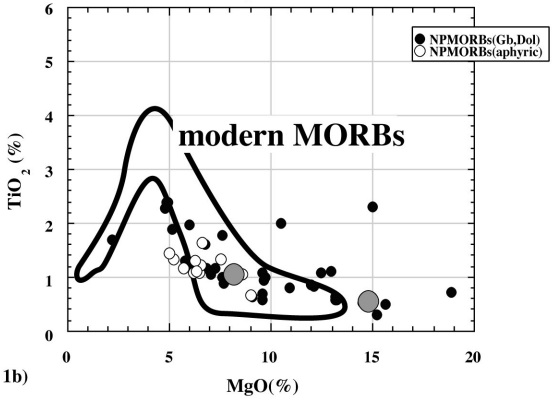


(Fig. 1b)

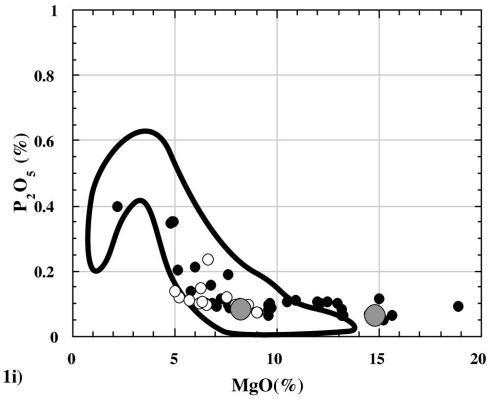


(Fig. 1i)

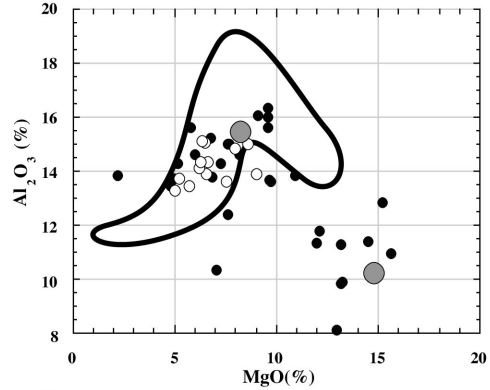


(Fig.1c)

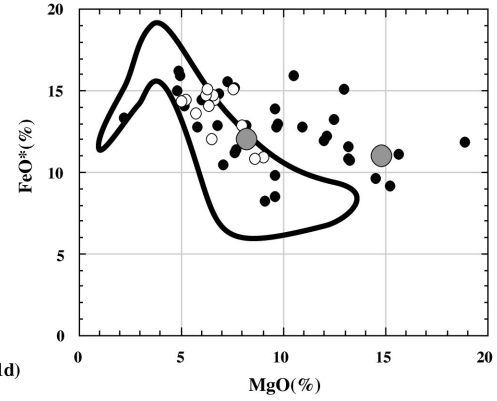


(Fig.1d)

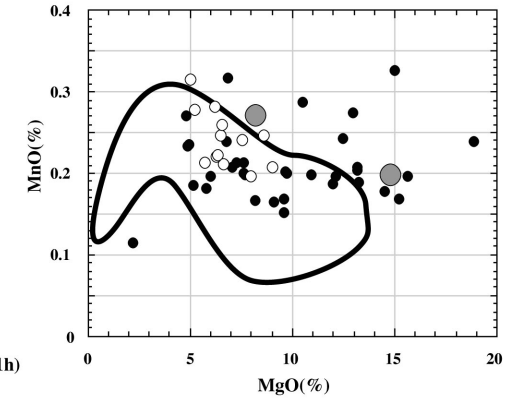


(Fig. 1h)

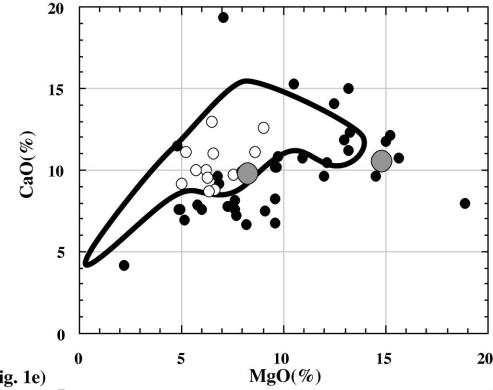


(Fig. 1e)

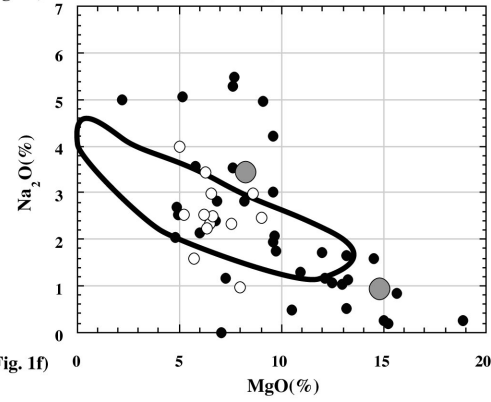


(Fig. 1f)

**Komiya 1999 Doctor Thesis Fig. VI-1**

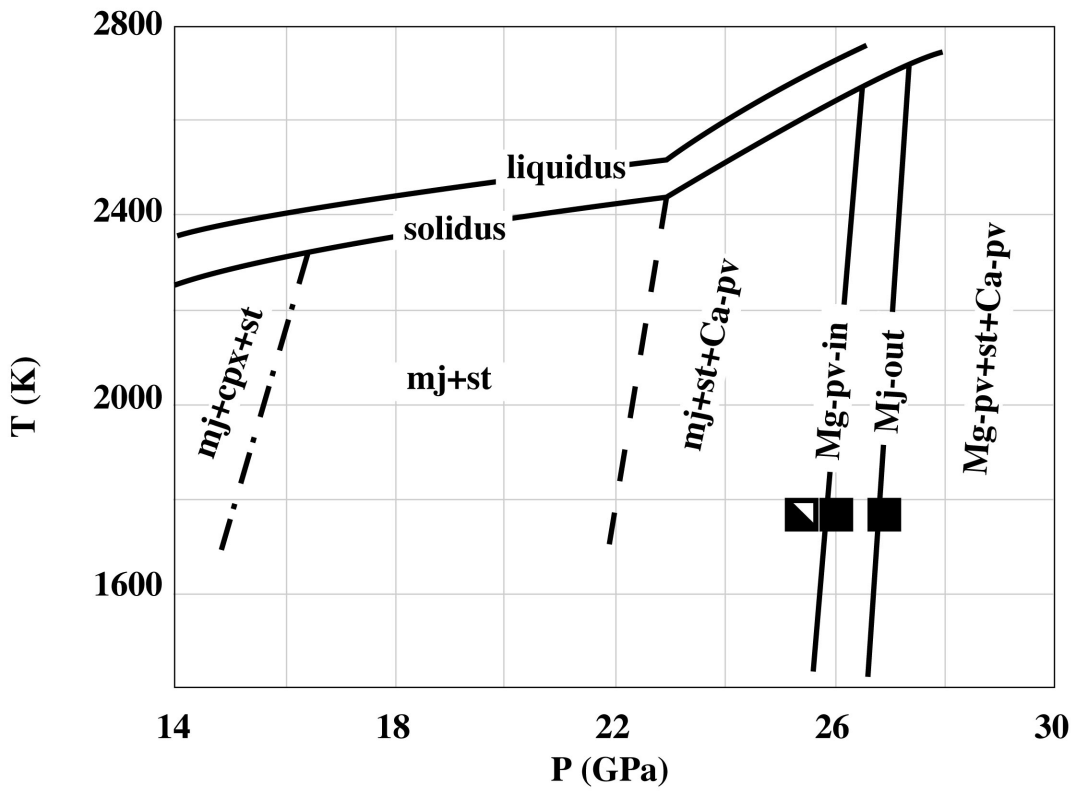


after Figure 2 of Hirose et al. 1998

Komiya 1999 Doctor Thesis Fig. 2a

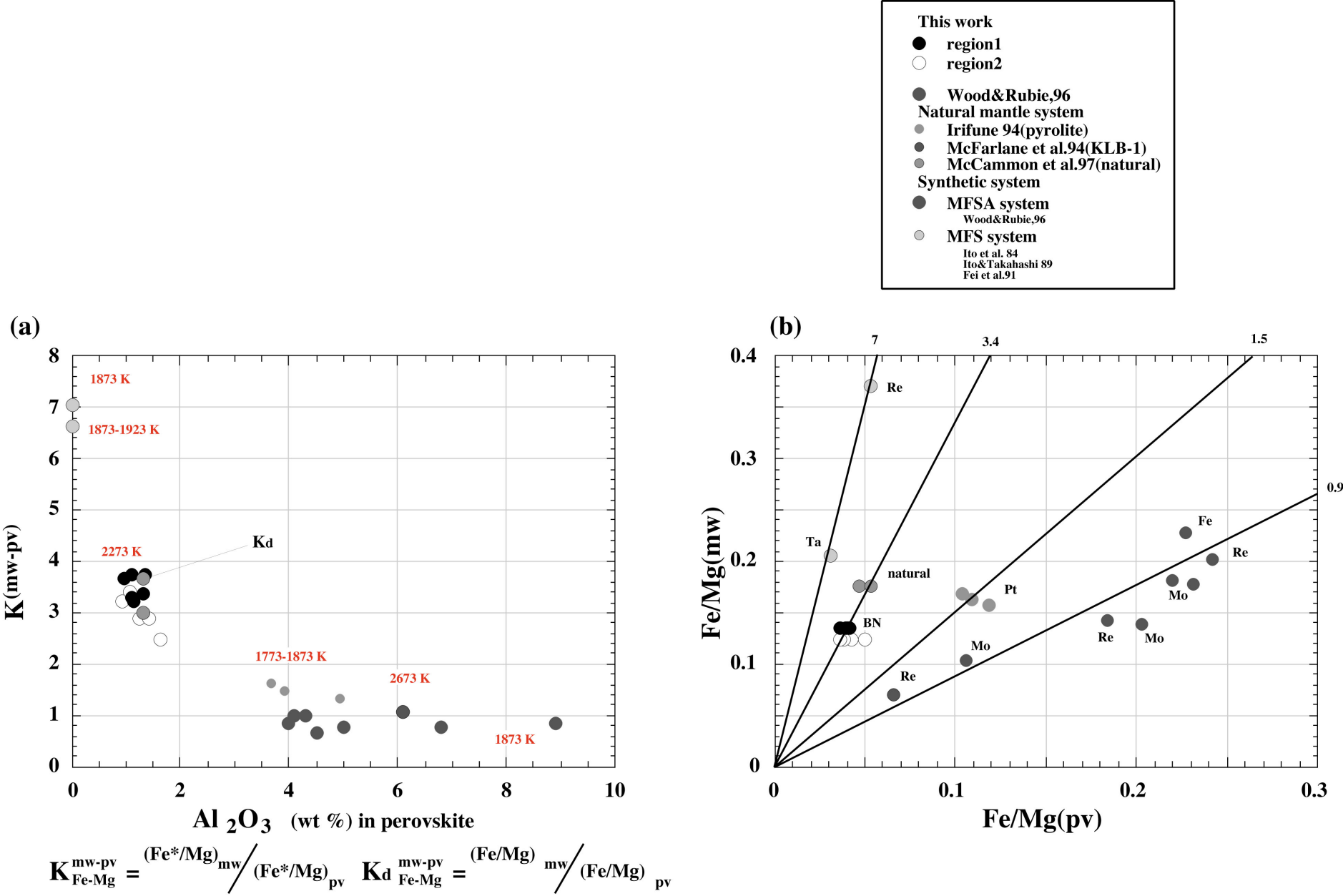


$$K_{Fe\text{-}Mg}^{mw\text{-}pv} = \frac{(Fe^*/Mg)_{mw}}{(Fe^*/Mg)_{pv}} \qquad Kd_{Fe\text{-}Mg}^{mw\text{-}pv} = \frac{(Fe/Mg)_{mw}}{(Fe/Mg)_{pv}}$$

**Komiya 1999 Doctor Thesis Fig. VI-2b**

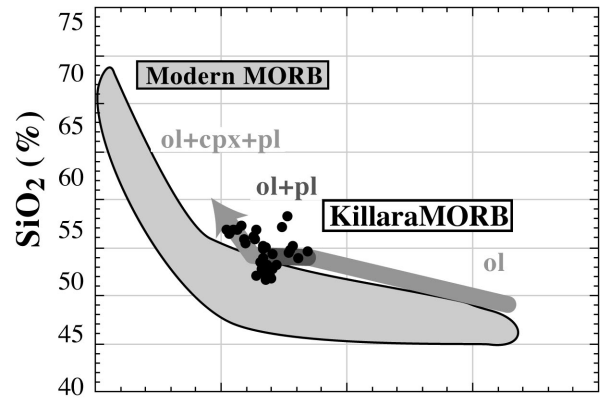


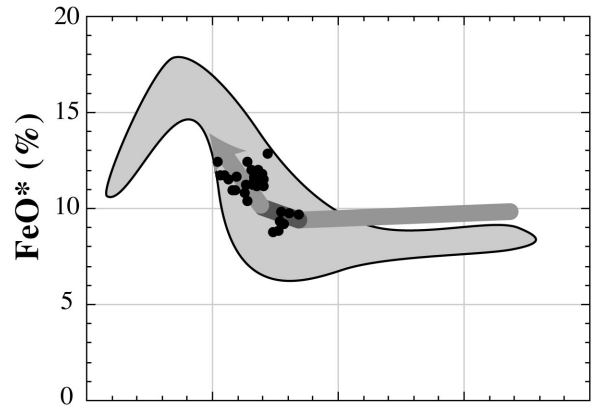


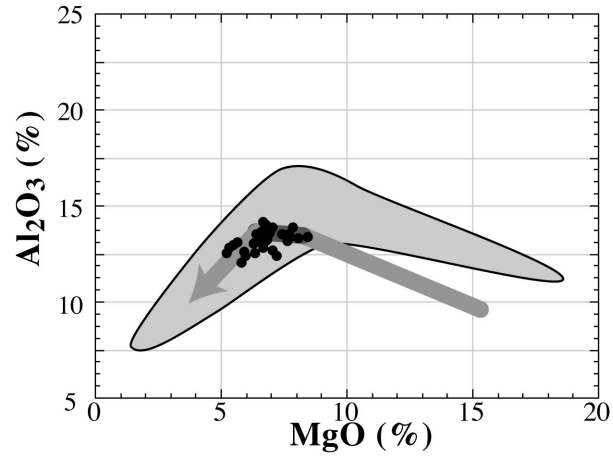


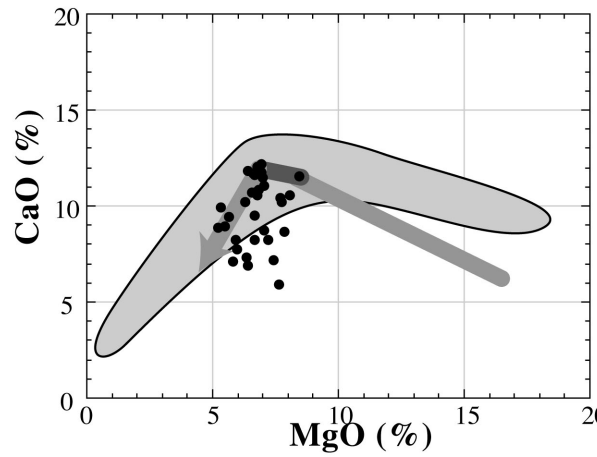


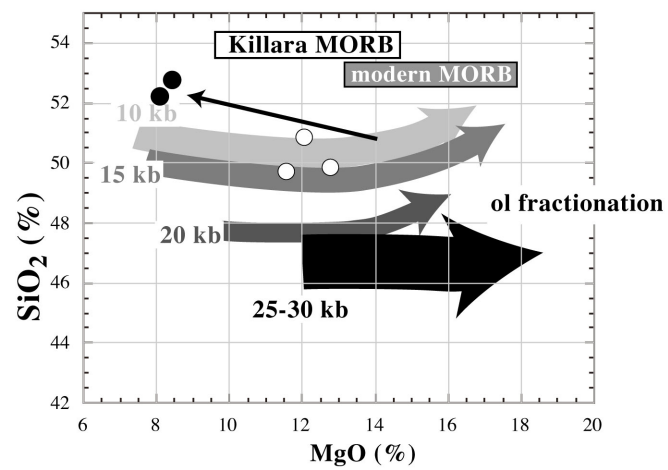


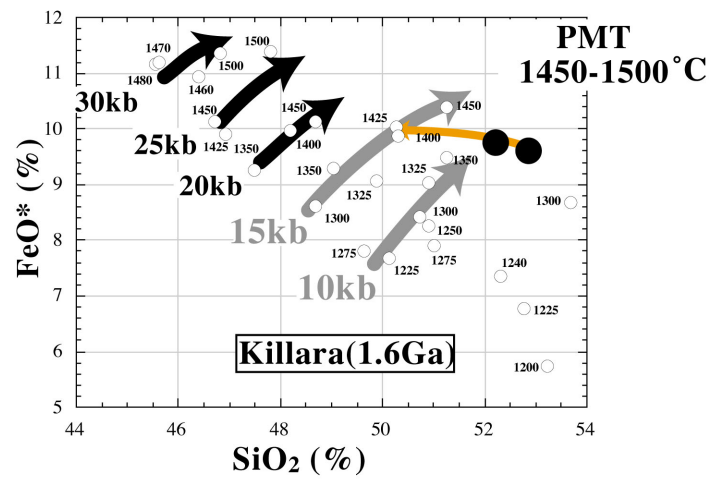


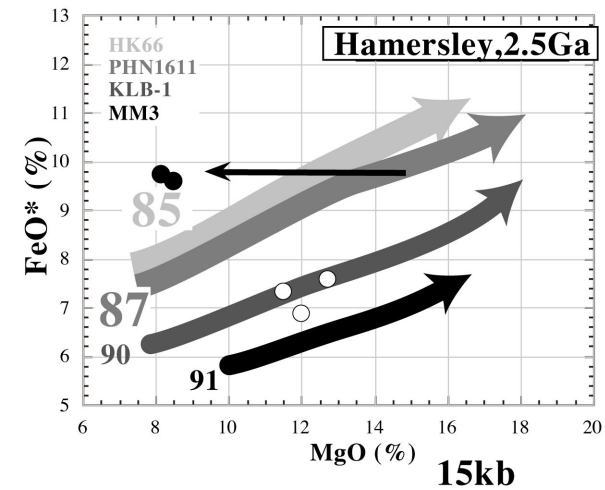


**Variation diagrams of major elements in Killara MORB(1.6Ga), compared with melt compositions by high pressure melting experiment**

## Results

**pressure-------10-15kb**

**FeO content in source mantle-----10% (Mg#=85-87)**

**PMT=1400-1500˚C**

Komiya 1999 Doctor Thesis Fig. VI-3

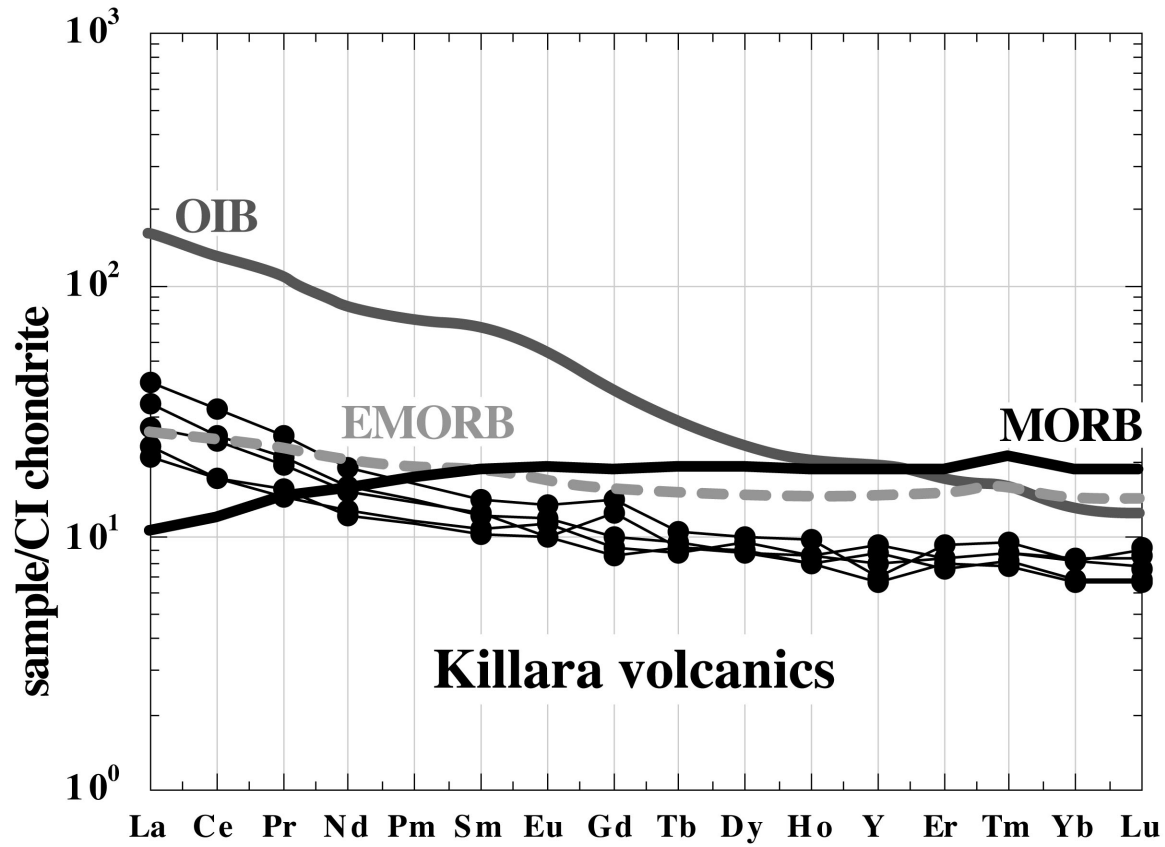


Komiya 1999 Doctor Thesis Fig. VI-4

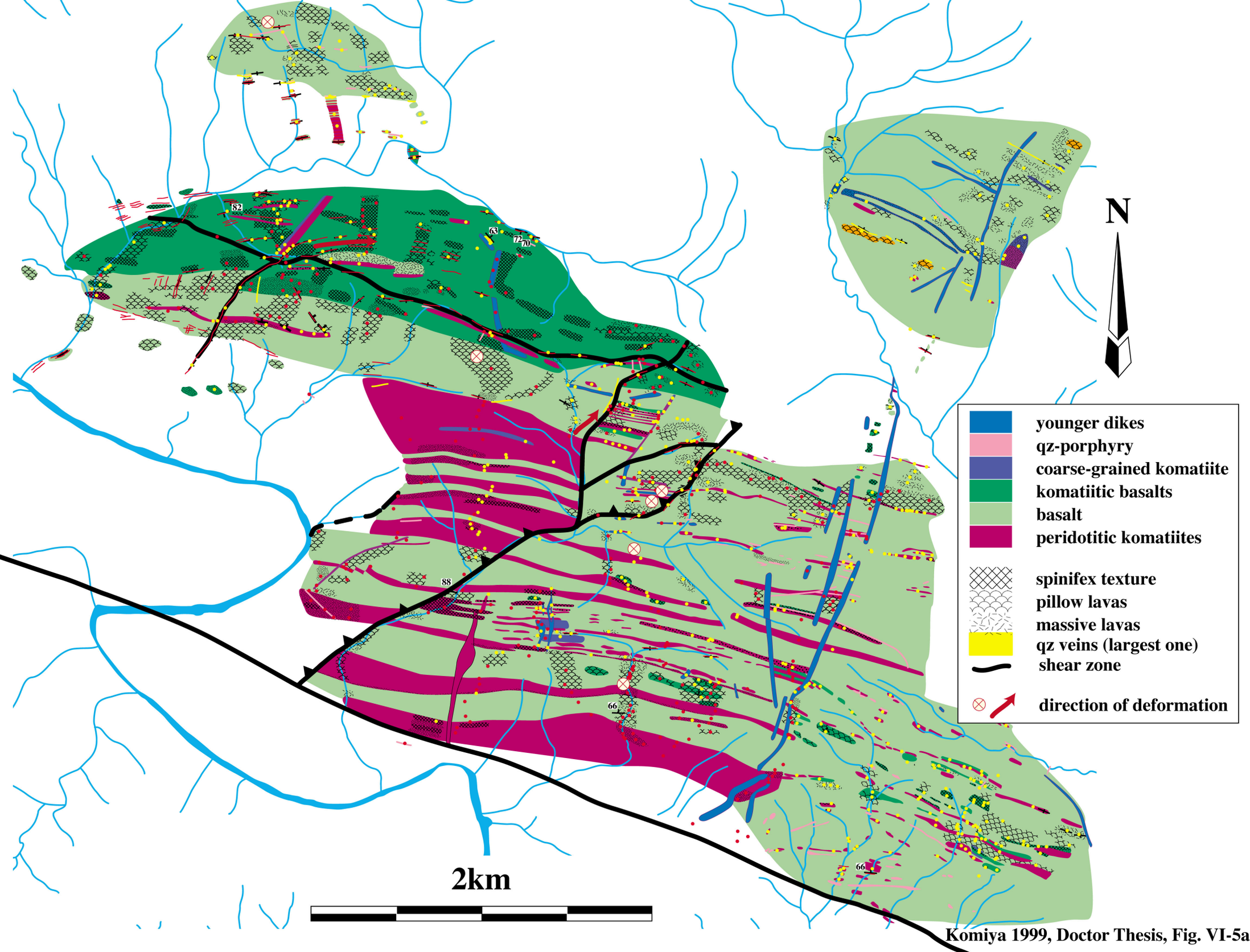


Komiya 1999, Doctor Thesis, Fig. VI-5a

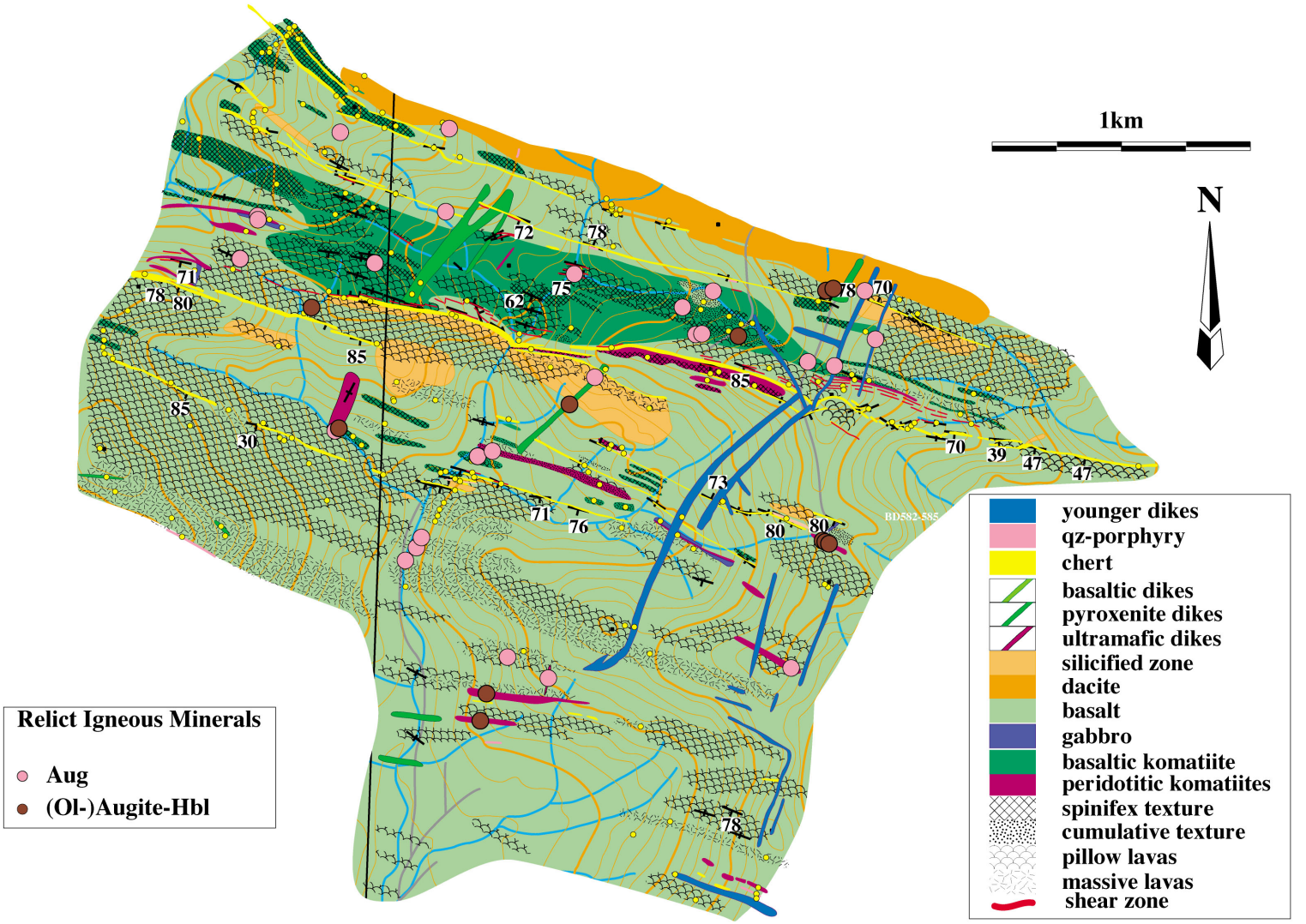


Komiya 1999, Doctor Thesis, Fig. VI-5b

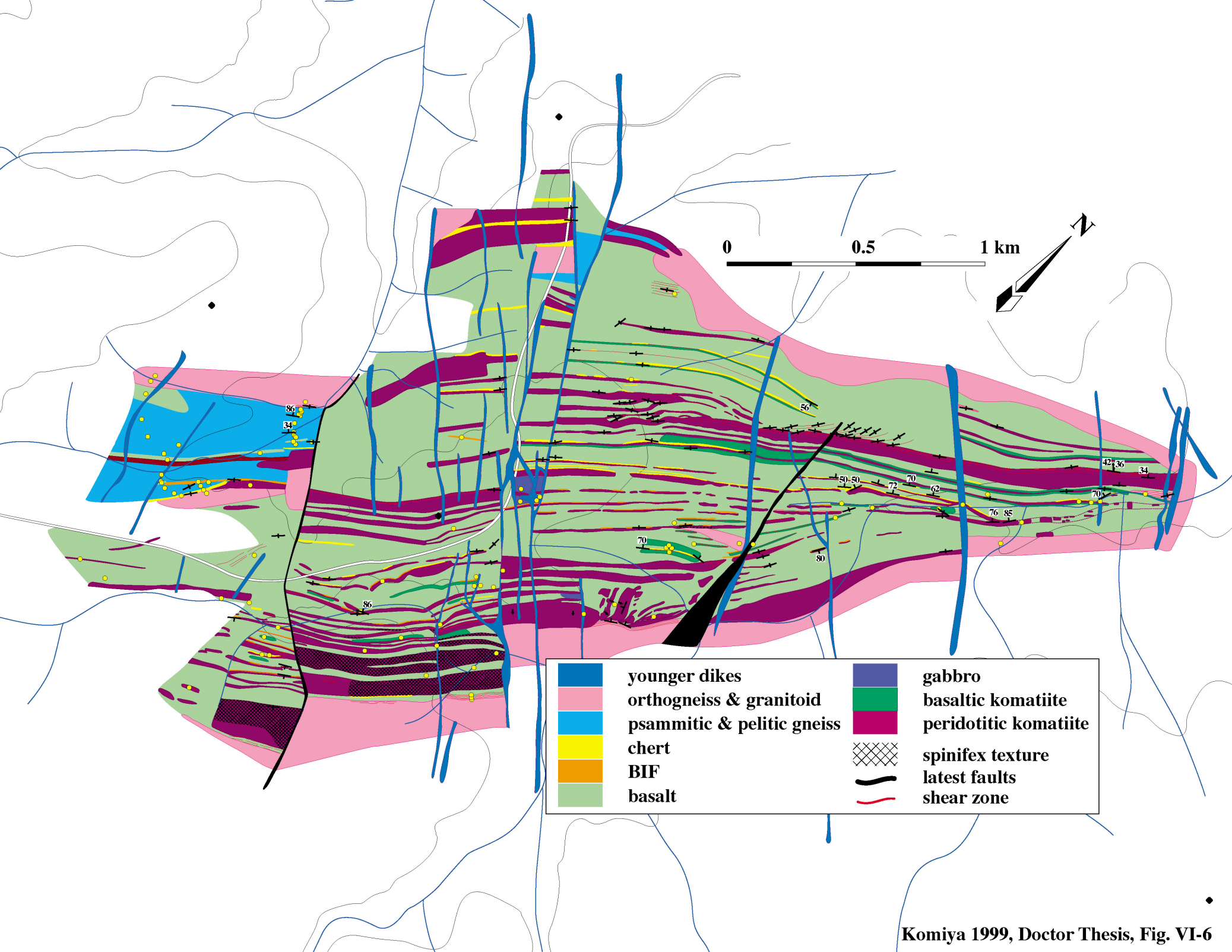


Komiya 1999, Doctor Thesis, Fig. VI-6

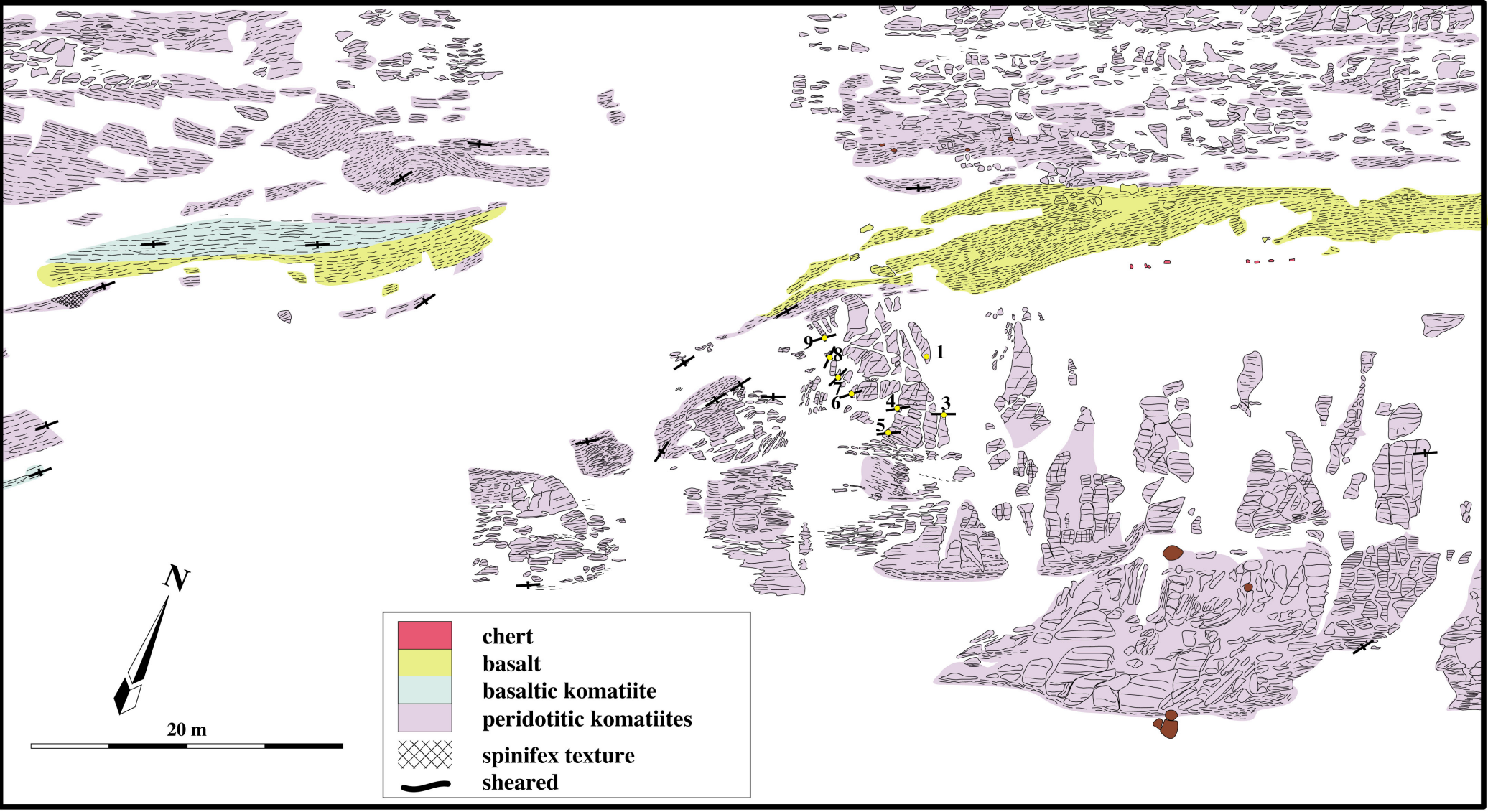


Komiya 1999, Doctor Thesis, Fig. VI-7

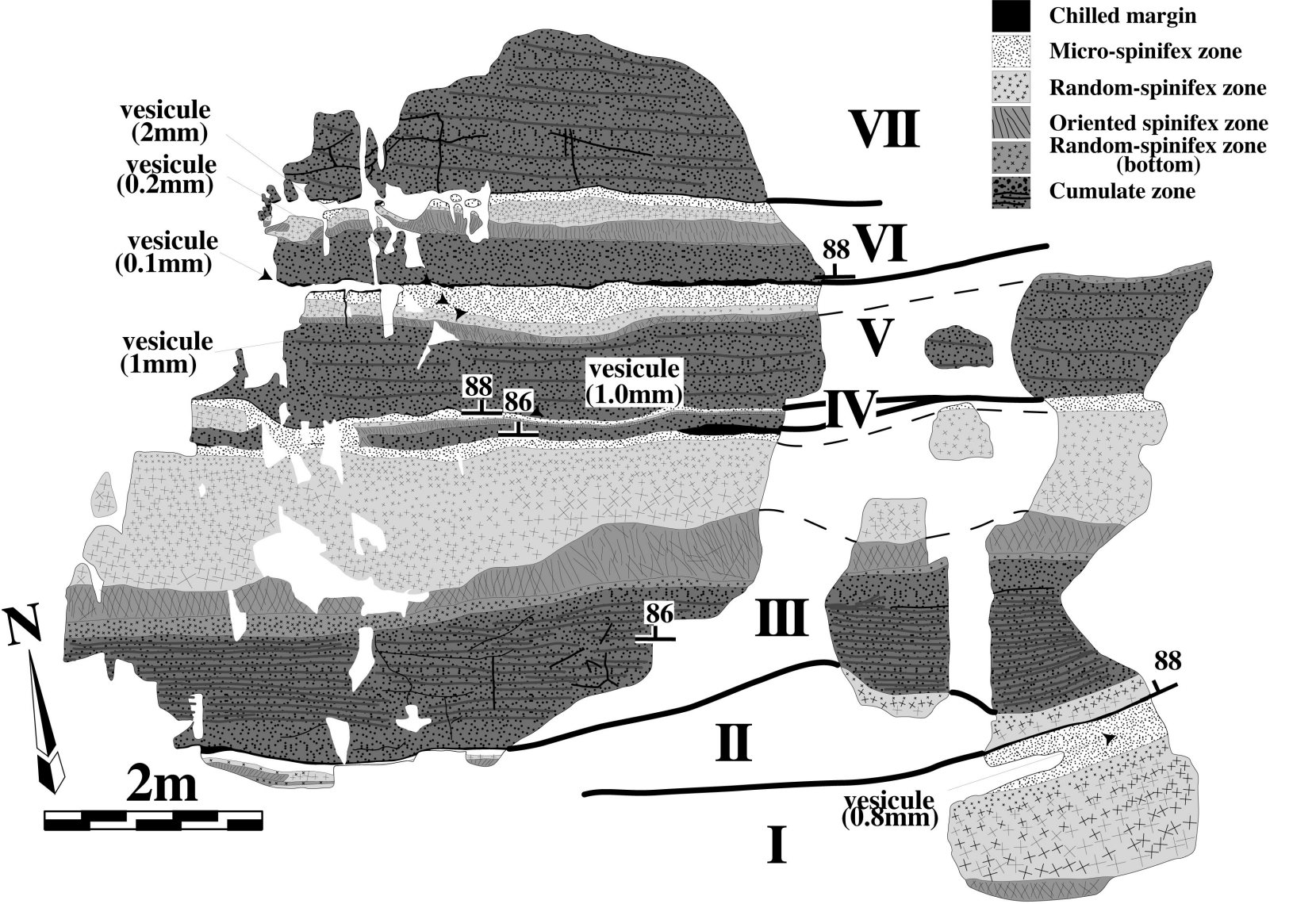


Komiya 1999 Doctor Thesis Fig. VI-8

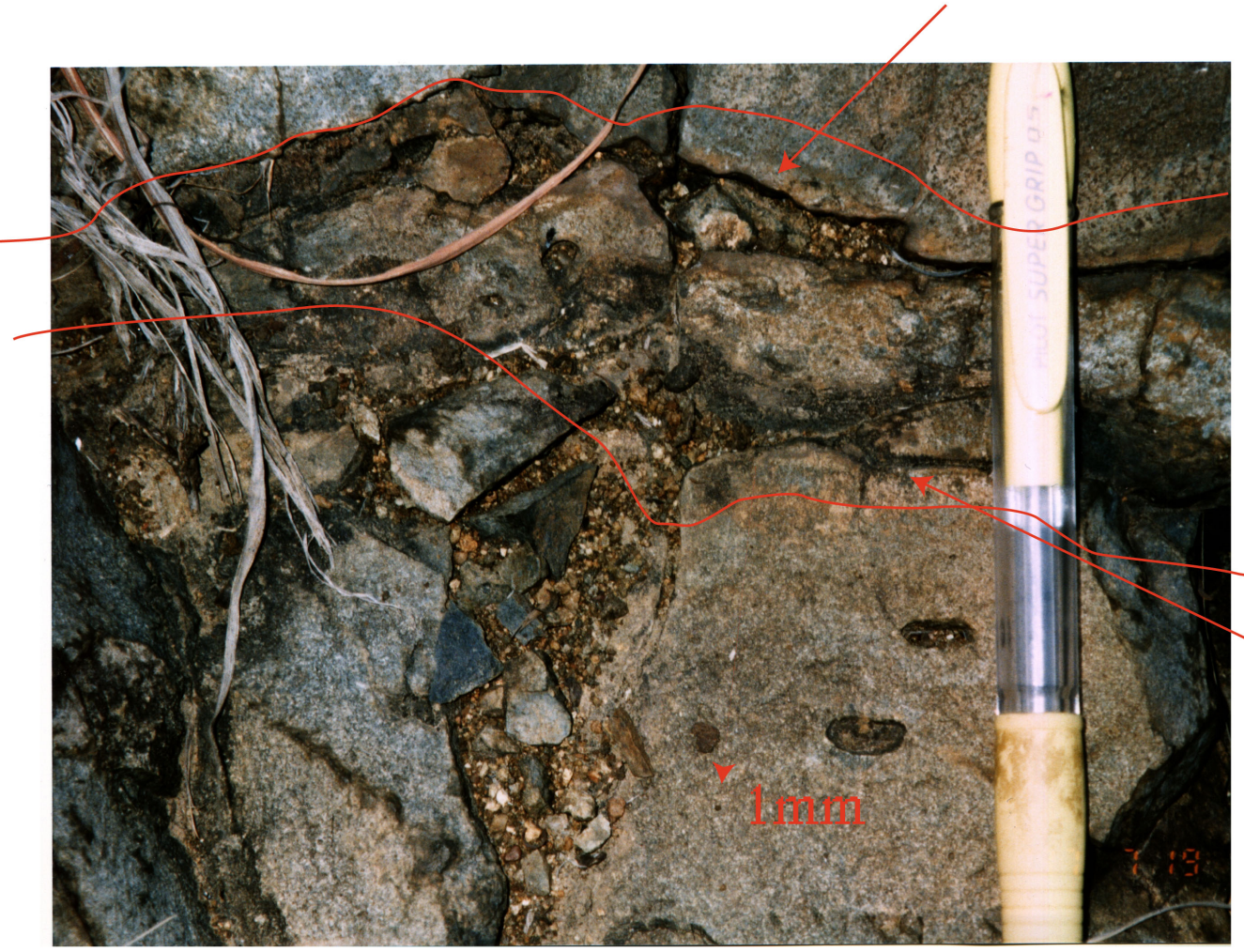


# Flow VI

chilled margin
(bottom)

chilled margin
(topmost)

# Flow III

10 cm

Komiya 1999 Doctor Thesis Fig. VI-9

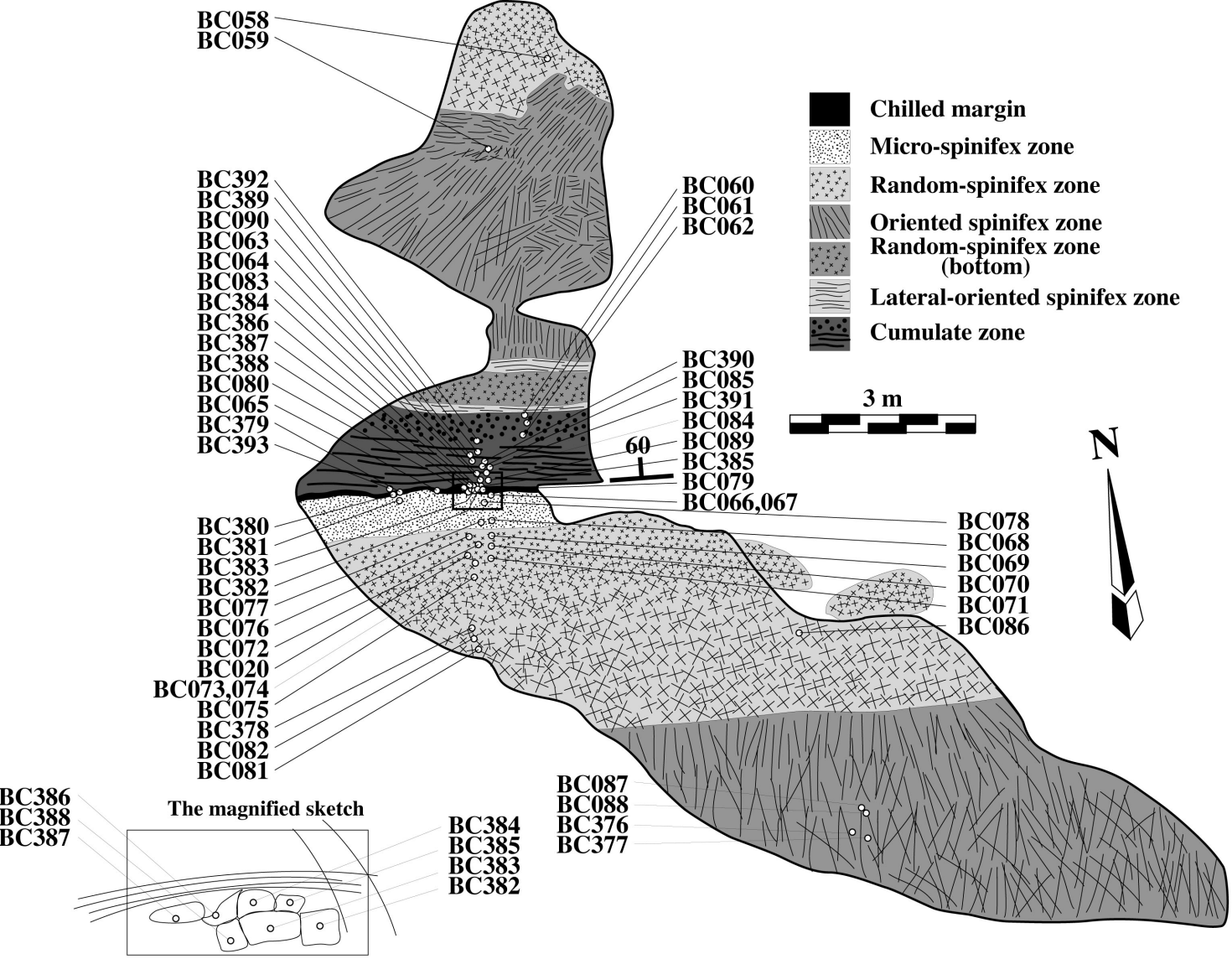


Komiya 1999 Doctor Thesis Fig. VI-10

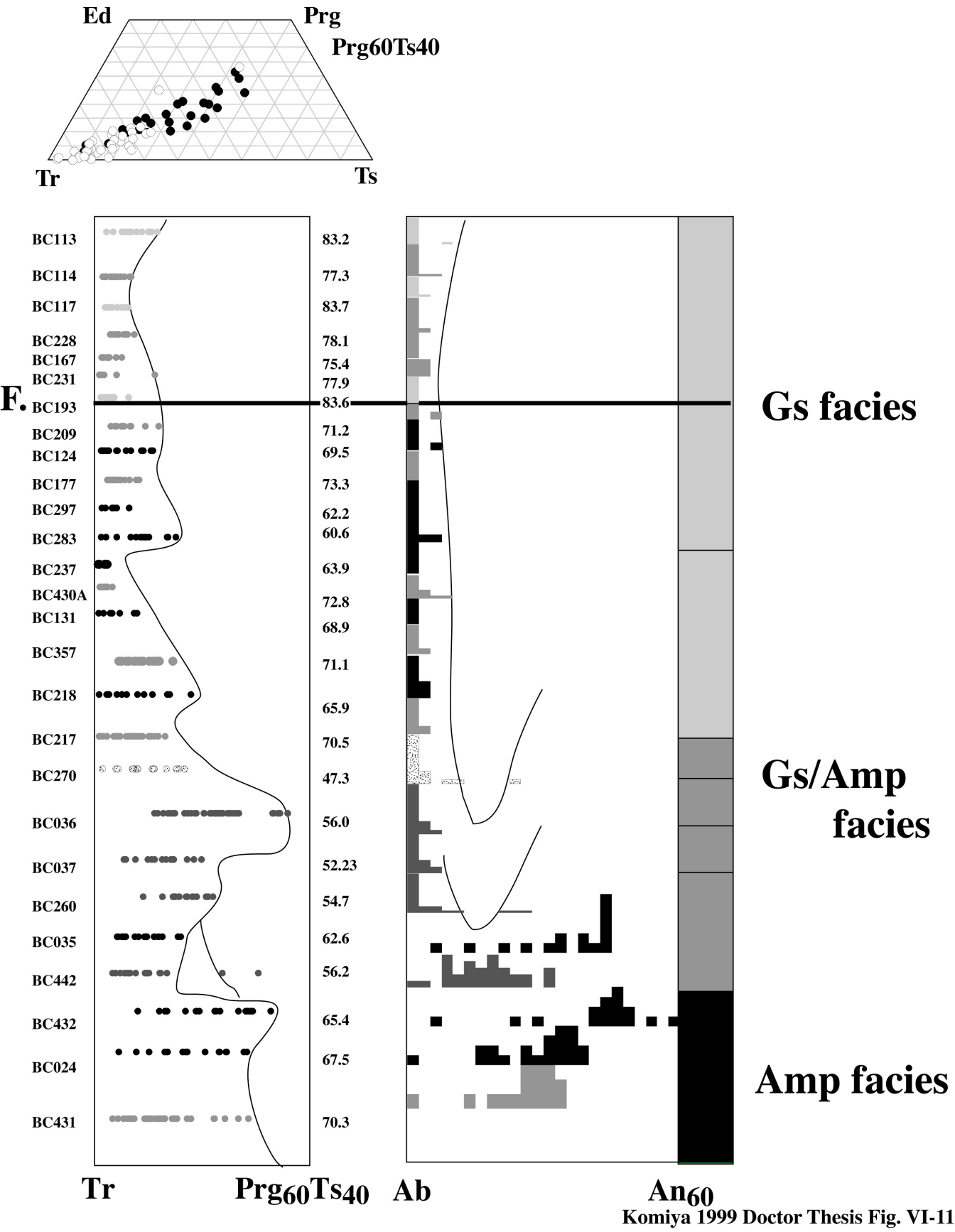


Komiya 1999 Doctor Thesis Fig. VI-11

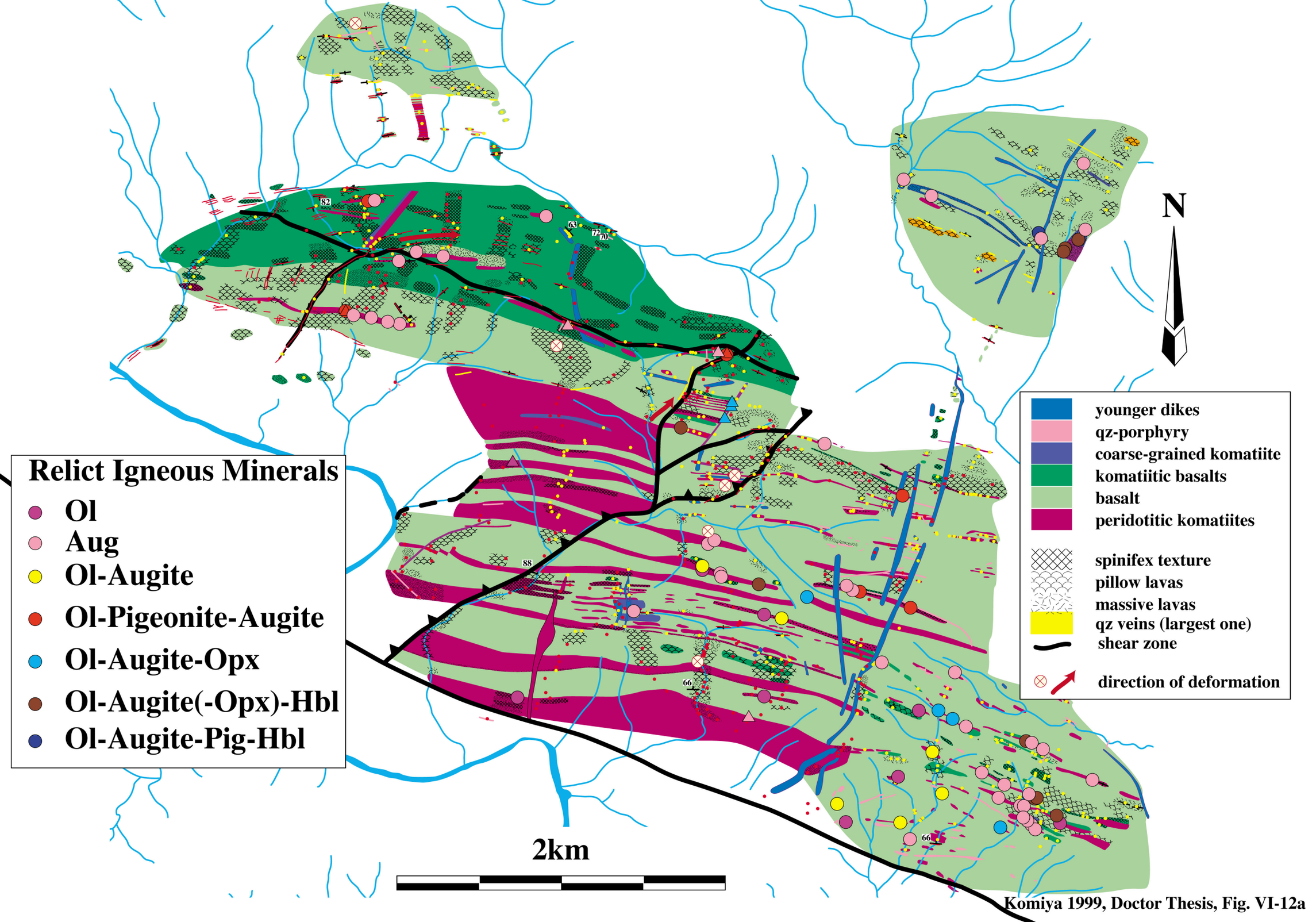


Komiya 1999, Doctor Thesis, Fig. VI-12a

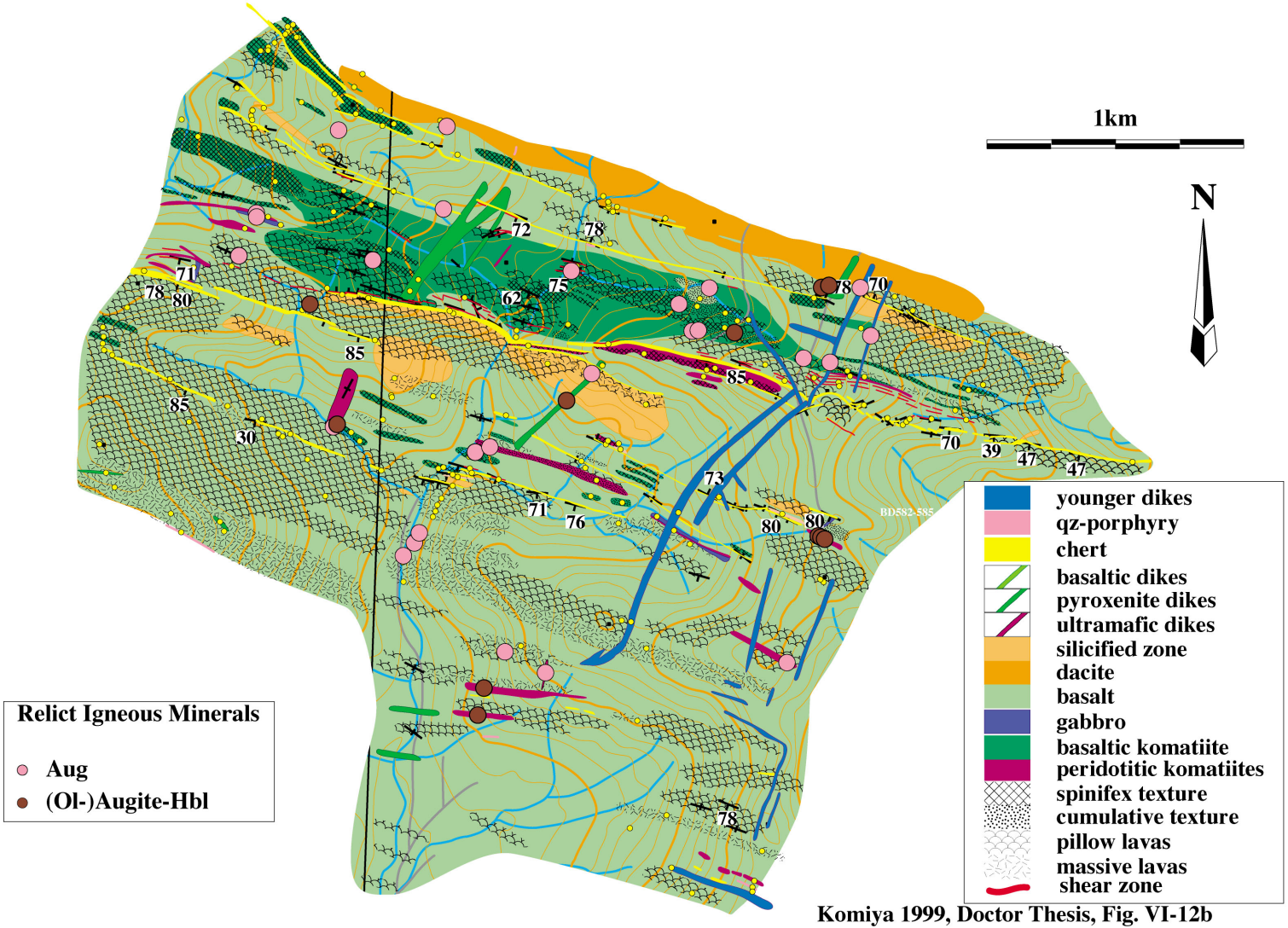
1km
N
Relict Igneous Minerals
Aug
(Ol-)Augite-Hbl
younger dikes
qz-porphyry
chert
basaltic dikes
pyroxenite dikes
ultramafic dikes
silicified zone
dacite
basalt
gabbro
basaltic komatiite
peridotitic komatiites
spinifex texture
cumulative texture
pillow lavas
massive lavas
shear zone
BD582-585
Komiya 1999, Doctor Thesis, Fig. VI-12b

# Original

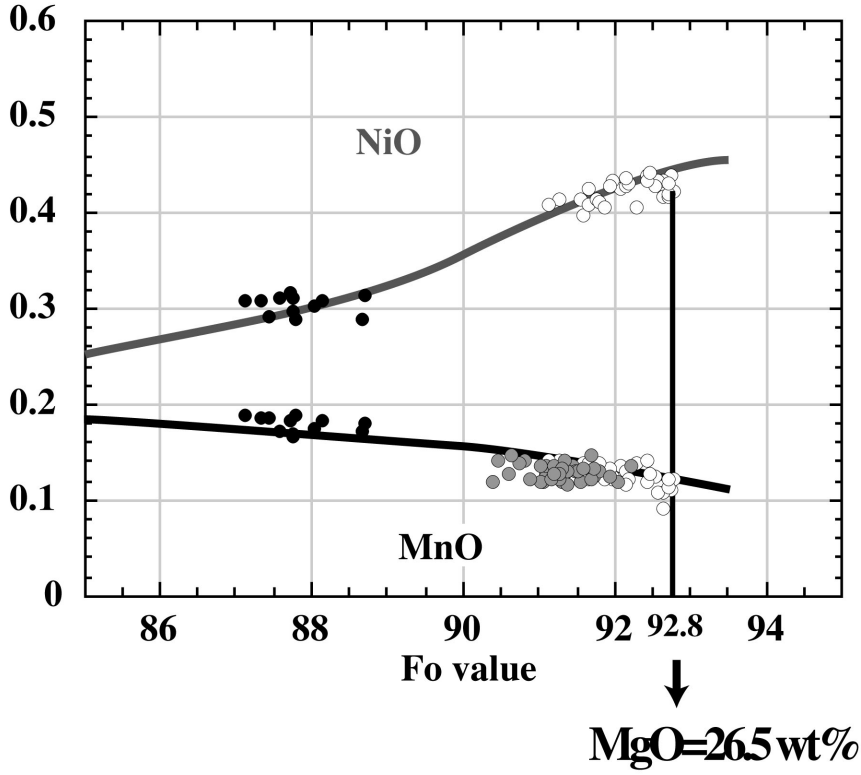


# Recrystallized

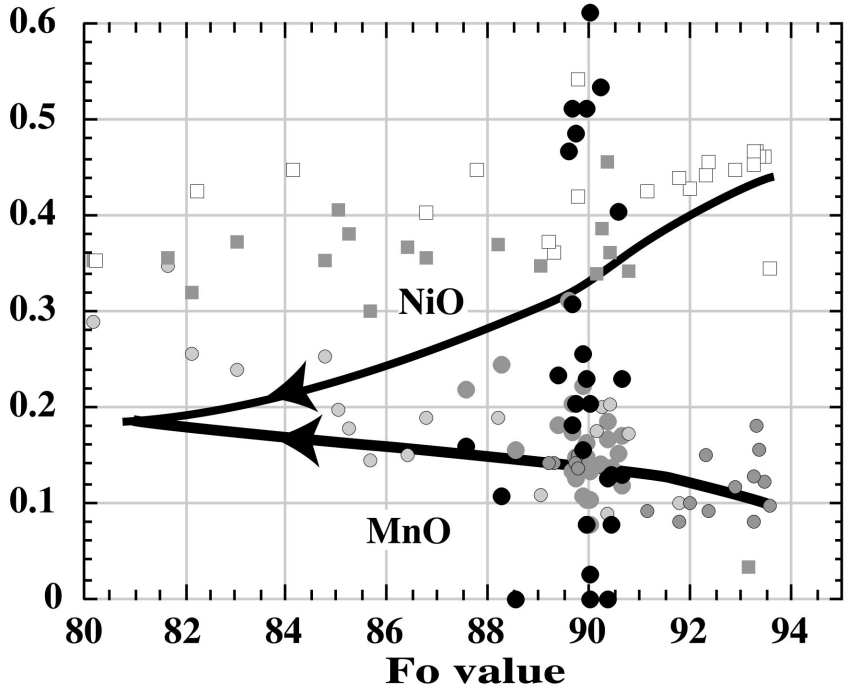


Komiya 1999 Doctor Thesis Fig. VI-13

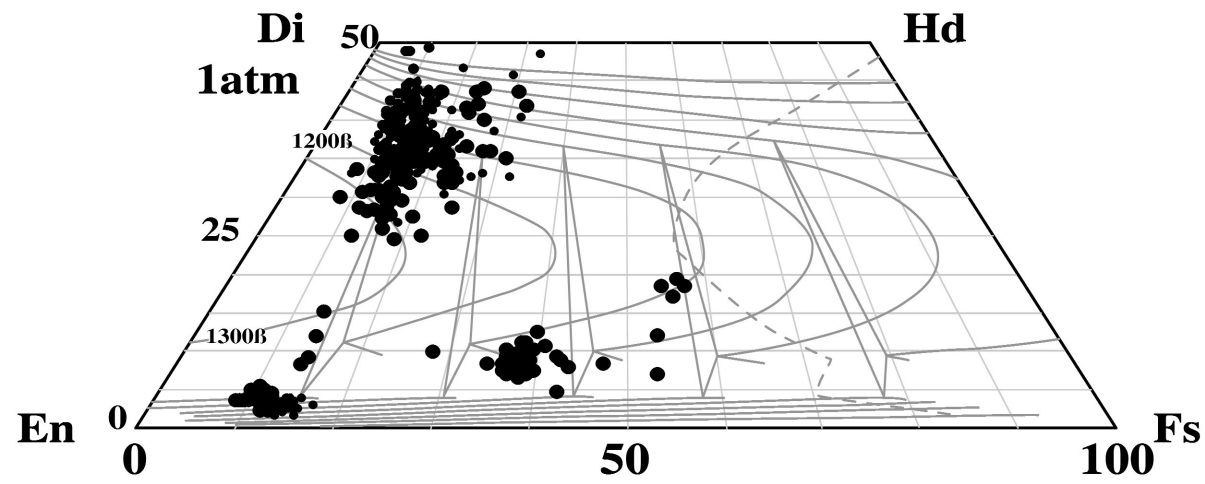


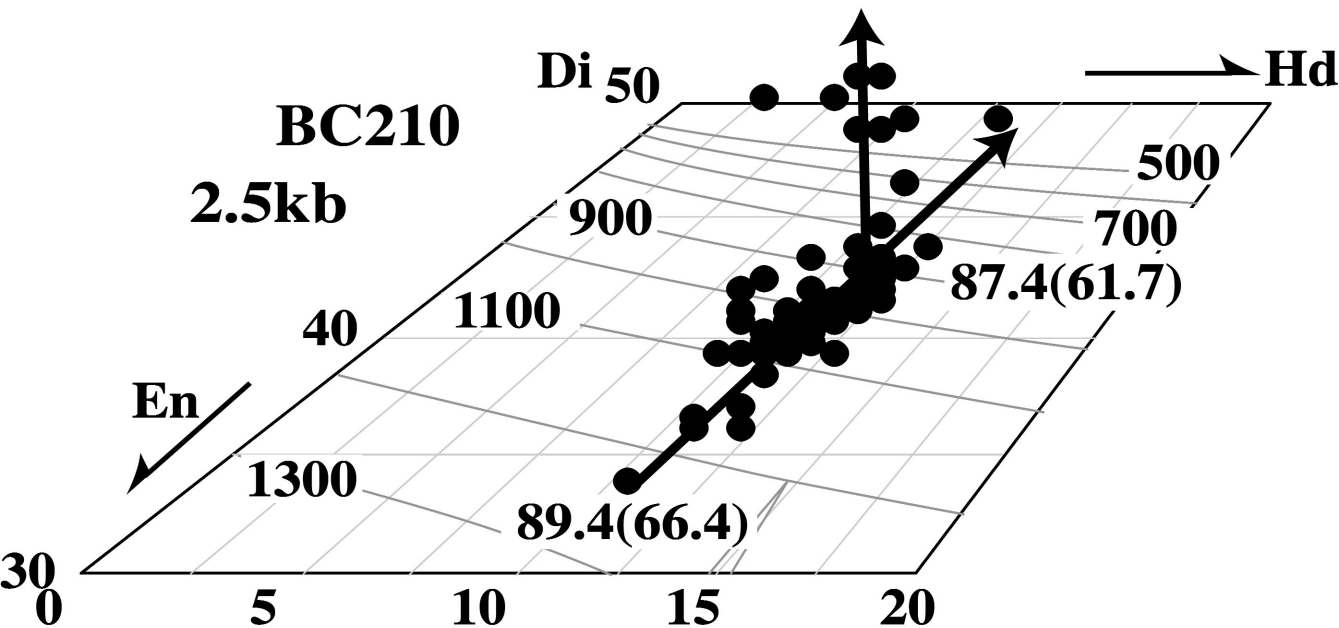


Komiya 1999 Doctor Thesis Fig. VI-14

# Textural relationship of olivine and pyroxenes

## (Type I) Ol-Spinifex peridotitic komatiites (inter-cumulus clinopyroxenes)

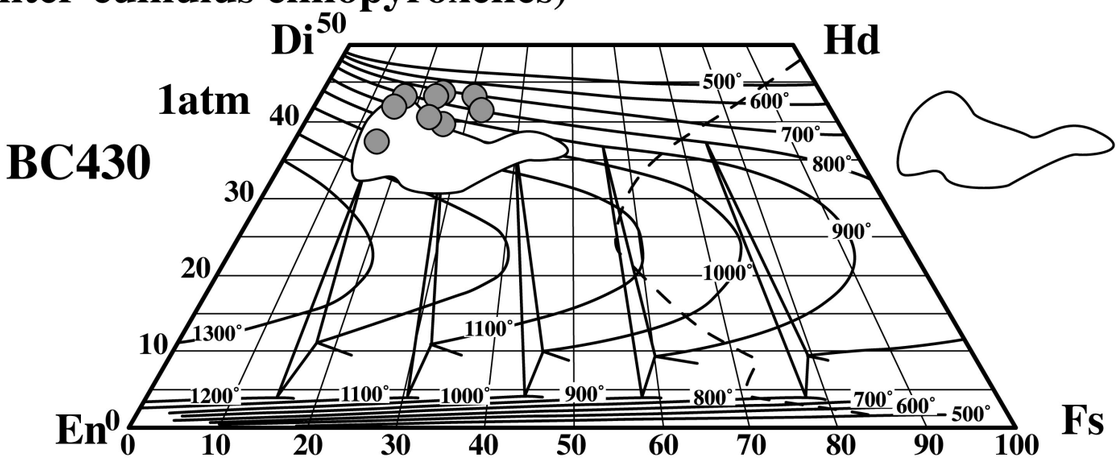


Parman et al.,1997

## (Type II) Ol cumulate (mesocumulate)

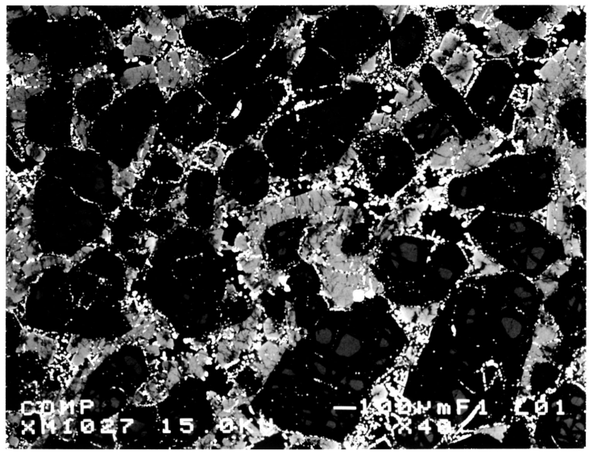

Ol-Pig-Aug

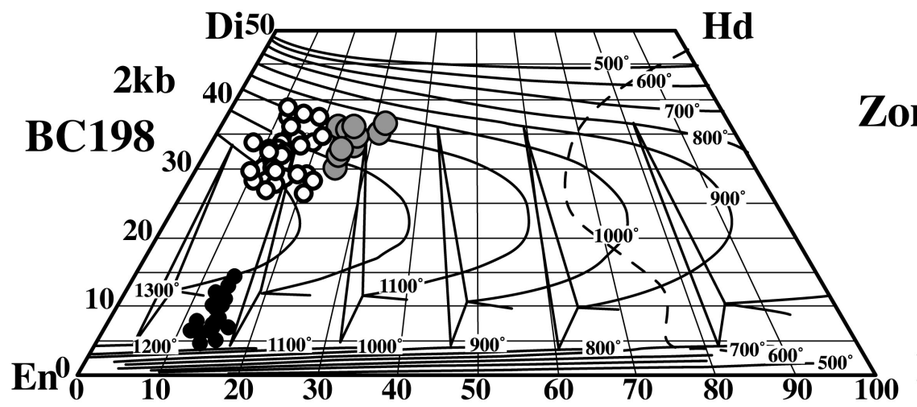


Zoning Pattern
- ● Pig
- ↓
- ○ Aug
- ↓
- ◎ Al-Aug

## (Type III) Ol cumulate (poikilitic, Ol-Cpx-Opx-Hbl)

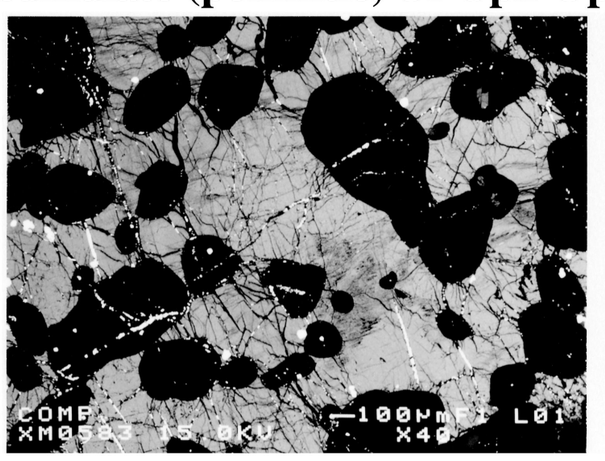

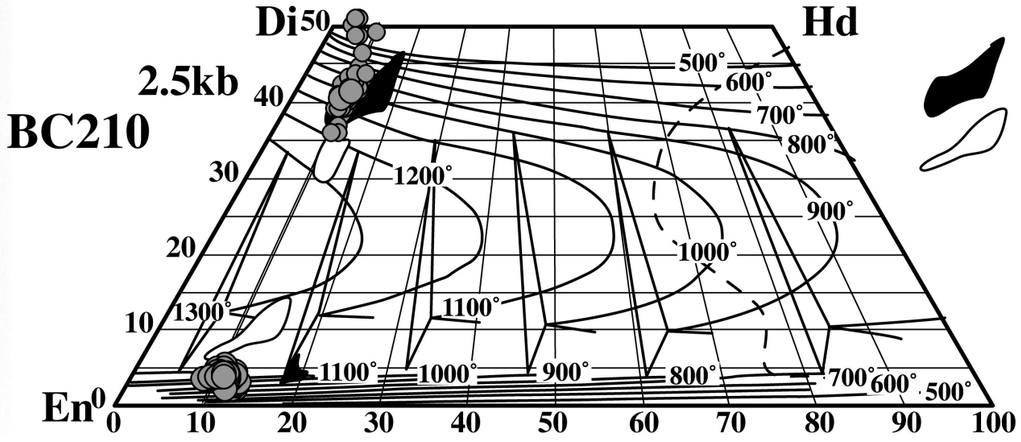


Wet (2kb)
Dry (1atm)
Parman et al.,1997

Komiya 1999, Doctor Thesis, Fig. VI-15

# Ol-Spinifex peridotitic komatiites
## (inter-cumulus clinopyroxenes)

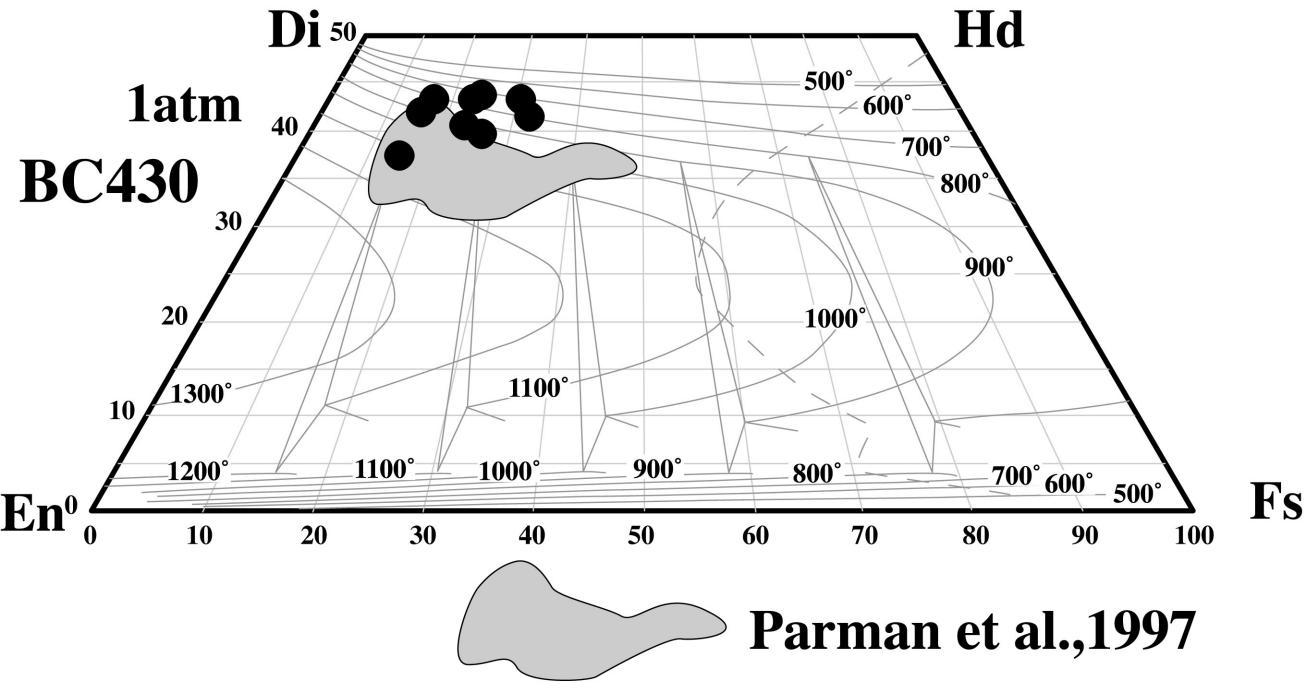




Parman et al.,1997

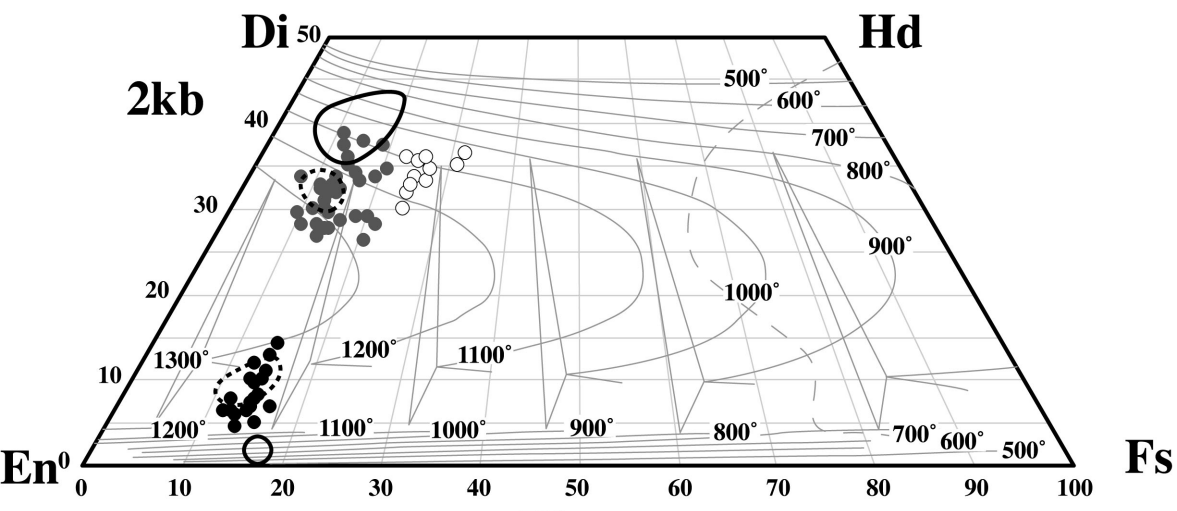


• Pig

Zoning Pattern • Aug

Wet (2kb)
Dry (1atm)

○ Al-Aug

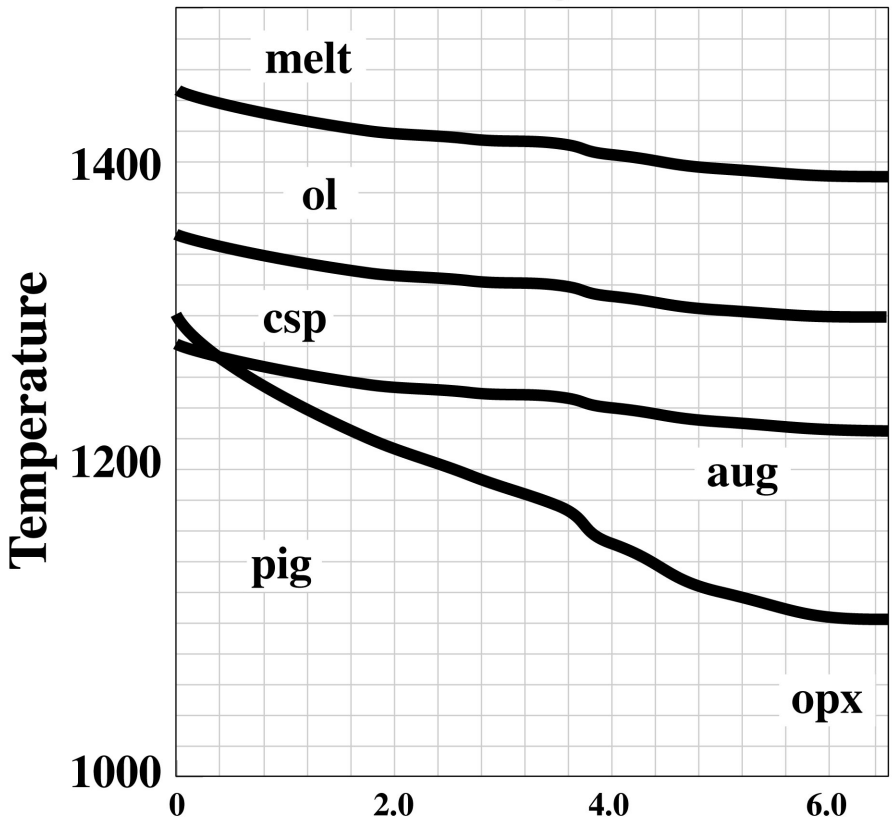


modified after Fig.5 in Parman et al.1997

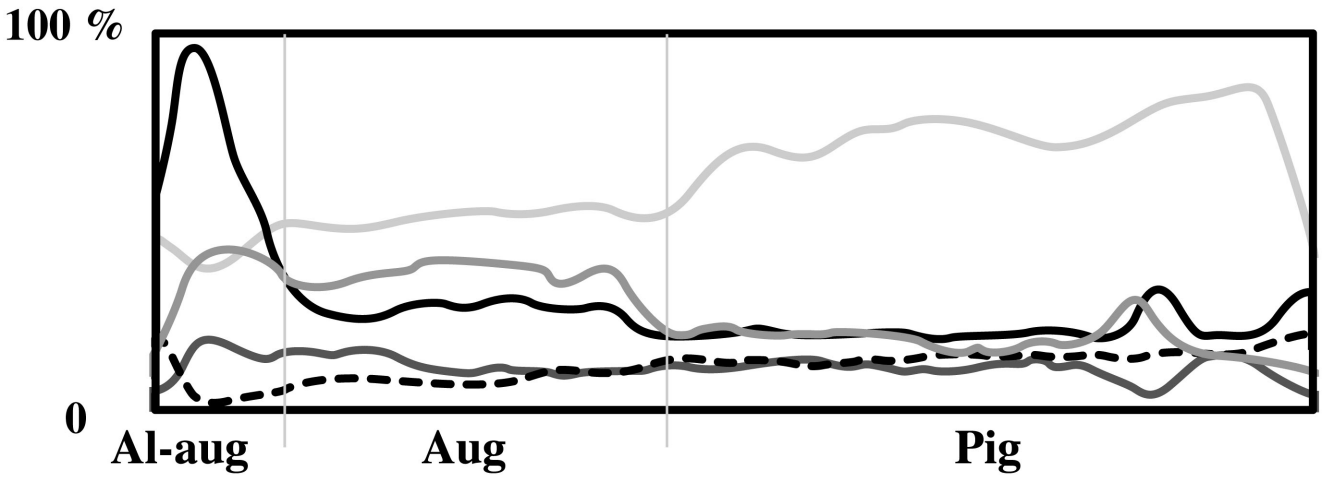


A

B

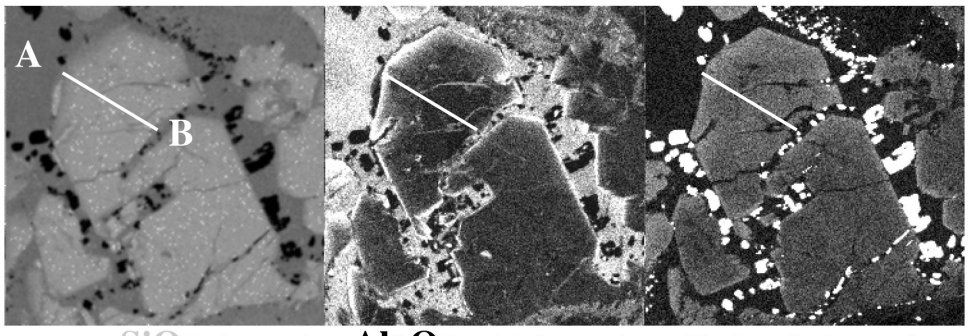


$SiO_2$ ( ) $Al_2O_3$ x10( ) FeO x2 ( )

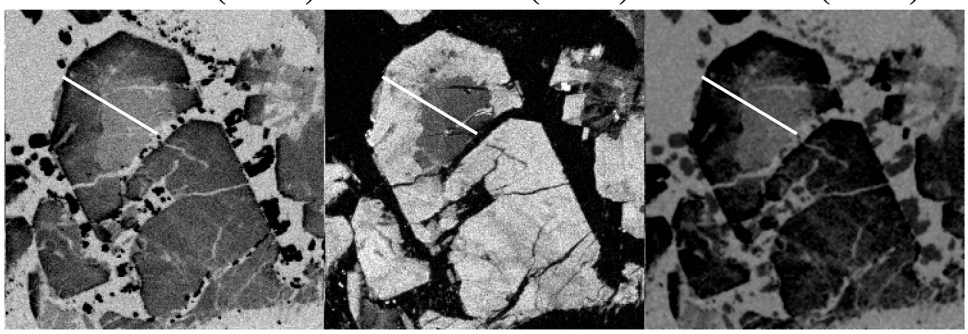

MgO ( ) CaO ( ) Mg#

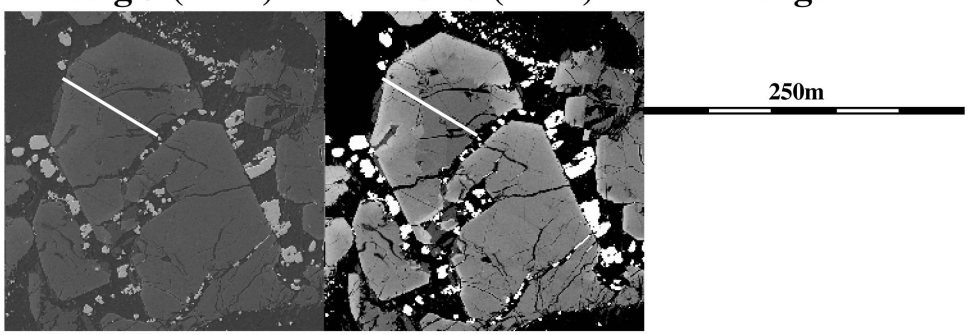


SEM BSI

Komiya 1999, Doctor Thesis Fig. VI-18

upper level

BD503

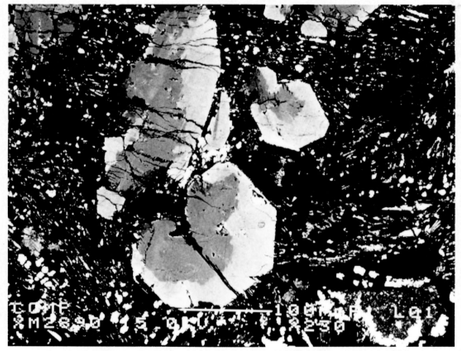


BD503

2300m

BD316

BD313

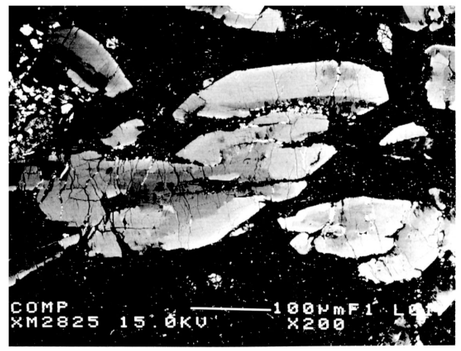


BC198

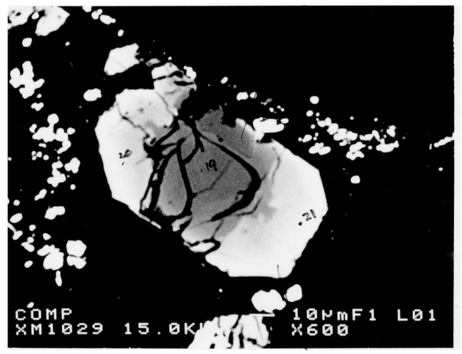


2100m

BD688

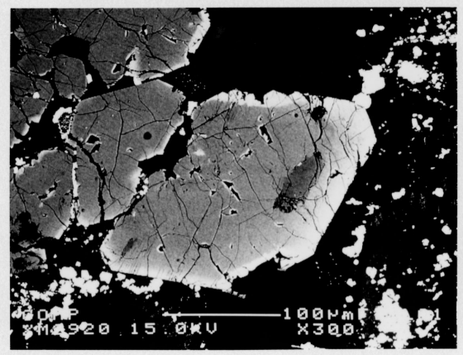


BD688

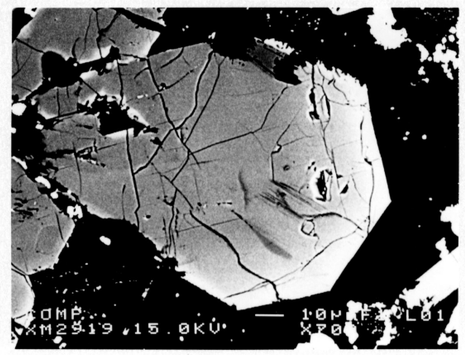


BD688

1900m

BD698

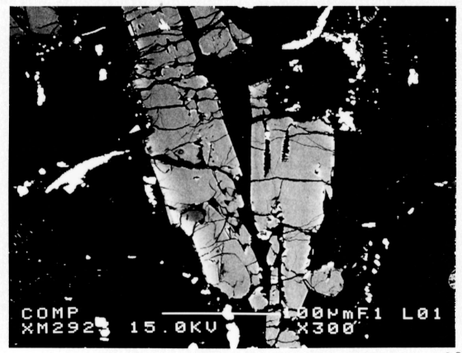


BD698

BD825

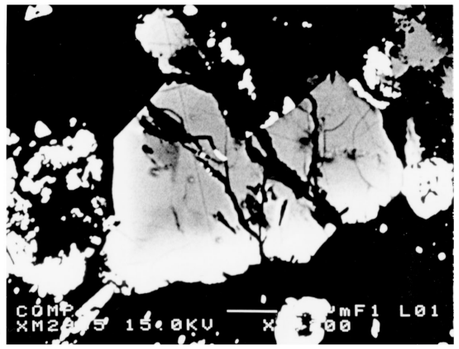


1300m

BD780

BD780

BD780

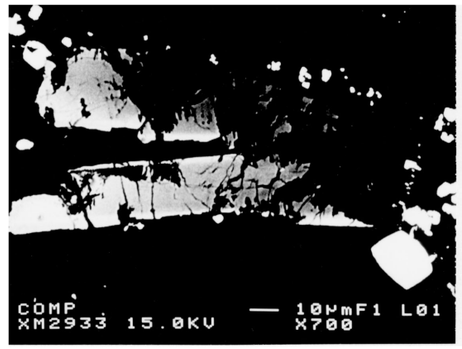


lower level

Komiya 1999, Doctor Thesis, Fig. VI-19

# Ol-Cumulate rock (Ol-Cpx-Opx-Hbl)
# (poikilitic cpx & opx)

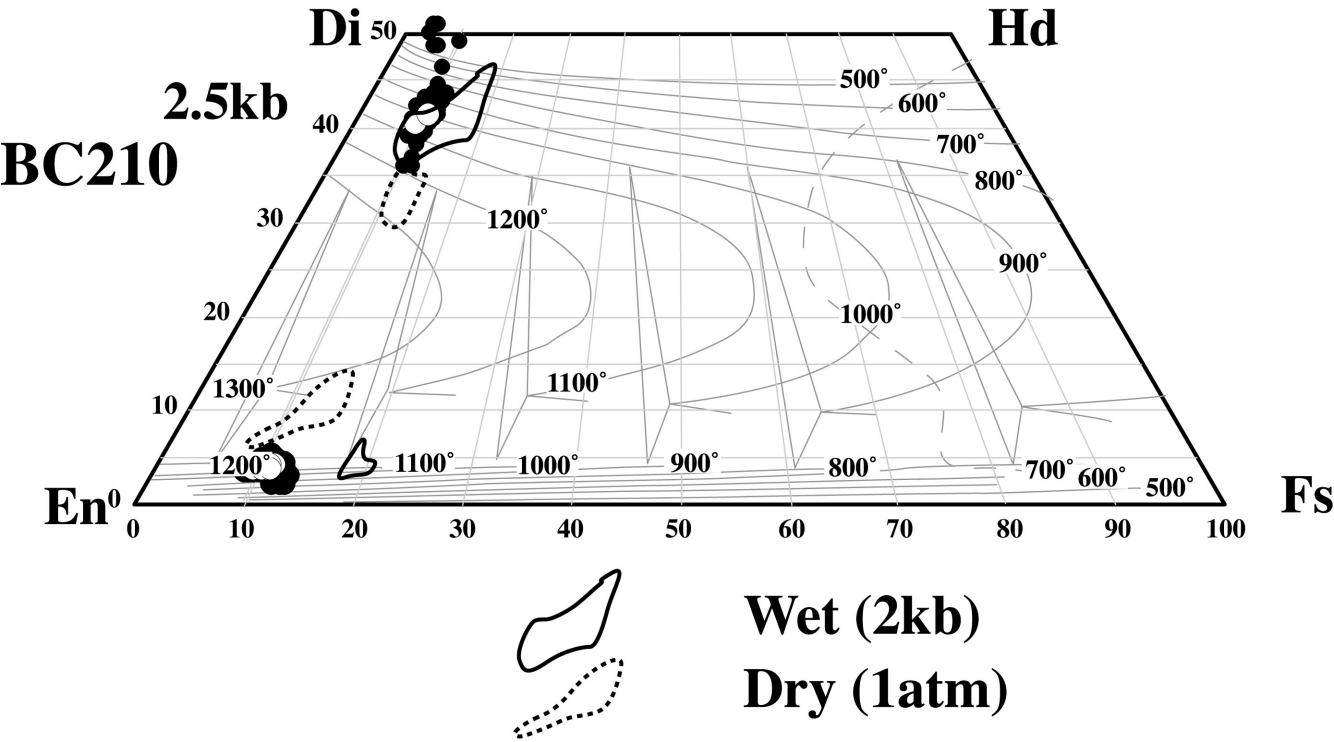


Wet (2kb)

Dry (1atm)

Komiya 1999 Doctor Thesis Fig. VI-20

## Area 9

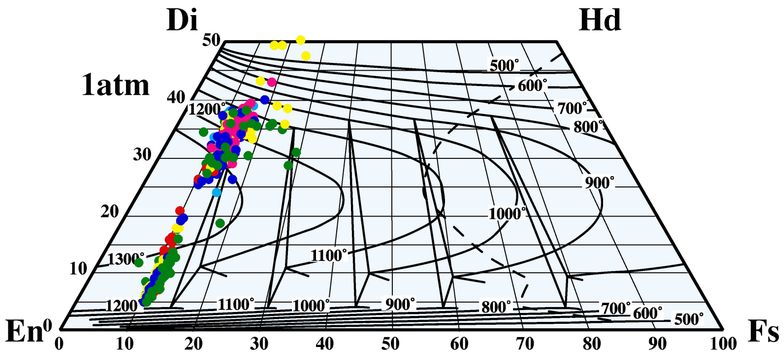


## Area 10

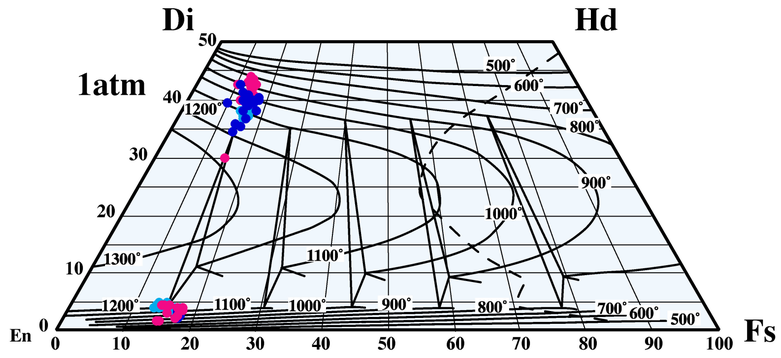


## Area 8

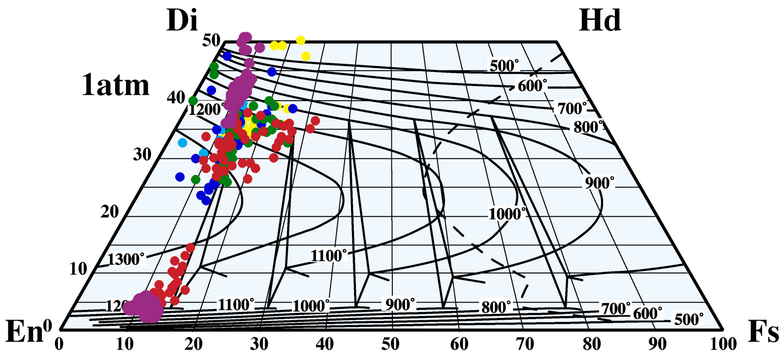


## Area 6

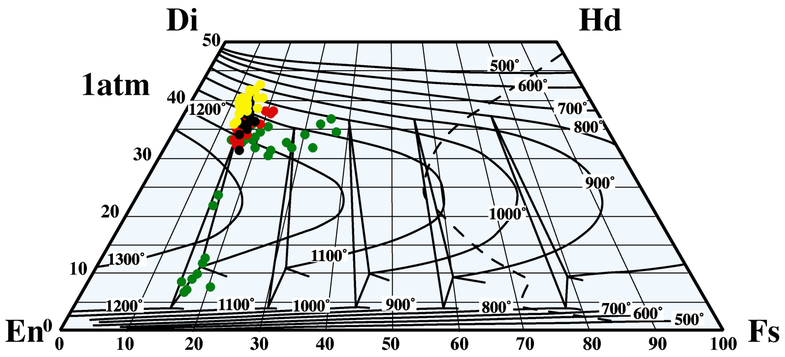


## Area 7

## Area 5

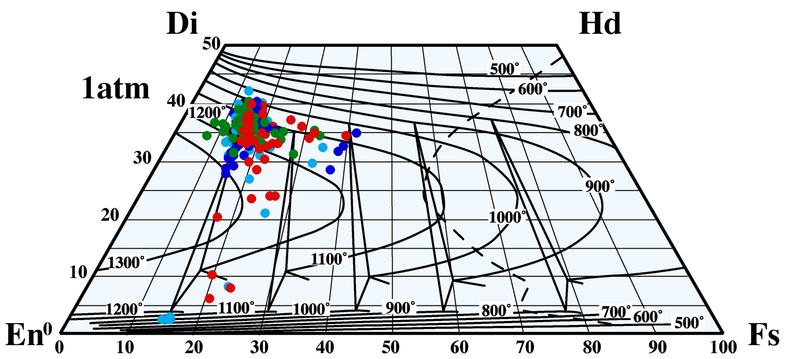


## Area 4

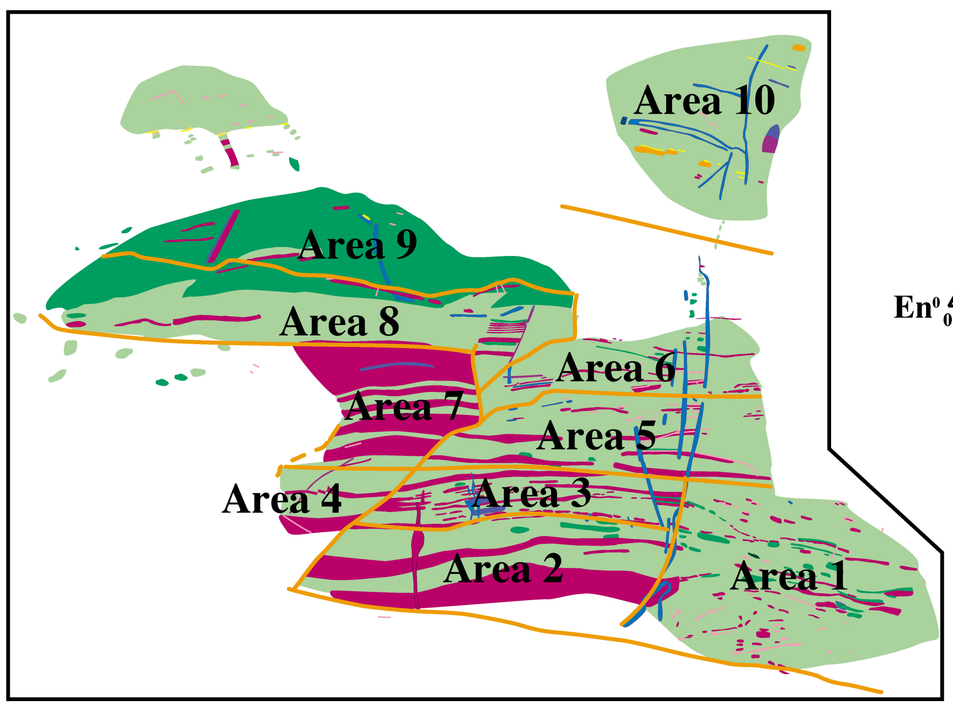


## Area 3

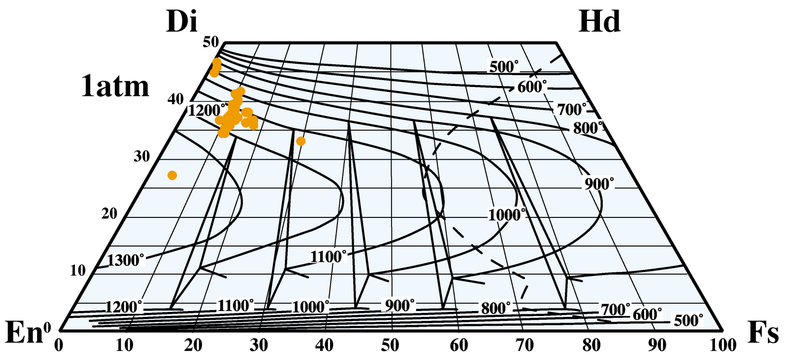


## Area 2

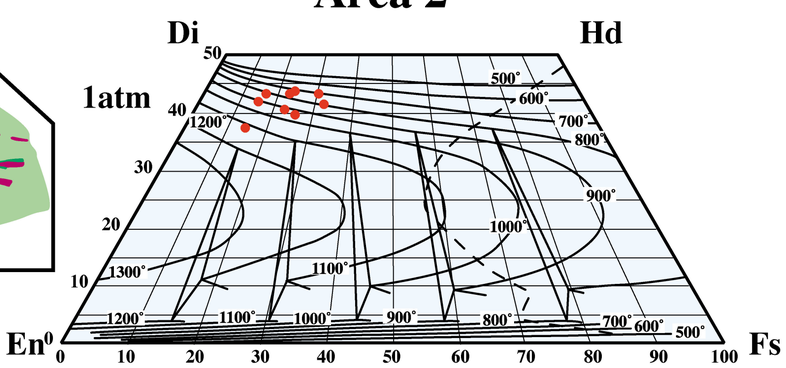


## Area 1

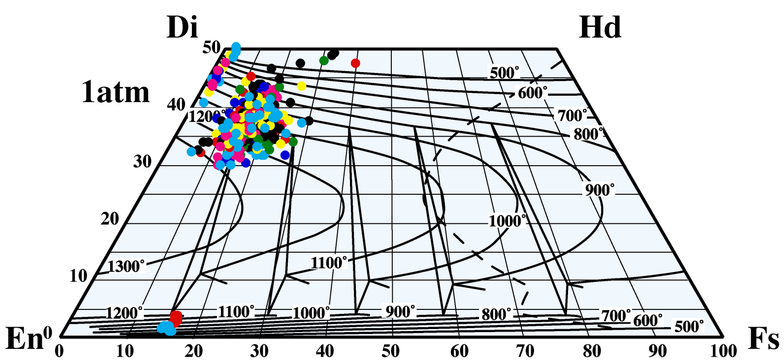


Komiya 1999, Doctor Thesis, Fig. VI-21

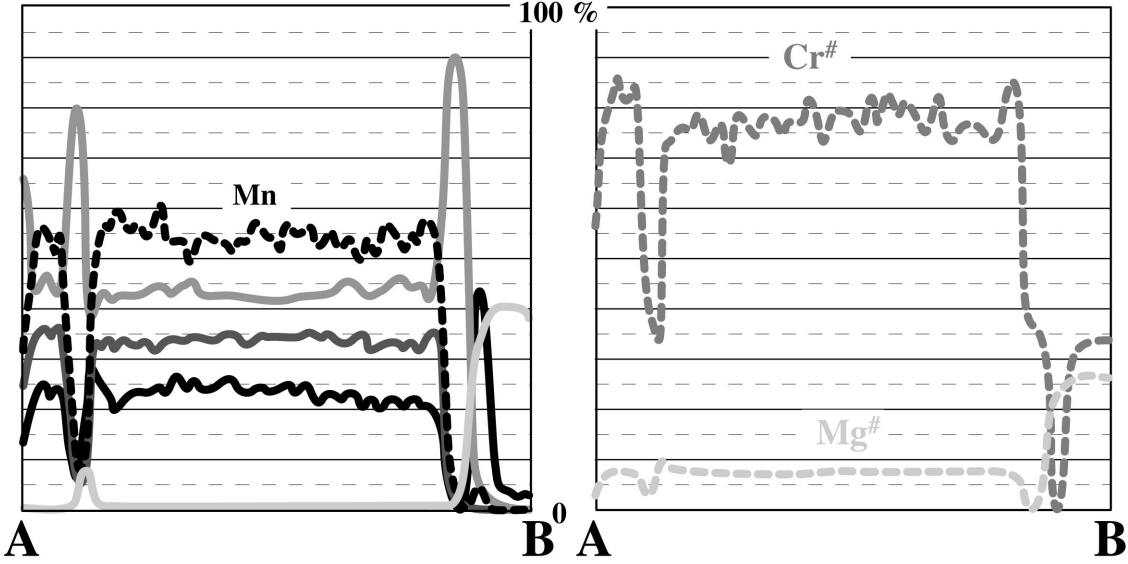


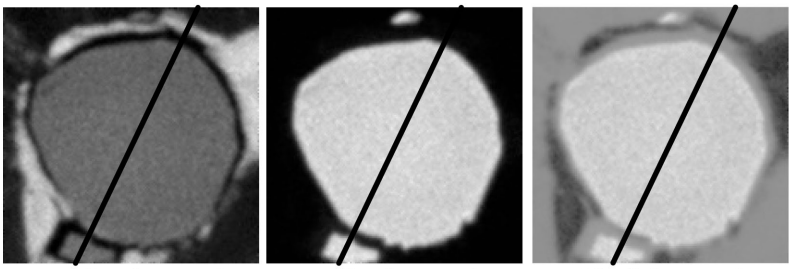


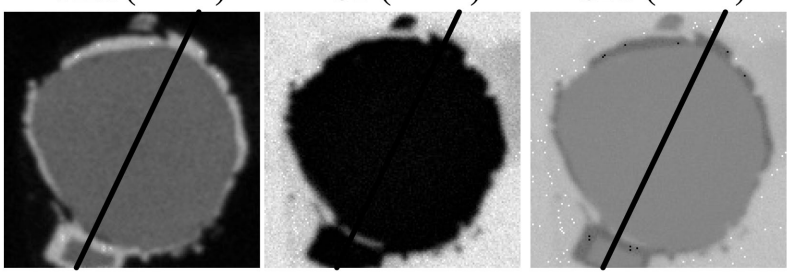


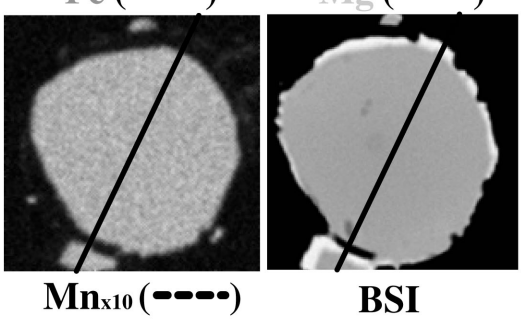

Komiya 1999 Doctor Thesis Fig. VI-23

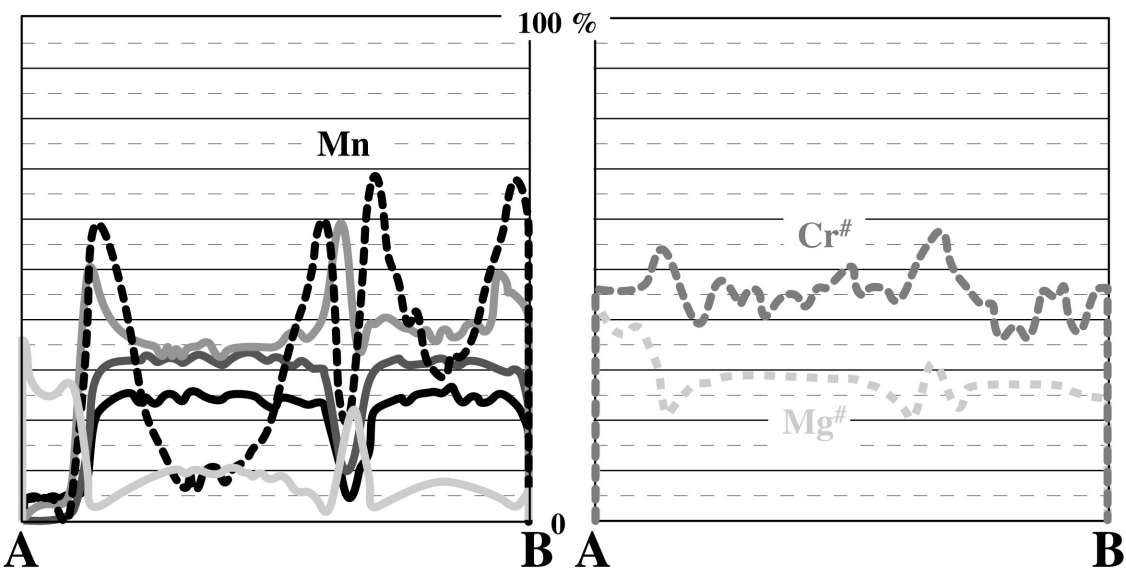


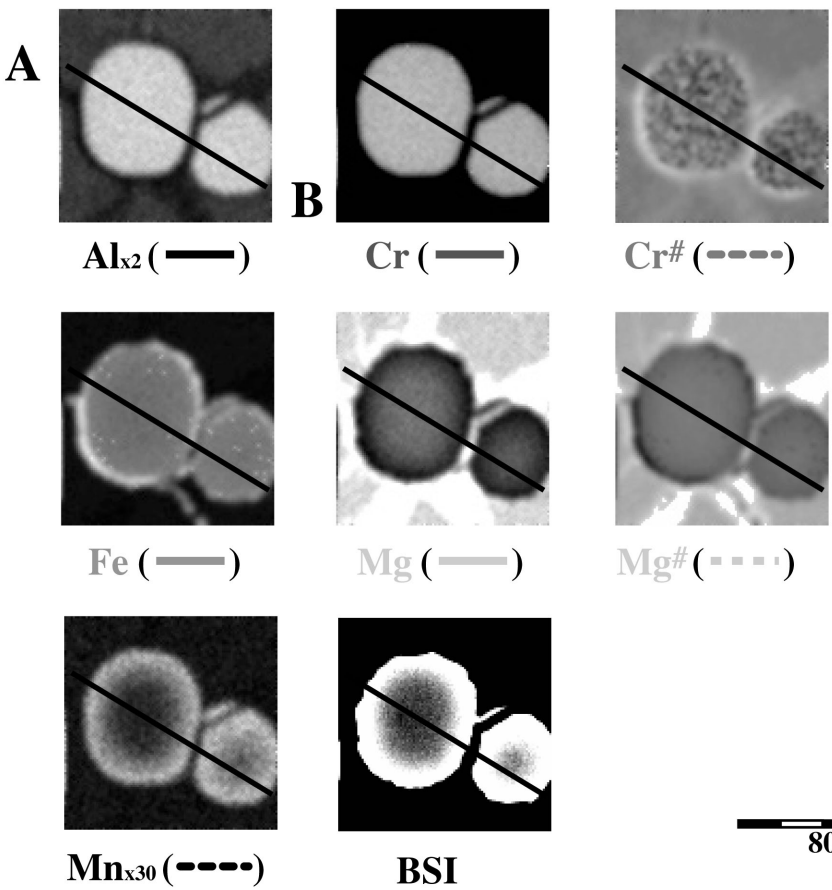


Komiya 1999 Doctor Thesis Fig. VI-24

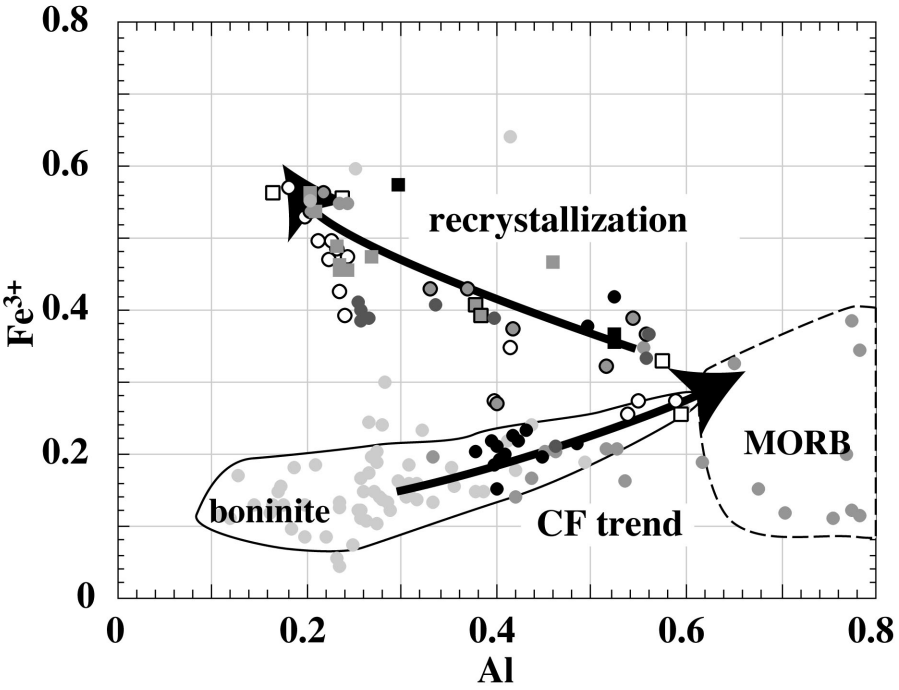


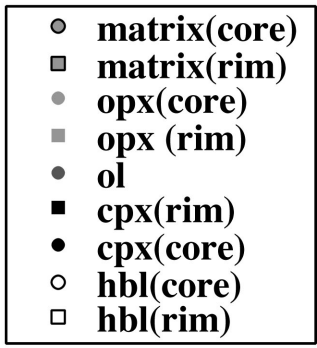


Komiya 1999 Doctor Thesis Fig. VI-25

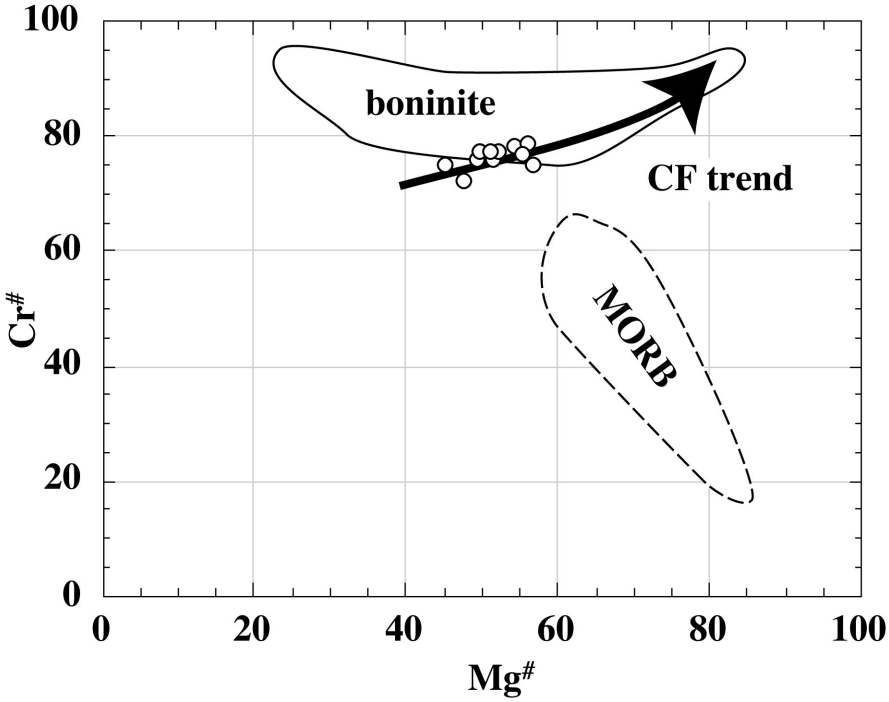


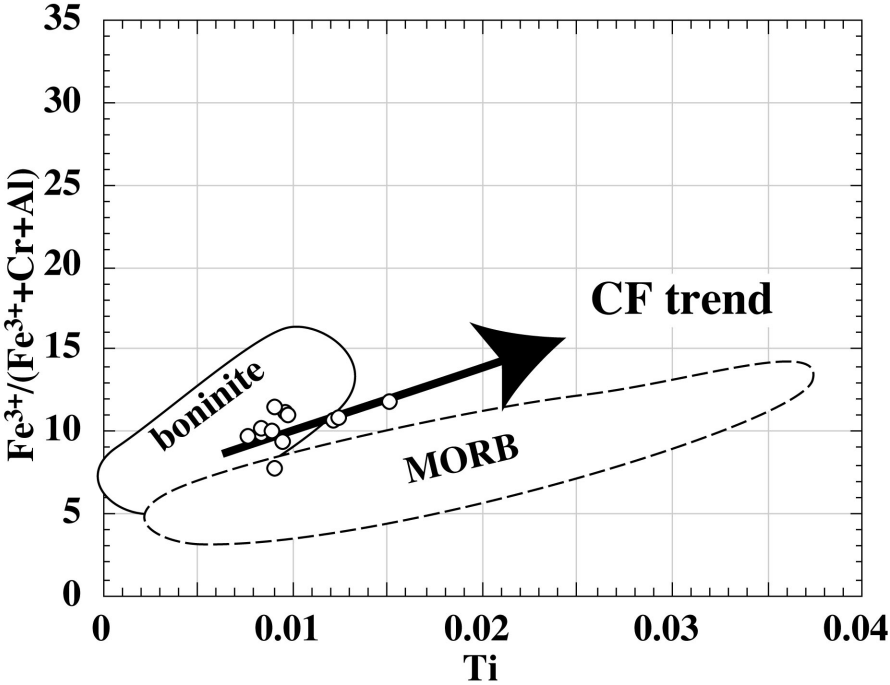


Komiya 1999 Doctor Thesis Fig. VI-26

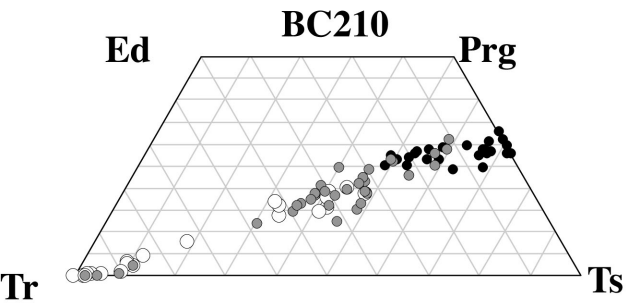


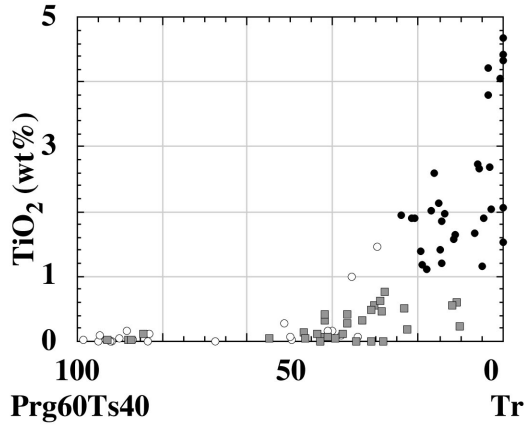


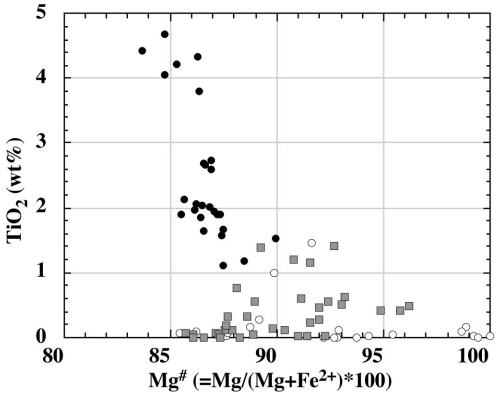


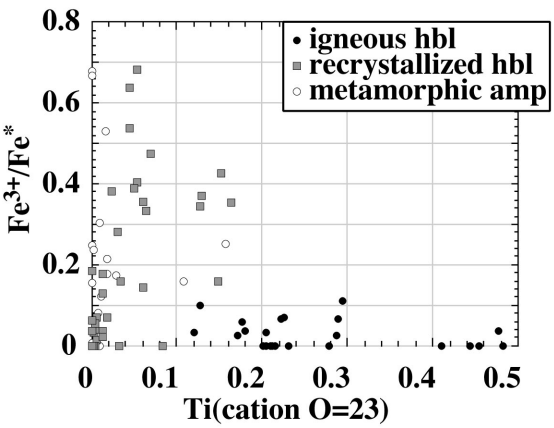


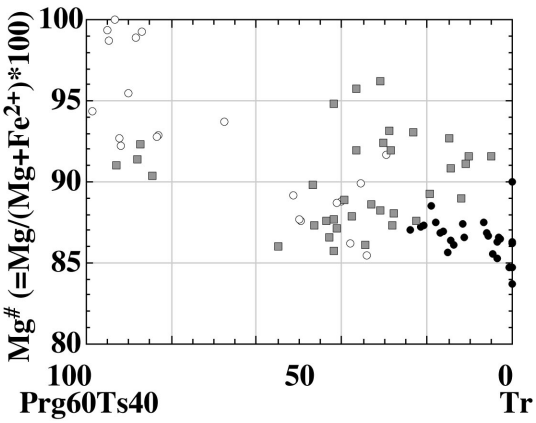


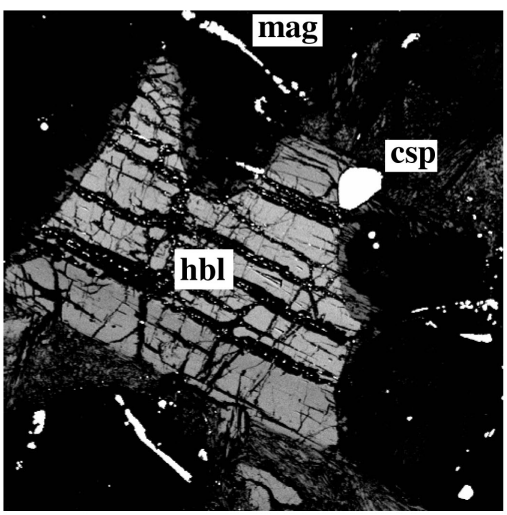


csp

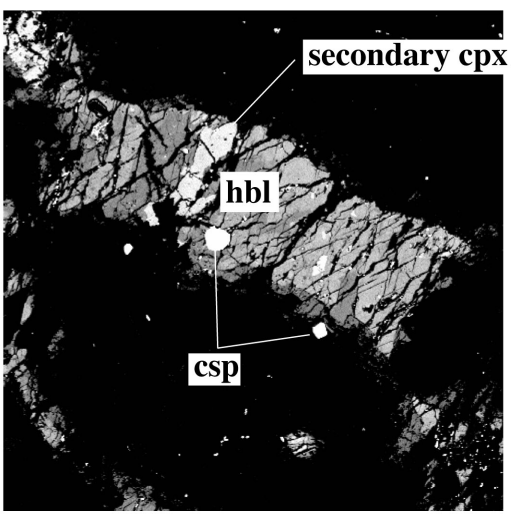


Komiya 1999, Doctor Thesis Fig. VI-27

**Barberton komatiites**

**(1) Primary magma**

**(1)MgO content---------26.5%**

**Fo=92.8**

**(2)water content---------0.5%**

**hydrous**

**vesicles**

**igneous hornblende**

**Aluminous pyroxenes**

**but less**

**ol → pig → aug → Al-aug**

**accompanied with**

**ol+cpx+opx (oikocrysts)+hbl(intercumulus)**

**(3)Degree of melting---------36%**

**trace elements (Ti) concetrations**

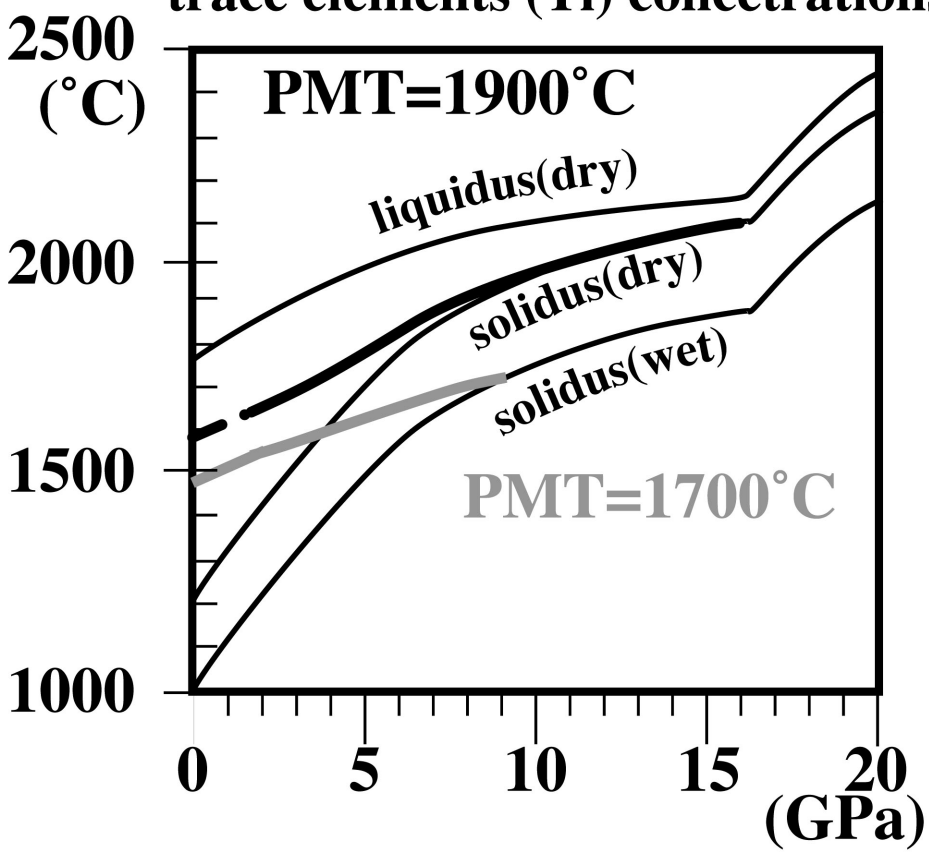


Komiya 1999 Doctor Thesis Fig. VI-28

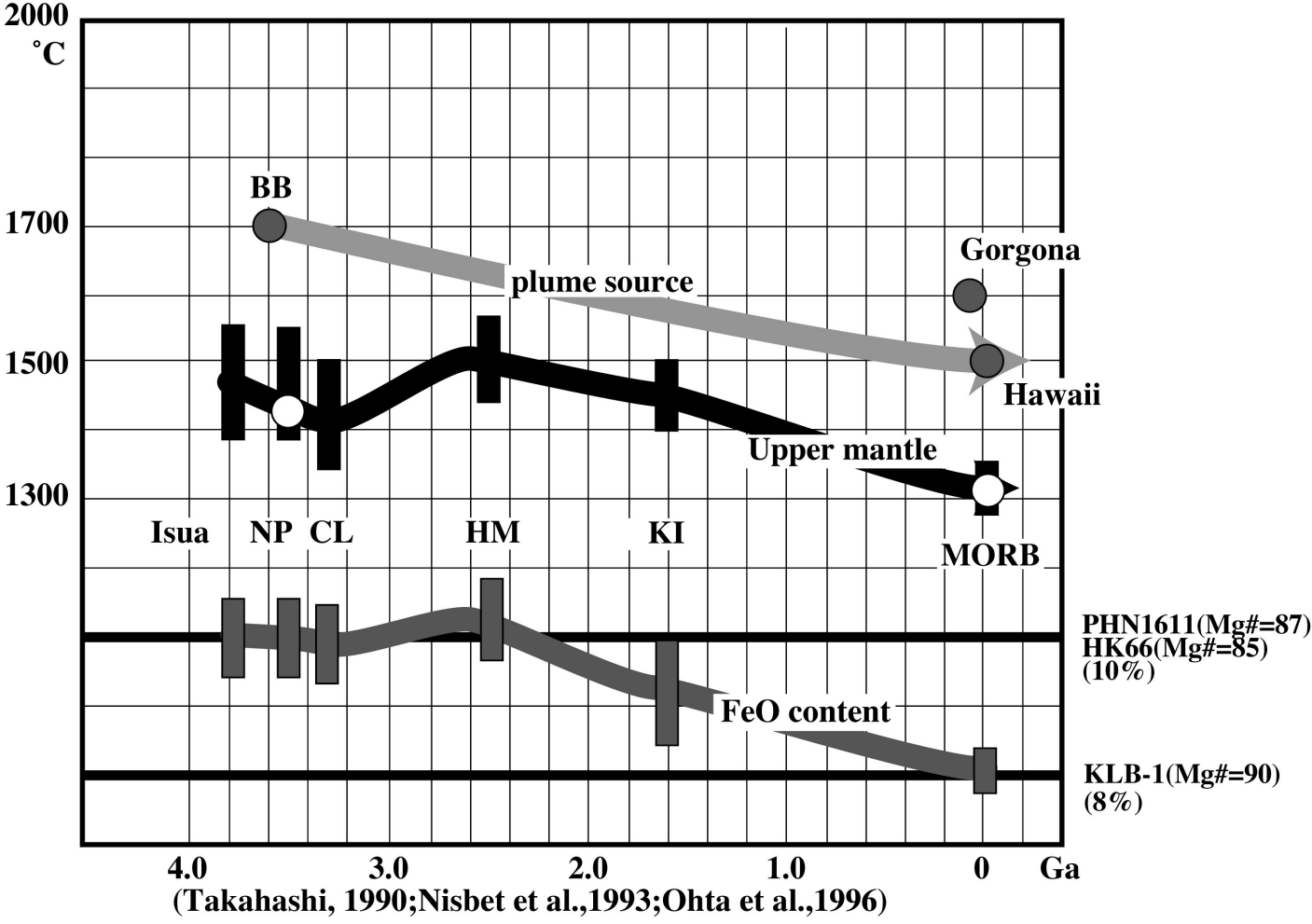


(Takahashi, 1990;Nisbet et al.,1993;Ohta et al.,1996)

Komiya 1999 Doctor Thesis Fig. 29

# Thickness of oceanic crust

## (1) Archean (i.e. life-span --- 10-20 My)

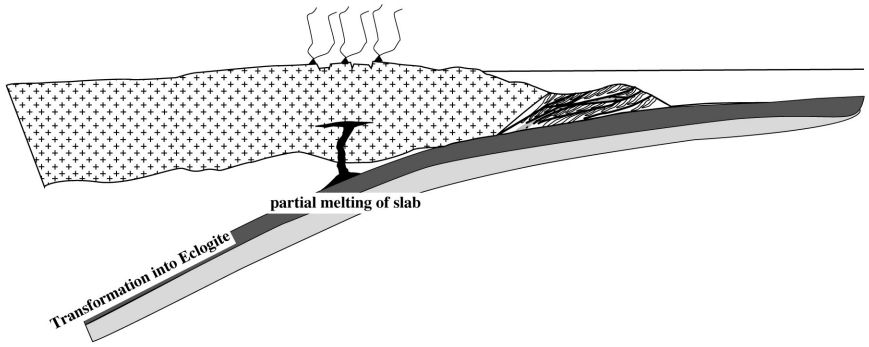


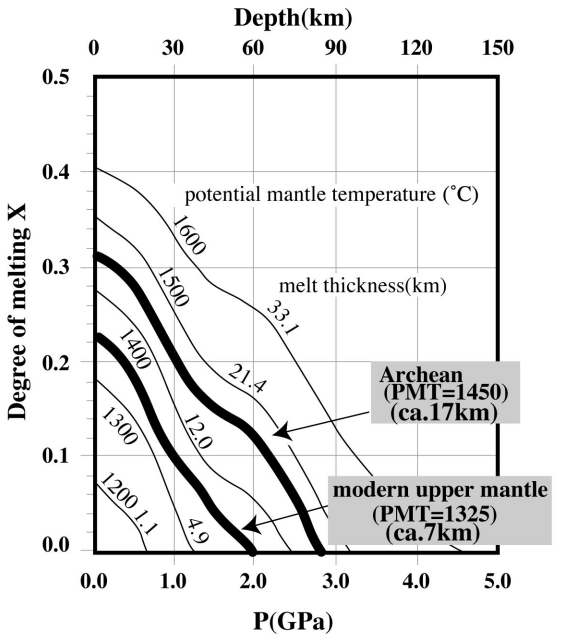


after Iwamori et al. 1995

## (2) present (i.e. life-span --- 60 My)

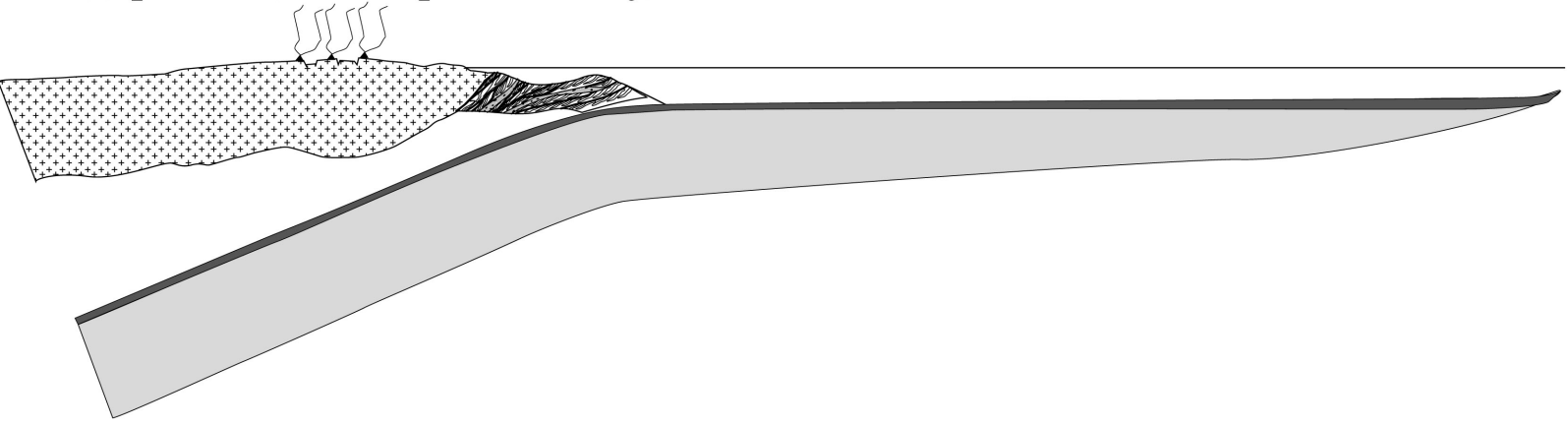

Komiya 1999, Doctor Thesis, Fig. VI-30

(a)

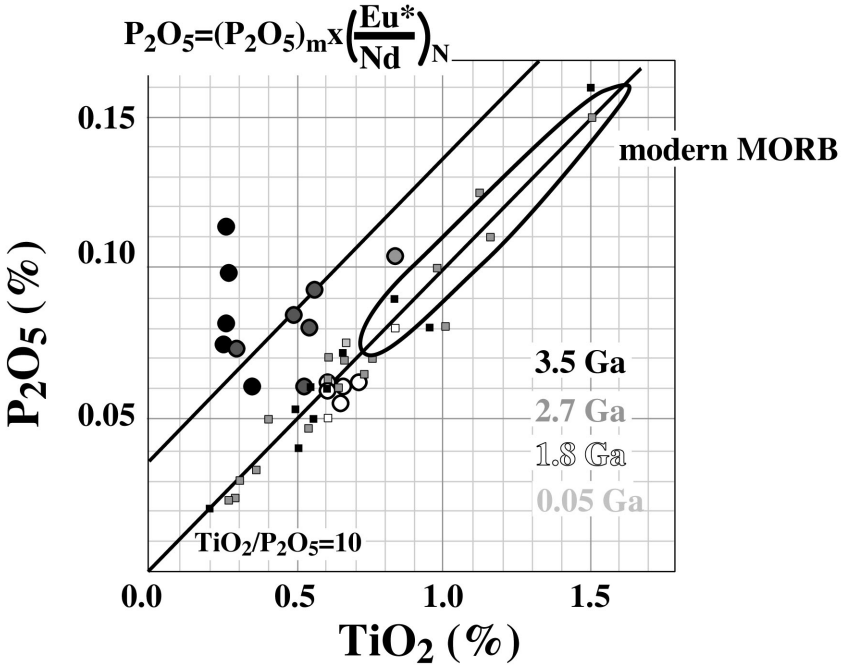


(b)

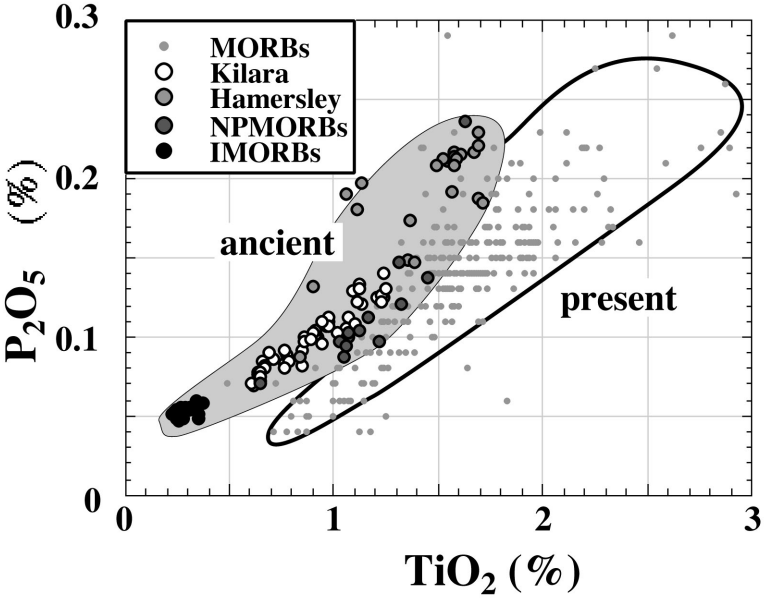


Komiya 1999, Doctor Thesis, Fig. VI-31

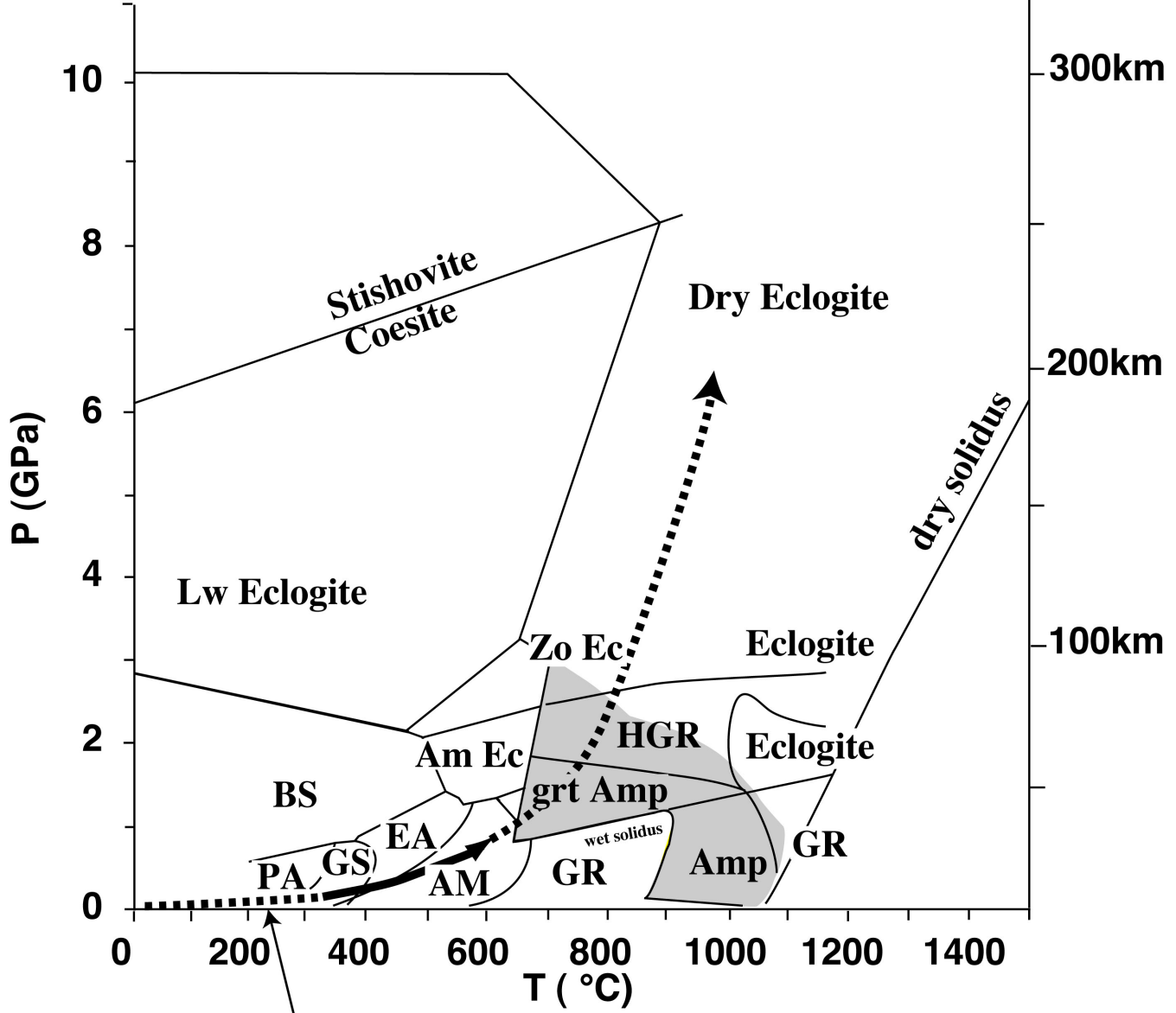


Isua supracrustal belt (3.8 Ga)
(Komiya et al. 1998)

Komiya 1999, Doctor Thesis, Fig. VI-32

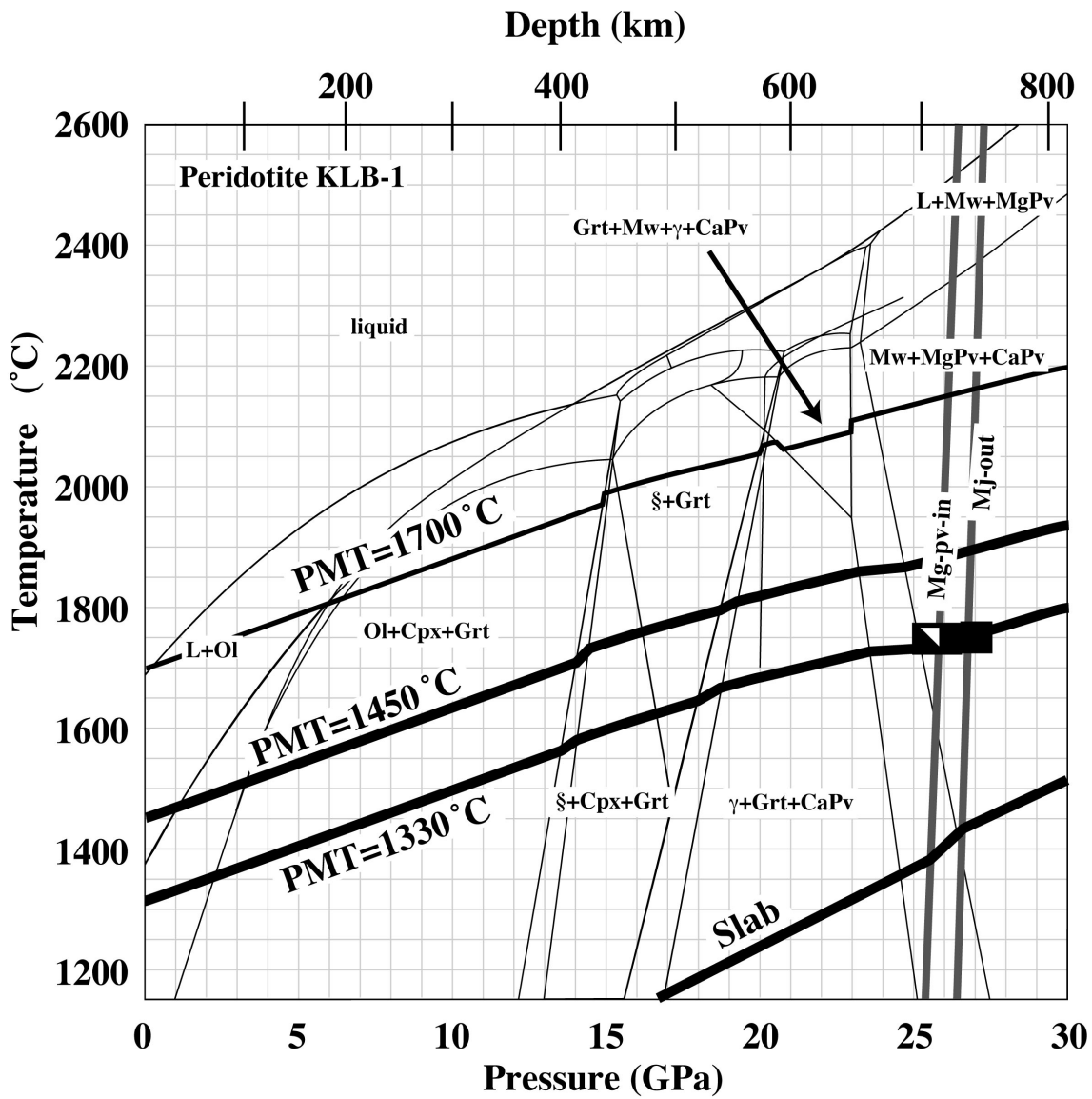


Komiya 1999 Doctor Thesis Fig. 33

# Isostasy

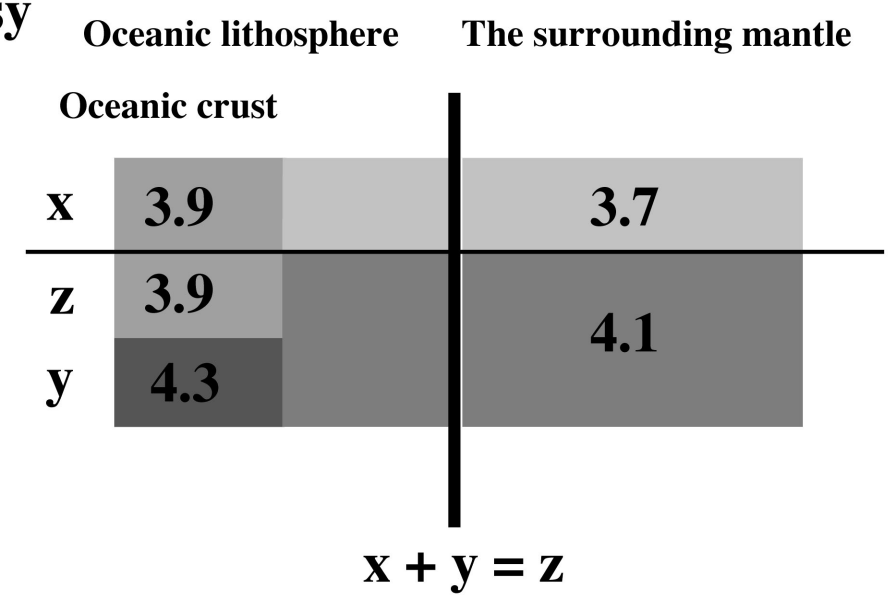


e.g. Surrounding mantle=1875 ˚C (PMT=1450 ˚C), Slab1400 ˚C-----z=40 km

e.g. Surrounding mantle=1725 ˚C (PMT=1330 ˚C), Slab1400 ˚C-----z=30 km

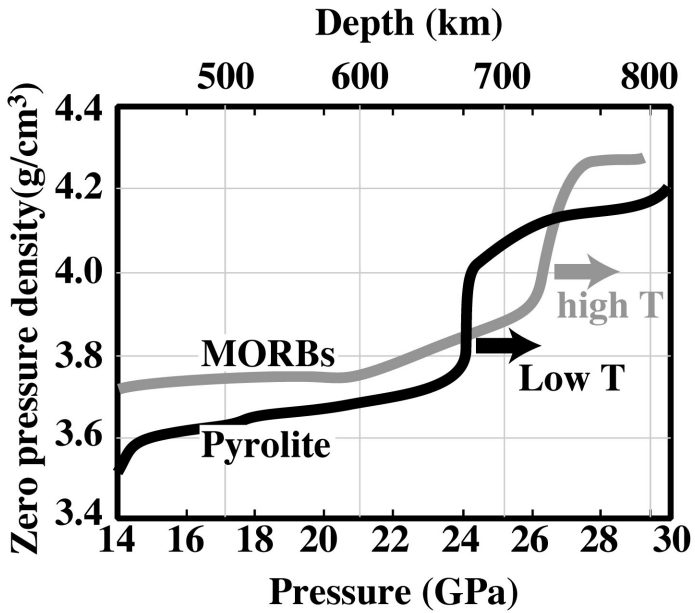


Komiya 1999, Doctor Thesis Fig. VI-34

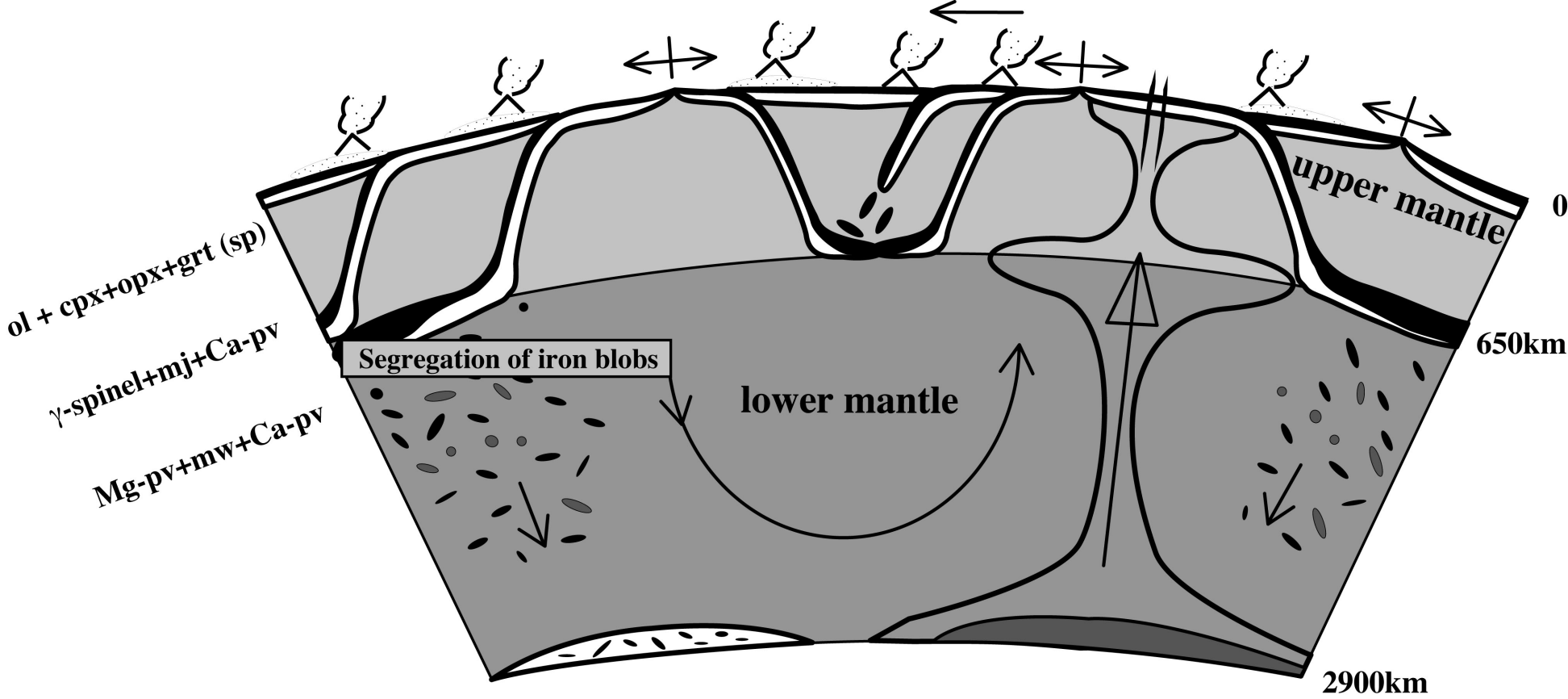


Komiya 1999, Doctor Thesis, Fig. VI-35

$TiO_2$= -0.0152xMgO+0.78558
(MgO= 51.68%, $TiO_2$=0%)

FeO* = -0.1534xMgO+14.987
(MgO= 39%, FeO*=9.0%)
(Mg/Si=1.3, FeO*=9.2%)

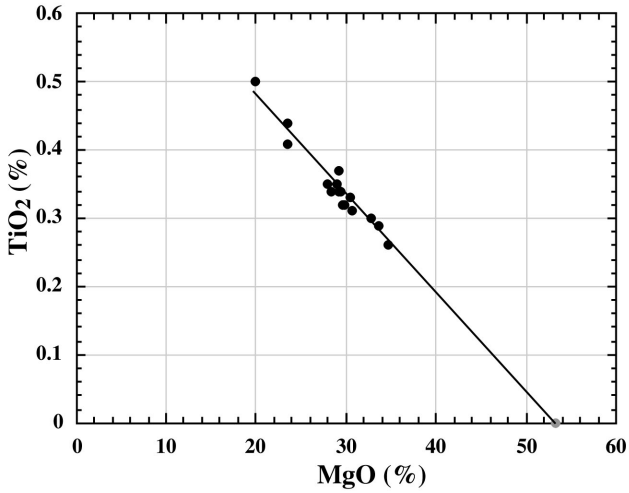


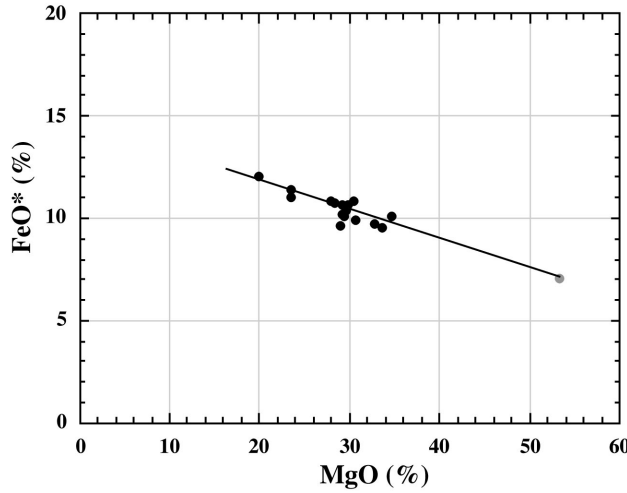


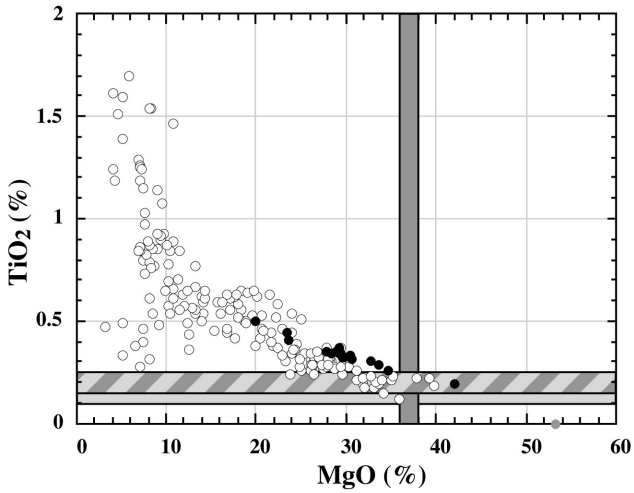


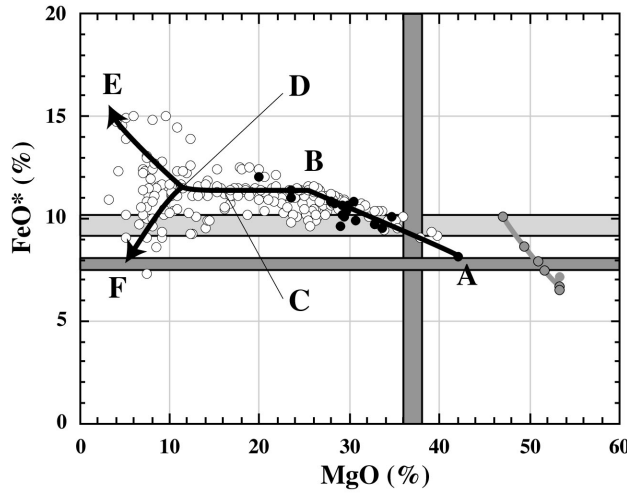


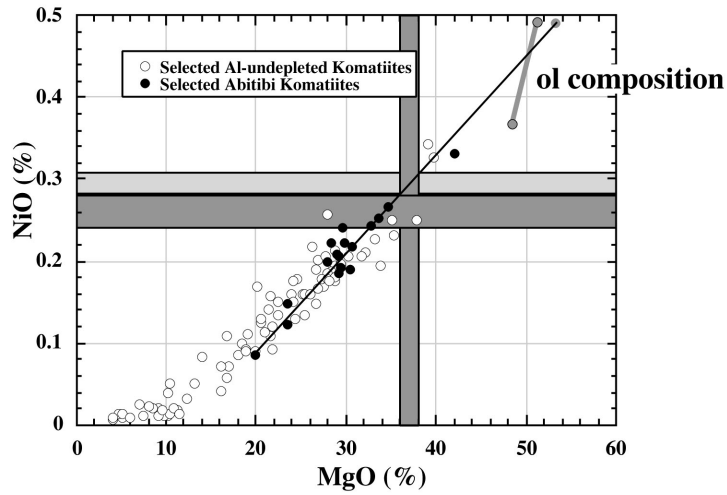


Komiya 1999 Doctor Thesis Fig. VI-36

Table 1 Chemical data for starting materials

| | 1 | 2 | 3 | 4 | 5 |
|---|---|---|---|---|---|
| | C017 | B106 | MAR02 | C017* | B106* |
| $SiO_2$ | 53.0 | 53.2 | 49.6 | 51.1 | 52.1 |
| $TiO_2$ | 0.26 | 0.38 | 1.64 | 0.55 | 1.03 |
| $Al_2O_3$ | 10.2 | 14.1 | 14.9 | 10.2 | 14.8 |
| $Cr_2O_3$ | 0.09 | 0.02 | | | |
| FeO | 11.0 | 12.0 | 11.4 | 11.0 | 12.8 |
| MnO | 0.09 | 0.08 | 0.18 | 0.20 | 0.20 |
| NiO | 0.00 | 0.04 | | | |
| MgO | 14.3 | 8.91 | 8.51 | 14.8 | 7.95 |
| CaO | 9.57 | 10.3 | 10.6 | 10.5 | 9.96 |
| $Na_2O$ | 1.08 | 0.92 | 2.90 | 0.93 | 1.0 |
| $K_2O$ | 0.44 | 0.06 | 0.12 | 0.61 | 0.08 |
| Total | 100.0 | 100.0 | 99.9 | 100.0 | 100.0 |
| | | | | | |
| Mg# | 69.9 | 56.9 | 57.0 | 70.5 | 52.4 |

1, 2, and 3 = EPMA analyses of the glass starting materials

4, and 5 = XRF analyses of bulk compositions of rock samples

Total iron as FeO

Tabel 2. Experimental Conditions and Run Products

| Run | P, GPa | T,℃ | Time, hours | samples | Run Products |
|---|---|---|---|---|---|
| LO#60 | 27 | 1500 | 6 | C017 | Mg-pv+st+Ca-pv+Al-phase |
| | | | | B106 | Mg-pv+st+Ca-pv+Al-phase |
| | | | | MAR02 | Mg-pv+mj+st+Ca-pv+Al-phase |
| LO#61 | 26 | 1500 | 8 | C017 | Mg-pv+st+Ca-pv+Al-phase |
| | | | | B106 | Mg-pv+mj+st+Ca-pv+Al-phase |
| LO#63 | 25.5 | 1500 | 12 | C017 | mj+st+Ca-pv+Al-phase |
| | | | | B106 | mj+st+Ca-pv+Al-phase |
| | | | | MAR02 | mj+st+Ca-pv+Al-phase |

Run products are Mg-pv, Mg silicate perovskite; mj, majorite; st, stishovite; Ca-pv, $CaSiO_3$ perovskite; Al-phase, aluminous phase

Table 3 Chemical data for starting materials

| | 1 | 2 | 3 | 4 |
|---|---|---|---|---|
| | En90+8%Al | En90+6%Al | En90+4%Al | En70+8%Al |
| $SiO_2$ | 53.5 | 54.6 | 55.7 | 50.6 |
| $Al_2O_3$ | 7.89 | 5.91 | 3.9 | 7.5 |
| FeO | 6.39 | 6.53 | 6.7 | 18.2 |
| MgO | 32.3 | 33.0 | 33.7 | 23.76 |
| Total | 100.0 | 100.0 | 100.0 | 100.0 |
| Mg# | 90.0 | 90.0 | 90.0 | 70.0 |

Table 4. Basic Quantities

| | At present | Archean | |
|---|---|---|---|
| Area of the earth | $5.10\times10^{8}$ | $5.10\times10^{8}$ | $km^2$ |
| Average life-time of oceanic plate | 60 | 20 | m.y. |
| Area of the sea floor | $3.0\times10^{8}$ | $3.0\times10^{8}$ | $km^2$ |
| Average thickness of oceanic crust | 7 | 20 | km |
| Production rate of oceanic crust | $3.5\times10^{7}$ | $3.0\times10^{8}$ | $km^3$/m.y. |
| Average degree of melting | 15 | 20 | % |
| Volume of upper mantle | $3.2\times10^{11}$ | $3.2\times10^{11}$ | $km^3$ |
| Volume of lower mantle | $6.0\times10^{11}$ | $6.0\times10^{11}$ | $km^3$ |
| Average density of upper mantle | $3.8\times10^{12}$ | $3.8\times10^{12}$ | $kg/km^3$ |
| Average density of upper mantle | $4.7\times10^{12}$ | $4.7\times10^{12}$ | $kg/km^3$ |
| Averege density of oceanic crust | $3.0\times10^{12}$ | $3.0\times10^{12}$ | $kg/km^3$ |
| FeO content of mantle | 8.1 | 10.2 | wt% |
| NiO content of mantle | 0.25 | 0.30 | wt% |
| $P_2O_5$ content of mantle | 0.021 | 0.029 | wt% |
| Pd content of mantle | 4.45 | 44.5 | ppb |
| Ir content of mantle | 1.84 | 18.4 | ppb |
| Os content of mantle | 3.4 | 34 | ppb |
| Re content of mantle | 0.28 | 2.8 | ppb |
| Mass of subducted oceanic crust | $1.1\times10^{20}$ | $9.0\times10^{20}$ | kg/m.y. |
| FeO content of oceanic crust | 12 | 12.5 | wt% |
| NiO content of oceanic crust | 0.032 | - | wt% |
| $P_2O_5$ content of oceanic crust | 0.1 | - | wt% |
| Pd content of oceanic crust | 0.7 | - | ppb |
| Ir content of oceanic crust | 0.017 | - | ppb |
| Os content of oceanic crust | 0.00104 | - | ppb |
| Re content of oceanic crust | 0.022 | - | ppb |
| Ferric to toral iron ratio of metamorphic rocks | 0.35 | - | |
| Volume of Mg-perovskite in subducted oceanic crust | 27.0 | - | vol% |
| $Al_2O_3$ content in Mg-perovskite | 15.1 | - | wt% |
| FeO* content in Mg-perovskite | 23.0 | - | wt% |
| MgO content in Mg-perovskite | 17.9 | - | wt% |
| Maximum solubility of $Fe^{2+}O$ in Mg-perovskite | 2.4 | - | wt% |
| $Fe^{3+}$ content in Mg-perovskite | 16.0 | - | wt% |
| Total amount of $Fe^{3+}$ in Mg-perovskite | $5.1\times10^{18}$ | $4.4\times10^{19}$ | kg/m.y. |
| Inherent amount of $Fe^{3+}$ in Mg-perovskite | $2.0\times10^{18}$ | $1.7\times10^{19}$ | kg/m.y. |
| Acquired amount of $Fe^{3+}$ in Mg-perovskite | $2.6\times10^{18}$ | $2.1\times10^{19}$ | kg/m.y. |
| Amount of $Fe^{2+}$ in Mg-perovskite | $5.2\times10^{17}$ | $4.5\times10^{18}$ | kg/m.y. |
| Amount of $Fe^{*}$ in Al-phase | $3.3\times10^{18}$ | $2.8\times10^{19}$ | kg/m.y. |
| Amount of $Fe^{*}$ in magnesio-wustite | $3.9\times10^{17}$ | $3.5\times10^{18}$ | kg/m.y. |
| Amount of $Fe^{*}$ in Ca-perovskite | $5.6\times10^{17}$ | $5.6\times10^{18}$ | kg/m.y. |
| Amount of $Fe^{*}$ in stishovite | $1.9\times10^{16}$ | $1.9\times10^{17}$ | kg/m.y. |
| Production rate of Fe | $2.6\times10^{18}$ | $2.1\times10^{19}$ | kg/m.y. |
| total Fe | $1.2\times10^{19}$ | $1.0\times10^{20}$ | kg/m.y. |
| 1200℃, 28GPa, $logfO_2$=0 | | | |
| Partition coefficient of Ni between metal and silicate | 2.4 | - | |
| Partition coefficient of P between metal and silicate | 3.8 | - | |
| Partition coefficient of PGEs between metal and silicat | 100 | - | |

Table 5

| Upper mantle | At present | Archean |
|---|---|---|
| How long could primordial mantle last? | 2.2 b.y. | 0.45 b.y. |
| How long does it takes to remove FeO content from 10.2 to 8.1 wt %? | 7.9 b.y. | 0.96 b.y. |
| How long does it takes to remove NiO content from 0.3 to 0.25 wt %? | 37 b.y. | 4.5 b.y. |
| How long does it takes to remove $P_2O_5$ content from 29 to 21 ppb? | 13 b.y. | 1.6 b.y. |
| How long does it takes to remove Pd content from 18.3 to 1.83 ppb? | $3.9x10^2$ b.y. | 47 b.y. |
| How long does it takes to remove Ir content from 18.4 to 1.84 ppb? | $1.6x10^4$ b.y. | $1.9x10^3$ b.y. |
| How long does it takes to remove Os content from 34 to 3.4 ppb? | $4.8x10^5$ b.y. | $5.8x10^4$ b.y. |
| How long does it takes to remove Re content from 2.8 to 0.28 ppb? | $1.9x10^3$ b.y. | $2.3x10^2$ b.y. |

| Whole mantle | | |
|---|---|---|
| How long could primordial mantle last? | 7.3 b.y. | 1.5 b.y. |
| How long does it takes to remove FeO content from 10.2 to 8.1 wt %? | 26 b.y. | 3.1 b.y. |
| How long does it takes to remove NiO content from 0.3 to 0.25 wt %? | $1.2x10^2$ b.y. | 15 b.y. |
| How long does it takes to remove $P_2O_5$ content from 29 to 21 ppm? | 42 b.y. | 5 b.y. |
| How long does it takes to remove Pd content from 18.3 to 1.83 ppb? | $1.3x10^3$ b.y. | $1.6x10^2$ b.y. |
| How long does it takes to remove Ir content from 18.4 to 1.84 ppb? | $5.2x10^4$ b.y. | $6.3x10^3$ b.y. |
| How long does it takes to remove Os content from 34 to 3.4 ppb? | $1.6x10^6$ b.y. | $1.9x10^5$ b.y. |
| How long does it takes to remove Re content from 2.8 to 0.28 ppb? | $6.1x10^3$ b.y. | $7.4x10^2$ b.y. |

Table 6 numerical values and the calculated result

| | Archean | at present | References |
|---|---|---|---|
| heat flux | | | |
| global | | | |
| $F_T$ | 0.208 W/m$^2$ | 0.082 W/m$^2$ | Richter1985 |
| oceanic | | | |
| $F_{O0}$ | | 0.098 W/m$^2$ | Richter1985 |
| $F_O(T)=F_{O0}(T_0/T_i)^{13}$ | 0.248 W/m$^2$ | | Davies 1992 |
| continental | | | |
| $F_{R0}$ | | 0.025 W/m$^2$ | Richter1985 |
| $F_{R(T)}=\pi^{1/2}(Ti-Tb)^{4/3}(g\alpha K^3/\kappa\nu(T))^{1/3}$ | 0.062 W/m$^2$ | | Richter1985 |
| material property | | | |
| gravity: g | 9.8 m/s$^2$ | 9.8 m/s$^2$ | Richter1985 |
| thermal expansion: α | 3.0E-05 1/℃ | 3.0E-05 1/℃ | Richter1985 |
| thermal conductivity: K | 4 W/m℃ | 4 W/m℃ | Richter1985 |
| thermal diffusivity: κ | 1.0E-06 m$^2$/s | 1.0E-06 m$^2$/s | Richter1985 |
| density: ρ | 3.3E+03 kg/m$^3$ | 3.3E+03 kg/m$^3$ | Richter1985 |
| specific heat: Cp | 1.2E+03 J/kg℃ | 1.2E+03 J/kg℃ | Richter1985 |
| mantle | | | |
| viscosity | | | |
| ν0 | | 3.0E+17 m$^2$/s | Richter1985 |
| $\nu(T)=\nu0(T_0/Ti)^{15}$ | 1.0E+17 m$^2$/s | | Richter1985 |
| latent heat: ΔL | 4.0E+05 J/kg | 4.0E+05 J/kg | Richter1985 |
| potential mantle temperature | | | |
| $T_0$ | | 1350 ℃ | Richter1985 |
| $T_i$ | 1450 ℃ | | this work |
| temperature of bottom of plate: $T_b$ | 1157 ℃ | 1157 ℃ | Richter1985 |
| scale length of crustal heat production: δ | 7.5 km | 7.5 km | this work |
| maximum thickness of oceanic lithosphere: Z | 70.7 km | 194.1 km | this work |

Table 7 Mantle composition estimated by composition of komatiite

| | Bickle et al. 1977 | Sun & Nesbitt 1977 | Sun 1982 | Beswick 1983 | this work |
|---|---|---|---|---|---|
| $SiO_2$ | 42.1-42.9 | 45-52 | 44.5 | 43.9-44.5 | 43.8 |
| $TiO_2$ | 0.08-0.11 | 0.18-0.24 | 0.2 | | 0.17 |
| $Al_2O_3$ | 2.7-2.4 | 3.59-4.94 | 4.3 | 2.1-2.6 | 4.03 |
| $Cr_2O_3$ | 0.47-0.27 | 0.44 | 0.4 | | 0.15 |
| FeO | 8.7-9.2 | 8.6-9.7 | 8.4 | 7.0-7.8 | 9.6 |
| MnO | | 0.15 | 0.1 | | 0.12 |
| NiO | 0.31-0.23 | 0.25 | 0.3 | | 0.26 |
| MgO | 42 | 38 | 38.0 | 44.8-42.5 | 37.2 |
| CaO | 0.5-2.5 | 2.96-4.07 | 3.5 | 2.2-2.9 | 4.19 |
| $Na_2O$ | | 0.32-0.43 | 0.4 | 0.1-0.13 | 0.39 |
| $K_2O$ | | 0.024-0.033 | 0.0 | 0.05-0.06 | 0.06 |
| $P_2O_5$ | | 0.018-0.024 | 0.0 | | 0.00 |
| Mg/Si | 1.49-1.46 | 1.26-1.09 | 1.27 | 1.42-1.52 | 1.27 |

Table 1 Chemical composition of K-series MORBs

| sample | KI-001 | KIA001 | KIA002 | KIA003 | KIA004 | KIA005 | KIA006 | KIA011 | KIA012 | KIA013 | KIA014 | KIA016 | KIA017 | KIA019 | KIA021 | KIA022 | KIA023 | KIA024 | KIA025 | KIA028 | KIA041 | KIA042 | KIB001 | KIB002T | KIB008 | KIB010T |
|---|---|---|---|---|---|---|---|---|---|---|---|---|---|---|---|---|---|---|---|---|---|---|---|---|---|---|
| $SiO_2$ | 59.1 | 52.9 | 53.1 | 53.3 | 53.3 | 51.7 | 51.1 | 52.0 | 50.1 | 50.2 | 49.6 | 49.9 | 49.5 | 50.4 | 50.3 | 49.2 | 49.8 | 49.5 | 49.9 | 51.9 | 52.0 | 50.6 | 53.0 | 51.9 | 53.9 | 54.6 |
| $TiO_2$ | 0.76 | 1.09 | 1.20 | 1.06 | 1.09 | 0.60 | 0.60 | 0.95 | 0.88 | 0.95 | 1.20 | 1.21 | 1.19 | 1.20 | 1.19 | 1.19 | 1.19 | 1.21 | 1.19 | 0.70 | 0.90 | 0.89 | 1.04 | 1.04 | 0.65 | 0.64 |
| $Al_2O_3$ | 12.9 | 13.9 | 13.6 | 14.1 | 14.0 | 14.4 | 14.4 | 14.3 | 14.0 | 14.2 | 14.7 | 15.0 | 14.6 | 14.8 | 14.8 | 14.9 | 14.6 | 14.8 | 14.5 | 14.4 | 14.2 | 14.2 | 13.8 | 13.5 | 14.5 | 14.1 |
| FeOt | 5.94 | 11.4 | 12.0 | 11.2 | 11.4 | 9.43 | 9.55 | 11.2 | 11.6 | 11.6 | 11.3 | 11.2 | 11.4 | 11.0 | 11.0 | 11.4 | 12.2 | 11.5 | 10.9 | 9.63 | 10.9 | 10.9 | 10.7 | 11.3 | 8.59 | 8.59 |
| MnO | 0.09 | 0.19 | 0.20 | 0.18 | 0.19 | 0.19 | 0.18 | 0.20 | 0.19 | 0.22 | 0.21 | 0.21 | 0.20 | 0.20 | 0.19 | 0.20 | 0.20 | 0.20 | 0.20 | 0.18 | 0.19 | 0.19 | 0.18 | 0.20 | 0.15 | 0.15 |
| MgO | 7.40 | 5.20 | 5.03 | 5.50 | 5.36 | 8.26 | 7.90 | 6.52 | 6.32 | 6.63 | 6.80 | 6.54 | 6.77 | 6.94 | 6.67 | 6.66 | 6.31 | 6.86 | 6.44 | 7.61 | 6.61 | 6.45 | 5.79 | 5.80 | 7.29 | 7.42 |
| CaO | 5.89 | 9.65 | 8.62 | 9.20 | 8.70 | 11.3 | 10.3 | 9.29 | 10.4 | 10.5 | 12.0 | 11.4 | 11.5 | 10.9 | 11.9 | 11.7 | 11.7 | 11.3 | 11.4 | 10.0 | 10.3 | 10.4 | 8.11 | 7.49 | 7.02 | 5.77 |
| $Na_2O$ | 0.26 | 0.84 | 1.00 | 0.84 | 0.98 | 0.47 | 0.45 | 0.92 | 0.30 | 0.71 | 0.17 | 0.19 | 0.17 | 0.20 | 0.15 | 0.19 | 0.17 | 0.15 | 0.17 | 1.01 | 0.54 | 0.30 | 0.36 | 4.11 | 0.91 | 4.89 |
| $K_2O$ | 6.46 | 2.01 | 2.01 | 1.84 | 2.22 | 1.52 | 3.31 | 2.11 | 2.81 | 2.11 | 2.22 | 2.31 | 2.44 | 2.59 | 2.24 | 2.37 | 2.18 | 2.57 | 2.46 | 2.51 | 1.99 | 2.89 | 5.14 | 1.50 | 4.85 | 1.11 |
| $P_2O_5$ | 0.09 | 0.13 | 0.14 | 0.13 | 0.13 | 0.07 | 0.07 | 0.11 | 0.10 | 0.11 | 0.12 | 0.12 | 0.12 | 0.12 | 0.12 | 0.12 | 0.12 | 0.12 | 0.12 | 0.08 | 0.10 | 0.10 | 0.10 | 0.11 | 0.08 | 0.08 |
| total | 98.8 | 97.3 | 96.9 | 97.3 | 97.4 | 98.0 | 97.9 | 97.6 | 96.7 | 97.3 | 98.3 | 98.1 | 97.9 | 98.3 | 98.5 | 98.0 | 98.5 | 98.3 | 97.3 | 98.1 | 97.8 | 96.9 | 98.3 | 96.9 | 98.0 | 97.4 |
| Mg# | 68.9 | 44.8 | 42.8 | 46.7 | 45.6 | 60.9 | 59.6 | 50.9 | 49.2 | 50.4 | 51.8 | 51.0 | 51.4 | 53.0 | 52.0 | 50.9 | 47.9 | 51.4 | 51.2 | 58.5 | 52.0 | 51.3 | 49.0 | 47.9 | 60.2 | 60.6 |
| | | | | | | | | | | | | | | | | | | | | | | | | | | |
| Ni | 60 | 41 | 36 | 44 | 41 | 68 | 61 | 50 | 50 | 50 | 55 | 57 | 58 | 53 | 57 | 63 | 62 | 62 | 53 | 76 | 51 | 54 | 45 | 40 | 70 | 73 |
| Rb | 7.4 | 22 | 26 | 22 | 26 | 17 | 19 | 32 | 28 | 29 | 1.6 | 4.5 | 3.1 | 7.9 | 2.8 | 4.1 | 2.7 | 2.7 | 2.8 | 51.0 | 15.2 | 10.9 | 17.1 | 63.4 | 26.1 | 29.9 |
| Sr | 56 | 198 | 185 | 208 | 202 | 174 | 276 | 220 | 191 | 196 | 204 | 195 | 204 | 197 | 227 | 199 | 196 | 211 | 201 | 222 | 238 | 310 | 217 | 203 | 204 | 178 |
| Y | 17 | 24 | 20 | 19 | 20 | 15 | 13 | 18 | 17 | 18 | 20 | 18 | 17 | 17 | 16 | 18 | 18 | 17 | 16 | 14 | 17 | 16 | 17 | 16 | 11 | 13 |
| Zr | 61 | 101 | 109 | 99 | 104 | 43 | 43 | 84 | 80 | 81 | 92 | 88 | 89 | 91 | 87 | 89 | 88 | 87 | 87 | 61 | 70 | 69 | 85 | 81 | 53 | 55 |
| Nb | 3.7 | 5.3 | 6.0 | 5.3 | 5.4 | 2.1 | 2.1 | 4.4 | 4.2 | 4.3 | 7.2 | 7.6 | 7.5 | 7.4 | 7.4 | 7.2 | 7.4 | 7.5 | 7.4 | 3.3 | 3.8 | 3.7 | 4.6 | 4.6 | 2.8 | 2.5 |
| Ba | 38 | 600 | 400 | 381 | 436 | 570 | 206 | 269 | 196 | 333 | 69 | 127 | 82 | 89 | 123 | 176 | 141 | 124 | 124 | 448 | 149 | 165 | 124 | 393 | 674 | 575 |
| Pb | 30 | 6.5 | 5.6 | 4.8 | 7.5 | 2.0 | 0.5 | 2.9 | 4.8 | 3.7 | 2.4 | 2.7 | 2.0 | 5.3 | 2.5 | 2.9 | 3.0 | 2.1 | 3.0 | 3.1 | 3.2 | 1.7 | 4.3 | 6.4 | 2.2 | 1.9 |
| Th | 3.2 | 5.4 | 6.0 | 5.2 | 4.8 | 1.4 | 1.0 | 3.7 | 3.7 | 3.7 | 2.1 | 2.2 | 2.0 | 2.4 | 1.6 | 1.6 | 1.8 | 1.7 | 2.2 | 2.6 | 2.3 | 3.2 | 4.6 | 3.8 | 2.6 | 2.5 |
| | | | | | | | | | | | | | | | | | | | | | | | | | | |
| La | | | | | | 5.306 | 4.691 | | | | | | | | | | | | | 9.653 | | | | | | 6.160 |
| Ce | | | | | | 10.357 | 9.928 | | | | | | | | | | | | | 19.470 | | | | | | 14.173 |
| Pr | | | | | | 1.281 | 1.324 | | | | | | | | | | | | | 2.222 | | | | | | 1.671 |
| Nd | | | | | | 5.734 | 5.329 | | | | | | | | | | | | | 8.596 | | | | | | 6.713 |
| Sm | | | | | | 1.507 | 1.395 | | | | | | | | | | | | | 1.966 | | | | | | 1.678 |
| Eu | | | | | | 0.609 | 0.524 | | | | | | | | | | | | | 0.731 | | | | | | 0.519 |
| Gd | | | | | | 1.761 | 1.569 | | | | | | | | | | | | | 2.709 | | | | | | 2.328 |
| Tb | | | | | | 0.302 | 0.309 | | | | | | | | | | | | | 0.374 | | | | | | 0.311 |
| Dy | | | | | | 2.287 | 2.010 | | | | | | | | | | | | | 2.394 | | | | | | 2.048 |
| Ho | | | | | | 0.448 | 0.438 | | | | | | | | | | | | | 0.522 | | | | | | 0.414 |
| Er | | | | | | 1.301 | 1.268 | | | | | | | | | | | | | 1.489 | | | | | | 1.193 |
| Tm | | | | | | 0.194 | 0.189 | | | | | | | | | | | | | 0.212 | | | | | | 0.168 |
| Yb | | | | | | 1.347 | 1.276 | | | | | | | | | | | | | 1.332 | | | | | | 1.043 |
| Lu | | | | | | 0.206 | 0.217 | | | | | | | | | | | | | 0.185 | | | | | | 0.161 |

Total iron as FeO

Table 1 (Continued)

| sample | KIB012T | KIB013 | KIB015 | KIB020 | KIB022 | KIB023 | KIB024T | KIB026 |
|---|---|---|---|---|---|---|---|---|
| $SiO_2$ | 51.1 | 53.6 | 52.2 | 52.0 | 51.9 | 50.3 | 51.1 | 54.4 |
| $TiO_2$ | 0.67 | 0.95 | 1.07 | 0.65 | 0.95 | 0.88 | 0.92 | 0.90 |
| $Al_2O_3$ | 14.4 | 14.2 | 13.6 | 14.8 | 13.9 | 13.6 | 13.8 | 13.4 |
| FeOt | 9.06 | 10.1 | 10.9 | 8.94 | 11.4 | 12.5 | 11.2 | 10.8 |
| MnO | 0.17 | 0.16 | 0.21 | 0.17 | 0.20 | 0.19 | 0.20 | 0.17 |
| MgO | 7.44 | 6.28 | 6.17 | 7.67 | 6.50 | 7.02 | 6.84 | 5.73 |
| CaO | 10.1 | 6.76 | 7.14 | 8.46 | 8.03 | 8.07 | 8.45 | 6.98 |
| $Na_2O$ | 2.68 | 0.57 | 0.65 | 1.06 | 1.15 | 1.08 | 3.39 | 0.51 |
| $K_2O$ | 1.31 | 5.09 | 4.86 | 3.82 | 3.63 | 3.90 | 1.20 | 5.54 |
| $P_2O_5$ | 0.09 | 0.10 | 0.10 | 0.08 | 0.10 | 0.10 | 0.11 | 0.10 |
| total | 97.0 | 97.9 | 97.0 | 97.6 | 97.7 | 97.6 | 97.1 | 98.5 |
| Mg# | 59.4 | 52.5 | 50.3 | 60.5 | 50.4 | 50.0 | 52.2 | 48.6 |
| | | | | | | | | |
| Ni | 74 | 55 | 38 | 81 | 54 | 57 | 54 | 52 |
| Rb | 46.7 | 9.3 | 10.3 | 35.2 | 39.1 | 28.6 | 48.3 | 13.0 |
| Sr | 224 | 149 | 84 | 267 | 374 | 167 | 321 | 58 |
| Y | 12 | 17 | 18 | 14 | 17 | 16 | 15 | 14 |
| Zr | 55 | 70 | 86 | 54 | 74 | 66 | 69 | 68 |
| Nb | 3.1 | 4.0 | 4.7 | 3.0 | 4.3 | 3.6 | 4.2 | 3.9 |
| Ba | 341 | 706 | 1232 | 945 | 486 | 867 | 442 | 353 |
| Pb | 3.3 | 1.8 | 2.8 | 3.1 | 2.6 | 2.0 | 2.6 | 1.1 |
| Th | 2.6 | 2.8 | 4.1 | 2.0 | 3.0 | 2.7 | 2.6 | 1.9 |
| | | | | | | | | |
| La | | | | 7.663 | | | | |
| Ce | | | | 14.786 | | | | |
| Pr | | | | 1.777 | | | | |
| Nd | | | | 6.958 | | | | |
| Sm | | | | 1.640 | | | | |
| Eu | | | | 0.616 | | | | |
| Gd | | | | 1.895 | | | | |
| Tb | | | | 0.330 | | | | |
| Dy | | | | 2.023 | | | | |
| Ho | | | | 0.413 | | | | |
| Er | | | | 1.147 | | | | |
| Tm | | | | 0.176 | | | | |
| Yb | | | | 1.082 | | | | |
| Lu | | | | 0.164 | | | | |

Total iron as FeO

Table 2 Chemical composition of PH-series MORBs

| sample | PHA011 | PHB046 | PHB062 | PHB070 | PHB073 | PHB074 | PHC046 | PHC047 | PHC048 | PHC049 | PHC050 | PHC053 | PHC054 | PHC055 | PHC057 | PHC062 | PHC063 | PHC065 | PHC070 | PHC057-2 | PHC63-2 |
|---|---|---|---|---|---|---|---|---|---|---|---|---|---|---|---|---|---|---|---|---|---|
| $SiO_2$ | 48.0 | 51.3 | 49.2 | 51.1 | 51.5 | 52.0 | 50.1 | 51.0 | 49.9 | 49.9 | 51.4 | 51.4 | 50.3 | 50.5 | 49.0 | 51.9 | 51.5 | 51.1 | 50.6 | 51.7 | 49.5 |
| $TiO_2$ | 1.20 | 0.88 | 0.81 | 0.82 | 0.98 | 0.91 | 1.09 | 1.08 | 0.74 | 0.83 | 0.83 | 0.75 | 0.76 | 0.73 | 0.63 | 0.62 | 0.62 | 0.64 | 0.86 | 0.63 | 0.63 |
| $Al_2O_3$ | 13.4 | 14.5 | 13.9 | 14.2 | 13.9 | 13.6 | 13.6 | 13.6 | 14.2 | 14.1 | 14.0 | 14.6 | 14.5 | 14.3 | 14.6 | 14.7 | 14.8 | 14.9 | 14.3 | 14.9 | 14.7 |
| FeOt | 14.0 | 10.4 | 10.6 | 10.4 | 11.0 | 10.1 | 12.4 | 12.4 | 9.44 | 10.5 | 10.2 | 9.65 | 9.83 | 9.77 | 9.48 | 8.72 | 8.61 | 8.85 | 10.7 | 8.67 | 9.52 |
| MnO | 0.23 | 0.19 | 0.21 | 0.18 | 0.20 | 0.18 | 0.21 | 0.21 | 0.18 | 0.19 | 0.18 | 0.20 | 0.21 | 0.17 | 0.18 | 0.17 | 0.17 | 0.19 | 0.18 | 0.17 | 0.18 |
| MgO | 6.96 | 7.15 | 7.80 | 7.46 | 6.48 | 6.53 | 6.52 | 6.19 | 7.83 | 7.43 | 7.61 | 7.69 | 7.62 | 7.82 | 8.79 | 7.81 | 7.83 | 7.89 | 6.78 | 7.82 | 8.94 |
| CaO | 9.41 | 9.92 | 10.9 | 10.4 | 9.3 | 10.6 | 10.4 | 10.8 | 11.9 | 11.4 | 10.2 | 11.3 | 11.4 | 11.4 | 12.0 | 11.4 | 11.1 | 9.58 | 10.6 | 11.2 | 12.1 |
| $Na_2O$ | 2.75 | 2.21 | 1.45 | 1.70 | 2.10 | 1.68 | 1.60 | 1.54 | 1.54 | 1.71 | 1.86 | 1.59 | 1.66 | 1.53 | 1.63 | 1.51 | 1.83 | 2.46 | 1.88 | 1.84 | 1.63 |
| $K_2O$ | 0.07 | 1.11 | 1.14 | 0.66 | 0.73 | 0.88 | 0.29 | 0.30 | 0.88 | 0.32 | 0.60 | 0.32 | 0.41 | 0.30 | 0.26 | 0.41 | 0.43 | 0.70 | 0.32 | 0.42 | 0.24 |
| $P_2O_5$ | 0.13 | 0.10 | 0.09 | 0.08 | 0.10 | 0.09 | 0.12 | 0.12 | 0.09 | 0.10 | 0.09 | 0.08 | 0.08 | 0.08 | 0.07 | 0.07 | 0.08 | 0.08 | 0.09 | 0.08 | 0.07 |
| total | 96.1 | 97.8 | 96.1 | 97.0 | 96.4 | 96.5 | 96.3 | 97.1 | 96.7 | 96.4 | 97.0 | 97.5 | 96.8 | 96.5 | 96.7 | 97.3 | 96.9 | 96.5 | 96.3 | 97.4 | 97.5 |
| Mg# | 47.1 | 55.0 | 56.6 | 56.1 | 51.1 | 53.4 | 48.4 | 47.2 | 59.6 | 55.8 | 57.2 | 58.7 | 58.0 | 58.8 | 62.3 | 61.5 | 61.8 | 61.4 | 53.2 | 61.6 | 62.6 |
| | | | | | | | | | | | | | | | | | | | | | |
| Ni | 61 | 68 | 80 | 59 | 51 | 49 | 50 | 48 | 76 | 64 | 67 | 63 | 62 | 64 | 98 | 69 | 64 | 67 | 60 | 98 | 64 |
| Rb | 1.1 | 51 | 47 | 16 | 19 | 25 | 7.0 | 7.0 | 34 | 8.0 | 18 | 7.2 | 11 | 6.2 | 6.2 | 10 | 13 | 21 | 11 | 6.2 | 13 |
| Sr | 108 | 158 | 151 | 172 | 182 | 154 | 118 | 133 | 149 | 163 | 143 | 127 | 134 | 123 | 153 | 143 | 169 | 236 | 170 | 153 | 169 |
| Y | 75 | 69 | 53 | 59 | 79 | 73 | 81 | 79 | 56 | 58 | 58 | 51 | 50 | 49 | 42 | 53 | 53 | 53 | 66 | 42 | 53 |
| Zr | 24 | 16 | 16 | 14 | 18 | 16 | 20 | 19 | 14 | 14 | 14 | 15 | 13 | 14 | 12 | 13 | 12 | 12 | 16 | 12 | 12 |
| Nb | 2.9 | 6.1 | 3.3 | 3.5 | 4.5 | 4.1 | 4.6 | 4.7 | 4.8 | 3.3 | 3.3 | 3.0 | 3.0 | 2.9 | 2.4 | 3.0 | 2.8 | 3.2 | 3.8 | 2.4 | 2.8 |
| Ba | 29 | 577 | 335 | 274 | 386 | 384 | 116 | 113 | 353 | 131 | 190 | 149 | 124 | 122 | 142 | 167 | 148 | 275 | 204 | 142 | 148 |
| Pb | - | 1.8 | 1.3 | 3.3 | 3.2 | 6.1 | 0.7 | 0.6 | 2.1 | 1.4 | 1.3 | 0.3 | 0.3 | - | 1.6 | 1.8 | 1.4 | 2.2 | 2.3 | 1.6 | 1.4 |
| Th | 0.4 | 2.2 | 1.4 | 2.6 | 4.0 | 3.8 | 1.7 | 2.1 | 1.2 | 1.7 | 1.9 | 2.1 | 1.3 | 1.7 | 1.4 | 2.4 | 2.2 | 2.5 | 2.4 | 1.4 | 2.2 |

Total iron as FeO

# ACKNOWLEDGEMENTS

Author would like to thank Prof. Shigenori Maruyama at Tokyo Institute of Technology. This project was financially and scientifically supported by his supervisor Prof. Shigenori Maruyama at Tokyo Institute of Technology. A special word of thanks to him for initiating the project and for his enthusiastic supports. I wish to thank them for assisting in the acquisition of analytical data and high pressure experiments: Prof. Yoshiyuki Tatsumi and Dr. Tetsu Kogiso (major elements analyses with XRF), Dr. Teruaki Ishii (trace elements analyses with XRF), Dr. Takahumi Hirata and Mr. Michinari Hattori (REE analyses with ICP-MS), Drs. Michihiko Nakamura, Hirokazu Tabata and Natsue Abe (microprobe analyses), Prof. Eiichi Takahashi and Dr. Kei Hirose (piston cylinder apparatus), Drs. Kei Hirose and Yingwei Fei (multi-anvil apparatus), Prof. Eiichi Takahashi (XRD), and Mr. Katayama (Laser Raman).

Working in the Greenland, author came into contact with several people who helped in various ways, but he wishes to thank them especially. To Mamoru Hayashi, Peter W. U. Appel, Stephen Moorbath, Susumu Nohda, Toshiaki Masuda, Chiho Morinaga, Mitsuru Ebihara, Tomonori Uchino, Haruka Minowa, and more recently, Masao Takano, and Yuichiro Ueno, my deepest gratitude. Christopher Parkinson revised our manuscript.

Working in Pilbara, special thanks to Drs. Gaku Kimura, Yasuhiro Kato, Hironao Shinjoe, Yukio Isozaki, Masaru Terabayashi, Taro Kabashima, Yoshihisa Suzuki, Tomoki Tsunematsu, Chihumi Kakuta, Hideki Masago, Toshiyuki Nanma, Kiwamu Ohguri, Yuichiro Ueno, Kouki Kitajima, and Yuki Masuda for supporting field works and arranging data.

Investigating in South Africa, although author can not fully discuss the geology and geochemistry of Barberton area for want of space in the manuscript, he wishes to thank Dr. Marthinus Cloete for the time he took to show author aspects of the mountain land that I would otherwise not have seen or been able to discuss. Author also wishes to acknowledge them for assisting in field survey and fruitful discussions: Drs. Kei Hirose, Kenji Shimizu, Toshiaki Tsunogae, Hikaru Iwamori, Hiroaki Ozawa, Kenji Nishikawa, and more recently Kazuaki Okamoto, Hiroshi Ohta, and Noriyuki Takahashi.

Investigating mantle evolution and dynamics, author wishes to thank Drs. Kei Hirose and Tetsu Kogiso for valuable discussions and revising his early draft.

Sincere thanks are also due to Drs. Shigenori Maruyama, Kiyoshi Nakazawa, Eiichi Takahashi, Katsuyuki Kawamura, Hisayoshi Yurimoto, and Gaku Kimura who constructively reviewed the manuscript.

Author also wishes thank other members of the Laboratory: Drs. Yoshiyuki Kaneko, Tsutomu Ohta, Yuji Orihashi, Ade Kadarusman, Akira Ishikawa, Atsushi Utsunomiya, Yuko Uchio, Hiroyuki Usui, Junnpei Yamamoto, Motohiko Murakami, and Toshio Yamanashi.

Lastly, author would like to thank Mr. Yoshihisa Suzuki, Mrs. Yoshiko Kogiso, Shio Watanabe, Miwako Katsuragi, and Miki Akimoto who have indirectly helped him through this project.